



NCPST



MPRC

**DEPOSITION OF HARD AND SOLID LUBRICANT
(TiN+MoS_x) COATING BY CLOSED-FIELD MAGNETRON
SPUTTERING**

A thesis submitted to School of Mechanical and Manufacturing Engineering under
the faculty of Engineering and Computing, Dublin City University
For the degree of Doctor of Philosophy (Ph.D.)

By

Md. Julfikar Haider, B.Sc. Eng.

Material Processing Research Center (MPRC)
National Centre for Plasma Science and Technology (NCPST) and
School of Mechanical and Manufacturing Engineering
Dublin City University, Ireland.

RESEARCH SUPERVISORS

Prof. M. S. J. Hashmi (B.Sc., M.Sc., Ph.D., D.Sc., C.Eng., FIMechE, FIEI, MASME)

Dr. Brian Corcoran (Dip. Eng., M.Sc., Ph.D., C.Eng., MIMechE, MIEI)

February 2005

DECLARATION

I, hereby, declare that the dissertation submitted for the fulfilment of the requirements for the degree of Doctor of Philosophy represents my own work and has not been previously submitted to this or any other institution for any degree, diploma or other qualification.

Signed: Md. Julfikar Haider

St. Id: 50161504

Md. Julfikar Haider

Date: 02-02-2005

ACKNOWLEDGEMENT

I extend my sincere respect, gratitude and appreciation to my supervisor Prof. M. S. J. Hashmi, Head, School of MME, DCU whose help, stimulating suggestions and encouragement helped me in all the time of research. He has not only guided me for research work but also in daily life like a real guardian offering help and suggestions in absence of my real guardian. It was a great honour to me to conduct this thesis under his supervision. I am also deeply indebted to him for the financial support during the course of this research.

I would also like to express my appreciation to my co-supervisor Dr. Brian Corcoran who always made himself available to offer advice and constructive comments during my research. His trademark Irish friendliness and generosity will always be remembered.

I would also like to acknowledge with much appreciation the crucial role of technicians especially Liam Domican in the School of MME, DCU. I would have never realized that how helpful and cooperative the Irish people are unless I would not work with him. Supports from other technicians Michael May and Allan Meehan have also been greatly acknowledged.

Many thanks are due to my undergraduate teacher Prof. Mahiuddin Ahmed, BUET, who gave me the opportunity to come to Ireland for pursuing higher study.

I wish to express my gratitude to Prof. David Cameron, School of Electronic Engineering, DCU for his continuous technical support during the rig upgradation. His kind support with regard to vacuum and thin film technology extended my depth of knowledge.

Many thanks go to Dr. Michael Murphy, former Ph.D. student in the sputtering laboratory. He helped me a lot to introducing the sputtering rig.

Particularly, I would like to give my special thanks to my parents for their support, inspiration and sacrifice to complete this work.

Thanks are also due to National Centre for Plasma Science and Technology (NCPST), DCU for its financial support and for providing nice environment for study.

Special thanks go to my co-worker Md. Mahfujur Rahman, post graduate student in the school of MME, DCU for his continuous support and suggestions in all course of this work.

Special thanks too go to Dr. Dermot Brabazon, School of MME, DCU to help me setting up the rotational control mechanism and also for introducing LabView programing.

I would like to express my gratitude to Dr. Paul Duggan and Dr. Denis Dowling, Enterprise Ireland for allowing me to use some of their characterization facilities. Their valuable suggestions helped me a lot to interpret the outcomes.

Many thanks are also due to Dr. Tofail Syed, University of Limerick for his generous help in characterizing of the coating by XPS analysis.

Needless to say, that I am grateful to my housemate Mahbub Hasan with whom I had been staying for over four years and friends and colleagues in the school of MME, DCU. Many more persons whose names are not mentioned participated in various ways during my research and I am thankful to them all.

DEDICATION

To
My Parents
And Late Grandfather
Mohammad Azhar Ali Mondol

NOMENCLATURE

A	= cross sectional area of the inlet pipe
A_w	= cross sectional area of the wear track
b	= width of coating/substrate
d	= geometrical dimension/interplanar spacing (nm)/depth of wear track (mm)
D_{mi}	= mass diffusion coefficient
E_b	= Binding energy
E_f	= Young's modulus of the coating
E_k	= Kinetic energy
E_s	= Young's modulus of the substrate
E_{ef}	= effective Young's modulus of the coating
E_{es}	= effective Young's modulus of the substrate
g_x, g_y, g_z	= acceleration component in x, y, and z directions respectively
g	= acceleration vector
h	= coating thickness/Plank's constant
H	= substrate thickness
k	= Boltzmann constant
K	= thermal conductivity
Kn	= Knudsen number
L	= normal load
M	= bending moment
M_i	= molecular weights of gas species
M_ϕ	= convergence monitor for degree of freedom ϕ
n	= molecular density/order of the diffraction/
N	= number of gas species/no of revolutions
P	= pressure
P_f	= force in the coating
P_s	= force in the substrate
P_i	= partial pressure of i^{th} species
P_{abs}	= absolute pressure
P_{rel}	= relative pressure
P_{ref}	= reference pressure
Q	= volume flow rate
r	= radius of the pin
\mathbf{r}	= position vector of the fluid particle
R	= Universal gas constant
Re	= Reynolds number
S_x, S_y, S_z	= source term in x, y, and z directions respectively
\mathbf{S}	= source term vector
Sc_i	= Schmidt number
t	= time
T	= temperature
T_d	= deposition temperature
T_r	= room temperature
v_x, v_y and v_z	= components of the velocity vector in the x, y and z directions respectively
\mathbf{v}	= velocity vector
V_w	= specific wear rate
V_x, V_y, V_z	= viscous loss terms in x, y, and z directions respectively
\mathbf{V}	= viscous loss vector
x, y, z	= global Cartesian co-ordinates
Y_i	= mass fraction for i^{th} species
Z	= total number of finite element nodes

GREEK LETTERS

β	= bulk modulus
λ	= mean free path/X-ray wavelength (nm)

θ	= Bragg diffraction angle
ν	= frequency
δ	= distance from the neutral axis to the interface
δ_m	= molecular diameter
ρ	= bulk density
ρ_0	= reference density
μ	= dynamic viscosity
μ_e	= effective viscosity
α_{bulk}	= bulk density, viscosity, conductivity or specific heat
α_i	= values of density, viscosity, conductivity or specific heat for species
κ_b	= curvature of a beam
κ	= number of iterations
ϕ	= degrees of freedom (pressure, velocity, temperature etc.)
$\Delta\varepsilon$	= misfit strain
σ_f	= stress in the coating
σ_s	= stress in the substrate
α_f	= thermal expansion coefficient of the coating
α_s	= thermal expansion coefficient of the substrate
ε_f	= strain in the coating
ε_s	= strain in the substrate
Σ	= beam stiffness

LIST OF ABBREVIATIONS

AFM	Atomic Force Microscopy
APDL	Ansys Parametric Design Language
Ar	Argon
BUET	Bangladesh University of Engineering and Technology
CFD	Computational Fluid Dynamics
CFUBMS	Closed-field Unbalanced Magnetron Sputtering
COF	Coefficient of Friction
CTE	Coefficient of Thermal Expansion
CVD	Chemical Vapor Deposition
DCU	Dublin City University
DLC	Diamond-like Carbon
DOF	Degrees-of-Freedom
DSMC	Direct Simulation Monte Carlo
EDX	Energy Dispersive X-ray
FD	Finite Difference
FEA	Finite Element Analysis
FEM	Finite Element Method
FV	Finite Volume
GAXRD	Glancing Angle X-Ray Diffraction
GUI	Graphical User Interface
HV	Vicker's Hardness
IBED	Ion Beam Enhanced Deposition
IBAD	Ion Beam Assisted Deposition
MEMS	Micro-Electro-Mechanical Systems
MME	Mechanical and Manufacturing Engineering
MoS ₂	Molybdenum Disulphide
MOVPE	Metalorganic Vapour Phase Epitaxy
MD	Molecular Dynamics
N ₂	Nitrogen
OP	Optical Microscope
PECVD	Plasma Enhanced Chemical Vapor Deposition
PLD	Pulsed Laser Deposition
PVD	Physical Vapor Deposition
RF	Radio Frequency
SEM	Scanning Electron Microscopy
SCCM	Standard Cubic Centimetre per Minute
TiN	Titanium Nitride
XPS	X-ray Photoelectron Spectroscopy
XRD	X-Ray Diffraction

DEPOSITION OF HARD AND SOLID LUBRICANT (TiN+MoS_x) COATING BY CLOSED-FIELD MAGNETRON SPUTTERING AND FINITE ELEMENT MODELLING

Md. Julfikar Haider, B.Sc. Eng.

ABSTRACT

Vapor deposited thin coatings have served well as mechanically hard coatings in different practical applications e.g., cutting and forming tool industries, decorative industries, biomedical industries etc. Some of these coatings (i.e., TiN) have a high coefficient of friction and can cause abrasion and rapid wear of the opposing surface. In a closed-system, a hard coating constitutes a source of abrasive particles upon spallation within the mechanism, which can lead to a worse result than the uncoated surface. Increasing number of reports in literature has suggested the use of a hard solid lubricant based coating to avoid this problem.

A sputtering rig was made operative as a closed-field magnetron sputtering system by re-establishing different systems (magnetron, water cooling, vacuum, electrical etc.). A heavy-duty impact-abrasion wear tester was modified for applying lower load on the coated sample during abrasion by a spring-loaded mechanism. A single-axis and double-axis rotary substrate table system was designed, manufactured and successfully installed in the existing sputtering system. This substrate table facilitated the rig for the deposition of multicomponent and multilayer composite coating by using different target materials and reactive gases. A rotational control mechanism has been developed to rotate the substrate table at slower speed in front of activated targets and faster speed in front of inactivated targets within a single rotation instead of rotating at constant speed. This system increased the deposition rate thus saving time and materials.

A three dimensional Computational Fluid Dynamics (CFD) study has been carried out using FLOTRAN-CFD code of the ANSYS analysis package to predict the velocity, pressure and concentration distribution of the process gas species (argon and nitrogen) across the sputtering chamber, inlets and outlet. The numerical predictions provided useful understanding of the multiple species process gas distribution and their mixing behaviour at various gas flow rates to some extent.

Modelling of thermal stress developed during cooling of a typical coating-substrate system (TiN-stainless steel) from deposition to room temperature was performed using the finite element code ANSYS. A parametric study was performed to analyse the effects of coating and substrate thickness, Young's modulus, deposition temperature etc. on the thermal stress. Radial, tangential, axial and shear stress distribution through the thickness of the coating and substrate were examined. The interface of the coating and substrate was recognised as the critical location from the failure point of view. Ti interlayer between TiN coating and substrate has significant influence on the reduction of thermal stress at the interface.

The deposition of composite hard and solid lubricant coatings (TiN+MoS_x) has been performed on a rotating substrate by closed-field magnetron sputtering using separate Ti and MoS₂ targets in a nitrogen gas environment. The composition of the coating was varied by controlling target current, gas pressure, and target to substrate distance. Compositional and structural analysis indicated the presence coating species (Ti, N, Mo and S) and incorporation of Mo and S atoms in the TiN matrix. The change of process parameters during deposition was also reflected in the measurements. For instance with the increase of MoS₂ target current, higher peak shifting and peak widening were observed in XRD study. The TiN+MoS_x coating showed slightly lower hardness than pure TiN coating but higher hardness than MoS_x coating. The hardness could not be directly correlated with the tribological properties. The adhesion test for all TiN+MoS_x coatings showed a better adhesion compared to pure TiN and MoS_x coatings. The TiN+MoS_x coating also showed lower coefficients of friction than TiN in Pin-on-disk wear tests possibly due to the solid lubrication effect from MoS₂ formed during sliding. This fact was also speculated based on the results of the optical investigation of the wear track.

KEYWORDS

Closed-field magnetron sputtering, Titanium nitride, Molybdenum disulphide, Hard-solid lubricant coating, Computational Fluid Dynamics, Gas mixing, Finite Element Method, Thermal stress.

TABLE OF CONTENT

	Page No
TITLE PAGE	
DECLARATION	I
ACKNOWLEDGEMENT	II
DEDICATION	III
NOMENCLATURE	IV
LIST OF ABBREVIATIONS	VI
ABSTRACT	VII
CHAPTER 1. INTRODUCTION	
1.1. SURFACE ENGINEERING	1
1.2. PROBLEMS ASSOCIATED WITH THIN HARD COATING	2
1.3. DESIGN AND SELECTION OF COATING SPECIES	3
1.4. COATING DEPOSITION METHOD	4
1.5. DEVELOPMENT OF MAGNETRON SPUTTERING RIG	4
1.6. GAS FLOW MODELING IN SPUTTERING CHAMBER	5
1.7. THERMAL STRESS MODELING IN THIN COATING	6
1.8. DEPOSITION AND CHARACTERIZATION OF HARD AND SOLID LUBRICANT COATING	6
1.9. PRINCIPAL OBJECTIVES	7
CHAPTER 2. SURFACE ENGINEERING: SPUTTERING AND ADVANCED COATINGS	
2.1. INTRODUCTION	8
2.2. SURFACE ENGINEERING	8
2.2.1. Definition	8
2.2.2. Objective of surface engineering	9
2.2.3. Benefits of surface engineering in manufacturing	10
2.2.4. Surface engineering techniques	10
2.2.4.1. <i>Surface treatment</i>	11
2.2.4.2. <i>Surface coating</i>	13
<u>Physical Vapour Deposition (PVD)</u>	13
<u>Chemical Vapour Deposition (CVD)</u>	15
2.3 SPUTTERING MECHANISM AND PLASMA SURFACE INTERACTIONS	16
2.3.1. Processes occurring at the target	16
2.3.1.1. <i>Sputter yield</i>	17
2.3.2. Process occurring at the substrate	19
2.4. DIFFERENT SPUTTERING TECHNOLOGIES	20

2.4.1.	Diode sputtering	21
2.4.2.	Triode sputtering	22
2.4.3.	Ion beam sputtering	22
2.4.3.1.	<i>Single ion beam sputtering</i>	22
2.4.3.2.	<i>Dual ion beam sputtering</i>	23
2.4.4.	Magnetron Sputtering	23
2.4.4.1.	<i>Development of magnetron sputtering</i>	24
2.4.4.2.	<i>Planar/conventional/balanced magnetron</i>	24
2.4.4.3.	<i>Unbalanced magnetron</i>	26
2.4.4.4.	<i>Closed-field unbalanced magnetron</i>	27
2.4.4.5.	<i>Power sources for sputtering</i>	28
2.4.4.6.	<i>Magnetron sputtering for high target utilization</i>	29
2.4.4.7.	<i>Other developments in magnetron sputtering</i>	29
2.5.	SPUTTER DEPOSITION MODES	30
2.5.1.	Reactive sputtering	30
2.5.1.1.	<i>Reactive sputtering mechanism and hysteresis effect</i>	30
2.5.2.	Co-sputtering	32
2.6.	FUNDAMENTAL PROPERTIES OF COATINGS	32
2.6.1.	Surface roughness	33
2.6.2.	Thickness	34
2.6.3.	Morphology	34
2.6.4.	Composition	37
2.6.5.	Hardness	37
2.6.6.	Adhesion	38
2.6.7.	Residual stress	39
2.6.8.	Wear	40
2.6.9.	Friction	41
2.7.	TRIBOLOGY OF THE COATED SURFACES	42
2.8.	COATINGS OF DIFFERENT GENERATIONS	43
2.9.	TiN AS A HARD COATING-SHORT REVIEW	47
2.10.	SOLID LUBRICATION	49
2.10.1.	Definition of solid lubricant	49
2.10.2.	Problems associated with liquid lubricants	50
2.10.3.	Why solid lubricants?	50
2.10.4.	Application of solid lubricant	51
2.10.5.	Characteristics of solid lubricant	51
2.10.6.	Types of solid lubricant	51
2.11.	MOS ₂ AS A SOLID LUBRICANT COATING-REVIEW	52
2.11.1.	General characteristics of MoS ₂	52
2.11.2.	Different forms of MoS ₂ in application	53
2.11.3.	Deposition methods for MoS ₂ coating	53

2.11.4.	Parametric effects on sputtered MoS ₂ coatings	55
2.11.4.1.	<i>Crystallographic orientation</i>	55
2.11.4.2.	<i>Composition</i>	57
2.11.4.3.	<i>Contamination during deposition</i>	57
2.11.4.4.	<i>Surface roughness</i>	58
2.11.4.5.	<i>Thickness</i>	58
2.11.4.6.	<i>Environment</i>	58
2.12.	NEW GENERATION COATING WITH SELF-LUBRICATION	59
2.12.1.	Composite solid lubricant coating	61
2.12.2.	Layered solid lubricant and hard coating	64
2.12.3.	Hard-solid lubricant coating	65
2.12.4.	Selected application area of low friction coatings	67
2.12.4.1.	<i>Dry cutting/machining industry</i>	67
2.12.4.2.	<i>Aerospace industry</i>	69
2.12.4.3.	<i>Automotive industry</i>	70
2.12.4.4.	<i>Biomedical industry</i>	70
2.13.	SUMMARY	71
CHAPTER 3. DEVELOPMENT OF EXPERIMENTAL RIG		
3.1.	INTRODUCTION	72
3.2.	DESCRIPTION OF MAGNETRON SPUTTERING RIG	72
3.3.	RE-ESTABLISHMENT OF DIFFERENT SYSTEMS	73
3.3.1.	Water supply system	73
3.3.2.	Electrical system	75
3.3.3.	Reactive sputtering controller	76
3.4.	FACILITATING THE RIG WITH CLOSED-FIELD UNBALANCED MAGNETRON SPUTTERING	78
3.5.	INSTALLATION OF MOS ₂ TARGET	79
3.6.	O-RING HOLDING METAL RING	80
3.7.	FIXING THE RESET SWITCH	81
3.8.	MAGNETRON SHIELD	81
3.9.	SHUTTER FOR MAGNETRON	82
3.10.	FACILITATE THE RIG FOR 3-D COATING	82
3.10.1.	Rotary shaft assembly	84
3.10.1.1.	<i>Rotary shaft</i>	84
	<u>Rotating union</u>	85
	<u>Extension pipe</u>	85
	<u>Ferrofluidic feedthrough</u>	85
	<u>Adapter flange</u>	85
	<u>Feedthrough insulator</u>	85
	<u>Shaft extension</u>	85

<u>Electrical connector</u>	85
<u>Shield</u>	86
3.10.1.2. <i>Rotary motion of the table</i>	86
3.10.1.3. <i>Water cooling of the rotary shaft</i>	86
3.10.2. Rotary table assembly	86
3.10.2.1. <i>One-axis rotary table</i>	86
3.10.2.2. <i>Two-axis rotary table</i>	87
<u>Sample table</u>	87
<u>Table support</u>	89
<u>Central substrate holing mechanism</u>	89
<u>Peripheral substrate holding mechanism</u>	89
<u>Kicker assembly</u>	89
<u>Metal plug</u>	91
3.11. TAP SELECTION FOR HIGHER TARGET CURRENT	91
3.12. ROTATIONAL CONTROL OF THE SUBSTRATE TABLE	92
3.12.1. Motor and motor controller	92
3.12.2. Why need rotational control?	92
3.12.3. Basic idea of rotational control	93
3.13. DESIGN CONCEPT OF THE ROTATIONAL CONTROL	94
3.13.1. Time control of motor speed	96
<u>Disadvantages of the time control method</u>	100
3.13.2. Position control of motor speed	100
<u>Advantage of position control of motor speed</u>	103
3.14. FACILITATE THE RIG FOR PLASMA NITRIDING	103
3.15. MODIFICATION OF THE WEAR-TESTING RIG	104
3.15.1. Brief description of the Impact-wear testing rig	104
3.15.2. Modification	106
3.15.3. Operational procedure	106
3.15.4. Advantages of the redesign	107
3.16. SUMMARY	107
CHAPTER 4. CFD MODELLING OF GAS FLOW IN SPUTTERING CHAMBER	
4.1. INTRODUCTION	108
4.2. COMPUTATIONAL FLUID DYNAMICS-A GENERAL INTRODUCTION	108
4.2.1. Basic processes in CFD	109
4.2.2. Importance of CFD	110
4.2.3. Applications of CFD	111
4.2.4. Limitations of CFD	111
4.2.5. Future of CFD	111
4.3. GAS FLOW IN LOW PRESSURE	112

4.4.	GAS FLOW MODELING APPROACHES AT LOW PRESSURE	114
4.5.	GAS FLOW MODELING IN VAPOR DEPOSITION METHODS	116
4.6.	MODELING APPROACHES IN SPUTTERING	117
4.7.	OBJECTIVE OF THIS STUDY	118
4.8.	NUMERICAL MODELING CONSIDERATIONS	119
4.8.1.	Description of physical problem	120
4.8.2.	Model formulations	121
4.8.3.	Experimental data collection	123
4.8.4.	Governing equations	124
4.8.4.1.	<i>Continuity equation</i>	124
4.8.4.2.	<i>Momentum equation</i>	125
4.8.4.3.	<i>Pressure field equation</i>	126
4.8.4.4.	<i>Partial pressure of the gas mixture</i>	126
4.8.4.5.	<i>Multiple species transport equation</i>	126
4.8.4.6.	<i>Multiple species property options</i>	127
4.8.5.	Process gas properties	128
4.8.6.	Analysis details	128
4.8.6.1.	<i>Element used in the model</i>	128
4.8.6.2.	<i>Meshing of the model</i>	129
4.8.6.3.	<i>Boundary conditions</i>	129
4.8.6.4.	<i>Numerical solution procedure</i>	130
4.9.	RESULT AND DISCUSSIONS	132
4.9.1.	Velocity vector plot of the gases	132
4.9.2.	Gas pressure distribution plot	133
4.9.3.	Gas mixture density plot	134
4.9.4.	Nitrogen concentration plot	135
4.9.5.	Nitrogen concentration at different positions in the chamber	136
4.9.6.	Nitrogen concentration at distances away from the chamber	137
4.9.7.	Nitrogen concentration at different flow rate	139
4.9.8.	Convergence problem of solution	141
4.9.9.	Model verification	141
4.9.10.	Model limitations	141
4.10.	SUMMARY	142
CHAPTER 5. THERMAL STRESS MODELLING IN THIN COATING		
5.1.	INTRODUCTION	143
5.2.	FINITE ELEMENT METHOD (FEM)	143
5.2.1.	Basic concept of Finite Element Method	144
5.2.2.	Basic steps in Finite Element Method	145
5.2.3.	Advantages of the Finite Element Method	146
5.2.4.	Disadvantages of the Finite Element Method	146

5.2.5. Finite Element Analysis (FEA) by ANSYS	147
5.3. RESIDUAL AND THERMAL STRESS IN THIN COATING	147
5.4. MODELING OF THERMAL STRESS IN COATING SUBSTRATE SYSTEM	150
5.5. THERMAL STRESS EQUATION IN THIN COATING	151
5.6. FINITE ELEMENT CONSIDERATIONS	155
5.6.1. Model formulation	155
5.6.2. Material properties	157
5.6.3. Analysis details	157
5.6.3.1. Element used in the model	157
5.6.3.2. Meshing of the model	158
5.6.3.3. Boundary conditions	159
5.6.3.4. Analysis through batch file	160
5.7. RESULTS AND DISCUSSIONS	160
5.7.1. Parametric studies	160
5.7.1.1. Effect of deposition temperature	161
5.7.1.2. Effect of coating Young's modulus	162
5.7.1.3. Effect of coating thickness	163
5.7.1.4. Effect of substrate thickness	163
5.7.1.5. Effect of coating thermal expansion coefficient	164
5.7.2. Stress distribution	165
5.7.2.1. Von Mises stress (σ_{eqv}) distribution	165
5.7.2.2. Tangential stress (σ_x) distribution	166
5.7.2.3. Shear stress (σ_{xy}) distribution	168
5.7.2.4. Axial stress (σ_y) distribution	170
5.7.3. Effect of interlayer	171
5.7.4. Model verification	173
5.7.5. Model limitations	174
5.8. SUMMARY	174

CHAPTER 6. COATING DEPOSITION AND CHARACTERIZATION TECHNIQUES

6.1. INTRODUCTION	176
6.2. RELATION AMONG SPUTTERING PARAMETERS	176
6.3. MATERIALS AND DEPOSITION PROCEDURE	177
6.3.1. Substrate materials	177
6.3.2. Coating materials	177
6.3.3. Substrate preparation	177
6.3.4. Substrate treatment	177
6.3.3.1. Chemical treatment	177
6.3.5. Deposition procedure	178
6.3.5.1. Loading of the sample	178

6.3.5.2.	<i>Pumping down of the chamber</i>	178
6.3.5.3.	<i>Plasma treatment</i>	178
6.3.5.4.	<i>Ti interlayer deposition</i>	178
6.3.5.5.	<i>TiN+MoS_x coating deposition</i>	179
	<u>MoS₂ sputtering target running in procedure</u>	179
6.4.	COATING CHARACTERIZATION TECHNIQUES	181
6.4.1.	Physical properties	182
6.4.1.1.	<i>Thickness of the coating</i>	182
	<u>Stylus profilometer</u>	183
	<u>Ball crater device</u>	184
6.4.1.2.	<i>Surface roughness</i>	187
	<u>Stylus Profilometer</u>	187
	<u>Optical profilometer</u>	187
	<u>Atomic force microscopy</u>	188
6.4.1.3.	<i>Density of the coating</i>	189
6.4.2.	Structural characterization	189
6.4.2.1.	<i>Optical Microscope (OM)</i>	189
6.4.2.2.	<i>Scanning Electron Microscope (SEM)</i>	190
6.4.2.3.	<i>X-Ray Diffraction (XRD)</i>	190
6.4.3.	Chemical composition characterization	192
6.4.3.1.	<i>Energy dispersive X-ray spectroscopy (EDS)</i>	192
6.4.3.2.	<i>X-ray Photo Electron Spectroscopy (XPS)</i>	194
6.4.4.	Mechanical and Physical characterization	194
6.4.4.1.	<i>Microhardness</i>	194
6.4.4.2.	<i>Adhesion</i>	195
	<u>Rockwell-C indentation tester</u>	196
	<u>Pull-off adhesion tester</u>	197
6.4.5.	Tribological properties	198
6.4.5.1.	<i>Pin-on-disk wear tester</i>	198
	<u>Specific wear rate measurement</u>	199
6.5.	SUMMARY	200
CHAPTER 7. RESULTS AND DISCUSSIONS		
7.1.	INTRODUCTION	201
7.2.	RESULTS	201
7.2.1.	Sputtering plasma characterization	201
7.2.1.1.	<i>Target voltage-current characteristics (Non-reactive)</i>	201
7.2.1.2.	<i>Target voltage-Ar flow rate characteristics</i>	202
7.2.2.	Optimization of stoichiometric TiN deposition	204
7.2.3.	Structural properties of TiN+MoS _x coating	206
7.2.3.1.	<i>Surface morphology of coating</i>	206

7.2.3.2. <i>Structural phases of the coating</i>	206
7.2.4. Chemical composition	207
7.2.4.1. <i>EDX analysis</i>	207
7.2.4.2. <i>XPS analysis</i>	208
7.2.5. Physical and Mechanical properties	208
7.2.5.1. <i>Thickness</i>	208
7.2.5.2. <i>Surface roughness</i>	209
7.2.5.3. <i>Hardness</i>	210
7.2.5.4. <i>Adhesion</i>	210
7.2.6. Tribological properties	211
7.2.6.1. <i>Coefficient of friction</i>	211
7.2.6.2. <i>Specific wear rate</i>	212
7.2.6.3. <i>Wear track observation by optical microscopy</i>	213
7.2.6.4. <i>Wear track observation by optical profilometry</i>	215
7.2.7. 3-D coating test	217
7.2.8. Coating deposition by rotational control	217
7.3. DISCUSSIONS	217
7.4. SUMMARY	222
CHAPTER 8. CONCLUSIONS AND SUGGESTIONS FOR FUTURE WORK	
8.1. GENERAL CONCLUSIONS	224
8.1.1. Experimental rig development	224
8.1.2. Coating deposition	224
8.1.3. Coating characterization	224
8.1.3.1. <i>Elemental and structural characterization</i>	224
8.1.3.2. <i>Physical and mechanical characterization</i>	225
8.1.3.3. <i>Tribological characterization</i>	225
8.1.4. Thermal stress modeling in thin film	225
8.1.5. CFD modeling of process gas flow	226
8.2. THESIS CONTRIBUTION	226
8.3. SUGGESTIONS FOR FUTURE WORK	227
8.3.1. Sputtering rig development	227
8.3.1.1. <i>Computer controlled operation of the rig</i>	227
8.3.1.2. <i>Closed-loop control system</i>	227
8.3.1.3. <i>Substrate rotation in front of target</i>	228
8.3.2. Process gas flow modeling	228
8.3.3. Thermal stress modeling	228
8.3.4. Coating deposition	228
REFERENCES	R1

APPENDIX A. DRAWINGS OF ROTARY TABLE

A 1. Diagram of base plate

ROTARY SHAFT

Shaft assembly

- A2. Diagram of water pipe extension*
- A3. Diagram of rotary feedthrough for sealing*
- A4. Diagram of adaptor flange*
- A5. Diagram of M5 Bolt insulator*
- A6. Diagram of feedthrough insulator*
- A7. Diagram of shaft extension*
- A8. Diagram of electrical connector*

Rotary shaft Shield

- A9. Diagram of upper shield*
- A10. Diagram of middle shield*
- A11. Diagram of lower shield*
- A12. Diagram of lower shield plate*

Rotary shaft driving motor

- A13. Diagram of support plate for motor*
- A14. Diagram of motor posts*

ROTARY TABLE (SINGLE AXIS)

- A15. Diagram of adaptor*
- A16. Diagram of central pole*
- A17. Diagram of sample plate (single axis)*
- A18. Diagram of collar*

ROTARY TABLE (DOUBLE AXIS)

Sample table

- A19. Diagram of sample plate (double axis)*
- A20. Diagram of bush*
- A21. Diagram of table support*
- A22. Diagram of plug*

Central substrate holding mechanism

- A23. Diagram of sliding carriage*
- A24. Diagram of sliding nut*
- A25. Diagram of locking thread*

Peripheral substrate holding mechanism

- A26. Diagram of sprocket*
- A27. Diagram of sprocket Shaft*

- A28. Diagram of sample post*
- A29. Diagram of sample clamp*

Kicker assembly

- A30. Diagram of kicker parts 1*
- A31. Diagram of kicker parts 2*
- A32. Diagram of M6 bolt insulator*
- A33. Diagram of kicker adaptor*

APPENDIX B. DRAWINGS OF MODIFIED WEAR TESTER	B1
<i>B1. Assembly diagram of spring loaded stylus</i>	
<i>B2. Diagram of modified M8 screw</i>	
<i>B3. Diagram of holding bar</i>	
<i>B4. Diagram of adapter plate</i>	
<i>B5. Diagram of designed cup</i>	
<i>B6. Diagram of modified M3 screw</i>	
APPENDIX C. COMPARISONS OF 2-D RESULTS FOR OUTLET POSITIONS IN GAS FLOW MODELLING	C1
APPENDIX D. INPUT FILE OF GAS MIXING IN SPUTTERING CHAMBER	D1
APPENDIX E. INPUT FILE OF THERMAL STRESS IN THIN COATING	E1

CHAPTER 1

Introduction

1.1. SURFACE ENGINEERING

Surface of any engineering materials has two aspects: functional and decorative. The former one has been paid the utmost importance as it meets all primary demands expected from any engineering material. Mankind has been searching for improved surfaces on various tools since antiquity. In the modern era that traditional surface improvement process is renamed as “surface engineering” which encompasses all of those techniques and processes utilized to induce, modify and enhance the performance (functions and/or service life) of engineering materials. Surface engineering through thin coatings has become a well-established technology and is extremely versatile means of improving component performance by optimising the surface properties. The processes of surface engineering tailor the surfaces of engineering materials to:

- control friction and wear,
- improve corrosion resistance,
- change physical property,
- alter dimension,
- vary appearance, e.g., colour and roughness and
- reduce cost.

Continuous evaluation of science and technology draws attention of the surface engineers to develop new materials and new methods to protect the surface of bulk materials. In many instances, the material, which is structurally required for a component, does not yield ideal surface properties for the application. Common surface engineering techniques can be divided into two major categories: treatments that cover the surfaces and treatments that alter the surfaces. The traditional surface engineering techniques such as salt nitriding for treatment of surface and subsurface or wet galvanizing for coating deposition are dominating the market due to their lower cost, fully optimised process, easy operational procedure etc. The advanced surface engineering techniques such as plasma nitriding for surface treatment and Physical Vapour Deposition (PVD), Chemical Vapour Deposition (CVD), Pulsed Laser Deposition (PLD) etc. for coating deposition available offer improved quality of surface engineering. Among the techniques plasma based surface engineering techniques are getting more popular than their counterparts. Surface engineering is used in a wide range of industrial sectors including the aerospace, automotive, cutting and forming tool, construction, biomedical, optical and microelectronic. The wide range of coating species (i.e., TiN, CN_x, DLC, TiAlN etc.) and

coating structures (multicomponent, multilayer, graded, nanocomposite, duplex coating etc.) are deposited by modern deposition techniques to meet several industrial demands. Chapter 2 lists different surface engineering techniques and discusses coating architectures briefly.

1.2. PROBLEMS ASSOCIATED WITH THIN HARD COATING

The main property requirements expected from thin coatings are generally tribological, electrical, optical, magnetic, heat resistant, corrosion resistant, biocompatible and decorative. The hard coatings deposited by advanced methods such as PVD, CVD etc. can meet those requirements with excellence. Although presently different kinds of thin hard coating are routinely used in industries for better service than the uncoated samples, still thin coating technology couldn't reach the market maturity. One important reason is that, coatings are routinely deposited with very good adhesion, but there is always the possibility of depositing a coating with poor adhesion, which leads coating failure. The coating failure is not a disaster on general component such as cutting tool. However, if a coating fails on a critical component in an engine or in general machinery, this can lead to a catastrophic failure of the whole assembly. Higher residual stress development in the coating and hardness gap between the coating and substrate are often addressed for poor adhesion. The advanced deposition techniques require higher capital investment and some methods have poor surface coverage over complex 3-D objects for practical application. The lower deposition rate compared to traditional coating deposition techniques is also another drawback. Again many of the coatings are not low friction and do not provide any protection for the opposing surface. Indeed, the coatings are very hard, and if the coated surface or the coating is rough, then they can cause abrasion and rapid wear of the opposing surface. If the coating is removed, this constitutes a source of abrasive particles acting like grits within the mechanism, which can lead the failure of the coating before the expected time. Friction can also cause higher power consumptions. Liquid lubricant can solve the friction problem but it involves huge cost and threat to environment. These performance limitations demonstrate the need for another high profile multifunctional coatings, which can provide wear resistance, load bearing and lubricating capability. Increasing number of reports in the literature has suggested the use hard-solid lubricant coating to avoid these problems in tribological applications. These coating requirements place demands upon the production equipment to provide higher throughput with more rigorous performance specifications. Thus, the deposition processes must provide higher

deposition rate for a wider range of material choices, while also providing improved large area thickness uniformity and lower defect levels. Chapter 2 discusses the different hard-low friction coatings and their possible impacts on different areas of practical importance.

1.3. DESIGN AND SELECTION OF COATING SPECIES

The growing interest for meeting the challenges in tribological applications has led to the commencement of this project. The complex requirements for surface engineering cannot be realized in a single homogeneous coating or a single surface treatment. New generation coatings such as multilayer, multiphase, gradient, duplex or composite coatings, therefore, seem to be the best compromise. Most of these studies have been concentrated on the improvement of the mechanical properties with little attention on the improvement of the tribological properties. To meet the ever-increasing demands for multifunctional properties under even more severe conditions a surface engineering approach with hard-solid lubricant coating has been proposed (Figure 1.1.).

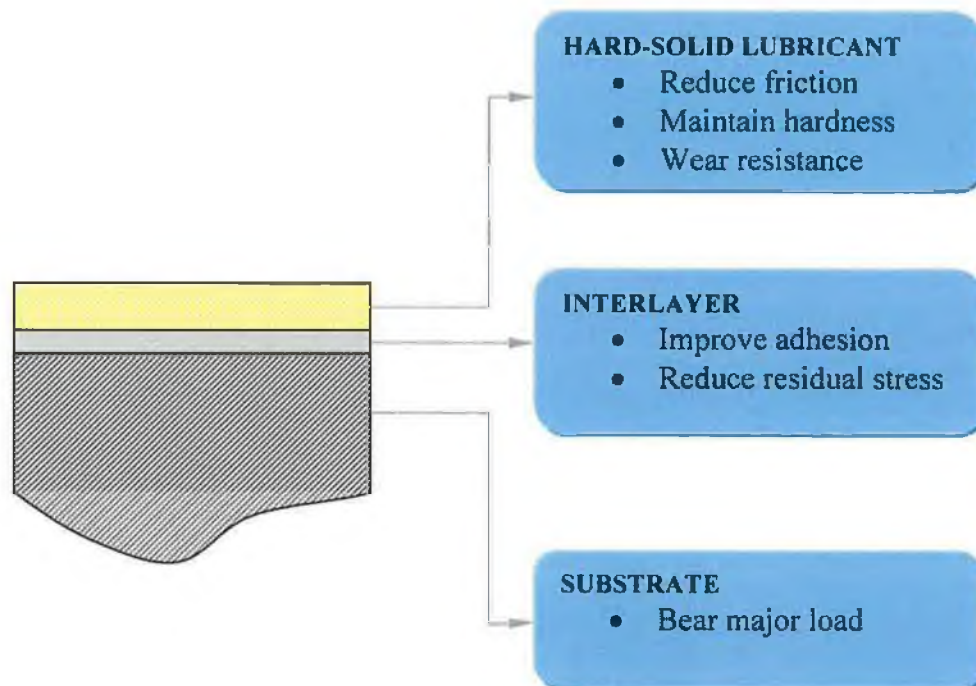


Figure 1.1. Design methodology for surface engineering through hard-solid lubricant coating.

The hard-solid lubricant coating will reduce the friction throughout the coating thickness while maintaining the hardness of the coating. The interlayer material will improve the adhesion between the coating and substrate. The proper selection of coating species and deposition method is critical factor for surface engineering approach. Titanium Nitride

(TiN) and Molybdenum Disulphide (MoS_2) were selected as hard and solid lubricant coating respectively, because they have already been accepted in various industrial applications as a hard and solid lubricant coatings.

1.4. COATING DEPOSITION METHOD

Generally, thin film deposition techniques can be categorized as Physical Vapour Deposition (PVD), Chemical Vapour Deposition (CVD) and Physical Chemical Vapour Deposition. PVD method is usually preferable than the other processes due its lower processing temperature and deposition capability of good quality coating. The method used for depositing thin hard-solid lubricating coating is unbalanced magnetron sputtering in a closed-field arrangement. This method is the latest development in the field of sputtering technology and has already proven its potential compared to conventional sputtering in depositing different new generation coatings with excellence not only in research and development but also in industrial applications. The main advantages include: (i) the closed-field configuration makes the coating to be well bonded and densified to the substrate due to higher ion bombardment (ii) the deposition rate of coatings is sufficient to meet economic and functional requirements in industrial production and is fully comparable to that achieved in other deposition techniques (iii) the process makes it possible to form coatings with new physical and functional properties and even coatings not obtainable by other techniques and (iv) the sputtering sources can be scaled up into large industrial coaters. Chapter 2 addresses the details of the magnetron sputtering mechanisms and different forms of magnetron sputtering.

1.5. DEVELOPMENT OF MAGNETRON SPUTTERING RIG

The magnetron sputter system used in this investigation had not been used for couple of years before starting this project. The system was configured for penning type magnetron system. The first phase of this project was to replace the existing system with closed-field magnetron sputtering system and set up the rig ready for deposition. Different systems (vacuum system, water-cooling system, electrical system etc.) have been reestablished as a part of the first phase. Significant amount of time has been spent for setting up the system to closed-field magnetron sputtering and especially for leak detection in the vacuum line hose, since it was an unusual place for leak. The second phase was to design and installation of a rotary substrate table for depositing multilayer, multicomponent, and

composite coatings on 3-D objects. Several attempts for installing the rotary substrate table have been failed previously. Since the design of rotary substrate table for facilitating the 3-D coating was a major part of the project, much time also had been spent communicating with the manufacturing company. The rotary substrate table was designed as part of the project by Teer Coating Company, England. After delivery of the rotary substrate table, several parts were assembled and successfully installed the whole system in the rig with proper vacuum sealing. The main concern for the rotary substrate table was the matching of rotary sealing with the existing hole on the base plate. Any deviation from the measurement during design stage could result bad vacuum sealing. The main versatility of the rotary table is that the substrates rotate around a central axis of the chamber passing in front of the target and also around its own axis, which allows the deposition of several new generation coatings over 2-D or 3-D objects. As only two magnetrons were activated during deposition due to shortage of power supply the deposition rate was very slow. Later a control system has been developed with microswitch and cam to rotate the substrate table at slower speed in front of the activated targets (deposition source) and at higher speed in front of the inactivated targets. This system has helped to increase the deposition rate. A wear-impact tester has also been modified by spring-loaded mechanism for measuring the coating wear with comparatively low load. Chapter 3 gives an overview of the development of the closed-field magnetron sputtering rig.

1.6. GAS FLOW MODELLING IN SPUTTERING CHAMBER

In thin coating deposition techniques e.g., CVD, PVD etc., process gases are fed into the deposition chamber to deposit thin coatings either by reacting among themselves or with other sources materials. Usually in the reactive sputtering process, argon gas is used as the process gas for sputtering and N_2 is added into the chamber to react with the sputtered material. The deposition of thin coating and their uniformity depends on the flow of the process gases inside the deposition chamber. In magnetron sputtering, many interdependent parameters control the deposition of coating, process gas flow and mixing being one of them. Experimentally, it is very difficult to track the flow of the gases inside the deposition chamber and the low pressure of the gases (not perfectly behave as continuum) makes the tracking of the flow even more difficult. It is worthwhile to simulate process gas flow, which might give some important information from process optimisation and deposition point of view. Computational Fluid Dynamics (CFD) has increasingly become the integral part for investing fluid flow phenomena along with the traditional

experimental methods. It has reached the maturity of simulating complex flow problem including multiphase and multiple species fluid flow. A three-dimensional Computational Fluid Dynamics (CFD) study has been carried out using FLOTRAN-CFD code of the ANSYS simulator to predict the velocity, pressure and concentration distribution of the process gas species (argon and nitrogen) in the sputtering deposition chamber. Chapter 4 presents the details of the multiple species gas flow modelling in magnetron sputtering chamber.

1.7. THERMAL STRESS MODELLING IN THIN COATING

Residual stress is the most common phenomenon appearing in coating irrespective of the deposition methods. The measurement of the residual stress is a huge issue for surface engineers as it is the determining factor for coating quality. In some deposition methods residual stress is completely intrinsic if the deposition temperature is low. But the extrinsic stress (thermal stress) sometimes become quite significant if the deposition temperature is high or the mismatch of thermal and physical properties of the coating and substrate is significant. Analytical equations have been developed to quantify thermal stress. But the analytical equations provide the average stress not the distribution throughout the coating. From the distribution of thermal stress the probability of the failure area could be identified. Significant amount of studies in the literature have proven the ability of finite element analysis in simulating the distribution of thermal stress in coating. Very few studies have dealt with the simulation of thermal stress in thin hard coating. No studies of simulating thermal stress distribution in sputtered TiN coating have been found so far. From that point of view a finite element model have been developed for analysing thermal stress in thin sputtered TiN coating by finite element package ANSYS. Chapter 5 points out the thermal stress modelling and analysing procedure in details.

1.8. DEPOSITION AND CHARACTERIZATION OF HARD-SOLID LUBRICANT COATINGS

From the literature it is evident that coating consisted of hard and solid lubricant phase definitely improves the tribological performance of sliding components as a low friction transfer layer is established on the matting surface. Co-deposition of TiN and MoS₂ on the rotating substrate has been performed by sputtering separate Ti and MoS₂ facing targets in N₂ gas environment. Composition of the different phases is controlled by varying the

respective target currents. Samples have been analysed by EDX to quantify the weight percentage of different elements and by XRD to determine the crystalline phases in the coating. Other physical, mechanical and tribological properties of the hard-solid lubricant coating have also been evaluated. Chapter 6 summarizes the deposition procedure of hard-solid lubricant coating and the characterization techniques for evaluating coating properties. Chapter 7 discusses the results obtained from hard-solid lubricant coating and Chapter 8 points out the conclusions from coating deposition and modelling.

1.9. PRINCIPAL OBJECTIVES

- [1]. Modify and commission the rig to facilitate closed-field magnetron sputtering.
- [2]. Upgrade the rig for 3-D coating by installing a single-axis and two-axis rotary substrate table.
- [3]. Incorporate a rotational control system to rotate the substrate table at different speeds within a single cycle.
- [4]. CFD modelling of the process gas flow in the magnetron-sputtering chamber.
- [5]. Modeling of residual thermal stress in thin coating by finite element method.
- [6]. Deposition of hard-solid lubricant coating ($\text{TiN}+\text{MoS}_x$) by co-sputtering of *separate* Ti and MoS_2 targets in N_2 gas environment.
- [7]. Characterizing physical, mechanical, chemical and tribological properties of the coatings and correlate these properties with the coating compositions.

CHAPTER 2

Surface Engineering: Sputtering and Advanced Coatings

2.1. INTRODUCTION

Surface engineering has become an integral part in the material processing industry. Several new generations coating species and coating architecture have been developed to meet the future demands in more severe conditions. The deposition of these coating have become possible with the development of advance processes such as magnetron sputtering, advanced power source such as Pulsed power supply, advanced process control system such as dynamic reactive sputtering controller, and insitu property characterization such as residual stress. In this chapter, magnetron sputtering, the most commonly used technique is briefly reviewed. Short description of the several new generation coatings and particularly the scope of hard-solid lubricant coating based on TiN and MoS₂ have been extensively reviewed.

2.2. SURFACE ENGINEERING

2.2.1. Definition

Probably the first comprehensive description of surface engineering was provided by Stafford et al. [1-3] in 1984. Surface engineering encompasses all of those techniques and processes, which are utilised to induce, modify and enhance the performance-such as wear, fatigue and corrosion resistance, and biocompatibility of surfaces and covers three major categories of interrelated activities: optimisation of surface properties, coating technology and characterization of coatings. Later another definition of surface engineering was given by Bell [4,5]: surface engineering involves the application of traditional and innovative surface technologies to engineering components and materials in order to produce a composite material with properties unattainable in either the base or surface material. Frequently the various surface technologies are applied to existing design of engineering components, but ideally, surface engineering involves the design of the component with a knowledge of the surface treatment to be employed. The main area of activity of surface engineering can be realised as design of surface layers, formation of surface layers, investigation of surface layers, and finally utilisation of surface layers [6]. The successful implementation of surface engineering requires an integrated approach at the design stage, involving collaboration between design and surface engineers, as is increasingly being realised by managers in diverse industrial sectors. The interaction between design,

properties, surface engineering technologies, and industrial sectors has been summarised using the 'road map' concept (Figure 2.1.) [7].

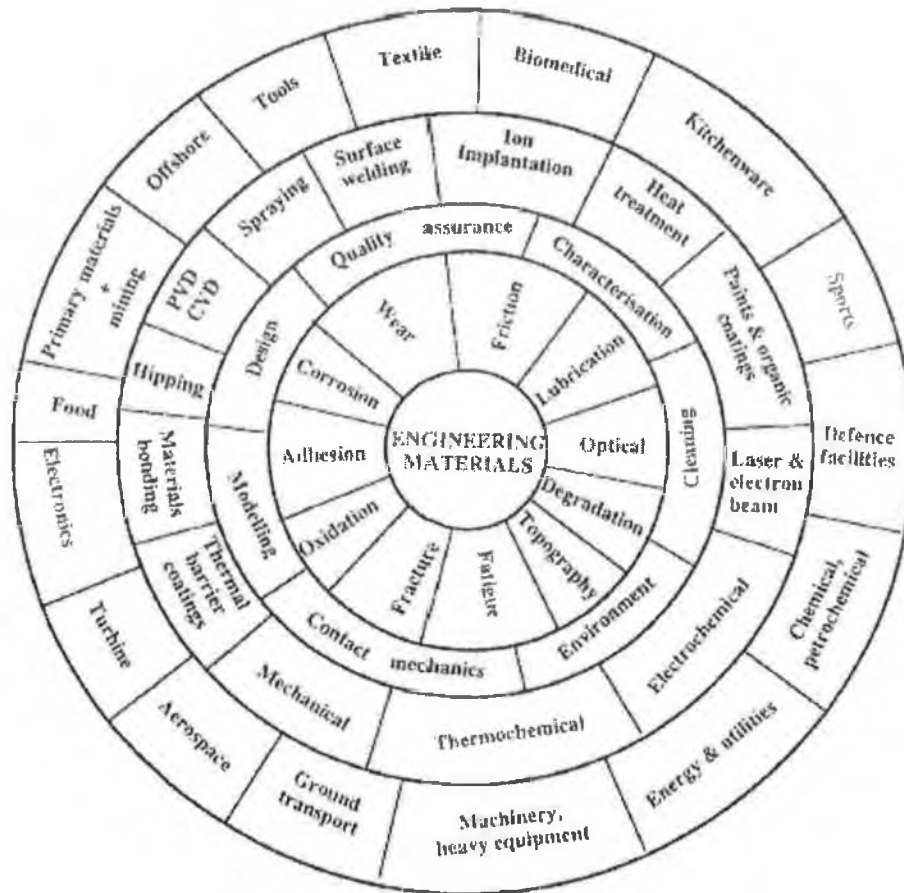


Figure 2.1. The surface engineering road map: a multisectoral, interdisciplinary technology [7].

2.2.2. Objective of surface engineering

It is often impractical, inefficient or uneconomical to manufacture components from a bulk material simply for its surface properties, it is far better to use a cheaper, more easily formed underlying material and coat it with a suitable high performance coating. The resulting product conserves scarce material resources, performs better than the original and may well be cheaper to produce. Improving the functionality of an existing product is only one aim of surface engineering. The choice of a surface material with the appropriate properties is crucial to its functionality.

2.2.3. Benefits of surface engineering in manufacturing

The surface engineering techniques have a profound influence on several engineering properties including tribological, mechanical, chemical, thermal, electronic and superconducting, optical, magnetic, aesthetic etc. This could enhance the manufacturing efficiency or the efficiency of the end products. The end result would be cost savings, enhanced quality in the product and the potential created for introducing high added value and therefore profitability. At the same time surface engineering creates the opportunities for the development of new products to meet the ever-increasing demands in diverse industrial sectors. At the very least surface engineering may allow the service life extension of an existing product. Surface engineering is important for all of these reasons and it is evident that in the present era of rapid change in the competitive manufacture, awareness and adoption of surface engineering techniques are crucial for enhanced profitability and may be even survival of a company. The economic benefits of surface engineering are enormous. According to a recent report [8,9] by 2005 the value of the UK coating market will be approximately £21.3 billion, and those coatings will critically affect products with a value greater than £143 billion.

2.2.4. Surface engineering techniques

The effectiveness (load-carrying capacity, wear resistance and coefficient of friction) of surface engineering depends on the particular technique. Numerous schemes have been tried for classifying the surface engineering techniques [10-18]. In reference [16], an approach for classifying the surface engineering methods by the depth and place of interaction and deposition of material is shown in the Figure 2.2. Another approach for surface engineering is atomic deposition (thin coating), bulk deposition (thick coating) and direct surface modification (surface treatment) [10]. Among the various surface engineering techniques plasma based techniques are in forefront in terms of research and practical applications [19]. In Figure 2.3. based on the literature, a general classification of surface engineering is attempted.

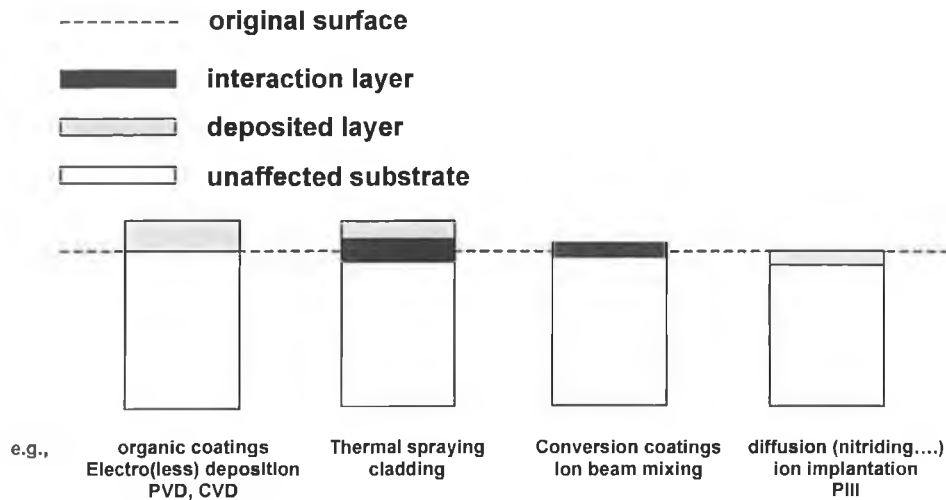


Figure 2.2. Classification of surface engineering processes [16].

2.2.4.1. Surface treatment

Surface treatments are usually performed for modifying the mechanical properties of the surface such as hardness, wear resistance, roughness, or sometime the bulk material. Usually this can be divided into two groups: microstructural treatment and chemical treatment. In the first method, the surface microstructure is modified without altering the substrate's chemical constitution and without or little change of the core. This treatment is mostly used for ferrous materials and performed either by heating or mechanical working. In the chemical treatment, both surface microstructure and composition is changed either by the incorporation of an element such as carbon, nitrogen, boron or occasionally other elements through diffusion (thermochemical diffusion treatment) or implantation (ion implantation) into the material by the application of the appropriate amount of heat, ion energy, time, and the surface catalytic reaction.

Plasma nitriding

Plasma nitriding is the most common method of surface treatment and now widely used for surface hardening of ferrous (steel) and non-ferrous materials (Ti and Al) in the manufacturing industry for surface modifications improving hardness, fatigue and wear resistance. It is more economical because it introduces faster nitrogen diffusion, which in turn allows for lower nitriding temperatures or shorter treatment times, environmentally friendly process, uniform treatment, and almost no distortion of the treated parts compared to conventional nitriding processes such as liquid or gas nitriding.

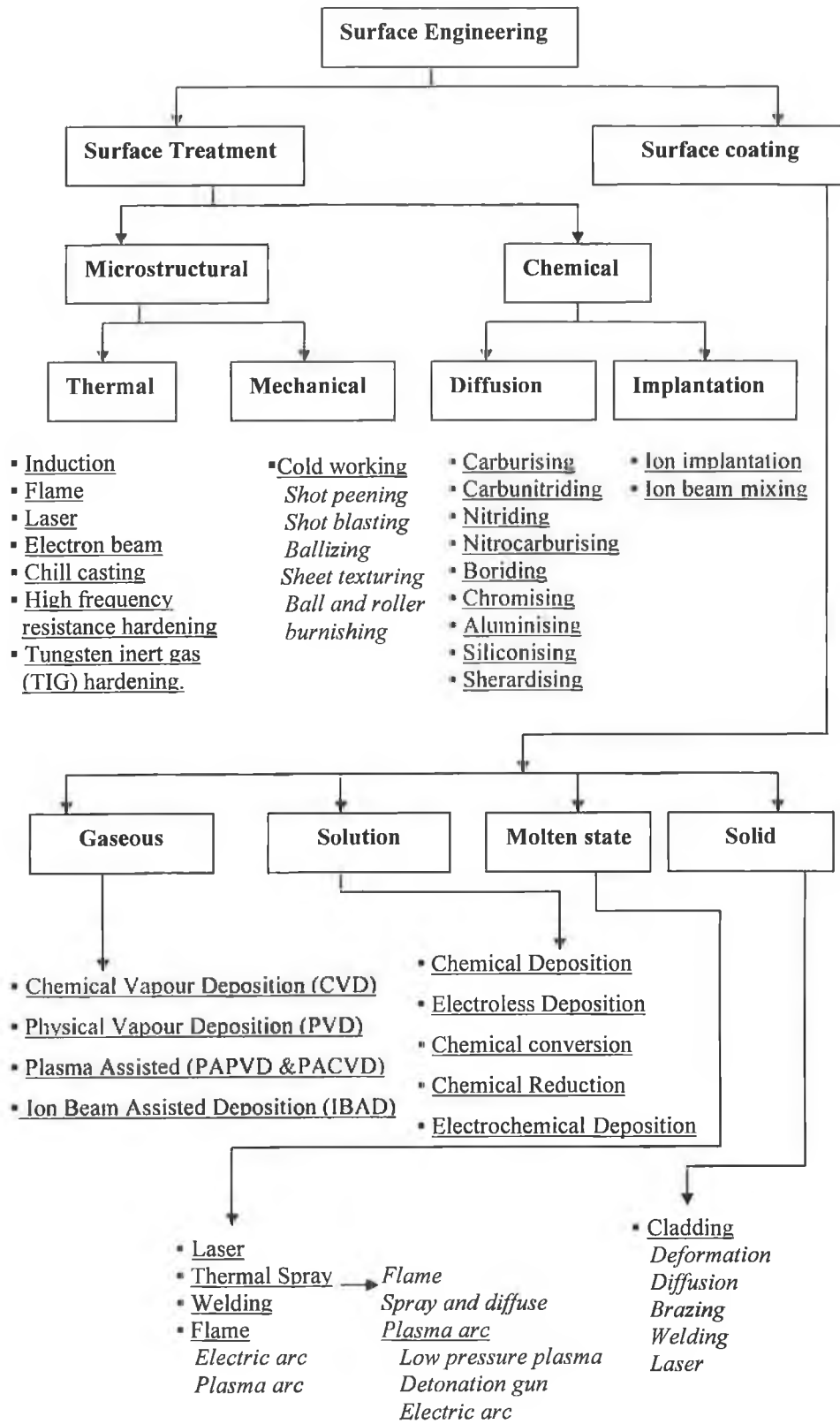


Figure 2.3. General classification of surface engineering.

2.2.4.2. Surface coating

Surface coating is a layer of material deposited artificially on the surface of an object made of another material, with the aim of obtaining required technical (mechanical, electrical, optical, and decorative) properties. All the coating deposition processes including PVD and CVD processes can be realised in terms of three steps in the formation of a deposit as shown in the Figure 2.4. [20]. For the vapour phase deposition methods, they are: creation of vapour phase, transport of vapour from source to substrate, and coating growth on the substrate. Among the entire surface coating methods the gaseous process are considered to have great potentials for depositing thin coatings compared to the traditional wet coating processes mainly due to the outcomes of hazardous chemicals. Furthermore, physical and chemical vapour depositions (PVD and CVD) offer a large variety of material coatings, higher quality coating (i.e., higher hardness, surface finish, adhesion), and high experimental flexibility as well as the minimisation of waste disposal [21,22]. The up to date history of the vacuum coating technology is given in reference [23]. Here the discussions about the surface coating will be restricted to thin ($\leq 10 \mu\text{m}$ [17]) vapour deposited (PVD and CVD) coatings.

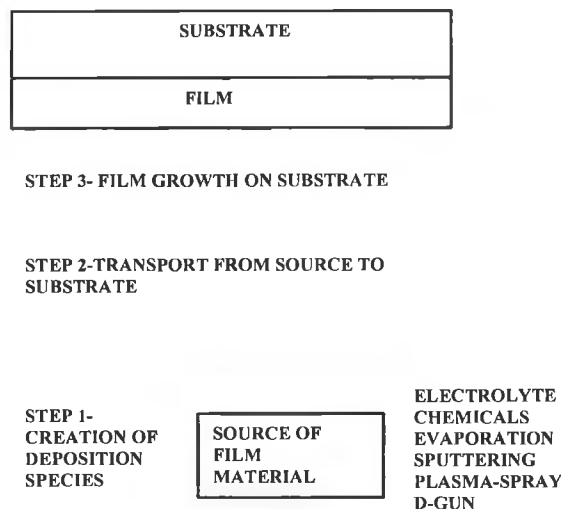


Figure 2.4. Different steps during coating formation [20].

Physical Vapour Deposition

Physical Vapour Deposition (PVD) processes are deposition processes in which atoms or molecules of a material are vapourized from a solid or liquid source, transported in the form of a vapour through a vacuum or low-pressure gaseous environment, and condense on a substrate. PVD processes can be used to deposit coatings of elemental, alloy, compound as well as some polymeric materials. PVD involves the generation of vapour phase species either via evaporation, sputtering, laser ablation or ion beam. In

evaporation atoms are removed from the source by thermal or electron means and in sputtering atoms are ejected from the target surface by the impact of energetic ions. Thermal evaporation has a limitation in multicomponent materials since one of the metallic elements typically evaporates before the other due to the differences in vapour pressures of the evaporating species. On the contrary, sputtering is capable of depositing high melting point materials such as refractory metals and ceramics, which are difficult to fabricate using evaporation. IBAD has the advantage of having more independent processing parameters than other PVD methods. Ion plating (concurrent bombardment of the coating during deposition) enhances adhesion of the coating [24]. Typically, PVD processes are used to deposit coatings with a thickness range of a few angstroms to thousands of angstroms. Process temperatures are relatively low, up to 400 °C, thus minimising distortion and preserving the heat-treated state of the substrate. Typical PVD deposition rates vary from 10-100 Å/sec. PVD processes have the advantage that almost any inorganic material and many organic materials can be deposited using pollution-free deposition processes. The deposits can be of single materials, layers with a graded composition, multi layer coatings, or very thick deposits. The several techniques under PVD process are shown in Figure 2.5. There are many references where different PVD techniques and their advantage and disadvantages are discussed in details [25-31]. In the next section among the various PVD techniques the sputtering techniques will be discussed in details.

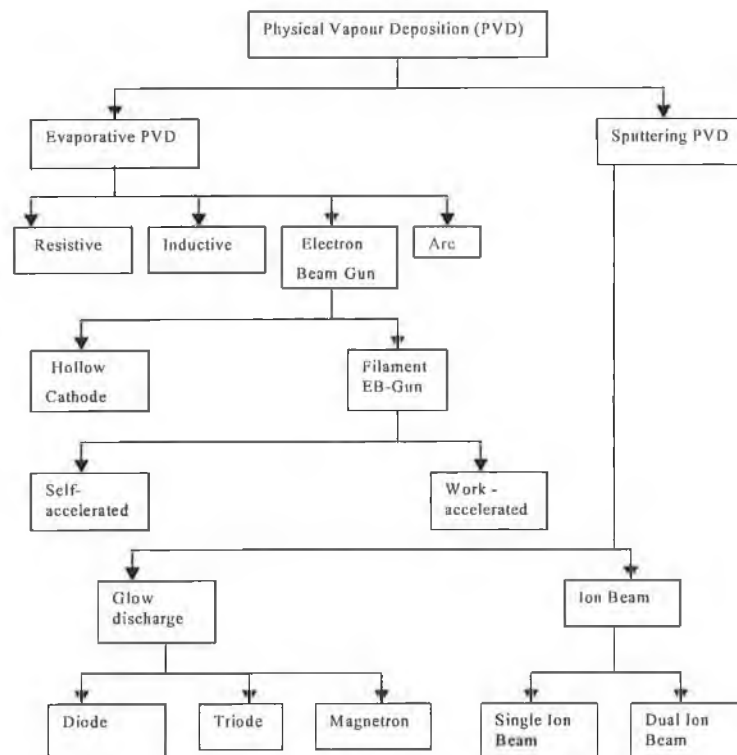


Figure 2.5. Classification of Physical Vapour Deposition processes.

Chemical Vapour Deposition (CVD)

Chemical Vapour Deposition (CVD) is a process where one or more gaseous adsorption species react or decompose on a hot surface to form stable solid products. In the basic CVD process gases containing volatile compounds of the element or elements to be deposited are introduced into a reaction chamber, and condense on to the substrate to form a coating. CVD is a more complex method of forming thin coatings than PVD. CVD exhibits several distinct advantages such as the capability of producing highly pure and dense coatings or fine particles at reasonably high deposition rates, and the capability of coating complex-shaped components uniformly due to its non-line-of-sight nature. CVD is widely used for the deposition of metallic, ceramic and semiconducting thin coatings. Figure 2.6. shows many derivatives of the basic CVD process. These have arisen in response to a need to achieve specific coating characteristics, such as epitaxial growth, improved hole penetration or lower deposition temperatures and pressures.

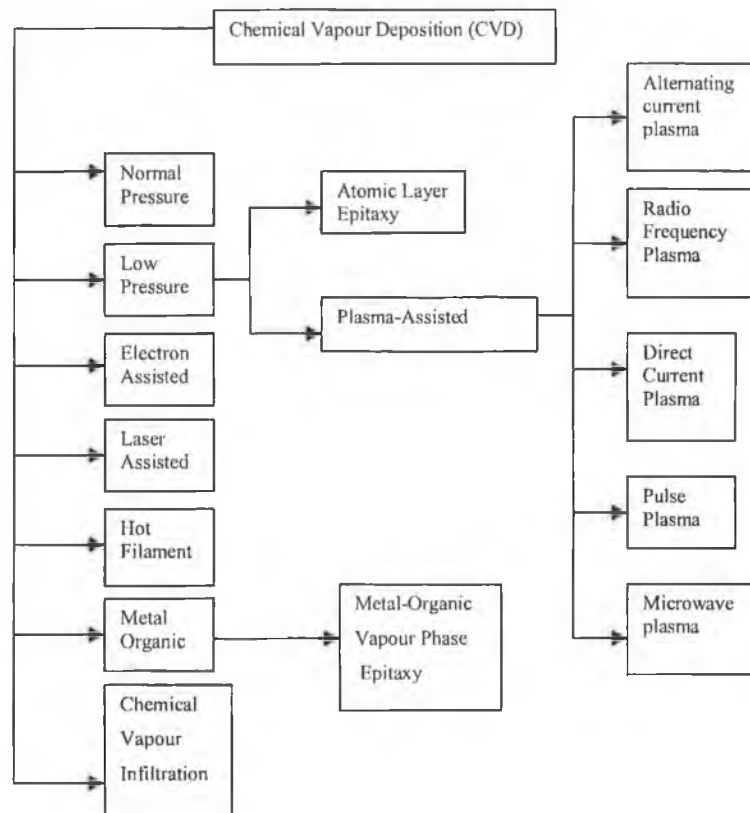


Figure 2.6. Some CVD based coating processes and ion based derivatives [14].

The deposition pressure in CVD can range from atmospheric to 1 Pa or less. Also there are various means of assisting the process, such as through the use of laser or electron beams, or by ion bombardment of the growing coatings. The latter method promises the benefit of reducing in coating temperatures necessary to obtain dense and well-adhered coatings. For

plasma assisted or enhanced CVD many of the beneficial effects are analogous with those observed for plasma assisted PVD. The versatility of the CVD process has been demonstrated by the wide variety of geometrical configurations into which it forms refractory metals, alloys, and refractory compounds. CVD compares favorably with other methods of plating and forming in its ability to produce high-density, high-purity, and high-strength materials. In general, CVD deposition process can vary from room temperature up to 2500 °C. Although CVD process is very effective for depositing hard coatings on cemented carbide tools but it was difficult to transfer the technology to steels until the advent of plasma assisted CVD because of high CVD processing temperature, which anneals steel. Choy [32] has recently reviewed the different aspects of chemical vapour deposition.

2.3. SPUTTERING MECHANISM AND PLASMA SURFACE INTERACTIONS

The basic sputtering process has been known for many years and many materials have been successfully deposited using this technique. The use of sputtered species as source material to deposit thin coatings is first reported in the literature in 1852 [33]. However, it is only relatively recently that sufficient understanding of the complex processes occurring during ion bombardment of the solid surfaces has been developed to allow the reproducible and controllable use of sputter deposition for growing high quality single crystals, complex alloys, superlattices and materials with tailored microstructures. The basic process in sputtering is like the other PVD methods i.e., creation of the vapour phase species, transportation of the source species from source to substrate and coating growth on the substrate. The basic sputtering process has been known for many years [34] and extensively reviewed in number of references [35-42].

2.3.1. Processes occurring at the target

Physical sputtering is a nonthermal vapourization process where surface atoms of a target (cathode) are physically ejected by momentum transfer from an atomic-sized energetic bombarding particle, which is usually a gaseous ion accelerated from a plasma or ion gun. Sputtering has also been observed for bombardment by ions, atoms, electrons and even photons. If the surface atom that has been struck attains enough energy, it will strike other atoms in the near-surface region and a “collision-cascade” will develop (Figure 2.7.).

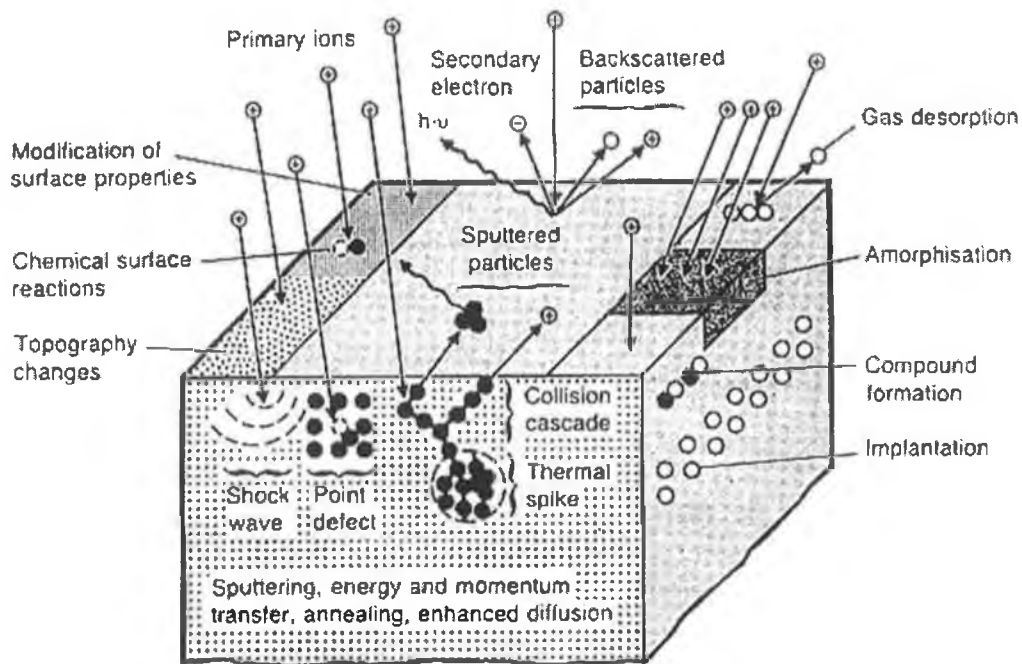


Figure 2.7. Plasma surface interaction during sputtering [43].

Multiple collisions can result in some momentum being directed back toward the surface and, if the energy attained by a surface atom, which is struck from below, is sufficient, it can be physically ejected from the surface, i.e., sputtered. The sputtered particles then condense on the substrate placed in front of the target. Secondary electrons are also emitted from the target surface as a result of the ion bombardment, and these electrons play an important role in maintaining the plasma. Most of the energy that is transferred by the bombarding particle appears as heat in the near-surface region.

2.3.1.1. Sputter yield

Sputtering is usually characterized by the ratio of the number of ejected target particles per incident particle, which is usually known as sputter yield, S .

$$S = (\text{Number of ejected atoms/each incident particle})$$

The sputtering rate is also synonymously used for sputtering yield. The sputtering yield mainly depends on the target species and the nature, energy, and angle of incidence of the bombarding species. There needs to be minimum ion energy for starting sputtering, called threshold ion energy, which is in the range of 20-40 eV depending on the target materials. After that sputtering yield is a nearly linear function of ion energy up to several hundred eV. At higher energy the dependency becomes sublinear. From the energy consumption point of view, linear region is most effective for sputtering process. For typical ion energy,

the sputtering yields of the most of the metals are near unity and within an order of magnitude of one another. Depending on the kinetic energy of the incident ion, different physical effects will be seen in the solid (Figure 2.8.): threshold sputtering (20-40 eV), knock on sputtering (20 eV up to perhaps 700-800 eV), collision-cascade sputtering (about 1000 eV to 50 keV) and implanted region (50 keV to MeV).

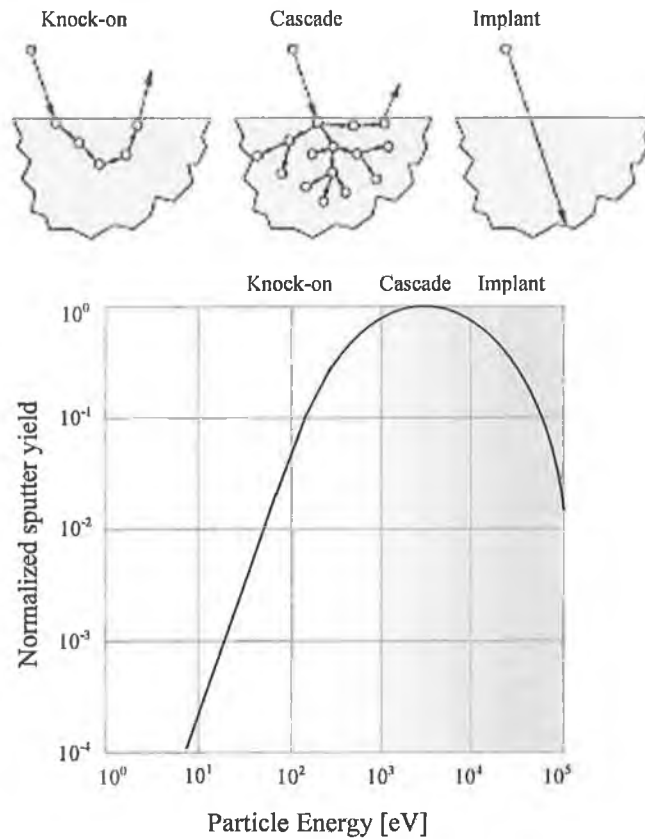


Figure 2.8. Typical sputtering yield curve with respect to incident ion energy [30].

The dependency of sputtering yield on ion angle incidence is shown in the Figure 2.9. The sputtering is most efficient 20-30 degrees from glancing angle position. The sputtering yields for the two elements in a binary alloy target are proportional to the number of different atoms present in the sputtering depth.

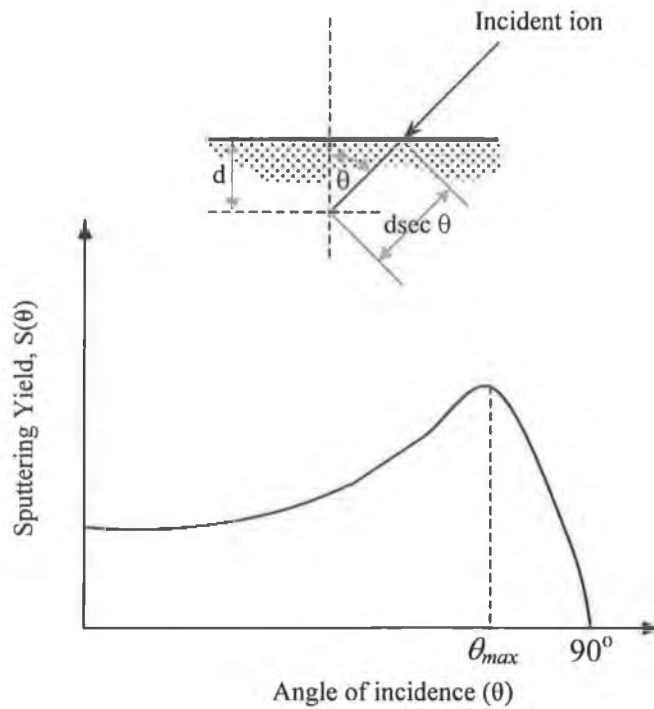


Figure 2.9. Schematic diagram of the variation of sputtering yield with ion angle incidence.

In equilibrium, the surface composition of the target changes such that the composition of the elements in the sputtered flux is the same as the original alloy composition provided that the target is sufficiently cooled to avoid any diffusion, and the target has to be a homogeneous alloy and not a simply mixture of two components. As physical sputtering is effectively a momentum and energy transfer process, the electrical state (charge) on the incident particle is mostly irrelevant. In reality the ions are typically neutralized as they approach a surface (within a few angstroms) and strike the surface as neutrals. Therefore, the sputter yield of an ion and a neutral are indistinguishable. The sputtering yield is relatively insensitive to the target temperature. At sufficiently high temperature, the evaporation rate becomes same or larger than the sputtering rate.

2.3.2. Process occurring at the substrate

The different steps occurring on the substrate during coating formation by sputtering is shown in Figure 2.10.

1. Diffusion of ad-atoms: Ad-atoms (atomic fluxes arrive at the substrates) diffuse around the substrate and the diffusivities are dependent on the interaction between the ad-atoms and temperature of the substrate.

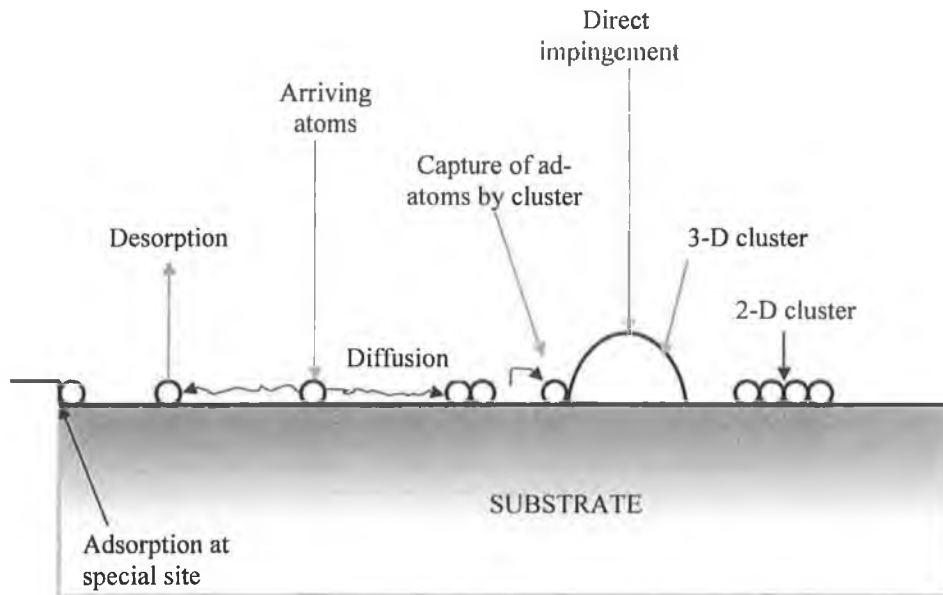


Figure 2.10. Coating formation steps during sputtering.

2. Doublet formation: In diffusing randomly the ad-atoms come across other ad-atoms and join them to form doublets, which have lower diffusivities.
3. Island formation: As more flux arrives at the substrate, the nuclei sizes grow and eventually islands are formed.
4. Continuous coating formation: These islands continue to grow and until they coalesce and form a continuous coating.

Depending upon the substrate temperature, flux and other process variables each island may conserve its own orientation and resulting coating will be turned out to be polycrystalline or amorphous. At higher temperature and low deposition rate, all the islands may reorient to adopt the most thermodynamically stable single orientation, leading to an epitaxial coating growth.

2.4. DIFFERENT SPUTTERING TECHNOLOGIES

Different sputtering techniques have been developed in order to increase the deposition rate, adhesion, and the deposition of higher quality coating. In this section different techniques of sputtering are discussed briefly.

2.4.1. Diode sputtering

Diode sputtering, the simplest and most widely used, consists of two electrodes, a cathode and an anode, and are placed 5-10 cm apart as shown in Figure 2.11. The anode holds the substrate and the cathode holds the target material (sputtering material). A low-pressure glow discharge, which is known as abnormal negative glow, is maintained between anode and cathode. The size of the electrode is important with respect to the distance between the electrodes because of the need to maintain electrically charged plasma between the electrodes to facilitate electron, ion, and atom movement.

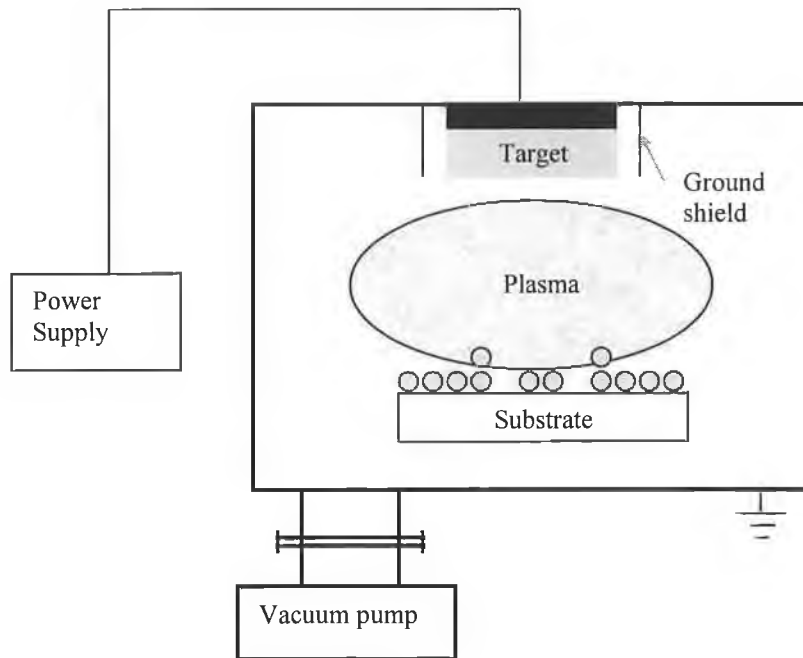


Figure 2.11. Schematic representation of the plasma in a planar diode sputtering source.

Due to the electrical potential drop the ions passing from the plasma volume experiences a strong electrical field, which accelerates the ions to impact the cathode. The sputtered material moves across the plasma and hits the substrate surface where it then becomes implanted as part of the coating surface. The amount of material, which is sputtered from the target onto the substrate, depends primarily on the pressure, voltage and current, the geometry of the substrate, the mean free path of the gas in the chamber, and the sticking coefficient between the target atoms and the substrate. The sputtering rate can effectively be increased by increasing the operating gas pressure at a given voltage. However, if the pressure is too high, the deposition rate starts to decrease due to the collision-dominated transport of the sputtered atoms. The collision-dominated transport also reduces the kinetic energy of the sputtered atoms at the substrate and results less dense coating. However, the

process is further limited by low ionization efficiencies in the plasma, and difficulties in compound formation by reactive sputtering.

2.4.2. Triode Sputtering

This method of sputtering is similar to the diode device except for the fact that there are three electrodes instead of two. The extra electrode is responsible for sustaining the glow discharge. The most common method of triode sputtering is hot-cathode sputtering. Electrons are emitted from the cathode thermionically rather than by ion bombardment. This relaxes the volume ionization requirement for sustaining the discharge. The hot-cathode triodes can be operated at low pressures (0.5 to 1.0 mtorr). The driving voltage of the thermoionic emitter is only 50-100 V, although the current may be several amperes. This method though permits a high deposition rate (hundreds of nm/min) at low pressures (mtorr range) and target voltage and large thicknesses are achievable. The low gas pressure also conserves the energy of the ions due to decreased collision. The problems with the triode sputtering are related to the difficulty in scale up and sensitivity of the thermoionic emitter with the reactive gas. Sputtering in a reactive environment is most likely to shorten the filament lifetime by oxidation.

2.4.3. Ion beam sputtering

Glow discharge sputtering is limited in the sense that the target current density and the voltage cannot be independently controlled except by varying the working gas pressure. Ion beam sputtering permits the independent control over the energy and the current density of the bombarding ions. Additionally, the angle of incidence of ions to a surface can easily be varied. The ion sources that are generally used are an aperture from a low-pressure arc or a hollow cathode ion sources. These devices were limited for practical deposition because of the small ion beam sizes (≈ 1 cm).

2.4.3.1. Single ion beam sputtering

A sputtering target is arranged to obliquely intersect an ion beam of given energy and flux density that is created by an independent ion source. Substrates are suitably placed to receive the coating flux as shown in the Figure 2.12. In addition to the independent control over the ion current and voltage, ion beam sources permit sputtered coatings to be

deposited at very low inert-gas pressure (≤ 0.1 mtorr) onto substrates that are not in contact with plasma.

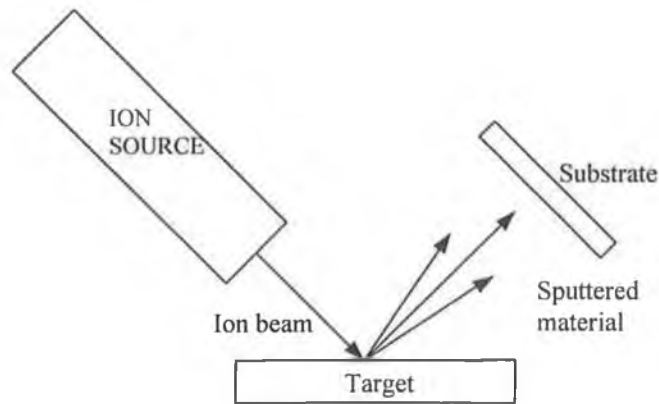


Figure 2.12. Schematic representation of single ion beam sputtering.

2.4.3.2. Dual ion beam sputtering

Dual ion beam sputtering is simply the combination of ion beam sputtering and ion beam deposition (Figure 2.13.). The advantage here is that more than one material can be deposited on the surface of the substrate at one time while maintaining control as in all ion beam deposition mechanisms.

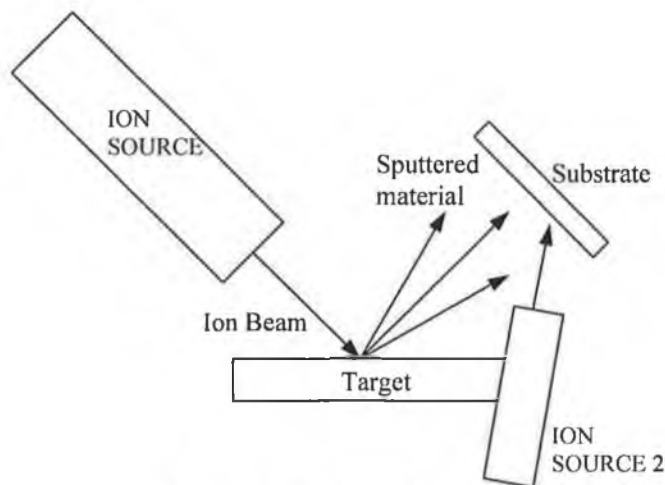


Figure 2.13. Dual ion beam sputtering.

2.4.4. Magnetron Sputtering

Conventional sputtering method suffers the limitations of lower deposition rate, higher voltage and pressure to sustain plasma, higher target temperature, lower ion current density to substrate etc. To overcome these difficulties magnetron sputtering has been developed.

2.4.4.1. Development of magnetron sputtering

In 1935 F. M. Penning first proposed to enhance the plasma density of a glow discharge by means of a magnetic field [44]. Then it took nearly 40 years until the *planar magnetron* with a closed loop tunnel of magnetic field lines was developed by J. S. Chapin in 1974 [45]. The introduction of *conventional or balanced magnetron* was an important step overcoming many limitations of conventional sputtering [46,47]. In 1986 B. Window and N. Savvides [48-50] developed the *unbalanced magnetron* sputtering to spread the plasma over a long distance for the substrate bombardment by energetic ions. In 1989, D. G. Teer [51] developed *closed-field unbalanced magnetron* sputtering for high quality and high rate deposition.

2.4.4.2. Planar /conventional/balanced magnetron

Magnetron sputtering configurations use a magnetic field, usually from permanent magnets near the target (cathode) surface, to confine the electrons near the surface. In magnetron, the magnets are arranged in such a way that one pole is positioned at the central axis of the target and the second pole is formed by a ring of magnets around the outer edge of the target. The cross section of a rectangular planar magnetron is shown in Figure 2.14.

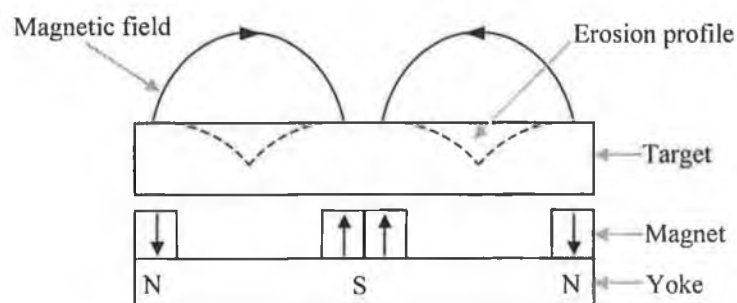


Figure 2.14. Cross-section of planar magnetron.

When an electron is ejected from the target surface, it is accelerated away from the surface by the electric field, but cross electric and magnetic field ($E \times B$) forces the electron to spiral around the magnetic field lines. The $E \times B$ force causes the electron to also move normal to the $E \times B$ plane and, if the magnetic field is arranged appropriately, the electrons will form a closed-path circulating current near the surface (Figure 2.15.). This closed circulating path can be easily produced on a planar surface or any surface of revolution such as a cylinder, cone, hemisphere, etc. Trapping the electrons in this way substantially increases the probability of an ionising electron-atom collision occurring. The increased ionization

efficiency of a magnetron results in a dense plasma in the target region. This, in turn, leads to increased ion bombardment of the target, giving higher sputtering rates and, therefore, higher deposition rates at the substrate. In addition, the increased ionization efficiency achieved in the magnetron mode allows the discharge to be maintained at lower operating pressures (typically, 10^{-3} mbar) and lower operating voltages (typically, -500V) than is possible in the diode sputtering mode.

In a conventional magnetron, the plasma is strongly confined to the target region. A region of dense plasma typically extends some 60 mm from the target surface. Coatings grown on substrates positioned within this region will be subjected to concurrent ion bombardment, which can strongly influence the structure and properties of the growing coating.

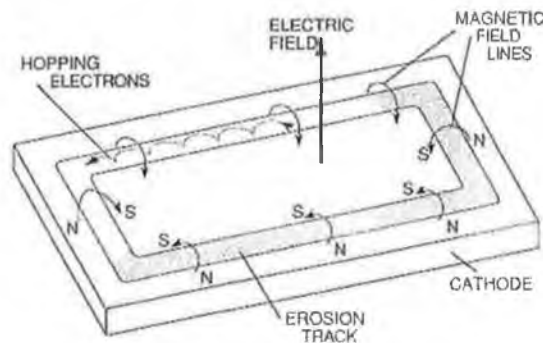


Figure 2.15. Applied fields and electron motion in magnetron.

Substrates placed outside this region, however, will lie in an area of low plasma density. Consequently, the ion current drawn at the substrate (typically, $<1 \text{ mA/cm}^2$) is generally insufficient to modify the structure of the coating. The energy of the bombarding ions can be increased by increasing the negative bias applied to the substrate. However, this can lead to defects in the coating and increased coating stress, and therefore, be detrimental to the overall coating properties. Thus, it is difficult to deposit fully dense coatings on large, or complex components using conventional magnetrons [52]. To deposit dense coatings without introducing excessive intrinsic stresses, a high flux ($>2 \text{ mA/cm}^2$) of relatively low energy ($<100 \text{ eV}$) ions is generally preferred [53]. These conditions are readily provided by unbalanced magnetrons.

2.4.4.3. Unbalanced magnetron sputtering

In an unbalanced magnetron, the central pole is strengthened relative to the outer pole (type-1) or the outer ring of magnets is strengthened relative to the central pole. In type-1, the field lines, which do not close in on themselves, are directed towards the chamber walls and the plasma density in the substrate region is low. This design is not commonly used, because of the resulting low ion currents at the substrate. In type-2, not all the field lines are closed between the central and outer poles in the magnetron, but some are directed towards the substrate, and some secondary electrons are able to follow these field lines. Consequently, the plasma is no longer strongly confined to the target region, but is also allowed to flow out towards the substrate. Thus, high ion currents can be extracted from the plasma without the need to externally bias the substrate. However, it was Windows and Savvides who first realised the significance of this effect when they systematically varied the magnetic configuration of a conventional magnetron [48-50,54]. They and other researchers have subsequently shown that substrate ion current densities of 5 mA/cm^2 and greater, i.e., approximately an order of magnitude higher than for a conventional magnetron, can be routinely generated when using an unbalanced magnetron [50,55]. A comparison between the plasma confinement obtained in different magnetron modes is shown schematically in Figure 2.16.

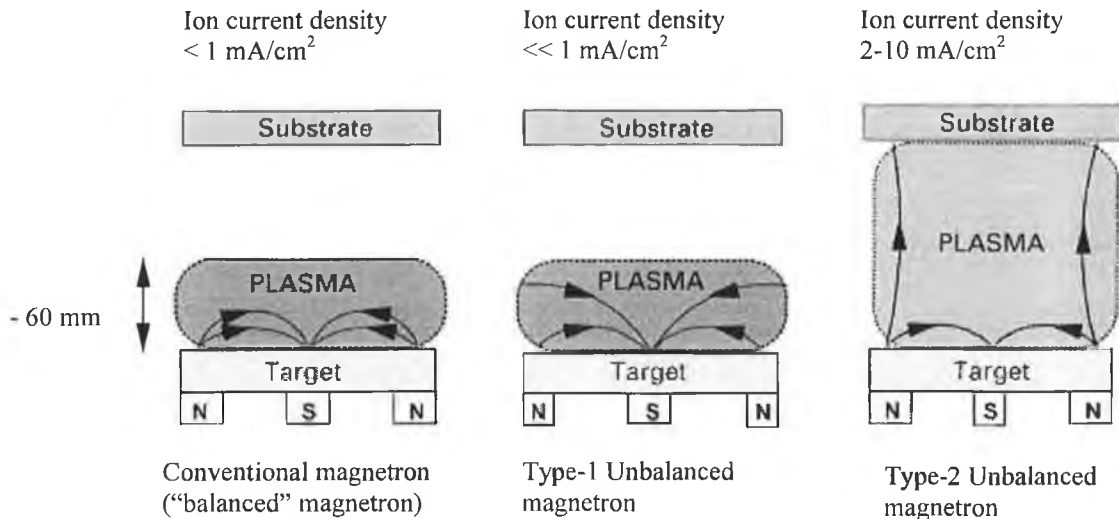


Figure 2.16. Schematic representation of the plasma confinement observed in conventional and unbalanced magnetrons [56].

Thus, in addition to providing a high flux of coating atoms (compared to a basic sputtering source), an unbalanced magnetron also acts as a very effective ion source. Furthermore, the

ion current drawn at the substrate is directly proportional to the target current. Deposition rate is also directly proportional to target current. As a result, and unlike other ion-plating processes, the ion-to-atom arrival ratio at the substrate remains constant with increasing deposition rate [57].

2.4.4.4. Closed-field unbalanced magnetron sputtering

Despite the benefits offered by unbalanced magnetrons, it is still difficult to uniformly coat complex components at acceptable rates from a single source. Therefore, in order to commercially exploit this technology, multiple magnetron systems have been introduced.

In a multiple magnetron system, the magnetic arrays in adjacent magnetrons can be configured with either identical, or opposite magnetic polarities. In the former case the configuration is described as “mirrored” and in the latter case “closed-field”, and both configurations are shown in Figure 2.17.

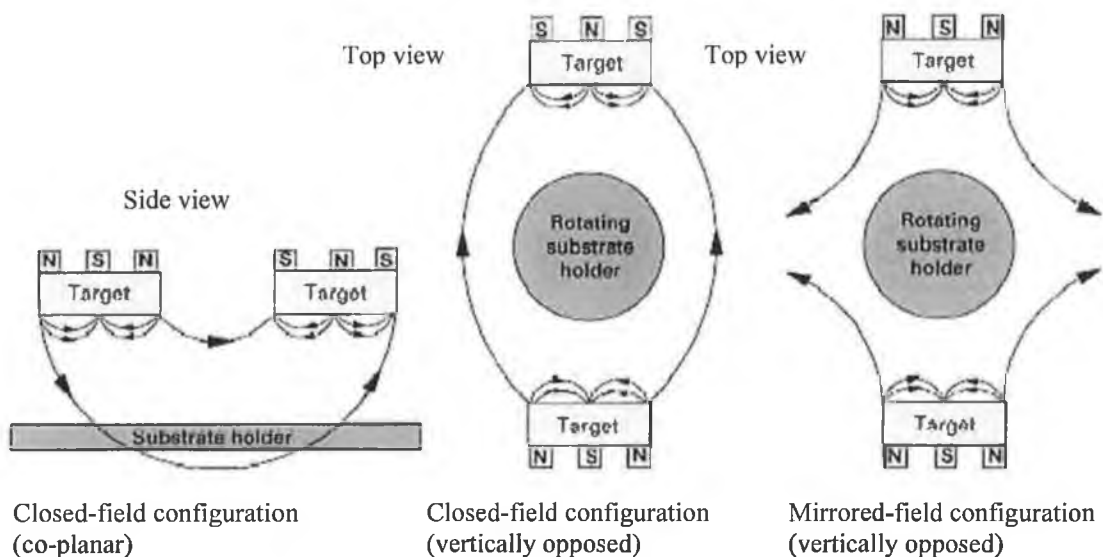


Figure 2.17. Different closed-field unbalanced magnetron configurations [56].

In the mirrored case, the field lines are directed towards the chamber walls. Secondary electrons following these lines are lost, resulting in a low plasma density in the substrate region. Conversely, in the closed-field configuration, the field lines are linked between the magnetrons. Losses to the chamber walls are low and the substrate lies in a high-density plasma region. The effectiveness of the closed-field configuration can be realized in terms of ion-to-atom ratio incident at the substrate (2-3 times greater) compared under the same

conditions in the mirrored, or single unbalanced magnetron configurations [58]. Also, the influence of the closed magnetic field on the ion-to-atom ratio becomes more marked as the distance from the target increases.

In UK, Teer Coatings Ltd. has developed closed-field unbalanced magnetron sputtering (CFUBMS) systems with an even number of vertically opposed magnetrons surround the rotating substrate holder. Adjacent magnetrons have opposite magnetic polarities and the field lines are closed. The major advantages of CFUBMS are high thickness uniformity, high stability of deposition rate for >100 hr uninterrupted production, good reproducibility of layer properties from day to day and from month to month, good adhesion and high density of deposited coatings, ability to deposit all kinds of metals including high melting point metals, metal alloys and compounds with precise control on coating composition, ability to deposit metal oxides, nitrides, carbides etc. with precise control of layer stoichiometry and ability to deposit tailored design coatings like multicomponent, multilayer, gradient, composite coating etc. The perspective of magnetron sputtering has been reviewed [59,60]. Magnetron sputtering more specifically CFUBMS has gained wide acceptance both in research and commercial purposes. The magnetron sputtering is routinely used in different industries like cutting tool, forming tool, semiconductor, optical, glass coating, decorative, biomedical etc.

2.4.4.5. Power sources for sputtering

Normally DC power sources are used in sputtering when the target is metallic. The incident ions on the target take electron from the target and become neutral. But if the target is not conductive the positive charge will build up and retard the sputtering. To deposit insulating coating from an insulating target, instead of DC, RF power supply is used. But it is difficult to maintain the same composition of the target in the coating due to the preferential effect during sputtering and deposition rate is slow too. The deposition of insulating coating can also be done by reactive DC sputtering of metallic targets. Arching and disappearing of anode (anodes covered by insulating coating material) are the very common problems which can affect the structure, composition and properties of the growing coating, and can also lead to damage of the magnetron power supply. Pulse power source in the medium frequency range (10-200 kHz) can significantly reduce the formation of arcs and, consequently reduce the number of defects in the resulting coating when depositing insulating coatings [61]. Furthermore, high deposition rate can also be achieved by pulsed reactive sputtering.

2.4.4.6. Magnetron sputtering for high target utilization

The sputtering capability of any target is mainly affected by the design of the magnetic field. Therefore, the position of the magnets in correlation to the target material as well as the selected magnetic force is very important. The highest plasma density and the highest localized sputter rate will be centred where the tangents of the field lines are parallel to the target surface. Therefore, an erosion groove is established where the magnetic field is most intense and results poor target utilization (25-30%). Target utilization is even lower when that target is magnetic because the erosion groove is further localized by the magnetic field from magnetic target. Variable field strength magnetrons [62], shunted magnetron (ToraMag) [63], planar magnetron with additional plasma confinement [64,65] have been developed to improve target utilization.

2.4.4.7. Other developments in magnetron sputtering

In the past few years, attention has begun to focus on magnetron sputtering with high deposition rate to shorten the coating formation time, which makes industrial production cheaper and to replace ecologically damaging galvanic coating processes by magnetron sputtering, higher ionization of the sputtered coating material to deposit dense coating from ions of the coating even in high aspect ratio trenches and to accelerate the reaction material during compound formation and in some cases the elimination of the inert sputtering gas from the deposition process. To fulfill the above mention objectives the following magnetron sputtering techniques are currently used: high-power pulsed magnetron sputtering [66], self-sputtering, low pressure sputtering, high rate sputtering, plasma-enhanced magnetron-sputtered deposition [67,68]. Several design of the magnetron has also been developed for higher deposition rate such as Electromagnetically moved plasma zone (Speed Mag), Dual magnetron sputtering (Twin Mag), Cylindrical Rotatable magnetron (C-Mag), Interpoles Target-Hollow magnetron (IPT-HM) [69,70]. Some hybrid sputtering process has also been developed such as magnetron sputtering combined with PLD [71], PECVD [72], Arc Ion Plating (AIP) [73] and cathodic arc evaporation [74].

Despite these developments there are still lot of issues like process repeatability, process control (i.e. temperature, reactive gas, particle formation etc), higher deposition rate for large-scale industrial development, and reduction of system cost needs to be addressed [75].

2.5. SPUTTER DEPOSITION MODES

In the following sections the different modes of sputtering has been discussed.

2.5.1. Reactive sputtering

Reactive sputtering can be defined as the sputtering of elemental targets in the presence of chemically reactive gases that react with both the ejected target material and the target surface. It has become a very popular technique in today's search for new material properties, for the deposition of a very wide range of compound and alloy thin coatings including oxides, nitrides, carbides, fluorides or arsenides. This can be applied to any of the previous methods of sputtering that have been discussed.

2.5.1.1. Reactive sputtering mechanism and hysteresis effect

As a reactive gas is added to the sputtering process, the gas atoms combine with depositing coating atoms to form compound coatings of varying stoichiometry. At this point, even though the additional gas is being added to the chamber, there is no rise in the chamber pressure because all of the gas atoms are absorbed by the coatings. With increasing the flow of reactive gas, the coatings become more and more reacted, and eventually at a sufficient high reactive gas flow, the coating reached their final reacted state. This is typically a stable, or "terminal" compound, such as Al_2O_3 , where the additional oxygen cannot be absorbed by the coating. Now any additional flow of reactive gas results in the formation of a reacted, compound coating on the cathode surface. This compound has almost invariably has a lower sputtering yield (by a factor of 10-20) than the pure metal cathode, which results in a reduction of the rate of metal atoms sputtered from the cathode and finally the process instability. This well-known phenomenon is called *target poisoning*. Reducing the rate of metal deposition reduces the rate at which the coating can absorb the reactive gas, further increasing the residual background of the reactive species. This, in turn, causes additional reaction on the cathode surface, which reduces metal sputtering rate even further. In effect the cathode undergoes a transition from metallic to a compound state, and the deposition process slows dramatically.

If the reactive gas flow rate is now lowered, the reverse transition does not occur at the same flow rate. This is due to the lower metal emission rate from the compound surface. A significantly lower gas flow rate is needed to make up for the low level of metal emission.

At a much lower flow the cathode switches back to the metallic mode, and all of the reactive gas is again absorbed in the coatings. This shows up in the Figure 2.18. as a *hysteresis loop*.

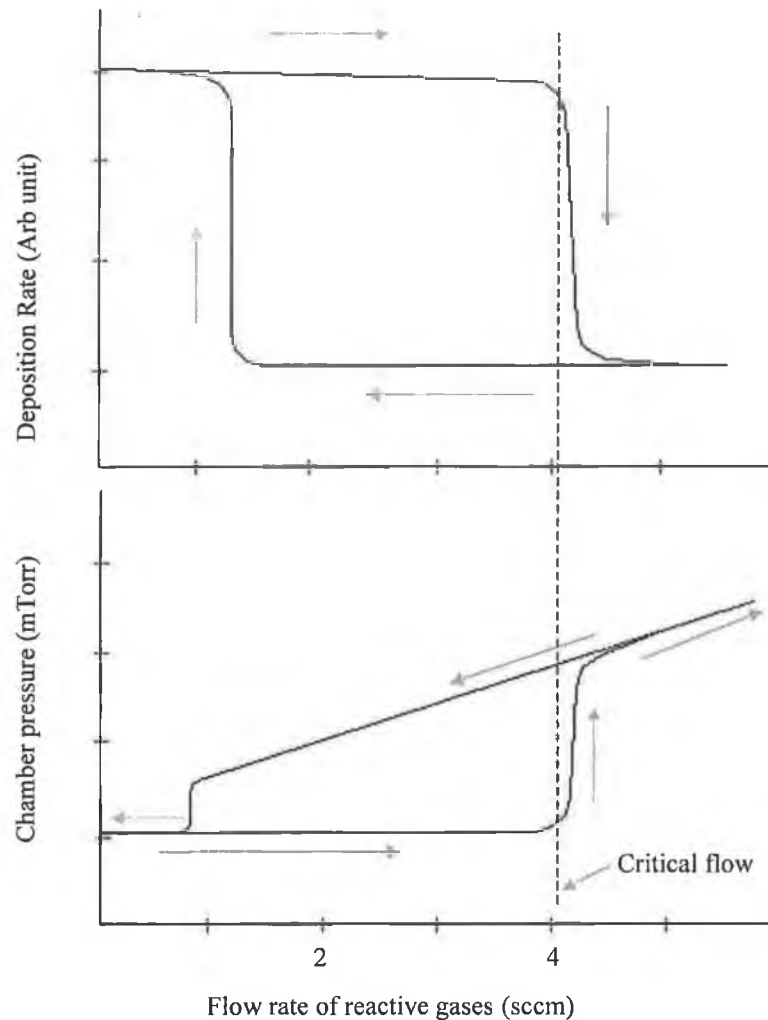


Figure 2.18. Hysteresis curve for the deposition rate and chamber pressure for the case of reactive sputtering.

Several methods have been tried to eliminate the hysteresis effect during reactive sputtering. If the deposition chamber is overpumped, the consumption of the reactive gas dominates that by the growing coating. Other processes are varying the target-to-substrate distance, or obstructing reactive gas flow to the cathode by a baffle or switching on and off the gas supply for very short periods. Several methods also have been developed for the control of the hysteresis effect. Among those, plasma emission monitoring, voltage control, successive plasma anodization (SPA) and successive pulsed plasma anodization (SPPA). These aspects of reactive sputtering have been reviewed in recent papers [76,77]. The advantages of the reactive sputtering are: (i) compounds can be formed using relatively

easy-to-fabricate metallic targets, (ii) insulating compounds can be deposited using DC power supplies and (iii) coatings with graded compositions can be formed. The primary disadvantage of this sputtering mode is that the gas injection rate affects the coating properties in a non-linear fashion and is difficult to predict. The effects are evident in the growth rate, composition, and coating structure.

2.5.2. Co-sputtering

It involves the simultaneous deposition of different materials from two or more targets. By this method multicomponent, multilayer, and composite coatings can be deposited. By regulating the power of different targets graded coating can also be deposited.

Other deposition modes of the sputtering so far includes bias sputtering, chemical sputtering and directional sputtering [78].

2.6. FUNDAMENTAL PROPERTIES OF COATING

Figure 2.19. illustrates the properties of the coating-substrate system, in terms of surface (coating dependent), bulk coating (coating and substrate dependent), and interfacial properties. If the performance of a coated component is to be fully understood, it is important to optimise each of these regions and to understand the interrelationships, which exist between each of them.

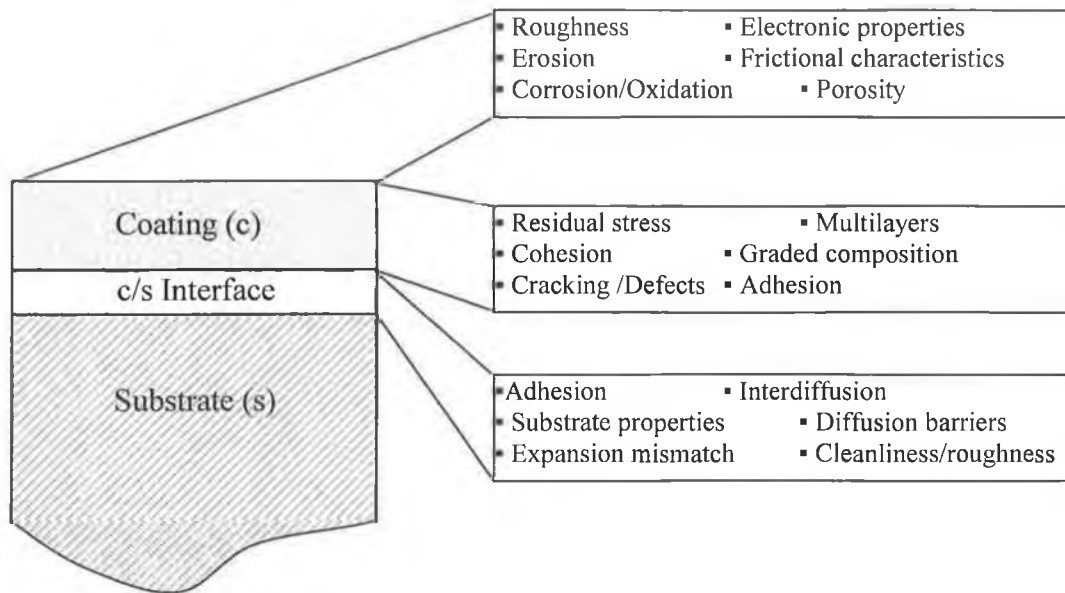


Figure 2.19. Properties of a coating-substrate system, which are important in determining its performance in technological applications [27].

2.6.1. Surface roughness

The surface finishing process controls the geometrical shape of the surface. Macroscopically smooth surface is not smooth and contains surface irregularities (asperities) when viewed microscopically. The Surface irregularities also referred as microroughness is shown schematically in Figure 2.20. Surface roughness is defined as that which distinguishes a real surface from a flat, featureless plain. The nature and degree of surface roughness is defined by the morphology of a surface. The main roughness parameters used are the peak to valley height, R_t , center line average value R_a , which is the arithmetic mean value of vertical deviation of the profile from centreline, the root mean square value, R_s , which is the square root of the arithmetic mean of the squares of the deviation from the centreline and R_{max} is the distance between two lines parallel to the mean line, which contact the extreme upper and lower profiles.

The substrate surface morphology, on the micron and submicron scale, is important to the morphology of the deposited coating, the surface coverage, and the coating properties. Typically fine ground surface for PVD coatings have gouging features (hills and valleys) and the coating tends to fill such troughs, thereby, improving the finish but the exact effects of the coatings depends on its own topography [14].

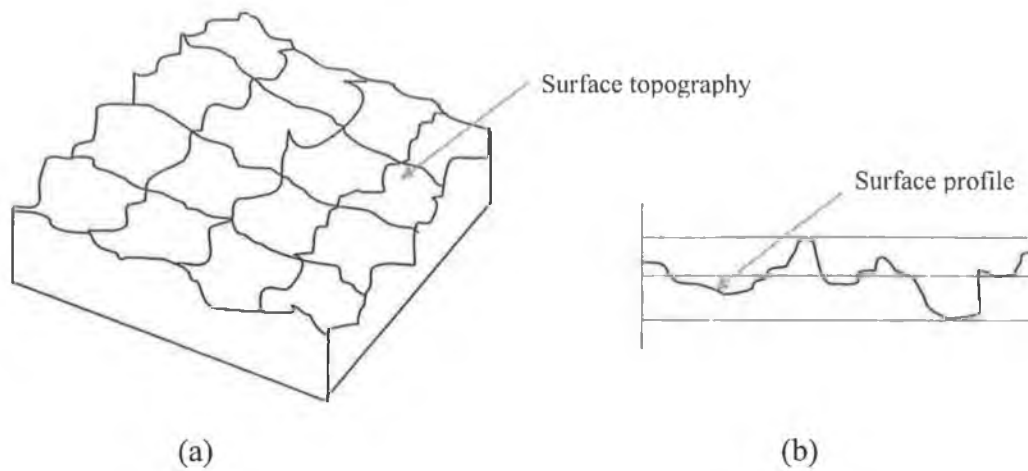


Figure 2.20. The shape of a surface characterized by (a) surface topography and (b) surface profile.

2.6.2. Thickness

Thickness is the most commonly used term to describe the amount of coating, which is critical to the final product's utility and cost. The coating property and behaviour depend on the thickness. In some applications such as decorative, metallurgical and protective coatings, the actual coating thickness is not particularly decisive for proper functioning. On the other hand in some applications such as microelectronic coatings the precise and reproducible coating thickness need to be maintained. A coating thickness may be defined in three ways: geometrical, mass and property. The geometrical thickness is the separation between surfaces and measures in nanometer, micrometer, angstrom etc. and does not take into account the density, composition, microstructure etc. Location of the surface and interface must be determined and surface morphology of the substrate is a factor. Mass thickness takes the density into consideration and expressed as weight per unit area ($\text{micrograms}/\text{cm}^2$). Property thickness measures some properties of the coating, which may be sensitive to the density, composition, microstructure etc.

2.6.3. Morphology

It is generally recognized that thin coatings prepared by PVD show a wide range of microstructures and properties. This has led to the development of the structure zone model (SZM) in providing an overview of the relationship between microstructure of the coatings and the most prominent deposition parameters [79-82]. The first such model was presented by Movchan and Demchisin [79] for evaporated metal coatings as a function of

T/T_m (where T is the actual coating temperature during deposition and T_m is the melting temperature, both in K) by three zones each of its own characteristics structure and physical properties.

The three zones can be identified as Zone 1 ($T/T_m < 0.3$), Zone 2 ($0.3 \leq T/T_m < 0.5$) and Zone 3 ($T/T_m \geq 0.5$). The Zone 1 structure consists of grains with domed tops and a high density of lattice imperfections and porous grain boundaries; hence the term 'porous columnar' is used to describe this type of structure. This structure is the consequence of atomic shadowing at low temperature. The atomic shadowing causes due to the surface roughness where high points on the growing surface receiving more coating flux than valleys, particularly when a significant oblique component is present in the flux. In this case the ad-atom mobility (diffusion) is insufficient to overcome the effect of shadowing. The Zone 2 structure is consisted of columnar grains with a smooth topography and no voids between the columns, which were defined by metallurgical grain boundaries with increased width. This structure forms due to the higher ad-atom mobility at higher temperature allowing surface diffusion processes to dominate and the structure is described as 'dense columnar'. Zone 3 is characterized by the large grains and dense strong grain boundaries where the grains may or may not be columnar in nature and the term 'fully dense' is used to describe the structure. This structure forms due to the bulk diffusion or recrystallization at higher temperature.

Thermally induced mobility has been considered [79] for SZM because that is sufficient for evaporation method. But for sputtering energetic particle bombardment induced mobility can be important process. Considering this fact, SZM is extended [79] to magnetron sputtered coatings by adding an axis to account for the effect of working Ar gas pressure as shown in Figure 2.21.

In this model a fourth zone consisting of a dense array of poorly defined fibrous grains identified between Zones 1 and Zone 2 and termed Zone T since it is believed to be a transition zone. Zone T forms by either thermally inducing greater ad-atom mobility or by ion bombardment. Momentum exchange then causes the coating atom to fill the boundary of loosely packed Zone 1 columns.

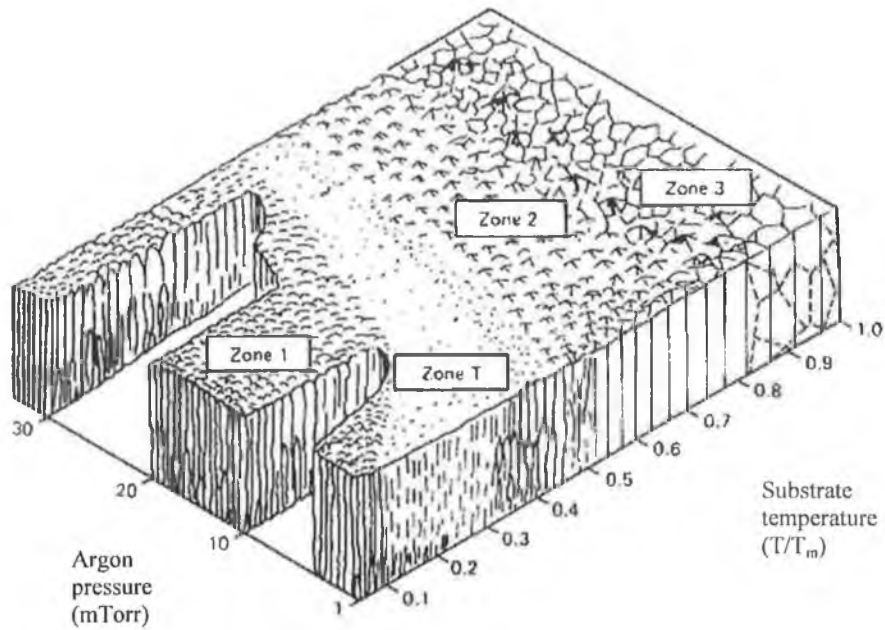


Figure 2.21. Structure Zone Model proposed by Thornton [82].

Messier et al. [83] have found that bias potential induced mobility appears to be more fundamental process affecting the physical structure rather than pressure induced bombardment to adatom mobility. So the pressure axis in Thornton's model is replaced by floating bias potential of the substrate to acknowledge the separate contribution of bombardment to adatom mobility. However, the application of substrate bias would also increase the total energy arriving at the substrate, so Musil et al. [84] have suggested the replacement of bias voltage with an energy parameter, E_p . Latter it has been found that E_p is not the universal parameter [85] rather ion-to-atom arrival ratio is the determining parameter [53,86].

It has become clear due to the formation of fully dense structures at relatively low substrate temperatures in the closed-field magnetron sputtering mode, which has been accounted for the ion-to-atom ratios incident at the substrate during deposition [87]. Kelly and Arnell [87] developed a novel three-dimensional SZM for closed-field magnetron sputtering in terms of homologous temperature, ion-to-atom ratio (to represent ion flux) and bias voltage (to represent ion energy) as shown in Figure 2.22. The model has considered the ion energy and ion flux separately to account for the concurrent ion bombardment on coating microstructure.

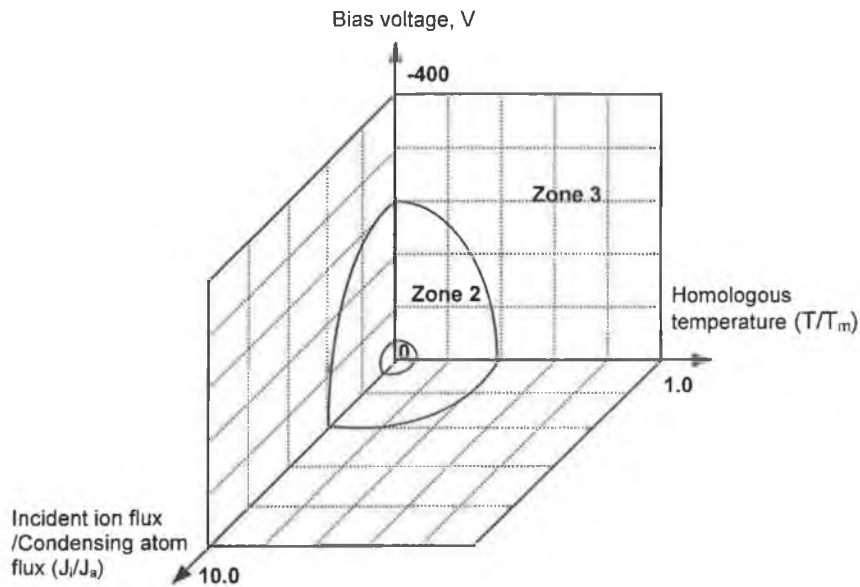


Figure 2.22. Structure zone model relating to the CFUBMS system [87].

2.6.4. Composition

Composition of a multi-elemental coating is an important parameter in many cases to be considered. Coatings composed of grains can be polycrystalline either random or textured and have preferred orientation, they may even be epitaxial, or in some cases they may be amorphous. Different structure of the coatings depends on the composition of the coating. Again the resulting composition of the coating is generally dependent on the deposition technique and the used growth parameters. Usually, metal nitride, carbide etc. with stoichiometric composition gives best performance in tribological applications. For example TiN with stoichiometric composition exhibits higher hardness and wear resistance. Sometimes the composition is varied continuously to deposit compositionally graded coating for improved performance.

2.6.5. Hardness

Hardness is defined as a phenomenological measure of resistance of a material to shear stresses under local volume compression by a body made of a harder material. Hardness is not a fundamental property of a material, it depends on how it is measured. A common definition to measure the H is the relationship between the peak contact load P and the projected area of impression A ($H = P/A$) [88]. The microhardness and nanohardness are commonly undertaken to evaluate coating's hardness. The hardness of a material may be influenced by the grain size, dispersed phases, defect structure, microstructure, density,

temperature, deformation rate, etc. When measuring a coated part, the hardness values that are obtained using large loads are very close to the substrate hardness values. As the load is decreased and the depth of penetration of the indenter decreases, the measured hardness value approaches that of the coating. Ideally, the depth of the indent can be maintained at about 20% or less of the coating thickness; then the hardness values accurately reflect the coating hardness. Surface effects may also influence the measurements for thin coatings, particularly those with oxide layers.

2.6.6. Adhesion

Adhesion is defined as the ability of the coating to remain attached to a substrate under required operating condition. Bond strength is also sometimes synonymously used as adhesion. American Society for Material Testing has defined the adhesion as “the state in which two surfaces are held together by interfacial forces which may consist of valence forces or interlocking forces or both.” This definition does not take account of the extraneous factors such as internal stress or defects within the coating. This led Mittal [89] to define the term practical adhesion by taking into account the extraneous factors. However, the practical adhesion will be dependant on application or test method. Holmberg and Matthews [14] latter suggested the term “effective adhesion” to take account of the observation that coatings with similar bond strengths may in practice exhibit different adhesion behaviour.

Generally, three basic mechanisms of adhesion can be distinguished [90]: (1) mechanical interlocking, (2) physical bonding and (3) chemical bonding. In all substrate/coating systems as well as in general joining technology, these mechanisms individually or together are responsible for adhesion. Very often, one of the mechanisms plays a dominant role. These mechanisms can be subdivided further (Figure 2.23). Mechanical interlocking can be divided into locking by friction and locking by dovetailing, physical bonding into van der Waals bonding and hydrogen bridge bonding, and chemical bonding into ionic, covalent and metallic bonding. In PVD technique several parameters such as residual stress in the coating, contamination at the interface, chemical bonding between the coating and the substrate, physical properties and roughness of the substrate and the precleaning chemical etc. affect the adhesion [91]. Several measures have been taken into consideration to enhance the adhesion such as chemical cleaning of the substrate to remove the organic or inorganic contaminants, plasma cleaning to remove oxide layer from the substrate

surface, interlayer (either multiple or graded) deposition [92] and thermochemical treatment of the substrate before the final coating deposition (duplex treatment) [93].

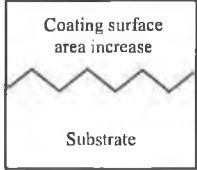
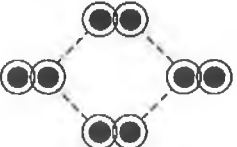
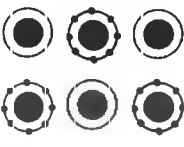
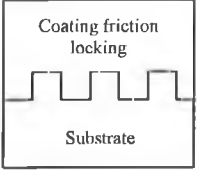

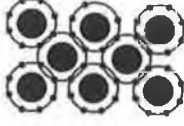
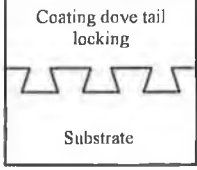

Mechanical interlocking	Physical bonding	Chemical bonding
 <p>Coating surface area increase</p> <p>Substrate</p>	<p>Van der Waals Bonds</p> 	<p>Ionic bond</p> 
 <p>Coating friction locking</p> <p>Substrate</p>	<p>Hydrogen bridge bond</p> 	<p>Covalent bond</p> 
 <p>Coating dove tail locking</p> <p>Substrate</p>		<p>Metallic bond</p> 

Figure 2.23. Schematic diagram of the different bonding mechanisms.

2.6.7. Residual stress

As-deposited coatings are vulnerable to residual stress irrespective of deposition techniques. The total stress is composed of growth (intrinsic) stress due to the structural damage during coating growth and thermal (extrinsic) due the difference in thermal expansion coefficient of coating and substrate. In low temperature deposition techniques growth stress is the major component while in high temperature deposition processes such as thermal CVD or thermal spray, thermal stress can be significant and sometimes even the major component of the residual stress. Residual stress increases the hardness of the coating but excessive stress can reduce the adhesion of the coating to substrate. The compromise between the hardness and residual stress has to be established for optimum performance. A compressive stress is often desired as many coating material are stronger in compression than in tension. Thin metal interlayer beneath the hard coating, multilayer coating with hard and soft layer, or graded coating can significantly reduce the residual stress. As the growth temperature is increased, the structure of the coatings will become denser and the net tensile growth stress will decrease to zero. Also, in the cases when energetic particle bombardment is used during growth, the defect annealing rate will

eventually become higher than the defect generation rate as the substrate temperature is increased and coatings free of growth stresses will result. However, as the temperature is increased the thermal stress will increase. A schematic representation of the total stress in the coatings (both the growth stress, and the thermal stresses are assumed to be of the same sign) as a function of growth temperature is given in Figure 2.24. More on residual stress can be found in Chapter 5.

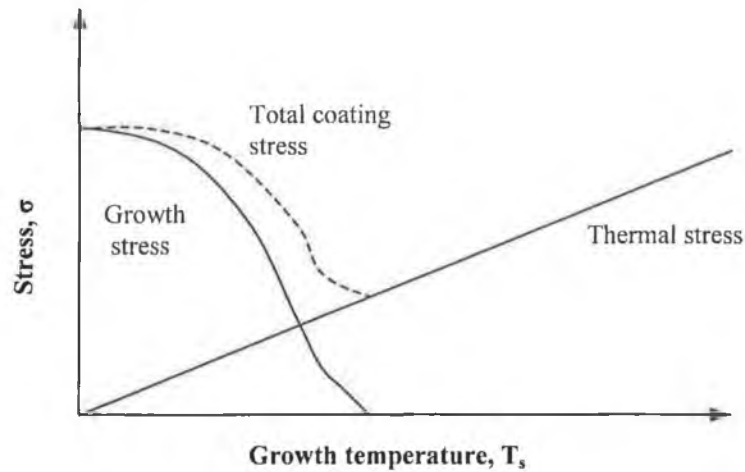


Figure 2.24. Schematic representation of the variation in growth, thermal, and total coating stresses as a function of the growth temperature T_s , [29].

2.6.8. Wear

Wear [11,14] involves the physical removal of material from a solid object in the form of fragments or debris and damage to the component surface as a result of the one contacting surface moving over another surface. Wear can be classified into several general categories: abrasive, erosive, adhesive, fatigue, fretting and chemical wear.

Abrasive wear can result from two surfaces rubbing together, with the harder surface grinding away the softer surface. It can be characterized by a rough appearance, due to the ploughing, scoring, wedge formation or grooving of the softer surface or by a relatively well-polished appearance, if the two interface materials are similar in hardness. Often, work hardening of the surface can take place. Two-body and three-body abrasive wear are commonly observed where the later refers to the situation in which hard particles are introduced between the moving surfaces. Thick, hard, well-adhered coatings are effective in relieving this problem.

Erosive wear, a subset of abrasive wear, is caused by hard particles striking the surface of a component with sufficient force that the surface material is removed by a “microcutting” or gouging action in the areas of impingement. It is characterized by a pitting appearance in the impinged area. Hard and tough coatings can be effective deterrents.

Adhesive wear, like abrasive wear, is caused by loaded surfaces rubbing together. With adhesive wear, high localized temperatures are created by friction at the tips of opposing asperities on rubbing surfaces. These tips can deform and “weld” together due to localized temperatures, only to break and fall away as debris. As the interfacial load increases, the adhesive wear rate increases. Adhesive wear is characterized by a non-oxidized, torn surface littered with coarse metallic debris. Adherent, inert and hard coatings with high thermal conductance can reduce adhesive wear.

Fatigue wear occurs whenever a surface is subjected to repeated high stress loads. With high loads on surfaces, as on gears and bearings, cracks often originate at the surface and progress inward. This is called contact fatigue wear. Eventually, fatigue cracks form on or below the surface, and the surface material breaks away or “pits.” Once initiated, pitting proceeds progressively until retarded by the increased strength of a work-hardened surface or by the application of an adherent hard coating.

Fretting wear occurs when tight-fitting contact surfaces subject to small, relative oscillatory motion or vibrational slip of extremely small amplitude. The process is characterized by the production of very fine oxidized wear debris. Process can also be associated with conditions of vibratory impact in which precursive and fatigue wear may be present.

Chemical wear involves the mechanical damage in the presence of significant detrimental chemical reactions in the contact, initiated by the influence of the environment, in combination with mechanical contact mechanisms.

2.6.9. Friction

Friction is the resistance to relative motion of contacting bodies when moves relative to each other. The degree of friction is expressed in terms of coefficient of friction (μ), which is the ratio of tangential or frictional force and normal force. Two types of friction are

generally observed: sliding and rolling friction. Traditionally, the friction between sliding surfaces are explained by the combined effects of adhesion between flat surfaces, ploughing by wear particles and hard surface asperity, and asperity deformation. On the other hand, adhesion, microslip, elastic hysteresis and plastic deformation are the major contributor for friction in rolling contact. A sliding contact passes through several stages of different frictional mechanism between the running-in period (initial period of sliding) and steady stage period before ending by destruction or breakdown period. The coefficient of friction (COF) is not an intrinsic property of a material and depends on a number of factors such as materials in contact, contact geometry, environment and surface conditions, and the load parameters. Significant reduction of coefficient of friction is possible by the application of thin coating on sliding surfaces; for example friction can be reduced by several orders of magnitude with thin MoS₂ or diamond-like carbon (DLC) coating.

2.7. TRIBOLOGY OF THE COATED SURFACES

The tribological process takes place as the two surfaces are moving in relation to each other and both physical and chemical changes are evident. The complete tribological process in a contact in relative motion is very complex because it involves simultaneously friction, wear and deformation mechanisms at different scale levels and of different types. Recently several tribological mechanism are identified [94-96] including macromechanical, micromechanical, nanomechanical, tribochemical, and material transfer mechanisms. Macromechanical mechanism is defined by the stress and strain field in the contact, plastic and elastic deformations and wear particle formation process and its dynamics and this mechanism can be influenced by coating properties such as hardness, thickness and surface finish and the size and hardness of debris in the contact. The micromechanical tribological mechanisms describe the stress and strain formation at an asperity-to-asperity level, the crack generation and propagation, material liberation and particle formation. In typical engineering contacts these phenomena are at a size level of about 1 µm or less down to the nanometre range. The chemical reactions taking place at the surfaces during sliding contact and also during the periods between repeated contacts, change the composition of the outermost surface layer and its mechanical properties. Increasing attention is being focussed on tribochemical reactions producing reaction products and transfer film, which often control contact behaviour. This has a considerable influence on both friction and wear. Nanomechanical mechanism can control the frictional behaviour at atomic level. Finally, material transfer mechanism can also have significant

effect on ensuing friction and wear behaviour. The relationship between the four described parameters will result in a number of different contact conditions characterized by specific tribological contact mechanisms. Twelve different contact situations can be grouped to represent eight characteristic wear mechanisms as schematically shown in Figure 2.25.

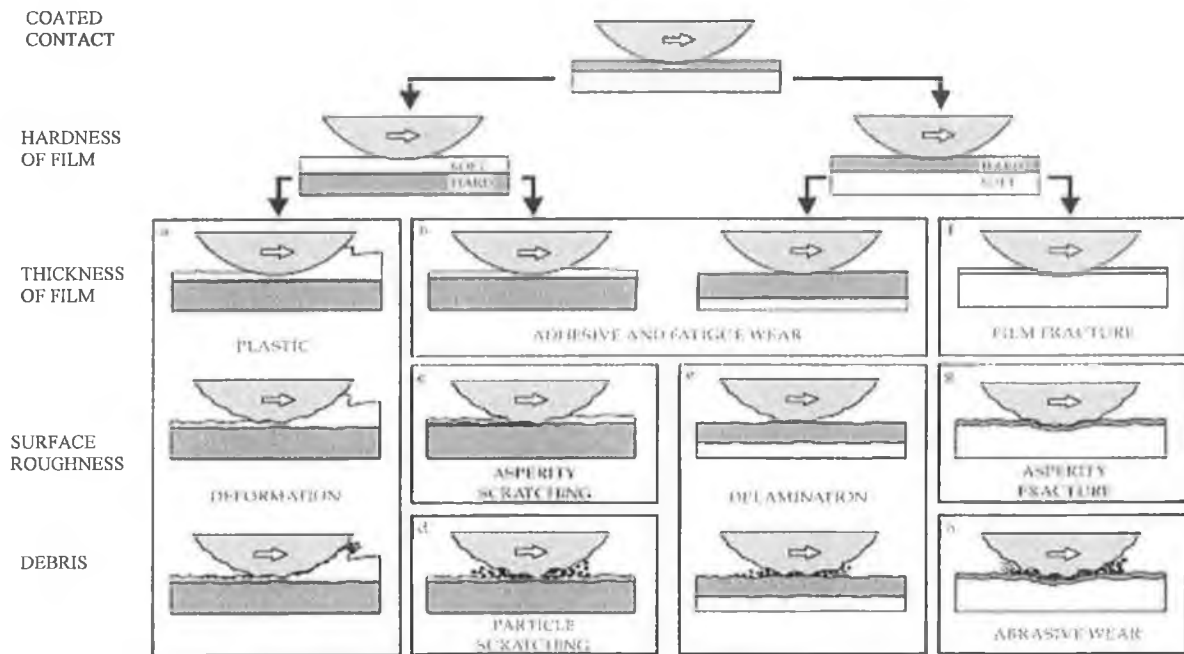






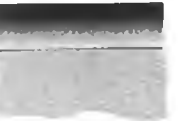
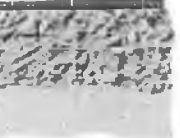
Figure 2.25. Wear mechanisms of coated surfaces [14].



2.8. COATINGS OF DIFFERENT GENERATIONS

For the last two decades many hard coating species like TiN, TiC, TiAlN, DLC etc. have been developed for tribological applications [97,98]. As the demand for advanced material is increasing, several new and modified design of the existing coatings are identified for the future applications [99-106]. In Figure 2.26., a concise development of different coating design for tribological applications is shown and Table 2.1. shortly describes them.

Table 2.1. Coatings of different generations.

COATING	ARCHITECTURE	DESCRIPTION	EXAMPLE	REFERENCE
Single component (Generation I)		<ul style="list-style-type: none"> ☐ Single component coating consists of a single homogeneous material. ☐ After developing the concept of coating for engineering surface, single component coatings are deposited. It is very easy to deposit this kind of coatings. ☐ Metal coatings are the first one to be considered as the single component coating. They have mainly developed for reducing the friction at the surface in tribological application or interconnector in microelectronic applications. 	Cu, Diamond, graphite, Au	
Multicomponent (Generation II)		<ul style="list-style-type: none"> ☐ Multicomponent coatings are composed of two or more constituents in the form of grains, particles or fibres. ☐ Depending on the non-metallic components, multicomponent coatings are nitride-, carbide-, boride- and oxide-based, whereas depending on metallic component multicomponent coatings are Ti-based and to some extent Cr-based and there are very few reports on Al and C based. ☐ The multicomponent coatings can be classified into the following three categories: binary, ternary, quaternary and higher component coatings. Multicomponent coatings are mainly deposited as a compound of metal(s) and non-metal (TiN, CrN, TiC, Al₂O₃, TiB₂) or non-metal and non-metal (SiC, SiN, CN). ☐ Metallic and non-metallic element/elements are added to the binary coating to form ternary quaternary and higher component coatings. ☐ Increasing the number of elements of the coating renders a finer microstructure and a small grain size (increase in strength and elasticity), formation of multi-phase structures (causing a better mechanical and thermal stability), solid solution strengthening, and formation of an external layer as a result of a partial reaction (the two latter effects promoting wear resistance) in thin hard coatings. 	TiN, TiAlN, (Ti, Al,Zr)N, Ti-Al-V-N-C	[99,100,102,103, 107-110]
Multilayer (Generation II)		<ul style="list-style-type: none"> ☐ Multilayer coatings are realised as a layered composite with numbers of repeated layers of two or more materials deposited one upon another. ☐ Better properties are observed in multilayer coatings due to the improvements in hardness, coating/substrate adhesion, load support, resistance for crack propagation and the reduction of the surface stresses. ☐ A multilayer coating with alternate hard and soft layers can allow deflection to occur under load without yielding of the hard layers. This provides combined properties of both hardness and elasticity. Much greater thickness can be achieved than the single layer coating due to lower stress and elasticity. ☐ A multilayered coating can be expected to improve the corrosion resistance due to the increase in coating thickness, discontinuous crystallite boundaries in the columnar structure and alternating interlayer of different compositions. 	Ti/TiN, TiN/TiAlN	[99,100,101,102 103,111-116]

<p>Superlattice (Generation III)</p>		<ul style="list-style-type: none"> ☐ Superlattice coatings consist of large number of isostructural (similar chemical bonding, similar atomic radii and lattice distances) single layer of different materials in the form of multilayer on a nanometer range scale, typically 2-10 nm thickness of the individual lamellae. ☐ Superlattice coatings exhibit entirely new materials with properties and characteristics not directly related individual layer materials. ☐ The high hardness (over 50 GPa) and toughness of the polycrystalline superlattice coatings indicate that they have real opportunity in cutting tool industry. ☐ Several explanations of the high hardness have been proposed including, dislocation blocking by layer interfaces, Hall-Petch strengthening, strain effects at layer interfaces, and the supermodulus effect. 	<p>TiN/VN, TiN/CrN</p>	<p>[117,118]</p>
<p>Gradient (Generation III)</p>		<ul style="list-style-type: none"> ☐ Gradient coatings are a type of multicomponent coating in which the compositions continuously change when moving from the substrate to the coating surface. ☐ This coating offers the possibility to vary the properties of the coating at different depths from the surface with no visible interface, which is common in conventional multi-layered coatings. ☐ A graded coating composition (Compositionally graded multicomponent coating) or structure (Functionally gradient multilayer coating) improves the load carrying capacity by offering smoother transitions in mechanical properties from those of the hard and stiff coating to those of the softer and more flexible substrate and expected to be more effective in terms of adhesion, wear, thermal shock and corrosion resistance. 	<p>TiAlN, Ti/TiC/DLC</p>	<p>[119-124]</p>
<p>Duplex coating (Generation III)</p>		<ul style="list-style-type: none"> ☐ Duplex surface engineering involves the sequential application of two (or more) established surface technologies to engineer the surface of the components in order to produce a surface composite with combined mechanical, metallurgical, and chemical properties because of the addition of the single process advantages and elimination of single process disadvantages. ☐ Among the most possible duplex coating systems, thermochemical treatment (nitriding, carburizing, nitrocarburizing etc.) and coating process (PVD, CVD) is the promising one. ☐ Better adhesion has also been observed due to the reduction of the hardness and stress gap between the coating and substrate avoiding any egg shell cracking and better crystallographic matching between the treated substrate (i.e., nitrided) and the deposited coating (i.e., TiN). Adhesion can be further improved by inserting an interlayer before depositing the coating. ☐ Duplex treatment also improves the fatigue resistance due to the compressive stress induced in the substrate. ☐ Better corrosion resistance has also been reported relating to the fact that the passivation power of the iron nitride compound layer formed during the plasma nitriding process. ☐ The performance of the duplex coating is further improved by the deposition of multilayer coating instead of single layer on treated substrate. 	<p>Plasma nitriding + TiN, Plasma carburising +TiC</p>	<p>[93,125-133]</p>

<p>Nano structured (<i>Generation III</i>)</p>		<ul style="list-style-type: none"> ■ Nanostructured coatings include nanocrystallized coatings with grain sizes in the nanometer range and nanocomposite coatings, as a logical progression of multicomponent coatings toward the nanoscale. ■ Nanocomposites include structures that combine amorphous phases with crystallized one. ■ The high hardness and high thermal stability of these coatings are very promising for surface engineering where they could be used as new advanced hard and protective coatings such as in cutting tool industry. 	<p>TiC/TiB₂, a-C/ TiC</p>	<p>[134-137]</p>
<p>Adaptive or smart (<i>Generation IV</i>)</p>		<ul style="list-style-type: none"> ■ Adaptive or smart coating is a multicomponent, multilayer or nanocomposite, which can change their properties to meet the requirements of the contact conditions depending upon the environment (cryogenic to high temperature or high humidity to low humidity). ■ Smart coatings imply a deep knowledge of the coating structure and composition dependence vs. temperature, contact pressure and environment. ■ The advantage of this coating is the ability of a single coating to act at different environment by self-adaptation. ■ Producing such coating requires following a complex deposition process and advanced deposition system. 	<p>Ti-TiC- TiC/DLC- MoS₂, WC/DLC/WS₂</p>	<p>[138-141]</p>

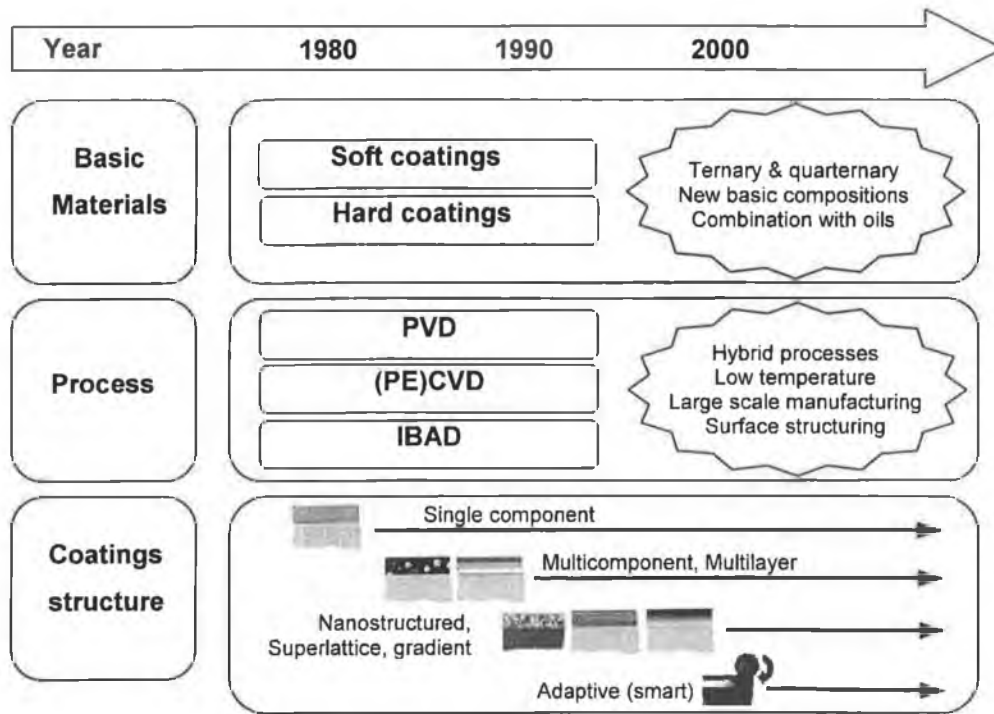


Figure 2.26. Developments of different tribological coatings [99].

2.9. TiN AS A HARD COATING-SHORT REVIEW

Titanium nitride is a member of the refractory transition metal nitrides family, which exhibits properties characteristic of both covalent and metallic compounds. TiN thin coatings have been investigated for more than 20 years mainly owing to their remarkable physical and chemical properties including high surface hardness, high melting point, chemical inertness, good adhesion to the substrate, good thermodynamic stability, pleasant golden colour, enhanced wear resistance, low resistivity and good corrosion resistance at room and elevated temperature [142-145]. These outstanding properties attracted different industrial areas for practical applications such as in cutting and forming tool industries as wear resistance coating, in biomedical industries as biocompatible coating, in semiconductor industry as diffusion barrier coating and in decorative industry as decorative coating.

So far TiN thin coatings have been synthesized by many different deposition methods such as PVD, CVD, and have been extensively studied on their microstructure, chemical composition, mechanical and tribological properties. The conventional CVD method with higher deposition temperatures is used for growing TiN on cemented carbide cutting tools. But conventional CVD methods are not suitable for depositing TiN on steel substrates

because the deposition temperature is higher than the softening temperature of the steels and there is a possibility of thermal damage of the coating itself. For the deposition of TiN on stainless steel PVD and plasma assisted CVD methods are suitable due to the lower deposition temperature. Magnetron sputtering system has been proved to be a successful technique and promoted to an industrial scale for many years. The closed-field magnetron sputtering has even further improved the coating quality and opportunity for depositing on complex shaped engineering commodities [145]. However, the physical and tribological properties of the sputter-deposited coatings were found to have strong correlations with the deposition parameters such as substrate bias, pressure and temperature [146-148]. Reactive sputtering is the very common way to produce TiN coating. But reactive sputtering has shortcomings such as target poisoning and covering of the chamber surface by the insulating coating material (disappearing anode problem). The first problem is usually addressed by using reactive sputtering controller to control the flow rate or partial pressure of nitrogen into the chamber [149]. This will also ensure the deposition of stoichiometric coating, which is important from the property point of view.

Typically the hardness of a fully dense TiN coating on a tool steel substrate is 2000-2500 kgf/mm², which is considered much harder than the substrate [150]. The hardness also depends on the method used and different operating parameters. TiN adheres well to the substrate, but as the thickness increases the adhesion decreases due to the developed residual stress. The deposition of an intermediate layer of Ti metal proves useful in enhancing the adhesion strength of the coating and reducing the overall corrosion speed of the TiN-coated tool steel [93]. The high hardness of TiN makes it suitable for tribological application to increase wear resistance, fatigue resistance etc. [151]. Substrate roughness, coating thickness, hardness and microstructure have substantial effect on the tribological behaviour of TiN coatings [150]. The mechanical properties of TiN are strongly related to its preferred orientation. Most results indicated that the TiN preferred orientation changed among (200), (111), and (220) as the parameters were varied. It has been reported that TiN coating with (111) preferred orientation possesses the highest hardness [152]. The colours of the deposited TiN coatings changed from metallic gray to gold and finally brownish red as the nitrogen content increases [153,154]. It is very easy to primarily access the quality of the golden colour, although colour alone is not the ultimate quality indicator. At the stoichiometric composition, TiN has the f.c.c. structure as shown in Figure 2.27. This phase is stable over a broad composition range, stoichiometric and overstoichiometric, concerning the nitrogen content. Different phases are observed at different nitrogen content

[148] and structural, mechanical and tribological properties vary accordingly [145,155]. Recently substoichiometric coating has also been investigated for wear resistance applications [156,157]. Residual stress is commonly encountered in TiN coating mainly due to the bombardment of the coating during deposition. This residual stress increases coating hardness but decreases adhesion to the substrate.

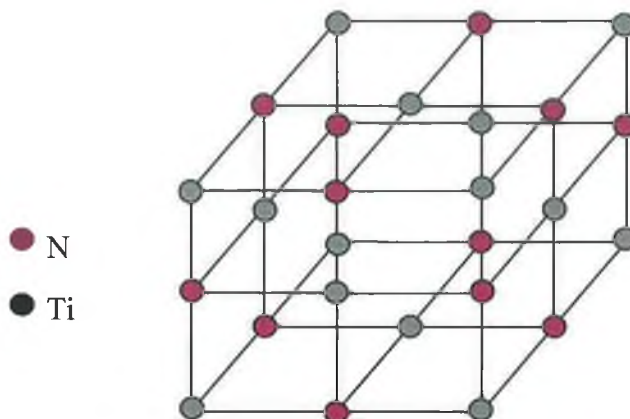


Figure 2.27. Crystal structure of TiN.

But upto now TiN has two main shortcomings in terms of high temperature oxidation resistance and corrosion resistance. The application of such coatings is limited to low temperatures since the TiN tends to oxidize at temperatures above about 600°C [158], with increasing temperature a rapidly multiplying growth rate of the surface oxide drastically contributes to the degradation of its wear resistance properties [159]. In an aggressive environment it does not show good corrosion resistance due to the through pinholes or micro-defects. But dense coating with higher thickness can enhance the corrosion resistance reducing pinhole defect [143]. Another problem in the tribological application is that the hard particles of TiN generated during sliding act as grits which fails the coating system very rapidly especially in a closed system.

2.10. SOLID LUBRICATION

2.10.1. Definition of solid lubricant

A solid lubricant is a material used as powder or thin coating to provide protection of the surface from damage during relative movement and to reduce friction and wear and the name of the lubrication process is called solid lubrication. Other terms commonly used for solid lubrication include dry lubrication, dry-film lubrication, and solid-film lubrication.

2.10.2. Problems associated with liquid lubricants

For centuries, liquid lubricants have been used to suppress or limit contact pressure, reduce friction and facilitate sliding. Liquids also remove frictional heat generated during sliding. Most lubricants contain environmentally harmful chemical additives. A significant amount of these lubricants are released to the environment, either on purpose or by accident. Again, as the contamination level is increased in the lubricant, the disposal cost increases. The liquid lubricant has several health hazard effects like skin damage, damage of respiratory organs and even cause cancer and it has several detrimental effects to the environment. In many cases (e.g., food or textile industry) the presence of liquid is not possible or recommended, or may be forbidden to avoid contamination [160].

Lubricant consumption: 1143 thousand tons(Tt) in a year

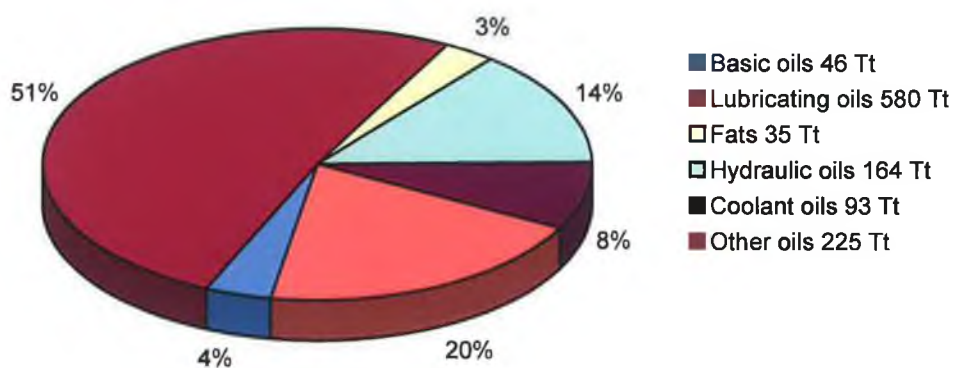


Figure 2.28. Total lubricant and coolant consumption in a year in Germany [161].

A report has shown that the annual consumption of lubricant in Germany amounted to be 1 million ton (Figure 2.28.) [161]. As a result lubrication free manufacturing process is the future demand for the clean environment. The cost of the solid lubricant may be more than offset by diminishing the high costs of recovering, storing, recycling and disposing of large quantities of used, often toxic oils.

2.10.3. Why solid lubricants?

More recently, because of safety and environmental concerns [162], solid lubricants have been rediscovered as a means of greatly reducing or even eliminating liquid flood lubrication. Therefore, there is a steady demand for materials and surface coatings with

solid lubricant ability and dry friction capability. By the use of solid lubricant either no lubricants at all are needed or the amount of lubricants used can be reduced drastically.

2.10.4. Applications of solid lubricant

The general applications of solid lubricant include extreme temperature conditions where other lubricants are prone to degradation or decomposition or solidification, high pressure condition where liquid lubricants squeezes out of the contact area, as additives to fluids and greases, inaccessible locations where servicing is difficult, high dust and lint areas where fluids may tend to pick up dust and lint and in the areas where there is a chance of migrating liquid lubricants.

2.10.5. Characteristics of solid lubricant

The properties important in determining the suitability of a material for use as a solid lubricant should possess some specific property including a lamellar crystal structure with an inherently low shear strength, good thermal stability with no undesirable phase or structural changes at high or low temperatures, good oxidation stability, low vapour pressure, chemically less reactive, higher melting point, sufficient hardness, and good electrical conductivity.

2.10.6. Types of solid lubricants

There are different kinds of solid lubricants found for reducing the friction in different conditions. A general classification was found in the literature as shown in Table 2.2. [163]. Among them the most common solid lubricants are MoS₂, WS₂, PTFE, DLC and graphite [164].

Table 2.2. General classification of solid lubricant coating [163].

TYPE	PRINCIPLE OF LUBRICATION	EXAMPLES
Soft materials	Pure metals	Pb, In, Sn, Ag, Au
	Soft materials at high temperatures	CaF ₂ or BaF ₂
	Other inorganic solids	PbO, PbS or CdO
Lamellar solids	Layered-lattice structure with strong, covalent bonding within the layers, but weak bonding between the layers	Dichalcogenides MoS ₂ , WS ₂ , TaS ₂ , etc., and similar ditellurides and di-selenides; talc
	Adsorbed vapours such as water or organic compounds are necessary to maintain easy shear (low friction)	Graphite and hexagonal boron nitride (BN _{hex})
	Layered structure with fluorination or intercalation used to insert atoms or molecules into the gap between planes, thus widening the spacing	Graphite fluoride or Ag, NbSe ₂
Organic polymers	Polymers with smooth molecular structures (i.e. no side groups), that can slide easily over one another	PTFE, FEP, PFA, PTFCE nylon, acetals, polyimides, metal soaps, waxes, solid fatty acids, esters
Chemical conversion	Surface oxides that reduce local cold-layers welding, and can be more easily sheared than the underlying metal	Oxide films
	Porous surfaces that provide a reservoir for solid or liquid lubricants	Anodized surfaces
	Surfaces with increased hardness to improve friction and wear characteristics	Phosphated surfaces

2.11. MoS₂ AS A SOLID LUBRICANT COATING-REVIEW

2.11.1. General characteristics of MoS₂

Molybdenum disulfide (MoS₂) has a layered molecular structure with individual sheets of molybdenum (Mo) and sulphur (S) atoms. The low shear strength is explained by its anisotropy. The material is comprised of hexagonally packed planes consisted of a layer of Mo bonded on each side by layer of S (Figure 2.29.) and each Mo atom is surrounded at equal distance by six sulphur atoms placed at the corners of a triangular prism. The forces holding the atoms together in each group of S:Mo:S layers are covalent bonds whereas the forces between the adjacent planes of sulphur atoms are weak van der Waals type bonds. All effective strong bonding is within the resulting sandwich planes. The bond strength between the neighbouring sandwiches is very weak. Thus, MoS₂ has a strong structure in

two dimensions and weak in the third [165]. As a result the adjacent planes of sulphur can readily slide over each other, and this is believed to be the low frictional resistance and hence low friction in the sliding direction. This implies that the basal plane of the crystals in polycrystalline coatings lies parallel to the sliding direction for good lubrication. A good book on the MoS₂ lubrication can be found in the reference [166].

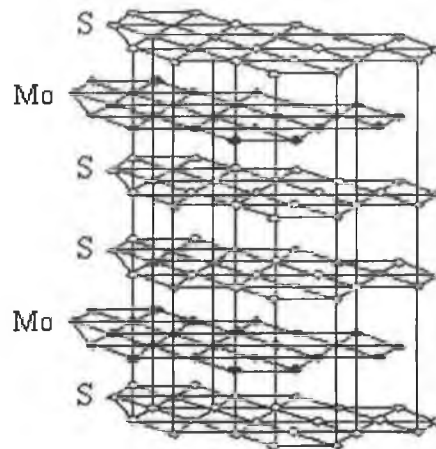


Figure 2.29. Crystal structure of MoS₂.

MoS₂ is an attractive solid lubricant because of extremely low co-efficient of friction of 0.01 in vacuum and the favourable tribological properties are retained from cryogenic temperature upto a maximum temperature of 300 °C or 400 °C (under favourable condition) in air and in high vacuum at temperature upto 800 °C [11,14,165].

2.11.2. Different forms of MoS₂ in application

Usually MoS₂ is used as a solid lubricant in three different forms: dry powders to facilitate assembly of parts or to provide lifetime lubrication, fine particle dispersions in fluids (petroleum oil, grease etc.) to reduce wear rate in a variety of industrial applications and surface coating to reduce friction and improve wear performance in tribological applications.

2.11.3. Deposition methods for MoS₂ coating

At the early stage, MoS₂ coatings are used to deposit either as formulations containing MoS₂ or produced by burnishing. Formulations made with binders and/or dispersants make the coating unsuitable for use in vacuum conditions due to problems of outgassing.

Burnishing has also been used to produce coatings, but these coatings suffer from low endurance due to poor adhesion and uneven transfer of the coating [167]. To solve these problems PVD has become the most common way of depositing MoS₂ coatings. Most of the early work involving the use of PVD methods has been carried out by RF sputtering due to the poor conductivity of the MoS₂ target, and this method is still very much the usual way of depositing MoS₂ coatings [168-170]. RF sputtering is usually carried out by sputtering either a MoS₂ target or a Mo target in a reactive gas atmosphere [171,172]. RF sputtered MoS₂ coatings show lower friction coefficients, better adherence and lower wear rate than coatings produced by burnishing. The influence of MoS₂ coating deposition techniques on performance is well illustrated by Figure 2.30. based on the experimental results of Roberts and Price [173]. The superiority of sputtered coatings is clear in this case. However, the deposition rate is low and a columnar MoS₂ tends to form with RF sputtering.

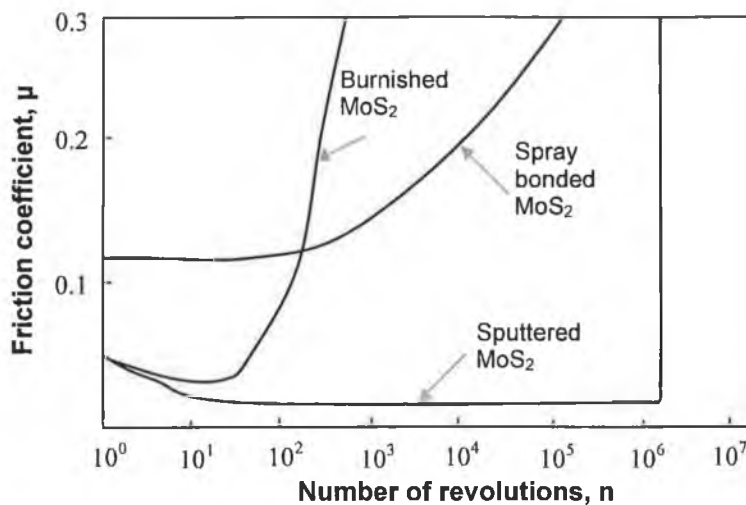


Figure 2.30. Co-efficient of friction of MoS₂ coatings in vacuum environment deposited by various techniques with a sliding speed of 1.2 m/s and a load of 50 N [173].

DC magnetron sputtering has been used for the deposition of MoS₂ coatings [174,175]. The quality of the coatings can be improved by applying a negative potential to the substrate, so that the growing coating is bombarded by energetic ions, thus densifying the structure and improving adhesion. MoS_x coating has also been prepared with an unbalanced DC magnetron-sputtering system by varying the DC power mode. MoS_x coatings deposited by simple DC power tend to form rougher surfaces, have higher edge orientation of crystallites, and have poorer tribological performance than those by bipolar-pulsed DC power [176].

DC closed-field unbalanced magnetron-sputter ion plating (CFUBMS) as a means of depositing MoS₂ overcomes some of these problems, and has the advantages of close compositional and microstructural control, good adherence and good uniformity. If the magnetic field of the magnetron is unbalanced, the intensity of the bombardment is increased and further improvements can be achieved using a multi-magnetron system, in which unbalanced magnetrons are used in the closed-field arrangement. Rechberger et al. [175] have studied the performance of cutting tools (such as end mills, drills) coated with MoS₂ coatings produced by CFUBMS and obtained good machining results with different alloys, the main improvements being in workpiece surface finish, productivity and tool life.

2.11.4. Parametric effects on sputtered MoS₂ coatings

Thin sputter-deposited MoS₂ coatings were developed some three decades ago and have been studied in great detail over the past 20 years because of their applications as solid lubricants principally for space lubrication applications [177]. The crystal structure of the coating, coating thickness, substrate material, roughness and the environment in which it operates especially humidity, have considerable influence on the tribological properties of the coating. Other factors that greatly affect the tribological properties of MoS₂ coatings are their densification and adhesion onto the substrate.

2.11.4.1. Crystallographic orientation

Two parameters related to the crystal structure of MoS₂ are thought to be of particular importance for solid lubrication [165,178]: the adhesion of the coating to the substrate surface, and the crystallographic orientation of the platelets in the coating. Previous studies have concluded that rubbing produces the parallel orientation in the MoS₂ coating [167,168,170,174]. Coating-substrate adhesion is believed to occur mainly through MoS₂ edge plane sites and should strongly influence the wear life of the coating: the stronger the adhesion, the longer the wear life. MoS₂ coating orientation should affect the coefficient of friction. Tribological studies have shown that a lower coefficient of friction is obtained with MoS₂ coatings on the condition that the (002) basal plane is preferentially oriented parallel to the sliding surface. Such a basal orientation also improves the resistance to oxidation. Conversely, the edge oriented planes such as (100) or (110) can easily react with oxygen and water vapour and result in the degradation of the lubricating and wear resistance of MoS_x coatings [179,180].

The first generation RF sputtered MoS₂ coatings were porous with a columnar plate morphology perpendicular to the substrate; these coatings are called Type I coatings [169] (Figure 2.31.). Type I coatings show basal plane orientation perpendicular to the substrate, although a layer of crystallites is formed at the interface between the substrate and the Type I coating, which have basal plane orientation parallel to the substrate due to the strength of chemical bonding between the MoS₂ 'edge' plane (100) and the substrate. Basal plane orientation parallel to the substrate is the optimum orientation of MoS₂ for good friction properties [181]; this type of coating known as Type II.

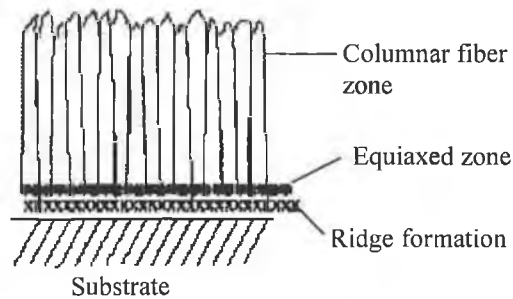


Figure 2.31. Initial MoS₂ RF sputtering.

Type I coatings are columnar and tend to be more porous than Type II coatings, and the former enhances the formation of MoO₃ in humid air, which results in an increase in friction coefficient and a decrease in coating endurance compared to Type II MoS₂ [170]. Type I coatings lubricate, as the columnar plates tend to detach near to the interface with the substrate and reorient in lubricating particles; this occurs after a few sliding runs [182] and results in the formation of a buffer layer a few tens of nm thick. This layer splits and separates from the bottom of the coating [183]. Detachment of the coating is promoted by the inherent porosity of the Type I structure [165]. Type II coatings are denser than Type I and the basal plane orientation develops in and below the wear track, due to stress-induced crystallisation [182]. These microstructures can be deposited by adjusting the deposition conditions (pressure, deposition rate) or by the incorporation of co-sputtered or multilayer dopants [183]. Crystal structure of sputtered MoS₂ has a strong influence on the behaviour of coating endurance and co-efficient of friction [165]. The amorphous coating act like an abrasive and exhibit poor lubricity i.e., high co-efficient of friction (0.4), whereas polycrystalline coating with proper stoichiometry exhibit effective lubrication with low co-efficient of friction (0.05) and long endurance life.

2.11.4.2. Composition

The coefficient of friction of MoS₂ coatings depends strongly on the stoichiometry i.e., the ratio of sulphur to molybdenum atoms [174,184-186]. The sputtered MoS_x has the x values in the range of 0.8-2.3 but most frequently reported values are in the range of 1.2-1.8 for better combination of wear and friction properties. Dimigen et al. [186] found that a rather low Ar pressure as well as a substrate bias potential can cause a high sulphur deficiency in the sputtered coating compared with the target material; this can be compensated by using an Ar-H₂S sputtering atmosphere. A low value of coefficient of friction is sustained even for a substantial Mo excess (S:Mo=1) whereas a further decrease in sulphur content can lead to abrupt increase in co-efficient of friction. Similar result also observed in another study [185].

It is known that MoS₂ with hexagonal structure exhibits an excellent friction reduction effect. The literature [187] reports the influence of the composition on the crystalline structure of MoS_x and points out that it is possible to form hexagonal structure of MoS₂ coating if the x value of the MoS_x coating is greater than 1.1. The content of the crystalline structure increases with increasing x values, which will improve the lubrication property of the MoS_x coating with a value of 1.287. The chemical composition of these MoS_x layers with respect to the x value is affected by various process parameters.

2.11.4.3. Contamination during deposition

Oxygen, carbon and hydrogen are often contaminants of the MoS_x coatings and affect the overall performance of the material. Contamination levels of O and C in the range 5-15 at.% are frequently reported [170]. The accumulation of oxygen as a substituent for sulphur is reported in literature [188]. Tests conducted at various O₂ partial pressure show that stoichiometric MoS_x exhibits friction independent of partial pressure of oxygen while nonstoichiometric coating has shown dependence of friction on the actual partial pressure of oxygen. This can be explained by the fact that the unsaturated bonds in the nonstoichiometric coatings may cause adsorption of ambient gases, which may strongly affect the coefficient of friction [189]. The presence of oxygen in the sputtering chamber has a major effect on the crystalline orientation, morphology, friction coefficient and wear life of MoS₂ coatings [190]. Results [169,170,182] have shown that very pure thin coatings of MoS₂ grown under ultrahigh vacuum conditions yield friction coefficients approximately an order of magnitude smaller (0.001) [191,192] than those obtained with conventional high-vacuum coatings. Most of these coatings were suitable only in vacuum

and at 0% humidity. To reduce the water vapour content in the vacuum chamber, a titanium target was sputtered during ion cleaning of the substrates prior to deposition to produce a gettering effect. The titanium was then used to deposit an interlayer, which led to an improvement in coating adhesion (critical load above 120 N) [193].

2.11.4.4. Surface roughness

The influence of surface roughness has been studied by Roberts and Price [173] and Roberts [194] and they have observed that with a higher roughness of $R_a=0.12 \mu\text{m}$, the coefficient of friction decreased from 0.02 to 0.01 with good (250,000 revolutions) coating endurance. For a smoother coated surface of $R_a=0.04$ the coefficient of friction was considerably higher, in the range 0.02 to 0.04 and the coating endurance only 20,000 revolutions. Roberts [195] suggests that for a $1 \mu\text{m}$ thick coating, there exists an optimum level of substrate surface roughness at which friction is minimized and coating endurance is maximized.

2.11.4.5. Thickness

The reported MoS_2 sputtered coatings with favourable tribological properties are in general very thin with thickness within the range of 0.1 to $2 \mu\text{m}$. Some decrease of thickness can be assumed to take place during sliding. Spalvins [165] has found that only a very thin coating of about $0.2 \mu\text{m}$ is required for effective lubrication. Minimum values of co-efficient of friction has been measured in another study [174] at coating thickness of about $3 \mu\text{m}$ for smooth surfaces and $1 \mu\text{m}$ for rougher surfaces in pin-on-disk experiments.

2.11.4.6. Environment

MoS_2 coatings have very favourable tribological properties in a vacuum environment. MoS_2 properties have been shown to degrade when in contact with humid air, which causes an increase in friction co-efficient and a decrease in coating lifetime. It is recommended that the humidity level should be below 5%, or failing this below 20%, to achieve a good tribological performance in an air environment [196].

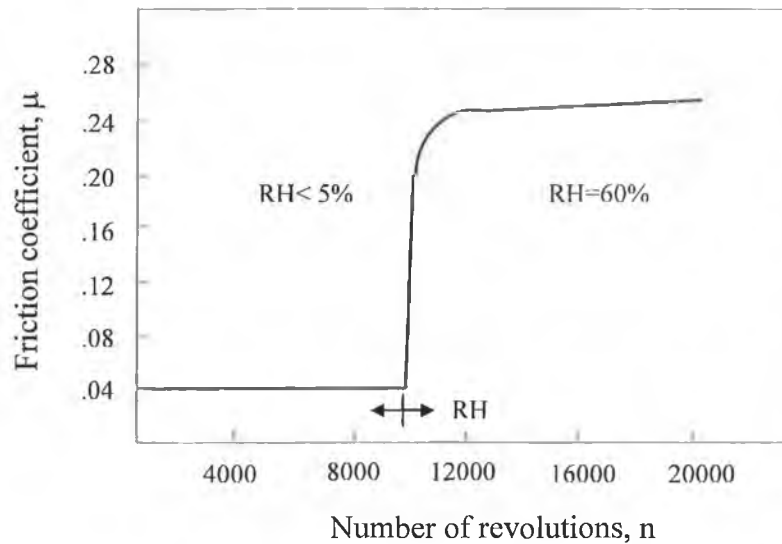


Figure 2.32. The influence of relative humidity on the co-efficient of friction [184].

The study of the effect of relative humidity on sputtered MoS_2 coating has revealed an increase in the coefficient of friction from 0.05 to 0.27 and a significant increase in wear when the relative humidity (RH) was increased from 5% to 60% as shown in Figure 2.32. [184]. Similar observation has also been reported by Niederhiiuser et al. [197]. The effect of humidity on the friction and wear of sputtered MoS_2 coatings has been explained as being due to the formation of oxides in the contact interlayers under humid condition and that oxidation product is not favourable for reducing friction. Fayeulle et al. [198] have discussed in detail the formation process of different Mo and Fe oxides that can be assumed to occur in these kinds of contacts. Experimentally they have observed that the wear rate of MoS_2 coatings is considerably lower in argon than air, which can be explained by the fact that molybdenum oxides are formed more slowly in argon than in air.

2.12. NEW GENERATION COATINGS WITH SELF-LUBRICATION

There has been considerable interest in identifying and developing solid lubricant coating system, which offer suitability in using higher temperature and pressure than liquid lubricants. In most of the cases solid lubricant coating has provided good lubrication but not very effective during sliding as the surface hardness is not high. Solid lubricants coatings, however, worn away rapidly and thus require some mechanical means for replenishment. Another problem with the solid lubricant is that some solid lubricants i.e., MoS_2 can provide good lubrication in vacuum or inert gas environment but they loose their lubrication property in humid weather. This is impractical for many hard-to-reach surfaces

in motion and has prompted recent attempts at extending sliding life of solid lubricant coatings [199].

Soft metal coatings [200] have been used as solid lubricants for space and other specialised applications but again, these have poor wear properties and cannot be considered for general wear protection. Diamond-like carbon (DLC) coatings [201] are hard and have lower friction than the hard nitride coatings and are starting to be used to protect some relatively lightly loaded mechanical components, but the true DLC coatings are very hard with high internal stresses and tend to be brittle, have poor adhesion and are unsuitable for highly loaded applications. In order to reduce the internal stresses, various metals are added. The Me:C coatings are less brittle and are also much softer [189]. They can be deposited with excellent adhesion and can be used at moderately high loads. The coefficient of friction is low, typically 0.15 and the wear properties are good. However, these coatings are not true solid lubricants in the sense that they do not provide an efficient transfer film on the opposing surface.

Ideal solid lubricant should have the properties of hard surface while providing lubrication. Several attempts have been made to improve the strength of the soft solid lubricant coating especially MoS₂ while maintaining good lubrication property in humid and terrestrial environment. Current researches have addressed the solid lubrication issues using three different approaches as follows (Figure 2.33.):

- (a) inclusion of metal doping in solid lubricant coating (Composite solid lubricant coating)
- (b) solid lubricant coating layer on top of hard coating layer (Layered solid lubricant and hard coating) and
- (c) inclusion of solid lubricant in a hard coating matrix (Hard-solid lubricant coating).

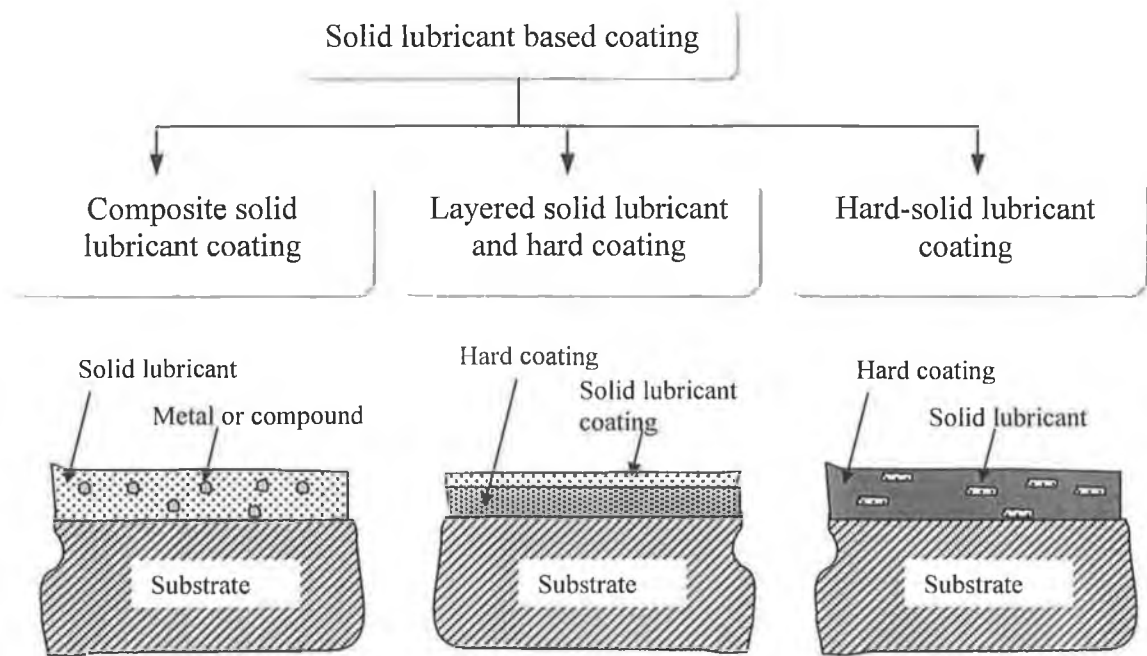


Figure 2.33. Classification of solid lubricant based coating.

2.12.1. Composite solid lubricant coating

As the solid lubricant coatings are soft, easily worn and some are prone to humid environment, the first step to modify the properties of the coating is to add metal or sometimes compound (dopants) in the form of composite or composite multilayer coating. The addition of dopants improves the tribological properties by changing the structure of coating. Metal or compound have been co-deposited with MoS_2 , as MoS_2 failed to provide lubrication in humid environment, although generally not with the primary intent to make the coating harder [197,202,203]. The range of concentration for the dopants has been varied up to as much as 50%. This group has showed an improved lifetime and hardness but it is not possible to reach high hardness because of the soft lubricating matrix.

The most widely studied metal inclusion in MoS_2 is Ti [204-211], which not only improves the overall tribological properties of MoS_2 , but also increases the hardness. More recent coatings of MoS_2 with titanium (MoST^{TM}) [212] deposited by closed-field unbalanced magnetron sputtering have exhibited high hardness (1000-2000 VHN), extremely low coefficient of friction (0.02-0.08) depending on the load and atmospheric condition (humidity), remarkably low wear rate and even at high humidity and excellent adhesion. A thin adhesion layer of Ti was deposited first and on top of that a coating consisting of MoS_2 and Ti is deposited for this composite coating. The coating thickness is typically 1

μm . The structure was amorphous or consisted of very small crystallites. No multilayer structure was observed.

It has been assumed that the distortion caused by the presence of Ti atoms within the MoS_2 structure is responsible for the increase in hardness and reduction in the sensitivity of the coating to humidity. Although the exact arrangement of the Ti atoms are unknown but it is believed that Ti atoms are situated between the neighbouring S planes as represented in Figure 2.34. The amount of metal in the coating is critical in defining the properties. When the amount of Ti in the coating is increased the hardness also increases to a maximum of about 2000 VHN at around 18% Ti content. Above this level, the solubility level of the Ti is exceeded and multilayers are formed. When this happens, the good tribological properties deteriorate. No real difference in the properties was observed from the addition of several other metals such as zirconium and chromium. The mechanism of metal introduction in the lattice parameter of MoS_2 was probably similar [206]. MoST coatings are now being used successfully in a wide range of applications. Many results in the field of metal cutting, metal forming, gears, bearings and various automotive applications have been published [213-215].

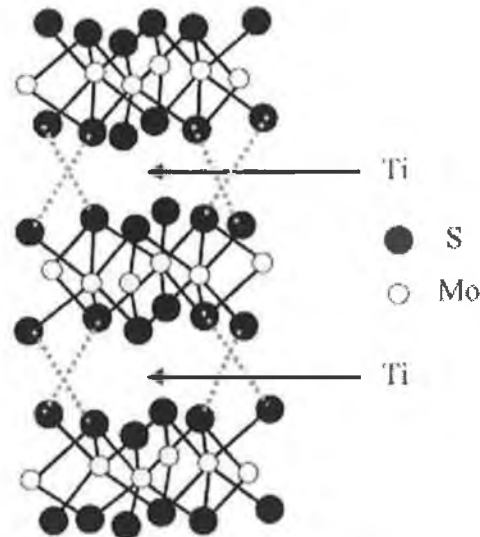


Figure 2.34. The structure of MoS_2 showing the probable positioning of the titanium atoms in the MoST structure.

With the same idea of Ti inclusion Cr has also been doped in MoS_2 coating to improve the wear resistance [181,216,217]. Optimum tribological properties again also depend on the correct amount (8%) of Cr doping. Au [218] may serve to saturate the active edge sites of the MoS_2 crystallites, thereby aiding the preferential growth of the tribologically

favourable basal plane. Other materials like Pb, Ni or Sb [219], Al [220] may preferentially oxidize, protecting the MoS₂ itself from oxidation and improved tribological properties. Another possibility of reducing the sensitivity of MoS₂ to water vapour and oxidation and to suppress the formation of porous, columnar microstructures is to add a moisture-repellent substance such as PTFE [221]. Co-sputtering metal oxide such as SbO_x, PbO and compounds like LaF₃ with MoS₂ have also been investigated [203,222].

Another technique for adding a metal or compound to solid lubricant is by the use of repeating layers, sometimes on the nanometer scale in thickness [223]. By optimising the metal layer thickness for a fixed MoS₂ thickness, and then optimising the MoS₂ for a fixed metal layer thickness, the sliding lifetime of 4-6 times has been increased than that of a comparable thickness, pure MoS₂ coating. MoS_x/Ti interfaces promoted the growth of the (002) basal plane and the degree of (002) basal orientation was dependent on the number of MoS_x/metal interfaces. [224,225]. The tribological performance of metal-MoS₂ multilayer coatings can be generally attributed to the optimisation of the MoS₂ structure, degree of basal orientation, grain sizes and density in nanoscaled layers [226]. WS₂/MoS₂ nanometer-scale multilayer coating (superlattice structured multilayer coating) having dry lubricating characteristics showed potential for improved endurance with respect to current MoS₂-based low friction coatings and may be suitable for use in more severe friction conditions [227].

Instead of considering MoS₂ as primary solid lubricant, dopant has also been added to the soft graphite to form carbon based coating. C-based composite solid lubricant coatings, graphit-iCTM with a thin adhesive Cr layer and a co-deposition of C and Cr on top of that and Dymon-iCTM, a hydrogenated, amorphous, carbon coating (a-C:H) have shown excellent tribological performance [228]. Again the amount of dopants (20% Cr or less) in the carbon is the crucial factor for optimum performance. C-Ag co-sputtered coatings substantially increased the wear resistance and decreased friction probably due to the small size of the Ag grains and also to the spherical structure of carbon nanocages entrapping them [229]. Multiple dopants (Cr, Ti, B and N) with carbon forming composite coatings (CrTiBCN+CCrTiB) have also exhibited high hardness, low coefficient of friction and low wear rate [230].

2.12.2. Layered solid lubricant and hard coating

In this group, normally soft or solid lubricant coatings are deposited on top of hard coatings with the intention to reduce the coefficient of friction by the top layer and load bearing and hardness effect from the hard layer. This combined approach can help to improve the performance of the coating in tribological contact but have shown an improvement over limited period of time because of the short lifetime of the soft lubricating top-layer.

Solid lubricant coating by PVD, CVD and polymer deposition techniques on top of hard coating layer (TiO_2 and Al_2O_3) by thermal spraying has improved wear resistance, compressive strength and load bearing capacity combined with low friction coefficients and a good tribological behaviour under dry sliding conditions [231]. Layered composite coating of $\text{TiN}+\text{MoS}_2$, where TiN coating deposited by ion plating and MoS_2 coating deposited on top of that by magnetron sputtering techniques has shown excellent fretting-resistant performance than the single layer TiN or MoS_2 coating under the same testing conditions. The solid lubrication property of MoS_2 coating could be fully developed by a strong support from the underneath TiN coating [232]. MoS_x thin coatings deposited by ion beam enhanced deposition (IBED) and magnetron sputtering (MS) onto the surface of IBED Si_3N_4 and TiN thin coatings [233] has shown better wear resistance than that of single IBED Si_3N_4 and TiN thin coatings.

The milling tests have confirmed the beneficial effect of a thin sputtered deposited MoS_2 layer deposited upon the multi-layer nitride coatings. The wear rate is very low for most of the tool life and grows rapidly only when the MoS_2 coating is completely removed from the cutting edge [234]. MoS_2 coating grown on TiN coated steel substrates in a graded structure by ion-beam-assisted deposition has been investigated [235]. The formation of graded structure is advantageous since it may extend the wear life of lubricating surface. The TiN rich interface provides good adhesion to the metal substrates as well as the required mechanical integrity. The presence of the TiN-rich interlayer can also help metal atoms from diffusing into the coating from the substrate, which often causes rapid degradation of the lubricating surface at elevated temperature. A thin MoS_2 layer on top of TiAlN has shown better result than TiN topped with MoS_2 for dry machining applications [236]. In this way, friction between the tool and the chip is considerably lowered, thus facilitating chip evacuation. Although the bulk of this relatively soft layer is removed very

quickly during machining, it is reported that its beneficial effect is maintained for extended periods. This is attributed to the fact that small quantities of MoS₂ remain trapped within the surface morphology of the hard coating where it remains active as a lubricant. The MoS₂ coating on top of TiN coating showed much better fretting behaviour than their single layer counterparts through the synergetic effect of single coatings [232].

MoS₂ top layer deposited on DLC interlayer by unbalanced magnetron sputtering technique has effectively improved the wear behaviour of MoS₂ coatings under various loading conditions and low friction coefficient of 0.05 even in atmosphere of 90% RH [237]. Friction-reducing double-layer coatings consisting of hard underlayers (B, TiB₂, B₄C, and BN) with an added upper layer of MoS₂ solid lubricant prepared by the dual fast atom beam technique has shown 50% lower friction coefficients and high durability [238]. Another multilayer approach with a hard coating like TiN, TiCN or TiAlN beneath MoS₂/Ti composite layer has proven better result for cutting and forming tools than the MoS₂/Ti composite layer. The exact reasons are unknown but the improvement is probably associated with the additional support offered by the hard coating [213]. MoS₂/Ti on top of CrN coating has also shown a promising alternative for high wear low friction applications [239]. Except the MoS₂, sputtered WC/C solid lubricant layer on top of arc evaporated TiAlN coating within the same chamber have resulted an excellent wear characteristics with low friction [240,241].

2.12.3. Hard-solid lubricant coating

Impregnation of solid lubricant in metal has proved significant improvement in tribological properties in the past years [11]. Instead of adding solid lubricant in the bulk material, similar idea can be extended to the addition of solid lubricant in hard coating for supplying lubrication during sliding. By combining materials having quite different properties (hard and low friction), it is hoped to tailor the functional characteristics of the coating to the needs of a particular application and tribological environment. The hard phase should provide wear, scratch and abrasion resistance and perhaps load-bearing capacity for the coated surface. The soft phase should lower the friction coefficient between the coated and counterpart (which may also be coated) surfaces. As the hard phase wears down and the lubricant is removed from the tribo-contact, new reservoirs of the lubricant are gradually exposed and friction remains low even after prolonged rubbing. The trade-off of the lubrication effect from soft phase with the expense of hardness of the hard phase has to be

properly controlled by the appropriate amount of lubrication phase in the hard phase. Because the lubricating phase is spread throughout the total thickness of the layer, the lubricating effect is maintained during the entire lifetime of the coating.

Co-deposition of Al_2O_3 and MoS_2 composites by resistive heating evaporation [242] with optimum weight percentage (40%) of MoS_2 has shown 2-9 times wear reduction than pure Al_2O_3 . Chemical vapour deposition (CVD) [243,244] of MoS_2 and TiN composite coating (distinct phases of TiN and MoS_2) rich in MoS_2 at the coating surface with TiN as the major phase near the substrate interface has demonstrated encouraging friction (0.07 to 0.3 in atmospheric conditions) and wear characteristics against silicon nitride. TiN- MoS_2 coatings produced by DC co-sputter deposition from a single unbalanced magnetron target composed of TiN and MoS_2 halves [245] have demonstrated high hardness exceeding 20 GPa and friction coefficients of about 0.1 by selecting suitable composition and deposition parameters. TiN- MoS_2 has also been deposited by co-sputtering Mo and Ti target in H_2S and nitrogen gas environment [246]. TiN+ MoS_x coating has been further deposited by combined PVD techniques such as cathodic arc evaporation for TiN deposition and dc magnetron sputtering for MoS_2 deposition [247] and E-gun evaporation for TiN deposition and magnetron sputtering for MoS_2 deposition [248]. Although these coatings haven't shown any distinct phases of MoS_2 but the improved tribological behaviours have been attributed to the formation MoS_2 during sliding from Mo and S elements.

Changing the base material similar composite coating has been developed by co-sputtering of MoS_2 and TiAlN. It is believed that using MoS_2 in a hard matrix of TiAlN₂ could hinder the oxidation process and improve the wear resistance of the material making it to an ideal solid lubricant [249]. TiB_2 has also been used as hard matrix to form solid lubricant based coating by incorporating MoS_2 or C as solid lubricant and has exhibited both high hardness and low friction coefficient [250-253]. A friction-reducing effect has been observed only at C concentrations above 66%, but at low concentrations of MoS_2 . With both types of lubricants, a trade-off between hardness and friction coefficient has been found. Nanocomposite TiC-C coatings with hard and soft phases (TiC phase, a distorted TiC* phase, and an amorphous carbon phase) have shown low wear rate and low friction due to the combined solid lubrication and hardness effect [254].

Metallic element such as silver has been added into hard matrix WC [255], TiN [256] and TiC [257] or copper into TiN [258] hard matrix to form composite hard solid lubricant

coating. Recently, TiN coating deposited by PACVD has shown to reduce the friction coefficient in ball-on-disc testing with low chlorine content. The drop of the friction coefficient to low values after a running-in period is attributed to the formation of an interfacial lubricant film on top of the TiN coating in combination with humidity. The chlorine is assumed to be easily released from the coating when its concentration is exceeding the solubility limit in TiN. But an upper temperature limit of 70 °C and a lower humidity limit of about 10% have been reported for this low-friction effect [259].

Instead of co-depositing the soft and hard phase together, there is another three-dimensional coating approach for inserting solid lubricant into the hard phase by intentionally made solid lubricant reservoir groove in the hard coating. Filling of MoS₂ in micrometer-sized grooves produced by laser in a Ti-TiC-TiC/DLC nanocomposite coating [260] has demonstrated the benefits of solid lubricant reservoirs in promoting a long wear life and low friction in dry environments due to a hard support with a constant lubricant supply to the friction contact.

2.12.4. Selected application area of low friction coatings

2.12.4.1. Dry cutting/machining industry

Today there is a strong tendency to move away from the use of conventional amounts of cooling lubricants in machining and cutting due to the huge cost involved in lubricant, lubrication system, disposal of the lubricants and most importantly environmental concern [161] despite having the beneficial effect of lubricant such as reduction of friction, removal of chips and transportation of heat from contact zone etc. [160]. Minimal lubrication is the new slogan. The preconditions for this technology are research activities, which are concentrated on the adoption of cutting conditions as well as on the development of new drilling tools with improved properties for dry machining by optimising manufacturing technologies, by alloying of cutting materials of sufficient toughness and high hot hardness, by adapting drill tool geometries and finally by coating of the tools [261].

Coatings for dry machining must satisfy several conditions, depending on the material to be machined. Conditions that are considered to be most important are resistance to the high temperatures associated with dry machining (i.e., high hot hardness and resistance to oxidation) combined with a low thermal conductivity for the protection of substrate

material from heat. In addition to this basic requirement, it is also desirable that the coating should be chemically inert with respect to the counterface to avoid adhesive interactions that may lead to edge build up, and that the coating display a low coefficient of friction to facilitate the transport of hot chips away from the cutting zone. Such a trend in machining technology has also been influenced decisively in the last 5 years by the development of new hard and protective coatings for industrial manufacturing. These include established coatings with a low coefficient of friction (e.g. diamond-like carbon (DLC) coating [262], MoS₂ [175], MoST [263], Dimon-iC and Graphit-iC [228]) and hard coatings with high resistance against aggressive wear and thermal load at the cutting edge (e.g. TiAlN, AlTiN, TiCN, TiAlCN and CrN coatings). Of all these hard coatings, Ti-Al based coatings (TiAlN with various Ti:Al ratio, TiAlCN multilayer and multilayered TiN/TiAlN structure) have been the most intensely studied and tested in practice for various machining operations, including dry cutting and high speed cutting (HSC) processes.

The combination of a hard coating and a solid lubricant coating has been proposed as a further step in improvement of dry cutting. Recent studies have suggested [240,241] that the deposition of a hard/lubricant (WC/C on TiAlN) coating on cutting tools seems to be a very interesting alternative to reduce the enormous amounts of cooling emulsion in metal cutting and to work with minimal or no lubrication in a number of applications. The combination of hard/soft coating layers allows improved chip flow with a lowered coefficient of friction and reduced cutting force. A possible mechanism on the role of the low friction coating during the drilling operation has also been offered (Figure 2.35.).

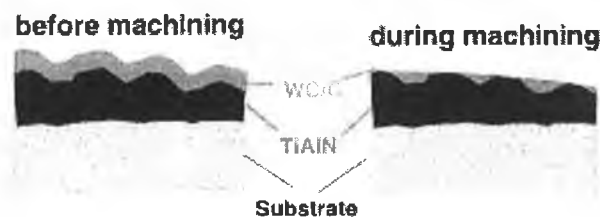


Figure 2.35. Schematic illustration of a possible mechanism on the role of the low-friction coating during a machining application [240].

Gilmore et al. [245] have suggested co-sputtered TiN-MoS₂ coating as cutting tool coating for dry machining. Another study has proved that suggestion due to the increased lifetime of drills by almost twofold with respect to the TiN coating and up to fivefold with respect to an uncoated drill with TiN+8%MoS_x coatings in a dry drilling operation [247]. MoS₂/Ti

coatings (MoST) deposited on top of TiN, TiCN and TiAlN have exhibited improved performance for several applications like cutting tools and forming tools under dry and lubricated conditions compared to their single layer counterpart [264,265].

The concept of combined coatings will open new fields for the use of light metal alloys in tribological applications and a significant decrease, or even replacement of grease and fluid lubricants is possible in many engineering applications with the proper hard/solid lubricant coating. It is not surprising that in future solid lubrication may be imposed by legislation (for example for environmental protection) and also for cost savings (as the treatment of used lubricants is very expensive) [264]. In that case the combination of solid lubricant and hard coating for dry machining might prove its potentiality [266]. The compromise of hardness and solid lubrication effect in the coating would depend on the particular requirement.

2.12.4.2. Aerospace industry

The mechanical, environmental and endurance requirements of the aerospace applications exceed the available lubrication and wear-reduction technologies, demanding novel materials and advanced technologies. So for aerospace applications new coatings combining the good tribological and environment endurance properties are necessary as soft lubricant coatings alone cannot provide that combined properties. The potential of new generation composite coatings with a soft lubricating phase for solid lubrication and a tough phase for bearing the load is worth mentioning in this regard.

Voevodin et al. [138] developed coatings consist of 1-2 nm WC and 5-10 nm WS₂ grains embedded in an amorphous DLC matrix. These WC/DLC/WS₂ nanocomposites demonstrate low friction and wear in tests performed in high vacuum, dry nitrogen and humid air. Coatings are found to adapt to the test conditions, which results in: (1) crystallization and reorientation of initially nanocrystalline and randomly oriented WS₂ grains; (2) graphitization of the initially amorphous DLC matrix; (3) reversible regulation of the composition of the transfer coating between WS₂ and graphite with environmental cycling from dry to humid; and (4) possible DLC/WS₂ synergistic effects, providing friction reduction in oxidizing environments. These adaptive mechanisms achieve low friction coefficients of 0.02-0.05 and an endurance above two million cycles in space simulation tests. This also provides stable coating performance and recovery of low friction in tests simulating ambient/space environmental cycling. Based on the similar idea

MoS₂ filled grooves on a functionally gradient Ti-TiC-TiC/DLC coating shown an ultra-low friction of 0.02 in conditions of low humidity [260]. When the humidity was raised, the base hard coating with the TiC/DLC layer provided a friction coefficient of about 0.15 and an extended wear life. The storage of an intact MoS₂ lubricant below friction contact ensured a good friction recovery when the humidity was cycled from high to low. Due to the better self-adaptation to friction environments and it might be possible candidate for aerospace applications subjected to the environment cycling. It is quite obvious that in near future this kind of composite soft-hard coating will be more attractive for the aerospace and vacuum environments.

The conventional solid lubricant coatings are sometimes oxidized by collisions with high velocity atomic oxygen combined with intense UV irradiation in aerospace applications. This causes the increase of friction of the coated surface. Surface oxidized BN/Cu low friction coating synthesized by magnetron co-sputtering combined with KrF excimer laser irradiation has been suggested for several aerospace applications. The low frictional property is maintained even after oxidization and prolonged UV irradiation [267].

2.12.4.3. Automotive industry

Due to the demand of high power and high-speed automotive engines, the engine moving parts have to be improved in tribological characteristics. High coefficient of friction among the engine parts leads lower fuel economy, durability, and environmental problems [268]. From an environmental point of view, lower fuel economy also means higher environmental pollution. In an engine, the major sources of frictions are valve train, piston system, crank and bearing system. Tailored hard-low friction coatings such as MoST [263] have significantly improved the service life of automotive parts such as fuel injection system, pistons, pistons rings etc. Besides lighter bulk material in sliding contact can also be used by applying hard-solid lubricant coating.

2.12.4.4. Biomedical industry

Application of biocompatible thin coating such as TiN, DLC etc. have been using on the surface of prosthetic implant such as artificial hip joint, knee joint etc. for quite a long time. TiN coating has good wear and biocompatible characteristics but it has relatively higher coefficient of friction which sometimes limits its service life in biomedical applications. DLC also has good biocompatibility, higher hardness and lower coefficient friction [201] due to the transformation of DLC into graphite (a solid lubricant) and the

build up of a transfer layer on the counterpart. But sometimes they are brittle with poor load bearing capacity and poor adhesion with implant materials. Carbon-based low friction coatings are alternative choices to avoid some of the limitations due to their low friction, sufficient hardness, high load bearing capacity, excellent biocompatibility etc. For example Cr doped low friction carbon coatings (Graphit-iC) appear to have potential for a number of biomedical applications [212]. Extrapolation from simple laboratory tests indicates that a Graphit-iC coated CoCr hip joint can have a lifetime in excess of 50 years where the uncoated hip joint can last only 10 years.

2.13. SUMMARY

Surface engineering will remain as a growing industry in the next decades, because surface-engineered products increase performance, reduce cost, and control surface properties independently of the substrate, thus offering enormous potential due to the followings: creation of entirely new products, solution of previously unsolved engineering problems, improved functionality of the existing products-engineering or decorative, conservation of scarce materials, ecological considerations, and reduction of power consumption and effluent output. It is evident from the mass of the literature that has emerged in recent years, and especially over the last decade or so, that the scope or potential of surface engineering is enormous and in some ways perhaps limited by the power of imagination rather than technical difficulties. However newer advanced plasma based deposition methods are failing to achieve their potential in several sector due to the cost constraints, including their unsuitability for use with cheap substrates such as mild steel or aluminum and due to their inability to provide certain benefits exhibited by the other coating methods [269]. In future, it is very obvious to expect that new generations of coatings (e.g., hard solid lubricant in tribological applications) deposited by advanced surface engineering techniques (e.g., closed-field magnetron sputtering) will be more popular because of their outstanding properties, which will compensate the cost.

CHAPTER 3

Development of Experimental Rig

3.1. INTRODUCTION

The magnetron-sputtering rig had not been used for the couple of years before starting this project. It was configured for the penning type magnetron sputtering system. A considerable amount of work has been done in order to make the whole system operational. This chapter discusses the modification of the existing rig in terms of facilitating the rig for the closed-field unbalanced magnetron sputtering and installing the rotary substrate table to facilitate the 3-D coating. Rotational control of the substrate table (i.e., slower speed in front of activated target and faster speed in front of inactivated target within one cycle) using time control and position control methods has been developed in order to achieve higher deposition rate. Other developments include design of O-ring holding metal ring for easier access in the deposition chamber, fixing the reset switch in the control panel, installing magnetron shield and facilitating the rig for plasma nitriding. The modification of the abrasion-impact wear test rig for measuring the wear characteristics at lower load has also been described.

3.2. DESCRIPTION OF MAGNETRON SPUTTERING RIG

The sputtering rig is consisted of custom built vacuum chamber with a upper plate and bottom plate. There are four magnetron holes on the chamber wall and one magnetron hole in the upper plate. There are other ports such as view port, pressure gauge ports on the chamber wall. The upper plate has rotatable shutter ports and plasma emission spectrometer ports. The bottom plate has thermocouple, substrate table, high vacuum, rough vacuum, swagelock water inlet and rotatable shutter feedthroughs. The upper plate or the chamber with upper plate is lifted up to load sample. The vacuum system is consisted of baffle, gate valve, diffusion pump, rotary pump, backing valve, roughing valve and foreline trap with a backing and roughing line. The detail of the chamber is described in the thesis of P. V. Kola [270]. The schematic diagram and photograph of the magnetron sputtering rig are shown in the Figure 3.1. and Figure 3.2. respectively.

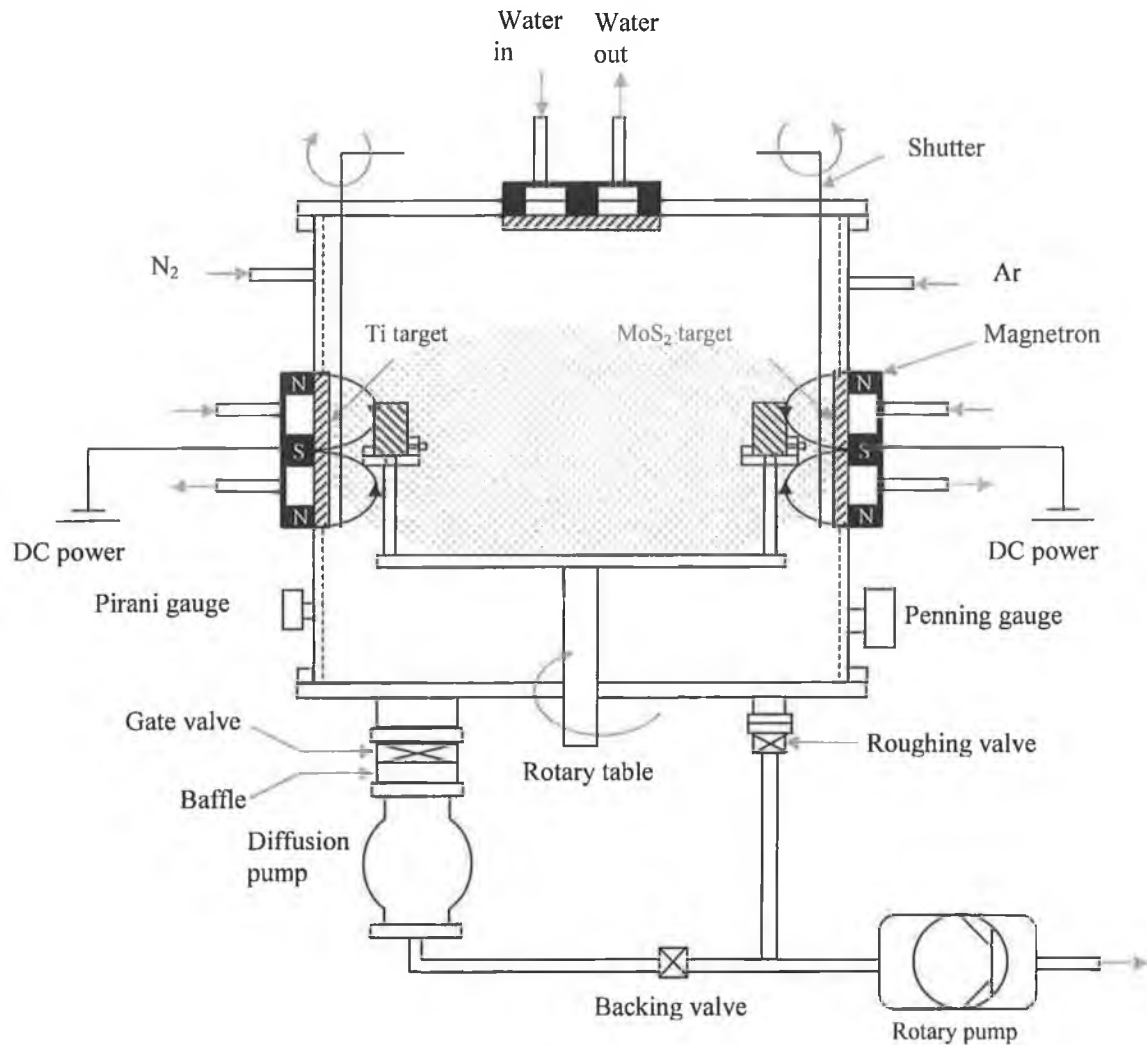


Figure 3.1. Schematic diagram of magnetron sputtering deposition facility.

3.3. RE-ESTABLISHMENT OF DIFFERENT SYSTEMS

Different systems like cooling water supply system, electrical system, reactive sputtering control system and temperature measurement system with the existing other systems such as gas supply system and compressed air flow system have been restored for the new configuration of closed-field magnetron sputtering system.

3.3.1. Water supply system

Certain parts including magnetron, diffusion pump, chamber wall and feedthrough with shaft of rotary substrate table in the magnetron-sputtering rig have to be cooled. The supplied water goes through a pump and the pressurized water goes to 6-port inlet manifold and is branched to different parts and returns to the outlet manifold. From the

outlet manifold the water goes to drain. The water-cooling system to different parts of the rig is shown in Figure 3.3.



Figure 3.2. Photograph of magnetron sputtering deposition facility.

As high power is supplied to the magnetron, it becomes very hot and eventually the target might be melt without cooling. Target cooling also allows for higher deposition rates due to their more efficient heat deposition. Sometimes chamber wall can get hot enough to cause the melting of the O-rings at the bottom and upper plate when deposition time is very long. Power applied on the rotary table shaft and feedthrough during substrate biasing and sputtering cleaning operation can generate heat in the feedthrough and shaft. High temperature may cause the degradation of the sealing properties of the feedthrough. Diffusion pump must have to cool for its sound operation. Any interruption from the water supply to the diffusion pump can cause damage of the diffusion pump. To avoid this problem, a water sensor is connected between the pump inlet and outlet manifold. If the water sensor does not sense any water, it will send a signal to the control panel. Then the control panel will turn off the diffusion pump automatically to prevent any further damage to the diffusion pump. If there is any water leak in the water carrying pipes, there might be flood in the room. To prevent this undesired flooding, a flood control water circuit is incorporated in the water supply line.

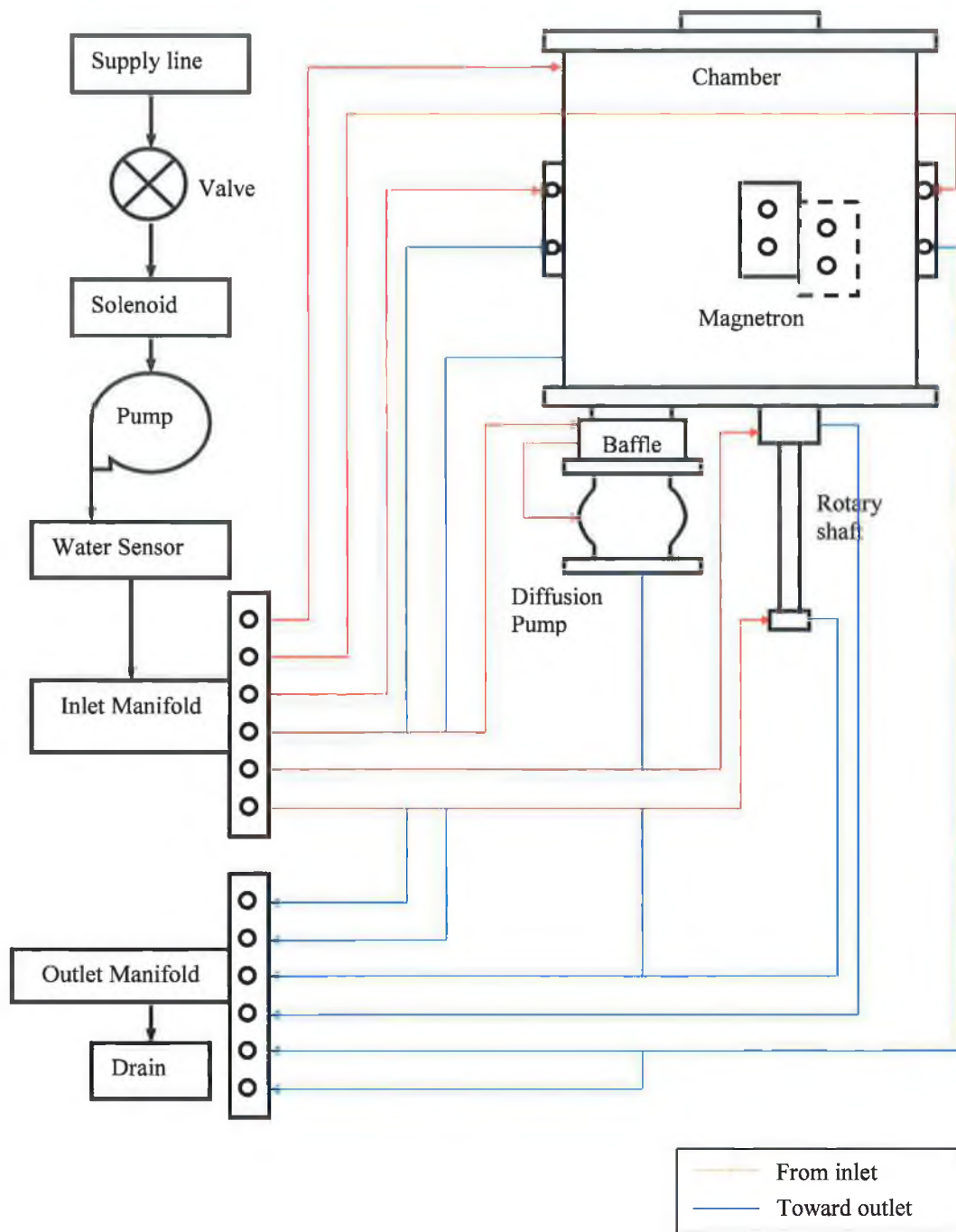


Figure 3.3. Schematic diagram of cooling water flow system.

3.3.2. Electrical system

Single-phase and three-phase powers are supplied in different parts of the rig depending on the requirements. Power supply to the rotary pump, diffusion pump, and different valves are maintained through the control panel. Advance energy MDX 5 kW power supply is used to supply power to magnetrons and during sputter cleaning and biasing. The electrical

connections to different parts and equipments have been established and shown schematically in Figure 3.4.

3.3.3. Reactive sputtering controller

During reactive sputtering, the target is poisoned with the coating material. The poisoned target gives coatings rich in reactive gas and low deposition rates. Target poisoning reduces the reactive gas consumption leading to an increase in the reactive gas pressure. To form the stoichiometric coating and stable operation during reactive sputtering the correct flow rate of reactive gas should be controlled. The sputtered material passes through the plasma where it is excited and emits light at characteristic wavelengths. The emission intensity is proportional to the density of the excited species i.e., to the product of the excitation probability and the density of the unexcited species. The Reactaflo™ unit monitors this plasma emission and uses it as a control signal for the reactive gas supply. If the monochromator is tuned to a metal emission line then this line will fall as the reactive gas is admitted (reverse control sense). If it is tuned to a reactive gas emission line then this will rise as the reactive gas is admitted (normal control sense). In either case the emission signal is a unique function of the reactive gas pressure. The Reactaflo™ unit dynamically controls the reactive gas flow to keep the chosen emission line constant. This eliminates the pressure instability and allows operation across the whole range of target conditions. The schematic diagram of the reactive sputtering control system is shown in the Figure 3.5.

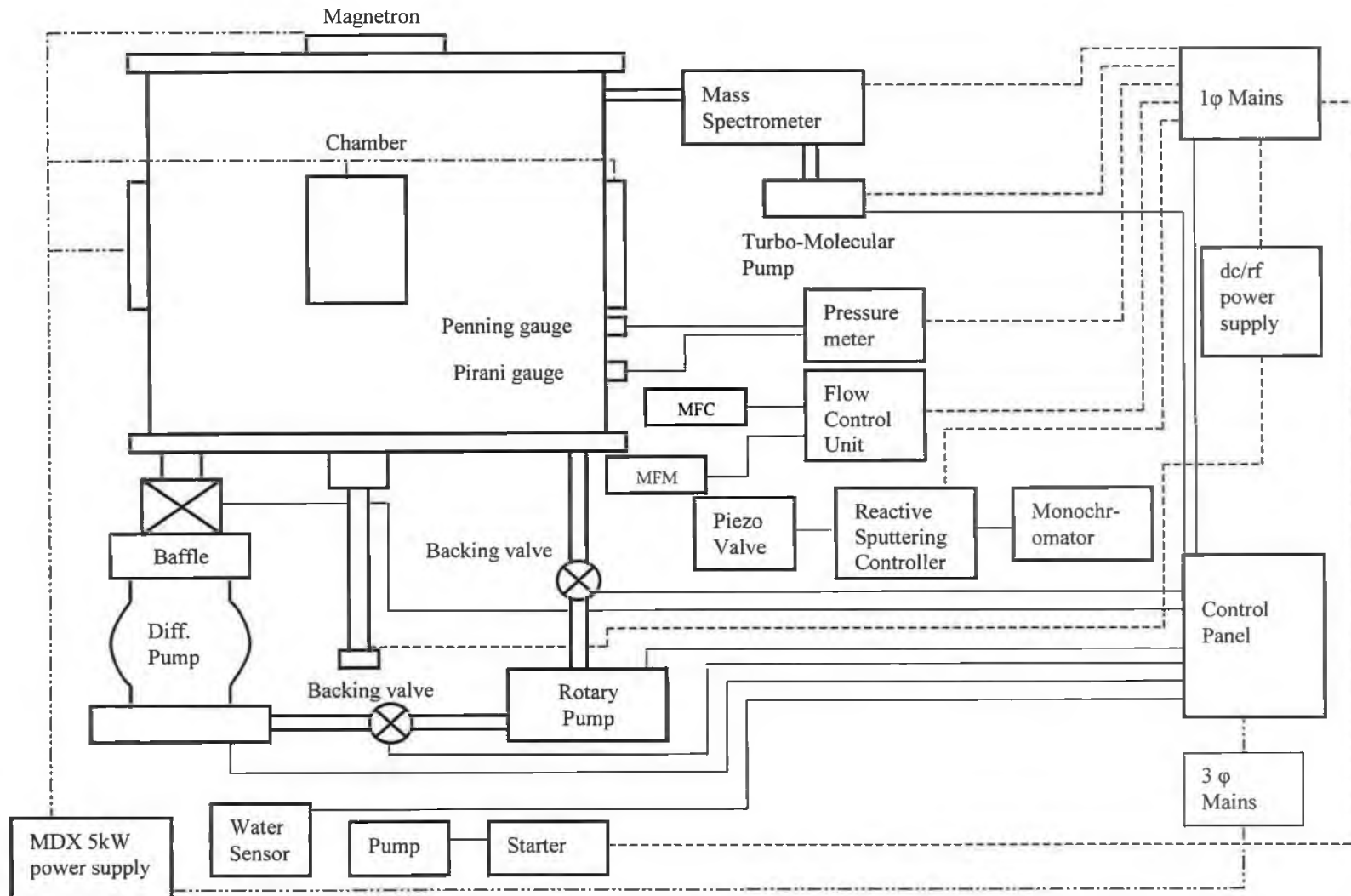


Figure 3.4. Schematic diagram of the electrical connections.

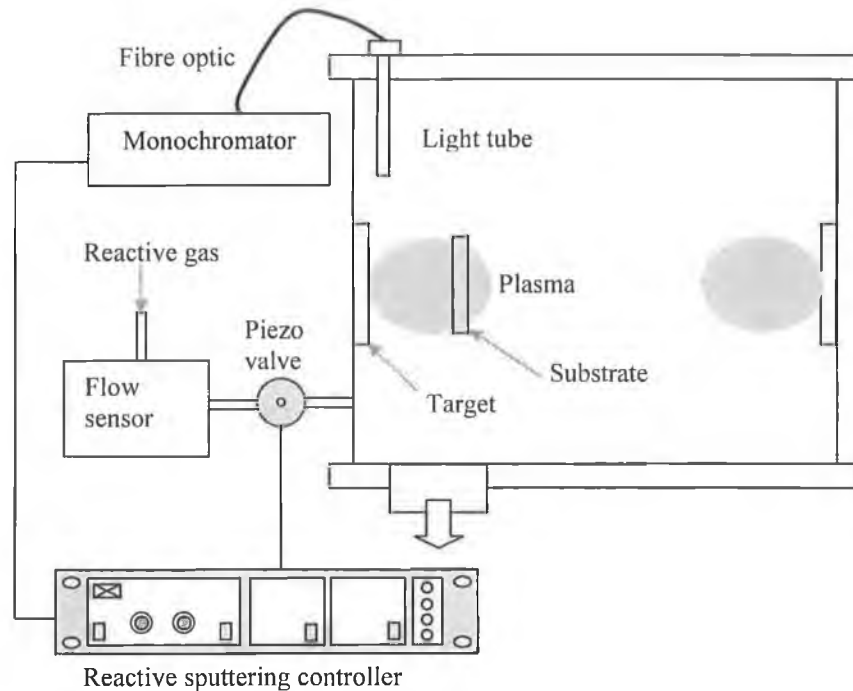


Figure 3.5. Schematic diagram of reactive sputtering control system.

3.4. FACILITATING THE RIG WITH CLOSED-FIELD UNBALANCED MAGNETRON SPUTTERING

The magnetron sputtering deposition chamber was configured for the penning type magnetron sputtering. The details of this configuration can be found elsewhere [271]. In the closed-field system, four unbalanced magnetrons are installed on the four-magnetron ports of the chamber uniformly arranged at 90° intervals around the vertical stainless steel vacuum chamber, which was approximately 603 mm internal diameter. Each magnetron was fitted with a 10 mm thick metallic target ($133 \times 330 \text{ mm}^2$). Three targets and one target each of titanium and molybdenum disulphide are employed. The magnetrons are positioned in such a manner that each magnetron has the opposite polarity from the nearby magnetron so that a closed magnetic field will be established and were magnetically unbalanced, their outer poles being stronger than their center poles. This novel system was developed by Teer coating company, England for depositing higher quality thin coating with high deposition rate [51]. There is another magnetron hole on the upper plate, which could be used along the other four magnetrons or separately. The cross-section of the closed-field unbalanced magnetron is shown in the Figure 3.6.

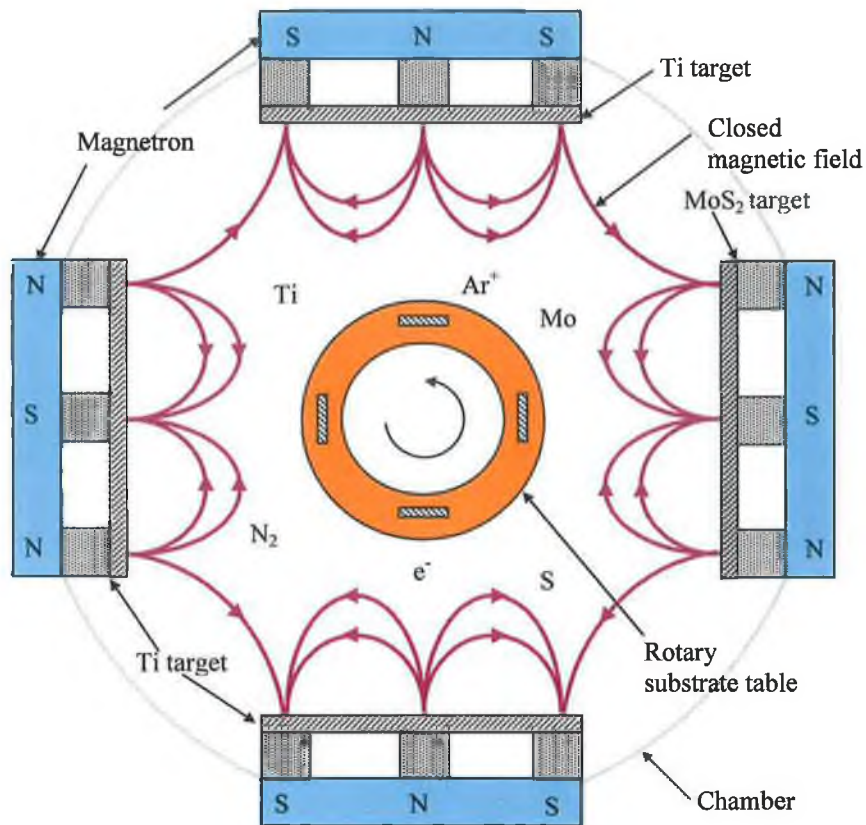


Figure 3.6. Cross-section of the closed-field unbalanced magnetron-sputtering system.

3.5. INSTALLATION OF MoS_2 TARGET

When using a new MoS_2 target for the first time it is important to follow certain steps to reduce the chances of damaging the plate.

- ❑ Two halves of MoS_2 target are attached to a copper plate with glue. When clamping the target to the magnetron body, it should be ensured that clamps are fitted to the target first to reduce the chance of debonding.
- ❑ The clamps should not be tight but are used only to hold the tiles in place. Overtightening can cause the target to crack when it is running and parts may delaminate.
- ❑ Due to the bending of the copper plate caused by the bonding process it is important to take great care when tightening the screws to attach the target to the backing plates. The screws should be tightened slowly and evenly around the target so that the bending is reduced slowly as the target is straightened on to the magnetron.
- ❑ Water pressure for cooling the magnetron should not exceed 3.0 bar. High pressure will cause the target to bow, which may lead to cracking and delamination of the

target. When turning the water-cooling on to the magnetron body, once the magnetron has been fitted into the coating chamber, this should be done very slowly with the output tap being turned on first. The input tap should then be opened gradually so that there is no large surge in water pressure. Large surges may cause the MoS₂ to crack as the copper flexes under the water pressure. Once the water is fully on and the full water pressure has been applied, this process should not need to be done again and the water can be turned on at the normal rate.

3.6. O-RING HOLDING METAL RING

The whole chamber with the upper plate would have to be lifted for the loading and unloading of the samples. In this way, it would be very difficult to set the samples inside the chamber. The loading of the sample in front of the target can be done by lifting the upper plate only. But the O-ring in the groove of the upper plate will fall down when the upper plate is lifted. The fitting of the O-ring in the groove is really a hard task to accomplish. A thin metal ring has been made for guiding a new O-ring that has smaller perimeter than the previous O-ring on the upper flange of the chamber. The metal ring perimeter and thickness are smaller than the O-ring so that when the upper plate is rested on the chamber flange, it would press the O-ring against the flange and prevent the metal-to-metal contact. There is no need to screwing up the upper plate with the chamber, because the weight of the upper plate on the O-ring is enough to hold the vacuum.

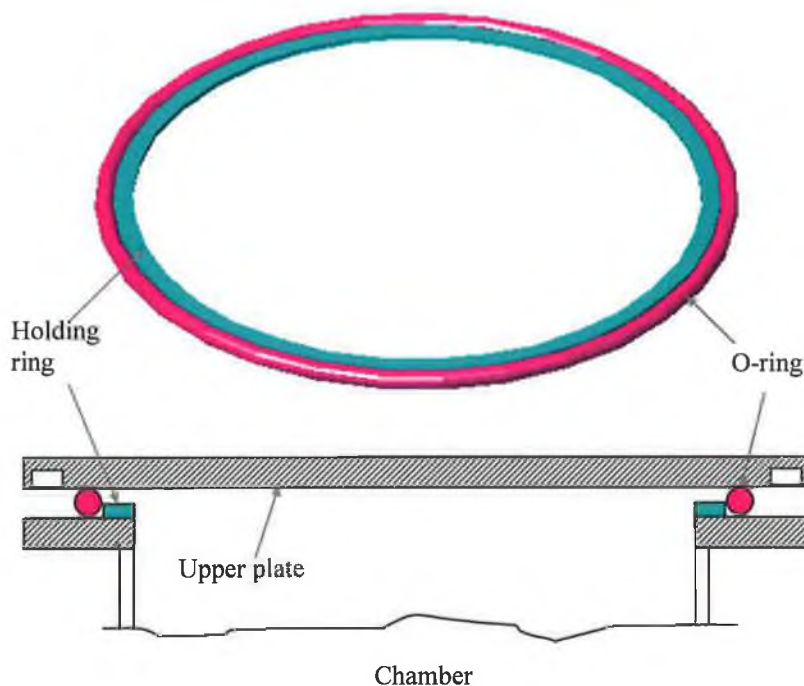


Figure 3.7. O-ring holding metal ring between the upper plate and the chamber.

Figure 3.7. shows the metal ring with O-ring and the cross sectional view of the whole system. This system facilitates the easy access for loading and unloading of the samples by lifting the upper plate only.

3.7. FIXING THE RESET SWITCH

The control panel has the switches for controlling power to the rotary pump, diffusion pump, gate valve, backing valve and roughing valve. There is sequence of operations for the pumps and valves during pumping down of the vacuum system. If the power shuts off everything will be shut off. When the power returns, pumps and valves will be started without maintaining that sequence. This may cause the damage of the valves and pumps. The idea of the reset switch in the main control panel is for safety operation. Nothing will get power as long as the reset switch is turned on. When the reset switch is turned on current passes through the solenoid coil, energize the coil and a contact is made in the circuit and everything will be in operation after turning on the respective switches. After that the reset switch is turned off. But it will not make the contact open and everything will be running as it was running before turning off the switch. Now if the main power shuts off there will no be current in the coil and everything will be shut off. As soon as the power returns nothing will get power as the reset switch is turned off. Then the reset switch has to be turned on manually to give the power supply to the panel. A relay has been installed for proper functioning of the control panel.

3.8. MAGNETRON SHIELD

During coating deposition the magnetrons act as cathode and carry high voltages of around 500-600V D.C.. If the magnetrons are touched, it will cause serious damage to human and may even cause death. Four metal shields had been made to isolate the high voltage magnetrons from human contact. First, holes for water pipes, power line and holding screw have been made in thin stainless steel sheet and then bent the sheet to form shields. The shield is attached to the magnetron by two butterfly screws. This will prevent any human contact with the magnetron. Figure 3.8. shows the magnetron shield installed on the magnetron.

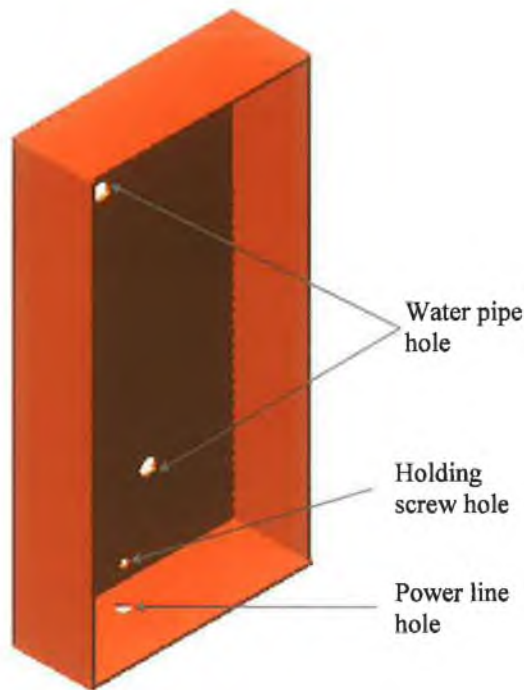


Figure 3.8. Metal shield for the magnetron.

3.9. SHUTTER FOR MAGNETRON

Shutter plays an important part in magnetron sputtering technique. During sputter cleaning the target is covered with the shutter to prevent any contamination of the target surface. After sputter cleaning the target is run for degassing, removing oxide from the target surface and getting thermal equilibrium. During this period shutter covering the target surface avoids any unwanted deposition on substrate. It is also very important when different target materials are used for deposition of multicomponent, multilayer or composite coating. By using the shutter the inactivated target surface are covered so that it cannot be contaminated with other target materials during deposition. In the upper plate of the chamber there are eight shutter feedthroughs two for each magnetron. Eight shutters have been designed, manufactured and installed in the chamber. Small O-ring is fitted in the shutter feedthrough to maintain the vacuum.

3.10. FACILITATE THE RIG FOR 3-D COATING

The basic set-ups for the production of multicomponent coatings can roughly be divided into two main groups: coatings deposited from static sources (e.g. sputter sources) on a static substrate and from static sources onto moveable substrates. The detailed choice of

the deposition process can give rise to entirely different coating structures and therefore, coating properties [272]. Especially the second group is very popular in industrial applications because of its capability for the coating of complexly shaped bodies. The need for extensive sample movement (rotation) in PVD techniques is addressed when the deposition comes from multi-source arrangements [273-275]. Usually three different kinds of motions are observed in thin coating deposition techniques for the movement of the substrate: linear, rotary and linear-rotary motion. During the coating deposition on small substrate the linear or up and down motion of the substrate table is not necessary. As the substrate is small, it can be placed in the middle position of the target to get better uniformity. But in case of bigger samples sometimes the linear-rotary motion might be helpful. For general applications simple planetary motion of the substrate table is desired. Planetary motion implies multiple rotations of the substrates and continuously varying angles of incidence, instantaneous deposition rates, and target-to-substrate distance. Such variation can affect the structure and properties of the deposited coatings [35]. During deposition of thin coating, the sample rotation is necessary for the following purposes:

- To increase the temperature uniformity where radiation heating is used
- To increase the thickness uniformity during coating deposition
- To deposit uniform coating on all surfaces of a 3-D object
- To deposit multicomponent, multilayer, graded or composite coating

To satisfy the first requirement, the rotation is almost always a simple rotation about the sample's central axis with the motion provided from the airside via a vacuum motion feedthrough. The second requirement is often satisfied by the simple rotation, but for more better result the complex double or triple axis planetary rotary device is necessary. The third and fourth requirements are also satisfied by simple rotation for simple-shaped object. For complex shaped objects, complex double or triple axis planetary rotary device is necessary. In the present system a one-axis and a two-axis rotary substrate table is installed into the deposition chamber. The detailed drawings of the table design will be found in the Appendix A.

The rotary substrate table can be divided into two major parts:

- a. Rotary shaft assembly
- b. Rotary table assembly

3.10.1. Rotary shaft assembly

3.10.1.1. Rotary shaft

The rotary shaft has the following parts: motor with pulley and belt, Deublin union, extension pipe, feedthrough, adapter flange, feedthrough insulator and shaft extension. The assembly diagram of the rotary shaft is shown in Figure 3.9.

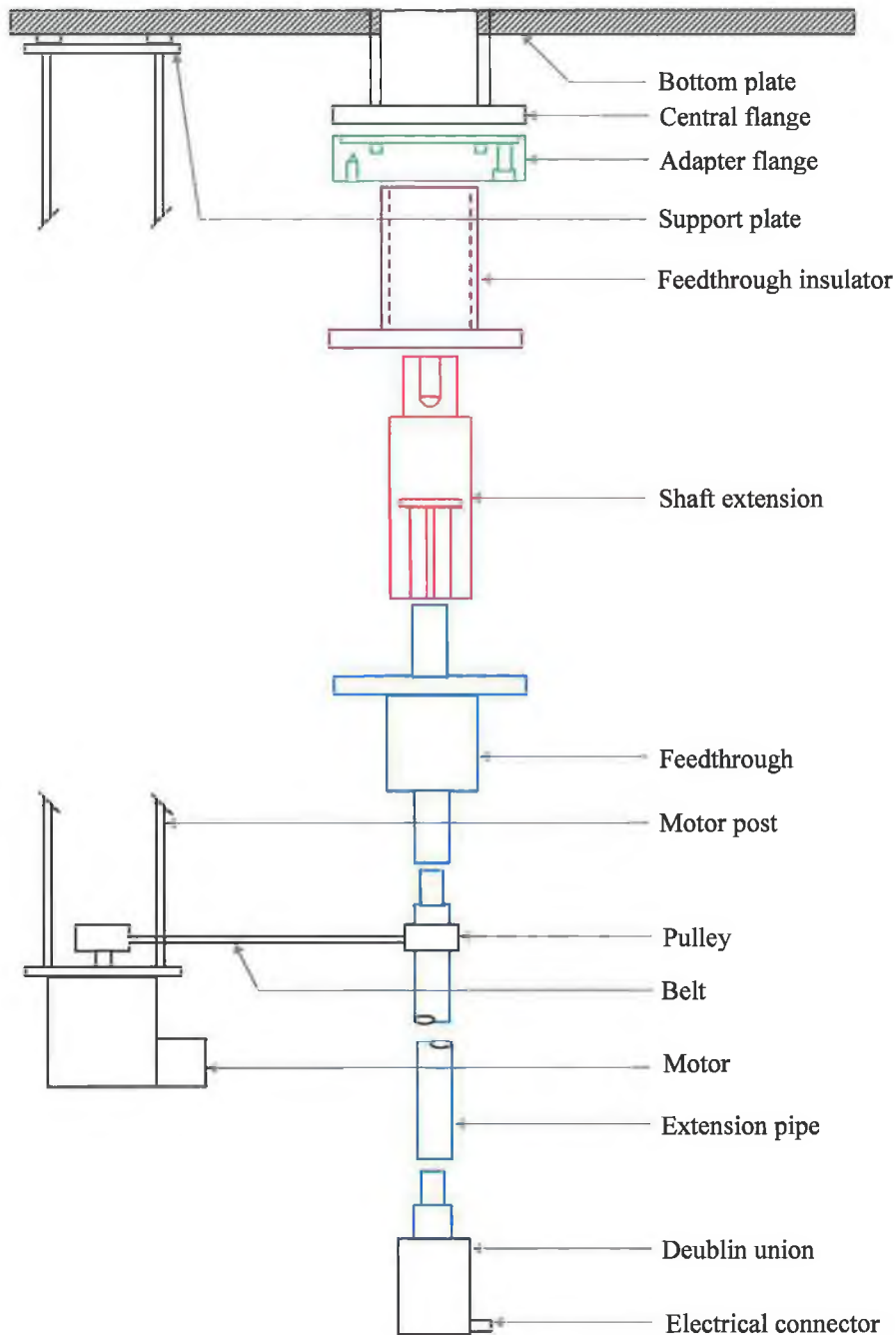


Figure 3.9. Assembly diagram of rotary shaft.

Rotating union

A rotating Deublin Union is a precision mechanical device used to convey fluid from a stationary source into rotating machinery.

Extension pipe

The one end of the extension pipe rotates resting on the Deublin Union while the Deublin Union itself remains stationary. For cooling the extension pipe another smaller diameter pipe goes through all along the extension pipe from the Deublin Union. The other end of the extension pipe is connected to the Ferro fluidic feedthrough.

Ferrofluidic feedthrough

The vacuum sealing between the shaft and base plate is maintained by a Ferro fluidic feedthrough during rotation. This seal conforms to the shaft perfectly, offering zero leakage in both static and rotary condition. It can even accommodate slight anomalies in the surface of the shaft and eccentricities in the rotating motion. Their lifetimes are reduced for higher applied loads, faster rotation speeds and high temperatures. These seals cannot be used for ultra high vacuum application because they are not bakeable and are susceptible to outgassing at pressure lower than about 8×10^{-10} mbar.

Adapter flange

The adapter flange is connected by screws to the flange of the base plate central hole. The Ferro fluidic feed through and extension pipe assembly is hanged from the adapter flange with bolt insulator for isolating the whole rotary table assembly from the chamber.

Feedthrough insulator

The feedthrough insulator between the Ferro fluidic feedthrough and base plate central hole electrically isolates the whole rotary shaft from the chamber.

Shaft extension

A shaft extension is connected with the Ferro fluidic feedthrough shaft by key. Both single-axis and two-axis table is connected to the shaft extension by key.

Electrical connector

A electrical connector is attached with the Deublin Union for supplying power during biasing (DC or RF) and sputter cleaning.

Shield

The rotary substrate table is covered by a shield for avoiding human contact with the shaft and provides ground path during biasing and sputter cleaning. The shield has three parts: upper shield for Ferro fluidic feedthrough, lower shield for Deublin Union and middle shield for extension pipe. The upper shield is connected with the adapter flange, middle shield is connected with the upper shield and lower shield is connected with the middle shield by screws. A lower shield plate covers the lower shield end.

3.10.1.2. Rotary motion of the table

A steel made motor support plate is attached by screws with the blanking plug underneath the base plate. From that plate a single-phase stepped motor is hanged by four threaded square bars (motor posts). One pulley is placed at the end of the driving shaft of the motor and other pulley is placed on the rotating shaft parallel to the first one. Both pulleys have same diameter. The rotary shaft gets the motion from the single-phase motor via a toothed belt connected between the pulleys. The rotational speed of the shaft is controlled by a controller (MOTOR CONTROL) from 0-10 rev/min.

3.10.1.3. Water cooling of the rotary shaft

Two separate water-cooling circuits are incorporated in the rotating shaft assembly as shown in the Figure 3.3. In the first circuit, water goes into the Ferro fluidic feedthrough and coming out from the other end of the feedthrough. The water circuit cools the magnetic poles in the feedthrough. In the other circuit, water enters into Deublin Union first, then goes through the smaller diameter pipe all along the length of the extension pipe and comes out through the annulus region between the smaller diameter pipe and extension pipe and finally drains out through the Deublin Union.

3.10.2. Rotary table assembly

There are two different types of rotary substrate tables: simple one-axis rotary table and two-axis rotary table.

3.10.2.1. One-axis rotary table

For the simple one-axis sample table, an adaptor is welded to a metal shaft (central pole). The adaptor with the central pole is placed on the shaft extension and locked by key. The sample table is made of 5 mm thick stainless steel. There are a series of small holes

around the outer edge of the table. A collar is screwed to the center of the sample table. The collar with the sample plate can slide along the length on the central pole and can be locked on the desired place of the central pole. The table plate is blanked in such a way that it looks like three ribs joining the outer ring and inner ring. The substrate is hanged from the small holes of the sample table by metal wire. The assembly diagram of one-axis rotary table is shown in the Figure 3.10. When the rotary shaft rotates the sample table and substrate rotates around the chamber. There is no motion of the substrate around its own axis but there is only single motion around the rotary shaft (one-axis).

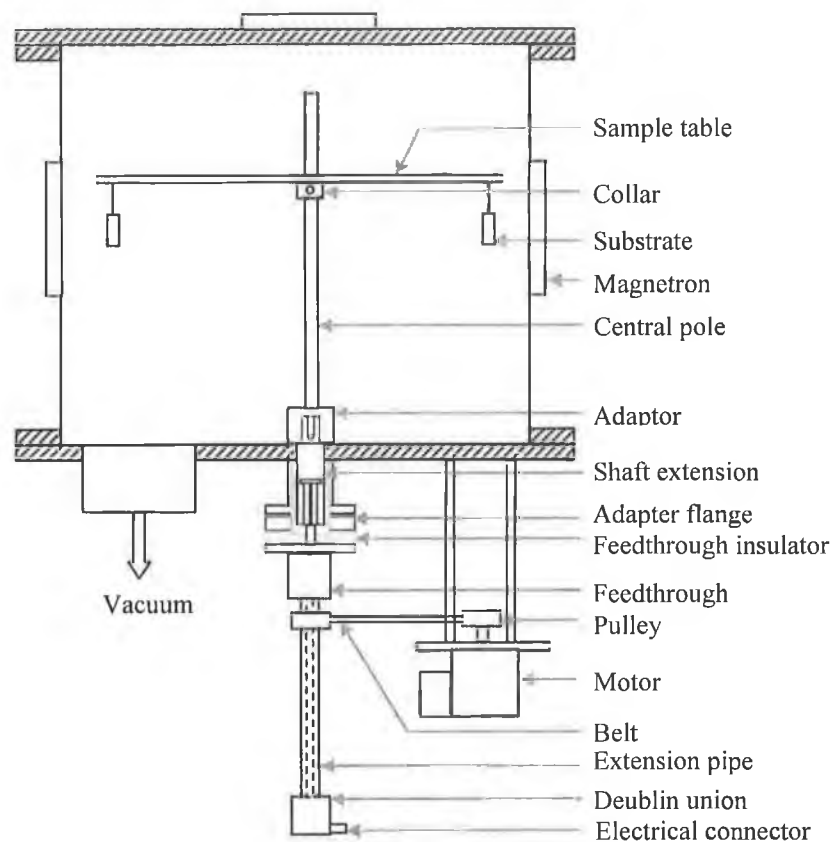


Figure 3.10. Simple one-axis rotary substrate table.

3.10.2.2. Two-axis rotary table

The assembly diagram and photograph of two-axis rotary table is shown in the Figure 3.11. and Figure 3.12. respectively.

Sample table

The two-axis rotary sample table is 450 mm in diameter and 12 mm thick stainless steel plate with eight blank holes. The holes in the plate will reduce the weight of the table. There are twenty holes with bushes on the table along two mutually perpendicular axes on the surface of the table. Five bushes are placed along one half of an axis starting at 50 mm

from the outer edge of the table and after every 30 mm towards the center. The holes can accommodate the substrate holders. For varying the target to substrate distance, the substrate holder is placed in different holes.

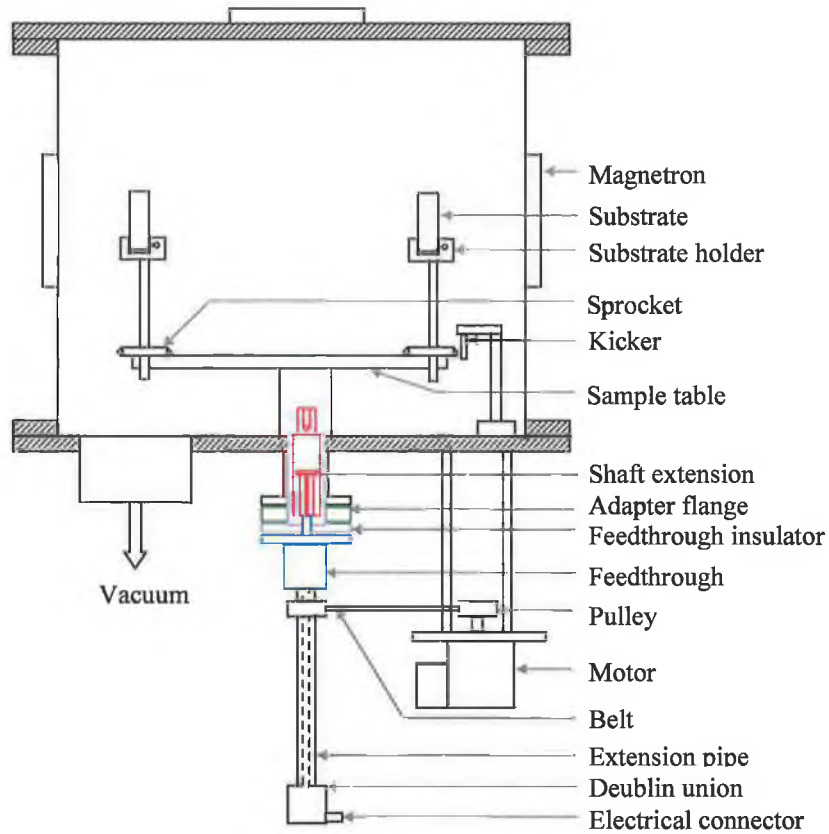


Figure 3.11. Two-axis rotary substrate table inside the chamber.

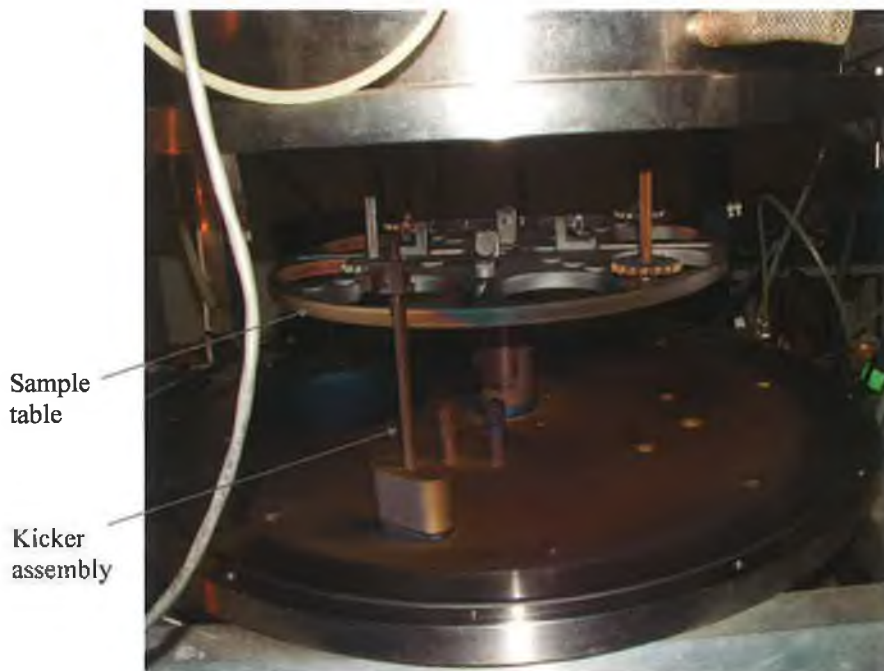


Figure 3.12. Photograph of the two-axis rotary substrate table.

Table support

A table plate support is placed on the shaft extension and locked by key. The sample table is placed on the table support and locked by screws.

Central substrate holing mechanism

There are four stepped grooves with sliding carriage and sliding nut along other two mutually perpendicular axes, which are at a 45° angle from the bush axes. The holding block can slide along the grooves. The purpose of the sliding carriage and nut is to hold any bigger substrate in the middle of the table. Two knurl screws are fitted with the sliding carriage. For holding any substrate all four sliding carriages are moved towards the center of the table by loosening the knurl screws underneath the table and fixed the position of the sliding carriages near the substrate by tightening the screw. Then the upper knurl screws will be pressed against the sample to hold the sample in the middle of the table.

Peripheral substrate holding mechanism

There is a sprocket with smaller shaft on one side and longer shaft with the substrate holder on the other side. The smaller shaft end is vertically placed through the bushes and tightened with the sample table by screws. There is slight clearance between the shaft and the bush hole so that the sprocket shaft can easily move in the bush. The longer shaft length with the substrate holder is chosen in such a way that the substrate holder will remain at the mid plane of the target. Four sprockets with substrate holder can be accommodated on the table at a time i.e., four substrates can be coated at a time in a single deposition cycle. When the rotary shaft rotates the sample table with the substrate rotates around the rotary shaft and gets the one-axis motion.

Kicker assembly

A kicker assembly is attached to the bottom plate of the chamber to provide the motion of the substrate around its own axis as shown in Figure 3.13. The kicker assembly consists of insulator, supporting flange, bolt insulator, shield, kicker post, kicker adapter, extension bar, rotating part for kicker and kicker. The supporting flange is screwed through the bolt insulator to the base plate sitting on top of the insulator. The insulator and bolt insulator keep the whole kicker assembly electrically isolated from the chamber. The shield prevents the coating getting onto the insulator and causing any arcing. One end of the kicker post is welded to supporting flange and kicker adapter is connected with the other end of the kicker post. Five different lengths of extension bars are connected to the

kicker adapter with screws. The length of individual extension bar can be adjusted with respect to the sprocket.

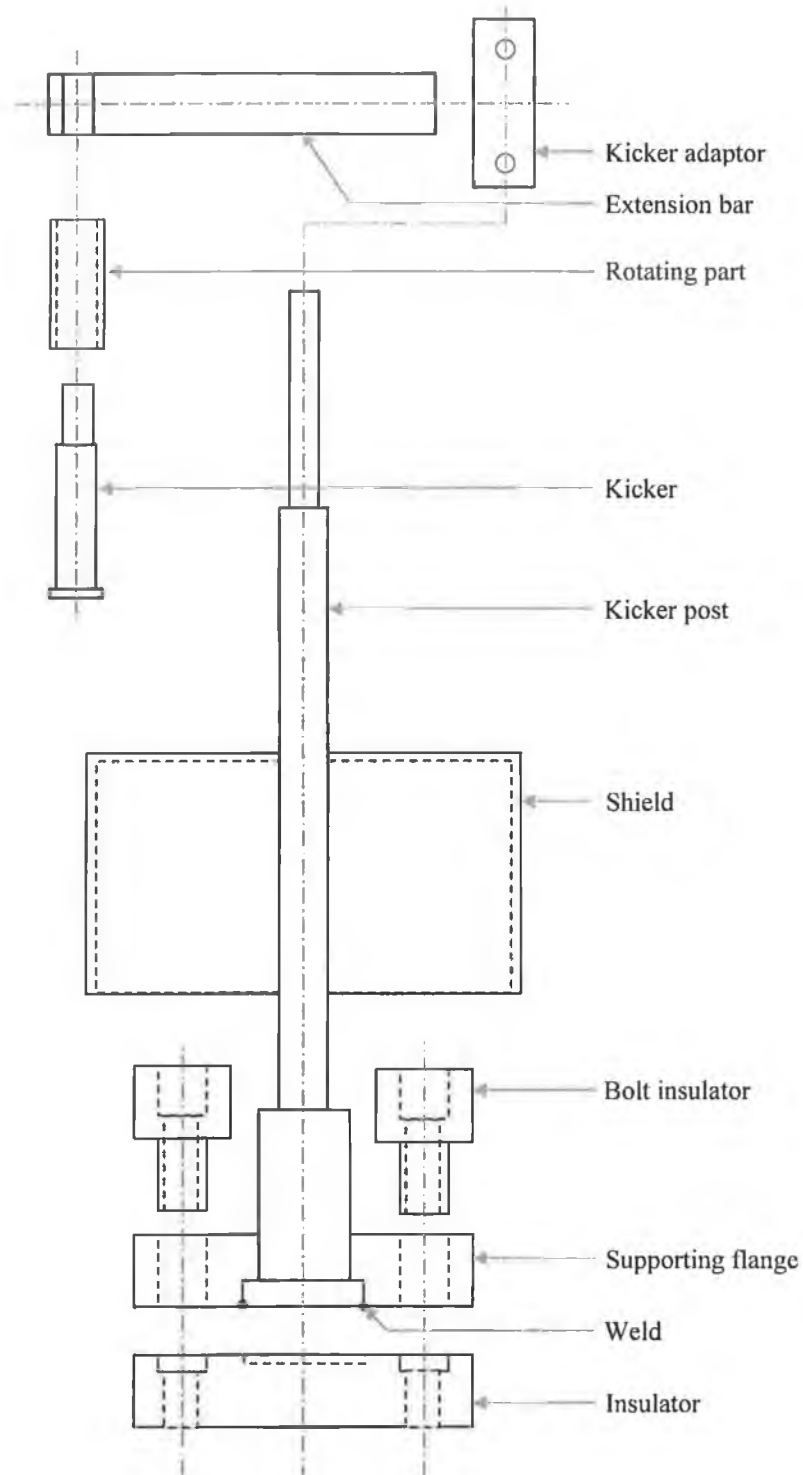


Figure 3.13. Assembly diagram of kicker parts.

The extension bar is adjusted so that the kicker can touch the sprocket. During the rotation of the table, as sprocket comes close to kicker, the kicker kicks the sprocket and the sprockets moves by one teeth and so does the substrate holder. For a complete rotation of the sprocket eighteen complete rotation of the table is necessary. This way the substrate

gets the motion around its own axis (two-axis). Five different lengths of extension bar will facilitate the kicking of the sprocket at five different distances from the target. That means target to sample distance can be varied by five different distances. The kicker with the rotating part is threaded to the extension bar. The rotating part on the kicker makes sure the flexible kicking of the sprocket.

Metal plug

As four sprockets can be fitted to four different bushes the other sixteen bush holes remain open. During deposition the bush holes will be coated by the coating material. As a result the sprocket shafts cannot be fitted into those bush holes. To avoid any undesired coating of bush holes metal plugs are placed on the bush holes.

3.11. TAP SELECTION FOR HIGHER TARGET CURRENT

It is well documented that the sputtering rate of the coating is proportional to the target current e.g., higher target current will give higher sputtering rate and in turn will give higher deposition rate. The MDX 5 kW magnetron power supply is used for supplying power to the magnetron. The MDX 5 kW power supply is equipped with a built-in impedance-matching transformer. These transformers are available in high-impedance, standard-impedance and low-impedance configurations. The power supply has three possible voltage taps so that three different voltage output ranges can be selected. Load impedances can further be modified by selecting from one of the three taps.

Table 3.1. Output voltage and current for different tap positions.

Tap no.	Low impedance		Standard impedance		High impedance	
	Output voltage range (V)	Maximum output current (A)	Output voltage range (V)	Maximum output current (A)	Output voltage range (V)	Maximum output current (A)
1	0-500	12.50	0-600	10.00	0-775	8.00
2	0-640	10.00	0-800	8.00	0-1000	6.40
3	0-800	7.75	0-1000	6.25	0-1250	5.00

Depending on the transformer configurations and tap settings load impedance requiring voltages from 400 V to 1250 V can be accommodated. Table 3.1. shows the maximum current that can be produced at each tap position. It also shows the range of output voltages available at each tap, when the unit is voltage regulation mode. Normally the MDX power supply is set to standard impedance configurations. It was configured at Tap no. 3 with the standard impedance configuration giving the maximum output current of 6.25 A. To get higher current from standard impedance configurations Tap no. 2 is selected for supplying the maximum current up to 8.0 A.

3.12. ROTATIONAL CONTROL OF THE SUBSTRATE TABLE

3.12.1. Motor and motor controller

An AC motor is employed to rotate the substrate table as shown in Figure 3.14. A Lenz 8200 smd frequency inverter (MOTOR CONTROL) is used to control the speed of the motor. From the MAINS the power is supplied to the MOTOR CONTROL that supplies power to the motor. The potentiometer (SPEED CONTROL) controls the speed of the motor by changing the resistance and thus the supplying voltage/frequency to the motor. The corresponding frequency for zero to 10 rev/min is zero to 50 Hz respectively. By turning the START/STOP switch the motor can be rotated to any particular speed specified at the SPEED CONTROL. There is a fuse between the MAINS and the MOTOR CONTROL to prevent any excessive current to the MOTOR CONTROL. The motor speed can be controlled from zero to 10 rev/min. Each revolution is divided into 100 divisions so that the motor speed can be controlled within the accuracy of two digits after any number of revolutions within the range. The motor rotates at a uniform speed within the range specified.

3.12.2. Why need rotational control?

During the deposition of thin coating by magnetron sputtering the highest deposition is anticipated only when the substrate comes in front of the magnetron. There are four magnetrons on the chamber wall. But at the moment due to the shortage of power supply only two magnetrons are activated during the deposition and the other two magnetrons are acted as dummy. The activated magnetrons are placed opposite to each other. One magnetron is equipped with Ti target and another one is with MoS₂ target.

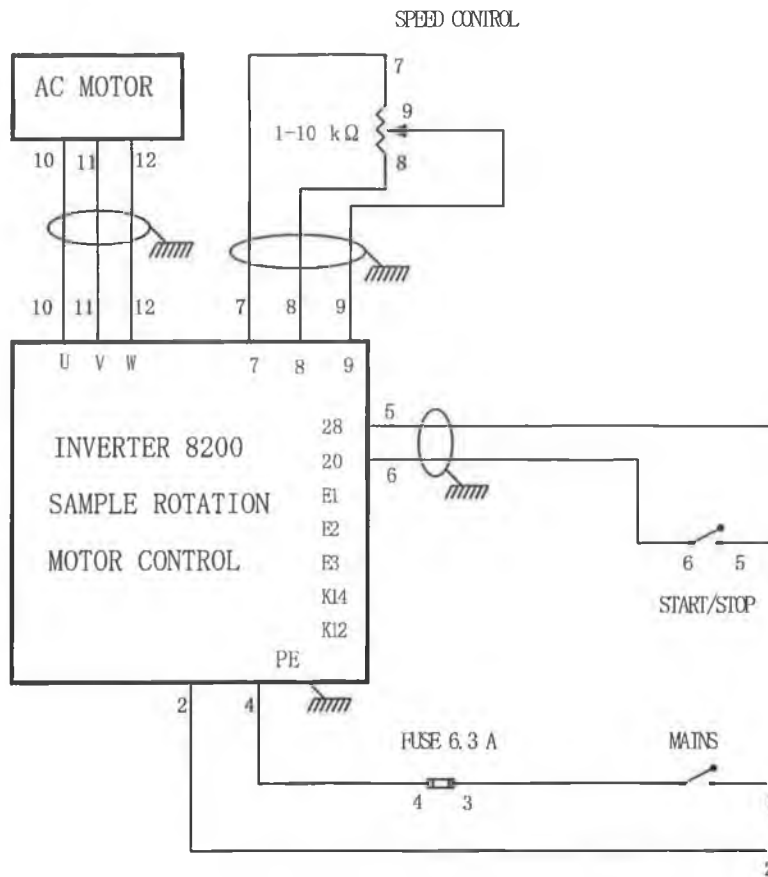


Figure 3.14. Connection diagram for constant speed rotational control.

The peripheral distance a magnetron covers on the chamber wall is less than $1/10^{\text{th}}$ of the chamber periphery. As a result, the substrate remains in front of the magnetron for a time less than $1/10^{\text{th}}$ of the time required to complete a full revolution while the substrate table is rotating. That's why the deposition rate was very slow. As for example the deposition rate was less than 500 nm/hr at a typical magnetron current of 3.0 A. To avoid this kind of problem there needs some control over the rotation of the substrate table so that the substrate can rotate slowly when it comes in front of the activated target and rotate fast when it goes out of the activated target. This will save lot of time for depositing coating with higher deposition rate.

3.12.3. Basic idea of rotational control

In the MOTOR CONTROL there are several terminals for control connections (Figure 3.14.). Terminal 20 (T-20) is the internal DC supply for digital input and terminal E1 (T-E1) is the configurable digital input and can be activated with the fixed set point 1 (JOG 1).

If T-20 and T-E1 are not connected, the table rotates at any specified speed set at the SPEED CONTROL. When the T-20 and T-E1 are connected then due to the internal dc supply voltage the speed of the motor increases to highest speed of 10 rev/min. In this position the voltage supplied to the motor bypasses the potentiometer at the SPEED CONTROL. Again when the T-20 and T-E1 are disconnected the voltage supply to the motor decreases to the original value set at the beginning and consequently it rotates to the previously specified speed. This is the basic idea of controlling the speed of the motor at different positions within a single cycle.

3.13. DESIGN CONCEPT OF THE ROTATIONAL CONTROL

To control the rotation of the substrate table according to the above-mentioned ideas, two configurations have been come up with.

1. When the targets are positioned opposite to each other: The substrate will rotate at a slower speed in front of the Ti target and rotate at faster speed when the substrate goes out of the target and again rotate at a slower speed in front of the MoS₂ target and at faster speed when the substrate goes out of the MoS₂ target (Figure 3.15. (a)).
2. When the targets are positioned side by side: The substrate table will rotate at a slower speed from the Ti target to the MoS₂ target and at a faster speed in the rest of the cycle (Figure 3.15. (b)).

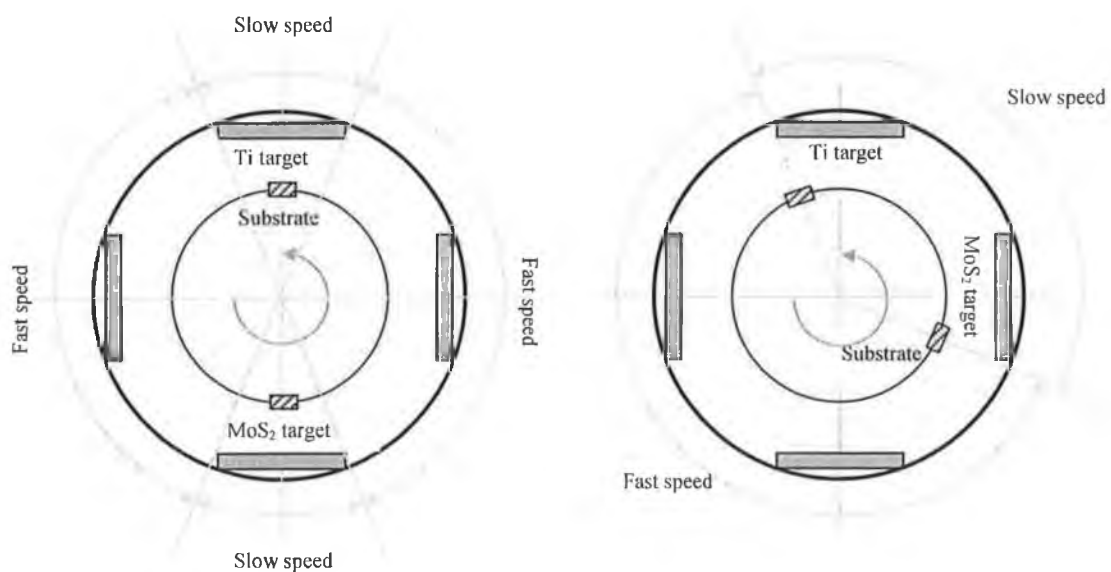


Figure 3.15. Fast and slow speed sequences of the rotary table within one cycle when the activated targets are (a) opposite to each other and (b) side by side.

The fast and slow speeds of 1 and 10 rev/min respectively are maintained. The minimum speed can be lowered to less than 1 rev/min. The speed versus angular distance profile for the rotary table is shown in the Figure 3.16. and Figure 3.17. for two different configurations.

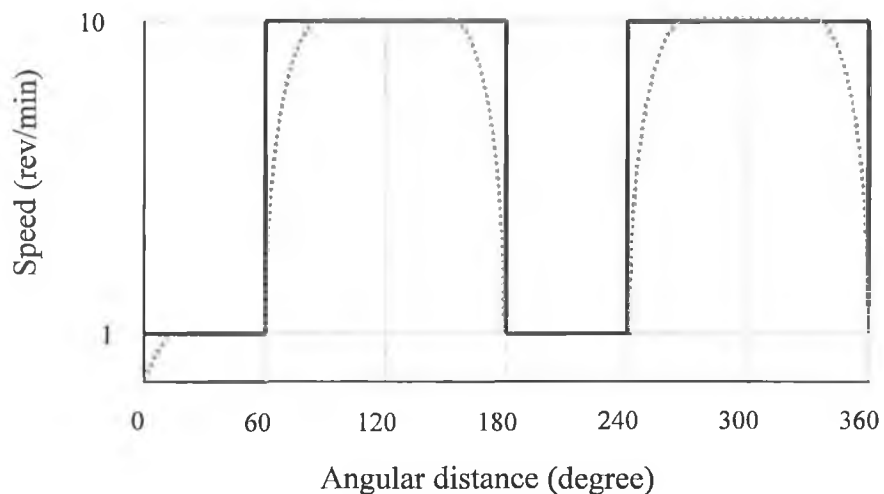


Figure 3.16. Speed versus angular distance profile within one cycle when the activated targets are opposite to each other.

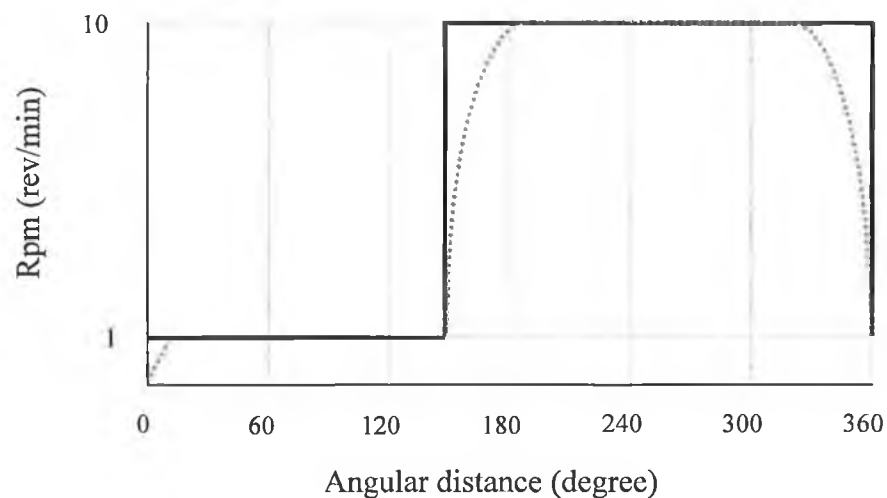


Figure 3.17. Speed versus angular distance profile within one cycle when the activated targets are positioned side by side.

Ideally the motor can jump directly from one speed to another speed without any time delay. But practically the speed should be changed gradually from slower to faster or faster to slower speed for avoiding any unwanted shock on the motor or rotary table. This can be achieved by controlling the acceleration and deceleration time in the MOTOR CONTROL.

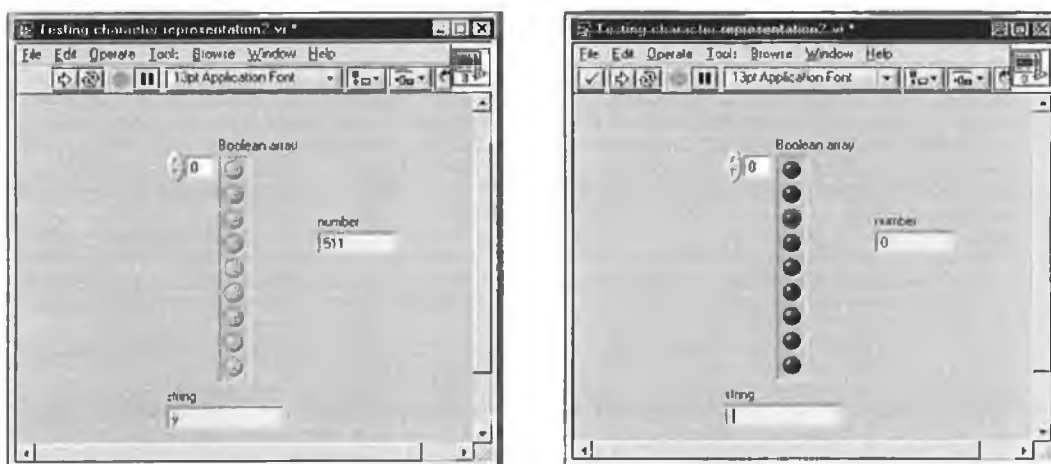
The motor speed control in a single cycle to match either of the above-mentioned profiles can be achieved by two different ways:

(a) Time control: In this method, the exact timing for slow and fast speed durations is controlled.

(b) Angular position control: In this method, the starting and ending positions for slow and fast speeds are determined and accordingly the speeds are controlled.

3.13.1. Time control of motor speed

LabVIEW software was used to control the timing of fast and slow speeds in a single cycle as explained in the previous section. The serial port of the computer was used as the voltage source for the MOTOR CONTROL. There are nine wires in the serial port (9-pin connector). By sending a certain ASCII (American Standard Code for Information Interchange) character to the serial port an output voltage of around 10 V is possible at the serial port. While sending another ASCII character to the serial port an output voltage of around 0 V is possible at the serial port. The computer converts ASCII characters to binary numbers zero (0) and one (1). Each ASCII character has a unique binary equivalent (0 and 1). To achieve two voltage levels from the serial port it is necessary to determine the ASCII characters that correspond to (0000 0000 0) and (1111 1111 1), which will set the voltage value to 0 V and 10 V respectively at the serial port. These characters are identified from the LabVIEW program as shown in the Figure 3.18. Figure 3.19 shows the block diagram for finding the corresponding characters for all nine bits as zero (0) and one (1).



(a)

(b)

Figure 3.18. Front panel of character testing for binary numbers (a) one (1) (b) zero (0).

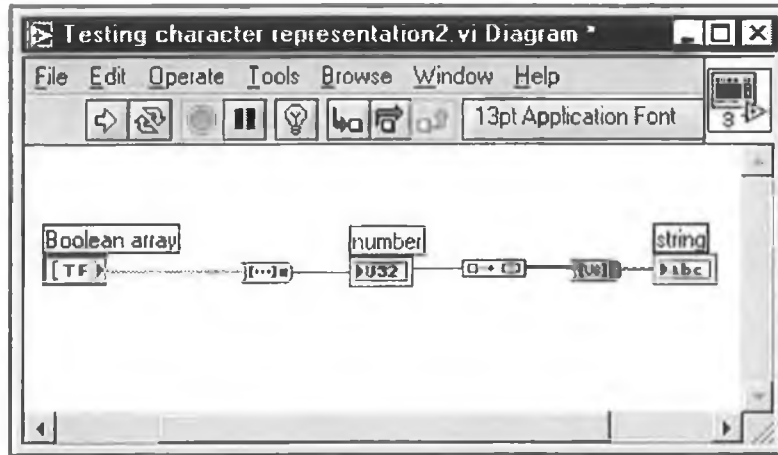


Figure 3.19. Character conversion code.

It was found that character “space” () corresponding to number 0 produced all the characters as zero while character “double dot over y” (ÿ) corresponding to number 511 produced all the nine bits as one. By sending the character space () to the serial port 0 V was produced while by sending the character double dot over y (ÿ) a 10 V was produced at the serial port output. The time duration for which the output voltage of either 0 or 10 V can be maintained depends on the number of characters sent by the computer. By controlling the number of space () and double dot over y (ÿ) characters, the time duration for slow and fast speed can be controlled.

A solid-state normally open relay is placed between the serial port output (neutral and live) and the MOTOR CONTROL (T-20 and T-E1) as shown in Figure 3.20. The input side of the relay is connected to the serial port output line and output side of the relay is connected to the MOTOR CONTROL. The input voltage rating of the relay is 3-32 V dc and the output voltage rating is 13 V. T-20 and T-E1 are open as the relay is normally open. The relay simply acts as a switch to open and close T-20 and T-E1 i.e., slow and fast speed.

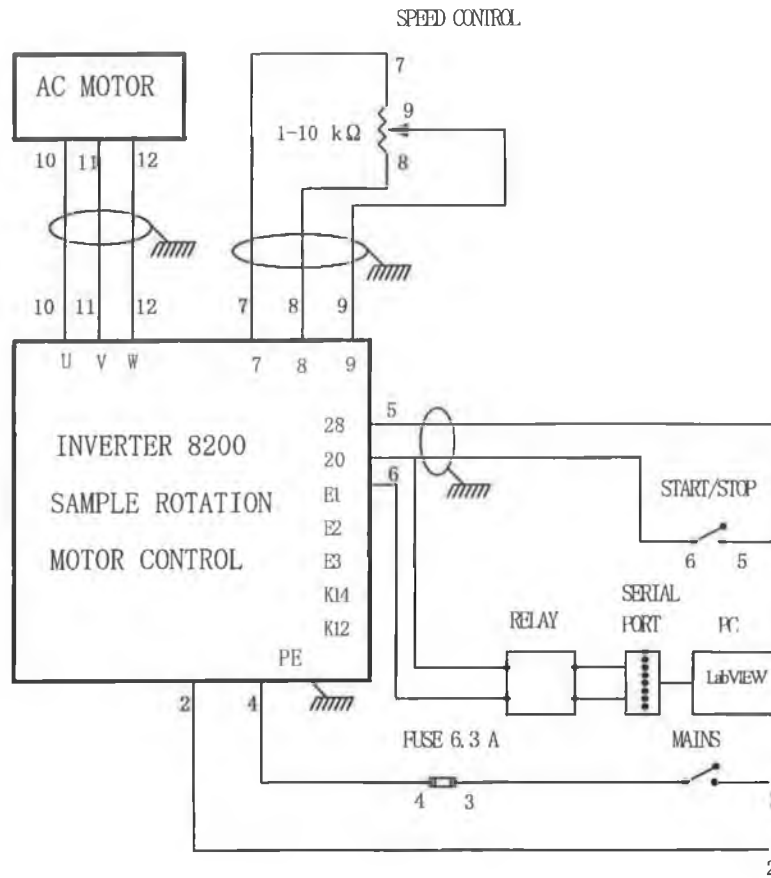


Figure 3.20. Modified connection diagram for time control of motor speed.

The opening and closing time durations are maintained by a code using LabVIEW. Figure 3.21. shows the front panel of the LabVIEW code to control the timing of different speeds. A certain number of space () characters (placed in the string 2) is sent and during that time there will be no voltage output at the serial port and it cannot close the relay and consequently T-20 and T-E1 remain open and no change in motor speed occurs. But when a certain number of double dot over y (ÿ) characters (placed in string 1) is sent to the computer, it produces voltage at the serial port output and that voltage closes the relay. As a result T-20 and T-E1 become short-circuited and the motor rotates at a higher speed. The run command in the front panel is a continuous run option, which can continuously send characters from the two different strings sequentially. The block diagrams of this code displaying the two different sequences (1 and 10 rev/min) are shown in the Figure 3.22. and Figure 3.23. respectively.

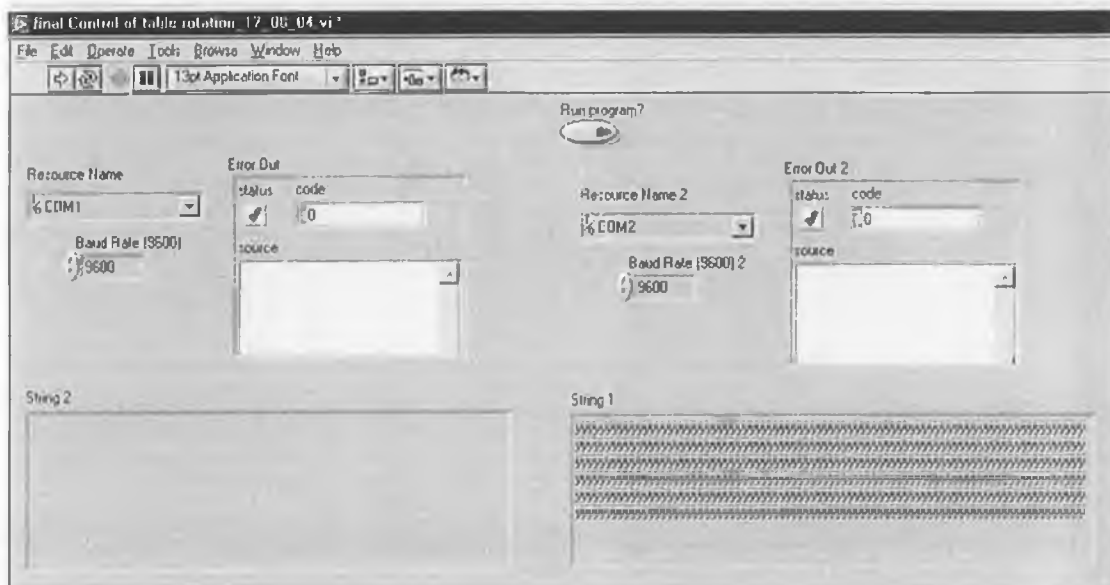


Figure 3.21. Front panel of the LabVIEW code for time control of motor speed.

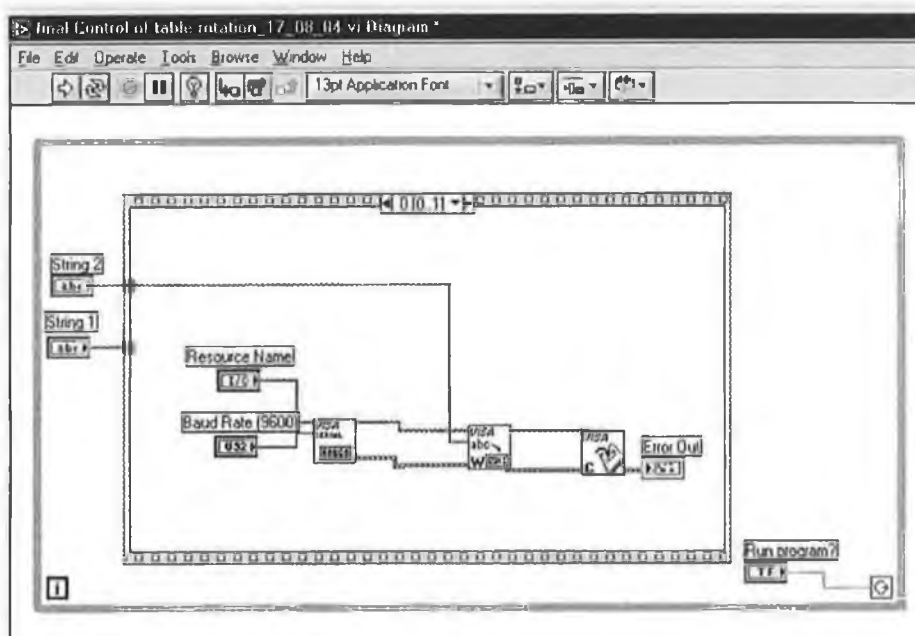


Figure 3.22. Block diagram showing the route of sending the space characters.

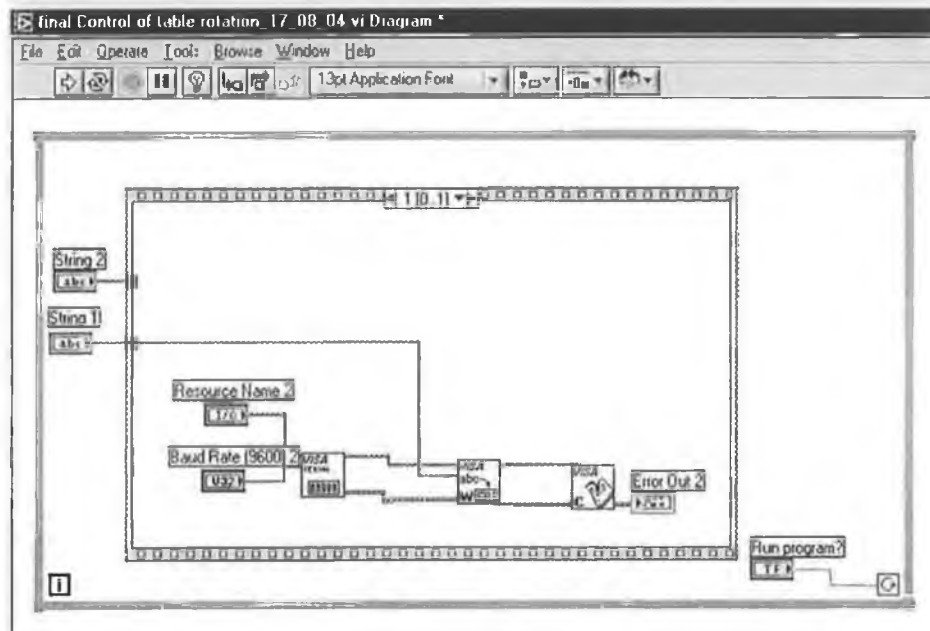


Figure 3.23. Block diagram showing the route of sending the double dot over y characters.

Disadvantages of the time control method

- Data communication through serial port is not very reliable in terms of accurate timing of events due to buffer delays.
- Before every operation the system has to be calibrated for correct positioning of the slow and fast speed.
- The control is an open loop system, which makes it impractical to maintain a constant position speed profile of the rotary substrate table. There is always a possibility of the substrate being shifted to a completely opposite position. It was found that after few revolutions the positions of the slow and fast speeds were shifted.

In order to achieve the position accuracy the control system must have a feed back loop or an event timer. This will make the control system more complicated. In the following section a more practical and easy approach has been employed.

3.13.2. Position control of motor speed

It is explained before that, time control system of motor speed has failed due to the position shifting of the substrate table. To solve this problem, position controlled system has been developed. The same basic idea of opening and closing the T-20 and T-E1 is also applied here. In this system a microswitch has been connected to the T-20 and T-E1 to

open and close the terminals (Figure 3.24.). When the microswitch is on, T-20 and T-E1 become short-circuited and speed increases to the higher value. Again when the microswitch is off, T-20 and T-E1 are open and speed decreases to the lower value specified. The sequencing of ON and OFF and the timing between the two events are maintained by a cam.

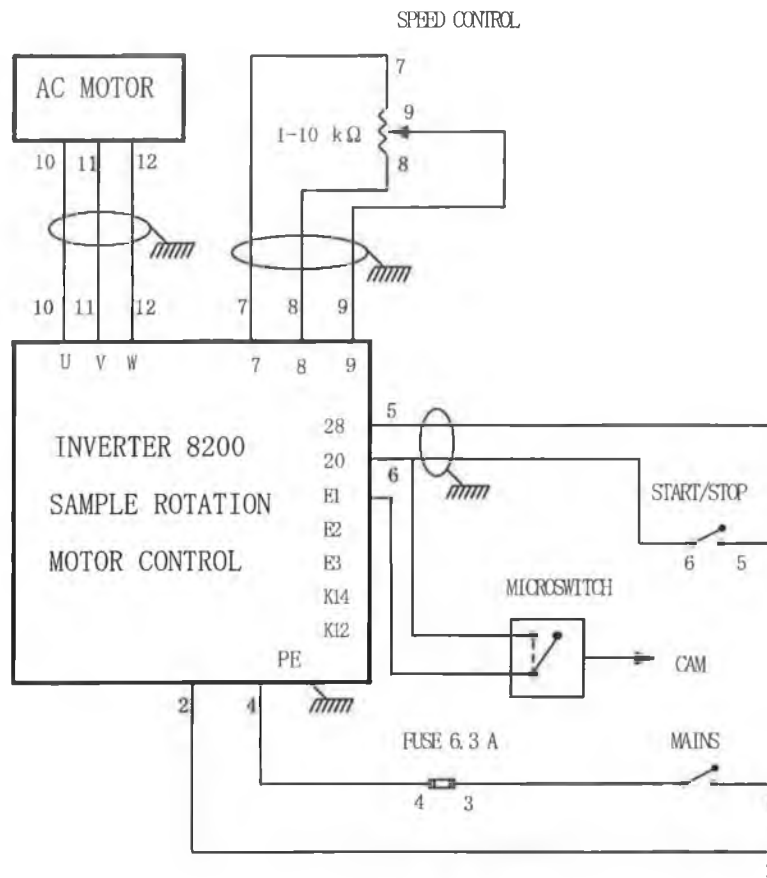


Figure 3.24. Modified connection diagram for angular position control of motor speed.

The cam is placed on top of the pulley attached to the motor shaft. This pulley is coupled with another pulley placed on the rotary substrate table shaft via a tooth belt and both pulleys have the same gear ratio i.e., one turn of the motor shaft will give one turn of the rotary substrate table shaft. The microswitch is placed vertically near the cam. Cams have been designed in such a way they have higher radii covering a certain angular distance and lower radii covering another certain angular distance. The cams have extended holes to screw them on the pulley with the advantage of adjusting their positions. When the higher radius comes in front of the switch it presses the lever of the microswitch so that the switch is on and consequently the table rotates at faster speed. But when the lower radius comes in front of the lever, it releases it and the table rotates at the preset speed. These events are schematically presented in the Figure 3.25.

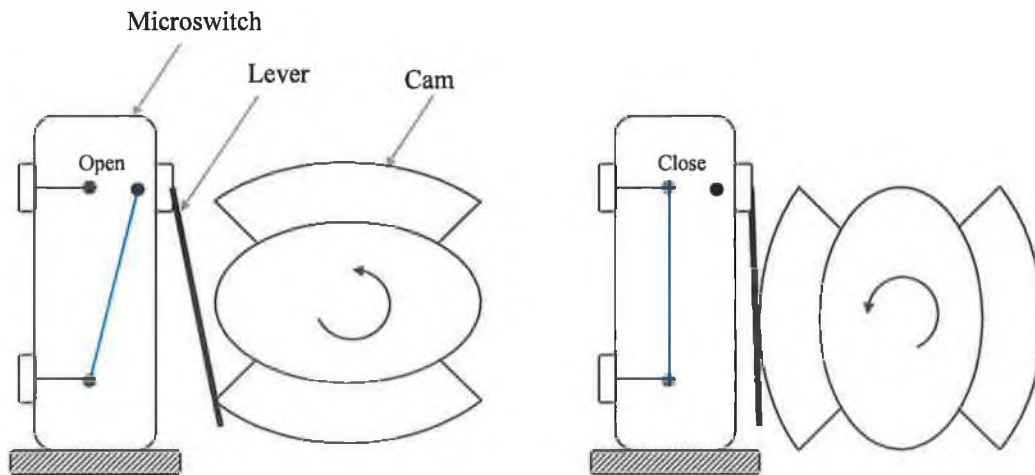


Figure 3.25. (a) Opening and (b) closing of microswitch with the help of cam.

The first cam has higher radius covering an angular distance of 120° and lower radius covering an angular distance of 60° and repeats the same sequence of higher and lower radius in the next 180° angular distance (Figure 3.26. (a)). This cam would turn the microswitch ON and OFF to follow the fast and slow speed sequences when the targets are opposite to each other (see Figure 3.15. (a)). The second cam has higher radius covering an angular distance of 210° and lower radius covering an angular distance of 150° (Figure 3.26. (b)). This cam would turn the microswitch ON and OFF to follow the fast and slow speed sequences when the targets are side by side (see Figure 3.15. (b)).

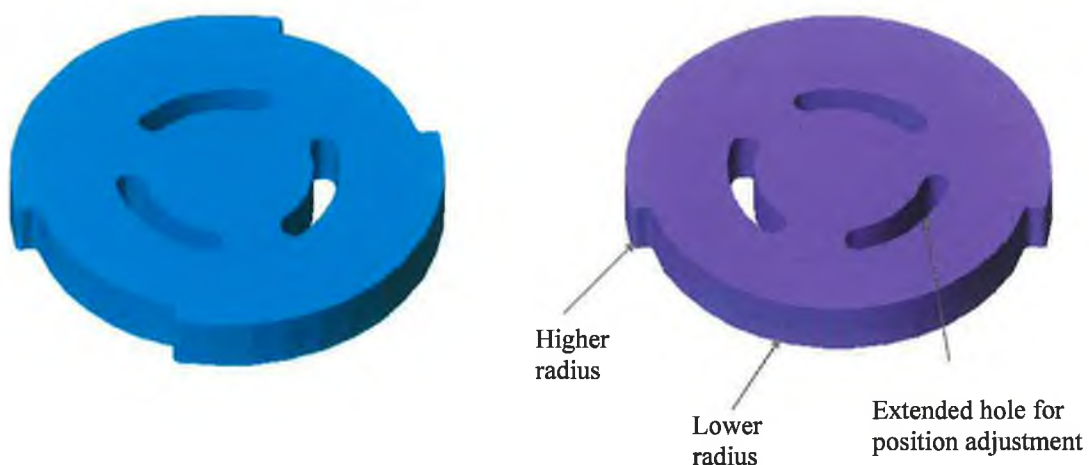


Figure 3.26. Designed cams to control angular position of the motor speed for (a) opposite target and (b) side-by-side target arrangements.

Advantage of position control of motor speed

The position control system is better than the time control system due to the fact that it is controlling the slow/fast speed sequence in terms of angular position via a fixed profile cam where there is very little chance of position errors. It is also a cheaper option than the previous system. During forming a multilayer coating the compositional period would be directly proportional to the rotational speed. By setting higher rotational speed (10 rev/min) very thin layers can be deposited while relatively thicker layer can be deposited by setting lower rotational speed (1 rev/min). For example in a 20 min long deposition period of TiN and MoS₂ layers with a rotational speed of 3 rev/min would produce approximately 60 compositional periods.

3.14. DEVELOPMENT OF THE RIG FOR PLASMA NITRIDING

The main motivation for facilitating the rig for plasma nitriding was to deposit the duplex surface treatment; nitriding the substrate first and then deposit a thin coating on the nitrided samples. The existing deposition chamber can be used for plasma nitriding. The substrate is made cathode attaching negative end of the power supply with the electrical connector at the end of the rotary substrate table and the whole chamber and other accessories attached to the chamber are made anode.

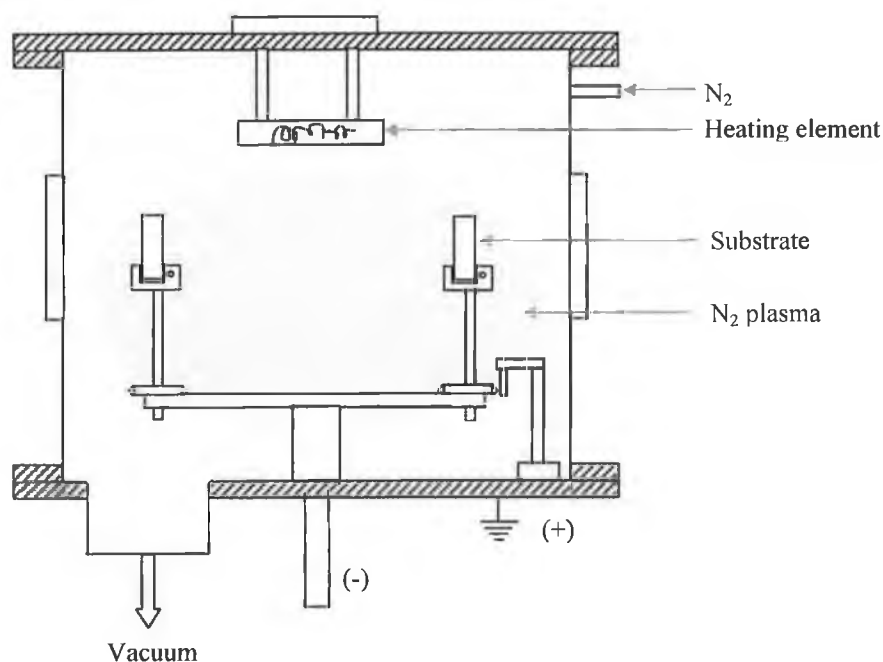


Figure 3.27. Schematic diagram of plasma nitriding.

After achieving high vacuum, nitrogen is backfield into the chamber and a high voltage (500-1000 V) is applied between anode and cathode to form a DC plasma of nitrogen. The nitrogen ion will bombard the substrate with high-energy and form a hard nitrided case with tough nitrogen diffused core, which will give the required platform for depositing hard coating. The schematic diagram for nitriding configuration is shown in Figure 3.27.

3.15. MODIFICATION OF THE WEAR-TESTING RIG

The abrasion-impact wear tester in the magnetron-sputtering lab is custom-built heavy-duty rig. In case of thin coating, light load should be applied on the coated sample to measure the coating wear without going further beyond the coating. The weight of the stylus itself is 180 g, which means that load less than 180 g cannot be applied on the sample. The rig has been modified for applying light load on the sample. The detailed description of the rig will be found in reference [276].

3.15.1. Brief description of the Impact-wear testing rig

The schematic diagram of the wear test rig is shown in Figure 3.28. The test rig performs the following main functions:

1. Direct abrasion (Sliding contact)
2. Direct impact
3. Compact impact-abrasion or dynamic abrasion conditions

1. Direct abrasion

Samples are held in position by two clamps and a locating fixture to the wear test table. The abrading stylus is located over the sample, in a linear drive unit driven by the motor. The load cell is placed over the stylus housing in a fixture and the normal load is placed onto this. The normal load is held on a bearing system in two guides, fixed to the linear drive unit. At the motor shaft, the linear displacement of the stylus and thus the sliding velocity can be set by adjusting the linear drive unit relative to the shaft center. In operation, the stylus rubs or abrades along the sample and produces the wear scar. Under sliding conditions, the impact operation is removed and pure rubbing occurs, producing a linear scar only. Sliding action in this test rig is reciprocating, causing the abrasion in both directions. This form of wear is considered more severe than one directional process.

2. Direct impact

The wear test table or the impact table is positioned on the test rig base plate by four vertical pillars and linear guide bearings. The pillars are fixed to the base plate of the test rig. These pillars allow the table to move vertically only for impact, driven by the cams through the use of knife-edges fixed to the table. Four bevel washers on the pillars act as a spring force to drive the table vertically upwards, producing impact while the cams are used to drive it downwards, opposing the spring action. In direct or pure impact only, the sliding velocity is reduced to zero by fixing the position of the crank end in the middle of the drive unit, and the stylus impact the sample each time in the same place. The number of cycles can be changed with the motor speed.

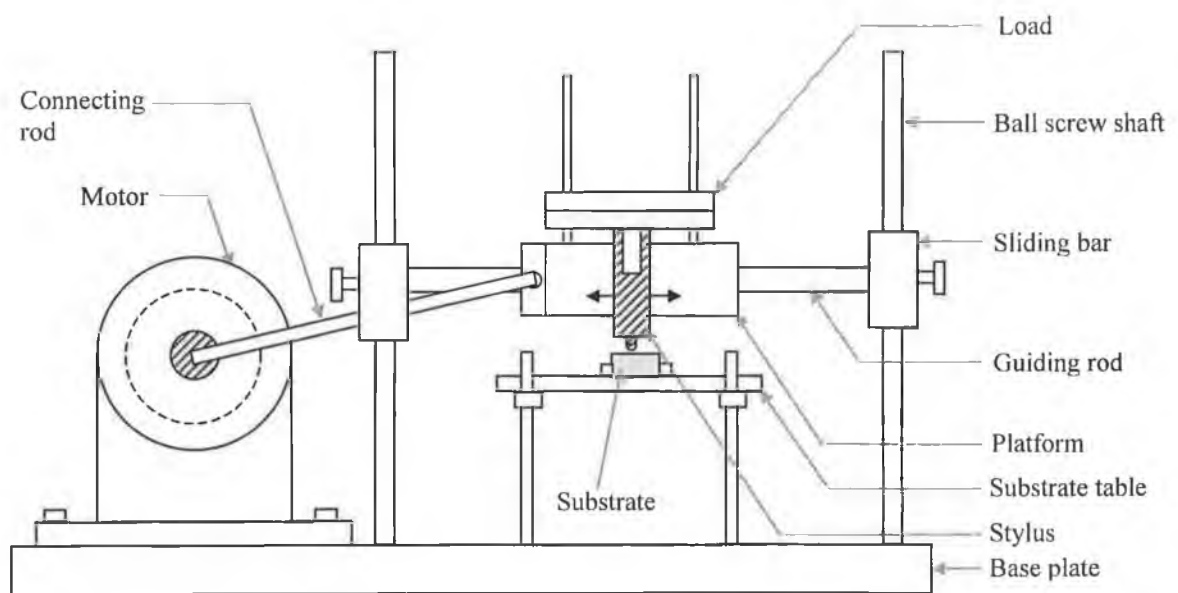


Figure 3.28. Schematic diagram of the wear rig.

3. Compact abrasion-impact

In this mode both sliding velocity is set to a particular value and impact motion is also set as described earlier to get a combined impact and abrasion.

Tests can be applied to both coated and uncoated substrates under identical conditions. Other applications of the test rig include a facility to change the sliding velocity and apply impact loads at any location along the abrasive wear scar. The test procedure is relatively fast and the applied forces of impact can be changed to suit test conditions. Other testing may include lubricated conditions to determine the effects of coolants or a lubricant on the wear conditions.

3.15.2. Modification

During sliding instead of putting physical load on the stylus, the force is applied on the stylus by a spring. The schematic diagram of the modified loading system is shown in Figure 3.29.

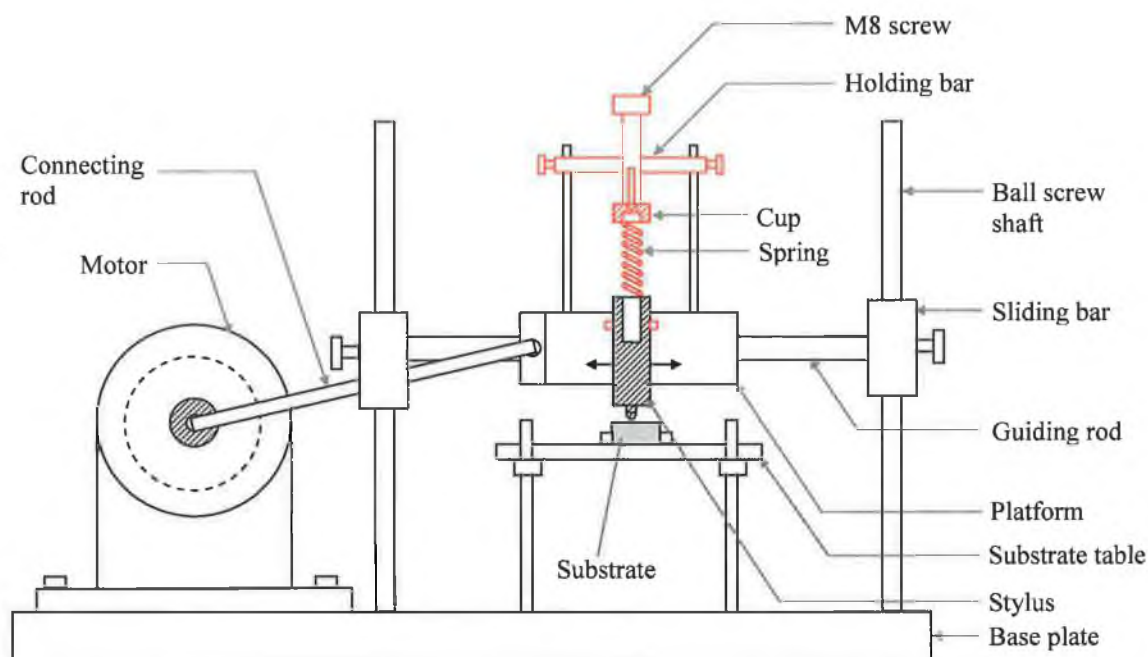


Figure 3.29. Modified loading system in wear testing rig.

A holding bar is placed in two guides of the wear test table with an adjusting screw. An M8 screw is positioned vertically on tapped through hole of the holding bar. There is also a tapped M4 hole at the end of the M8 screw. An M4 screw is attached with a cup using an adaptor plate screwed onto the cup. The M4 screw is attached in the tapped hole of the M8 screw. The M4 screw can easily rotate in the cup. A spring is attached with the cup by a pin. The other end of the spring is attached with the stylus holder by similar pin. The detailed drawings will be found in Appendix B.

3.15.3. Operational procedure

By moving the M8 screw upward the stylus can be hanged freely. As the M8 screw is moving downward the whole cup-spring-stylus assembly will move downward. When the stylus will touch the sample, it will not give any force on the sample as it is hanged from the spring. By further moving the M8 screw downward, the cup-spring-stylus assembly

will move downward and the stylus will be pressed against the sample by the spring force. Eventually force will be applied on the sample. A load cell is positioned between the stylus and the sample to measure the load on the sample. The force on the sample will be calibrated against the M8 screw movement. By continuously moving the M8 screw, a continuously varying load can be applied on the sample. The spring is chosen so that load on the sample can be varied from 20 g to 1000 g.

3.15.4. Advantages of the redesign

- Very light loads can be applied on the sample depending on the spring constant.
- Loads on the sample can be varied with very small load gap between the successive loads.
- This design will allow operating the rig both for heavy duty and light duty purpose interchangeably with very minute change in the assembly.

3.16. SUMMARY

The development of magnetron sputtering rig is briefly reviewed in this chapter. The detail drawing of the designs are provided in the appendix. The closed-field magnetron sputtering along with one-axis and two-axis rotary substrate table has facilitated the rig for deposition of multicomponent, multilayer, duplex and composite coatings. Higher deposition rate is expected from the rotational control of being slow speed in front of the activated target and faster speed in front of the inactivated target instead rotating at uniform speed within one cycle.

CHAPTER 4

CFD modelling of gas flow in sputtering chamber

4.1. INTRODUCTION

In thin coating deposition techniques e.g., as Chemical Vapor Deposition (CVD), Physical Vapor Deposition (PVD) etc., process gases are fed into the deposition chamber to deposit thin coatings. Usually in the reactive sputtering process, argon gas is used as the process gas for sputtering and N_2 is added into the chamber to react with the sputtered material. The deposition of thin coating and their uniformity depends on the flow of the process gases inside the deposition chamber. It is worthwhile to simulate process gas flow, which might give some important information from process optimisation and deposition point of view. Computational Fluid Dynamics (CFD) is the ideal method for understanding the fluid flow phenomena through arbitrary geometries. FLOTRAN-CFD code of the ANSYS simulation package has been used to gain an insight of the gas flow characteristics in a magnetron-sputtering chamber before igniting the plasma. Multiple species gas flow analyses have been performed to visualise the mixing behaviour of the process gases inside the deposition chamber. The results showed that the location of gas inlet ports and substrate has a greater influence on the gas distribution inside the chamber and over the substrate where the reactive gas will react to form compound coating. Results are presented in terms of velocity profiles, pressure profiles, and species distributions, density profile of the mixed gas species across the chamber, inlets and outlet for various gas flow rates and arrangements of substrate positions.

4.2. COMPUTATIONAL FLUID DYNAMICS-A GENERAL INTRODUCTION

Computational Fluid Dynamics (CFD) is a computer-based simulation tool that solves a set of equations governing the fluid flow over any geometrical configuration whilst advancing the solution through space or time to obtain a numerical description of the complete flow field of interest. The equations can represent steady or unsteady, compressible or incompressible, inviscid or viscous, Newtonian or non-Newtonian, multiple or multiphase fluid flows and also including non-ideal and reacting fluid behavior. The particular form is chosen depending on the intended application. The state of the art is characterized by the complexity of the geometry, the flow physics, and the computer time required to obtain a solution. The role of CFD in engineering predictions has become so important that today it may be viewed as a new branch of fluid dynamics, the other two branches being the classical cases of pure experiment and pure theory (Figure 4.1.).

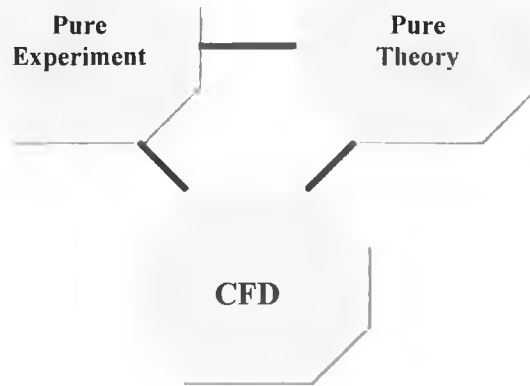


Figure 4.1. The three branches of fluid dynamics.

4.2.1. Basic processes in CFD

The equations governing the fluid flow problem are the continuity (conservation of mass), the momentum (conservation of momentum) and the energy (conservation of energy) equations. The starting point for any description of a flow field is the solution of the Navier-Stokes equations, which can be described as the variation of the three components of velocity (u , v , w) in both space and time, coupled to the pressure gradients in x , y and z directions. These equations form a system of coupled non-linear partial differential equations (PDEs), which require numerical methods to obtain solutions.

To start a CFD analysis first task is to identify a real fluid flow problem and create a physical model of the flow field by considering the nature of the flow. A simplified mathematical model is then created from the knowledge of the physical problem. This means replacing of the differential equations governing the fluid flow with a set of algebraic equations. This is done by the discretization (meshing) of the fluid domain into cells, with each cell having a grid point at its vertex. The well-known discretization methods used in CFD are Finite Difference Method (FDM), Finite Volume Method (FVM), Finite Element Method (FEM) and Boundary Element Method (BEM) [277]. The mesh covers the whole fluid area and associated boundaries, inlets and outlets. These boundaries are described as boundary conditions and show how the flow is contained inside the domain. The boundary conditions are specified in terms of velocities, pressures, temperatures etc. to carry out the numerical solution by digital computer. The fluid's physical properties (viscosity, density etc.) are applied to flow domain. The solution method depends on the type of problem being modelled and can vary between laminar and

turbulent, incompressible and compressible, transient and non-transient etc. After the solution the results are obtained in different forms. Finally, the sequence of physical model, mathematical model, and numerical solution, together with the computed results are interpreted to provide the final description of the flow field. The different steps of applying computational fluid dynamics are shown in Figure 4.2.

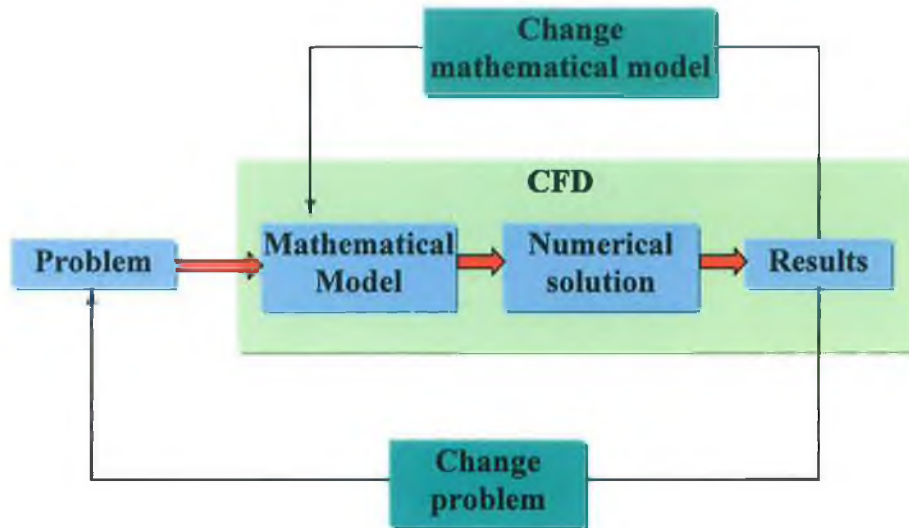


Figure 4.2. Steps in applying computational fluid dynamics.

4.2.2. Importance of CFD

CFD is considered as a virtual fluid mechanics laboratory where thousands of experiments can be performed on the computer. It also allows design engineers to solve practical flow problems within reasonable time and cost constraints. It can provide the values of all the relevant variables (such as velocity, pressure, temperature, turbulence intensity etc.) throughout the domain of interest, even in the inaccessible areas where experimental measurement are not obvious. This wide range of information can save lot of time and cost during the physical prototype stage. In simulation techniques, realistic models i.e., large or small dimensions, low or high temperatures, fast or slow processes, and toxic or flammable substances can be achieved. There is no need for scaling down or scaling up the models. Due to this vast variation in parameters, ideal situations can easily be achieved, thus removing the interference from irrelevant effects. The visualisation techniques for the flow process are very sophisticated giving the end-user valuable insights in the flow behaviour, which would be impossible with experimental techniques.

4.2.3. Applications of CFD

There is a wide range of applications of CFD in different industries including aerospace propulsion systems, nuclear power-plant heat exchangers, passively or actively cooled high-power electronic components and systems, reactor design and delicate artificial heart valves. CFD has increasingly been used to deal with multiphase and multiple species flows taking place in different industrial sectors.

4.2.4. Limitations of CFD

CFD has the inherent limitation of approximating a continuous system with finite length (discrete approximation). Computational techniques rely totally on the validity of the analytical models in the coding. If these are wrong, or the understanding of the physical phenomena is not yet available, simulation techniques cannot be used. Experimental investigation on the other hand will still produce a result. Some examples where a mathematical description is still lacking, includes complex turbulent flows, certain non-Newtonian fluids and some combustion processes. Even where the mathematical description is correct, some small-scale effects, like small-scale turbulence, if they are to be modelled for every location in the computational domain, will provide prohibitively expensive in computer power. It should be noted that the numerical solution of a computational problem is a small part of the total engineering process. It is a must to understand the physical flow problem to successfully implement CFD.

4.2.5. Future of CFD

During the last 10–15 years, computational fluid dynamics (CFD) has become a very powerful tool in the process industry not only for research and development of new processes but also for understanding and optimisation of existing ones. Although a large volume of research publications have appeared in recent years on numerical flow simulation, the potential for further research is expanding at an ever-increasing rate. In the decades to come, it appears that many more powerful algorithms will be evolved and several complex flow/heat transfer problems will be successfully simulated. Many commercial softwares have been developed [278,279] and many more to come. It is also likely that more industries would consider CFD vigorously for product developments.

4.3. GAS FLOW IN LOW PRESSURE

Gas flow at below or above atmospheric pressure is commonly encountered in fluid dynamics calculations. The behaviour of gas at low pressure is quite different from those at normal pressure. As a reduction in pressure occurs in a flow system, the gas will be rarefied passing through several flow regimes. Rarefied gas flows are in general encountered in flows through small geometries such as Micro-Electro-Mechanical Systems (MEMS) and in low-pressure applications such as in high-altitude flying or vacuum coating deposition chamber.

The mean free path (λ) concept is extremely important in low-pressure engineering calculations. It defines the boundary between different types of gas flow regimes. The mean free path is defined as the mean path distance, which each gas molecule covers between two collisions with other molecules and is expressed by the following relations.

$$\lambda = \frac{1}{\sqrt{2}n\delta_m^2} \quad \text{-----} \quad (4.1)$$

At higher pressure, the mean free path is much smaller than the dimensions of the gas container; the gas behavior is dominated by intermolecular interactions and the gas behaves much like a liquid. But at low pressure, the mean free path is larger than container dimensions, the gas behaviour is dominated by collisions with walls rather than intermolecular collision, no viscosity prevails among the gas molecules and the gas behaves like discrete molecules.

The degree of gas rarefaction can be expressed through a dimensionless Knudsen number (Kn), which combines the mean free path and the characteristic dimension of the gas container (d). Physically it provides an indication that how many times the mean free path is larger than the container dimension.

$$Kn = \frac{\lambda}{d} \quad \text{-----} \quad (4.2)$$

In terms of pressure and temperature Knudsen number can be represented by the following equation:

$$Kn = \frac{KT}{\sqrt{2}\pi P\delta_m^2 d} \quad \text{-----} \quad (4.3)$$

Different flow regimes distinguished according to Knudsen number are [280-282]: viscous (continuum) regime, transition (Knudsen) regime and the molecular regime as shown in Figure 4.3.

Continuum flow starts to occur when Knudsen number is smaller than 0.01. After reaching Knudsen number value 0.001, perfectly viscous flow is obtained. There is no slip flow at the wall of the container. In this regime, mean free path is much less than the dimensions of the (flow domain) container ($\lambda \ll d$), the molecules are in a constant state of inter-collision, and gas behavior is dominated by the interactions between the particles. Such interactions result in viscous force and cause good communications throughout the gas. For this reason this regime is sometimes also called viscous flow regime. This will be found almost exclusively in atmospheric pressure to rough vacuum range. Viscous flow includes turbulent flow, where the flow is irregular with substantial eddies, and laminar flow, where the flow is regular with no eddies. Laminar flow in a container with parabolic velocity distribution is known as *Poiseuille flow*. This special case is found frequently in vacuum technology.

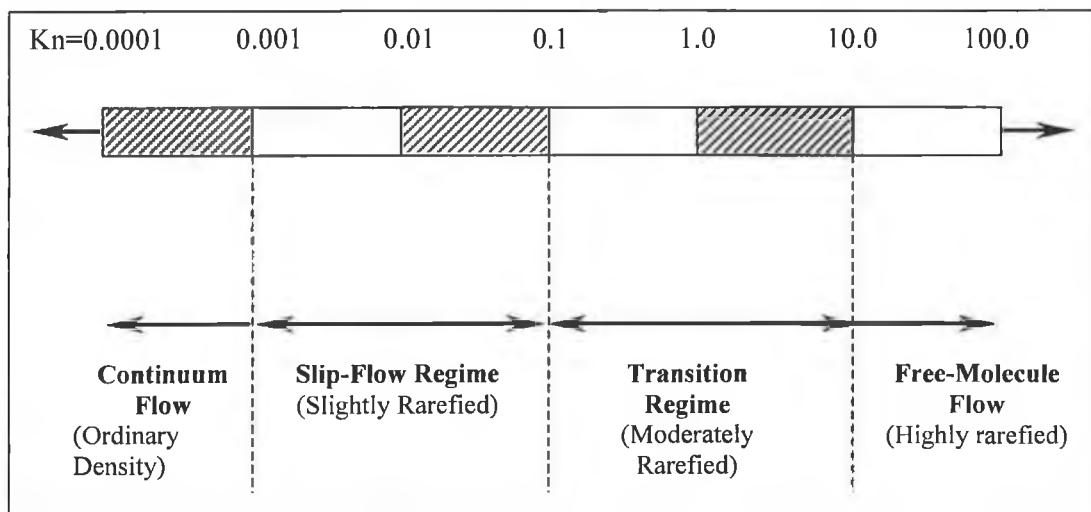


Figure 4.3. Gas flow regimes under different Knudsen numbers [280].

A characteristic quantity describing the viscous flow state is the dimensionless Reynolds number, Re . It is common to evaluate the Reynolds number and compare it to the transitional number to determine whether the flow is laminar or turbulent. Reynolds number is the product of the pipe diameter, flow velocity, density and reciprocal value of the viscosity (internal friction) of the gas, which is flowing.

$$\boxed{\text{Re} = \frac{\rho v d}{\mu}} \quad \text{-----} \quad (4.4)$$

Flow is turbulent where $\text{Re} > 2200$ and laminar where $\text{Re} < 2200$. The phenomenon of *choked flow* may also be observed in the viscous flow situation. It plays a part when venting and evacuating a vacuum vessel and where there are leaks.

The gas flow can still be considered as continuum upto Knudsen number value of 0.1. But at this situation, there is substantial amount of slip at the wall of the container, called slip-flow regime.

Molecular flow is present where the mean free path length for a particle is very much larger than the dimension of the container: $\lambda \gg d$ i.e., Knudsen number is in excess of 10. In this regime the molecules can move freely colliding more frequently with the walls rather than any mutual interference. The statistical motion of the independently moving molecules then governs gas behavior. Molecular flow prevails in the high and ultrahigh vacuum ranges.

The transitional range between viscous flow and molecular flow is known as Knudsen or transition flow. Knudsen flow occurs when Knudsen number lies between .1 and 10. Behaviour of both of the viscous and molecular flow regimes exists in this case. It is prevalent in the medium vacuum range.

4.4. GAS FLOW MODELLING APPROACHES AT LOW PRESSURE

In many low pressure or vacuum applications, the gas velocities involved are comparatively small and the gas density is such that the flow varies from viscous to molecular. As the gases behave distinctly in different flow regimes, there needs particular modelling approaches in each flow regimes. The different gas flow modelling approaches are reviewed in reference [280] as shown in Figure 4.4. Gas flow modelling is usually done by molecular (at low pressure) and continuum modelling (at high pressure).

Modelling of continuum regime is accomplished by deterministic methods such as computational fluid dynamics (CFD). Continuum mechanics equations are valid in this regime. In CFD, the velocity, density, pressure, etc., are defined at every point in space and

time, and conservation of mass, energy and momentum lead to a set of nonlinear partial differential equations (Euler, Navier–Stokes, Burnett, etc.) and the solution of these equation actually describes the flow field.

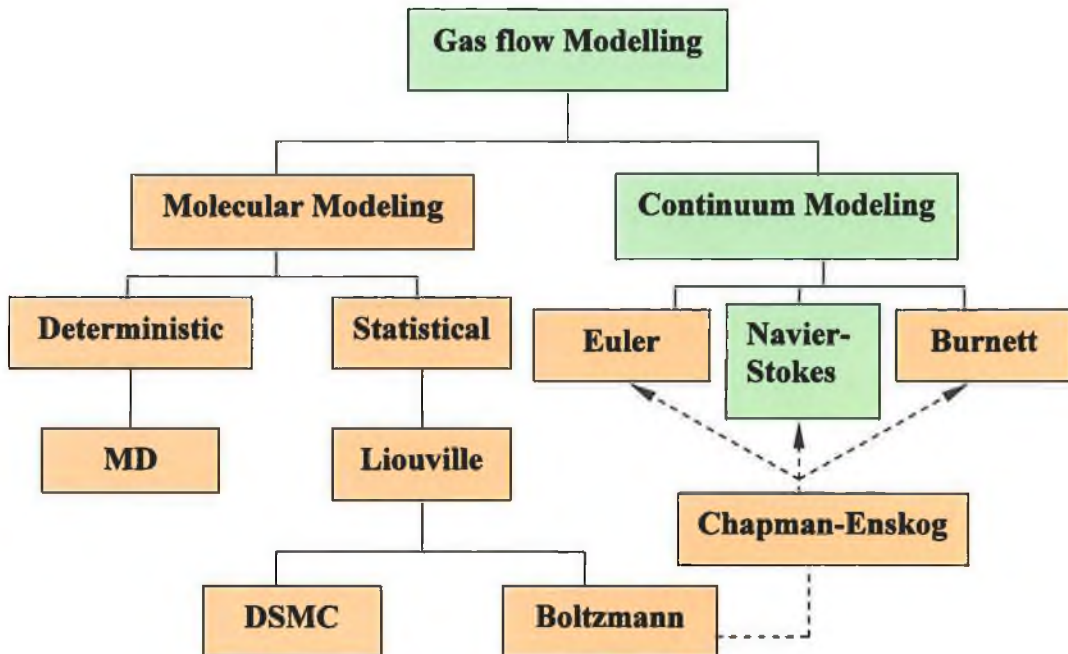


Figure 4.4. Gas flow modelling approaches [280].

In the continuum models, the macroscopic fluid properties are the dependent variables while the independent variables are the three spatial coordinates and time. A continuum fluid implies that the derivatives of all the dependent variables exist in some reasonable sense. In other words, local properties such as density and velocity defined as averages over elements are large compared with the microscopic structure of the fluid but small enough in comparison with the scale of the macroscopic phenomena to permit the use of differential calculus to describe them. Additionally, the flow must not be too far from thermodynamic equilibrium. The former condition is almost always satisfied, but it is the latter which usually restricts the validity of the continuum equations. The continuum model is easier to handle mathematically than the alternative molecular models. Thus, continuum models should be used as long as they are applicable by taking careful considerations of the validity of the Navier–Stokes equations.

The modelling of molecular/rarefied flow regime are usually accomplished using deterministic methods such as Molecular Dynamics (MD) or probabilistic methods such as Direct Simulation Monte Carlo (DSMC) [283] and solving kinetic energy equation (Boltzmann equation). The molecular models recognize the fluid as a myriad of discrete

particles: molecules, atoms, ions and electrons. The goal is to determine the position, velocity and state of all particles at all times. Provided that there is a sufficient number of microscopic particles within the smallest significant volume of a flow, the macroscopic properties at any location in the flow can then be computed from the discrete-particle information by a suitable averaging or weighted averaging process. Monte Carlo simulation estimates actual molecular trajectories necessary in the molecular regime to make accurate calculations. These methods can also be applied to some degree of transitional flow. Navier-Stokes equations cannot be used in this regime, even the modified one.

However, in a mixed or transitional flow regime with rarefied and continuum conditions, a combination of both techniques can provide a predictive method that enjoys the advantages of each technique in its suitable flow domain [284]. The solution of continuum region is obtained with CFD, which in turn provides an inflow boundary for molecular region. By combining the continuum and non-continuum solutions, flow fields with order of magnitude changes in density from continuum to rarefied flow can be obtained without the complexity of strong coupling, but with the advantage of using the best method in each region.

4.5. GAS FLOW MODELLING IN VAPOR DEPOSITION METHODS

Gas flow mechanisms in the different coating deposition reactors have attracted greater practical scientific and engineering interests. Simulations of low-pressure CVD have been used in semiconductor growth to study the deposition over micron-sized trenches and flow through and around the substrates. Ikegawa and Kobayashi [285] and Coronell and Jensen [286] have analyzed the flow in and around systems of wafers in CVD chambers by DSMC method. Recently, CFD has been used to simulate the vapour-phase process in CVD to optimize uniform deposition across each wafer and from wafer to wafer, and step coverage over topographical features by correctly choosing the total pressure, composition of the entering gas, and spacing of the wafers. Kotecki et al. [287] have developed a CFD model to enhance the performance of a CVD process. It has been shown that the model can provided information to improve wafer and gas phase temperature uniformity and the thickness uniformity in terms of reactor geometry. ANSYS-FLOTRAN has been used to investigate and optimise the gas flow system in a Plasma Enhanced Chemical Vapor Deposition (PECVD) reactor [288]. The simulated results showed that the reactor

geometry and the deposition process pressure have high influence on the velocity distribution curves. It has also been shown that it is necessary to change the geometry of the reactor to achieve improved uniformity in deposited thin coating. Similarly, a room temperature CVD reactor has been optimised in terms of gas flow and thickness variation of the deposited TiN coating thickness by using computational-fluid-dynamics (CFD) software PHOENICS-CVD [289]. The study has been restricted to the physical parameters to get an insight into the thermodynamic behavior of the different gas species in the chamber and to receive at least viable directions for optimising gas flow, temperature conditions, pressure conditions and gas inlet layouts. The numerical simulation of organometallic chemical vapour deposition (OMCVD) of copper coatings has been performed using PHOENICS-CVD simulation tool, which includes the treatment of all relevant transport phenomena [290]. The radial course of deposition rates and their dependence on wafer temperature have been calculated and compared with deposition experiments. The simulation represents the main experimental trends and appears to be suitable for process and equipment optimisation. Computational fluid dynamics has been used to model SiC deposition by chemical vapour deposition [291]. Results presented in terms of flow patterns, species distributions, and growth parameters at various reactor pressures have provided an understanding of the flow patterns, the temperature, and the species distributions in the reactor, and how these affect deposition rate, uniformity, and coating composition. Three-dimensional finite element modelling of transport phenomena in a close-spaced Metalorganic Vapour Phase Epitaxy (MOVPE) reactor has been performed to see the effects of operating conditions and reactor geometry on flow patterns, growth rate and growth rate uniformity. Experiments on the growth of GaAs/AlAs epilayers are consistent with numerical predictions [292].

4.6. MODELLING APPROACHES IN SPUTTERING

Magnetron sputtering is the most versatile deposition procedure among the PVD techniques having the additional advantage of low deposition temperature (room temperature to $400\text{ }^{\circ}\text{C}$) as discussed in Chapter 2. As a deposition technique, the success of magnetron sputtering has turned it into the subject of numerous modelling and simulation efforts. Sputtering process is complex phenomena and it can be divided into four different stages: gas flow and mixing at low pressure (in case of reactive sputtering), plasma generation, physical sputtering of the target and transport of the sputtered neutral species to the substrate. As there are different physical phenomena involved in different

stages, any single model will not be enough to describe all the situations. The modelling of physical and chemical processes involved in each stage and correlating them can be daunting. For each of the steps different kinds of mathematical and numerical modelling are required as suggested in reference [293]. Mathematical models and experimental investigations are usually applied to calculate the plasma parameters [294]. Steady-state plasma model are required to find out the flux and energy of Ar ions striking the target and the substrate. A molecular dynamics sputtering model for the energy distribution, angle distribution, and yield of the sputtered atoms from the target [295,296], and a direct simulation Monte Carlo (DSMC) model for the transport atoms through the low-pressure argon gas to the deposition substrate [297,298]. Gas transport system in TiN reactive sputtering system has been modeled using DSMC methods [299,300]. The different modelling approaches in the magnetron sputtering are reviewed in reference [298].

4.7. OBJECTIVE OF THIS STUDY

Very little can be known from the literature about the gas transport system of the sputtering process. In general it is assumed that the process gases are dispersed all around the chamber at low pressure. Though the plasma effects are very important, neutral gas particle distribution also has effects on the film composition in reactive sputtering. Gas transport system must be included to model any sputtering apparatus. But there are very few studies [285] so far found on the gas flow simulation of PVD deposition process as there are other complex plasma process are involved in PVD compared to CVD process. Further lower pressure is used in PVD than CVD, which is a problem for using the CFD continuum approach. But when the local Knudsen number is ≤ 0.1 , the flow generally is accepted upper limit for applicability of CFD solutions with slip boundary conditions [280,282]. Since CFD solutions can be obtained an order of magnitude or faster than corresponding DSMC solutions, the CFD approach can be used to speed up design turnaround times. CFD simulations using slip boundary conditions are compared to DSMC simulations in an instrumented vacuum test cell typical of semiconductor equipment chambers [301]. The CFD solution matched up well with DSMC simulations within selected range of pressure and gas flow rate. Additionally, there are no commercially available DSMC codes with the support and ease-of-use features that are seen in many CFD software packages, which are already in common use in the industry.

It is evident from the literature that CFD has the capability of simulating the gas flow and mixing behaviour in a deposition chamber. It can also provide better visualization of the flow situation, as it is quite difficult to understand that experimentally. In this study, the main focus will be on CFD modelling of the gas flow inside the magnetron-sputtering chamber during the reactive deposition of TiN assuming the gas flow is continuum and by applying basic fluid mechanics concepts to describe the fluid dynamics and mass transfer. The main parameters that affect the nature of gas flow in deposition chamber are [32]: deposition temperature, deposition pressure, gas flow rate, properties of gas (e.g., density), and deposition chamber geometry. The results of the fluid model, i.e., gas pressure and velocity, might give some useful information during plasma modelling or sputtered particle transport modelling mentioned before.

4.8. NUMERICAL MODELLING CONSIDERATIONS

In this investigation the simulation of process gas flow in a magnetron-sputtering chamber has been conducted by finite element analysis CFD code ANSYS-FLOTRAN. The earliest CFD codes were based on Finite Difference (FD) or Finite Volume (FV) methods and have been applied already to a large number of incompressible and compressible flow problems. One of the disadvantages of these two methods is that, to date, commercial codes are based on a structured grid and difficulties are encountered in applying them to complex geometries. Unlike the FD and FV methods, there is no inherent difficulty for FEM in modelling complex geometries [302]. FLOTRAN combines the advantages of existing finite difference and finite volume methods. Its capability of modelling a wide range of fluid flow and heat transfer problems is reviewed in reference [303]. The model simply deals with the gas flow from pure fluid dynamics point of view before igniting the plasma ignoring the complex phenomenon of the plasma processes during the deposition of thin coatings. The effects of operating parameters (gas velocity and pressure), position of the inlets along the circumference of the chamber on the gas flow and mixing behaviour under isothermal condition have been investigated. Emphasis has also been laid upon the distribution of nitrogen over the substrate at different positions inside the chamber and its possible impact on the composition of coating.

4.8.1. Description of physical problem

The vertically positioned magnetron sputtering deposition chamber is a cylinder with 610.0 mm in height and the internal diameter of 603.0 mm. There are 12 gas inlets on the middle of the chamber body at 90° interval with three inlets vertically in line at each position. The diffusion pump (outlet) is connected off axis with the bottom plate of the chamber. There is a rotary substrate table with four substrate holders inside the chamber. Besides, there are ports on the chamber wall for different kinds of feedthroughs. The different dimensions of the chamber are shown in Figure 4.5.

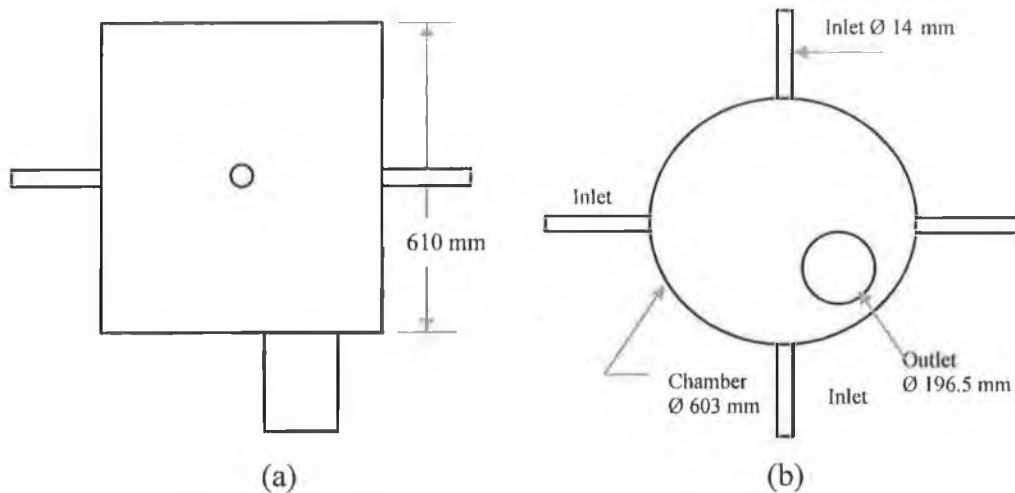


Figure 4.5. Schematic diagram of (a) vertical and (b) horizontal cross-section of the deposition chamber.

The deposition chamber is first evacuated roughly by the rotary pump from atmospheric pressure to 5×10^{-2} mbar (5 Pa). And finally the chamber is evacuated to low pressure with a value of 5×10^{-6} mbar (5×10^{-4} Pa) by the diffusion pump. At this position the working gas are continuously feed into the chamber and vacuum pumps continuously drive the gases out of the chamber. As the inlet gas flow rate is higher than the pumping speed (measured by outlet flow rate) a residual pressure will build up in the chamber and steady state condition will be established within few seconds. By controlling the inlet gas flow rates the chamber pressure is raised to some working pressure value $1-5 \times 10^{-3}$ mbar ($1-5 \times 10^{-1}$ Pa). Argon and nitrogen gases are introduced into the chamber at a rate of 35-40 sccm (standard cubic centimeter per minute) and 5-10 sccm respectively to drive the pressure towards the final value of working pressure for a typical deposition condition of TiN coating depending on the sputtering rate. From the flow rate it can be seen that the major portion of the gas mixture is argon. The gas flow system is shown in the Figure 4.6.

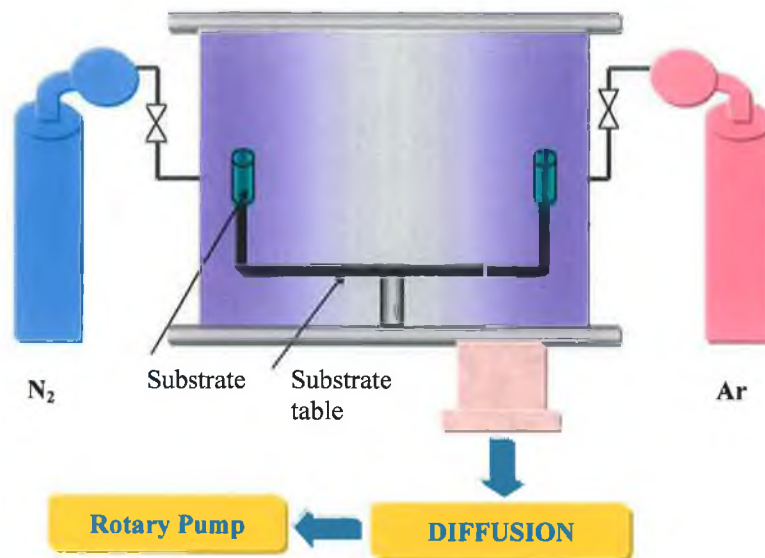


Figure 4.6. Gas flow details in the chamber.

4.8.2. Model formulations

A 2-D model has the advantage of reduced computational time, better visualization and simplifying complex configuration over a 3-D model. As the chamber had no axial symmetry, it would be very difficult to get the perfect symmetry of all the features by taking into consideration of a single cross section either through vertical or horizontal axis to establish 2-D model. So a three-dimensional model was deemed more realistic in this case. There was a limitation on the number of nodes available in ANSYS, so for a full model the available number of nodes was not sufficient to capture the entire flow phenomenon. By considering all these circumstances, one quarter of the full model was considered in this analysis. Although the outlet was off-axis, the outlet was considered in the middle of the bottom plate of the chamber to exploit the advantage of applying a symmetry boundary condition. As the chamber was very big and analysis was mainly focused near the area of the chamber where the substrate is located, so the location of the outlet would not impose a significant effect on the final results (see Appendix C). The inlets were modelled at the middle of the chamber perpendicular to each other. In the model N_2 was introduced through the top inlet (*nitrogen inlet*) and argon was introduced through the right inlet (*argon inlet*). The CFD model was equal to the real geometry in terms of all design points.

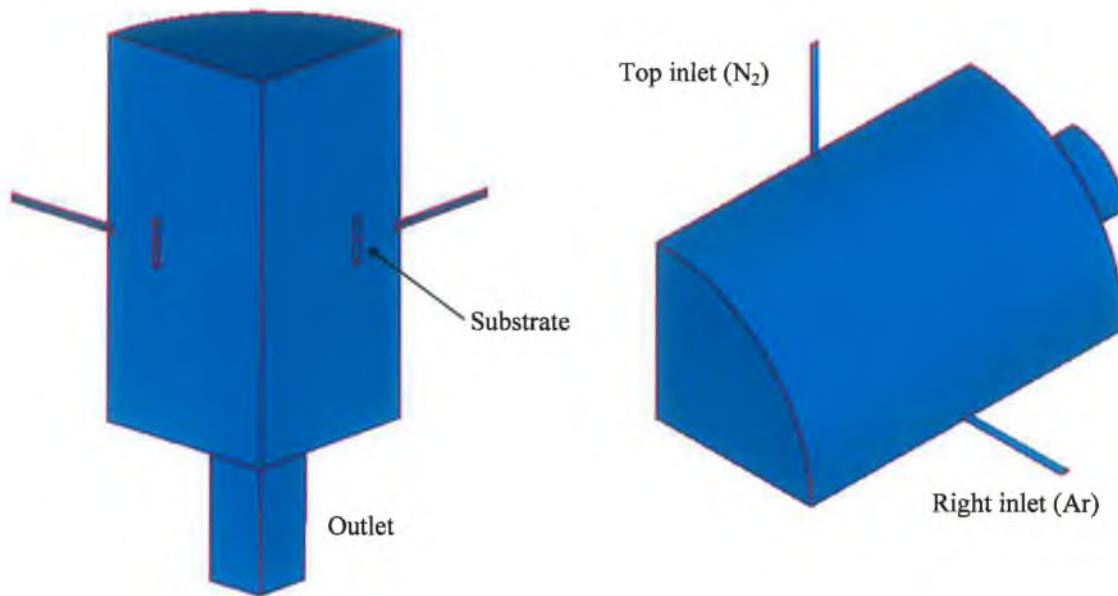


Figure 4.7. One-quarter model of the deposition chamber, inlets and outlets.

A substrate with a length of 70 mm was modelled at three different positions inside the chamber: in front of the nitrogen inlet, in front of argon inlet and between the nitrogen and argon inlet to find out the distribution of nitrogen on the substrate. The substrate was also modelled at four different distances away from the chamber (30, 50, 70 and 100 mm) to see the variation of the nitrogen concentration on the substrate surface. By applying symmetry boundary conditions on the inside surfaces, the quarter model can be considered as full model. All dimensions used in the model were in SI units. Figure 4.7. shows the one-quarter model of the deposition chamber.

Several assumptions were made during the analysis of gas flow in the PVD chamber. The process gas species were considered argon and nitrogen without considering other neutral particles i.e., Ti and TiN. Usually in reactive sputtering nitrogen gases are consumed to form TiN. As very little volume of nitrogen takes part in the reaction, no consumption of nitrogen was considered. The pumping speed was assumed constant. The calculated Knudsen number in the region of interest was sufficiently small enough to consider the flow as continuum. The gas flow regime inside the chamber was considered as laminar according to the calculated Reynolds number. The viscous heating of the gas due to the dissipation was neglected since velocity gradients were not large. Due to low Reynolds numbers in the mixing chamber, the mixing of gases was considered mainly by mass diffusion. The investigated fluid was considered incompressible and steady-state flow rate

was considered as it simulates the average operating conditions. The gaseous mixture was considered to be an ideal fluid with a Newtonian behaviour, which is a reasonable assumption for a low-density gas. The effect of the slow substrate rotation on flow was neglected in the model. As Ar gas was inert, so no reaction was considered between the gas species argon and nitrogen. As the gas temperature was same as the atmospheric temperature, no buoyancy effect due to gravity and no temperature dependant gas properties [304] were taken into consideration.

4.8.3. Experimental data collection

As it is explained in the previous section that when the flow rate of the gas is increased the chamber pressure increases and after a certain time it reaches the steady state. Several steady-state pressures were gathered by varying the flow rate of argon and nitrogen. The following two tables (Table 4.1 and Table 4.2) give the recorded values of steady-state chamber pressure, flow rate of the gas species and their corresponding velocities at the inlet with constant nitrogen and constant argon flow rate. The velocities of the gas species were calculated by dividing the flow rate with the inlet cross-section.

$$\boxed{v = \frac{Q}{A}} \quad \text{-----} \quad (4.5)$$

Table 4.1. Chamber pressure and velocities of Ar at different flow rates of Ar and at constant N₂ flow rate.

Pressure (Pa)	Ar flow rate (sccm)	N ₂ flow rate (sccm)	Ar velocity (mm/s)	N ₂ velocity (mm/s)
0.1	15	8	1.62	0.866
0.4	35	8	3.79	0.866
0.7	51	8	5.52	0.866
0.9	60	8	6.50	0.866

Table 4.2. Chamber pressure and velocities of N₂ at different flow rates of N₂ and at constant Ar flow rate.

Pressure (Pa)	Ar flow rate (sccm)	N ₂ flow rate (sccm)	Ar velocity (mm/s)	N ₂ velocity (mm/s)
0.4	35	8	3.79	0.866
0.42	35	10	3.79	1.08
0.44	35	13	3.79	1.41
0.46	35	15	3.79	1.62

4.8.4. Governing equations

ANSYS-FLOTRAN discretizes the partial differential equations of conservation of mass, momentum and energy using finite elements based techniques [305]. In ANSYS, the velocities are obtained from the conservation of momentum principle, and the pressure is obtained from the conservation of mass principle. The temperature, if required, is obtained from the conservation of energy principle. In addition to that when there is a situation of mixing two or more fluid species, a mass balance equation is solved to get species distribution.

4.8.4.1. Continuity equation

The conservation of mass transfer can be considered as the continuity equation. The continuity equation is as follows:

$$\frac{\partial \rho}{\partial t} + \frac{\partial(\rho v_x)}{\partial x} + \frac{\partial(\rho v_y)}{\partial y} + \frac{\partial(\rho v_z)}{\partial z} = 0 \quad \text{-----} \quad (4.6)$$

The continuity equation can be written in the following vector form:

$$\frac{\partial \rho}{\partial t} + \nabla(\rho \mathbf{v}) = 0 \quad \text{-----} \quad (4.7)$$

In case of incompressible flow, the continuity equation can be written as follows:

$$\nabla \cdot \mathbf{v} = 0 \quad \text{-----} \quad (4.8)$$

Incompressible flow condition

If the density of the fluid changes insignificantly with pressure, the flow can be considered as incompressible. The rate of change of density can be related to the rate of change of pressure according to the following equation:

$$\boxed{\frac{\partial \rho}{\partial t} = \frac{\partial \rho}{\partial P} \frac{\partial P}{\partial t} = \frac{1}{\beta} \frac{\partial P}{\partial t}} \quad \text{-----} \quad (4.9)$$

A relatively large value is set for β to make the rate of change of density to zero.

4.8.4.2. Momentum equation

Velocity field is the result of the solution of the momentum balance defined by the Navier-Stokes differential equation, which is used for turbulent and laminar flow. The general differential form of the momentum equation of the fluid flow in X, Y and Z directions can be written as:

$$\boxed{\frac{\partial \rho v_x}{\partial t} + \frac{\partial (\rho v_x v_x)}{\partial x} + \frac{\partial (\rho v_y v_x)}{\partial y} + \frac{\partial (\rho v_z v_x)}{\partial z} = \rho g_x - \frac{\partial P}{\partial x} + S_x + \frac{\partial}{\partial x} \left(\mu_e \frac{\partial v_x}{\partial x} \right) + \frac{\partial}{\partial y} \left(\mu_e \frac{\partial v_x}{\partial y} \right) + \frac{\partial}{\partial z} \left(\mu_e \frac{\partial v_x}{\partial z} \right) + V_x} \quad \text{-----} \quad (4.10)$$

$$\boxed{\frac{\partial \rho v_y}{\partial t} + \frac{\partial (\rho v_x v_y)}{\partial x} + \frac{\partial (\rho v_y v_y)}{\partial y} + \frac{\partial (\rho v_z v_y)}{\partial z} = \rho g_y - \frac{\partial P}{\partial y} + S_y + \frac{\partial}{\partial x} \left(\mu_e \frac{\partial v_y}{\partial x} \right) + \frac{\partial}{\partial y} \left(\mu_e \frac{\partial v_y}{\partial y} \right) + \frac{\partial}{\partial z} \left(\mu_e \frac{\partial v_y}{\partial z} \right) + V_y} \quad \text{-----} \quad (4.11)$$

$$\boxed{\frac{\partial \rho v_z}{\partial t} + \frac{\partial (\rho v_x v_z)}{\partial x} + \frac{\partial (\rho v_y v_z)}{\partial y} + \frac{\partial (\rho v_z v_z)}{\partial z} = \rho g_z - \frac{\partial P}{\partial z} + S_z + \frac{\partial}{\partial x} \left(\mu_e \frac{\partial v_z}{\partial x} \right) + \frac{\partial}{\partial y} \left(\mu_e \frac{\partial v_z}{\partial y} \right) + \frac{\partial}{\partial z} \left(\mu_e \frac{\partial v_z}{\partial z} \right) + V_z} \quad \text{-----} \quad (4.12)$$

The momentum equation can be written in the following vector form:

$$\boxed{\frac{\partial \rho \mathbf{v}}{\partial t} + \mathbf{v} \cdot \nabla \mathbf{v} = \rho \mathbf{g} - \nabla P + \mathbf{S} + \mu_e \nabla^2 \mathbf{v} + \mathbf{V}} \quad \text{-----} \quad (4.13)$$

For a laminar case, the effective viscosity, μ_e is merely the dynamic viscosity of fluid, μ . \mathbf{S} represents any source terms necessary for the particular fluid flow investigated. An

example is distributed resistance (flow through screens and porous media), used to model the effect of some geometric feature without modelling its geometry. In the present study, the effect of \mathbf{S} can be neglected. The viscous loss term \mathbf{V} can be eliminated in the incompressible, constant property case. The general momentum equation for gas flow in the deposition chamber can be written in the following vector form:

$$\boxed{\frac{\partial \rho \mathbf{v}}{\partial t} + \mathbf{v} \cdot \nabla \mathbf{v} = \rho \mathbf{g} - \nabla P + \mu \nabla^2 \mathbf{v}} \quad \text{-----} \quad (4.14)$$

4.8.4.3. Pressure field equation

For numerical accuracy a relative pressure is solved in ANSYS rather than an absolute pressure. Pressure field in the investigated area is solved by the following equation with considering no rotating co-ordinate system:

$$\boxed{P_{abs} = P_{ref} + P_{rel} + \rho_0 (\mathbf{g} \cdot \mathbf{r})} \quad \text{-----} \quad (4.15)$$

In the absence of gravity and a rotating reference frame, the absolute pressure is the sum of the FLOTRAN (relative) pressure and the reference pressure.

4.8.4.4. Partial pressure of the gas mixture

Total pressure of the gas can be defined by Dalton's law

$$\boxed{P = \sum_{i=1}^N P_i} \quad \text{-----} \quad (4.16)$$

4.8.4.5. Multiple species transport equation

In ANSYS, the multiple species transport capability enables the tracking of several different fluids one at a time, subjected to the limitation that a single momentum equation is solved for the flow field. The properties for this equation are calculated from those of the species fluids and their respective mass fractions by specifying the composite gas option for density or the composite mixture option. If these options are not invoked, the species fluids are carried by a bulk fluid, with the momentum equation solved with properties of a single fluid. The governing equations for species transport are the mass balance equations for each of the species. For $i = 1, \dots, N-1$.

$$\boxed{\frac{\partial (\rho Y_i)}{\partial t} + \nabla \cdot (\rho Y_i \mathbf{V}) - \nabla \cdot (\rho D_{mi} \nabla Y_i) = 0} \quad \text{-----} \quad (4.17)$$

The equation for the N^{th} species, which is selected as the algebraic species, is not solved directly. The mass fraction for the N^{th} species as a function of space is calculated at each node from the identity ensuring that the mass fraction of all the species upto 1 everywhere.

$$\boxed{Y_N = 1 - \sum_{i=1}^{N-1} Y_i} \quad \text{-----} \quad (4.18)$$

The diffusion information available for the specific fluid is sometimes represented in terms of a Schmidt number for a species. The relationship between the Schmidt number and the mass diffusion coefficient is as follows:

$$\boxed{Sc_i = \frac{\mu}{\rho D_{mi}}} \quad \text{-----} \quad (4.19)$$

In the above expression, the density and the viscosity are those of the bulk carrier fluid, or the average properties of the flow. The multiple species transport equation can be written in terms of laminar Schmidt number associated with the species diffusion:

$$\boxed{\frac{\partial(\rho Y_i)}{\partial t} + \nabla \cdot (\rho Y_i V) - \nabla \cdot \left(\frac{\mu}{Sc_i} \nabla Y_i \right) = 0} \quad \text{-----} \quad (4.20)$$

4.8.4.6. Multiple species property options

Based on the key issue of determining how large a mass fraction of the overall flow field the species to be traced, there are choices among three mixture types for analysis: dilute mixture, composite mixture, and composite gas.

Dilute Mixture: In a dilute mixture analysis, small mass fractions of species fluids are tracked in a flow field, and the species properties do not significantly influence the flow field.

Composite Mixture: A composite mixture analysis calculates the properties used in the solution from a linear combination of the species, weighted by mass fraction as a function of space. The solution of the momentum equation depends on the species distribution, so the momentum and transport equations are strongly coupled.

$$\boxed{\alpha_{bulk} = \sum_{i=1}^n Y_i \alpha_i} \quad \text{-----} \quad (4.21)$$

Composite Gas: In a composite gas analysis, at each node the fluid density is calculated as a function of the mass fractions and molecular weights of the gases.

$$\rho = \frac{P}{RT \sum_{i=1}^N \frac{Y_i}{M_i}} \quad \text{----- (4.22)}$$

4.8.5. Process gas properties

The required thermodynamic and transport properties of Ar and N₂ gases for simulation include density, viscosity, mass and gas diffusivity as shown in the Table 4.3. The gas species were considered as isotropic. All the properties were taken at standard pressure (1 atm.) and temperature (300 K).

Table 4.3. Thermophysical properties of the gases used.

Gas	Density ρ (kg/m ³)	Dynamic viscosity μ (Pa.s)	Gas diffusivity	Molar Mass M (kg/kmol)
Ar	1.623	2.125×10^{-3}	1.31×10^{-3}	1.67
N ₂	1.138	1.663×10^{-3}	1.37×10^{-3}	1.40
Air	1.225	1.789×10^{-3}	1.46×10^{-5}	1.40

4.8.6. Analysis details

4.8.6.1. Element used in the model

The element used for the analysis was 3-D isoparametric, quadrilateral, 8-node FLOTRAN 142. The element has six degrees of freedom: velocity, pressure, temperature, turbulent kinetic energy, turbulence dissipation rate, mass fraction of species (upto 6 species). Figure 4.8. shows the geometry, node locations, and the coordinate system for this element. A tetrahedral-shaped element, wedge-shaped element, or a pyramid-shaped element can be formed by rearranging different node numbers.

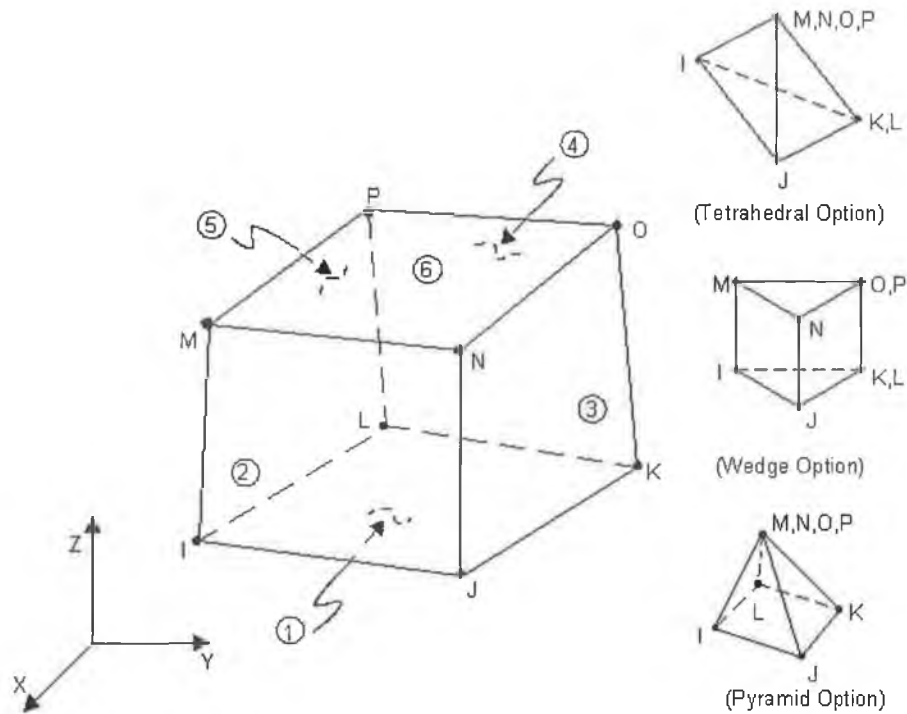


Figure 4.8. FLUID 142 element.

4.8.6.2. Meshing of the model

Unstructured meshing enjoys the advantage of easier meshing of a circular geometry using automatic grid generation. Unstructured or free meshing with tetragonal shaped elements was used to mesh the quarter model as the model involves curved areas (Figure 4.9.). The general finite element philosophy of putting more elements in regions with higher solution gradients was applied here. The mesh ratio chosen results in smaller elements near the inlet where the flow is developing, and near the expansion because of the high solution gradients in those regions. Small elements were also introduced near the substrate. Furthermore, mesh biasing was applied in the inlet and outlet wall lines. The mesh size of the model used in this study was refined to an acceptable level (63000 nodes).

4.8.6.3. Boundary conditions

The degrees of freedom applied to the simulated model were the velocity and pressure. Argon velocity varying from 1-4 mm/sec was applied at the right inlet of the model. Similarly nitrogen velocity varying from 0.1-0.4 mm/sec was applied at the top inlet of the model. Velocity components at all the outer walls of the model were set to zero ($V_x = 0$, $V_y = 0$ and $V_z = 0$) to comply with the non-slip condition at the wall. The reference pressure was set to from 0.1-0.9 Pa (corresponds to the working pressure) depending on different flow rates (Table 4.1 and Table 4.2) and the relative outlet pressure

was set to 0.0 Pa. The different boundary conditions applied in the model are shown in Figure 4.10.

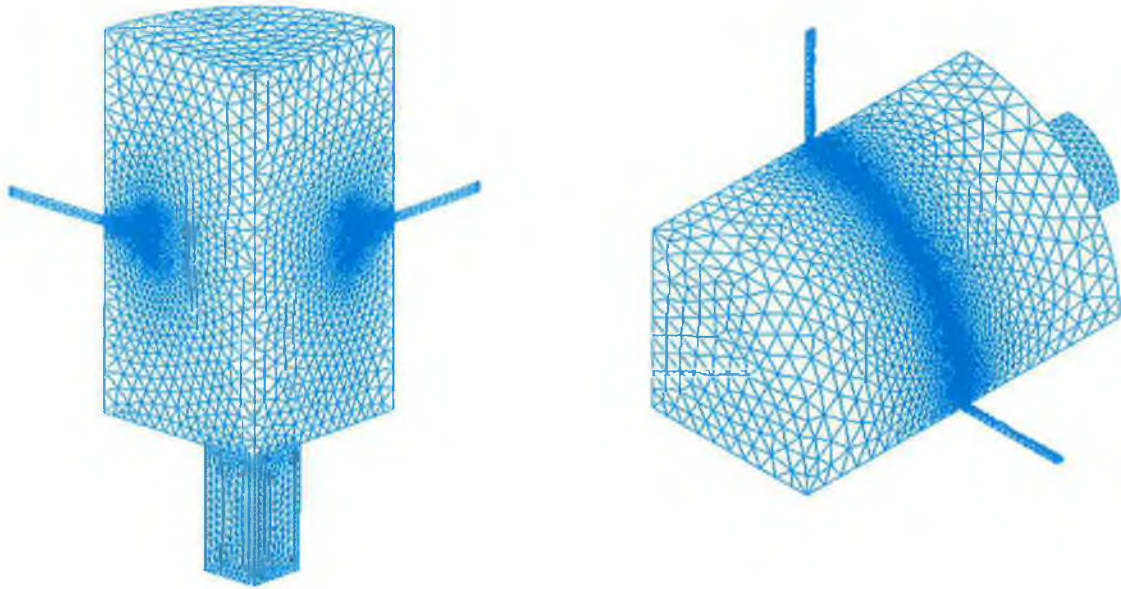


Figure 4.9. Finite element model of the PVD deposition chamber.

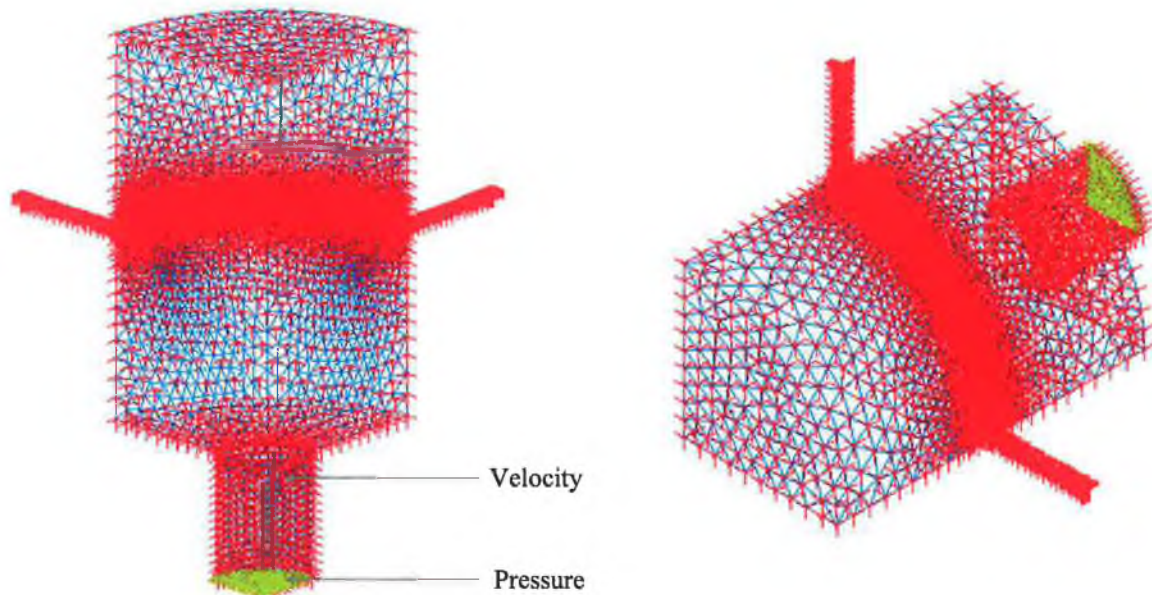


Figure 4.10. Boundary conditions (velocity and pressure) applied in the model

4.8.6.4. Numerical solution procedure

The solution output associated with the element takes the form of nodal quantities. A segregated sequential solver algorithm was used (i.e., the matrix system derived from the finite element discretization of the governing equation for each degree of freedom was solved separately). The flow problem was nonlinear and the governing equations were coupled together. The sequential solution of all the governing equations, combined with

the update of any temperature- or pressure-dependent properties, constituted a global iteration. The governing equations for the fluid flow were discretized using the second order upwind scheme and solved by an iterative method. A multigrid technique based on the "Full Approximation Scheme" for the coupled non-linear system of equations was used to speed up the convergence rate and the standard SIMPLEF pressure correction algorithm was employed. When momentum, energy, species transport, turbulence or the compressible pressure equations are solved, the advection term plays a significant role in the solution. When the advection term dominates over other terms in the governing equations, it can lead to numerical instabilities. Accordingly, careful consideration must be taken with the discretization of this particular term. The advection term for momentum was discretized using Streamline Upwind/Petrov-Galerkin (SUPG) approach and the advection term for pressure was discretized using Monotone Streamline Upwind (MSU) approach. Bulk modulus parameter β (defined by Equation 4.9.) was set to a very high value (10^{15} J/kg) for specifying incompressible fluid. Bulk, nominal and total temperatures were set to 27 °C. The internal flow (velocity) behavior was analyzed as a function of the relative supply pressure, which lead to reasonable velocity. This might reduce the possibility of instability during the convergence of the solution. In this analysis first the flow field was solved for single species (e.g., air) only. Nitrogen and argon were introduced into the chamber then and solved for multiple species. The number of species set during the analysis was argon and nitrogen. The transport equations were solved for the mass fractions of each species. To minimize numerical error, the nitrogen was selected as the algebraic species (n^{th} species). The bulk properties of the mixture were considered to be a linear combination of the species properties (composite mixture) by setting the property type option CMIX. Mass fraction capping was activated to prevent producing unrealistic results. The gas species boundary condition is specified by the mass fraction at the inlets. In FLOTTRAN, the overall convergence of the segregated solver was measured through the convergence monitoring parameter M_ϕ by calculating a convergence monitor for each degree of freedom at each global iteration. Convergence monitor is roughly the normalized rate of change of the solution from one global iteration to the next and is calculated as follows:

$$M_\phi = \sum_{i=1}^Z \frac{|\phi_i^k - \phi_i^{k-1}|}{|\phi_i^k|} \quad (4.23)$$

After some initial fluctuations, convergence monitors decreased as the analysis approached towards convergence. The number of global iterations required to achieve a converged solution may vary considerably, depending on the size and stability of the problem. A minimum of 100 iterations was required to obtain the desired convergence for the results. An M_ϕ value lower than 10^{-5} was adopted for the convergence criteria. The input file for the analysis is given in Appendix D.

4.9. RESULTS AND DISCUSSIONS

The results of the gas flow modelling in the magnetron-sputtering deposition chamber are mainly obtained in the form of velocity, pressure, density and gas concentration plots. In the next sections gas flow behaviour in the deposition chamber are presented.

4.9.1. Velocity vector plot of the gases

Velocity vectors provide a good understanding of the flow phenomena in the deposition chamber. In the vector plot the direction of the arrow indicates the direction of the flow whereas the length of the arrow indicates the proportionate velocity of the gas. Figure 4.11. shows the simulated velocity vector plot inside the inlet, chamber and outlet.

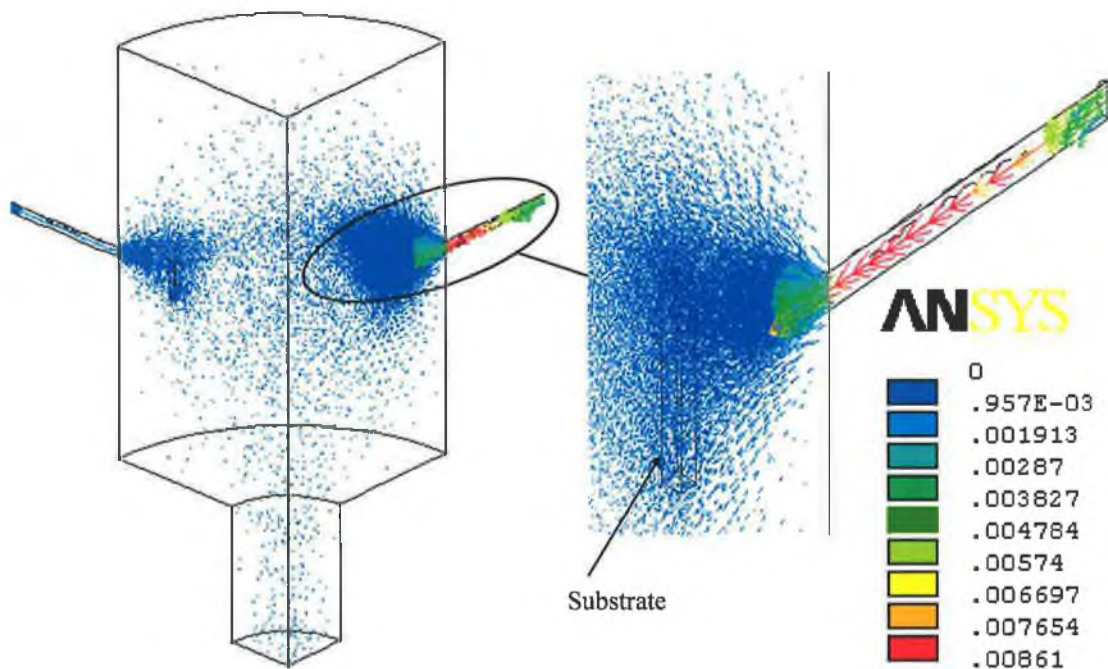


Figure 4.11. Velocity (m/sec) vector diagram of the gas species.

Higher gas velocities were found in the inlets and outlets but in the substrate region the velocities were quite low. Velocity vectors showed very small length near the wall, which indicated the flow was nearly zero at those positions. The resulting vector plot showed the recirculation region that occurred in the upper region of the chamber. In this region the gas species were hardly moving. No backflow of the gases from the outlet was observed. As compared to the maximum velocity in the entrance the gas velocity was much lower near the middle of the chamber. This was due to the expansion of the gas as a jet from the smaller diameter inlet to much larger diameter chamber. More vectors were visible close to the finer mesh area. In the inlet pipe higher velocity in the middle of the pipe was observed due to the parabolic distribution of fluid velocity through circular pipe.

4.9.2. Gas pressure distribution plot

Figure 4.12. shows the pressure distribution inside the chamber. Pressure is proportional to the inlet velocity. As it was seen before that the maximum velocity was observed at the inlet, so the maximum pressure was also observed at the inlet. As the chamber diameter was much larger than the inlet diameter, the nitrogen pressure steeply decreased in the region very close to the inlet and after that decreased slowly inside the chamber.

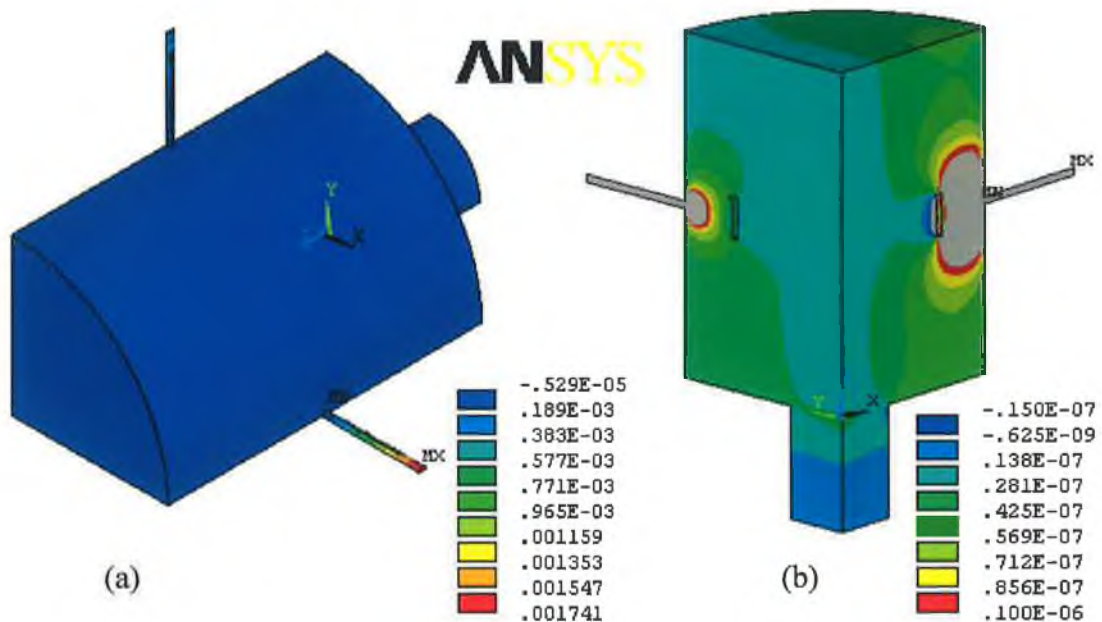


Figure 4.12. Pressure (Pa) distribution plot (a) full range (b) selected range.

A similar decrease of pressure was observed by Kobayashi [299] in a Monte Carlo simulation of gas transport in TiN magnetron sputtering apparatus. It was also observed that the higher pressure was observed in the argon inlet than the nitrogen inlet. This is

simply because argon has higher velocity than the nitrogen. Even if the same velocity was used for both nitrogen and argon higher pressure was observed in the argon inlet due to the higher density of argon than nitrogen.

4.9.3. Gas mixture density plot

Figure 4.13. shows the gas mixture density inside the chamber, outlet and inlet at 35 sccm of argon and 8 sccm of nitrogen flow rate. The density of the gas mixture in the whole chamber was seen as single colour inside the chamber due to small variation of density inside the chamber (Figure 4.13. (a)). To see the variation of density plot inside the chamber, a particular range of concentration was selected. In Figure 4.13. (b) the density variation can be seen clearly in the chamber within the selected range.

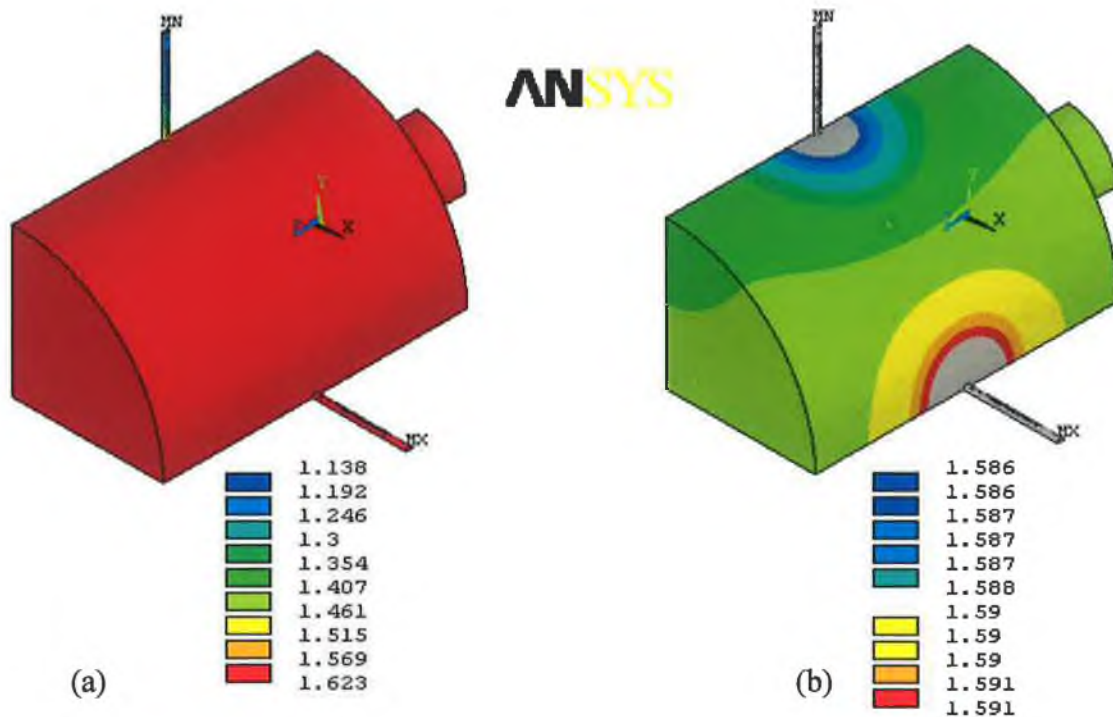


Figure 4.13. Gas mixture density (kg/m^3) plot inside the chamber (a) full range (b) selected range.

Minimum density (nitrogen density) was observed at the nitrogen inlet, while maximum density (argon density) was observed at argon inlet as only nitrogen is fed though the nitrogen inlet and argon was fed through the argon inlet. The density of the gas mixture inside the chamber was remained between the nitrogen and argon density and varies slightly as the density of the gas mixture is the linear combination of gas species. The mixture density was slightly lower than the argon density due to the higher density and

velocity of argon than nitrogen. The density plot suggested that the nitrogen and argon gas species were sufficiently mixed inside the chamber. Similar distribution of gas mixture viscosity was observed across the chamber, inlets and outlets.

4.9.4. Nitrogen concentration plot

Figure 4.14. shows the nitrogen concentration inside the chamber, outlet and inlet at 35 sccm of argon and 8 sccm of nitrogen flow rate. The concentration of nitrogen in the whole chamber was seen as single colour inside the chamber due to small variation of nitrogen concentration inside the chamber (Figure 4.14. (a)). To see the variation of concentration inside the chamber, the range of concentration, which fell only inside the chamber, was selected. In Figure 4.14. (b), the concentration variation can be seen clearly in the chamber within the selected range.

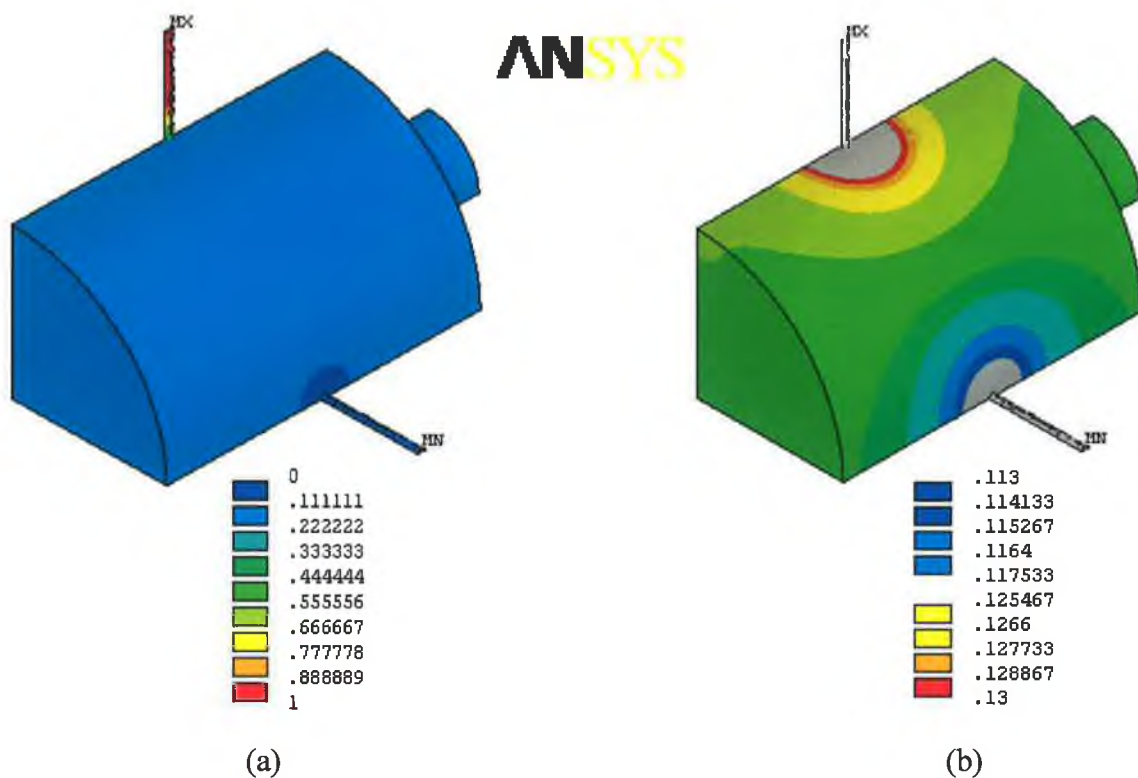


Figure 4.14. Nitrogen concentration ($\times 100\%$) plot inside the chamber (a) full range (b) selected range.

Higher nitrogen concentration was observed near nitrogen inlet and decreased towards the center of the chamber. Lower nitrogen concentration was observed near argon inlet and increased towards the center of the chamber. In the middle the concentration is almost constant. As a result, nitrogen concentration became almost constant in the middle of the

chamber. There was only two percent variation observed inside the chamber. How this variation of nitrogen would affect the deposition of coating on the substrate is discussed latter. ANSYS has the limitation of plotting a single species at one time. If Argon and nitrogen could be plotted together then the visualisation would be more realistic.

4.9.5. Nitrogen concentration at different positions in the chamber

The structural, mechanical, electrical, chemical properties and the colour of TiN coating deposited by magnetron sputtering are influenced by the nitrogen content in the coating to a great extent [142,145,153]. The distribution of nitrogen concentration along the substrate for three different positions of the substrate inside the chamber: in front of argon inlet, in front of nitrogen inlet and between nitrogen and argon inlet was plotted in Figure 4.15. for particular nitrogen flow rate of 13 sccm and a distance of 30 mm away from the chamber.

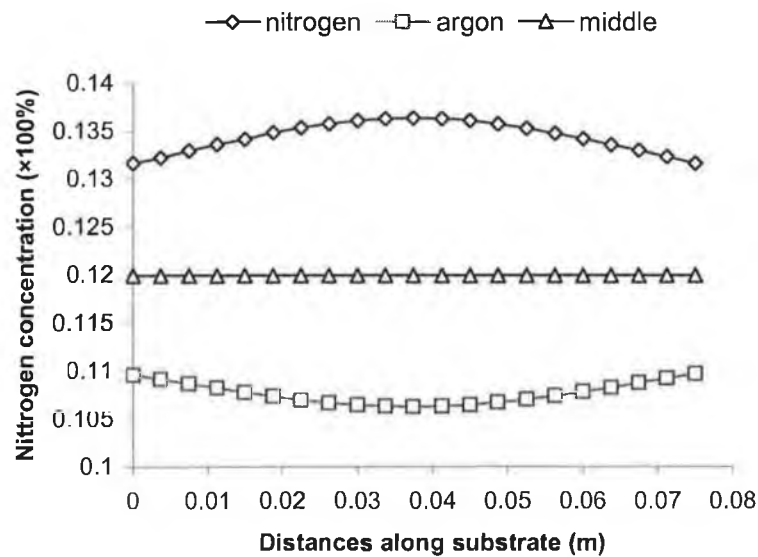


Figure 4.15. Nitrogen concentration along the substrate near argon inlet, nitrogen inlet and middle of argon and nitrogen inlet 30 mm away from the chamber wall and at a nitrogen flow rate of 15 sccm.

It was observed that in the middle of the substrate nitrogen concentration was higher than the edge when the substrate was in front of nitrogen inlet, lower in the middle than the edge when the substrate was in front of argon inlet and almost constant when the substrate was in the middle of argon and nitrogen inlet. This indicated that when the substrate was in the middle between argon and nitrogen inlet (in front of target), uniform distribution of nitrogen concentration was observed. The deposition of TiN would occur when the

substrate would come into the position between argon and nitrogen inlet. From the distribution of nitrogen over the substrate at this position, it is reasonable to consider that uniform percentage of nitrogen would be present in the coating. By modelling the right distance of the the substrate from the chamber or target, indirect information of coating nitrogen concentration can be obtained also.

4.9.6. Nitrogen concentration at distances away from the chamber

The distance between the substrate and chamber wall was varied from 30 mm to 100 mm for each different positions of the substrate as explained in the previous section. When the substrate was in front of nitrogen inlet (Figure 4.16.) higher nitrogen concentration was found in the middle of the substrate than the edge. This was because nitrogen was directly coming onto the substrate from the nitrogen inlet. At different distances away from the chamber the nitrogen concentration decreased as the distances was increased and maximum concentration of nitrogen in the middle of the substrate was found at the minimum distance (30 mm) due to the impinging nitrogen directly in the middle of the substrate.

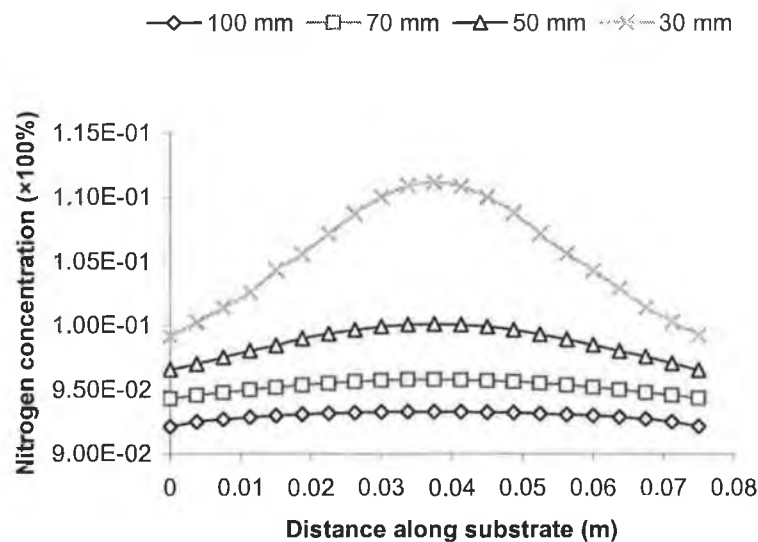


Figure 4.16. Nitrogen concentration along the substrate at different distances away from the chamber wall near nitrogen inlet and with a nitrogen and argon flow rate of 10 and 35 sccm respectively.

When the substrate was in front of argon inlet (Figure 4.17.) the opposite phenomenon was observed e.g., lower nitrogen concentration was found in the middle of the substrate than the edge. This was because argon was directly coming onto the substrate from the argon

inlet and drove away nitrogen from the middle of the substrate. At different distances away from the chamber the nitrogen concentration decreased as the distances of the substrate from the chamber decreased and maximum concentration of nitrogen in the middle of the substrate was found at the maximum distance (100 mm) due to the fact that at the maximum distance argon couldn't drive that amount of nitrogen away as it did at minimum distance.

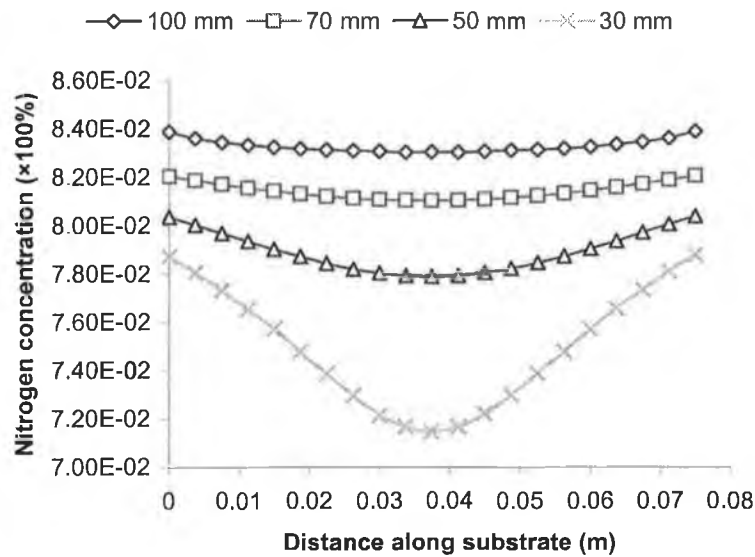


Figure 4.17. Nitrogen concentration along the substrate at different distances away from the chamber wall near argon inlet and with a nitrogen and argon flow rate of 10 and 35 sccm respectively.

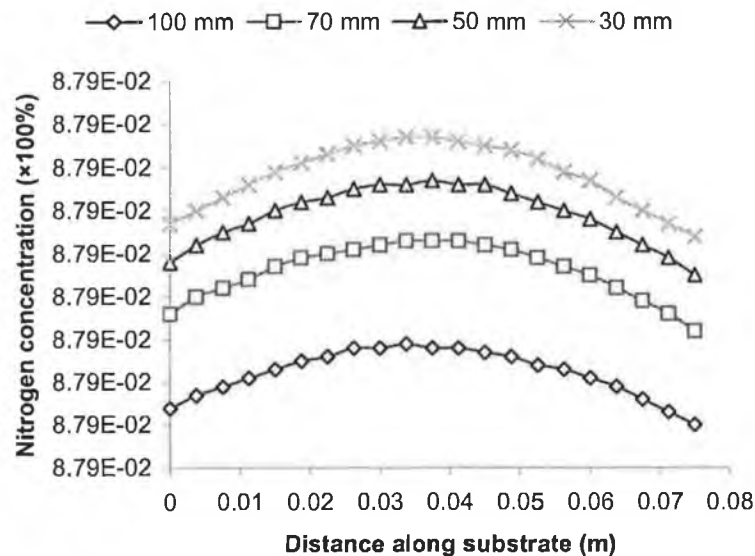


Figure 4.18. Nitrogen concentration along the substrate at different distances away from the chamber wall between argon and nitrogen inlet and with a nitrogen and argon flow rate of 10 and 35 sccm respectively.

When the substrate was positioned between argon and nitrogen inlet (Figure 4.18.) higher nitrogen concentration was found in the middle of the substrate than the substrate edge and nitrogen concentration increased as the distances between the chamber and substrate decreased. But the concentration variation at this position was very small (i.e., variation was in third digit). Higher percentage of nitrogen in the coating would be present as the distances between the substrate and chamber wall decreased.

4.9.7. Nitrogen concentration at different flow rate

Nitrogen flow rate also affects the distribution of nitrogen over the substrate at any particular position of the substrate. Figure 4.19. shows the distribution of nitrogen over the substrate when the substrate was in front of argon inlet and at 30 mm away from the chamber wall. It was observed that with the increase of nitrogen flow rate, nitrogen concentration over the substrate increased. The nitrogen concentration was lower in the middle than the edge of the substrate due to the positioning of the substrate near argon inlet as explained before.

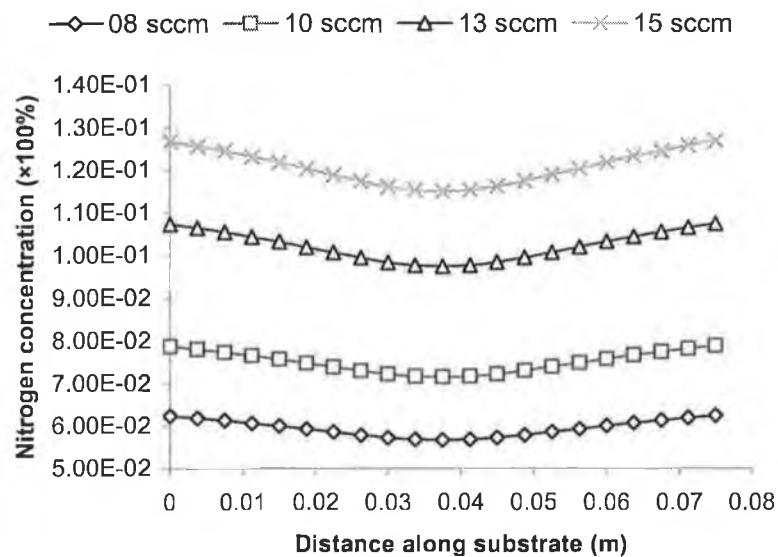


Figure 4.19. Nitrogen concentration along the substrate in front of argon inlet at different flow rate of nitrogen (constant argon flow of 35 sccm and substrate was 30 mm away from the chamber wall).

The similar behaviour of higher nitrogen concentration with the increase of nitrogen flow rate was observed in Figure 4.20. and Figure 4.21. when the substrate was positioned near nitrogen inlet and between the nitrogen and argon inlet respectively. Near nitrogen inlet,

nitrogen concentration was higher in the middle of the substrate than the edge as it was in front of nitrogen inlet. The substrate positioned between argon and nitrogen inlet follow the similar behaviour but the variation of nitrogen concentration over the substrate for any particular position was almost constant as explained before. Similar trend was also found when argon flow rate was varied.

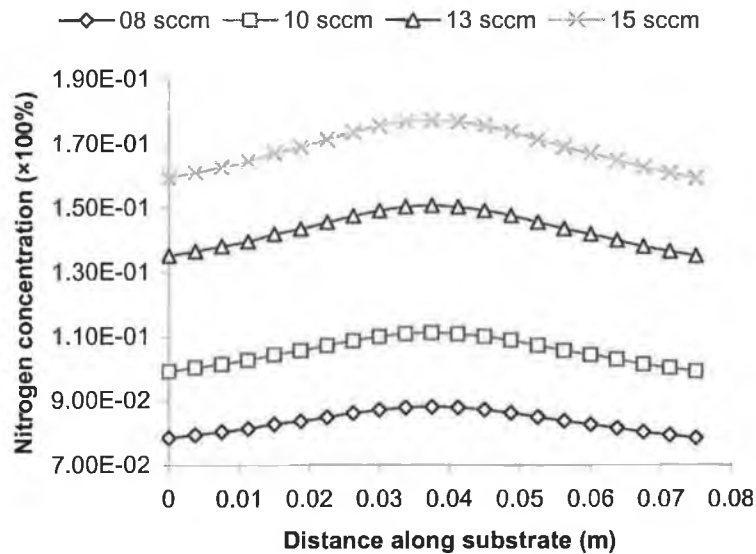


Figure 4.20. Nitrogen concentration along the substrate in front of nitrogen inlet at different flow rate of nitrogen (constant argon flow of 35 sccm and substrate was 30 mm away from the chamber wall).

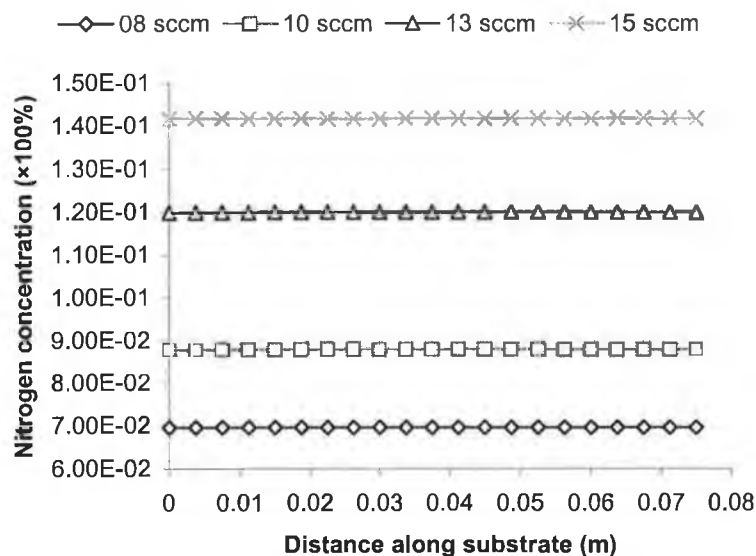


Figure 4.21. Nitrogen concentration along the substrate between nitrogen and argon inlet at different flow rate of nitrogen (constant argon flow of 35 sccm and substrate was 30 mm away from the chamber wall).

4.9.8. Convergence problem of solution

As the fluid flow simulation was considered non-linear process, there had been huge difficulties in reaching the convergence of the solution. Instabilities in the analysis can arise from a number of sources: the matrices may have poor condition numbers because of the finite element mesh or very large gradients in the actual solution. The fluid phenomena being observed could be unstable in nature. The reasons, which are worthwhile to mention for the present analysis are: short length of the inlet pipe in which the flow is not fully developed, application of vacuum pressure and a backflow from the outlet. First the inlet pipe was modelled with the same length as it was in the original chamber. As the length was shorter it was giving instability in the convergence of the solution. The length of the inlet pipe is then extended to allow fully developed flow. Sometimes putting very low pressure as the reference pressure caused the divergence of the solution.

4.9.9. Model verification

The numerical approach used to model the fluid flow in the deposition chamber needs to be validated against the experimental data. Validation of gas flow analysis in deposition chamber is difficult due to unavailability of reliable measured data at different positions of the chamber. The check of the numerical results was performed by using the law of mass balance. The difference between mass flow rate on inlet and on outlet is obtained from average velocities and pressures on base equation for steady-state isothermal fluid flows. Results showed that the mass flow rate in the outlet was almost same as the mass flow rate in inlet.

4.9.10. Model limitations

The full deposition chamber model couldn't be modelled due to the limitations of no of nodes. The available no of nodes were insufficient to capture the fluid flow in a full chamber model. According to the calculations from the Knudsen number the gas flow was not perfectly continuum rather continuum with slip in the wall. But no slip flow on the chamber wall was considered. This might affect the results slightly. The model considers the mixing of gas from completely fluid flow phenomena. There are other issues such as thermal diffusion, composition-dependent gas properties, surface reaction etc. that have to be considered to make it more close to the real system.

4.10. SUMMARY

CFD modelling was carried out to simulate the gas flow and the mixing behaviour in a magnetron-sputtering thin coating deposition chamber by ANSYS-FLOTRAN commercial code. CFD modelling showed the potential to be an important tool for simulating multicomponent gas flows and mixing behaviour in terms of gas velocity, pressure and gas species concentration distribution in sputtering deposition chamber. Higher velocity at the inlet dropped to a low velocity inside the chamber due to the large expansion of geometry from the inlet to the chamber. Maximum pressure was also found at the inlet and dropped to a low value due to the same reason of large expansion of geometry from inlet to the chamber. With the same velocity of nitrogen and argon higher pressure was observed for argon due to the higher density of argon than nitrogen. Argon has higher concentration in the chamber than nitrogen due to the higher flow rate of argon than nitrogen. Nitrogen concentration over the substrate increased with the increase of higher nitrogen flow rate and with the decrease of substrate to chamber wall distance. Higher nitrogen concentration was observed in the middle of the substrate than the edge when the substrate is in front of nitrogen inlet and lower nitrogen concentration was observed when the substrate was in front of argon inlet. But when the substrate was between argon and nitrogen inlet the nitrogen was uniformly distributed over the substrate. This indicated a uniform percentage of nitrogen would be present in the coating at this position. This information can help to modify the reactor geometry and gas flow openings and the position of the gas flow openings for better gas flow over the substrate which in turns gives an indirect indication of the composition of compound coating on the substrate.

CHAPTER 5

Thermal Stress Modelling in Thin Coating

5.1. INTRODUCTION

Residual stresses are very common in most of the surface coatings either thin or thick. The presence of residual stress in coatings can lead to cracking, debonding or spallation of the coating, though it might have positive effects such as the resistance of the coating to wear and fatigue propagation. In this chapter the focus is mainly on a particular type of residual stress called extrinsic or thermal stress, which develops due to the difference in thermal (e.g., thermal expansion coefficient) and physical properties (e.g., Young's modulus, Poisson's ratio etc.) between the coating and substrate materials. A 2-D finite element model has been developed using ANSYS to estimate the thermal residual stress in thin vapour deposited (magnetron sputtering) TiN coating on stainless steel substrate when cooled down to room temperature from deposition temperature. An analytical model has also been employed to compare with the Finite Element (FE) results. Radial, shear and axial stresses both in the coating and substrate have been analysed. Several parametric studies i.e., the effect of coating thickness, coating Young's modulus, coating thermal expansion coefficient, substrate thickness and deposition temperature on thermal stress have been performed to get the description of the thermal stress states after cooling the coating-substrate system. The effect of an interlayer on thermal stress has also been studied.

5.2. FINITE ELEMENT METHOD (FEM)

The finite-element method is a general technique for constructing approximate solutions to boundary-value problems. The method involves dividing the domain of interest into a finite number of simple subdomains, the finite elements, and using variational concepts to construct an approximation of the solution over the collection of finite elements. Most practical problems in engineering and applied science are mathematical models of physical systems and governed by differential or integral equations. The solutions to these equations would provide an exact, closed-form solution to the particular problem being studied. However, complexities in the geometry, properties and in the boundary conditions that are seen in most real-world problems usually means that an exact solution cannot be obtained or obtained in a reasonable amount of time or by simplifying the problem. Current product design cycle times imply that engineers must obtain design solutions in a short amount of time. The objective is to obtain approximate solutions that can be readily obtained in a reasonable time frame and with reasonable effort. The FEM is one such numerical

procedure for obtaining approximate solutions to many of the problems encountered in engineering analysis. The basic steps in finite element methods are same as in analytical method except the breaking down of the problem domain in finite elements (Figure 5.1.).

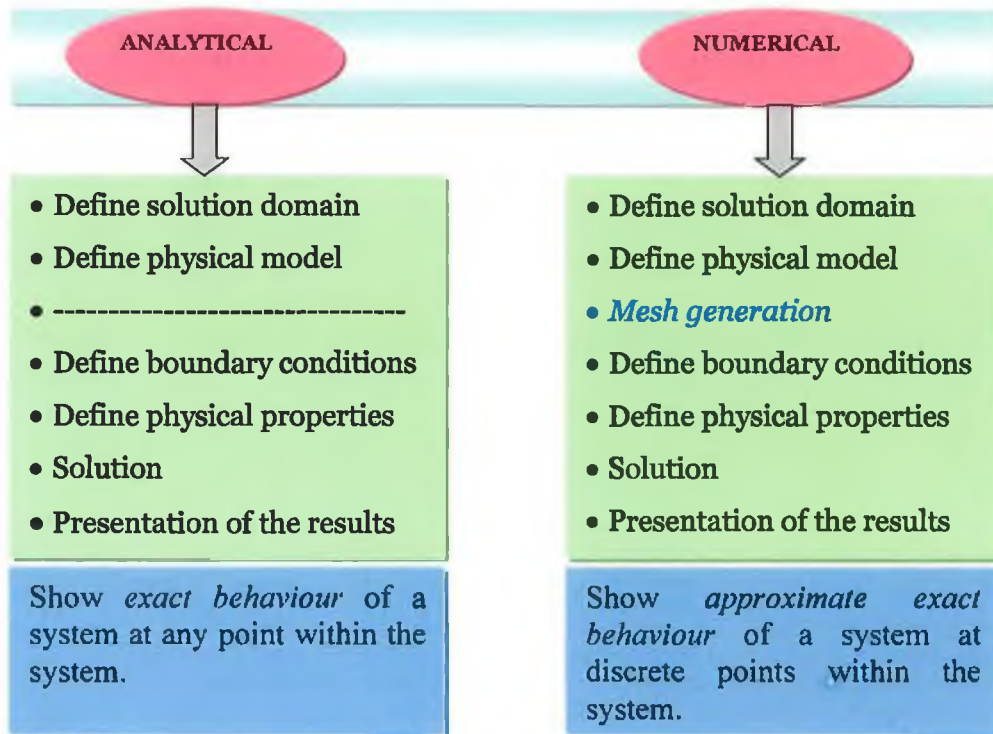


Figure 5.1. Basic difference between analytical and finite element method.

5.2.1. Basic concept of the Finite Element Method

Finite Element Analysis is a computer based numerical method of deconstructing a complex system defining a continuum into very small geometric shapes (of user-designated size) called elements, which are interconnected at specific points in the elements called nodes. The process of breaking a continuous problem into smaller parts is termed discretization (meshing). The properties and the governing relationships are assumed over these elements and expressed mathematically in terms of unknown values at nodes. An assembly process is used to link the individual elements to the given system. When the effects of loads and boundary conditions are considered, a set of linear or nonlinear algebraic equations is usually obtained. The finite element method uses integral formulations rather than difference equations, which are used in the finite difference method to create a system of algebraic equations. The software implements equations and solves them all, creating a comprehensive explanation of how the system acts as a whole. Solution of these equations gives the approximate behavior of the continuum or system.

The continuum has an infinite number of degrees-of-freedom (DOF), while the discretized model has a finite number of DOF. This is the origin of the name, finite element method. The more will be the no of elements, the better will be the results. These results then can be presented in tabulated, or graphical forms. This type of analysis is typically used for the design and optimisation of a system far too complex to analyze by hand. Systems that may fit into this category are too complex due to their geometry, scale or governing equations. The number of equations is usually rather large for most real-world applications of the FEM, and requires the computational power of the digital computer.

5.2.2. Basic steps in Finite Element Method

The basic three steps of finite element method can be summarised as follows:

Pre-processing phase

1. Geometric description of the model and discretization into nodes and elements.
2. Representation of the physical behaviour of an element by assuming a shape function (linear, quadratic or cubic).
3. Developing equations for an element and arranging them in a matrix form.
4. Constructing the global stiffness matrix by assembling the elemental matrix to present the entire problem.
5. Applying boundary conditions, initial conditions and loading.

Solution Phase

6. Solving a set of linear or non-linear algebraic equations simultaneously to obtain nodal results (Gaussian elimination, Wavefront methods etc.) such as displacement values at different nodes.

Post-processing phase

7. Obtaining other important information (at nodal points or Gauss points) like values of principal stresses from the nodal displacement values and presenting in the form of table, contour plots or graphs.

5.2.3. Advantages of the Finite Element Method

Finite element method provides a greater flexibility than finite difference and finite volume methods. It has been widely used in solving wide variety of engineering problems such as structural, mechanical, heat transfer, fluid dynamics and electromagnetics etc. Complex geometry, analysis types (vibration, transients, nonlinear, heat transfer, fluids etc.), loading (node-based loading e.g., point loads; element-based loading e.g., pressure; thermal and inertial forces e.g., time or frequency dependent loading) and restraints (indeterminate structures) can be handled in finite element method. Bodies comprised of nonhomogeneous materials (every element in the model could be assigned a different set of material properties) and nonisotropic materials (orthotropic, anisotropic) can be modeled and analyzed. Special material effects (temperature dependent properties, plasticity, creep, swelling etc.) and geometric effects (large displacements, large rotations, contact (gap) condition etc.) can also be modeled. FEM reduces the amount of prototype testing by simulating multiple “what-if” scenarios quickly and effectively in a virtual environment. FEM also can simulate designs that are not suitable for prototype testing e.g., surgical implants, such as an artificial knee. With the finite element virtual prototyping technique, product can be optimized long before the manufacturing is started which enables a reduction in the level of risk. The ultimate gains are cost savings, time savings (reduction of time to enter a product into market) and creation of more reliable and better-quality product.

5.2.4. Disadvantages of the Finite Element Method

In spite of the great power of FEA, the disadvantages of computer solutions must be kept in mind. The FEM is applied to an approximation of the mathematical model of a system. Generally these approximations are made in geometry, material properties, loading conditions and constraints. Due to these approximations different kinds of error such as discretization, formulation and numerical error are built-in problem in FEM. A general closed-form solution, which would permit one to examine system response to changes in various parameters, is not produced. The user has to be expert to handle the software for the correct incorporation of certain effects (buckling, large deflections and rotations, material nonlinearities and other nonlinearities) that are not included automatically. Experience and judgment are needed in order to construct and analyze a good finite element model. The FEM has little practical value if the digital computer is not available.

Reliable FEM software is also essential to avoid any kind of computer software error. Sometimes the input and output data may be large and tedious to prepare and interpret. It is very susceptible to user-introduced modelling errors (poor choice of element types, distorted elements, geometry not adequately modeled) and can be fatal. Finally the finite element results have to be validated against experimental or analytical results for the proper use of derived information from FEA.

5.2.5. Finite Element Analysis (FEA) by ANSYS

ANSYS is general-purpose finite element analysis software. It has excellent pre-processing facilities and is very easy to use. The pre-processing, solution and post-processing drivers are all contained within the same graphical user interface. The governing equations of elasticity, fluid flow, heat transfer and electro-magnetism can all be solved by the finite-element method in ANSYS. ANSYS can solve transient problems as well as nonlinear problems. The multifaceted nature of ANSYS also provides a means to ensure that users are able to see the effect of a design on the whole behavior of the product, be it electromagnetic, thermal or mechanical.

5.3. RESIDUAL AND THERMAL STRESS IN THIN COATING

Residual stress in thin coatings is a stress under no external loading and the sum of growth stress and thermal stress (Figure 5.2.). It is very common in almost all of the coating deposition techniques such as plasma spraying, physical vapour deposition, chemical vapour deposition etc. The stress state in coating is very complicated and could vary within the thickness of the coating. Higher stress gradient between the coating and substrate is observed in case of thin coating system. The residual stresses can be tensile or compressive depending on the process parameters during deposition. Residual stress can strongly influence coating quality and the performance of a coated system since it is directly related to the other coating properties such as hardness, wear resistance, fatigue strength, adhesion, etc. [306]. In coatings, the strength of the bonded system is governed by a number of variables [307]: the thermal and elastic mismatch effect; the plastic flow stress of the metal; the relative substrate/coating thickness; the thickness of interlayers and the fracture resistance of the interface; and the flaw distributions in the coating and at the interface. Residual stress can give rise to deformation of coated workpieces by several stress relaxing mechanism such as adhesive failure (delamination at the interface) or cohesive failure

(spalling or micro-cracking within the coating) of the coating or subsurface fracture (substrate failure) [308]. In most of the cases first two mechanisms are very likely to occur because thin coatings on metal surface usually have poor adhesion. Near the edges, a complex stress state will be present, but away from the edges, this appears to a simple stress state where the stresses normal to the substrate and the shear stresses are zero [307,309].

On the other hand, since the residual stress in the coating must be balanced by an opposing stress in the substrate, the residual stress induced by the coating may be used to affect the failure properties of the substrate. A coating which induces a compressive stress in the surface of a brittle substrate is expected to increase the fracture strength of the substrate since an applied tensile stress must overcome the residual compressive stress in the substrate before crack opening and subsequent growth can be initiated [310].

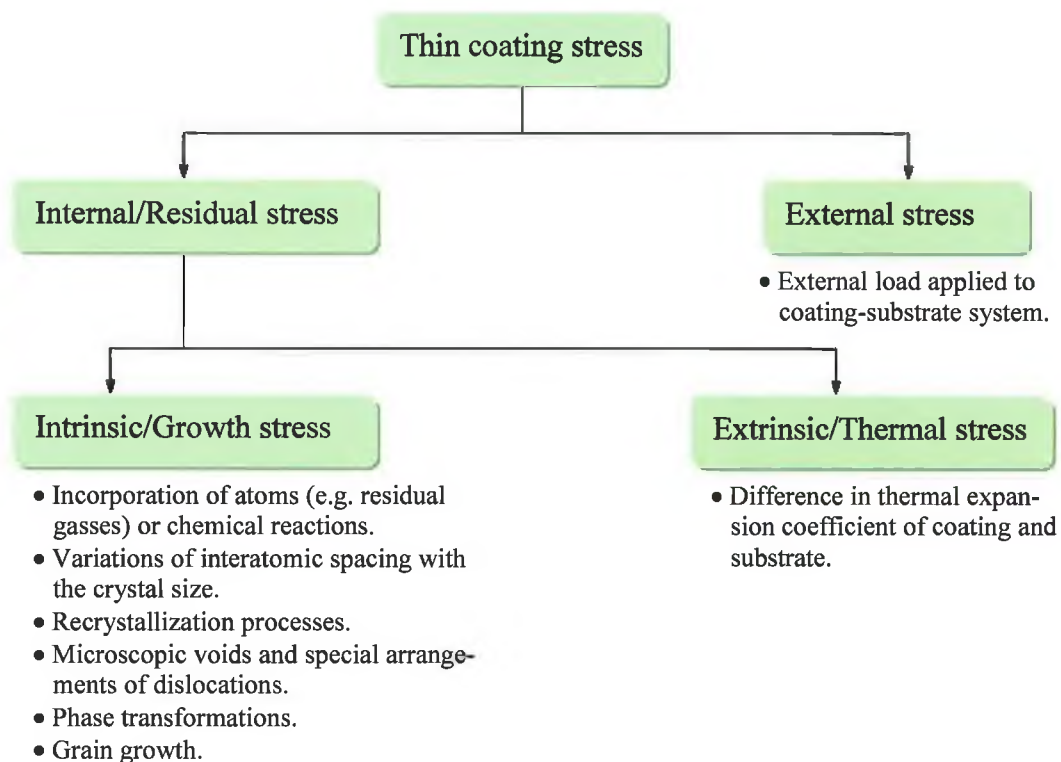


Figure 5.2. Classification of stress in thin coating.

The growth stress (also called intrinsic stress) in coatings can result from a number of mechanisms related to lattice imperfection including [311,312]: incorporation of atoms (e.g. residual gasses) or chemical reactions, variations of interatomic spacing with the crystal size, recrystallization processes, microscopic voids and special arrangements of dislocations and phase transformations. Mainly rapid solidification and intense

bombardment effect during thin coating deposition process are the sources of lattice imperfection related mechanisms. It has been shown that intrinsic stresses in magnetron sputtered thin coatings can be significantly influenced by the deposition parameters such as deposition gas pressure, target to substrate distance, bias voltage etc., as these strongly influence the energy of the species condensing onto the substrate. Residual stress changes from compressive at lower working pressure to tensile stress at higher working pressure. A transition from tensile to compressive or from very low compressive to high compressive stress has also been noted when the substrate bias is increased [310]. Substrate based influences on stress include substrate roughness and substrate temperature during deposition [313].

The other component of residual stress called thermal stress (also called extrinsic stress) is also very familiar in coating deposition techniques. Thermally induced stress results from the physical and thermal property mismatch between the coating and the substrate when cooled to room temperature from the deposition temperature [314]. The various physical parameters of both coating and substrate on which thermal stress depend can be listed as thermal expansion coefficients, Young's modulus of elasticity, Poisson's ratio, thickness, thermal conductivity, temperature histories during deposition and cooling and stress relaxation mechanisms [315]. Generally, thermal stresses are developed at the interface between coating and substrate when coating and substrate materials with substantially different properties are bonded together [316]. Cracking or delamination of the coating can occur due to the differences in elastic and plastic properties between the coating and the substrate [317]. This thermal stresses are superimposed on growth stress during cooling, resulting in the total stress level. From the literature, it was found that major component of the residual stress in the sputtered coatings come from growth stress. Usually the thermal stresses are neglected for approximation. But sometimes the thermal stress would also be significant (as high as 20-25% of the total stress [318]) if the deposition temperature or the mismatch of elastic and thermal properties of the coating and substrate materials is high. Therefore, the residual stresses in the sputtered coating cannot be regarded as entirely growth in nature. Stress management has been an essential aspect of coating manufacturing and stress estimation has increasingly become a matter of great importance for the soundness of the coating-substrate system. In order to improve the long-term performance of PVD coating, it is important and necessary to acquire the knowledge of the distribution of thermal stress.

5.4. MODELLING OF THERMAL STRESS IN COATING-SUBSTRATE SYSTEM

Generally, analytical solutions have been developed to describe the uniform biaxial thermal stress states in coating-substrate system for linear-elastic or simple elastic-plastic materials [319]. For more general 2-D or 3-D problem, numerical methods such as finite element analysis (FEA) has been successfully established in the area of macroscopic analysis. The application of FEM overcomes the difficulties associated with the laborious solution of the complex form of analytical equations. Thermal stresses in engineering materials with different temperature gradients [320] or cooling down of two different bonded materials from the fabrication temperature [321] are simulated using finite element analysis.

Recently finite element analysis has been used to simulate the behaviour of thermal stress in coating-substrate system in a number of studies [322-329]. The results showed that the level of the thermal stresses is influenced by combination of coating, substrate and interlayer materials, coating thickness, interlayer material thickness, impurity phase state and the mismatch of the thermal and mechanical properties between coating and substrate materials. Stress concentration arising at the coating-substrate interface can give rise to the propagation of cracks parallel to the coating-substrate interface and therefore, causes coating delamination [330]. Several methods of reducing the thermal stress level in the coating-substrate system have been considered, including the application of an interlayer [326,327,331] and the gradient interface or functionally graded coating [309,332-334]. The interlayer material decreases thermal stresses in coating and there is significant effect on thermal stress levels with interlayer material thickness. This is due to the smoother changes in temperature gradients in interlayer coating layers and more uniform temperature distributions in small thickness in comparison to the thick layers. Therefore, interlayer materials can increase the bonding strength by reducing the level of thermal stresses. In the functionally gradient coating, the graded layer can accommodate part of the thermal stresses generated due to CTE mismatch and an improvement in composite strength with the use of the graded coating would be expected. The more uniform the gradient near the interface, the more it can reduce the thermal stress [335]. Most these studies have been performed for thick coatings deposited mainly by thermal spraying. Thermal stress analysis using FEM in thin coating is performed in wafer processing technology to simulate wafer processing, variation of the wafer bow as a result of temperature increase and examine the correlation between temperature variation and stress distribution inside the wafer during

different stages of the process [336,337]. The deformation characteristics of thin oxide scales due to the developed thermal stress during cooling from oxide formation temperature have been studied by FEA [338-341]. There are few studies of thermal stress modelling by FEA in thin hard coating for mechanical applications [342,343].

Thus FEA can be considered an attractive tool to simulate thermal stress problem in coating-substrate systems because of its ease with solving problems in complex geometries including material nonlinearity or geometric nonlinearity and formulations of different types of problems. The objective of this study is to study the distribution of thermal stress in thin TiN coating on stainless steel substrate resulted due to the cooling from deposition to room temperature by finite element analysis package ANSYS. The effect of interlayer on the reduction of thermal stress has also been investigated.

5.5. THERMAL STRESS EQUATION IN THIN COATING

Tsui and Clyne [344] developed the analytical model to determine the thermal stress in progressively deposited coating for simple planar geometry.

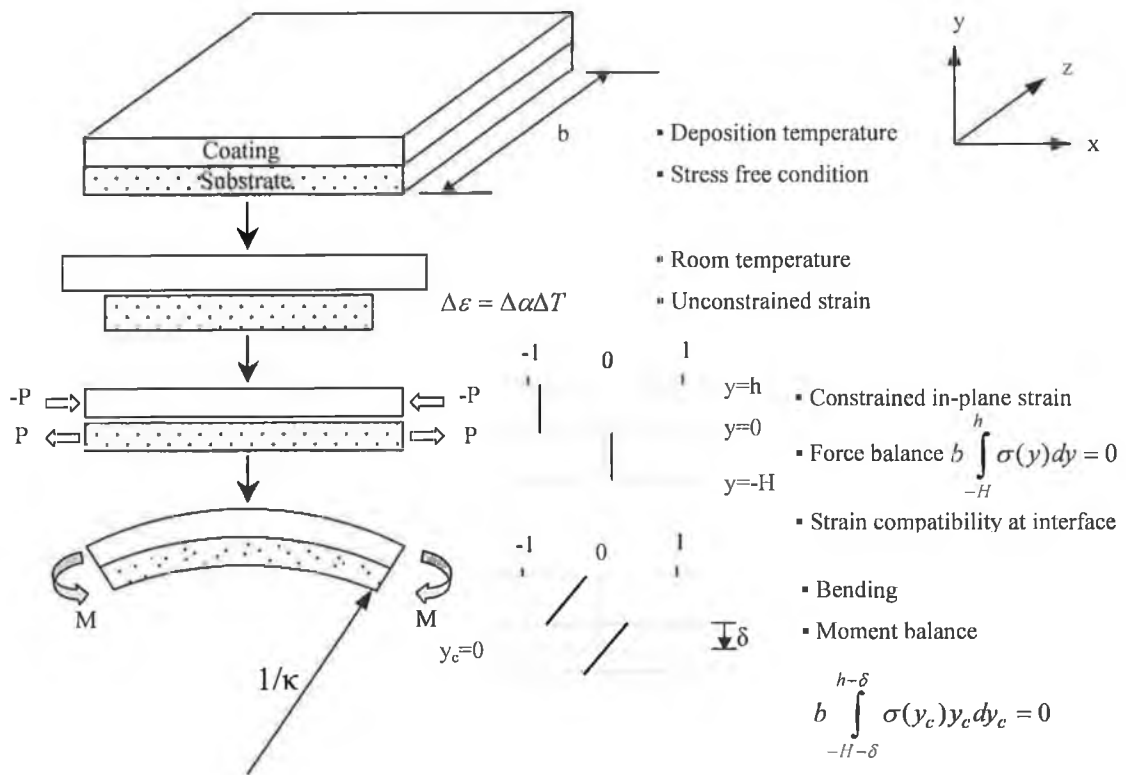


Figure 5.3. Schematic diagram of curvature generation in bimaterial flat plate due to thermal strain.

Consider two bonded plates cooled from a stress free temperature (deposition temperature, T_d) to room temperature (T_r) so that a misfit strain, $\Delta\varepsilon$, due to the CTE mismatch is created. Imposition of this misfit strain results in equal and opposite forces of magnitude P , being set up in both the coating and substrate (Figure 5.3.).

$$\begin{aligned} \text{Force in the coating,} & \quad P_f = -\sigma_f \times (h \times b) \\ \text{Force in the substrate,} & \quad P_s = \sigma_s \times (H \times b) \end{aligned}$$

Now the corresponding strains in the coating and substrate are

$$\varepsilon_s = \frac{\sigma_s}{E_s} = \frac{P_s}{HbE_s} \quad \varepsilon_f = \frac{\sigma_f}{E_f} = -\frac{P_f}{hbE_f}$$

As the forces in the coating and substrate are equal and opposite, $P_s = P_f = P$, so the thermal misfit strain can be written as

$$\begin{aligned} \Delta\varepsilon = \varepsilon_f - \varepsilon_s &= -\frac{P_f}{hbE_f} - \frac{P_s}{HbE_s} \\ \frac{P}{b} &= -\Delta\varepsilon \left(\frac{E_f E_s h H}{E_f h + E_s H} \right) \end{aligned} \quad \text{----- (5.1)}$$

where, σ = stress, α = thermal expansion coefficient, ε = strain, and E = Young's modulus. Subscripts s and f indicate substrate and coating. h, H, and b are coating thickness, substrate thickness, and width of coating/substrate respectively.

The resultant stress distribution, $\sigma_x (y)$, and curvature, κ_b , can be obtained from simple beam bending theory. Firstly, the misfit strain is removed by the application of two equal and opposite forces ($-P$ and P). When the two plates are joined, this results in an unbalanced moment. Balancing this moment generates curvature of the composite plate. The moment, M is given by

$$M = P \left(\frac{h + H}{2} \right) \text{----- (5.2)}$$

Now, the curvature of a beam, κ_b , (equal to the through-thickness gradient of strain) can be expressed as the bending moment divided by the beam stiffness,

$$\kappa_b = \frac{M}{\Sigma} \text{-----} (5.3)$$

From Equation (5.1) and (5.2),

$$M = -\frac{1}{2}b\Delta\varepsilon \left(\frac{E_f E_s h H}{E_f h + E_s H} \right) (h + H) \text{-----} (5.4)$$

Where the negative curvature changes represents the deposit surface being more convex (or less concave), as expected if $\alpha_s > \alpha_f$ ($\Delta\alpha$ is positive). The composite beam stiffness, Σ is given by

$$\begin{aligned} \Sigma &= b \int_{-H-\delta}^{h-\delta} E(y_c) y_c^2 dy \\ &= bE_f h \left(\frac{h^2}{3} - h\delta + \delta^2 \right) + bE_s H \left(\frac{H^2}{3} - H\delta + \delta^2 \right) \text{-----} (5.5) \end{aligned}$$

Here δ is the distance from the neutral axis ($y_c = 0$) to the interface ($y = 0$). It is positive when lies within the deposited coating and its value is given by [345],

$$\delta = \frac{E_f h^2 - E_s H^2}{2(E_f h + E_s H)}$$

Putting this value of δ in Equation (5.5),

$$\Sigma = \frac{b(E_f^2 h^4 + E_s^2 H^4 + 4E_f E_s h^3 H + 6E_f E_s h^2 H^2 + 4E_f E_s h H^3)}{12(E_f h + E_s H)} \text{-----} (5.6)$$

Combining Equation (5.3), (5.4) and (5.6),

$$\kappa_b = -\frac{6E_f E_s h H (h + H) \Delta\varepsilon}{E_f^2 h^4 + E_s^2 H^4 + 2E_f E_s h H (2h^2 + 3hH + 2H^2)} \text{-----} (5.7)$$

From Stoney's equation [346] we can find the relation for curvature for thin coating on thick substrate,

$$\kappa_b = \frac{6\sigma_f h}{E_s H^2} \text{-----} (5.8)$$

From Equation (5.7) and (5.8),

$$\sigma_f = - \frac{E_f E_s^2 H^3 (h+H) \Delta \varepsilon}{E_f^2 h^4 + E_s^2 H^4 + 2E_f E_s hH (2h^2 + 3hH + 2H^2)} \quad (5.9)$$

When $h \ll H$ and considering the first order approximation, equation (8) becomes

$$\sigma_f = - \frac{E_f E_s H \Delta \varepsilon}{E_s H + 4E_f h} \quad (5.10)$$

Again the thermal misfit strain can be written as

$$\Delta \varepsilon = \int_{T_d}^{T_r} (\alpha_s(T) - \alpha_f(T)) dT \quad (5.11)$$

The whole coating-substrate system is considered as a composite beam, where coating is thin compared to substrate e.g., biaxial stress ($\sigma_x = \sigma_z = \sigma$ and $\sigma_y = 0$) state can be assumed. So from the three-dimensional stress-strain relation

$$\varepsilon_{xx} = \frac{1}{E} [\sigma_{xx} - \nu(\sigma_{yy} + \sigma_{zz})]$$

$$\sigma = \frac{E}{1-\nu} \varepsilon = E_e \varepsilon$$

Here E_e is the effective Young's modulus and substituting E_f and E_s by effective Young's modulus of coating (E_{ef}) and substrate (E_{es}) respectively and putting the value of $\Delta \varepsilon$ in Equation (5.10)

$$\sigma_f = - \left[E_{ef} \int_{T_d}^{T_r} (\alpha_s - \alpha_f) dT \right] / \left[1 + 4 \left(\frac{E_{ef}}{E_{es}} \right) \left(\frac{h}{H} \right) \right] \quad (5.12)$$

If the average thermal expansion coefficients are used

$$\Delta \varepsilon = (\alpha_s - \alpha_f) \Delta T \quad (5.13)$$

Using average thermal expansion coefficients Equation (5.10) can be written as

$$\sigma_f = - \frac{E_f E_s H (\alpha_s - \alpha_f) \Delta T}{E_s H + 4E_f h} \quad (5.14)$$

Again considering zero order approximation ($h \ll H$) Equation (5.14) reduces to the following simple form:

$$\sigma_f = -E_{ef} (\alpha_s - \alpha_f) \Delta T \text{-----(5.15)}$$

Although this simple Equation (5.15) does not include the effect of coating to substrate thickness ratio and coating to substrate Young's modulus ratio, it can give very close value to that of Equation (5.14). Thus, the thermal stress in the coating is simply proportional to the Young's modulus of the coating, the mismatch between the thermal expansion coefficients of coating and substrate and the difference between the deposition temperature and room temperature. The greater these values, the higher will be the resulting thermal stress magnitudes.

5.6. FINITE ELEMENT CONSIDERATIONS

The analytical equation of thermal stress can be applied only to a simple-shaped structure to get the average value in the coating or substrate but not the local stress at any particular point in complex shaped object. On the other hand, the finite element method (FEM) is very effective for calculating and displaying the stress distribution at any particular location in the coating-substrate system.

5.6.1. Model formulation

For the modelling of residual thermal stress generated in TiN coating deposited by sputtering method, a simple cylindrical shape stainless steel sample (20 mm diameter and 0.05 mm thick) with coating on top of the sample (typical thickness 5 μm) was considered. Although the substrate was quite thin, it was thick enough in comparison to the coating thickness. This was done to keep the models reasonably sized [338] and to allow the coating-substrate system bending after the development of thermal stress. The substrate was long enough to ensure that the boundaries were sufficiently removed, so as not to affect the stress calculations [337]. The cylindrical specimen geometry was chosen for this analysis to treat three-dimensional model by using two-dimensionally structured computer programs [320]. This would save both time and money without losing much accuracy. An axisymmetric plane parallel to global XY plane through the thickness of coating and substrate was taken as 2-D model. To study the influence of the interlayer material and its

thickness on the thermal stress levels, Ti interlayer with a thickness ranging from 0.5 to 2.5 μm was also modelled. The schematic diagram of 3-D and the corresponding 2-D geometry used in the finite element model is shown in Figure 5.4.

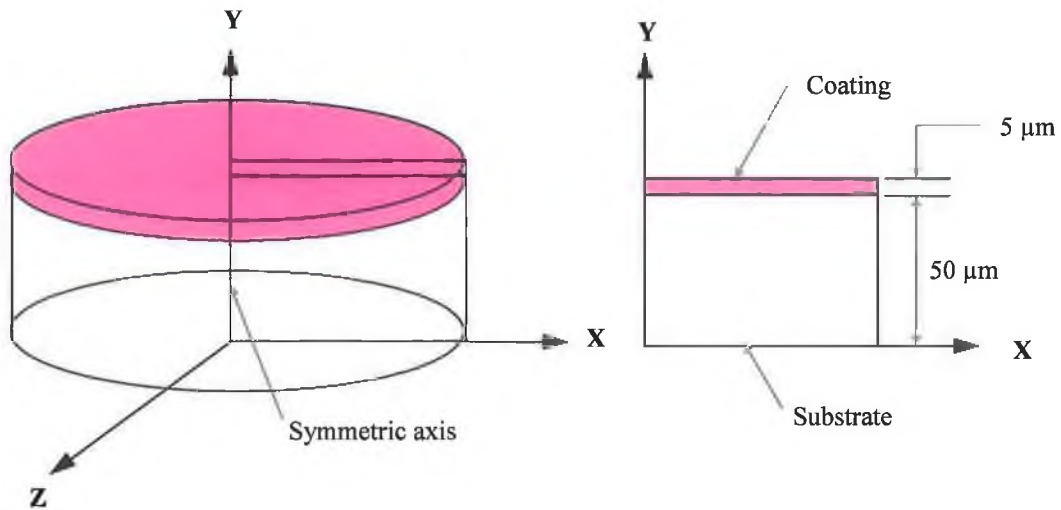


Figure 5.4. Schematic diagram of 3-D and 2-D solid model.

Several assumptions were made for simplicity of calculations [339,342]. The coating and substrate were assumed to be well bonded or in finite element terminology, nodes were shared at all interfaces to get the perfect adhesion. In order to model thermal stress values in thin coatings it is common to neglect growth stresses, which depends on complex interdependent process parameters and can hardly be quantified. Coating was only considered on one side of the substrate to allow the bending of the substrate as no bending is induced by the thermal stress because of the symmetric geometry when coatings are considered on both sides. Since strain hardening was not considered, the coating and substrate material were assumed as homogeneous, isotropic and linear thermoelastic. The assumption of linear thermoelastic material model is reasonable as the hard coating material (brittle) considered here deforms elastically until fracture. It is important to include temperature dependent and thickness dependent material properties in the calculation during thermal stress modelling. But these kinds of material properties are rarely available in the literature for thin TiN coating and can be considered constant values within the temperature range and thickness used in this investigation [347]. It was assumed that the final result would not be affected much without including these effects. As the surface area of the coating was very large compared to the thickness of the coating, plane stress was assumed. Time-dependent processes such as creep was not considered, since the effect of creep has negligible effect in the analysis. Interfaces were considered to be abrupt

boundaries along which the materials were in constant contacts without gaps or flaws e.g., flat and smooth.

5.6.2. Material properties

The physical and thermal material properties of coating (TiN) and substrate (stainless steel) taken from the literature are shown in Table 5.1. [92,318,332,348,349]. The reported coating properties are not consistent in the literature due to the variation of sputtering techniques, coating quality (affected mainly by processing parameters for any particular deposition method), thickness and the evaluation techniques of the coating properties. Thermal expansivity is the most significant property in elastic layers, while the yield strength is most critical in plastic layers [350].

Table 5.1. Physical and thermal properties of coating, substrate and interlayer materials.

Property	Materials		
	Ti	TiN	Stainless steel
Young's modulus (GPa)	140	600	200
Poisson's ratio	0.41	0.25	0.3
Thermal expansion coefficient ($^{\circ}\text{C}$) $\times 10^{-6}$	10.48	9.4	13.0

5.6.3. Analysis details

Numerical simulation of thermal stresses generated during the deposition of TiN coating on stainless steel by magnetron sputtering was simulated using the ANSYS finite element analysis code [351].

5.6.3.1. Element used in the model

A structural finite element analysis with thermal loading was executed for the model using four-node structural plane and quadratic element PLANE 42 (Figure 5.5.), which has two degrees of freedom (translations in the nodal x and y dimensions) per node. The element can be used either as a plane element (plane stress or plane strain) or as an axisymmetric element. This element has also plasticity, large strain and large deflection capabilities.

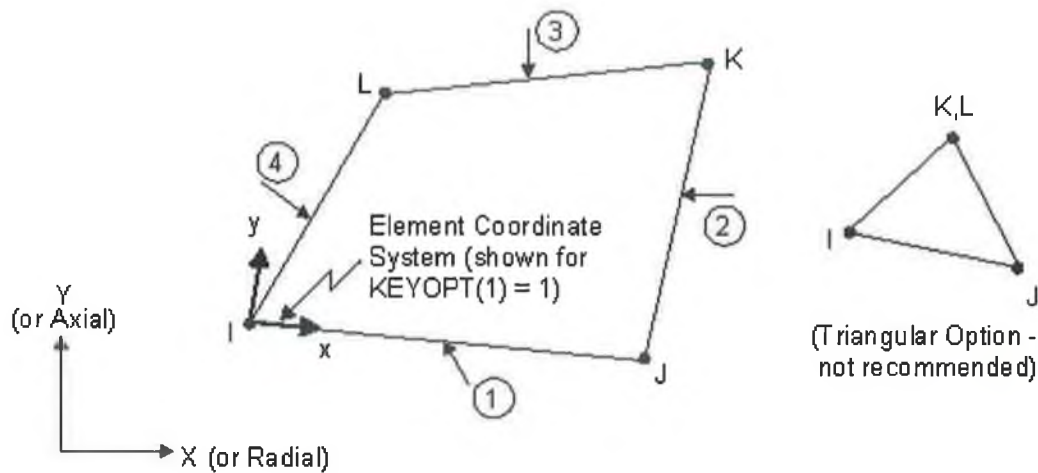


Figure 5.5. PLANE42, 2-D structural solid element.

5.6.3.2. Meshing of the model

The mapped meshing with quadrilateral-shaped elements was used to mesh the model. A fine mesh was introduced into model across the plane in such a way that the element size was minimized in a graded fashion both from coating and substrate side near the coating-substrate interface [321] (Figure 5.6.), as this area is very prone to high stress concentration [306,316,338]. A fine mesh was also introduced near the edge in a graded fashion across the thickness of the coating and substrate [329].

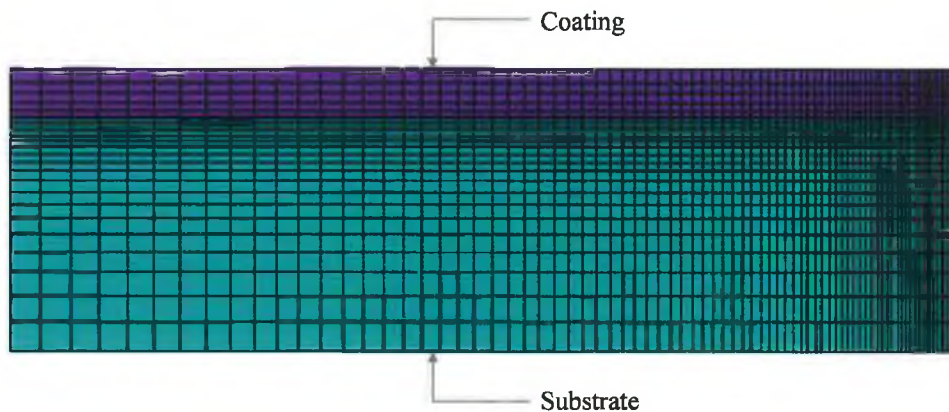


Figure 5.6. Typical meshed model of the coating-substrate system.

The mesh was refined until a very small change in the results obtained, although the mesh couldn't be refined indefinitely because of the limitations of the number of elements generated in ANSYS. This will indicate that a sufficiently fine mesh was used. Figure 5.7 shows the convergence curve with the increasing no of elements used in the model. The finite element mesh was consisted upto 27000 elements depending on the mesh refinements required.

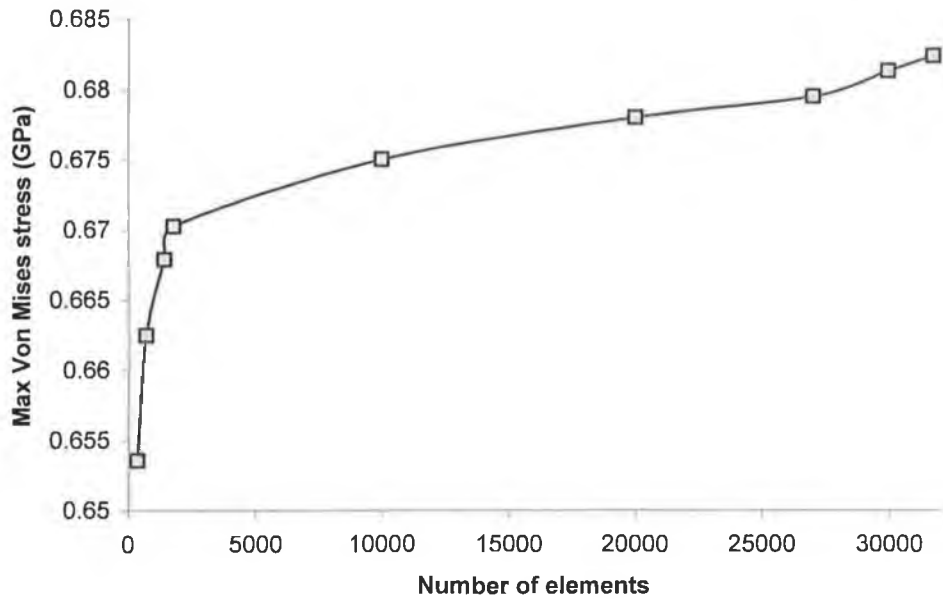


Figure 5.7. Convergence of finite element model.

5.6.3.3. *Boundary conditions*

The physical boundary condition is important for correct modelling as it reflects the physical situation. When a composite body is subjected to uniform change in temperature, no stress is induced if the body can freely deform but stress is induced only when it is restrained against free deformation. The left side of the model was used as the axis of axisymmetric model. The bottom corner of the axisymmetric model was pinned to restrict any movement in all directions.

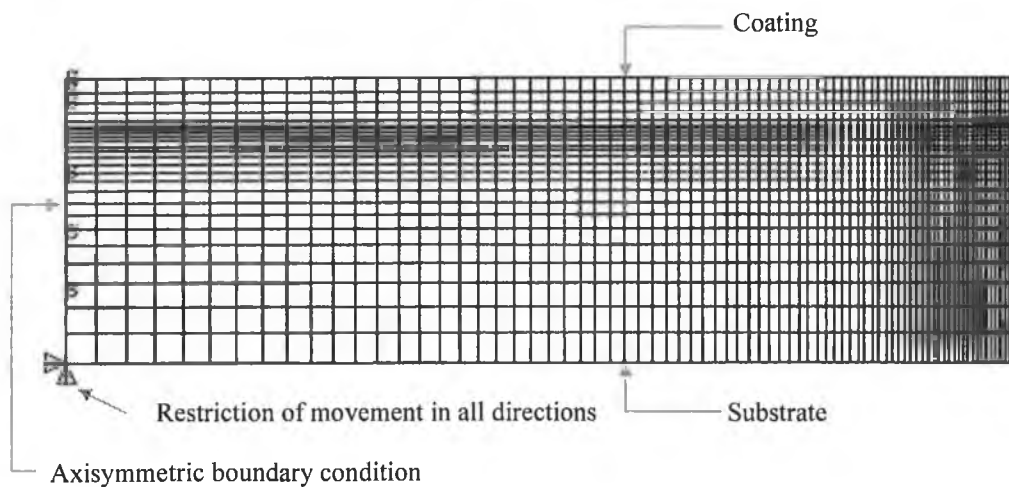


Figure 5.8. Physical boundary conditions applied in the model.

Fixing only one corner allows the coating-substrate system to respond to thermal stresses with minimum interference from the boundary condition, and thus stress and distortion

analyses can be carried out with reasonable accuracy [352]. All other edges were free so that bending was permitted to take place during cooling [321]. The physical boundary conditions applied to the model are shown in the Figure 5.8. Thermal loading was applied by cooling the model from deposition temperature (500 °C) to room temperature (25 °C). The deposition temperature was set to reference temperature and room temperature was set to uniform temperature in ANSYS.

5.6.3.4. Analysis through batch file

The analysis was performed using batch mode instead of Graphical User Interface (GUI) mode by using the Ansys Parametric Design Language (APDL). The main advantage of the batch mode analysis over GUI mode analysis is small file size (10-100 K) for documenting an entire model, mesh and solution description. Batch processing is highly modular. Once the batch file is created, changing dimensions, material properties, mesh densities, loads etc. is a snap. This helps to save lot of time to optimize or make several ANSYS runs without having to do everything by hand. A macro was written to compare the analytical and FEA results for parametric studies. The analysis in batch mode is shown in the Appendix E as an input file.

5.7. RESULTS AND DISCUSSIONS

5.7.1. Parametric studies

A parametric study was performed on the model in order to determine the effects of various parameters on the maximum stress developed in the coating and compared with analytical equation (Equation 5.14). The parameters in this investigation were deposition temperature, coating thickness, substrate thickness, coating thermal expansion coefficient, and coating elastic modulus. Five sets of finite element analyses were performed by varying one of the parameters and holding four other parameters constant as shown in Table 5.2.

Table 5.2. Values of the parameters used in the parametric studies.

Parameters	Range of values	Increment	Constant value used for analysis
Deposition temperature (°C)	0-500	50	500
Coating thickness (μm)	1.0-5.0	0.5	3.0
Substrate thickness (mm)	0.05-0.5	0.05	0.1
Coating thermal expansion coefficient (1/°C) × 10 ⁻⁶	6.5-9.5	0.5	9.4
Coating elastic modulus (GPa)	200-600	50	600

5.7.1.1. Effect of deposition temperature

Deposition temperature in magnetron sputtering technique depends on the power supply to the target, target to substrate distance etc. Typically in the sputtering technique, deposition temperature varies between 100-500 °C. The typical thermal stress of TiN was found to reach about 1 GPa upon cooling from 450 °C to room temperature [349].

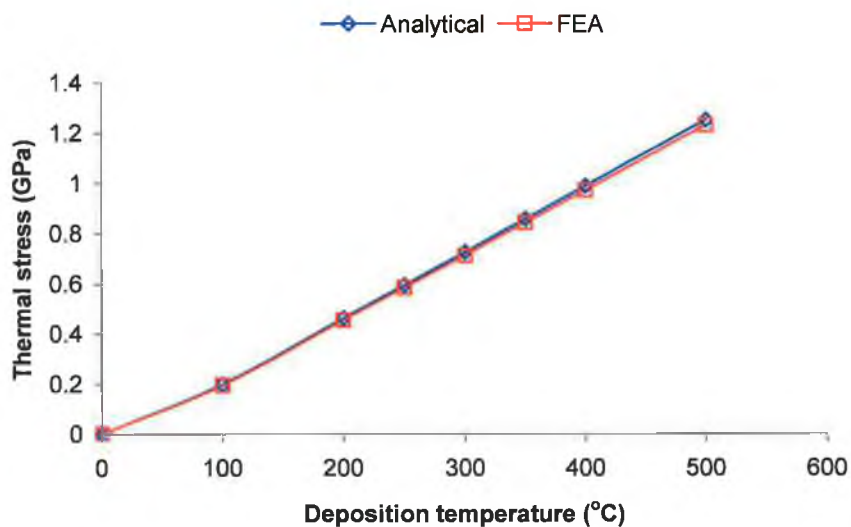


Figure 5.9. Variation of analytical (average stress in the coating) and FEA (Max Von Mises stress) thermal stress with deposition temperature.

From Figure 5.9. it is seen that thermal stress varies linearly with the deposition temperature. From Equation (5.14) it is quite clear that if the other parameters are constant then thermal stress is proportional to deposition temperature. This proportionality has been reflected in the graph both for analytical and finite element analysis within the temperature range considered here. Deposition temperature may contribute a big boost for the thermal

stress development, as it can be seen from the graph that almost one order of magnitude more stress is induced with increasing the temperature from 100 °C to 600 °C.

5.7.1.2. Effect of coating Young's modulus

The Young's modulus of the coating deposited by PVD techniques depends on the PVD deposition techniques and the processing parameters (deposition pressure, deposition current, N₂ percentage in the coating etc.) and of course the determination techniques of Young's modulus. Usually understoichiometric TiN has lower Young's modulus values whereas overstoichiometric TiN coating has higher Young's modulus [348]. The reported values of Young's modulus of TiN coating in the literature vary within the range of 250-600 GPa. From Figure 5.10. it is seen that thermal stress calculated by FEM increases with coatings Young's modulus agreeing with the analytical calculations. This plotting will give an indication of the error introduced in the thermal stress calculation with different Young's modulus of the coating.

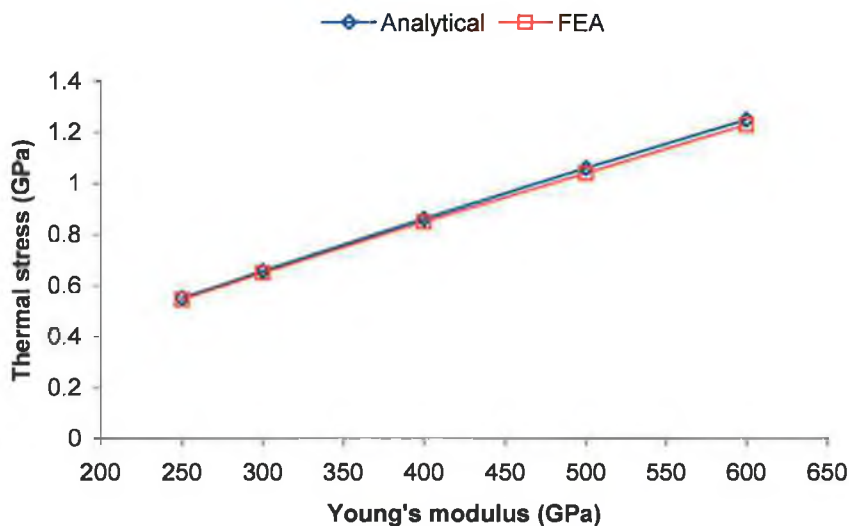


Figure 5.10. Variation of analytical (average stress in the coating) and FEA (Max Von Mises stress) thermal stress with different Young's modulus of coating.

Thermal stress has become double from the minimum value to the maximum value of Young' modulus used here. The main reason for variation the reported TiN Young's modulus is the porosity induced in the coating during deposition. As the porosity increases in the coating the Young's modulus and thermal conductivity values decreases while Poisson's ratio decreases [328]. This plotting will give an indirect relationship between the coating porosity and thermal stress; thermal stress decreases with the increased porosity in the coating due to the lower thermal gradient [328,334].

5.7.1.3. Effect of coating thickness

Coating thickness has an impact of the thermal stress developed in the coating. Thermal stress decreases with the increase in the coating thickness [324]. This is true for both analytical and finite element analysis and can be seen in Figure 5.11. This is due to the bending-induced stress relaxation at high coating thickness [353] and is consistent with the analytical solution in other study. When the coating-substrate system is bent, the stress in coating and substrate is reduced in proportion to the bending strain. This bending effect is negligible for thin coatings, due to their very low stiffness; it is significant as coating thickness increases. When other conditions are same, a larger coating thickness causes larger bending curvature in the coating-substrate system. Hence, the increase of coating thickness results in considerable bending-induced stress relaxation [324] and consequently lower stress in the coating.

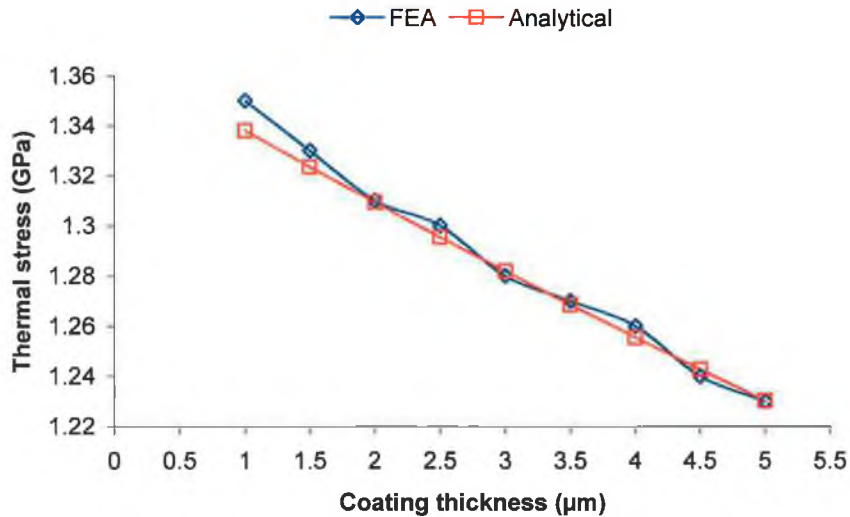


Figure 5.11. Variation of analytical (average stress in the coating) and FEA (Max Von Mises stress) thermal stress with coating thickness.

5.7.1.4. Effect of substrate thickness

Like the coating thickness, thermal stress also increases with the substrate thickness as shown in Figure 5.12. Analytical and finite element analyses are also in good agreement in this regard. With lower substrate thickness, the stress in the coating is relaxed by the deformation of the substrate while for higher substrate thickness bending is prevented due to the higher substrate thickness and consequently higher thermal stress develops in the coating.

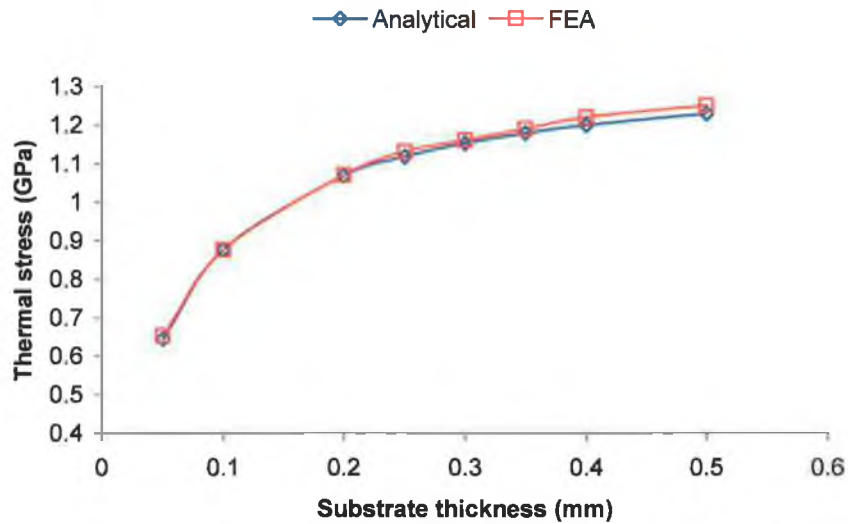


Figure 5.12. Variation of analytical (average stress in the coating) and FEA (Max Von Mises stress) thermal stress with substrate thickness.

5.7.1.5. *Effect of coating thermal expansion coefficient*

Again for TiN coating, the thermal expansion coefficient (CTE) is not constant. It depends on the deposition methods and the processing parameters. The reported values of CTE of TiN lie with the range of 6.5×10^{-6} to $9.4 \times 10^{-6} / ^\circ\text{C}$ [332,347].

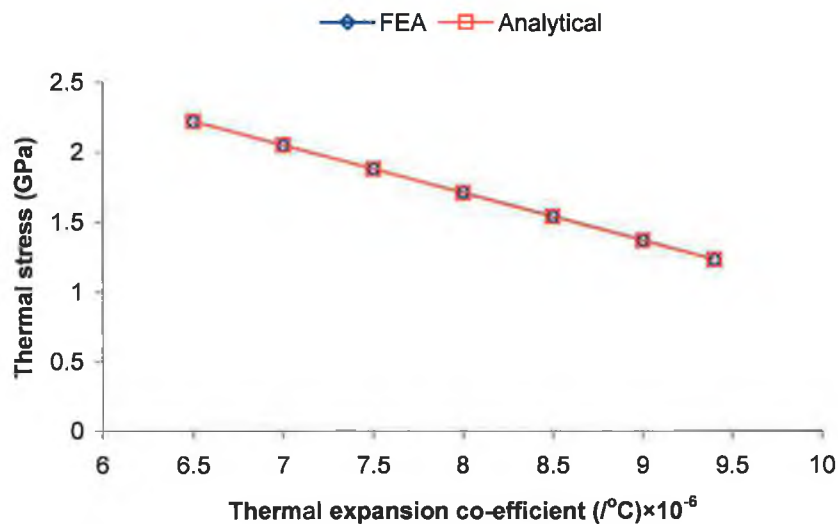


Figure 5.13. Variation of analytical (average stress in the coating) and FEA (Max Von Mises stress) thermal stress with thermal expansion of coating.

From the Equation (5.14) it is seen that thermal stress is proportional to the CTE difference between the coating and substrate if the other parameters are constant. This fact is reflected

in Figure 5.13. for both analytical and finite element calculations. As CTE of the coating is increased, the difference of CTE decreases and consequently thermal stress decreases.

5.7.2. Stress distribution

The coating failure mechanisms are mainly controlled by the magnitude and the distribution of radial (σ_x) or tangential stress (σ_z), axial stress (σ_y) and shear stress (σ_{xy}) at or near the radial free edge of the specimen or near the specimen's axis of symmetry (y-axis) [321,322]. The above-mentioned stresses were obtained and analysed in the next sections.

5.7.2.1. Von Mises stress (σ_{eqv}) distribution

For isotropic materials, elastic deformation ceases and yielding commences when the von Mises yield criterion is satisfied. This is the criterion used to detect the initiation of plastic deformation and to determine the plastic zone boundary. Theoretically, maximum stress should arise at the interface between the coating and substrate due to joining two different types of materials. Von Mises stress distribution away from the edge in the coating and substrate with individual colour legend is shown separately in Figure 5.14. to visualize the stress variation more clearly. The maximum von Mises stress arises at the interface between the coating and substrate.

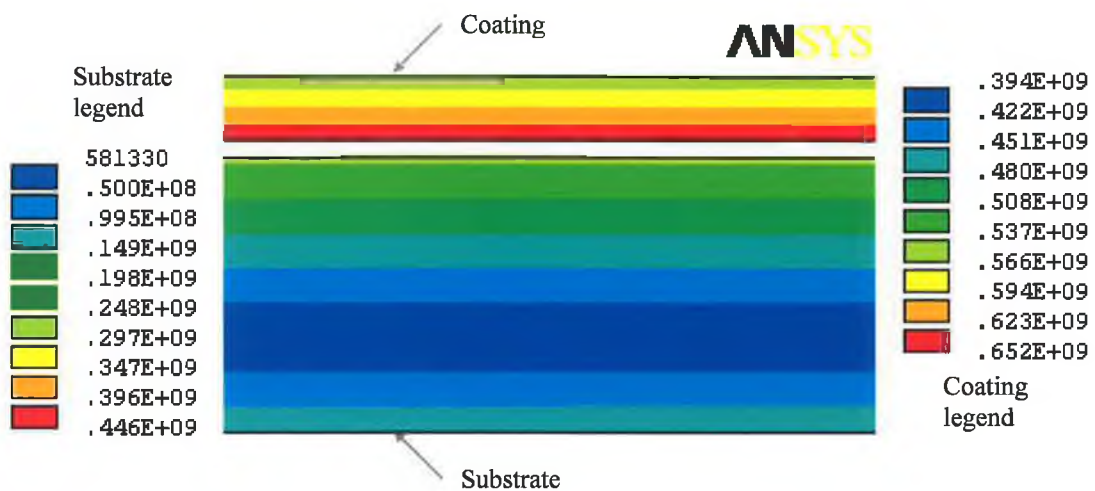


Figure 5.14. Von Mises stress distribution separately in the coating and substrate after cooling the coating-substrate system from deposition temperature to room temperature.

The strain distribution also supports the von Mises stress distribution as shown in Figure 5.15.

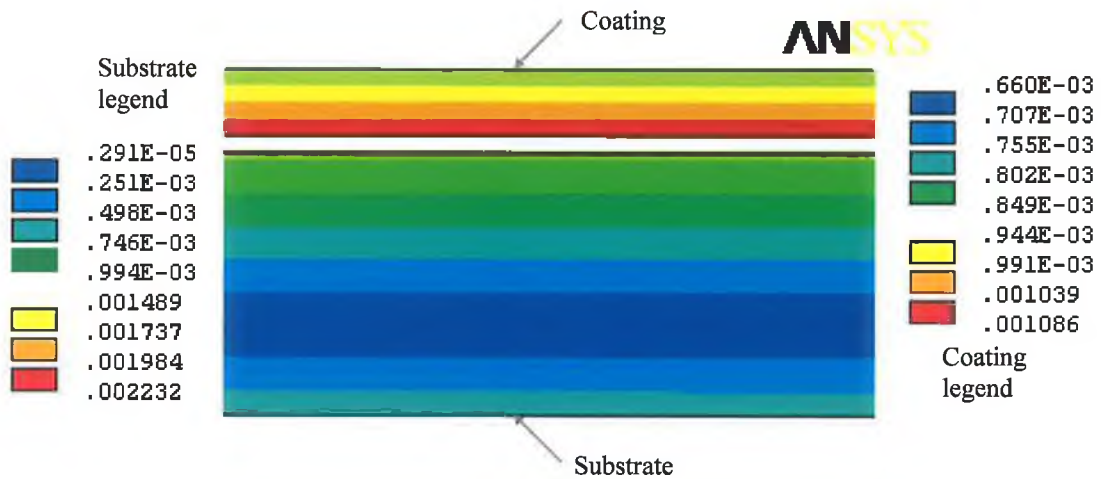


Figure 5.15. Strain distribution separately in the coating and substrate after cooling the coating-substrate system from deposition temperature to room temperature.

When the coating and substrate are plotted together with high coating to substrate thickness ratio maximum stress value corresponding to a particular colour exists throughout the coating area while minimum stress corresponding to a particular colour exists throughout the substrate. This happens due to the huge gap between the maximum and minimum stress values and joining of two dissimilar materials. It should be noted that stress values from the analysis could be seen varied through the thickness. This variation can be seen in Von Mises stress plot if the coating and substrate are plotted separately.

5.7.2.2. *Tangential stress (σ_x) distribution*

Figure 5.16. shows the tangential stress plot separately in the coating and substrate away from the edge with their corresponding colour legends. Through the thickness of the substrate from bottom to top surface stress gradient and stress reversals (compressive to tensile) were observed. In the bottom surface of the substrate compressive stress appeared; stress reversals occurred after a distance of around one third of the substrate thickness; and reached maximum value near the interface between the coating and substrate. Through the thickness of the coating from bottom to top surface slight stress gradient was observed but no stress reversal was observed. Compressive stress increased from the top surface of the coating towards interface and reached the maximum value at the interface.

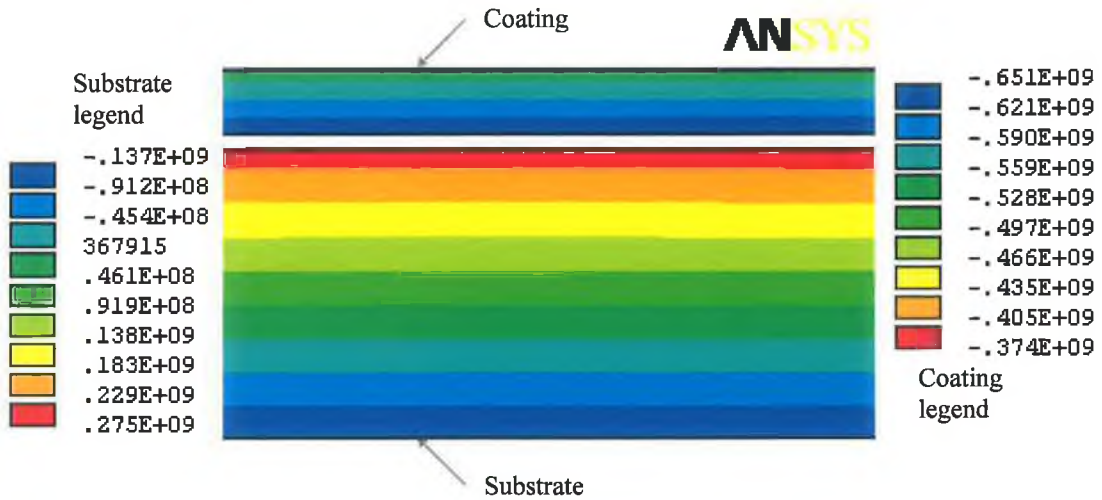


Figure 5.16. Tangential stress distribution separately in the coating and substrate after cooling the coating-substrate system from deposition temperature to room temperature.

Figure 5.17. shows the distribution of tangential stress along the thickness of the coating and substrate at different distances away from the edge of the coating-substrate system. The graph mimics the stress distribution as seen in the stress plot.

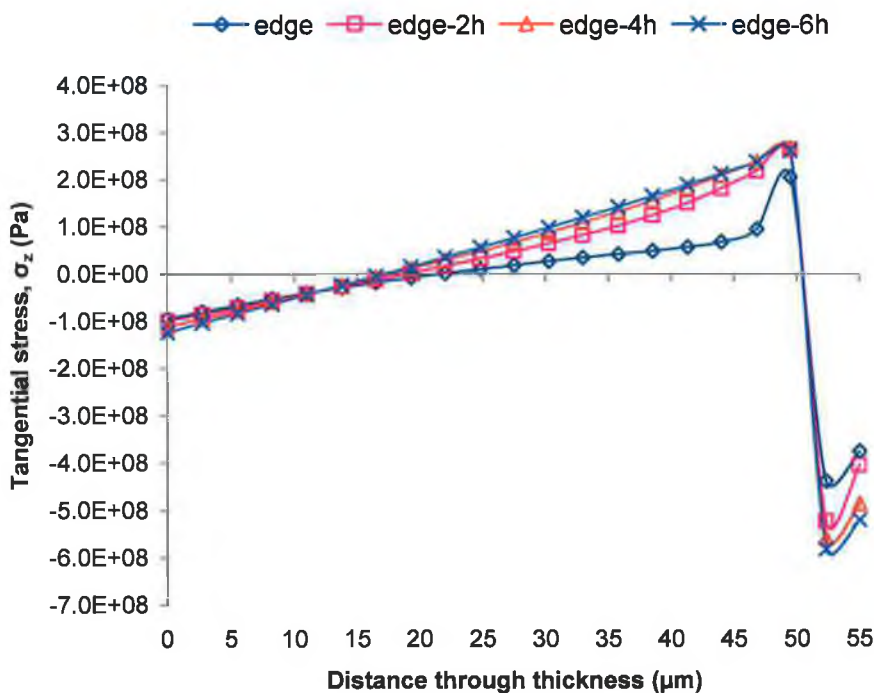


Figure 5.17. Tangential stress (σ_z) distribution through thickness at different position from the edge to the center.

The minimum tangential stress value in the coating appears at the edge while stress values increase away from the edge. At around a distance of 5h (h is coating thickness) stresses

reach close to the maximum value and remain constant throughout the rest of the coating. Since the substrate-to-coating thickness ratio is large, the compressive stress in the coating is larger than the tensile stress in the substrate [338]. The radial stress also followed the same stress distribution as tangential stress, which indicated that the biaxial stress assumption was right. If the radial or tangential stress exceeds the interfacial bond strength, coating failure may occur by spallation [354].

When the coating-substrate bends a linear stress gradient (along Y axis) in the coating and substrate develops as shown in Figure 5.18. [318,355]. The tangential or radial thermal stress distribution follows the similar stress gradient through the thickness of the coating and substrate when the coating-substrate system is cooled from deposition temperature to room temperature (see Figure 5.17.).

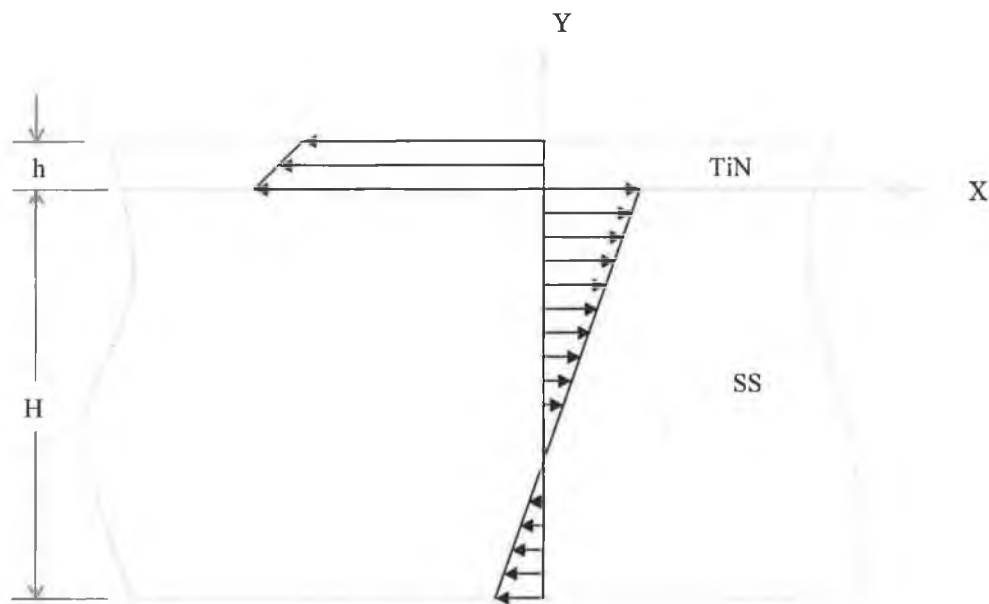


Figure 5.18. Schematic diagram of typical thermal stress distribution through the thickness of coating and substrate.

5.7.2.3. Shear stress (σ_{xy}) distribution

Figure 5.19. shows the contour plot of the shear stress distribution in the coating and substrate. The maximum shear stress was found at the interface between the coating and substrate near the edge and is consistent with other studies [322].

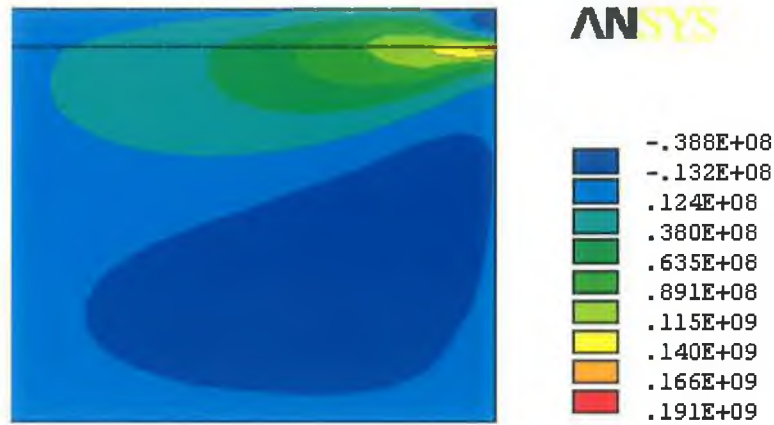


Figure 5.19. The contour plot of shear stress distribution in the coating and substrate near edge.

Figure 5.20. shows the distribution of shear stress through the thickness of the coating and substrate at different distances away from the edge. The shear stress values were smaller than the other stress components except near the edge. The maximum tensile shear stress appeared at the interface near the edge of the coating and decreased to very small compressive stress at the top surface of the coating.

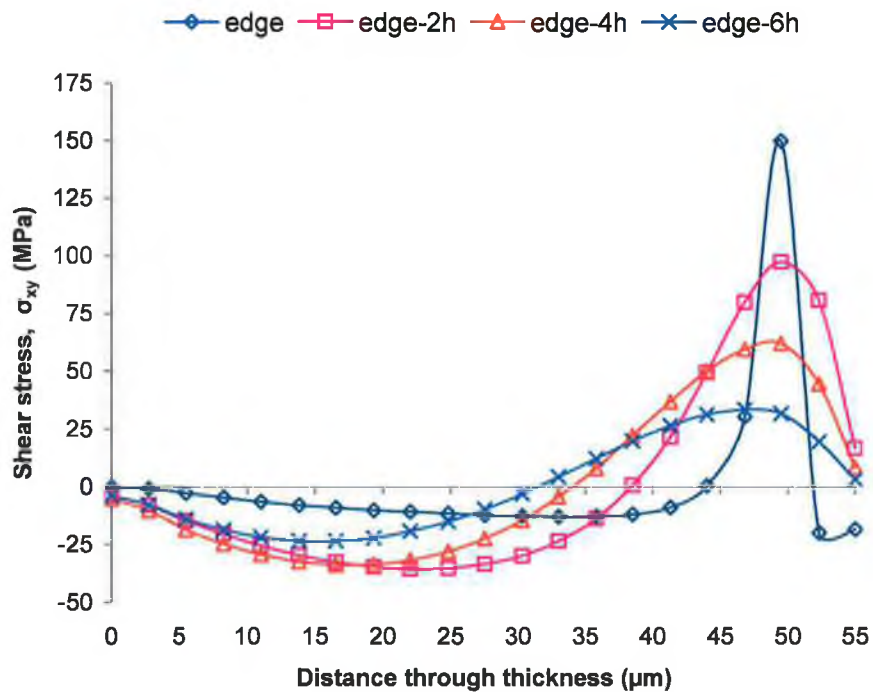


Figure 5.20. Shear stress (σ_{xy}) distribution through thickness at different distances away from the edge.

But away from the edge no stress reversal in the coating was observed and the tensile stress at the top surface of the coating reached to very small value due to the free surface phenomenon. While at the edge of the substrate, the maximum tensile stress at the interface decreased to very small value at the bottom surface. Stress reversal from tensile at the interface to compressive towards the bottom surface was also observed. Away from the edge the shear stress values at the interface decreased. But the general trend for shear stress distribution in the coating and substrate remained same as explained before. The shear stress is equivalent to the adhesion strength of the coating [307]. As the maximum shear stress is at the interface between the coating and substrate, the spallation of the coating is expected to occur from this position if the shear stress is greater than the bonding strength between the coating and substrate. As expected there is small shear stresses along the axisymmetric line and top surface of the coating.

5.7.2.4. Axial stress (σ_y) distribution

Figure 5.21. shows the axial stress plot near the edge of the model. Maximum tensile stress in the coating and maximum compressive stress in the substrate was observed at the edge.

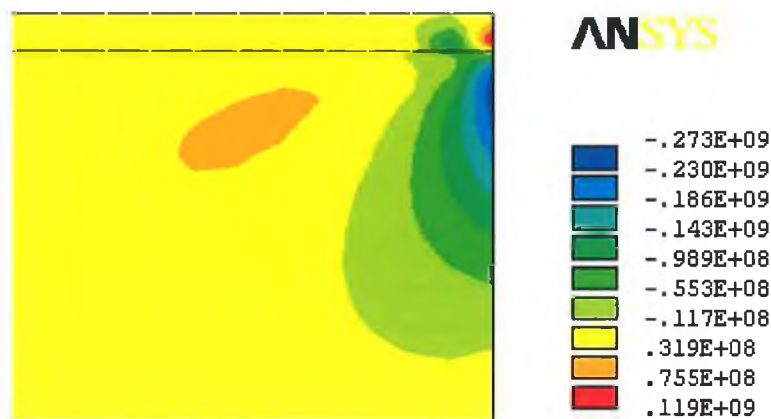


Figure 5.21. The contour plot of axial stress distribution in the coating and substrate near edge.

Figure 5.22. shows the axial stress distribution through the thickness of coating and substrate at different distances away from the edge. The graph reflects the similar stress distribution as in the contour plot. At the edge the maximum tensile stress in the coating is smaller than the maximum compressive stress in the substrate. The edge of the coating-substrate system can be considered the critical location from the failure standpoint as the maximum tensile stress was found at the edge of the coating. But away from the edge the compressive stress in the substrate turned into tensile stress and tensile stress in the coating remained tensile.

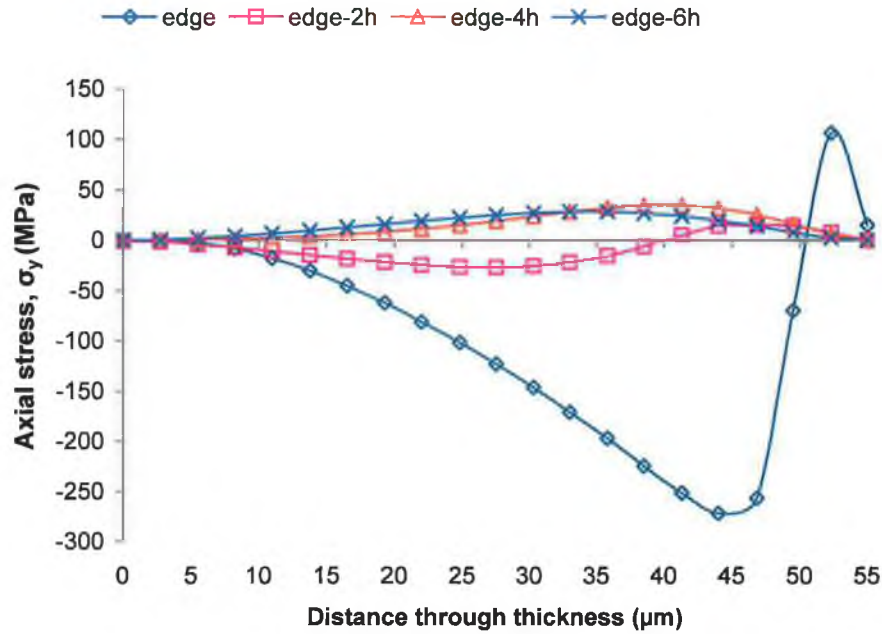


Figure 5.22. Axial stress (σ_y) distribution through the thickness of the coating and substrate at different distances away from the edge.

It is well known that in the case of planar specimens with thin coatings, in-plane biaxial stresses (σ_x , σ_z) in the coating are far higher than the out-of-plane through-thickness stresses (σ_y). This is evident from the axial stress distribution in the coating little bit away from the edge.

5.7.3. Effect of interlayer

The property variation in hard coating on soft substrate is substantial at the interface in coatings prepared by various PVD techniques. One of the reasons for not getting good adhesion is due to the sharp interface with a thickness of less than a nanometre. The residual stress generated at the interface can also play an important role for poor adhesion. It is generally acknowledged that in the vapour deposition method a Ti interlayer is introduced between TiN coating and steel to enhance the adhesion of the coating to substrates and reduce the thermal mismatch between them, as well as prolong the service life of the coating [92,350]. Chemically, diffused mixing of elements forming a broad interface and strong epitaxial relation between the TiN and Ti layers is attributed for better adhesion with Ti interlayer. Mechanically, the titanium interlayer acts as a soft flexible layer, reducing the shearing stresses at the coating-substrate contact and stopping the propagation of cracks in the inter-surface area.

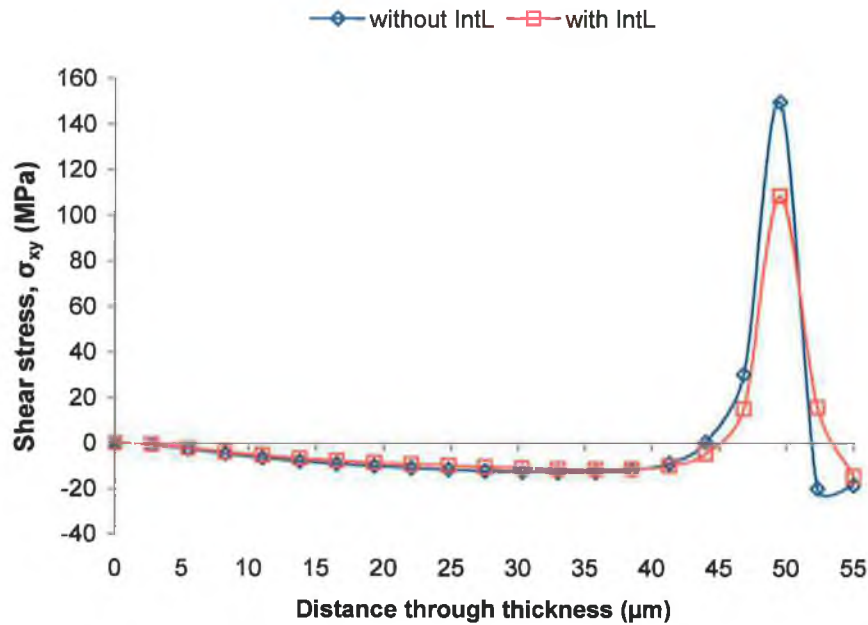


Figure 5.23. Shear stress (σ_{xy}) distribution through thickness at the edge without and with interlayer (interlayer thickness is 2 μm).

TiN coating on stainless steel substrate is modelled with and without Ti interlayer. It was seen in the previous Section (5.7.2.3.) that shear stress is maximum at the edge and near the interface. The shear stress distribution through the thickness of the coating and substrate at the edge of the coating-substrate model with and without interlayer is shown in Figure 5.23. A significant reduction of shear stress is evident with introducing Ti interlayer and is consistent with the literature [92]. Smooth transition of thermal properties from TiN to stainless steel and accommodation of shear stress by the deformation of soft Ti layer would be recognised as the possible reasons for the reduction of shear stress.

The increase of Ti interlayer thickness can reduce the shear stress levels but not very significant reduction was observed (Figure 5.24.). When the interlayer thickness is half of the typical coating thickness the shear stress value reaches near the minimum value. After that increasing the interlayer thickness the shear stress value does not change in a great deal. At lower thickness the Ti interlayer cannot accommodate the shear stress with significant amount, that's why the shear stress is little bit higher than the shear stress with higher interlayer thickness. It was also found that the other stress components e.g., radial or tangential stress and axial stress can also be reduced by introducing the Ti interlayer.

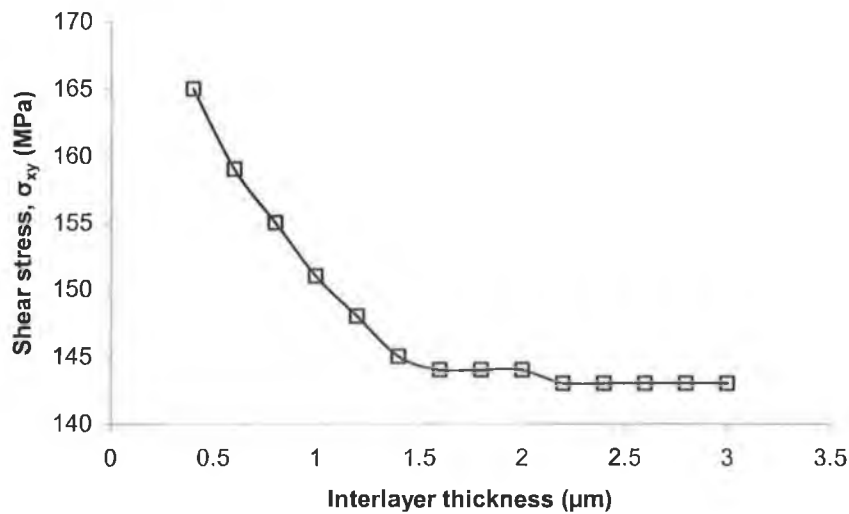


Figure 5.24. Variation of shear stress (σ_{xy}) with the interlayer thickness.

5.7.4. Model verification

Checking the results of finite element model is vital. Comparisons with experimental or analytical results are necessary. Numerical verification of the model was done by comparing the FE results with the analytical equation of thermal stress in thin coating (Equation 5.14). The thermal stress generated in the coating after deposition could be compressive or tensile depending on the thermal expansion coefficients of the coating and substrate. If the coating thermal expansion coefficients are lower than the substrate, during cooling substrate will try to contract with a higher rate than the coating. As a result a compressive stress will generate in the coating. The opposite phenomenon occurs when the coating thermal expansion coefficients are higher than that of substrate [306]. When the coating-substrate system is cooled, thermal stress will generate and by symmetry, the coated substrate will take up a spherical curvature in the region away from the edges. By convention, positive stress value refers to a tensile stress state, in which the substrate is bowed towards the coating (concave), while negative stress value corresponds to a compressive stress state, in which the substrate is bowed away from the coating (convex) [314]. It has been observed that the coating-substrate system bows away from the coating (convex), which implies that coating is in compressive stress state. Analytical and finite element calculations yield the similar results of compressive stress in the coating.

Theoretically the coating-substrate system should bow towards the coating (concave) when heated from room temperature to deposition temperature i.e., compressive stress generates

in the substrate and tensile stress in the coating (Figure 5.25.). This idea was verified using ANSYS by heating the substrate from 25 to 500 °C.



Figure 5.25. Bending of the coating-substrate system after the generation of thermal stress in finite element modelling.

Verification of the model has been done by making the coating thickness zero which produces zero stresses, as there is no restriction on expansion or contraction of the substrate. Verification of the model has also been done by putting the same value of room temperature for deposition temperature and putting no restriction in physical movement in the finite element analysis. Theoretically both events will contribute no thermal stress. Finite element analysis also didn't produce any stress at those situations.

5.7.5. Model limitations

Analytical and numerical simulated results do not differ much (e.g., see Figure 5.8.) along most of the radius of the model, however the mismatch of the results increases significantly at bond edges. This is due to the fact that analytical model gives the average stress while the FE model gives the distribution of stress in the coating-substrate system. Furthermore, the thickness ratio of coating and substrate is less than the practical thickness ratio. Although the modelling studied here have provided an important insight into thermal stresses generated in coating and substrate, their impact has been diminished because it has not been possible to experimentally verify the results and thereby, confirm the validity of the assumptions and approximations made in the modelling.

5.8. SUMMARY

Simulation of thermal stress developed in thin TiN sputtered coating on stainless steel substrate has been performed by finite element package ANSYS and verified with appropriate analytical calculations. The wide ranging parametric studies performed on the

verified model under different conditions showed the sensitivity of the maximum stress values in the coating with the various material properties and dimensions. It has been found that deposition temperature, coating thickness, thermal expansion coefficient, and elastic modulus have the most effect on the maximum stress developed in the coating. For minimum peak stress the coating thickness and thermal expansion coefficient should be increased whilst the deposition temperature and the elastic modulus should be reduced as much as practicable. The radial (σ_x) stress distribution and tangential (σ_z) stress distribution are quite similar except near the edge, which reflects the biaxial model consideration. The highest tangential stress values found at the interface between the coating and substrate indicates that the interface between the coating and substrate is the critical location from the failure point of view. Along the interface higher shear stresses were found at the edge because of stress concentration. Higher axial stress was also found at the edge of the coating-substrate system. This will cause the start of the spallation of the coating from the edge. Results also showed that insertion of Ti interlayer between the TiN coating and substrate can significantly reduce the stress components especially the shear stress. However, the interlayer thickness has little effect on stress reduction. Finally, FEM analysis offers detailed information about all stress components and proves very useful in providing better understanding of thermal stress developed during cooling down of the thin coating-substrate system.

CHAPTER 6

Coating Deposition and Characterization Techniques

6.1. INTRODUCTION

PVD is advantageous among the different thin coating deposition techniques in terms of depositing new coating species and new generation coating architecture. The method used for depositing coatings was closed-field unbalanced magnetron sputtering, which is comparatively a new technique under the PVD category. In this chapter the deposition procedure for TiN, MoS₂ and TiN+MoS_x coatings is briefly described. The different methods for characterizing physical, chemical, structural, mechanical and tribological properties of the coatings are also briefly discussed.

6.2. RELATION AMONG SPUTTERING PARAMETERS

Sputtering is complex process, which is highly dependent on number of process parameters namely, deposition pressure, discharge voltage, discharge current, target to substrate distance, process gas flow rate, reactive gas flow rate in case of reactive sputtering, substrate biasing, etc. The effect of gas pressure and target current on the target voltage was investigated for both Ti and MoS₂ targets. In the first case the target current was fixed to a constant value and the Ar gas flow rate was increased from the point where the plasma can be sustained. In the second case the discharge pressure was fixed to a constant value and the target current was changed step by step to investigate the effect of current on voltage. The gate valve was fully opened during the investigation. The power supply to the target can be supplied through three different modes i.e., voltage mode, current mode and power mode. The current control mode is the easiest one to control the discharge. The current control mode was used throughout this experiment. The plasma is sustainable down to 1×10^{-4} mbar in Ar process gas in this method. This is, at least, two orders of magnitude lower pressure than the conventional magnetron sputtering [56]. The range of parameters varied during the investigation is as follows:

- Deposition pressure: $1.0 \times 10^{-4} - 1.0 \times 10^{-2}$ mbar
- Ar flow rate: 8.0-75.0 sccm
- N₂ flow rate: 0.0-10.0 sccm
- Ti target current: 0.0-5.0 A.
- MoS₂ target current: 0.0-2.25 A.

6.3. MATERIALS AND DEPOSITION PROCEDURE

6.3.1. Substrate materials

The substrate material used for depositing coating was 316L stainless steel. The chemical composition of 316L stainless steel is shown in Table 6.1. Glass slide and Si wafer substrates have also been used as substrate in some cases to suit certain characterization techniques such as XRD, SEM etc.

Table 6.1. Chemical composition of AISI 316L stainless steel (wt.%).

C	Mn	Ni	Cr	Ni	Mo	Fe
0.03 max	2.0	14.0	18.0	10.0	3.0	Balanced

6.3.2. Coating materials

The coating materials deposited in this investigation were TiN (hard coating), MoS₂ (solid lubricant coating) and TiN+MoS_x (hard-solid lubricant coating).

6.3.3. Substrate preparation

The substrate was prepared as discs with a diameter of 30 mm and a thickness of 10 mm cutting from a long circular rod of 316L stainless steel. The substrates was previously ground and polished with the different grades of SiC paper (250, 600, 800, 1200) sequentially. Smooth surfaces with an average roughness of $R_a=0.02 \mu\text{m}$ were obtained after polishing the samples with $0.3 \mu\text{m}$ alumina powder. Just before chemical cleaning, the substrate was polished with $0.25 \mu\text{m}$ diamond suspensions.

6.3.4. Substrate treatment

6.3.4.1. Chemical treatment

The substrate was chemically cleaned by warm acetone (around 40 °C) for 20 min in an ultrasonic cleaner before being placed in the chamber. This treatment will remove any dirt, grease or loose particle attached with the substrate. The sample was then cleaned by

detergent and dried in hot air to remove water particle, which might affect the pumping down of the chamber.

6.3.5. Deposition procedure

6.3.5.1. Loading of the sample

The sample was loaded by opening the upper plate of the chamber or the whole chamber with upper plate. The sample was attached with the rotary substrate holder with facing the substrate surface parallel to the chamber wall. When only TiN or MoS₂ is deposited, the substrate holder was positioned in front of the Ti or MoS₂ target.

6.3.5.2. Pumping down of the chamber

After loading the sample, the chamber was evacuated roughly (5.0×10^{-2} mbar) using the rotary pump. The chamber was then evacuated to high vacuum (7.0×10^{-6} mbar) using the diffusion pump backed by the rotary pump.

6.3.5.3. Plasma treatment

After achieving high vacuum, the substrate was sputter cleaned in argon plasma with an overall pressure of 10^{-2} mbar for 15-20 minutes. For sputter cleaning the power supplier was run in voltage mode. By setting to 1000 V the current was approximately 50-100 mA. A plasma zone was created in front of the substrate. This plasma will sputter and heat the substrate and effectively remove the contaminated surface oxide layer from the surface of the sample. During sputter cleaning the targets were covered by the shutter so that the sputtered material from the sample surface could not contaminate the target surface.

6.3.5.4. Ti interlayer deposition

It is well documented that Ti interlayer deposition before depositing TiN coating can increase the adhesion [92]. With that in mind a thin Ti interlayer was deposited on the substrate. After plasma cleaning the Ar flow rate was decreased to give a chamber pressure of 3×10^{-3} mbar and shutter for Ti was opened. During this period the MoS₂ target was covered with the shutter so the sputtered Ti coating cannot deposit MoS₂ target surface.

6.3.5.5. TiN+MoS₂ coating deposition

MoS₂ sputtering target running in procedure

When applying current to the MoS₂ sputtering target for the first time or after a long time this should be done very gradually. The target has probably absorbed a large amount of water vapour, which needs to be released from the target gradually to prevent unnecessary cracking of the surface. The MoS₂ target current was ramped from zero to the usual sputtering current level of 0.8 A over the period of 1 hour. This would allow the surface to release water vapour gradually without affecting the pressure in the chamber. The target was then left at the coating current level for a further 2 hours to ensure that all moisture was removed. A titanium target was run together at this time (to getter to system) where the titanium target current was not higher than the MoS₂ current. The ramp procedure was followed for all other targets at the same time to reduce contamination of the new MoS₂ target with the other sputtering target materials.

The coatings were deposited using a closed-field magnetron sputtering (CFUBMS) technique by varying the process parameters such as the Ar/N₂ flow rate, magnetron power and bias voltage. The details can be seen in the Table 6.2. The deposition pressure varies from 1×10^{-3} to 5×10^{-3} mbar as measured by penning gauge. The substrate holder was designed to allow the target-to-substrate distance for each magnetron to be varied independently. Thus, each run produced four sets of coatings deposited under otherwise identical conditions, but at different values of target-to-substrate distance. The distance between the magnetron target and the substrate was 75 and 105 mm. The substrates were fixed to a rotatable two-axis substrate holder, which was electrically isolated from the grounded deposition chamber. This will facilitate substrate biasing and sputter cleaning. The temperature of the samples during the coating was measured by K-type thermocouple. The deposition time was normally 30-80 min depending on whether substrate rotation control was used or not. The thickness of the coatings can be controlled by varying a combination of the target current, deposition pressure, bias voltage, target to substrate distance and deposition time.

Table 6.2. Production cycle of TiN+MoS_x in the CFUBMS system.

PROCESS STEPS	PROCESS DATA	DURATION
1. Loading of substrate	Atmospheric pressure: (10 ³ mbar)	-
2. High vacuum	P ₀ = 10 ⁻⁵ mbar	-
3. Plasma cleaning <ul style="list-style-type: none"> ● Gas inlet ● Bias voltage to substrate ● Bias current to substrate ● Pressure 	Ar U = -1000 V I = 100 mA P = 10 ⁻² mbar	15 min
4. Interlayer (Ti) deposition <ul style="list-style-type: none"> ● Gas inlet ● Sputtering target ● Ti target voltage ● Ti target current ● Working pressure ● Ar flow rate 	Ar Ti U = 410 V I = 6.5 A P = 3.0 × 10 ⁻³ mbar f _{Ar} = 40 sccm	10 min
5. Hard-solid lubricant (TiN+MoS_x) coating <ul style="list-style-type: none"> ● Gas inlet ● Sputtering target ● Ti target current ● Ti target voltage ● MoS₂ target current ● MoS₂ target voltage ● Working Pressure ● Bias voltage to substrate ● Ar flow rate ● N₂ flow rate ● Ti peak intensity ● Set point 	Ar + N ₂ Ti and MoS ₂ I _{Ti} = 6.5 A U _{Ti} = 410 V I _{MoS2} = 0.2, 0.4, 0.6 A U _{MoS2} = 390, 425, 540 V P = 3.0 × 10 ⁻³ mbar U _b = -50 V f _{Ar} = 45 sccm f _{N2} = 15 sccm I _{Ti} = 830 I _{set} = 457	55 min
6. Vacuum cooling	P = 4.0 × 10 ⁻² mbar	60 min
7. Venting	Air	5 min

A Ti target (99.99% purity) was used for the deposition of hard TiN coating and a MoS₂ target (99% purity) was used to deposit the soft solid lubricant coating. The sputtering system contains four unbalanced magnetron sources to elicit maximum ion current densities. Two facing magnetrons fitted with Ti and MoS₂ targets were activated during deposition. The other two facing magnetrons equipped with Ti targets were acted as dummy to make the closed-field and the Ti surface acted as the gettering surface to reduce the contamination [207,246]. Ti interlayer also act as a Mo stabilizer in oxidizing environment [211]. The rotary substrate holder was rotated continuously at a speed of 3 rev/min inside the chamber. Standard procedure of degassing targets was followed before deposition of coating. Advanced Energy MDX 5 kW DC power source was used to supply

power during sputtering of the targets. The magnetron drivers were operated in current regulation mode. Another Advanced Energy MDX 5 kW DC power source was used for biasing the substrate by operating in voltage regulation mode.

The hard-solid lubricant coating was deposited as a multilayer coating as it passes in front of Ti and MoS₂ targets in the nitrogen gas environment. The relative concentration of the metals in the coating was controlled by the relative sputtering power on each target. The nitrogen flow rate was controlled by the use of plasma emission feed back control loop monitoring the Ti peak. Plasma emission monitoring was achieved with a Verity Instruments monochromator detector of 0.2 m focal length. This monochromator was used in conjunction with Reactflo reactive sputtering controller from Megatech Ltd. The titanium intensity was (I_0 , pure Ti peak height represented as 100%) measured by with the optical emission monitor and set I (55% of the initial value of I_0). The Reactflo reactive sputtering controller controls the flow of nitrogen through a high-speed Peizo valve so the intensity decreases from I_0 to I. This ensured that the nitrogen admitted into chamber was sufficient to deposit stoichiometric TiN. For the change from Ti to TiN layer, the bias voltage and N₂ flow were changed slowly and simultaneously over few min to ensure a less abrupt coating-substrate interface. After the deposition the substrate was cooled in vacuum and vented to air.

To investigate the interlayer effect, four different interlayers (only Ti, only stoichiometric TiN, Ti-TiN_{0.33}-TiN, and Ti-TiN_{0.2}-TiN_{0.47}-TiN) with fixed thickness but at different graded composition was deposited underneath the TiN+MoS_x coating. The graded Ti-TiN interlayer was deposited by gradually changing the set point in the reactive sputtering controller. For reference, TiN and MoS_x coatings were also deposited either by activating the Ti target in Ar and N₂ gas environment or MoS₂ target in only Ar gas environment. In all cases the coating thicknesses were maintained approximately same.

6.4. COATING CHARACTERIZATION TECHNIQUES

Surface characterization means the assessment of relevant properties of surface by means of physical, chemical and technological effects. Characterization of surface coatings in terms of composition, microstructure, physical, chemical, mechanical and tribological properties is the crucial step for developing surface engineering because the outcome determines whether or not the specific design requirements can be achieved. It is also an

important feature for quality assurance when any particular surface engineering process has gone into production. A great variety of powerful techniques exists both to characterize surface and coatings that the quality is adequate. This section will address the different techniques for the determination of the properties of thin coating.

6.4.1. Physical properties

6.4.1.1. Thickness of the coating

Various techniques are available for thickness measurement and can be categorized as contacting and non-contacting. Some measurement techniques can achieve good accuracies; they all have both strong and weak points. The choice of different methods depends on the thickness, properties, the accuracy desired and the application of coating. One of the most accurate methods is stylus profilometer. Ball cratering is also very useful for measuring the thickness of any kind of material but suffers the limitation of measuring very thin coating (nanometer level). Optical methods are only suitable for transparent coating. There are other techniques for thickness measurement based on electrical, magnetic, and electromagnetic principles. Some methods are suitable for thicker coating and some are for thinner coating. A comparison of common thickness measurement results performed by different methods is shown in Figure 6.1.

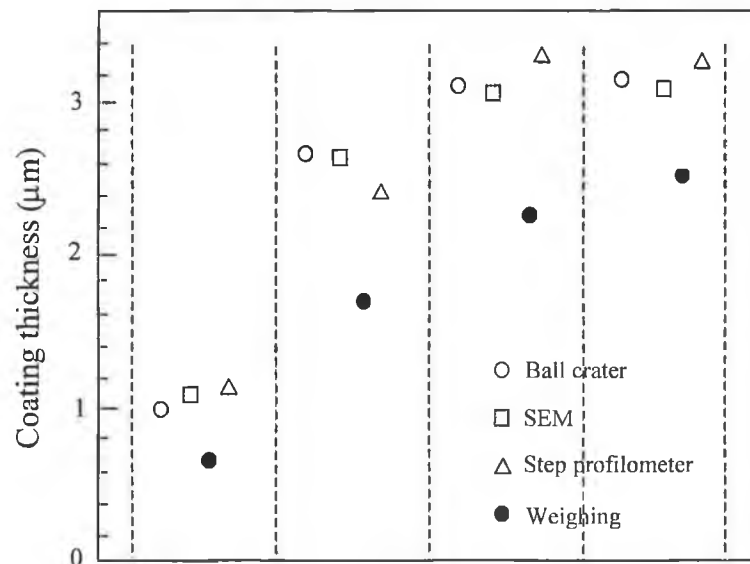


Figure 6.1. Comparison of common thickness measurement results performed by four different methods [356].

Ball crater, SEM and step profilometer give thickness with satisfactory accuracy while weighing underestimates the thickness. The different methods for measuring coating

thickness, their advantages, and disadvantages are reviewed [11,14,26,27]. Stylus and ball cratering methods are discussed in this section.

Stylus profilometer

The stylus instrument amplifies and records the surface topography from the vertical motion of a stylus moved over the surface at a constant velocity. A diamond needle stylus serves as the electromagnetic pick up. The electrical signal from the pick up represent the relative movement between the stylus and the pickup body. The schematic diagram is shown in Figure 6.2.

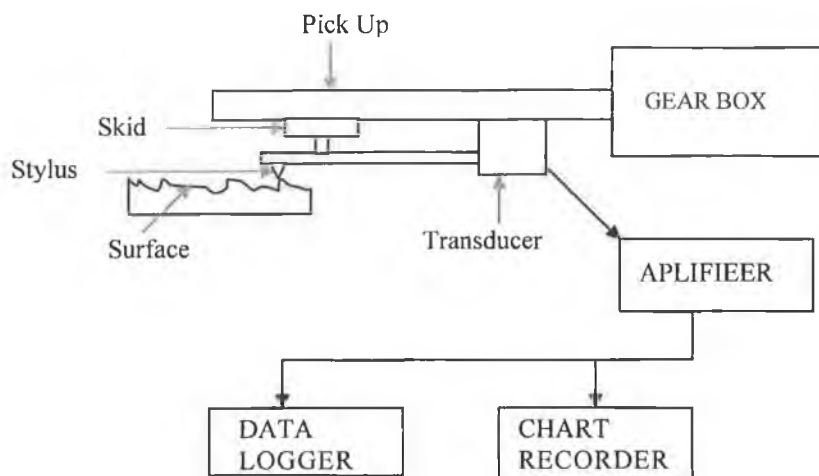


Figure 6.2. Schematic diagram of a typical stylus instrument.

Stylus profilometers have the advantage that they offer long-scan profiling, ability to accommodate large-sized surfaces and pattern recognition. The best stylus profilometers can give a horizontal resolution of about 100 \AA and a vertical resolution as fine as 0.5 \AA , although $10\text{-}20 \text{ \AA}$ is more common. The leveling and measurement functions are controlled by computer in modern instruments. The vertical movement is digitized and data can be processed to magnify areas of interest and yield best profile fits.

The stylus method measures the thickness of a coating by the mechanical movement of a stylus by tracing the topography of a coating-substrate step. Usually a step is made by masking a portion of the substrate during deposition of coating and removing that after deposition. Coating thickness is directly measured as the height of the resulting step-contour trace as shown in Figure 6.3. Several factors limit the accuracy of the measurement from a stylus profilometer such as stylus penetration and scratching of very soft coatings, introduction of excessive noise in case of rough surface, vibration of the equipment and

roughness, flatness and abruptness of the step. The measurement of coating thickness from 200 nm to 10 μm with an inaccuracy of few percents is possible due to the wide variety of vertical amplification available. Stylus profilometer is also used for measuring the surface roughness of the coating and substrate and wear track depth and width to quantify the wear rate.

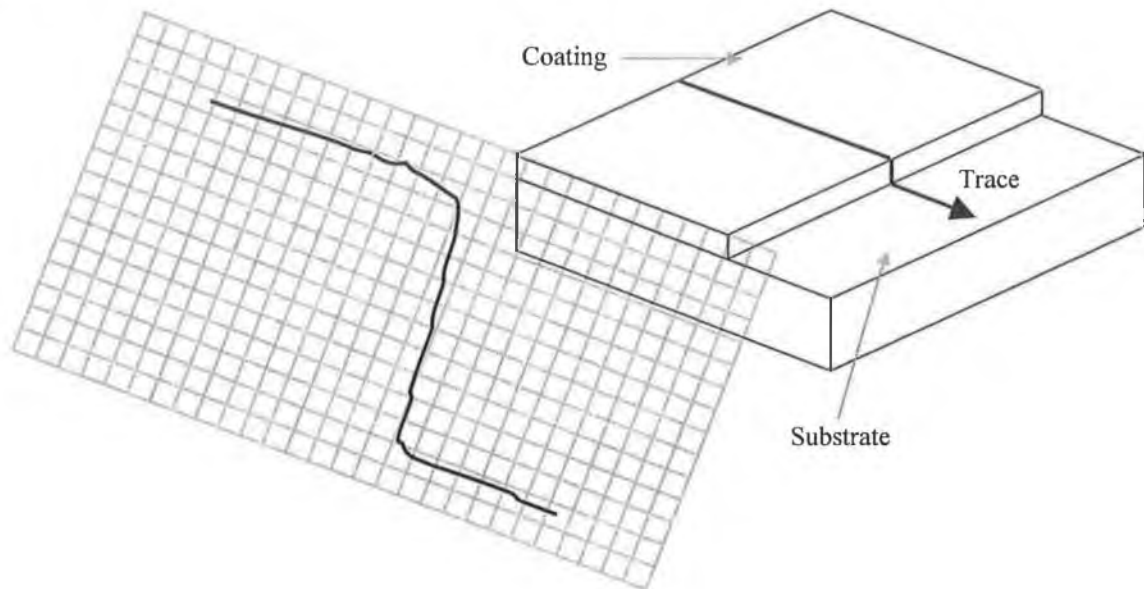


Figure 6.3. Schematic diagram of topography tracing of a coating-substrate system.

A Talysurf stylus profilometer (Surftest 402, series 178, Mitutoyo Corporation) was used to measure the surface roughness of the coating and substrate and the thickness of the coatings. The stylus of the profilometer used in the present study is cone of 5 μm tip radius. The profilometer can be operated in two modes: profile mode for measuring coating thickness and roughness mode for measuring roughness. The profilometer gives two types of reading of the roughness value: digital display by roughness tester or data logger and graphical display by a chart recorder (Mini Recorder for Surftest 402, series 178, Mitutoyo Corporation) in roughness mode. The roughness tester can represent the roughness values in terms of the following parameters: R_a , R_z , R_q , and R_{max} . The chart recorder can also represent the roughness curve in the roughness mode. The coating thickness was determined by measuring the step height of the coating-substrate system from the chart recorder.

Ball crater device

Ball cratering is a very simple, quick, and inexpensive method originally used for assessing the thickness of thin coating. This is achieved by grinding a small crater in a

coating with a ball of known geometry to provide a tapered cross-section of the coating when viewed under an optical or scanning electron microscope. Measurements of the resultant crater can then be made to allow the calculation of the coating thickness without the need to fracture the sample. Examination of the crater can also give qualitative information on coating adhesion and interface condition. Application to complex graded and multi-layered coatings allows the analysis of adhesion layers, layer colours, layer thicknesses and interfaces. Structural or compositional analysis of thin coatings can also be made using additional techniques such as EDX, AES or TEM. A ball crater is also promising to quantify the amount of wear and plastic deformation when applied to wear track created by pin-on-disk. When applied to a scratch test, the ball crater can reveal the failure mechanism. Coating thickness less than 1 μm requires very smooth surface. The other aspects of the ball cratering device is reviewed by Gee et al. [357]. Schematic diagrams of front and side view of the ball crater equipment used for the analysis are shown in Figure 6.4. and Figure 6.5. respectively.

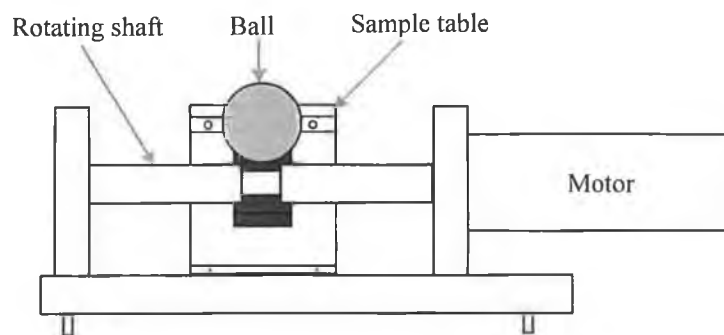


Figure 6.4. Schematic diagram of the front view of the Ball Crater device.

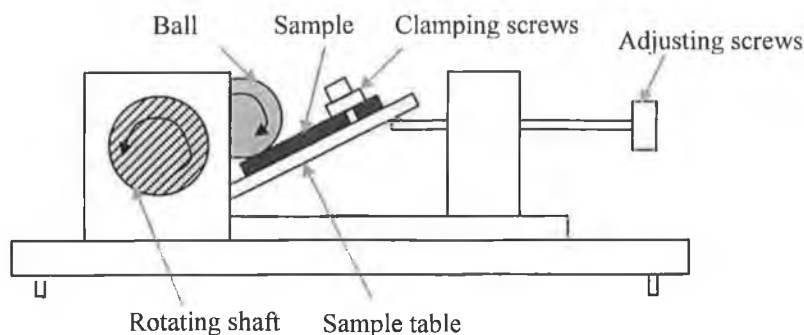


Figure 6.5. Schematic diagram of the side view of the Ball Crater device.

Equation for coating thickness measurement

From the geometry of Figure 6.6 the coating thickness becomes

$$t = (R^2 - b^2)^{1/2} - (R^2 - a^2)^{1/2}$$

$$= R \left[\left(1 - \frac{b^2}{R^2}\right)^{1/2} - \left(1 - \frac{a^2}{R^2}\right)^{1/2} \right]$$

When $\frac{b^2}{R^2}$ and $\frac{a^2}{R^2} \ll 10^{-3}$

$$t = \frac{1}{2R}(a+b)(a-b) \text{-----(6.1)}$$

$t = xy/\text{ball diameter}$

-----(6.2)

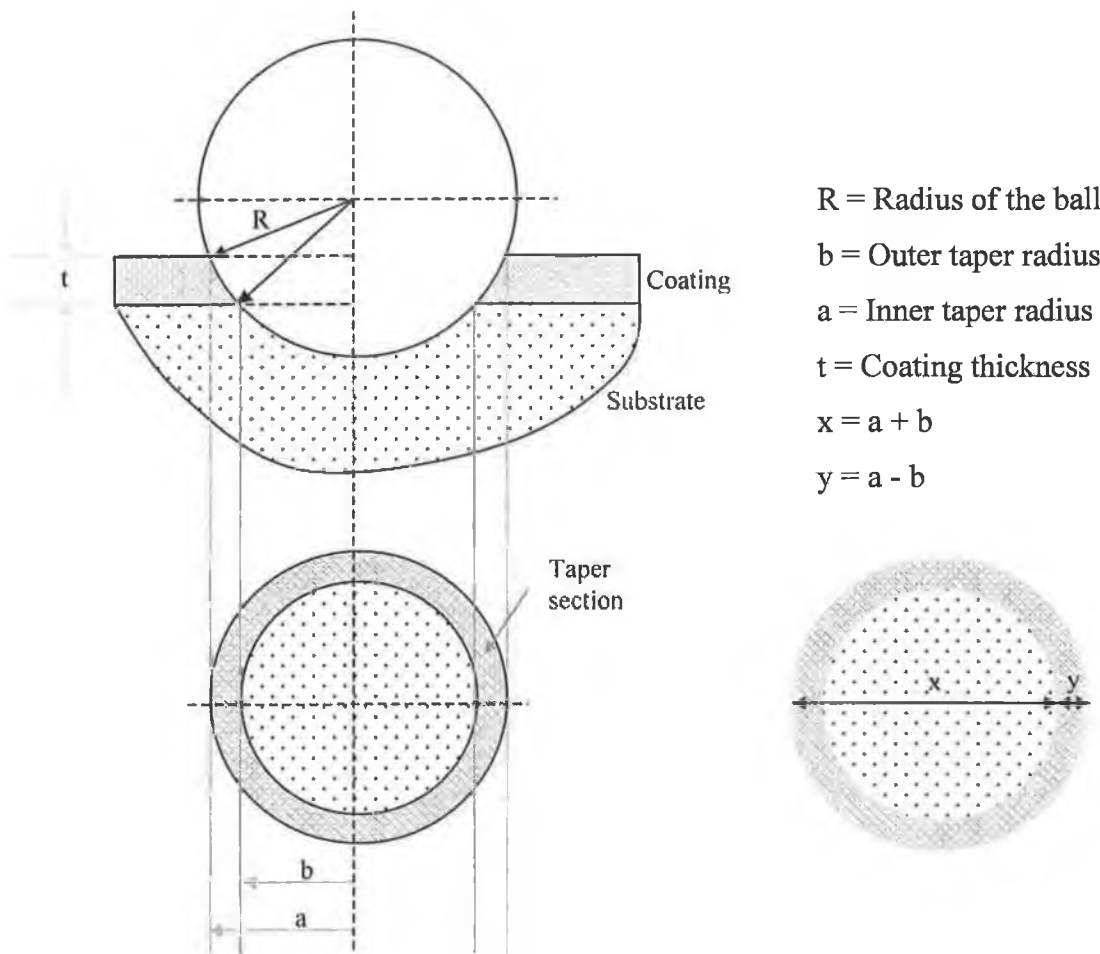


Figure 6.6. A schematic diagram of the crater and the geometry used for coating thickness determination.

Teer bc-2 ball cratering instrument was used to measure the coating thickness from the optical measurement of the crater formed on the sample. The ball crater was also used to

evaluate coatings appearance and the visualization of interface. Sample thickness was determined by an average of five ball-cratering experiments and confirmed by optical and stylus profilometer.

6.4.1.2. Surface roughness

Profilometers are instruments for measuring (or visualizing) the surface roughness. There are two categories of surface profilometers. One is the contacting type (stylus profilometer), which uses a stylus in contact with the surface that moves over the surface, and the other is the non-contacting type, which does not contact the surface (optical profilometer). The contacting types can deform the surface of soft materials. Other methods for surface roughness measurement include confocal scanning microscopy, Scanning Tunneling Microscopy (STM), Atomic Force Microscopy (AFM) etc.

Stylus Profilometer

Talysurf stylus profilometer was also used for measuring the coating and substrate roughness. The profilometer was calibrated against the standard sample before measuring the roughness.

Optical profilometer

Optical profilers offer fast, non-contact three-dimensional measurement of surface topography. Optical profilometer consists of a microscope, an interferometer, a detector array, and support electronics. The surface profile measurement is based on two-beam optical interference and requires a reference surface, which is mounted on a piezo-electric transducer permitting the use of phase shifting techniques to measure the phase of the interference pattern, which is proportional to the surface height at that location. The combination of speed, non-contact, and large field of view makes the optical profiler an ideal metrology tool for a vast majority of applications e.g., coating thickness, uniformity and roughness, all in a single measurement of a few seconds in duration. The image analysis software enables the comprehensive three-dimensional view of the surface of the coating. An optical profiler measures thickness for every point in the field of view, highlighting variations in thickness and uniformity across an area compared to other techniques such as ellipsometry providing only a single average thickness value, with little indication of coating uniformity. The method also extends to thickness measurement of opaque or semi-transparent on metallic or non-metallic coatings. An optical profiler's

range extends to the measurement of thickness upto several millimeters compared to other techniques such as ellipsometer (few microns).

Veeco NT-1000 optical profilometer was used to measure the surface roughness, coating thickness and to inspect the wear tracks for analyzing the wear mechanisms and the wear depth and width.

Atomic force microscopy (AFM)

The Atomic Force Microscope (AFM), which is sometimes called the Scanning Force Microscope (SFM), is capable of visualizing and imaging surface features as small as a carbon atom (0.25 nm) and as large as the cross section of a human hair (80 μm). An atomically sharp tip is scanned over a surface by a piezo-electric scanners to maintain the tip at a constant force (to obtain height information) or height (to obtain force information) above the sample surface. The AFM head employs an optical detection system in which the tip is attached to the underside of a reflective cantilever. A diode laser is focused onto the back of a reflective cantilever. As the tip scans the surface of the sample, moving up and down with the contour of the surface, the laser beam is deflected off the attached cantilever into a photodetector. The motion of the cantilever is then directly proportional to the output of the photo-detector. Motions as small as 1 nm are routinely measured in AFM. A feedback control is used to keep the probe in a "fixed" relationship with the surface while a scan is measured. The different components of AFM are shown in Figure 6.7. From the motion of the probe a three-dimensional image of the surface is constructed by the two measures of resolution: in plane resolution and vertical resolution. In general, the sharper the probe the higher the resolution of the AFM image is.

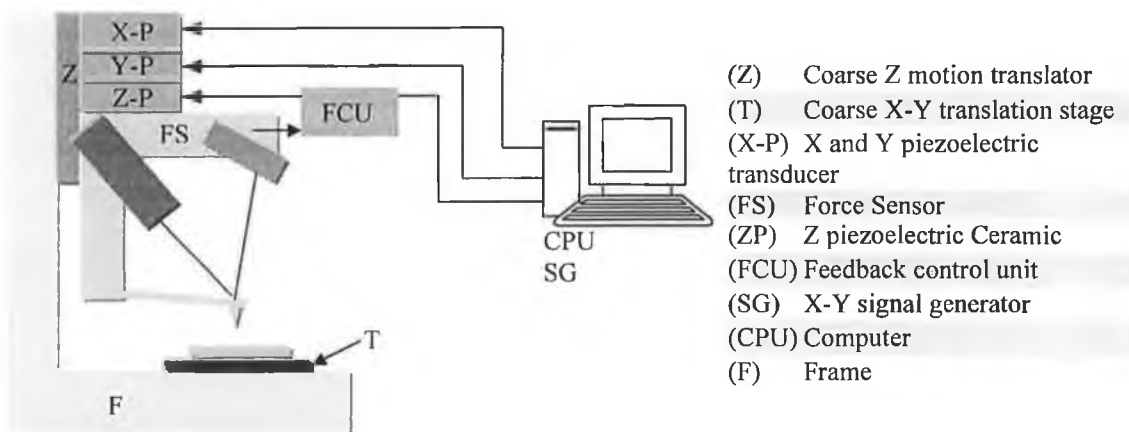


Figure 6.7. The components of AFM.

Because there is no current flow, the AFM can be used on electrically conductive or non-conductive surfaces and in air, vacuum, or fluid environment. The AFM can be operated in three modes: contact, noncontact and tapping. The contact mode takes advantage of van der Waal's attractive forces as surfaces approach each other and provides the highest resolution. In the non-contacting mode, a vibrating probe scans the surface at a constant distance and the amplitude of the vibration is changed by the surface morphology. In the tapping mode, the vibrating probe touches the surface at the end of each vibration exerting less pressure on the surface than in the contacting mode. This technique allows the determination of surface morphology to a resolution of better than 10 nm with a very gentle contacting pressure (Phase Imaging).

Pacific Nanotechnology Nano-RTM AFM scanner was employed to perform the surface analysis of the coating using contact mode. The NanoRule+™ AFM image analysis software was used to viewing and analyzing the images from AFM.

6.4.1.3. Density of the coating

The density of the coatings was determined by dividing the mass by the volume of the coating [164]. The volume was measured as surface area multiplied by thickness and the mass of the coating was measured as mass increase of the substrate before and after the deposition of the coating with a high precision (nearest to ± 0.0001 g) digital balance.

6.4.2. Structural characterization

The microstructure of hard coatings defines the physical properties and therefore, the performance of a coating-substrate composite in an engineering application. Some common techniques used in this investigation have been described.

6.4.2.1. Optical Microscope (OM)

The optical microscope is simple and quick way to observe surface topography and microstructure before viewing in advanced techniques such as SEM. The optical microscope works on the principle of reflection of light in case opaque material. Contrast between different regions when viewed in reflected light can arise from variations in surface topography and differences in reflectivity (e.g., of different phases, different grain orientations, or boundary regions). Transmission mode can be used when the specimen is transparent. The magnification of up to one hundred to one thousand times is achievable.

The Reichert “MeFe2” Universal Camera Optical Microscope was employed for the observation of the polished substrate surface, Rockwell C indentation for adhesion measurement, coating surface morphology, ball cratering spot for coating thickness, wear and coating deformation mechanism, and pin-on-disk wear track to evaluate wear mechanisms. The digital camera connected with the optical microscope can provide image analysis in the computer with the help of Buehler Omnimet Image analysis software.

6.4.2.2. Scanning Electron Microscope (SEM)

A surface can be viewed in an optical-like form using the Scanning Electron Microscope (SEM). Instead of light, the SEM uses secondary electrons emitted from the surface to form the image [358,359]. The intensity and angle of emission of the electrons depend both on the surface topography and the material. The angle of emission depends on the surface morphology so the spatially-collected electrons allow an image of the surface to be collected and visually presented. The magnification of the SEM can be varied from several hundred diameters to 250 kx magnification. However, the image is generally inferior to that of the optical microscope at less than 300x magnification. The technique has a high lateral and vertical resolution. Stereo imaging is possible in the SEM by changing the angle of viewing of the sample. This can be done by rotating the sample along an axis normal to the electron beam. The SEM can also be used to measure the thickness of the coating.

Stereoscan 440 (Lecia Cambridge Ltd.) SEM was used to observe the surface topography and coating microstructure of the deposited coating. It has the capability of holding samples up to 100 mm by 100 mm and has height clearance of 30mm. The probe current, focus and accelerating voltage was 4 nA, 15 mm and 15 keV respectively.

6.4.2.3. X-Ray Diffraction (XRD)

X-ray diffraction (XRD) is commonly used to investigate the microstructure of thin hard coatings, since it is a non-destructive and relatively simple technique. Figure 6.8. shows the basic features of XRD equipment, where the diffraction angle 2θ is the angle between the incident and diffracted X rays. In a typical equipment, the diffracted intensity is measured as a function of the orientation of the specimen, which yields the diffraction pattern. When there is constructive interference from X rays scattered by the atomic planes in a crystal, a diffraction peak is observed. The condition for constructive interference from planes with spacing d is given by Bragg's law:

$$\lambda = 2d\sin\theta \quad \text{-----(6.3)}$$

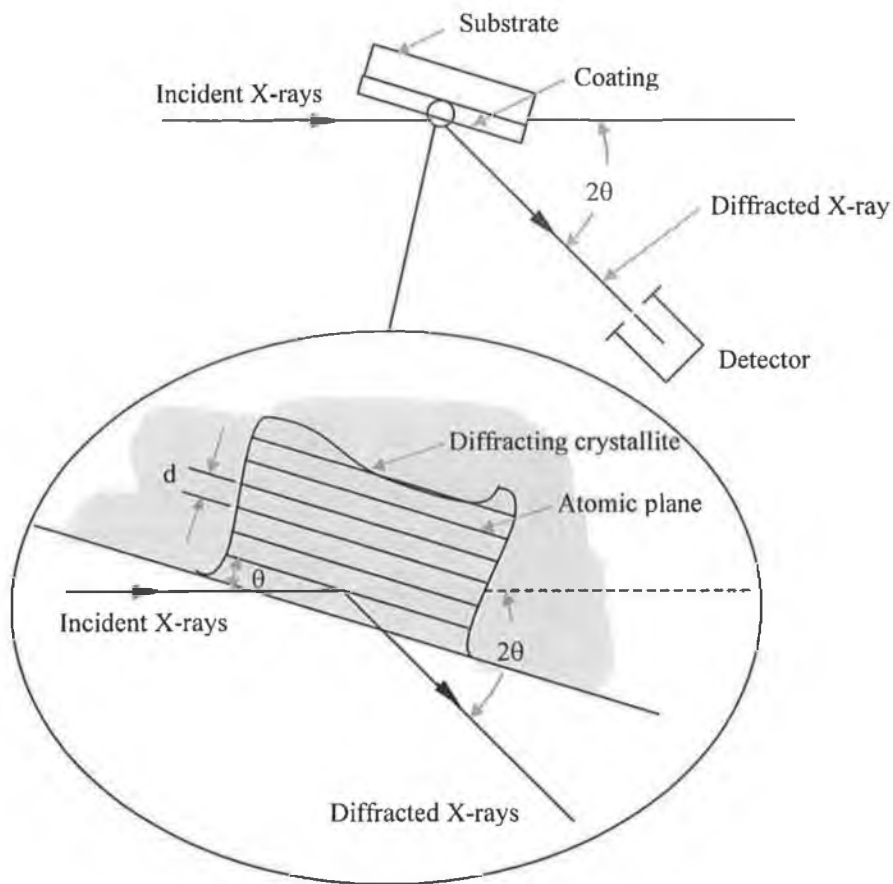


Figure 6.8. Basic features of a typical XRD experiment [360].

The following parameters are measured in XRD study: the peak positions, to evaluate the lattice parameter, the integral intensities for texture analysis, and the peak shape parameters for domain size (particle size) and microstrain. XRD is also used to determine the thickness of thin coatings and multilayers, and atomic arrangements in amorphous materials (including polymers) and at interfaces. Phase identification for polycrystalline thin coating, using standard equipment and diffraction geometries, is also possible down to thicknesses of 100 Å. Materials composed of any element can be successfully studied with XRD, but XRD is most sensitive to high-Z elements, since the diffracted intensity from these is much larger than from low-Z elements. As a consequence, the sensitivity of XRD depends on the material of interest. XRD is noncontact and nondestructive, which also makes it ideal for in situ studies.

Two different geometries are usually employed in XRD: the conventional Bragg Brentano geometry and the parallel beam grazing angle geometry (GAXRD). The penetration depth of the X-ray beam can be controlled using the latter technique by varying the angle of incidence to a very small value. When coupled to a synchrotron radiation X-ray source (to produce an intense, parallel X-ray beam) monolayer sensitivity can be achieved and used for the extreme situation of surface structure, or epitaxial relationships at the interfaces of coatings by GAXRD.

Glancing Angle X-ray Diffraction (GAXRD) measurement with a Bruker D8 diffractometer was performed by using a CuK_α radiation source at an incident angle of 3° for microstructural analysis of the samples. The cathode voltage and current of the X-ray source were 40 KV and 40 mA respectively. The X-ray profiles were acquired in the detector scan mode. The diffraction angles scanned was between $2\theta=10^\circ$ and 90° .

6.4.3. Chemical composition characterization

The elemental composition of a coating can be important to the coating properties and is an indication of process reproducibility. In many cases, the elemental composition can change with thickness and some technique must be used that allows depth profiling of the elemental composition. Energy dispersive X-ray spectroscopy (EDX), X-ray Photoelectron Spectroscopy (XPS), Auger Electron Spectroscopy (AES), Ion Scattering Spectroscopy (ISS) and Secondary Ion Mass Spectroscopy (SIMS) are the most common methods to characterize compositions. The first two methods are employed in this study.

6.4.3.1. Energy dispersive X-ray spectroscopy

In EDX, electrons emitted from the filament (cathode) are accelerated with high energy to strike the specimen (anode) to be analysed. Electrons of the inner shells of the specimen atoms are excited by interaction with the electron beam and X-rays are emitted from the irradiate area due the electron transitions between different shells (Figure 6.9).

If the electron transition occurs between L and K shells, K_α X-Rays are produced. Different X-Rays are generated from different electron transitions, e.g., K_β X-Rays from $\text{M}\rightarrow\text{K}$, and L_α X-Rays from $\text{M}\rightarrow\text{L}$ electron transitions. The difference in energy between the levels involved in the electron transitions determines the energy (wavelength) of the emitted X-rays. Each atom shows a unique set of K, L M, etc. X-ray spectral lines that

serve to identify an element. Identification of the atom and determination of the concentration of the atoms in the specimen can be performed by analysing the X-ray energies and by a count of the numbers of X-rays emitted respectively [361]. Most EDX systems are interfaced with SEMs to excite characteristics X-rays by electron beam from the area of the specimen being probed. The EDX spectroscopy can analyze all elements in the periodic table, provided a suitable light element X-ray window is used. Peak overlapping problem sometimes occurs in multicomponent samples during analyzing of neighboring elements in the periodic table. Quantitative analysis in multicomponent coatings is quite complicated. The expected X-ray yield depends on number of factors such as intensity of the electron beam, the atomic concentration, the ionization cross-section, X-ray absorption coefficient etc. It is simpler practice to calibrate the yields against the standard composition.

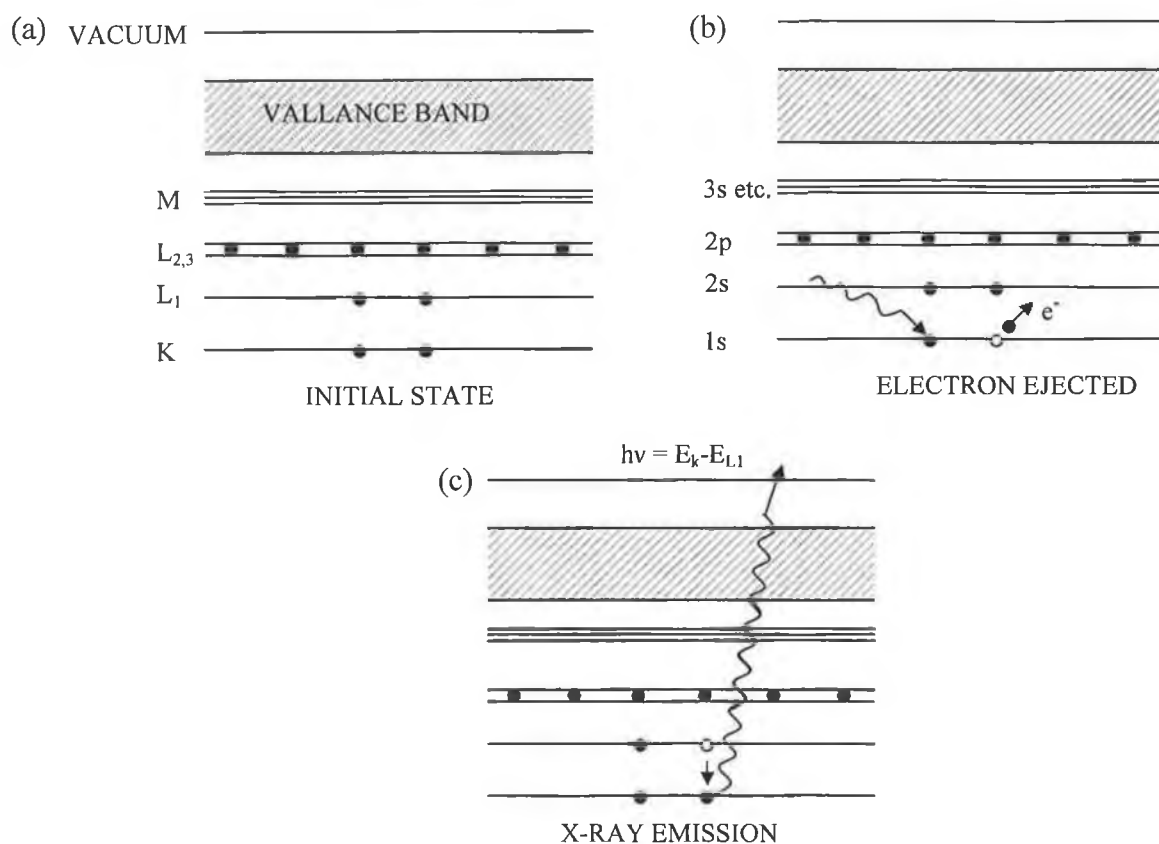


Figure 6.9. Schematic diagram of electron energy transition: (a) initial state; (b) incident photon (or electron) ejects K shell electron (c) X-ray emission when 2s electron fills vacancy [311].

EDX analysis was carried out with a Princeton Gamma-tech spectrometer attached to the Stereoscan 440 (Lecia Cambridge Ltd.) SEM. The EDX together with IMIX software offers

the qualitative and quantitative measurements of elements present in any particular sample by analyzing and processing both X-ray and image data. From the Ti K_{α} , N K_{α} , Mo L_{α} and S K_{α} peak areas, the EDX quantification software (incorporating an automatic ZAF matrix correction and peak separation procedure) was employed to obtain the chemical composition. Higher probe current (3.0-5.0 nA) was used to get higher X-ray count rate (more than 100 cps). The total no of X-ray count was more than quarter of a million in all cases. For EDX analysis the focus distance in the SEM was higher (25 mm) than those for taking images. The magnification was between 3.0-8.0 kx.

6.4.3.2. X-ray Photoelectron Spectroscopy (XPS)

X-ray photoelectron spectroscopy (XPS) has been employed to determine the chemical composition of thin coatings for many years. In XPS, X rays of a fixed wavelength, $h\nu$, eject core-level electrons from atoms in the sample. The kinetic energy, E_k of these photoelectrons is measured by the difference between the energy of the X-ray photon ($h\nu$) and the binding energy (E_b) of the electrons ($h\nu - E_k$), thereby, allowing the determination of the core level E_b , which provides an atomic identification and chemical state information. XPS technique provides identifications of elements and information about their chemical states present in the outermost ~ 5 nm of the sample's surface due to its excellent element selectivity, quantitative character and high surface sensitivity. Titanium nitride TiN and other nitride coatings have been widely studied and their chemical states are usually characterized by the binding energy position of the N 1s and the respective metal or nitride-forming element line [362].

The X-ray photoelectron spectroscopic study was performed on the as-introduced samples using a Kratos Axis 165 spectrometer. A monochromatic Al K_{α} (Energy = 1486.6 eV) radiation source with an energy resolution of 0.4 eV at pass energy of 20 eV was used with 15 mA current and 15 kV voltage.

6.4.4. Mechanical properties

6.4.4.1. Microhardness

The most conventional hardness tests involve a hard indenter (diamond for example) that is pressed vertically into the surface of the sample being tested. Two common microhardness tests are Knoop microhardness and Vickers microhardness. They measure the hardness of a material from the size of an impression produced under load by a

pyramid-shaped diamond indenter. The method most commonly used in test laboratories is the Vickers hardness test. The indenter used in this technique is a square-base diamond pyramid having included face angles of 136° . The advantage of this indenter geometry is that the law of proportional resistance is obeyed. That is, the applied test force is directly proportional to the indentation area, making a Vickers hardness value fundamentally independent of the selected test force (load). In this test a very small diamond pyramid is placed on the sample and a small load of 1 to 1,000 gf is used. This low amount of load creates a small indent that must be measured under a microscope. The schematic diagram of the created indent is shown Figure 6.10.

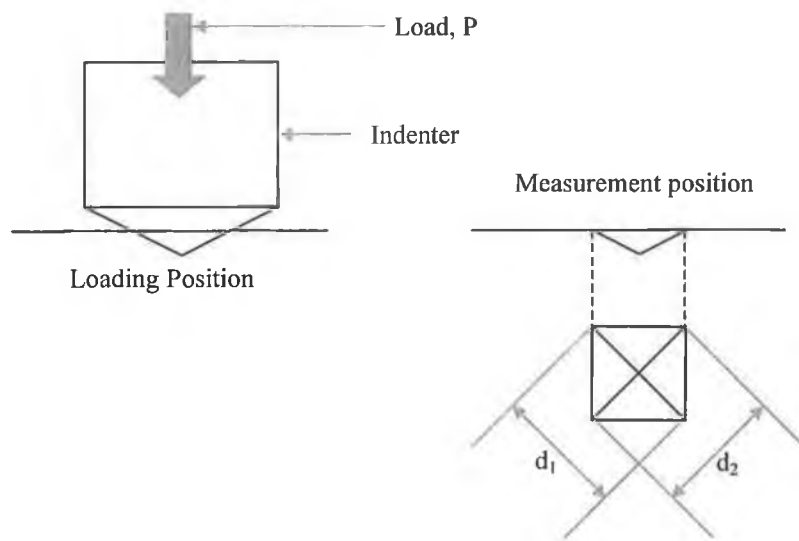


Figure 6.10. Schematic of Vicker indenter and plan view of the indentation area.

The Vickers number (HV) is calculated using the following formula [363,364]:

$$\boxed{HV = 1.854(P/d^2)} \text{(6.4)}$$

P is the indentation load in kgf, and d is the mean diagonal (average of two measured diagonals d_1 and d_2) of indentation.

Micro-hardness measurements were carried out using a Leitz MiniLoad micro-hardness tester. The measurement was carried out using Vickers indenter and a maximum load of 15 gm minimizing any substrate effects and the dwell time of indentation was approximately 20 sec. The plastic hardness value was then calculated by averaging data from 10 indentation values of the same coating on different spots.

6.4.4.2. Adhesion

The different methods for measuring adhesion have been reviewed by Steinmann et al. [365]. Among various techniques Rockwell C indentation test has particularly accepted as standard method for measuring adhesion. In this section Rockwell C and pull-off test are discussed.

Rockwell C indentation tester

In this method, a 120° Sphero-conical diamond indenter is pressed against a coated sample with a certain standard load (60, 100, and 150 kg) as shown in Figure 6.11. When the indenter penetrates the coating cracks propagate from the indentation point towards the edge of the sample.

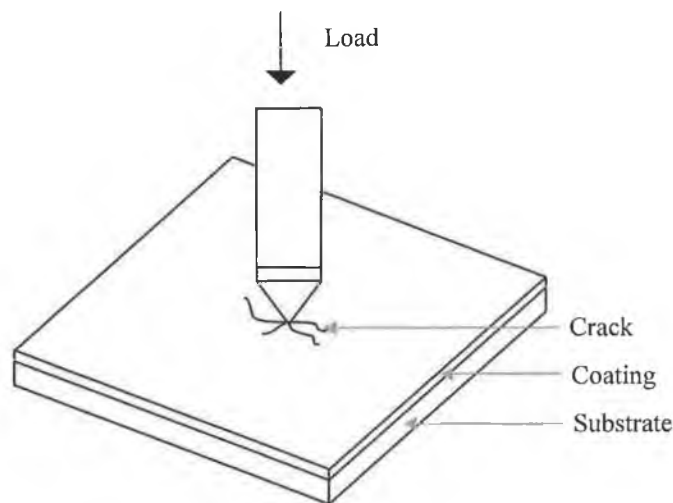


Figure 6.11. Rockwell C set-up for adhesion measurements.

This technique does not give any absolute measurement of adhesion but a comparative measurement indenting with same load for all samples. This gives the pictures of comparative adhesion properties considering the crack network from the indentation spot under optical or scanning electron microscope. This test also gives a qualitative measure of the toughness of coating. The Rockwell-C adhesion test was developed in Germany and is standardized in the VDI guidelines 3198, (1991) [366,367]. A scale is considered from HF1 to HF6 (HF is the German short form of adhesion strength) showing the adhesion property in a sequential way (Figure 6.12.). HF1 shows excellent adhesion property with a few crack networks while HF6 shows the poorest adhesion properties showing complete delamination of the coating. The damage of the coating is compared with a defined scale to find out the adhesion strength quality. This test method is very easy to perform and is especially useful for quality control during manufacture.

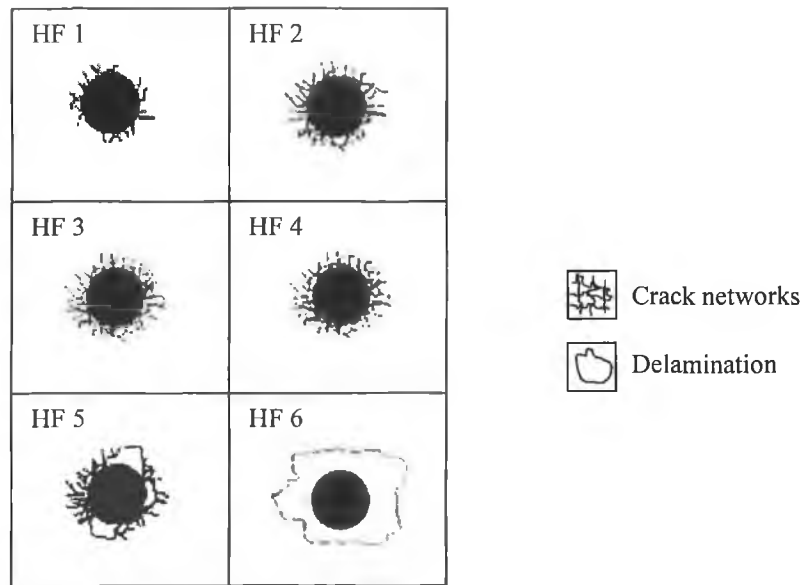


Figure 6.12. Adhesion strength quality HF 1 to HF 6.

An Indentec hardness tester was used to assess the adhesion of the coatings. This test method uses a standard Rockwell-C load (maximum applied load, 100 kg) causing layer damage adjacent to the boundary of the indentation. After indentation an optical microscope was used to evaluate the test. On each sample three indentations were produced. The damage to the coating was compared with a defined adhesion strength quality.

Pull-off adhesion tester

In this method some kind of pulling device (dolly or stud) is attached to the surface of the coating with solder or high strength adhesives forming a bond and then applying a force to pull it off in a direction normal to the interface. The testing method is shown schematically in Figure 6.13. The load at which the pulling device falls down and strips the coating gives a measure of the adhesion. It is important in the latter case to ensure that the loading is purely normal and that no bending moments are applied at the interface. In case of porous coating the pull-off method is not suitable as there is chance to diffuse the adhesive into the coating [364]. The coating surface must be cleaned before gluing the stud and cured for the amount of time recommended by the manufacturer.

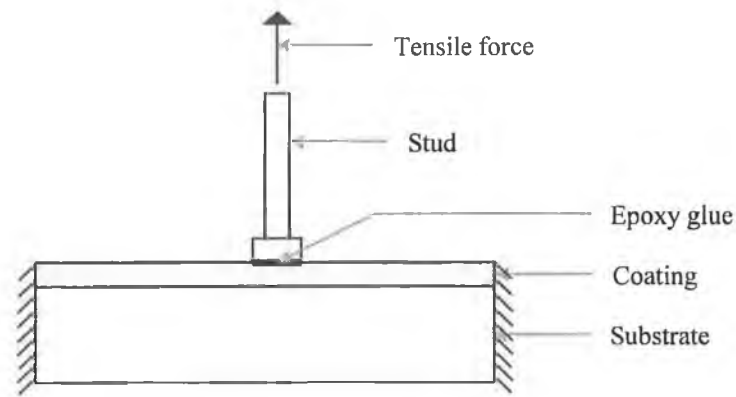


Figure 6.13. Schematic diagram of Pull-off test for adhesion measurement.

6.4.5. Tribological properties

6.4.5.1. Pin-on-disk wear tester

The schematic diagram of the pin-on-disk apparatus is shown in Figure 6.14. This system is consisted of a tribometer and data acquisition system. A test disk is mounted in a cup that revolved around a vertical axis. A pin is attached to one end of a precision balanced lever arm, which is used to apply vertical loads (normal force) on the test sample and read the friction force (tangential force) on the pin. A load cell on the top platform is used to measure the friction force when hooked up the lever arm via a side arm.

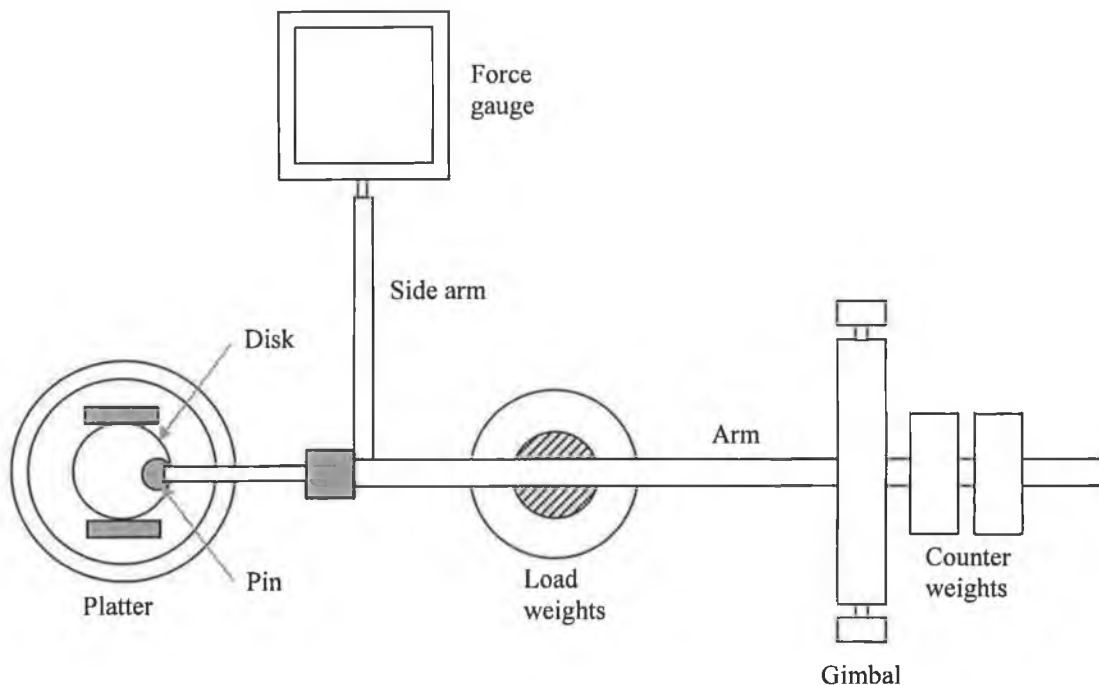


Figure 6.14. Pin-on-disk wear tester.

Before applying the load the lever arm is balanced by adjusting the counter weights. When the load is applied on the lever arm, the pin came in contact with the test sample and upon rotating the cup or sample a circular wear track of a given diameter is created due to the friction between the pin and test sample. The sliding motion of the sample under the wear pin provides a frictional force, which is a property of the coating and is proportional to the load applied. Different wear track diameters allow a number of tests to be performed on one sample. The same linear speed can be used for all tests by adjusting the rotational speed for each diameter. The analog friction output signal is transmitted to the computer. The software calculated the coefficient of friction from the normal and tangential force and is displayed as coefficient of friction vs no of revolutions on the screen. By examining the resulting plot an indication of the friction characteristics and endurance of a particular coating is obtained. Wear is usually expressed as wear depth per number of revolutions or worn volume per unit load per unit sliding distance [14].

Specific wear rate measurement

The cross-sectional area of the wear track on the sample created by pin-on-disk was assumed to be a circular segment (Figure 6.15.) and could be calculated as:

$$A_w = r^2 \sin^{-1} \left(\frac{w}{2r} \right) - \frac{w}{4} \sqrt{4r^2 - w^2} \quad \text{-----(6.5)}$$

$$w = 2\sqrt{2rd - d^2}$$

$$A_w = r^2 \sin^{-1} \left(\frac{\sqrt{2rd - d^2}}{r} \right) - \sqrt{2rd - d^2} (r - d) \quad \text{-----(6.6)}$$

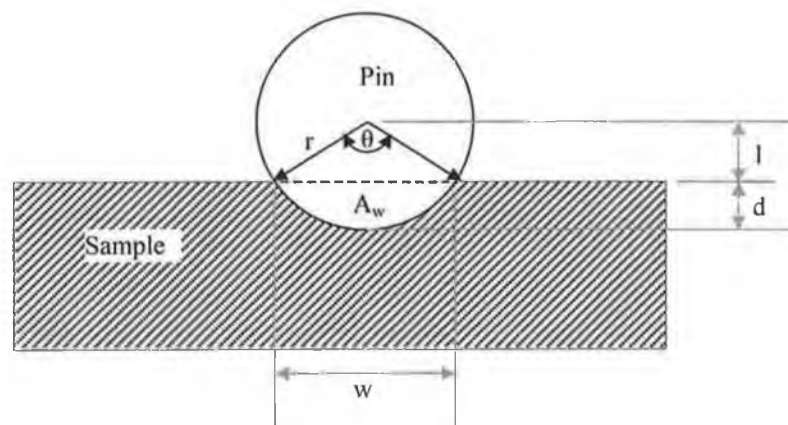


Figure 6.15. Geometry used in calculation of cross-section area of wear track.

Specific wear rate can be calculated as:

$$\text{Wear rate } V_w = \frac{\text{Wear volume}}{\text{Normal load} \times \text{Sliding distance}}$$

$$V_w = \frac{r^2 \sin^{-1} \left(\frac{\sqrt{2rd - d^2}}{r} \right) - \sqrt{2rd - d^2} (r - d)}{L \times N} \times 10^{-9} \text{ (m}^3 / \text{N-m)} \quad \text{-----(6.7)}$$

where, r = radius of the pin (mm)

d = depth of the wear track (mm)

L = normal load (N)

N = number of revolutions

An Implant Sciences ISC-200PC tribometer was used to measure the wear and coefficient of friction. Before wear tests, the ball and the disk specimens were cleaned with ethanol to remove remaining contaminants. Each sample was tested to 9,000 revolutions, at a speed of 60 rev/min and a cylindrical track diameter of 9 mm in laboratory air (40-50% RH) and room temperature (25 °C). The total sliding distance was around 250 m. A load of 200 g on a 3 mm diameter tungsten carbide (WC) ball (counterpart/pin) was also used for each sample. The test was carried out under dry or unlubricated conditions. Friction coefficients were continuously recorded in the hard disk. Worn surfaces were investigated by optical microscope and optical profilometer. Optical profilometry was carried out across the wear track on each sample at ten different locations to measure the wear depth and width. EDX analyses were performed on the wear track to find out the composition of the worn surfaces. Wear lifetime of the coating was defined by observing the friction coefficient value to rise abruptly to the value of substrate.

6.5. SUMMARY

TiN+MoS_x coating has been successfully deposited by closed-field unbalanced magnetron sputtering from separate Ti and MoS₂ target in a nitrogen gas environment. Several characterization techniques and their experimental procedure for measuring chemical, structural, physical and mechanical properties have been briefly reviewed to present the derived results from the measurements in the next chapter.

CHAPTER 7

Results and Discussions

7.1. INTRODUCTION

The hard-solid lubricant TiN+MoS_x coating has been characterized to evaluate the coating's performance in terms of physical, chemical, structural, mechanical and tribological properties. This chapter discusses different characteristics of the coatings. The relationship between the target voltage, target current and gas flow rate for different targets have also been presented.

7.2. RESULTS

7.2.1. Sputtering plasma characterization

7.2.1.1. Target voltage-current characteristics

The relation between target voltage and current at different pressures for Ti and MoS₂ targets in Ar gas is shown in Figure 7.1. and Figure 7.2. respectively. The Ti target voltage increased with the increase of the target current at a particular discharge pressure. At lower target current range (0.0-1.0 A), the rate of increasing voltage was faster than the rate at higher current range (0.1-5.0 A). In both ranges, the target voltage increased linearly with the target current. At any particular target current the target voltage decreased with the increase of discharge pressure.

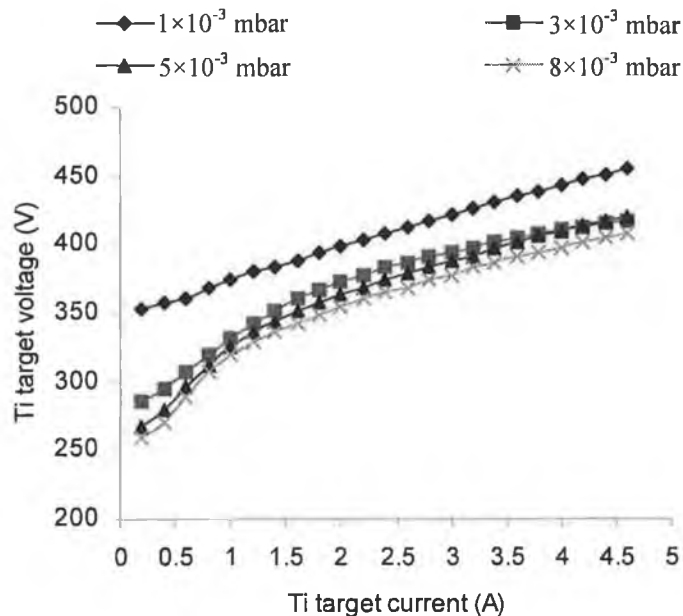


Figure 7.1. Variation of Ti target voltage with respect to Ti target current at different pressures.

Similar behaviour of increasing target voltage with the increase of target current at any particular discharge pressure and decreasing of target voltage with the increase of discharge pressure at any particular target current were also found for MoS₂ target. But the rate of increasing voltage with current for MoS₂ target was higher than that of Ti target. The reasoning was obvious as Ti was more conductive than the MoS₂.

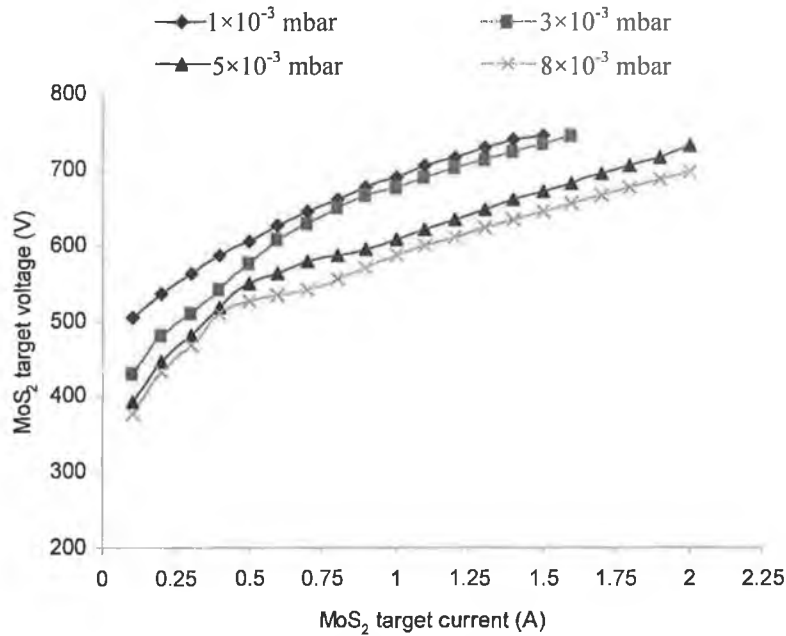


Figure 7.2. Variation of MoS₂ target voltage with respect to MoS₂ target current at different pressures.

7.2.1.2. Target voltage-Ar flow rate characteristics

The target voltage was also dependent on the discharge pressure or Ar flow rate (i.e., discharge pressure is proportional to the Ar flow rate). With the increase of Ar flow rate, the Ti target voltage decreased sharply and finally it became more or less constant with the further increase in Ar flow rate (Figure 7.3.). At constant Ar flow rate, the Ti target voltage increased with the target current following the previous current-voltage relationship.

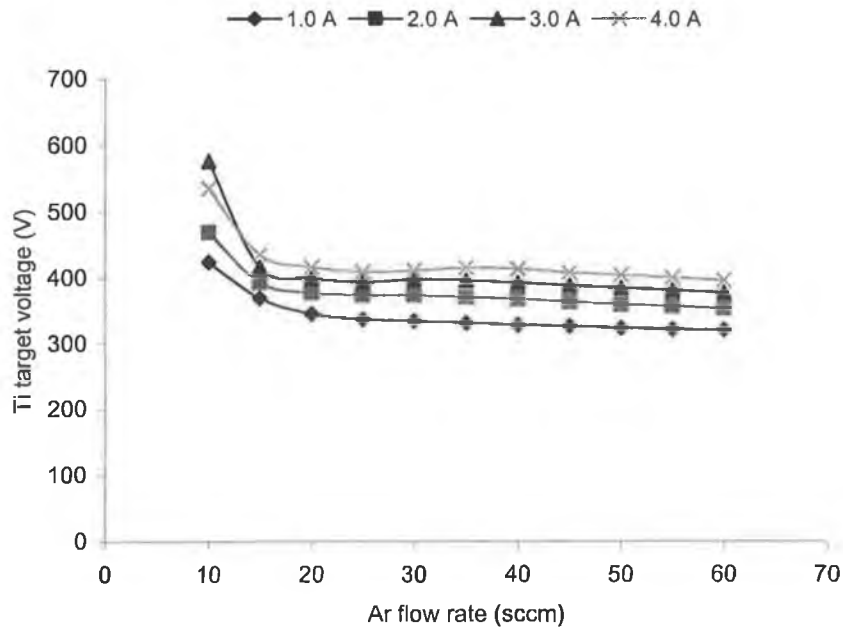


Figure 7.3. Variation of Ti target voltage with Ar flow rate at different Ti target currents and constant MoS₂ target current (both Ti and MoS₂ targets are on).

Similar relation between target voltage and Ar flow rate was also found for MoS₂ target but the discharge voltage was higher than in Ti target as MoS₂ was less conductive than Ti (Figure 7.4.). In both cases, there existed a minimum flow rate (approximately 10 sccm) to trigger the discharge.

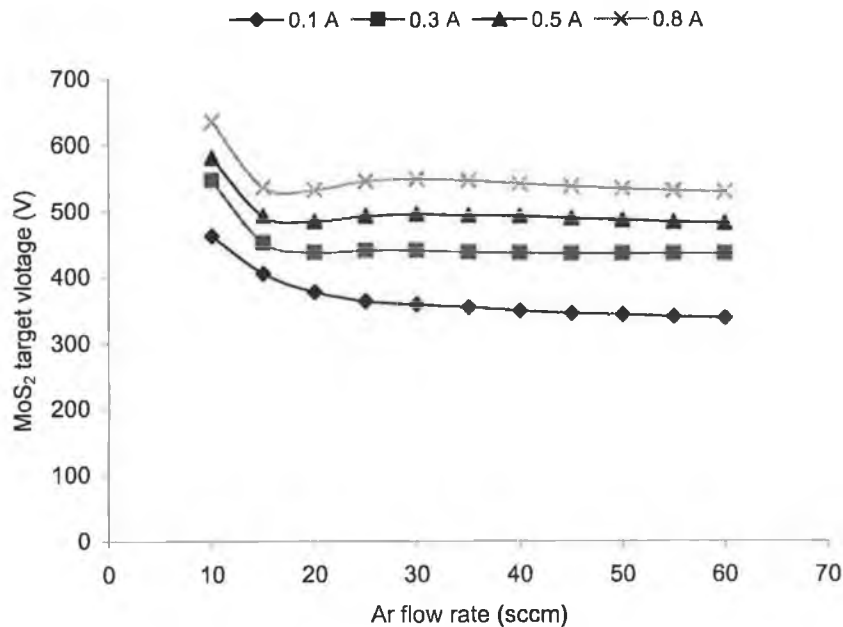


Figure 7.4. Variation of MoS₂ target voltage with Ar flow rate at different MoS₂ target currents and constant Ti target current of 3.0 A (both Ti and MoS₂ target are on).

7.2.2. Optimisation of stoichiometric TiN deposition

Deposition of stoichiometric TiN (50% Ti and 50% N) by reactive sputtering requires the optimisation of many parameters such as target current, deposition pressure, Ar flow rate, N₂ flow rate, target to substrate distance, bias voltage etc. Furthermore there is always a possibility of target poisoning (see Chapter 2) during reactive sputtering for an extended period of time. Reactive sputtering controller not only allows correct flow rate of reactive gas just to form stoichiometric compound but also prevents target poisoning [368]. Series of experiments have been performed to optimise the deposition of stoichiometric TiN by the reactive sputtering controller. For this analysis a particular current value was supplied to the Ti target at any particular discharge pressure. For that particular current the 100% Ti peak intensity was recorded and then Ti emission intensity was set at different set point in the reactive sputtering controller to allow different flow rate of N₂. The deposition parameters used in the experiment are given in the Table 7.1.

Table 7.1. Typical experimental data for TiN deposition.

Parameters	Value
Base pressure	9.0×10^{-6} mbar
Gate valve position	Fully open
Deposition pressure	3.1×10^{-3} mbar
Ar flow rate	32.0 sccm
Deposition current	3.0 A

TiN coatings from understoichiometric to overstoichiometric were deposited by allowing different nitrogen flow rate in the deposition chamber through reactive sputtering controller system. The compositions of the coatings were analysed by EDX to find out the atomic percentage of N₂ in the coatings formed with different nitrogen flow rates. Figure 7.5. shows the N₂ flow rate and atomic percentage of N₂ in TiN coatings at different set points in the reactive sputtering controller.

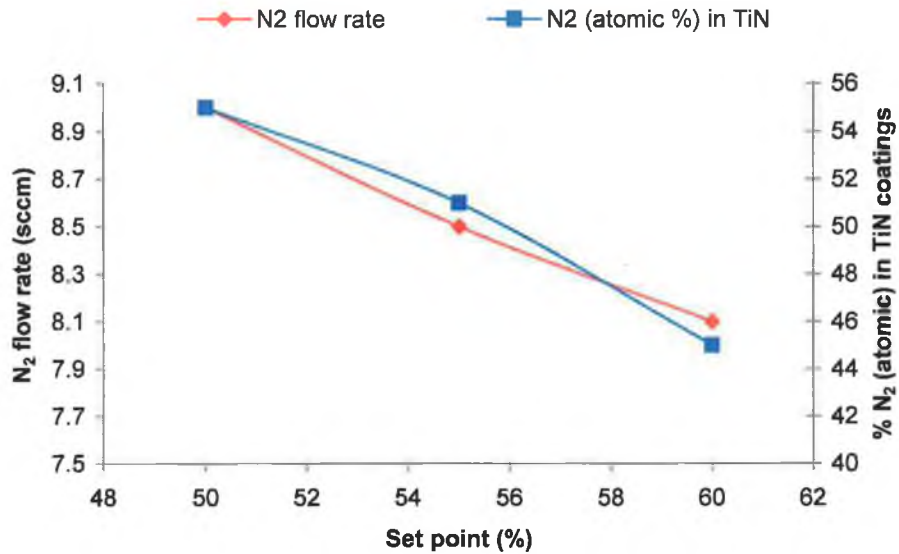


Figure 7.5. Flow rate of N₂ at different set points and corresponding atomic percentage of N₂ in the TiN coating.

The nitrogen content in the TiN coating increased with the increase of N₂ flow rate. The atomic concentration of N₂ in TiN_x coatings were at 45, 49 and 54% at set points of 60, 55 and 50% giving the stoichiometric factor $x=0.82, 0.98,$ and 1.17 respectively.

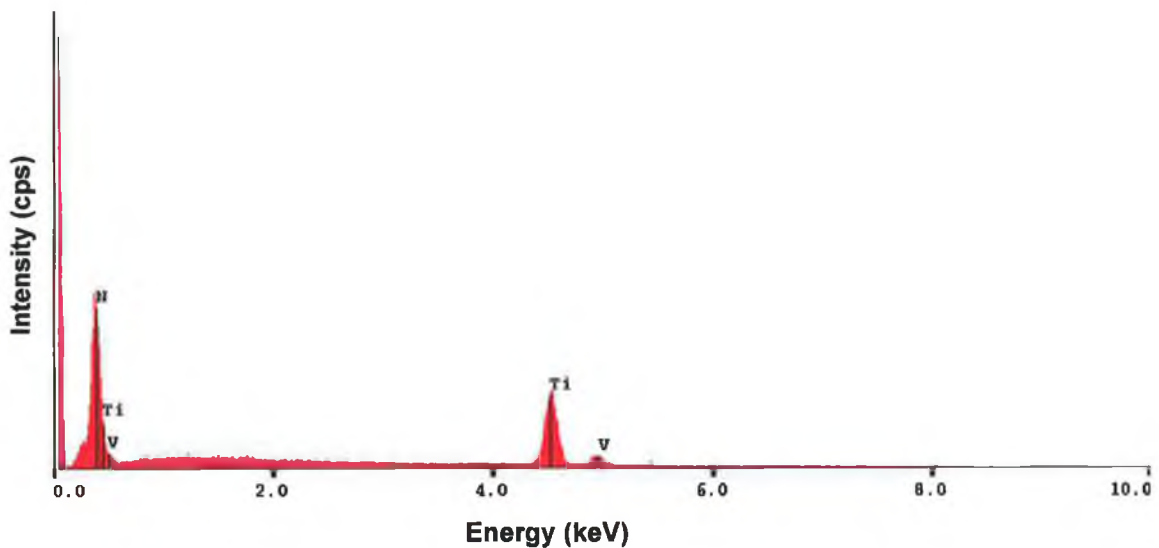


Figure 7.6. Typical EDX spectra of TiN coating.

Figure 7.6. shows a typical EDX analysis performed on TiN coating. The EDX spectra showed peaks corresponding to elements (Ti, N and V) that were present in the coating and the substrate. It can be noticed that no peak corresponding to any impurity element such as

C or O other than those supposed to be present in TiN coating found in EDX spectrum. The presence of Vanadium couldn't be explained. EDX analysis at different spots on the surface of the TiN coating confirms the uniform distribution of the elements.

7.2.3. Structural properties of TiN+MoS_x coating

7.2.3.1. Surface morphology of coating

A typical picture in Figure 7.7. taken from AFM shows the 3-D surface topography of the coating. On the AFM images of the surfaces protuberances with corn structures can be identified. The scanning distance was 20 μm×20 μm.

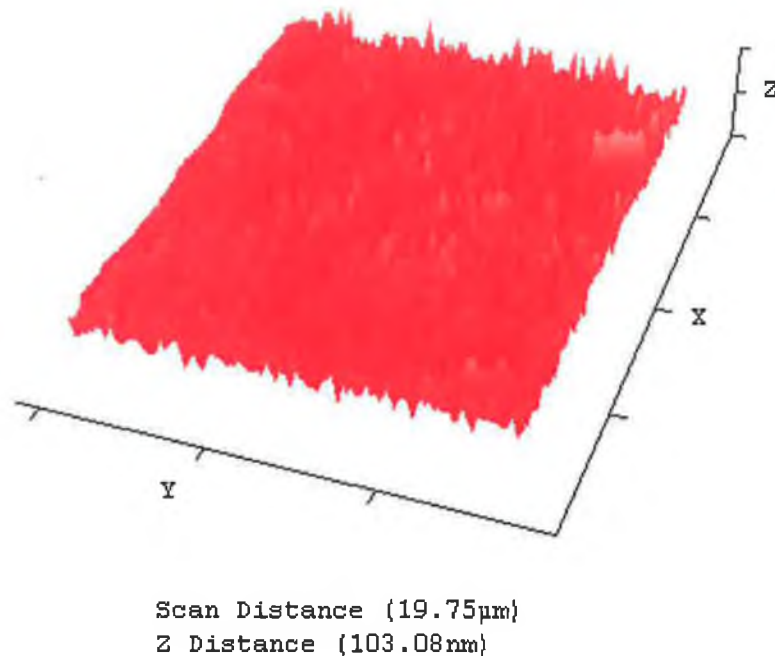


Figure 7.7. AFM surface topography of TiN+MoS_x coatings.

7.2.3.2. Structural phases of the coating

The phase compositions of the coatings were determined by comparing the XRD diffraction peak positions with the standard data. Figure 7.8. shows the GAXRD spectra of pure TiN and TiN+MoS_x coating with different MoS_x content superimposed one upon another. Both types of coatings exhibited the f.c.c. structure in the XRD spectrum. In the TiN+MoS_x coatings, peaks were shifted to lower angles, which indicated an increase in the lattice parameter. Peaks in TiN+MoS_x coatings were also slightly widened compared to pure TiN coating, which was the indication of a reduction in grain size of the coating. No MoS_x phase was observed in any of these coatings suggesting the possible incorporation of

Mo and S atoms into the cubic TiN lattice or segregated at the grain boundaries. This theory was also supported by other researchers [245,248]. With the higher current of MoS₂ target, higher peak shifting and peak widening were observed. This suggested that higher concentration of Mo and S atoms were incorporated in TiN coating with higher MoS_x target current used during the deposition of TiN+MoS_x coating.

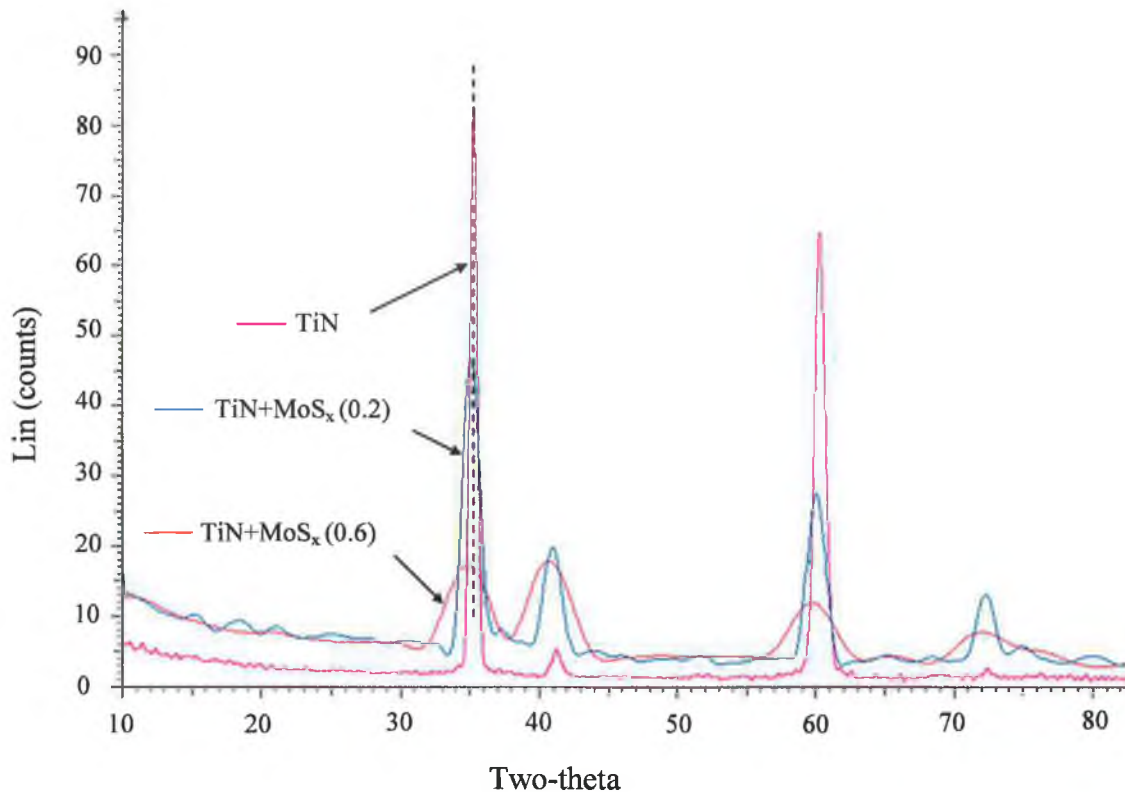


Figure 7.8. XRD spectra of TiN and TiN+MoS_x coatings with MoS₂ target current of 0.2 and 0.6 A.

7.2.4. Chemical composition

7.2.4.1. EDX analysis

Despite having the peak-overlapping problem in EDX, Mo+S percentage in the TiN+MoS_x coating was measured approximately 3.0, 7.0, and 11.0 wt % corresponding to MoS₂ target currents of 0.2, 0.4 and 0.6 A. This indicated the variation of MoS_x content in the TiN+MoS_x coating with the MoS₂ target current [247]. This result also supports the XRD findings of higher peak shifting and peak widening in the coatings deposited with the higher MoS₂ target current. Figure 7.9. shows a typical EDX analysis performed on TiN+MoS_x coating. EDX line spectrum analysis showed an increment of N₂ concentration

from Ti interlayer towards the TiN+MoS_x coating due to the diffusion effect upon the subsequent growth of TiN and MoS_x [120].

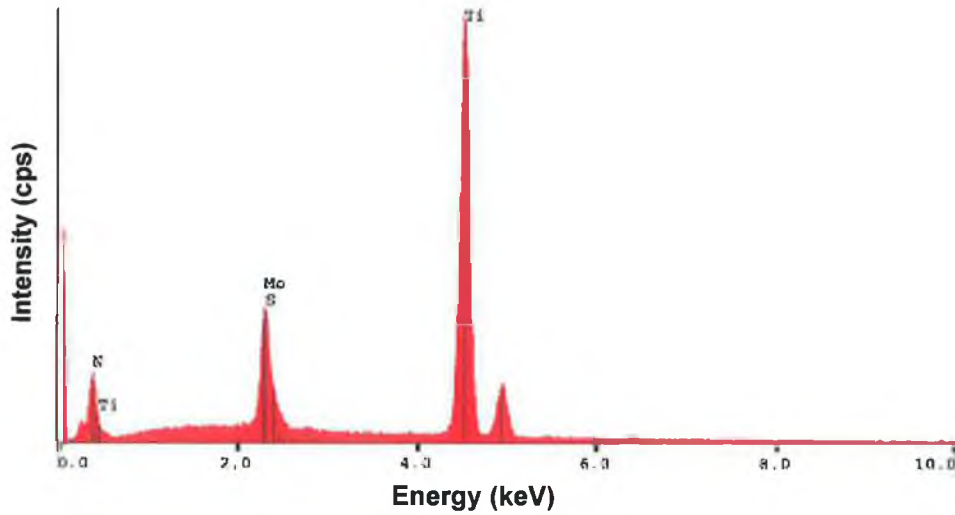


Figure 7.9. EDX spectra of TiN+MoS_x coating.

7.2.4.2. XPS analysis

Preliminary XPS analysis on TiN+MoS_x coating showed the presence of Ti, N, Mo and S elements. Furthermore, O and C were present in the coatings, which is commonly observed contamination during deposition of MoS₂ [170]. But after sputter etching the coating surface showed decrease level of contamination [246]. The bonding of TiN was evident but there was no evidence of MoS_x phase in the coating, which also supports the findings in the XRD results. At different spots of the coating surface, the analysis was performed to test the uniformity of the coating species. It has been observed that the composition was uniform with slight variation.

7.2.5. Physical and mechanical properties

7.2.5.1. Thickness

The ball cratering experiments revealed the structure of the coating and allowed the determination of the coating and interlayer thickness from the measurements in the optical micrographs. Figure 7.10. shows a typical micrograph of ball cratering spots revealing the interlayers and top coating. The coating thickness was measured approximately 1.9 μm from the ball-cratering device. These findings were confirmed by the thickness measurement from stylus and optical profilometer with 5-10% variations.

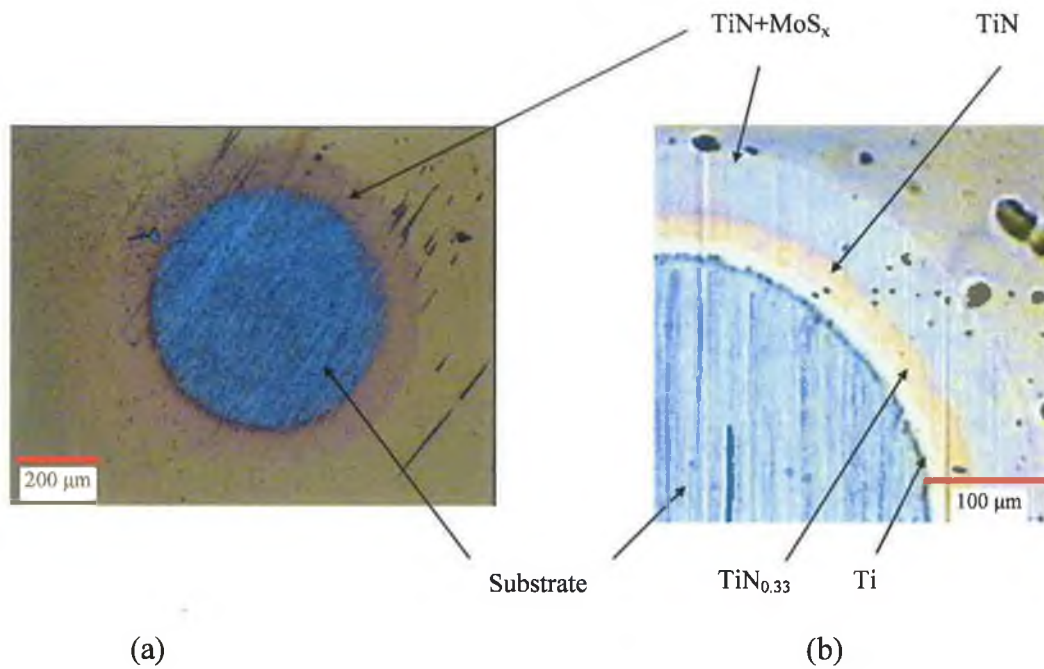


Figure 7.10. Optical micrograph of the ball cratering spot showing substrate, interlayer and coating in (a) TiN+MoS_x coating (b) TiN+MoS_x coating with Ti-TiN graded interlayer.

7.2.5.2. Surface roughness

The surface roughness of the TiN+MoS_x coating was slightly lower compared to TiN coating and substrate but there was no significant difference in optical profilometry. An average surface roughness (R_a) value of around 14-18 nm was recorded in the coating from optical profilometry measurement. Pinholes in the TiN coatings were suppressed by the MoS_x introduction in the TiN+MoS_x coating.

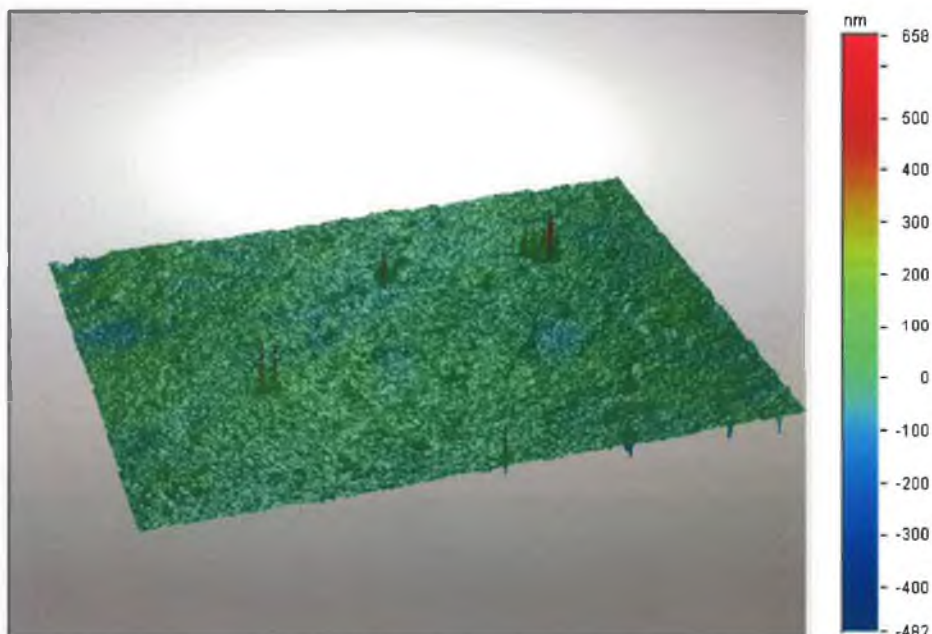


Figure 7.11. 3-D surface profile of the TiN+MoS_x coating from optical profilometer.

Figure 7.11. shows 3-D optical profilometer plot of the surface roughness of the TiN+MoS_x coating. Similar results have also been observed in AFM.

7.2.5.3. Hardness

Figure 7.12. shows the comparison of microhardness of the TiN+MoS_x coating with pure TiN, MoS_x and substrate. The TiN+MoS_x coating showed lower hardness than pure TiN but higher hardness than MoS_x. But there was no significant difference of hardness among the TiN+MoS_x coatings with different contents of MoS_x.

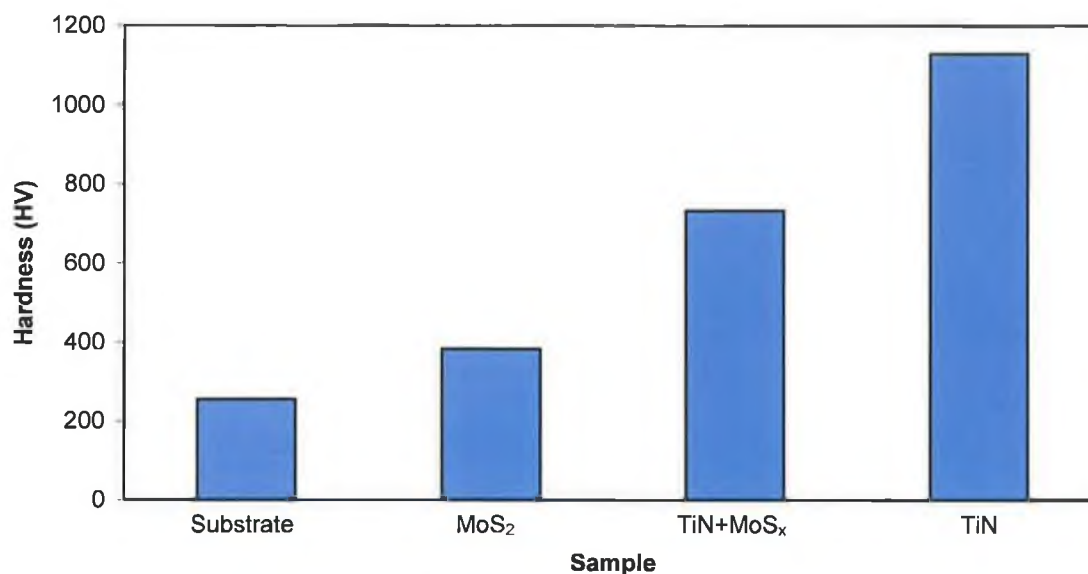


Figure 7.12. Comparison of the Vickers hardness of the coatings and substrate.

7.2.5.4. Adhesion

Figure 7.13. shows the optical micrographs of Rockwell C indentation on MoS_x, TiN and TiN+MoS_x coatings. The Rockwell C indentation test for all TiN+MoS_x coatings showed an acceptable adhesion, i.e. class HF3 which is connected to the chipping and short cracks around the indentation. Chipping corresponds to the removal of little pieces of the coating or very small breakout areas. However, it was not necessarily an indication of poor adhesion. The chipping could originate from a surface crack or from an internal crack.

On the other hand, poor adhesion was found for pure TiN and MoS_x i.e., class HF5, which is connected with the delamination or flaking of the coating around the indentation. Flaking or delamination corresponds to the large breakout areas exposing the substrate. Flaking was observed when the cracks propagated along the interface of the coating-substrate, and this was an indication, in general, of poor adhesion.

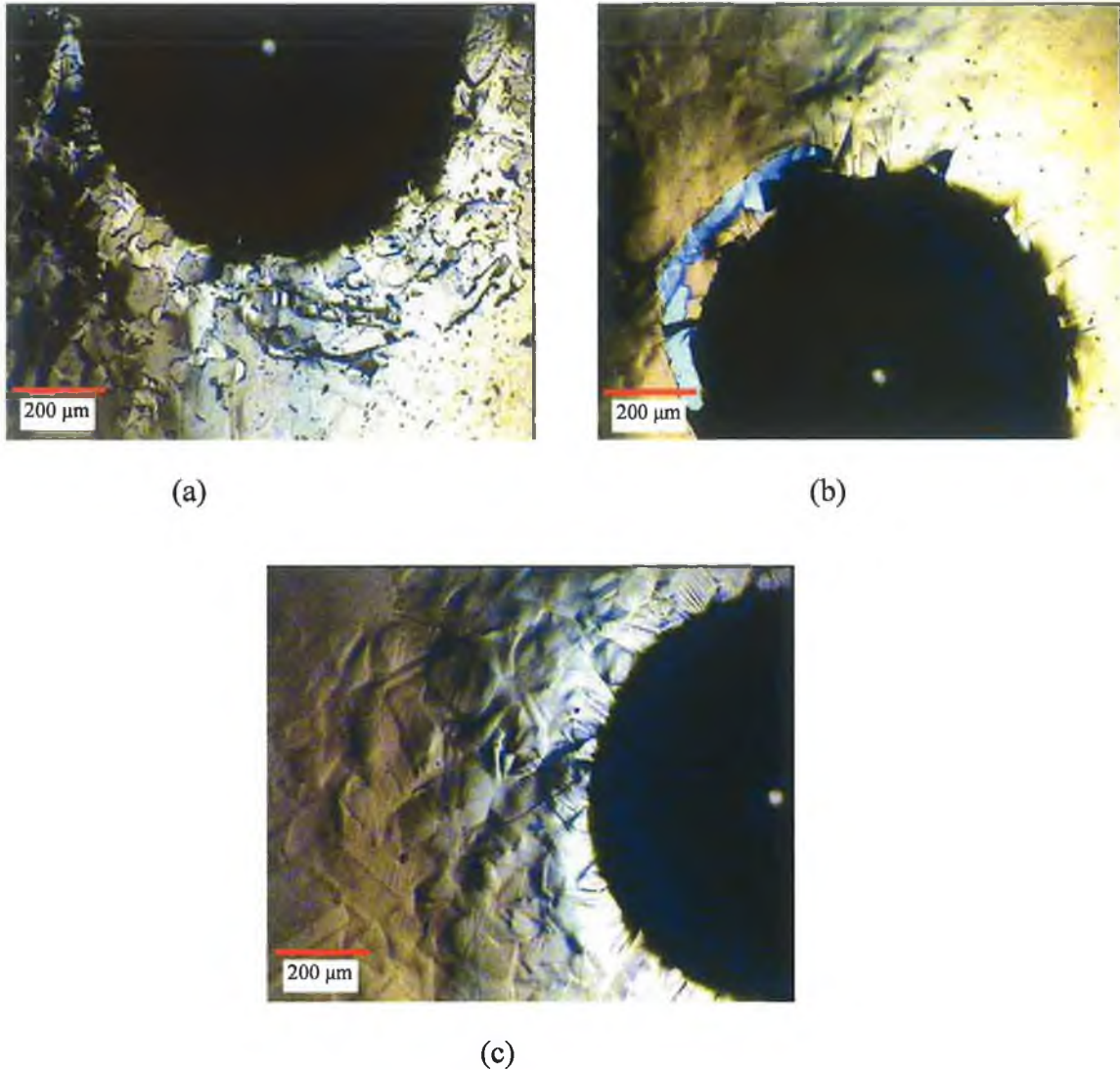


Figure 7.13. Rockwell C adhesion test of (a) TiN and (b) MoS₂ (c) TiN+MoS_x coatings (load 100 kg).

7.2.6. Tribological properties

7.2.6.1. Coefficient of friction

Figure 7.14. shows the comparison of the friction curves of TiN, MoS₂ and TiN+MoS_x coating as a function of no of revolutions against the WC ball under same experimental conditions. TiN+MoS_x coating showed lower friction coefficient than pure TiN but higher value than pure MoS_x. This fact can be explained by the formation of MoS_x from Mo and S atoms in the wear track during the run-in period as explained by Goller et al. [247]. Lower coefficient of friction was observed in MoS_x coating due to easy shearing of the material during sliding [165]. High friction coefficient in the TiN results from highly abrasive wear debris resulting from ploughing wear leading to high friction force.

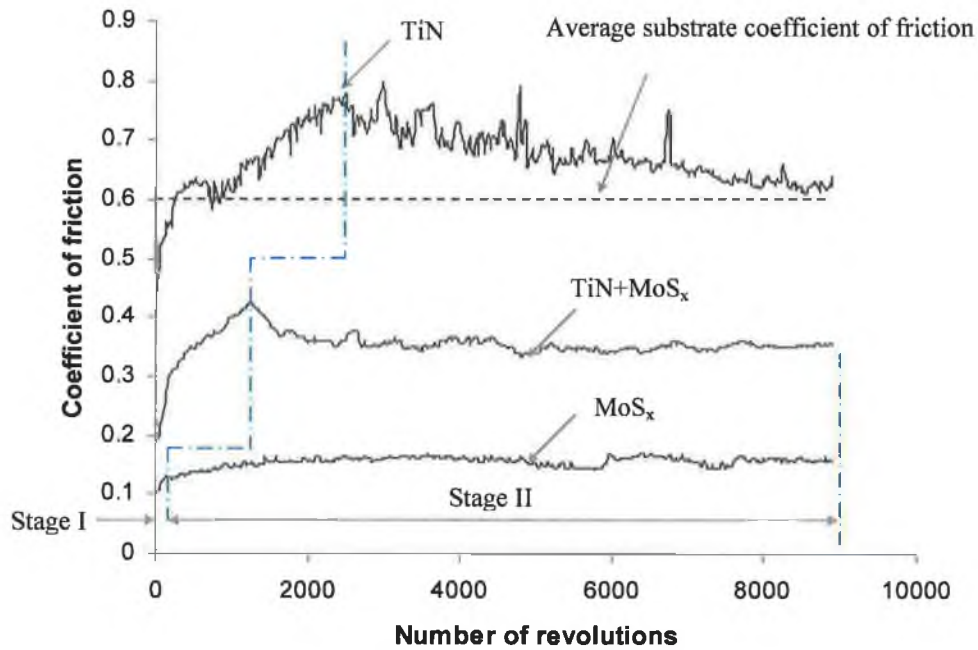


Figure 7.14. Curves of coefficient of friction of different coated samples obtained by pin-on-disk test.

Friction curves can be divided into two parts: the first part represents run-in (Stage I), while the second part represents the steady-state (Stage II) wear regime. During the run-in period (Stage I) an increase of co-efficient of friction to the highest value followed by a steady-state friction in the steady-state-period (Stage II) was observed. Similar behaviour was also observed in TiN+MoS_x coating from another study [245]. Compared to TiN+MoS_x coating TiN coating had longer run-in period while MoS₂ had much shorter run-in period and low level of friction coefficient in the TiN+MoS_x coating, which remained constant till destruction of the coating, was attributed to steady-state wear according to Ref. [14].

7.2.6.2. Specific wear rate

In addition to the decrease in coefficient of friction, the wear resistance of the TiN+MoS_x coated samples improved with respect to both TiN and MoS₂ coatings. Figure 7.15. shows the comparison of wear depth of TiN+MoS_x with pure TiN and MoS_x coatings. The wear depth and width was taken as the average of at least 10 readings from the optical profilometry measurement. TiN+MoS_x coating showed the least wear among the different coatings under the same operating conditions. TiN coating was broken through with the same no of cycles i.e., the wear depth was at least the thickness of the coating. Generally, the harder the surface the lower the wear rate is. This cannot be directly

correlated with the hardness values of different coatings. Although TiN+MoS_x has lower hardness value than TiN coating, but it showed lower wear rate possibly due to some lubrication effect from the MoS_x phase formed during sliding operation.

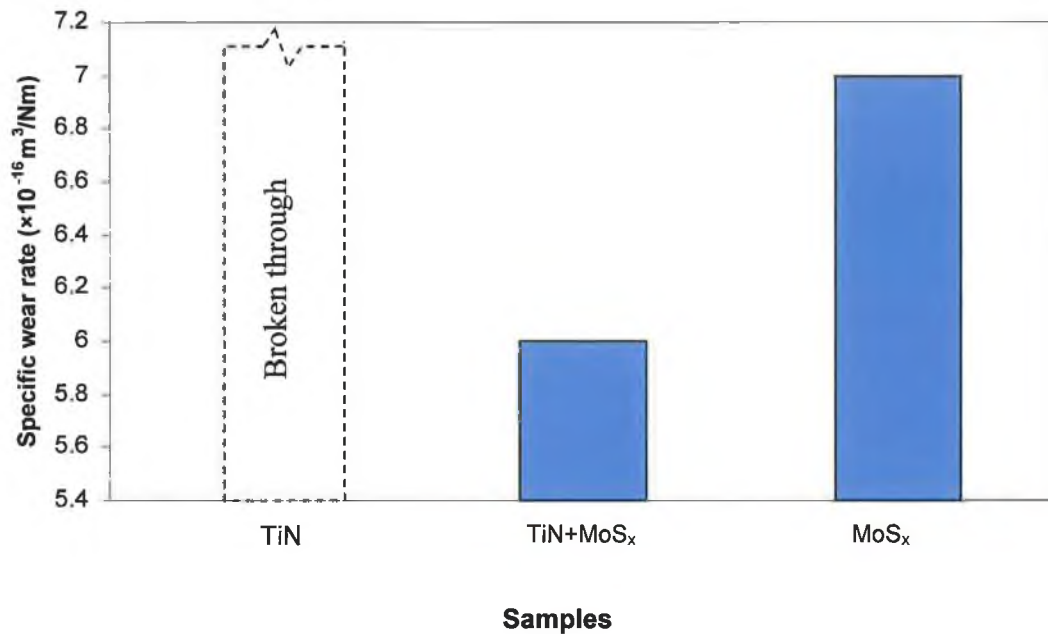


Figure 7.15. Comparison of the wear rate of the TiN+MoS_x coating with pure TiN and MoS_x.

The wear depth of TiN+MoS_x decreased to approximately an order of magnitude lower than that of TiN coating possibly due to the low friction transfer layer in the steady-state period and proper hardness effect from the hard phase. The wear rate was affected by the applied load i.e., higher load causes quick wear of the coating.

7.2.6.3. Wear track observation by optical microscopy

The visualization of the wear track under optical microscope performs a good tool to analyse wear behaviour [113,204]. At the end of pin-on-disk test the wear tracks of the coated samples were observed by optical microscopy and at least ten images were recorded at different positions across the wear track. Optical micrographs revealed significant difference in the surface wear characteristics among MoS_x, TiN, TiN+MoS_x coatings as shown in Figure 7.16.

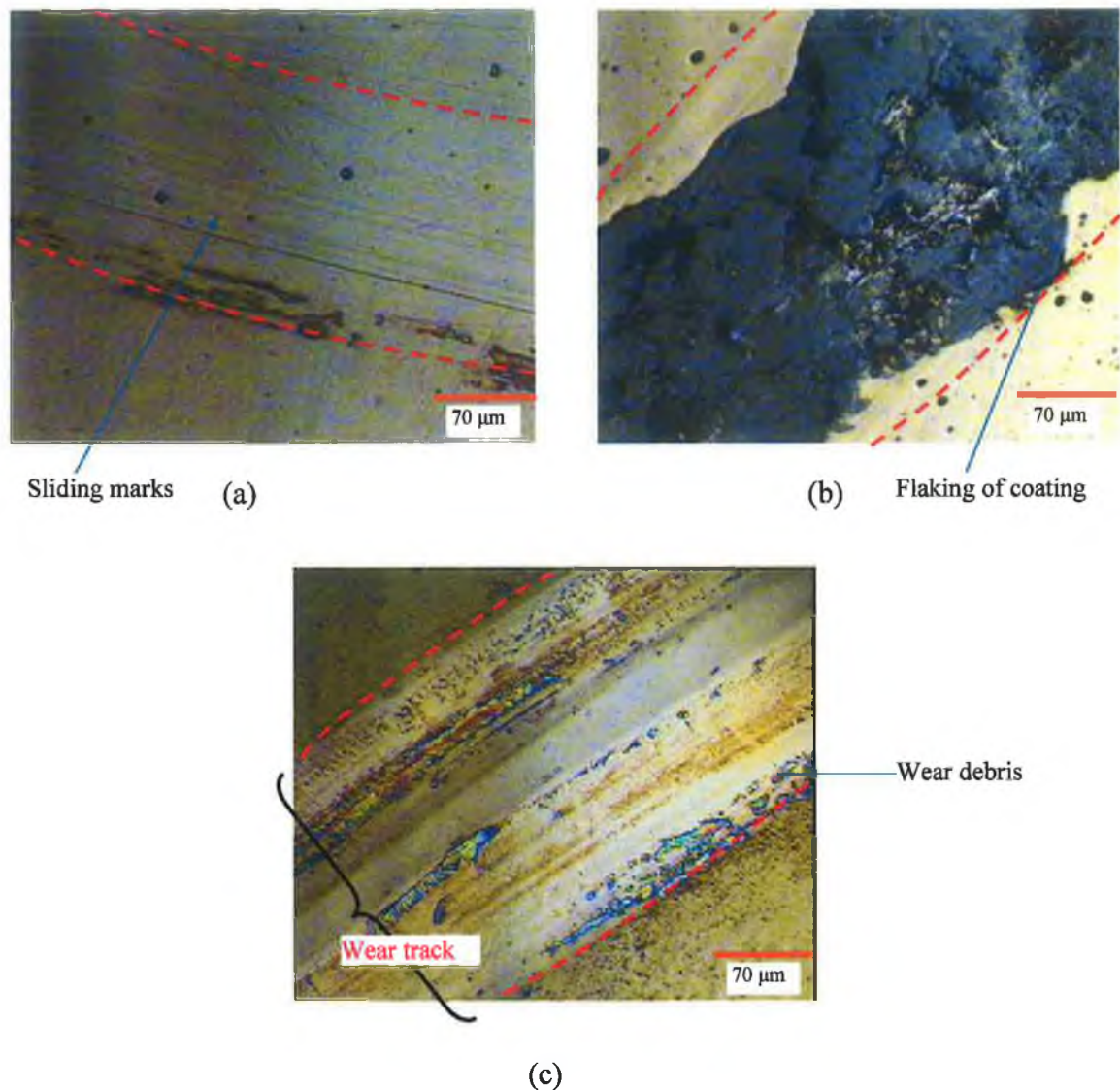


Figure 7.16. Optical micrograph of wear track profile created by pin-on-disk for (a) MoS_x (b) TiN and (c) TiN+ MoS_x coatings.

Wear grooves with features of microcutting and microploughing, typical for a severe abrasive mechanism was observed in the TiN coating. The generation of hard abrasive debris due to the progressive removal of the TiN coating have contributed to a pronounced abrasion mechanism and a local removal of the TiN coating in the form of flakes exposing the substrate.

Comparatively smooth surface was observed in TiN+MoS_x coating than TiN coating. The material transfer from the TiN+MoS_x coating was not uniform and there are some places where comparatively deep groove was observed. MoS₂ coating has smoother surface than TiN and TiN+MoS_x coatings, there was no sign of nonuniformity and complete failure of the coating was not observed.

In some locations the wear track of TiN+MoS_x coating had a blue colour, different from the colour of the coating, being difficult to understand if the coating has been completely worn out or not. In this respect the optical microscopy analysis was not always conclusive enough to identify the zones of the wear tracks where the coating has been completely worn out.

7.2.6.4. Wear track observation by optical profilometry

Visualization and quantification of the wear track by 3-D optical profilometry can overcome the problems associated with optical microscope and have increasingly been reported as an important tool to gain fundamental understanding of the wear process [127,259]. The 3-D visualization of the wear track by optical profilometer can provide colour legend at different places around the wear track to indicate height and depth at different places. This would help to identify the depth of the worn area.

Figure 7.17. shows the 3-D wear track of TiN coating. Similar abrasion and flaking of the coating were evident as observed in optical microscope. The maximum height indicated by red colour and maximum depth indicated by blue colour were higher than the coating thickness. This confirms the complete delamination of the coating. The coating indicated by green colour was still in the groove.

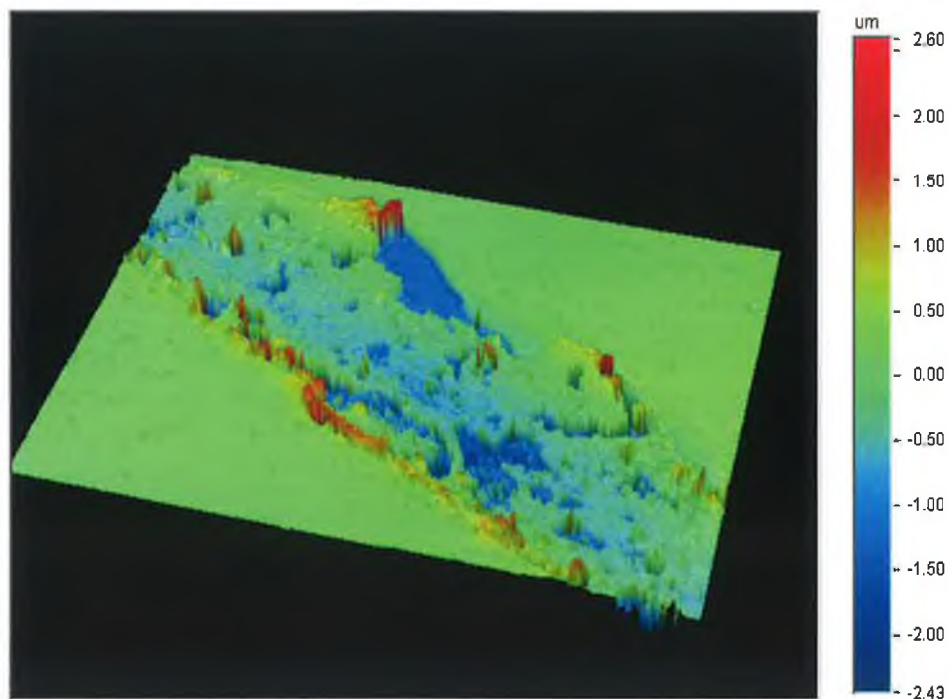


Figure 7.17. 3-D optical profilometry images of the wear tracks of TiN coating.

Figure 7.18. shows the 3-D wear track of TiN+MoS_x coating. Loose wear debris (aggregates of fine powdery particles) were observed at the periphery of the coating wear track.

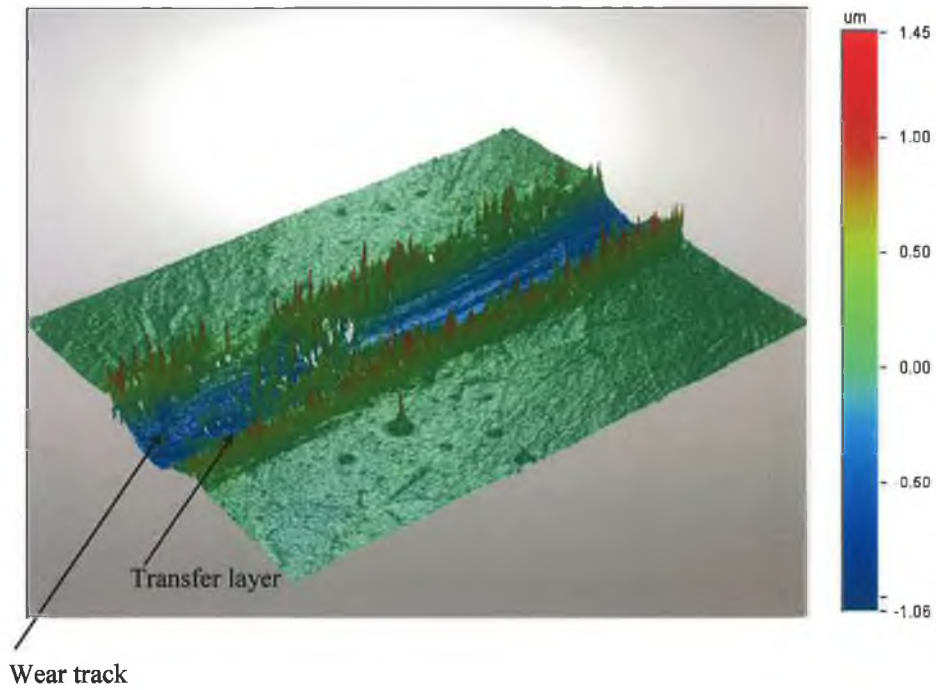


Figure 7.18. 3-D optical profilometry images of the wear tracks of TiN+MoS_x coating.

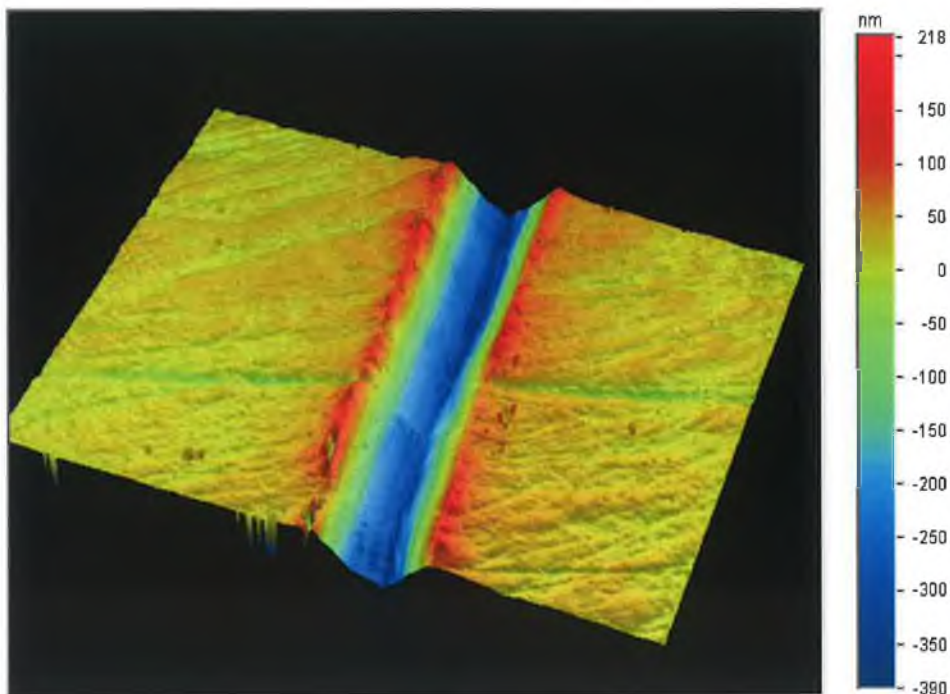


Figure 7.19. 3-D optical profilometry images of the wear tracks of MoS_x coating.

Very smooth wear track with very little wear debris was found for MoS₂ coating as shown in Figure 7.19. The wear track was barely visible in optical microscope as if no wear track was formed. But the wear track was clearly visible in the optical profilometry.

7.2.7. 3-D coating test

Initial test for 3-D coating was performed by depositing TiN and TiN+MoS_x coating on square and cylindrical bar. The coating was uniform all around the substrate, which demonstrated the successful coating deposition on 3-D objects by the two-axis rotary substrate table. Further investigations are necessary to demonstrate the effectiveness of sputtering system for 3-D coating by depositing on deep trench, grooves etc.

7.2.8. Coating deposition by rotational control

It was found that the deposition rate of the TiN+MoS_x coating was less than 2.0 μm/hr when the substrate table was rotated at a constant speed within each rotation. The deposition rate increased to double after using the rotational control of the substrate (slow rotation in front of activated target and fast rotation of inactivated targets) within each rotation. Similar physical, mechanical, chemical and tribological properties were obtained using rotational control compared to those not using the rotational control.

7.3. DISCUSSIONS

Ideally, set point 50% in the sputtering controller is required to form stoichiometric TiN coating. But the optimisation of TiN study showed that set point of 55% in the reactive sputtering controller was required to form nearly stoichiometric TiN_x (x=49/51). The set point is fixed on the basis of Ti intensity collected from the light tube located above the target (see Figure 3.5.). The distance between the light tube and target surface is shorter than the target-to-substrate distance. At distances away from the target the flux of the target material decreases. As a result at any particular set point, Ti and N atomic concentration ratio is higher near the light tube than the position where substrate is located. This is why a higher setpoint in the sputtering controller compensates the decrease of Ti and N atomic concentration ratio near the substrate. For example at 55% set point Ti and N concentration ratio is 55/45 near the light tube and the ratio would decrease to 49/51 near the substrate.

In the literature four different deposition techniques have been used to form TiN+MoS_x coatings so far: chemical vapour deposition with Ti((CH₃)₂N)₄, MoF₆, NH₃ and H₂S precursors [243], unbalanced magnetron sputtering of a composite target composed of TiN and MoS₂ halves in Ar and N₂ gas environment [245], hybrid technique using cathodic arc evaporation of Ti and sputtering of MoS₂ target in Ar and N₂ gas environment [247] and hybrid technique using E-gun evaporation of Ti and sputtering of MoS₂ target in Ar and N₂ gas environment [248]. In this investigation, TiN+MoS_x coating was deposited using closed-field unbalanced magnetron sputtering from separate Ti and MoS₂ target in Ar and N₂ gas environment. From the deposition point of view, the present deposition technique showed another unique way depositing TiN+MoS_x hard-solid lubricating coating. Although TiN+MoS_x coating was deposited as a multilayer coating when the substrate passes in front of Ti and MoS₂ targets in the N₂ gas environment, no evidence of multilayer was found in the SEM observation of the ball crater spot on the coating possibly due to the diffusion of Mo and S atoms in the TiN phase. The word “composite coating” (referred by some other researchers) has not been used to name TiN+MoS_x coating, as there was no discrete phase of TiN and MoS₂ were found.

As the N₂ content in the gas discharge guides the nitrogen composition, it is the key parameter in colour control for TiN_x sputtered coatings [153]. Colours from yellow to gold and finally brownish red were observed in the TiN coating as the nitrogen mass flow was raised in the gas discharge. With the introduction of grey colour MoS₂, the gold colour of TiN turned into yellow-grey in TiN+MoS_x coating [248]. The colour of TiN+MoS_x coating turned into more greyish with higher MoS_x content controlled by using higher MoS₂ target current during deposition. This also gave a rough indication of the incorporation of MoS_x in TiN coating during co-deposition.

The width of the diffraction peak in XRD test represents the crystallinity of the coating and the broader width of the diffraction peak indicates inferior crystallinity. The widening of the peaks in the TiN+MoS_x coating indicated nanocrystalline nature. Peak broadening can also be related to the presence of microstrain or higher nitrogen concentration in the coating [369]. As the deposition parameters of TiN and TiN+MoS_x was identical, so it was reasonable to assume that the peak broadening occurred only due to small crystallite size. Rapid widening of peak width in TiN-MoS_x coating was observed in reference [245] with the increase of MoS₂ percentage, which could happen when there was a competition of TiN and MoS₂ phase growth. There was no rapid widening of peak in this study, which

also supported the postulate of being Mo and S atoms into the cubic TiN lattice. With the increase of Mo+S content in TiN+MoS_x coating TiN peak started to disappear and completely disappeared at sufficiently higher content (~30 wt%). This suggested that there was a certain optimum concentration of MoS_x where TiN phase could form. Beyond that limit the excessive MoS_x hindered the formation of TiN and the coating completely loses its crystallinity and becomes amorphous. No peak was found for pure MoS₂ coating in the XRD analysis or the peak was too weak to detect, which hinted that the MoS₂ were in amorphous or nanocrystalline form. Similar poor crystalline MoS₂ was also observed in another study of MoS₂ deposited by closed-field magnetron sputtering [211].

The main problem in quantifying the atomic percentage of Ti and N in the TiN coating by EDX analysis was to find out the correct parameters (i.e., accelerating voltage). EDX analysis are not very sensitive to lower atomic no elements. These elements produce soft X-rays that are hard to detect and easily absorbed before it reaches to detector.

The adhesion is considered good if the cracks propagated through the substrate. The small flakings found adjacent to the boundary of the indentation suggested the evidence of adhesive failure. As Rockwell C indentation test is a combined measure of adhesion and toughness of the coating, the present results are in agreement. One explanation of the overall lack of adhesion of the coatings can be given considering the mechanical properties of the substrate. If the substrate were soft compared to the coating, there would be an increased possibility of damage under indentation [123,370].

In the pin-on-disk test results the friction values decreased at higher load indicating that TiN+MoS_x coating was behaving in elastic manner [215]. The fluctuation of coefficient of friction in the TiN+MoS_x coating was very small. Similar behaviour was also observed in another study of TiN+MoS_x coating where Mo and S atoms were supposed to present as discrete atoms [247]. But a typical “saw-tooth” type friction curve was observed in TiN+MoS_x coating where TiN and MoS₂ were existed as separate phase [245] and in MoS₂ filled Ti-TiC-TiC/DLC nanocomposite coating [260]. The “saw-tooth” behaviour was explained by the discrete supply of solid lubrication during sliding. As no “saw-tooth” type behaviour was observed in this study, so it could be expected that the constant supply of lubrication was obvious. At higher load periodic peaks were observed in the friction curve of TiN+MoS_x coatings. First it was thought that breaking of the coating caused these peak appearances. But close observation revealed that the coating was not broken. This peak

appearance can be explained by “stick slip” phenomenon referred by Cosemans et al. [248]. During pin-on-disk test debris material build up in front of pin counterface. When this debris reaches a certain critical volume it collapses and causes peaks in the friction curve. To realise the solid lubrication effect in TiN+MoS_x coating, there needs some run in period where the Mo and S atoms combines and lowers the friction. But it should be noted that even in that period the coefficient of friction is much lower than pure TiN coating. Steady-state friction value for long sliding distance can be related to the formation of transfer layer during sliding. This ensured the reliable behaviour during service. The low friction can also be associated with the low adhesion between the contact surfaces. TiN+MoS_x coatings showed lower coefficient of friction in normal environment indicating its suitability as hard-solid lubricant coating. The reproducibility of the friction behaviour was quite good (within the limit of 5-10%).

In general, tribological behaviour of thin coating is dominated by four main parameters: the ratio of coating to substrate hardness, the coating thickness, the surface roughness and the debris in the contact [14]. During the pin-on-disk testing, the transferred materials were compacted and mechanically mixed with coating materials, forming the surface layer usually referred to as a tribofilm or wear debris, which plays an important role in controlling the wear and friction behaviour [371,372]. The formation of tribofilm is a complex phenomenon depending on environment, sliding conditions, load etc. The tribochemical mechanism can be divided two main surface phenomena: the formation of thin microfilm on hard coatings and the oxidation of soft coatings [14].

The detachment of the TiN coating can also be attributed to the loss of adhesion and the presence of debris originating from the steel substrate [127]. As the hardness of TiN is higher than TiN+MoS_x coating, it should show high wear resistance. It showed lower wear upto a certain sliding distance and the abrasive particle formed in the wear track propagated the failure of the coating rapidly [232].

The good lubrication property of MoS₂ is generally ascribed to the ease of sliding of the basal planes of its hexagonal structure, which are held together by weak van der Waals bonding [165]. It is interesting to note that there was no evidence of MoS₂ hexagonal phase in either MoS₂ or TiN+MoS_x coating. However, the reduction of friction can be explained by the structural reorientation of MoS₂ in MoS₂ coating and combining of Mo and S atoms and then structural reorientation in TiN+MoS_x coating during sliding. This phenomenon is

not contradictory with the literature where it is reported that poorly crystalline or amorphous phases of MoS₂ transforms into well-developed hexagonal phases in sliding friction [164, 211,260,372,373].

Abrasive effect in the TiN+MoS_x coating is diminished by the solid lubricant effect coming from the solid lubricant part of the coating. The low wear and friction in the TiN+MoS_x coating can be related to the fact that a low friction layer produced in the opposing surface (pin) in the pin-on-disk wear test. This type transfer film formation was observed by several researchers in different types of coatings such as MoS₂ and C film in MoS₂:C:TiB₂ coating [253] or graphite like carbon film in DLC coating [374]. More recently, direct evidence of tribofilm controlling friction and wear during sliding has been obtained with insitu tribometer incorporating optical microscopy and Raman spectroscopy. Singer et al. [372] has shown that amorphous Pb-Mo-S was lubricated by MoS₂ transfer film by insitu Raman spectroscopy. At present this type of characterization is developing. Hopefully, in future the tribofilm formation mechanism from in situ characterization will broaden the present understanding. The low coefficient of friction of TiN+MoS_x coating compared to TiN could be one of the reasons for lower wear rate in the coating [371]. The addition of MoS₂ increases the adhesion of the TiN+MoS_x coating. This enables higher load bearing capacity of the coating and is one of the reasons for increased life-time [215]. In TiN+MoS_x coating although the middle of the wear track was very smooth, there were very few places on the side of the track deeper groove. This can be explained by the spalling of relatively bigger debris where there was lack of lubrication. Figure 7.20. shows a schematic diagram of possible wear mechanism in the TiN+MoS_x coating during dry sliding.

The low wear in MoS₂ coating compared to TiN can be attributed to the easy sliding of the pin over the coating and possibly due to the formation of transfer layer on the pin making the contact only between the low friction layers. Although much lower friction observed in MoS₂ coating, the comparative higher wear rate than TiN+MoS_x can be related to the lower hardness of MoS₂ coating.

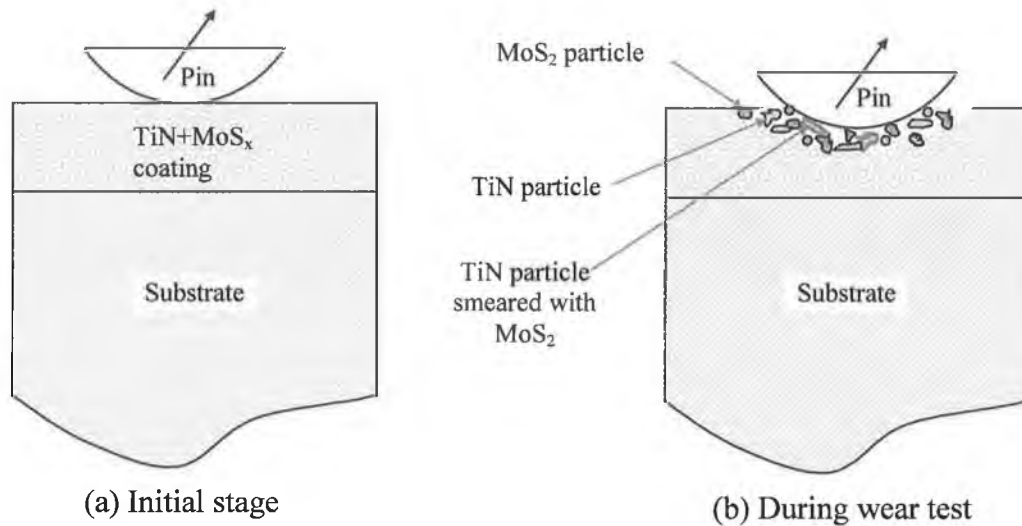


Figure 7.20. Schematic diagram of possible wear mechanism in TiN+MoS_x coating during pin-on-disk test.

The present wear test results suggested that hardness alone is not the main factor affecting wear behavior. Since there is no clear correlation between the hardness and of the coatings and their tribological performance, it is inferred that the lubricity from MoS_x in the TiN+MoS_x coatings may be playing a role in the tribological properties.

EDX analysis performed in the wear track of TiN+MoS_x coatings revealed the presence of Ti, N, Mo, and S. There was no sign of Fe peak from the wear track. This suggested that the coating was not broken through. But there are very few places in the wear track of the TiN+MoS_x coating where Fe peak was evident indicating the delamination of the coating. But in case of TiN, Fe peak was evident in the wear track, which suggested that the coating was broken through in most of the places due to the digging of the pin. This is the general scenario in most places of the wear track of the TiN coating.

TiN+MoS_x coatings with graded interlayer (Ti-TiN_{0.33}-TiN, Ti-TiN_{0.2}-TiN_{0.47}-TiN) showed further improvement in tribological performance due to the solid lubricant effect from the top layer as well as better load bearing capacity from the graded interlayer.

7.4. SUMMARY

TiN+MoS_x coatings deposited by closed-field magnetron sputtering from separate Ti and MoS₂ target in N₂ gas environment exhibited enhanced wear resistance compared to pure

TiN and appeared to be promising for applications where low wear and low friction are required. It can protect the matting surfaces during sliding operations by combining hard and solid lubrication effect. It has been speculated that Mo and S atoms was incorporated in the TiN hard phase from XRD analysis and lubrication effect arises from the MoS_x phase formed during sliding. This lubrication effect is evident from the lower coefficient of friction and wear rate compared to the pure TiN coating in the pin-on-disk test results. The tribological data together with the optical inspection of the worn areas have given detailed insight of wear mechanism involved in different coatings.

CHAPTER 8

Conclusions and Suggestions for Future Work

8.1. GENERAL CONCLUSIONS

The following general conclusions can be drawn from the sputtering rig development, coating deposition and characterization, thermal stress and gas flow modelling.

8.1.1. Experimental rig development

The magnetron sputtering rig has been developed to a closed-field arrangement by reestablishing different systems such as magnetron, vacuum, electrical, water-cooling, reactive sputtering controller etc. The design and installation of one-axis and two-axis rotary substrate table has enabled the deposition of new generation coatings such as multicomponent, multilayer, composite etc. The slow and fast rotational control of the substrate table in front of activated and inactivated targets respectively within a single cycle of rotation has been established.

8.1.2. Coating deposition

TiN+MoS_x coating has been deposited by a closed-field unbalanced magnetron sputtering from separate Ti and MoS₂ targets in reactive N₂ gas environment by rotating the substrate inside the chamber. The coating deposition rate of the TiN+MoS_x coating was quite slow; 1.8-1.9 μm per hour with the uniform rotation of the substrate table. But by the introduction of slow and fast rotational control of the substrate table twofold increase of the deposition rate was realized.

8.1.3. Coating characterization

8.1.3.1. Elemental and structural characterization

EDX analysis showed that Mo+S percentage in the TiN+MoS_x coating was approximately 3.0, 7.0, and 11.0 wt % corresponding to 0.2, 0.4 and 0.6 MoS₂ target current. This indicated the variation of MoS_x content in the TiN+MoS_x coating with the MoS₂ target current. Pure TiN and TiN+MoS_x coatings exhibited the f.c.c. structure in the XRD spectrum. In the TiN+MoS_x coatings, peaks were shifted to lower angles and slightly widen compared to pure TiN coating, which indicated an increase in the lattice parameter and a reduction in grain size respectively. With the higher current of MoS₂ target higher peak shifting and peak widening were observed. No MoS_x phase was observed in any of

these coatings suggesting the possible incorporation Mo and S atoms into the cubic TiN lattice or segregated at the grain boundaries.

8.1.3.2. Physical and mechanical characterization

The coating surface was quite smooth and an average surface roughness value of 14-18 nm was found from optical profilometer and AFM. TiN+MoS_x coating showed lower hardness than pure TiN but higher hardness than MoS_x. But there was no significant difference of hardness among the TiN+MoS_x coatings with different contents of MoS_x. The Rockwell C indentation test for all TiN+MoS_x coatings showed a better adhesion, i.e. class HF3 compared to the adhesion of pure TiN and MoS_x (HF5).

8.1.3.3. Tribological characterization

TiN+MoS_x coating showed lower friction coefficient than pure TiN but higher value than pure MoS_x. This fact can be explained by the formation of MoS_x from Mo and S atoms in the wear track during the run-in period. TiN+MoS_x coating showed the least wear among the different coatings under the same operating conditions. This cannot be directly correlated with the hardness values of different coatings. Although TiN+MoS_x has lower hardness value than TiN coating, but it showed lower wear rate possibly due to some lubrication effect from the MoS_x phase formed during sliding operation. Similar evidence of lubrication effect was also found from the study of the wear scar morphology. Around the wear track of TiN coating brittle flaking was observed whereas comparatively smooth surface was observed in TiN+MoS_x coating with no brittle flaking.

8.1.4. Thermal stress modelling in thin film

Thermal stress modelling of TiN coating on stainless steel substrate by finite element analysis revealed that the coating was in compression throughout the thickness and the substrate was in tension at top surface but in compression at bottom surface. The highest radial (σ_x) and tangential (σ_z) stress values found at the interface between the coating and substrate indicated that the interface between the coating and substrate was the critical location from the failure point of view. Along the interface higher shear stresses were found at the edge because of stress concentration. Higher axial stress was also found at the edge of the coating-substrate system. This would cause the start of spallation of the coating from the edge. The insertion of Ti interlayer between the TiN coating and substrate significantly reduced the stress components particularly the shear stress.

8.1.5. CFD modelling of process gas flow

The simulation of process gas flow and the mixing behaviour in a magnetron-sputtering deposition chamber was carried out by Ansys-FLOTRAN CFD code. Higher values of velocity and pressure at the inlet dropped to lower values inside the chamber due to the large expansion of geometry from the inlet to the chamber. Argon has higher concentration in the chamber than nitrogen due to the higher flow rate of argon than nitrogen. Nitrogen concentration over the substrate increased with the increase of higher nitrogen flow rate and with the decrease of substrate to chamber wall distance. Slightly higher nitrogen concentration was observed in the middle of the substrate than the edge when the substrate was in front of nitrogen inlet and lower nitrogen concentration was observed when the substrate was in front of argon inlet. But when the substrate was between argon and nitrogen inlet the nitrogen was uniformly distributed over the substrate. This indicated that uniform percentage of nitrogen would be present in the coating at this position. This information can help to modify the reactor geometry and gas flow openings and the position of the gas flow openings for better gas flow over the substrate which in turns gives an indirect indication of the compound coating uniformity on the substrate.

8.2. THESIS CONTRIBUTION

- ❑ The sputtering rig has been developed to closed-field arrangement from Penning type arrangement. Design and installation of a single axis and two-axis rotary substrate table facilitated the deposition of multicomponent, multilayer, graded and composite coating.
- ❑ A novel rotational control of the substrate table has been developed to increase deposition rate by maintaining slower speed in front of the activated targets and faster speed in front of the inactivated targets instead of rotating at uniform speed.
- ❑ New generation hard-solid lubricant coating ($\text{TiN}+\text{MoS}_x$) deposited by a new technique (sputtering from separate Ti and MoS_2 target in N_2 gas environment) showed better wear characteristics (hardness effect from TiN) and lower coefficient of friction (lubrication effect from MoS_2) than pure TiN coating.
- ❑ A method of simulating thermal stress in thin hard coating has been developed by finite element package Ansys and verified with appropriate analytical equation. The method can be useful for predicting thermal stress distribution for any kind of

coating material on any kind of substrate materials if the material properties are known.

- ❑ A simple model for simulating process gas flow in magnetron sputtering chamber has been developed by finite element package Ansys-Flotran. The method can give important information for process gas flow distribution, their mixing behaviour, and possible impact on the uniformity of the composition of the coating.

8.3. SUGGESTIONS FOR FUTURE WORK

8.3.1. Sputtering rig development

8.3.1.3. Computer controlled operation of the rig

The magnetron-sputtering rig is operated manually. This operating system can be upgraded to control from the computer through Programmable Logic Controller (PLC) and a suitable programming language (LabView).

8.3.1.2. Closed-loop control system

It has been explained in Chapter 3 that the controlling of the substrate motion by time control method was not precise due to the open-loop control system. This controlling system can be extended to closed-loop control system by incorporating a sensor providing feedback of the position of the substrate table (Figure 8.1.).

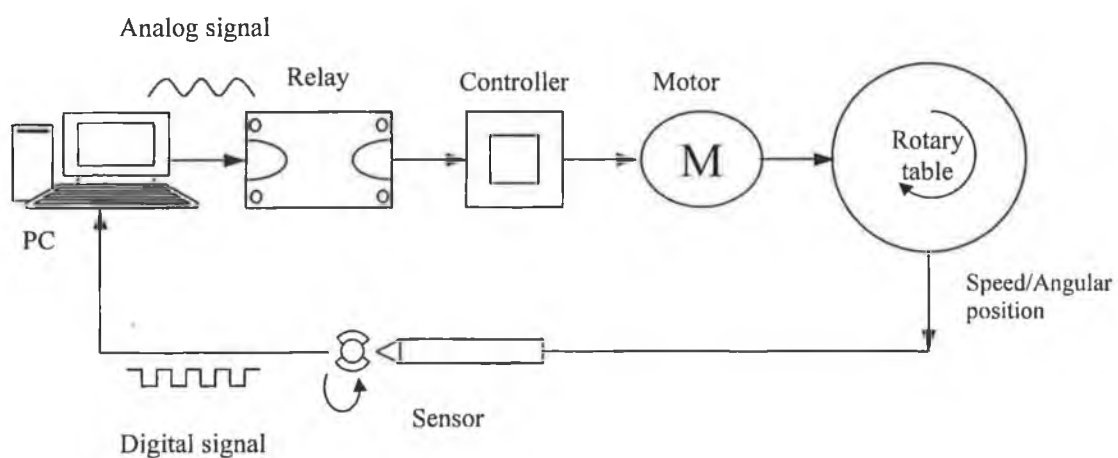


Figure 8.1. Schematic diagram of closed-loop control system diagram.

8.3.1.3. Substrate rotation in front of target

For depositing a single species coating on 3-D objects it is necessary to rotate the substrate remaining in front of the target. This can be performed by simple gear arrangements with the help of the main motion from the central shaft.

8.3.2. Process gas flow modelling

Due to the node number limitation, the full magnetron-sputtering chamber couldn't be modelled. The full model of the chamber can be modelled by the fluent software to get further insight of the gas flow and mixing behaviour. The temperature distribution inside the deposition chamber can be modelled by taking the magnetron as heat source.

8.3.3. Thermal stress modelling

The thermal stress modelling can be extended to the any type of coating-substrate system if the material properties are known. At the moment the model does not include any temperature dependent material properties. Further work can be carried out to investigate the effects of temperature dependent material properties on thermal stress.

8.3.4. Coating deposition

Further study can be carried out to improve the adhesion of TiN+MoS_x coating to evaluate the coating's ultimate performance on cutting tool. TiN+MoS_x coating can also be deposited on plasma nitrided sample performed within the same chamber. Plasma nitriding would improve the load bearing capacity and hard-solid lubricant coating would provide better wear characteristics with low friction. Other combination of hard (CrN) and solid lubricant coatings (Ag) can also be studied.

REFERENCES

1. K. N. Strafford, P. K. Datta and C. Googan (eds.). Coating and surface treatments for Corrosion and Wear Resistance. Ellis Horwood, Chichester, U.K. (1984).
2. K. N. Strafford and C. Subramanian, Surface engineering: an enabling technology for manufacturing industry. *J. Mater. Process. Tech.*, 53 (1995) p. 393.
3. K. N. Strafford, Tribological properties of coatings-expectations, performance and the design dilemma. *Surf. Coat. Tech.*, 81, (1996) p. 106.
4. T Bell, Surface engineering: past, present and future. *Surf. Eng.*, 6 (1990) p. 31.
5. T. Bell, Towards designer surfaces. *Ind. Lubr. Tribol.*, 44 (1992) p. 3.
6. T. Burakowski and T. Wierzchon, Surface engineering of metals: Principles, Equipment, technologies. edited by Brian Ralph (1999).
7. T. Bell, Towards a universal surface engineering road map. *Surf. Eng.*, 16 (2000) p. 89.
8. A. Matthews, R. Artley and P. Holiday, "2005 Revisited; The UK Surface Engineering Industry to 2010".
9. A. Matthews, A. Leyland and P. stevenson, Widening the market for advanced PVD coatings. *J. Mater. Proces. Technol*, 56 (1996) p. 757.
10. A. Matthews, Advances in surface processing technology. In: surface engineering practice. Strafford K. N., Datta P. K. and Gray J. S. (eds), Chichister, UK, Ellis, Horwood, (1990) p. 33.
11. B. Bhushan and B. K. Gupta, Handbook of tribology; materials, coatings and surface treatments, McGraw-Hill, New York (1991).
12. D. S. Rickerby, A. Matthews, (eds) Advanced surface coatings: A handbook of surface engineering. Glasgow, UK, Blackie, (1991) p. 364.
13. W. Gissler, H. A. Jehn (eds), Advanced techniques for surface engineering. Kluwer Academic publishers, Dordrecht, The Netherlands, (1992) p. 397.
14. K. Holmberg and A. Matthews, Coatings tribology. Elsevier, New York (1994).
15. K. Seshan, Handbook of Thin-Film Deposition Processes and Techniques-Principles, Methods, Equipment and Applications (2nd Edition) Noyes (2002).
16. R. S. Cowan, W. O. Winer, Surface engineering...an enigma of choices. *J. Phys. D.* 25 (1992) p. A 285.
17. S. Hogmark, S. Jacobson and M. Larsson, Design and evaluation of tribological coatings. *Wear*, 246 (2000) p. 20.
18. B. Podgornik and J. Vižintin, Tribology of thin films and their use in the field of machine elements. *Vacuum.*, 68 (2002) p. 39.
19. A. Matthews, A. Leyland, B. Dorn, P. R. Stevenson, M. Bin-Sudin, C. Rebholz, A. Voevodin, and J. Schneider, Plasma-based surface engineering processes for wear and corrosion protection. *J. Vac. Sci. Technol.*, A 13 (1995) p. 1202.
20. R. F. Bunshah and C. V. Deshpandey, Plasma assisted physical vapor deposition processes: A review. *J. Vac. Sci. Tech. A*, 3 (1985) p. 553.
21. B. Navinsek, P. Panjan and I. Milosev, PVD coatings as an environmentally clean alternative to electroplating and electroless processes. *Surf. Coat. Tech.*, 116-119 (1999) p. 476.
22. H. A. Jehn, PVD and ECD-competition, alternative or combination. *Surf. Coat. Tech.*, 112 (1999) p. 210.
23. D. M. Mattox, Foundations of Vacuum Coating Technology. William Andrew Publishing/Noyes (2003).
24. D. M. Mattox, Ion plating-past, present and future. *Surf. Coat. Tech.*, 133-134 (2000) p. 517.

25. D. M. Mattox, Physical Vapor Deposition (PVD) Processes. *Metal Finishing*, 98 (2000) p. 410.
26. D. M. Mattox, *Handbook of Physical Vapor Deposition (PVD) Processing*. William Andrew Publishing/Noyes, (1998).
27. R. F. Bunshah, *Handbook of Deposition Technologies for Films and Coatings: Science, Technology, and Applications*. Second Edition, Noyes Publications, New Jersey (1991).
28. J. E. Mahan, *Physical Vapor Deposition of Thin Films*. John Wiley & Sons, (2000).
29. R. F. Bunshah, *Handbook of Hard Coatings*. William Andrew Publishing/Noyes (2001).
30. S. M. Rossnagel, Thin film deposition with physical vapor deposition and related technologies. *J. Vac. Sci. Technol. A* 21 (2003) p. S74.
31. A. Matthews, Plasma-based physical vapor deposition surface engineering processes. *J. Vac. Sci. Technol. A* 21, (2003) p. S224.
32. K. L. Choy, Chemical vapour deposition of coatings. *Progress in Materials Sci.*, 48 (2003) p.57.
33. W. R. Grove, "On the Electrochemical Polarity of Gases," *Philosophical Trans. Royal. Soc. (London) B*, 142 (1852) p. 87.
34. P. Sigmund, Theory of sputtering. I. Sputtering yield of amorphous and polycrystalline targets. *Phys. Rev.*, 184 (1969) p. 383.
35. J. L. Vossen, *Thin film processes*. Werner Kern-New York: Academic Press (1978).
36. B. N. Chapman, *Glow Discharge Processes*. Wiley-Interscience, New York (1980).
37. S. M. Rossnagel, J. J. Cumo and W. D. Westwood, *Handbook of plasma processing technology: fundamentals, etching, deposition*. Park Ridge, N. J: Noyes Publications (1990).
38. J. L. Vossen, *Thin film processes II*. Werner Kern-Boston, Academic Press (1991).
39. S. M. Rossnagel, *Sputter Deposition*. In: W.D. Sproul and K.O. Legg Editors, *Opportunities for Innovation: Advanced Surface Engineering*, Technomic Publishing Co, Switzerland (1995).
40. D. A. Glocker and S. I. Shah, *Handbook of thin film process technology*. Bristol and Philadelphia, Institute of Physics Publishing (1995).
41. A. Kinbara, E. Kusano and I. Kondo, *Fundamentals of plasma and sputtering processes*. *Vacuum.*, 51 (1998) p. 475.
42. S. M. Rossnagel, Sputter deposition for semiconductor manufacturing. *IBM J. Res. Devel.* 43 (1999) p. 163.
43. C. Weissmantel, Applications of ion beams for the preparation of thin films. *Proc. IX IVC-VICES*, Madrid, Spain (1983) p. 300.
44. F. M. Penning, Coating by Cathode Disintegration. (filed December 1935 in Germany), U.S. Patent #2,146,025 (Feb.7, 1939); also *Physica (Utrecht)*, 3 (1936) p. 873.
45. J. S. Chapin, Sputtering Process and Apparatus. (filed Jan. 1974), U.S. Patent # 4,166,018 (1979).
46. J. A. Thornton, Magnetron sputtering: basic physics and application to cylindrical magnetrons. *J. Vac. Sci. Technol.*, 15 (1978) p. 171.
47. R. K. Waits, Planar magnetron sputtering. *J. Vac. Sci. Technol.*, 15 (1978) p. 179.
48. B. Window and N. Savvides, Charged particle fluxes from planar magnetron sputtering sources. *J. Vac. Sci. Technol. A*, 4 (1986) p. 196.
49. B. Window and N. Savvides, Unbalanced DC magnetrons as sources of high ion fluxes. *J. Vac. Sci. Technol. A*, 4 (1986) p. 453.
50. N. Savvides and B. Window, Unbalanced magnetron ion-assisted deposition and property modification of thin films. *J. Vac. Sci. Technol. A*, 4 (1986) p. 504.

51. D. G. Teer, Technical note. A magnetron sputter ion-plating system. *Surf. Coat. Technol.*, 39/40 (1989) p. 565.
52. J. Musil and S. Kadlec, Reactive sputtering of TiN films at large substrate to target distances. *Vacuum.*, 40 (1990) p. 435.
53. F. Adibi, I. Petrov, J. E. Greene, L. Hultman and J. E. Sundgren, Effects of high-flux low-energy (20–100 eV) ion irradiation during deposition on the microstructure and preferred orientation of Ti_{0.5}Al_{0.5}N alloys grown by ultra-high-vacuum reactive magnetron sputtering. *J. Appl. Phys.*, 73 (1993) p. 8580.
54. W. D. Münz, The unbalanced magnetron: current status of development. *Surf. Coat. Technol.*, 48 (1991) p. 81.
55. W. D. Sproul, High-rate reactive DC magnetron sputtering of oxide and nitride superlattice coatings. *Vacuum.*, 51 (1998) p. 641.
56. P. J. Kelly and R. D. Arnell, Magnetron sputtering: a review of recent developments and applications. *Vacuum.*, 56 (2000) p. 159.
57. P. J. Kelly and R. D. Arnell, Characterization studies of the structure of Al, Zr, and W coatings deposited by closed-field unbalanced magnetron sputtering. *Surf. Coat. Technol.*, 97 (1997) p. 595.
58. P. J. Kelly and R. D. Arnell, The influence of magnetron configuration on ion current density and deposition rate in a dual unbalanced magnetron sputtering system. *Surf. Coat. Technol.*, 108–109 (1998) p. 317.
59. J. Musil, J. Vlcek, A perspective of magnetron sputtering in surface engineering. *Surf Coat Tech.*, 112 (1999) p. 162.
60. P. J. Kelly, R. D. Arnell, W. Ahmed and A. Afzal, Novel engineering coatings produced by closed-field unbalanced magnetron sputtering. *Mater. Des.*, 17 (1996) p. 215.
61. R. D. Arnell, P. J. Kelly and J. W. Bradley, Recent developments in pulsed magnetron sputtering. *Surf. Coat. Tech.*, 188–189 (2004) p. 158.
62. Gencoa Product Information: V-Tech Magnetrons. Gencoa, 4 Wavertree Boulevard South, Liverpool L7 9PF, UK. Web address: www.Gencoa.com.
63. J. R. German, A Simple Low Cost Method for Increased Performance of Planar Magnetron Sputtering Targets. <http://www.soleras.com/shunt/shunt.htm>
64. J. Musil, K. Rusnak, V. Jezek and J. Vlcek, Planar magnetron with additional plasma confinement. *Vacuum.*, 46 (1995) p. 341.
65. J. Musil, Rectangular magnetron with full target erosion. *J. Vac. Sci. Technol. A* 17 (1999) p. 555.
66. K. Macák, V. Kouznetsov, J. Schneider, and U. Helmersson and I. Petrov, Ionized sputter deposition using an extremely high plasma density pulsed magnetron discharge. *J. Vac. Sci. Technol. A*, 18 (2000) p. 1533.
67. J. Musil, Recent advances in magnetron sputtering technology. *Surf. Coat. Technol.*, 100–101 (1998) p. 280.
68. J. Musil, Low-pressure magnetron sputtering. *Vacuum.*, 50 (1998) p. 363.
69. R. Kukla, Magnetron sputtering on large scale substrates: An overview on the state of the art. *Surf. Coat. Tech.*, 93 (1997) p. 1.
70. B. Window, Recent advances in sputter deposition. *Surf. Coat. Tech.*, 71 (1995) p. 93.
71. J. G. Jones and A. A. Voevodin, Magnetron sputter pulsed laser deposition: technique and process control developments. *Surf. Coat Technol.*, 184 (2004) p. 1.
72. N. M. Renevier, H. Oosterling, U. König, H. Dautzenberg, B. J. Kim, L. Geppert, F. G. M. Koopmans and J. Leopold, Performance and limitation of hybrid PECVD (hard coating)—PVD magnetron sputtering (MoS₂/Ti composite) coated inserts tested for dry high speed milling of steel and grey cast iron. *Surf. Coat. Technol.*, 163–164 (2003) p. 659.

73. K. H. Kim, S. R. Choi and S. Y. Yoon, Superhard Ti–Si–N coatings by a hybrid system of arc ion plating and sputtering techniques. *Surf. Coat. Tech.*, 161 (2002) p. 243.
74. P. Eh. Hovsepian, D. B. Lewis, C. Constable, Q. Luo, Y. N. Kok and W. -D. Münz Combined steered cathodic arc/unbalanced magnetron grown C/Cr nanoscale multilayer coatings for tribological applications. *Surf. Coat. Technol.*, 174-175 (2003) p. 762.
75. B. Window, Issues in magnetron sputtering of hard coatings. *Surf. Coat. Technol.*, 81 (1996) p. 92.
76. I. Safi, Recent aspects concerning DC reactive magnetron sputtering of thin films: a review, *Surf. Coat. Technol.*, 127 (2000) p. 203.
77. J. Musil, P. Baroch, J. Vlček, K. H. Nam and J. G. Han, Reactive magnetron sputtering of thin films: present status and trends. *Thin Solid Films*, In Press (2004).
78. S. M. Rossnagel, D. Mikalsen, H. Kinoshita and J. J. Cuomo, Collimated magnetron sputter deposition. *J. Vac. Sci. Technol. A*, 9 (1991) p. 261.
79. B. A. Movchan and A.V. Demchisin, *Phys.Met. Metallogr.* 28, (1969) p. 83.
80. D. M. Mattox, The effect of processing variables on coating morphology. *J. Vac. Sci. Technol.*, 20 (1982) p. 1345.
81. J. A. Thornton, The microstructure of sputter-deposited coatings. *J. Vac. Sci. Technol. A*, 4 (1986) p. 3059
82. J. A. Thornton, Influence of apparatus geometry and deposition conditions on the structure and topography of thick sputtered coatings. *J. Vac. Sci. Technol.* 11 (1974) p. 666.
83. R. Messier, A. P. Giri, R. A. Roy, Revised structure zone model for thin film physical structure. *J. Vac. Sci. Technol. A*, 2 (1984) p. 500.
84. J. Musil, S Kadlec, V. Valvoda, Ion-assisted sputtering of TiN films. *Surf. Coat. Technol.*, 43/44 (1990) p. 259.
85. S. Munsterer and K. Kohlhof, in *Thin Films*, edited by G. Hecht, F. Richter, and J. Hahn (DGM Informationsgesellschaft), Verlag (1994) p. 121.
86. K. Ino, T. Shinohara, T. Ushiki, and T. Ohmi, Ion energy, ion flux, and ion species effects on crystallographic and electrical properties of sputter-deposited Ta thin films. *J. Vac. Sci. Technol. A*, 15 (1997) p. 2627.
87. P. J. Kelly and R. D. Arnell, Development of a novel structure zone model relating to the closed-field unbalanced magnetron sputtering system. *J. Vac. Sci. Technol. A*, 16 (1998) p. 2858.
88. D. Tabor, *The Hardness of Metals*. Oxford C. Press, New York (1951).
89. K. L. Mittal, Adhesion measurement of thin films. *Electrocomponent Sci. Technol.*, 3 (1976) p. 21.
90. H. Weiss, Adhesion of advanced overlay coatings: mechanisms and quantitative assessment. *Surf. Coat. Technol.*, 71 (1995) p. 201.
91. K. Koski, J. Hölsä, J. Ernoult and A. Rouzaud, The connection between sputter cleaning and adhesion of thin solid films. *Surf. Coat. Technol.*, 80 (1996) p. 195.
92. F. S. Shieu, L. H. Cheng, M. H. Shiao and S. H. Lin, Effects of Ti interlayer on the microstructure of ion-plated TiN coatings on AISI 304 stainless steel. *Thin Solid Films.*, 311 (1997) p. 138.
93. B. Škorić, D. Kakaš, M. Rakita, N. Bibić and D. Peruškob, Structure, hardness and adhesion of thin coatings deposited by PVD, IBAD on nitrided steels. *Vacuum.*, 76 (2004) p. 169.
94. K. Holmberg, H. Ronkainen and A. Matthews, Tribology of thin coatings. *Ceram. Int.*, 26 (2000) p. 787.
95. K. Holmberg, A. Matthews and Helena Ronkainen, Coatings tribology-contact mechanisms and surface design. *Tribol. Int.*, 31 (1998) p. 107.

96. A. Matthews, A. Leyland, K. Holmberg and H. Ronkainen, Design aspects for advanced tribological surface coatings. *Surf. Coat. Technol.*, 100-101 (1998) p. 1.
97. W. D. Sproul, From metallurgical coatings to surface engineering. *J. Vac. Sci. Technol. A*, 21 (2003) p. S222.
98. M. Van Stappen, M. Kerkhofs, L. M. Stals and C. Quaeyhaegens, State of the art for the industrial use of ceramic PVD coatings. *Surf. Coat. Tech.*, 74-75 (1995) p. 629.
99. C. Donnet and A. Erdemir, Historical developments and new trends in tribological and solid lubricant coatings. *Surf. Coat. Tech.*, 180-181 (2004) p. 76.
100. C. Subramanian, and K. N. Strafford, Review of multicomponent and multilayer coatings for tribological applications. *Wear*, 165 (1993) p. 85.
101. H. Holleck, Material selection for hard coatings. *J. Vac. Sci. Technol. A*, 4 (1986) p. 2661.
102. H. A. Jehn, Multicomponent and multiphase hard coatings for tribological applications. *Surf. Coat. Tech.*, 131 (2000) p. 433.
103. W. D. Sproul, Multilayer, multicomponent, and multiphase physical vapour deposition coatings for enhanced performance. *J. Vac. Sci. Technol. A*, 12 (1994) p. 1595.
104. A. Matthews, Developments in PVD tribological coatings (IUVSTA highlights seminar-vacuum metallurgy division). *Vacuum.*, 65 (2002) p. 237.
105. J. S. Zabinski and A. A. Voevodin, Recent developments in the design, deposition, and processing of hard coatings. *J. Vac. Sci. Technol. A*, 16 (1998) p. 1890.
106. W. D. Sproul, Physical vapor deposition tool coatings. *Surf. Coat. Tech.*, 81 (1996) p. 1.
107. L. P. Ward, K. N. Strafford, C. Subramanian and T. P. Wilks, Observations on the structure, hardness and adhesion properties of a selection of multicomponent refractory element nitride coatings. *J. Mater. Proces. Technol.*, 56 (1996) p. 375.
108. E. J. Bienk, H. Reitz and N. J. Mikkelsen, Wear and friction properties of hard PVD coatings. *Surf. Coat. Technol.*, 76-77 (1995) p. 475.
109. O. Knotek, W. D. Münz, and T. Leyendecker, Industrial deposition of binary, ternary, and quaternary nitrides of titanium, zirconium, and aluminum. *J. Vac. Sci. Technol.* 5 (1987) p. 2173.
110. O. Knotek, M. Böhmer, and T. Leyendecker, On structure and properties of sputtered Ti and Al based hard compound films. *J. Vac. Sci. Technol. A*, 4 (1986) p. 2695.
111. H. Holleck and V. Schier, Multilayer PVD coatings for wear protection. *Surf. Coat. Technol.*, 76 (1995) p. 328.
112. S. Yang, E. Wiemann and D. G. Teer, The properties and performance of Cr-based multilayer nitride hard coatings using unbalanced magnetron sputtering and elemental metal targets. *Surf. Coat. Technol.*, 188-189 (2004) p. 662.
113. J. Deng and M. Braun, DLC multilayer coatings for wear protection. *Diamond Rel. Mater.*, 4 (1995) p. 936.
114. H. Holleck, M. Lahres, P. Woll, Multilayer coatings-influence of fabrication parameters on constitution and properties. *Surf. Coat. Technol.*, 41 (1990) p. 179.
115. M. Berger, U. Wiklund, M. Eriksson, H. Engqvist and S. Jacobson, The multilayer effect in abrasion-optimising the combination of hard and tough phases. *Surf. Coat. Technol.*, 116-119 (1999) p. 1138.
116. S. J. Bull, A. M. Jones, Multilayer coatings for improved performance. *Surf. Coat. Technol.*, 78 (1996) p. 173.
117. P. E. Hovsepian, D. B. Lewis and W. D. Munz, Recent progress in large-scale manufacturing of multilayer/superlattice hard coatings. *Surf. Coat. Technol.*, 133-134 (2000) p. 166.
118. Q. Yang and L. R. Zhao Dry sliding wear of magnetron sputtered TiN/CrN superlattice coatings. *Surf. Coat. Technol.*, 173 (2003) p. 58.

119. X. Zeng, S. Zhang and J. Hsieh, Development of graded CrTiN coatings. *Surf. Coat. Technol.*, 102 (1998) p. 108.
120. C. Fernández-Ramos, J. C. Sánchez-López, A. Justo, T. C. Rojas, I. Papst, F. Hofer and A. Fernández, Microstructural characterization of Ti-TiN/CN_x gradient-multilayered coatings. *Surf. Coat. Technol.*, 180-181 (2004) p. 526
121. A. A. Voevodin, M.A. Capano, S. J. P. Laube, M.S. Donley and J.S. Zabinski, Design of a Ti/TiC/DLC functionally gradient coating based on studies of structural transitions in Ti-C thin films. *Thin Solid Films.*, 298 (1997) p. 107.
122. A. A. Voevodin, J. M. Schneider, C. Rebholz and A. Matthews, Multilayer composite ceramic-metal-DLC coatings for sliding wear applications. *Tribol. Int.*, 29 (1996) p. 559.
123. K. L. Choy and E. Felix, Functionally graded diamond-like carbon coatings on metallic substrates. *Mater. Sci. Eng. A*, 278 (1999) p. 162.
124. X. Qiao, Y. Hou, Y. Wu and J. Chen, Study on functionally gradient coatings of Ti-Al-N. *Surf. Coat. Technol.*, 131 (2000) p. 462.
125. K. E. Cooke, S. Yang, C. Selcuk, A. Kennedy, D. G. Teer and D. Beale, Development of duplex nitrided and closed field unbalanced magnetron sputter ion plated CrTiAlN-based coatings for H13 aluminium extrusion dies. *Surf. Coat. Tech.*, 188-189 (2004) p. 697.
126. J. C. A. Batista, C. Godoy, V. T. L. Buono and A. Matthews, Characterisation of duplex and non-duplex (Ti, Al)N and Cr-N PVD coatings. *Mater. Sci. Eng. A*, 336 (2002) p. 39.
127. M. H. Staia, A. Fragieli, S. P. Brühl, J. N. Feugeas and B. J. Gomez, Behavior of the pulsed ion nitrided AISI 4140 steel/CVD TiN coatings as tribological pair. *Thin Solid Films.*, 377-378 (2000) p. 650.
128. J. P. Celis, D. Drees, M. Z. Huq, P. Q. Wu and M. De Bonte, Hybrid processes — a versatile technique to match process requirements and coating needs. *Surf. Coat. Tech.*, 113 (1999) p. 165.
129. O. H. Kessler, F. T. Hoffmann and P. Mayr, Combinations of coating and heat treating processes: establishing a system for combined processes and examples. *Surf. Coat. Tech.*, 108-109 (1998) p. 211.
130. T. Bell, H. Dong and Y. Sun, Realizing the potential of duplex surface engineering. *Tribol. Int.*, 31 (1998) p. 127.
131. H. Dong, Y. Sun and T. Bell, Enhanced corrosion resistance of duplex coatings. *Surf. Coat. Tech.*, 90 (1997) p. 91.
132. Y. Sun and T. Bell, Plasma surface engineering of low alloy steel. *Mater. Sci. Eng. A*, 140 (1991) p. 419.
133. M. Zlatanovic, Deposition of (Ti,Al)N coatings on plasma nitrided steel. *Surf. Coat. Technol.*, 48 (1991) p. 19.
134. S. C. Tjong and H. Chen Nanocrystalline materials and coatings. *Mater. Sci. Eng. R*, 45 (2004) p. 1.
135. S. Zhang, D. Sun, Y. Fu and H. Du, Recent advances of superhard nanocomposite coatings: a review. *Surf. Coat. Technol.*, 167 (2003) p. 113.
136. J. He and J. M. Schoenung, Nanostructured coatings. *Mater. Sci. Eng. A*, 336 (2002) p. 274.
137. S. Veprek, P. Nesládek, A. Niederhofer, F. Glatz, M. Jílek and M. Sítma, Recent progress in the superhard nanocrystalline composites: towards their industrialization and understanding of the origin of the superhardness. *Surf. Coat. Technol.*, 108-109 (1998) p. 138.
138. A. A. Voevodin, J. P. O'Neill and J. S. Zabinski, Nanocomposite tribological coatings for aerospace applications. *Surf. Coat. Technol.*, 116/119 (1999) p. 36.
139. J.-H. Wu, D.A. Rigney, M.L. Falk, J.H. Sanders, A.A. Voevodin and J.S. Zabinski, Tribological behavior of WC/DLC/WS₂ nanocomposite coatings. *Surf. Coat. Technol.*, In Press (2004).

140. A. A. Voevodin, T. A. Fitz, J. J. Hu, and J. S. Zabinski, Nanocomposite tribological coatings with "chameleon" surface adaptation. *J. Vac. Sci. Technol. A*, 20 (2002) p. 1434.
141. A. A. Voevodin, J. J. Hu, T. A. Fitz and J. S. Zabinski, Tribological properties of adaptive nanocomposite coatings made of yttria stabilized zirconia and gold. *Surf. Coat. Technol.*, 146-147 (2001) p. 351.
142. F. Vaz, J. Ferreira, E. Ribeiro, L. Rebouta, S. Lanceros-Méndez, J. A. Mendes, E. Alves, Ph. Goudeau, J. P. Rivière, F. Ribeiro et al., Influence of nitrogen content on the structural, mechanical and electrical properties of TiN thin films. *Surf. Coat. Technol.*, In Press (2004).
143. B. F. Chen, W. L. Pan, G. P. Yu, J. Hwang and J. H. Huang, On the corrosion behavior of TiN-coated AISI D2 steel. *Surf. Coat. Technol.*, 111 (1999) p. 16.
144. P. V. Kola, S. Daniels, D. C. Cameron and M. S. J. Hashmi. Magnetron sputtering of tin protective coatings for medical applications. *J. Mater. Proces. Technol.*, 56 (1996) p. 422.
145. R. D. Arnell, J. S. Colligon, K. F. Minnebaev and V. E. Yurasova, The effect of nitrogen content on the structure and mechanical properties of TiN films produced by magnetron sputtering. *Vacuum.*, 47 (1996) p. 425.
146. P. Patsalas, C. Charitidis and S. Logothetidis. The effect of substrate temperature and biasing on the mechanical properties and structure of sputtered titanium nitride thin films. *Surf. Coat. Technol.*, 125 (2000) p. 335.
147. H. Oechsner Process controlled microstructural and binding properties of hard physical vapor deposition films. *J. Vac. Sci. Technol. A*, 16 (1998) p. 1956.
148. V. Valvoda, Structure of thin films of titanium nitride. *J. Alloys Compounds*, 219 (1995) p. 83.
149. R. Hübler, Transition metal nitrides thin films deposition using a dynamically controlled magnetron sputtering apparatus. *Surf. Coat. Technol.*, 158-159 (2002) p. 680.
150. J. Takadom and H. H. Bennani, Influence of substrate roughness and coating thickness on adhesion, friction and wear of TiN films. *Surf. Coat. Technol.*, 96 (1997) p. 272.
151. S. Wilson and A. T. Alpas TiN coating wear mechanisms in dry sliding contact against high speed steel. *Surf. Coat. Technol.*, 108-109 (1998) p. 369.
152. H. Ljungcrantz, M. Oden, L. Hultman, J. E. Greene and J.-E. Sundgren, Nanoindentation studies of single-crystal (001)-, (011)-, and (111)-oriented TiN layers on MgO. *J. Appl. Phys.*, 80 (1996) p. 6725.
153. P. Roquiny, F. Bodart and G. Terwagne, Colour control of titanium nitride coatings produced by reactive magnetron sputtering at temperature less than 100°C. *Surf. Coat. Technol.*, 116-119 (1999) p. 278.
154. Q. Fang and J. -Y. Zhang, Nano-porous TiN thin films deposited by reactive sputtering method. *Int. J. Inorganic Mater.*, 3 (2001) p. 1193.
155. J.-H. Huang, K.-W. Lau and G.-P. Yu, Effect of nitrogen flow rate on structure and properties of nanocrystalline TiN thin films produced by unbalanced magnetron sputtering. *Surf. Coat. Technol.*, In Press (2004).
156. J. Kohlscheen, H. -R. Stock and P. Mayr, Substoichiometric titanium nitride coatings as machinable surfaces in ultraprecision cutting. *Surf. Coat. Technol.*, 120-121 (1999) p. 740.
157. S. Yang, D. B. Lewis, I. Wadsworth, J. Cawley, J. S. Brooks and W. D. Münz Investigation of substoichiometric titanium nitride grown by unbalanced magnetron sputtering. *Surf. Coat. Technol.*, 131 (2000) p. 228.
158. S. PalDey and S. C. Deevi, Single layer and multilayer wear resistant coatings of (Ti,Al)N: a review. *Mater. Sci. Eng. A*, 342 (2003) p. 58
159. E. Arslan and İ. Efeoğlu, Effect of heat treatment on TiN films deposited by CFUBMS. *Mater. Characterization.*, 53 (2004) p. 29
160. H. K. Tonshoff and A. Mohlfeld, PVD-Coatings for wear protection in dry cutting operations. *Surf. Coat. Tech.*, 93 (1997) p. 88.

161. T. Cselle and A. Barimani, Today's applications and future developments of coatings for drills and rotating cutting tools. *Surf. Coat. Technol.*, 76-77 (1995) p. 712.
162. G. Byrne, Environmentally Clean Machining Processes, A strategic Approach. *Annals of CIRP*, (1993), p. 42.
163. P. Sutor, Solid lubricants: overview and recent developments. *MRS Bull.*, (1991) p. 24.
164. J. -P. Hirvonen, J. Koskinen, J. R. Jervis and M. Nastasi, Present progress in the development of low friction coatings. *Surf. Coat. Technol.*, 80 (1996) p. 139.
165. T. Spalvins, A review of recent advances in solid film lubrication. *J. Vac. Sci. Technol. A*, 5 (1987) p. 212.
166. A. R. Lansdown, Molybdenum Disulphide Lubrication. *Tribology series*, 35, D. Dowson 230. (Ed.) (1999) p. 380.
167. H. Waghay, T. S. Lee and B. J. Tatarchuk, A study of the tribological and electrical properties of sputtered and burnished transition metal dichalcogenide films. *Surf. Coat. Technol.*, 76/77 (1995) p. 415.
168. T. Le Mogne, C. Donnet, J. M. Martin, A. Tonck and N. Millard Pinard, Nature of super-lubricating MoS₂ physical vapor deposition coatings. *J. Vac. Sci. Technol. A*, 12 (1994) p. 1998.
169. P. D. Fleischauer, Fundamental aspects of the electronic structure, materials properties and lubrication performance of sputtered MoS₂ films. *Thin Solid Films.*, 154 (1987) p. 309.
170. G. Jayaram, N. Doraiswamy, L. D. Marks and M.R. Hilton, Ultrahigh vacuum high resolution transmission electron microscopy of sputter-deposited MoS₂ thin films. *Surf. Coat. Technol.*, 68/69 (1994) p. 439.
171. J. Moser, F. Levy and F. Bussy, Composition and growth mode of MoS_x sputtered films. *J. Vac. Sci. Technol. A*, 12 (1994) p. 494.
172. J. A. Obeng and G. L. Schrader, Reactive sputtering of molybdenum sulfide thin films. *Surf. Coat. Technol.*, 68-69 (1994) p. 422.
173. E. W. Roberts, and W. B. Price, In vacuo, tribological properties of "high-rate" sputtered MoS₂ applied to metal and ceramic substrates. *Mat. Res. Soc.*, 140 (1989) p. 251.
174. A. Aubert, J. Ph. Nabot, J. Ernoult and Ph. Renaux, Preparation and properties of MoS_x films grown by d.c. magnetron sputtering. *Surf. Coat. Technol.*, 41 (1990) p. 127.
175. J. Rechberger, P. Brunner and R. Dubach, High performance cutting tools with a solid lubricant physically vapour deposited coating. *Surf. Coat. Technol.*, 62 (1993) p. 393.
176. J. Wang, W. Lauwerens, E. Wieers, L. M. Stals, J. He and J. P. Celis. Effect of power mode, target type and liquid nitrogen trap on the structure and tribological properties of MoS_x coatings, *Surf. Coat. Technol.*, 153 (2002) p. 166.
177. M. R. Hilton, P. D. Fleischauer, Applications of solid lubricant films in spacecraft. *Surf. Coat. Technol.*, 54-55 (1992) p. 435.
178. S. V. Didziulis, P. D. Fleischauer, B. L. Soriano and M. N. Gardos, Chemical and tribological studies of MoS₂ films on SiC substrates. *Surf. Coat. Technol.*, 43/44 (1990) p. 652.
179. J. R. Lince. MoS_{2-x}O_x solid solutions in thin films produced by RF-sputter-deposition. *J. Mater. Res.*, 5 (1990) p. 218.
180. M. R. Hilton and P. D. Fleischauer, TEM lattice imaging of the nanostructure of early-growth sputter-deposited MoS₂ solid lubricant films. *J. Mater. Res.*, 5 (1990) p. 406.
181. G. Weise, A. Teresiak, I. Bacher, P. Markschlager and G. Kampschulte, Influence of magnetron sputtering process parameters on wear properties of steel/Cr₃Si or Cr/MoS_x. *Surf. Coat. Technol.*, 76/77 (1995) p. 382.
182. F. Levy and J. Moser, High-resolution cross-sectional studies and properties of molybdenite coatings. *Surf. Coat. Technol.*, 68/69 (1994) p. 433.
183. M. R. Hilton, Fracture in MoS₂ solid lubricant films. *Surf. Coat. Technol.*, 68/69 (1994) p. 407.

184. J. Nabot, A Aubert, R. Gillet, P. Renaux, Cathodic sputtering for preparation of lubrication films. *Surf. Coat. Technol.*, 43/44 (1990) p. 629.
185. W. Lauwerens, Jihui Wang, J. Navratil, E. Wieërs, J. D'haen, L. M. Stals, J. P. Celis and Y. Bruynseraede, Humidity resistant MoS_x films prepared by pulsed magnetron sputtering. *Surf. Coat. Technol.*, 131 (2000) p. 216.
186. H. Dimingen, H. Hübsch, P. Willich and K. Reichelt. Stoichiometry and friction properties of sputtered MoS_x layers. *Thin Solid Films.*, 12 (1985) p. 79.
187. J. L. Grosseau-Poussard, P. Moine and J. P. Villain, Microstructural and tribological characterization of MoS_x coatings produced by high-energy ion-beam-assisted deposition. *Thin Solid Films.*, 224 (1993) p. 52.
188. J. R. Lince, M. R. Hilton and A. S. Bommannavar, EXAFS of sputter-deposited MoS₂ films. *Thin Solid Films.*, 264 (1995) p. 120.
189. H. Dimigen and H. Hubsch, Applying low-friction wear-resistant thin solid films by physical vapour deposition. *Philips. Technol. Rev.*, 41 (1983) p. 186.
190. J. R. Lince, M. R. Hilton and A.S. Bommannavar, Oxygen substitution in sputter-deposited MoS₂ films studied by extended X-ray absorption fine structure, X-ray photoelectron spectroscopy and X-ray diffraction. *Surf. Coat. Technol.*, 43/44 (1990) p. 640.
191. J. M. Martin, C. Donnet and T. Le Monge, Superlubricity of molybdenum disulphide. *Physical Review B*, 48 (1993) p. 10583.
192. J. M. Martin, H. Pascal, C. Donnet, Th. Le Mogne, J. L. Loubet and Th. Epicier. Superlubricity of MoS₂: crystal orientation mechanisms. *Surf. Coat. Technol.*, 68-69 (1994) p. 427.
193. V. Bellido-Gonzales, A. H. S. Jones, J. Hampshire, T. J. Allen, J. Witts, D. G. Teer, K. J. Ma and D. Upton, Tribological behaviour of high performance MoS₂ coatings produced by magnetron sputtering. *Surf. Coat. Technol.*, 97 (1997) p. 687.
194. E. W. Roberts, B. J. Williams and J. A. Ogilvy, Effect of substrate surface roughness on the friction and wear of sputtered MoS₂ films. *J. Phys. D: Appl. Phys.*, 25 (1992) p. A65.
195. E. W. Roberts, Thin solid lubricant films in space. *Tribol. Int.*, 23 (1990) p. 95.
196. E. W. Roberts, Towards an optimized sputtered MoS₂ lubricant film. *Proc. 20th AMS. NASA Lewis, Cleveland, NASA publications 2423, (1986) p. 103.*
197. P. Niederhauser, M. Maillat, H.E. Hintermann, Moisture resistant MoS₂-based composite lubricant coatings. *Proc. First European Symposium on Space Mechanisms and Tribology, Neuchâtel, Switzerland, ESA SP-196 (1983) p. 119.*
198. S. Fayeulle, P D. Ehni, and I L. Singer, Role of transfer films in wear of MoS₂ coatings. In: *Mechanics of coatings*. Dowson D & al. eds, Tribology series 17, Elsevier, Amsterdam, (1990) p. 129.
199. N. J. Mikkelsen, G.Sorensen, Ion beam modification of MoS_x films on metals. *Mater. Sci. Eng. A*, A115 (1989) p. 343.
200. T. Spalvins, NASA TN D-7169 (1973).
201. R. Hauert, An overview on the tribological behavior of diamond-like carbon in technical and medical applications. *Tribol. Int.*, 37 (2004) p. 991.
202. B. C. Stupp, Synergistic effects of metals co-sputtered with MoS₂. *Thin Solid Films.*, 84 (1981) p. 257.
203. M. R. Hilton, G. Jayaram and L.D. Marks, Microstructure of cosputter-deposited metal- and oxide-MoS₂ solid lubricant films. *J. Mater. Res.*, 13 (1998) p. 1022.
204. S. K. Kim, Young Hwan Ahn and Kwang Ho Kim. MoS₂-Ti composite coatings on tool steel by d.c. magnetron sputtering. *Surf. Coat. Tech.*, 169-170 (2003) p. 428.
205. V. Rigato, G. Maggioni, A. Patelli, D. Boscarino, N. M. Renevier and D. G. Teer, Properties of sputter-deposited MoS₂/metal composite coatings deposited by closed field unbalanced magnetron sputter ion plating. *Surf. Coat. Tech.*, (2000) p. 206.

206. N. M. Renevier, V. C. Fox, D. G. Teer and J. Hampshire, Coating characteristics and tribological properties of sputter-deposited MoS₂/metal composite coatings deposited by closed field unbalanced magnetron sputter ion plating. *Surf. Coat. Tech.*, 127 (2000) p. 24.
207. M. C. Simmonds, A. Savan, E. Pflüger and H. Van Swygenhoven, Mechanical and tribological performance of MoS₂ co-sputtered composites. *Surf. Coat. Tech.*, 126 (2000) p. 15.
208. I. Bertóti, M. Mohai, N. M. Renevier and E. Szilágyi, XPS investigation of ion beam treated MoS₂-Ti composite coatings. *Surf. Coat. Tech.*, 125 (2000) p. 173.
209. J. H. W. Siu and Lawrence K. Y. Li, An investigation of the effect of surface roughness and coating thickness on the friction and wear behaviour of a commercial MoS₂-metal coating on AISI 400C steel. *Wear.*, 237 (2000) p. 283.
210. D. G. Teer, V. Bellido-Gonzalez, J. Hampshire and V. Fox, The tribological properties of MoS₂/metal composite coatings deposited by closed field magnetron sputtering. *Surf. Coat. Tech.*, 94-95 (1997) p. 572.
211. D. Y. Wang, C.-L Chang, Z.-Y. Chen and W.-Y. Ho, Microstructural and tribological characterization of MoS₂-Ti composite solid lubricating films. *Surf. Coat. Tech.*, 120-121 (1999) p. 629.
212. D. G. Teer, New solid lubricant coatings. *Wear.*, 251 (2001) p. 1068.
213. N. M. Renevier, J. Hampshire, V. C. Fox, J. Witts, T. Allen and D. G. Teer, Advantages of using self-lubricating, hard, wear-resistant MoS₂-based coatings. *Surf. Coat. Tech.*, 142-144 (2001) p. 67.
214. N. M. Renevier, V. C. Fox, D. G. Teer and J. Hampshire, Performance of low friction MoS₂/titanium composite coatings used in forming applications. *Mater. Des.*, 21 (2000) p. 337.
215. V. C. Fox, N. Renevier, D. G. Teer, J. Hampshire and V. Rigato, The structure of tribologically improved MoS₂-metal composite coatings and their industrial applications. *Surf. Coat. Tech.*, 116-119 (1999) p. 492.
216. W. H. Kao, Tribological properties and high speed drilling application of MoS₂-Cr coatings. *Wear*, In Press (2004).
217. W. H. Kao and Y. L. Su, Optimum MoS₂-Cr coating for sliding against copper, steel and ceramic balls. *Mater. Sci. Eng. A*, 368 (2004) p. 239.
218. T. Spalvins, Frictional and morphological properties of Au-MoS₂ films sputtered from a compact target. *Thin Solid Films.*, 118 (1984) p. 375.
219. B. C. Stupp, Air Force Tribology. Technical Review (1989) p. 592.
220. J. J. Nainaparampil, A. R. Phani, J. E. Krzanowski and J. S. Zabinski, Pulsed laser-ablated MoS₂-Al films: friction and wear in humid conditions. *Surf. Coat. Tech.*, 187 (2004) p. 326.
221. P. Niederhäuser, H.E. Hintermann and M. Maillat, Moisture-resistant MoS₂-based composite lubricant films. *Thin Solid Films.*, 108 (1983) p. 209.
222. D.-Y. Yu, J. -A. Wang and J. -L. O. Yang, Variations of properties of the MoS₂-LaF₃ cosputtered and MoS₂-sputtered films after storage in moist air. *Thin Solid Films.*, 293 (1997) p. 1.
223. M. R. Hilton, R. Bauer, S. V. Didziulis, M. T. Dugger, J. Keem and J. Scholhamer, Structural and tribological studies of MoS₂ solid lubricant films having tailored metal-multilayer nanostructures. *Surf. Coat. Tech.*, 53 (1992) p. 13.
224. M. C. Simmonds, A. Savan, H. Van Swygenhoven and E. Pflüger, Characterisation of magnetron sputter deposited MoS_x/metal multilayers. *Thin Solid Films.*, 354 (1999) p. 59.
225. M. C. Simmonds, A. Savan, H. Van Swygenhoven, E. Pflüger and S. Mikhailov, Structural, morphological, chemical and tribological investigations of sputter deposited MoS_x/metal multilayer coatings. *Surf. Coat. Tech.*, 108-109 (1998) p. 340.
226. S. Mikhailov, A. Savan, E. Pflüger, L. Knoblauch, R. Hauert, M. Simmonds, and H. Van Swygenhoven, Morphology and tribological properties of metal (oxide)-MoS₂ nanostructured multilayer coatings. *Surf. Coat. Tech.*, 105 (1998) p. 175.

227. S. Watanabe, J. Noshiro and S. Miyake, Tribological characteristics of WS₂/MoS₂ solid lubricating multilayer films. *Surf. Coat. Tech.*, 183, (2004) p. 347.
228. S. K. Field, M. Jarratt and D. G. Teer, Tribological properties of graphite-like and diamond-like carbon coatings. *Tribol. Int.*, 37 (2004) p. 949.
229. D. Babonneau, T. Cabioch, A. Naudon, J. C. Girard and M. F. Denanot, Silver nanoparticles encapsulated in carbon cages obtained by co-sputtering of the metal and graphite. *Surf. Sci.*, 409 (1998) p.358.
230. S. Yang, A. H. S. Jones and D. G. Teer, The development of sputtered carbon based coatings incorporating Cr, Ti, B and N. *Surf. Coat. Tech.*, 133-134 (2000) p. 369.
231. R. Gadow and D. Scherer, Composite coatings with dry lubrication ability on light metal substrates. *Surf. Coat. Technol.*, 151-152 (2002) p. 471.
232. G. Xu, Z. Zhou, J. Liu and X. Ma, An investigation of fretting behavior of ion-plated TiN, magnetron-sputtered MoS₂ and their composite coatings. *Wear.*, 225-229 (1999) p. 46.
233. Z. Daming, L. Jiajun, Z. Baoliang and L. Wenzhi, A study of the friction and wear performance of MoS_x thin films produced by ion beam enhanced deposition and magnetron sputtering. *Wear.*, 210 (1997) p. 45.
234. V. Imbeni, C. Martini, E. Lanzoni, G. Poli and I. M. Hutchings, Tribological behaviour of multi-layered PVD nitride coatings. *Wear*, 251 (2001) p. 997.
235. L. E. Seitzman, R. N. Bolster, I. L. Singer, X-ray-diffraction of MoS₂ coatings prepared by ion-beam-assisted deposition. *Surf. Coat. Tech.*, 52 (1992) p. 93.
236. M. Lahres, O. Doerfel and R. Neumüller, Applicability of different hard coatings in dry machining an austenitic steel. *Surf. Coat. Tech.*, 120-121 (1999) p. 687.
237. D. Y. Wang, C. L. Chang and W. Y. Ho, Microstructure analysis of MoS₂ deposited on diamond-like carbon films for wear improvement. *Surf. Coat. Tech.*, 111 (1999) p. 123.
238. H. Kuwano and K. Nagai, Friction-reducing coatings by dual fast atom beam technique. *J. Vac. Sci. Technol. A*, 4 (1986) p. 2993.
239. S. Carrera, O. Salas, J. J. Moore, A. Woolverton and E. Sutter, Performance of CrN/MoS₂(Ti) coatings for high wear low friction applications. *Surf. Coat. Tech.*, 167 (2003) p. 25.
240. V. Derflinger, H. Brändle and H. Zimmermann, New hard/lubricant coating for dry machining. *Surf. Coat. Tech.*, 113 (1999) p. 286.
241. B. Navinsek, P. Panjan, M. Cekada and D. T. Quinto, Interface characterization of combination hard/solid lubricant coatings by specific methods. *Surf. Coat. Tech.*, 154 (2002) p. 194.
242. A. Srivastav, A. Kapoor and J. P. Pathak, The role of MoS₂ in hard overlay coatings of Al₂O₃ in dry sliding. *Wear*, 155 (1992) p. 229.
243. Y. W. Bae, W. Y. Lee, T. M. Besmann, C.S. Yust and P.J. Blau, Preparation and friction characteristics of self-lubricating TiN-MoS₂ composite coatings. *Mater. Sci. Eng. A*, 209 (1996) p. 372.
244. Y. W. Bae, W. Y. Lee, C. S. Yust, P. J. Blau and T. M. Besmann, Synthesis and friction behavior of chemically vapor deposited composite coatings containing discrete TiN and MoS₂ phases. *J. Am. Ceram. Soc.*, 79 (1996) p. 819.
245. R. Gilmore, M. A. Baker, P. N. Gibson, W. Gissler, M. Stoiber, P. Losbichler and C. Mitterer, Low-friction TiN-MoS₂ coatings produced by dc magnetron co-deposition. *Surf. Coat. Tech.*, 108-109 (1998) p. 345.
246. Y. Jing, J. Luo and S. Pang, Effect of Ti or TiN codeposition on the performance of MoS₂-based composite coatings. *Thin Solid Films.*, 461 (2004) p. 288.
247. R. Goller, P. Torri, M. A. Baker, R. Gilmore and W. Gissler, The deposition of low-friction TiN-MoS_x hard coatings by a combined arc evaporation and magnetron sputter process. *Surf. Coat. Tech.*, 120-121 (1999) p. 453.

248. P. Cosemans, X. Zhu, J. P. Celis and M. Van Stappen, Development of low friction wear-resistant coatings. *Surf. Coat. Tech.*, 174-175 (2003) p. 416.
249. C. Heinisch, K. Piplits, F. Kubel, A. Schintlmeister, E. Pflüger and H. Hutter, SIMS investigation of MoS₂ based sputtercoatings. *Appl. Surf. Sci.*, 179 (2001) p. 270.
250. R. Gilmore, M. A. Baker, P. N. Gibson and W. Gissler, Preparation and characterisation of low-friction TiB₂-based coatings by incorporation of C or MoS₂. *Surf. Coat. Tech.*, 105 (1998) p. 45.
251. R. Gilmore, M. A. Baker, P. N. Gibson and W. Gissler, Comparative investigation of multilayer TiB₂/C and co-sputtered TiB₂-C coatings for low-friction applications. *Surf. Coat. Tech.*, 116-119 (1999) p. 1127.
252. M. A. Baker, R. Gilmore, C. Lenardi, P. N. Gibson and W. Gissler, Microstructure and mechanical properties of multilayer TiB₂/C and co-sputtered TiB₂-C coatings for cutting tools. *Vacuum.*, 53 (1999) p. 113.
253. M. Steinmann, A. Müller and H. Meerkamm, A new type of tribological coating for machine elements based on carbon, molybdenum disulphide and titanium diboride. *Tribol. Int.*, 37 (2004) p. 879.
254. M. Stüber, H. Leiste, S. Ulrich, H. Holleck and D. Schild, Microstructure and properties of low friction TiC-C nanocomposite coatings deposited by magnetron sputtering. *Surf. Coat. Tech.*, 150 (2002) p. 218.
255. J. L. Endrino, J. J. Nainaparampil and J. E. Krzanowski, Magnetron sputter deposition of WC-Ag and TiC-Ag coatings and their frictional properties in vacuum environments. *Scripta Materialia*, 47 (2002) p. 613.
256. T. de los Arcos, P. Oelhafen, U. Aebi, A. Hefti, M. Düggelin, D. Mathys and R. Guggenheim, Preparation and characterization of TiN-Ag nanocomposite films. *Vacuum.*, 67 (2002) p. 463.
257. J. L. Endrino, J. J. Nainaparampil and J. E. Krzanowski, Microstructure and vacuum tribology of TiC-Ag composite coatings deposited by magnetron sputtering-pulsed laser deposition. *Surf. Coat. Technol.*, 157 (2002) p. 95.
258. H. S. Myung, Hyuk M. Lee, Leonid R. Shaginyan and J. G. Han, Microstructure and mechanical properties of Cu doped TiN superhard nanocomposite coatings. *Surf. Coat. Technol.*, 163-164 (2003) p. 591.
259. E. Badisch, G. A. Fontalvo and C. Mitterer, The response of PACVD TiN coatings to tribological tests with different counterparts. *Wear.*, 256 (2004) p. 95.
260. A. A. Voevodin, J. Bultman and J. S. Zabinski, Investigation into three-dimensional laser processing of tribological coatings. *Surf. Coat. Tech.*, 107 (1998) p. 12.
261. S. R. Bradbury and T. Huyanan, Challenges facing surface engineering technologies in the cutting tool industry. *Vacuum.*, 56, (2000) p. 173.
262. R. Hauert and U. Müller, An overview on tailored tribological and biological behavior of diamond-like carbon. *Diamond Related Mater.*, 12 (2003) p. 171.
263. V. C Fox, A. Jones, N. M. Renevier, and D. G. Teer, Hard lubricating coatings for cutting and forming tools and mechanical components. *Surf. Coat. Tech.*, 125 (2000) p. 347.
264. N. M Renevier, N. Lobiondo, V. C Fox, D. G Teer and J. Hampshire, Performance of MoS₂/metal composite coatings used for dry machining and other industrial applications. *Surf. Coat. Tech.*, 123 (2000) p. 84.
265. N. M. Renevier, H. Oosterling, U. König, H. Dautzenberg, B. J. Kim, L. Geppert, F. G. M. Koopmans and J. Leopold, Performance and limitations of MoS₂/Ti composite coated inserts. *Surf. Coat. Tech.*, 172 (2003) p. 13.
266. H. L. Coldwell, R. C. Dewes, D. K. Aspinwall, N. M. Renevier and D. G. Teer, The use of soft/lubricating coatings when dry drilling BS L168 aluminium alloy. *Surf. Coat. Tech.*, 177-178, (2004) p. 716.

267. M. Goto, A. Kasahara, M. Tosa, J. Hobley, M. Kishimoto, K. Yoshihara, and H. Fukumura, Low frictional coating by cosputtering in combination with excimer laser irradiation for aerospace applications. *J. Vac. Sci. Technol.*, 20 (2002) p. 1458.
268. A. Erdemir, Review of engineered tribological interfaces for improved boundary lubrication. *Tribol. Int.*, In Press (2004).
269. A. Matthews, R. J. Hartley, P. Holiday, and P. R. Stevenson, *The UK Engineering Coatings Industry in 2005*. University of Hull Press, Hull (1992).
270. P. V. Kola, Magnetron sputtering of thin nitriding films. PhD. Thesis, Dublin City University, Ireland, (1995).
271. M. J. Murphy, Planar sputter magnetron technology. PhD. Thesis, Dublin City University, Ireland, (1996).
272. C. Eisenmenger-Sittner, Condensation and structure of multiphase thin films. *Vacuum.*, 61 (2001) p. 183.
273. B. Rother, H. A. Jehn and H. M. Gabriel, Multilayer hard coatings by coordinated substrate rotation modes in industrial PVD deposition systems. *Surf. Coat. Technol.*, 86-87 (1996) 207.
274. H. A. Jehn and B. Rother, Homogeneity of multi-component PVD hard coatings deposited by multi-source arrangements. *Surf. Coat. Technol.*, 112 (1999) p. 103.
275. B. Rother, G. Ebersbach and H. M. Gabriel, Substrate-rotation systems and productivity of industrial PVD processes. *Surf. Coat. Technol.*, 116-119 (1999) p. 694.
276. D. M. Kennedy, Dynamic abrasion resistance of advanced coating systems. PhD. Thesis, Dublin City University, Ireland (1995).
277. N. Dombrowski, E.A. Foumeny, A. Riza, Know the CFD codes, *Chem. Eng. Prog.*, 89 (1993) p. 46.
278. H. P. Langtangen, K.-A Mardal and R. Winther, Numerical methods for incompressible viscous flow. *Adv. Water Resour.*, 25 (2002) p. 1125.
279. TECHNICAL BRIEF: Selected Benchmarks from Commercial CFD Codes. ASME newsletter, Fluids Engineering division.
<http://www.asme.org/divisions/fed/newsletter/techbriefs.html>
280. M. Gad-el-Hak, Flow physics in MEMS. *Mécanique & Industries*, 2 (2001) p. 313.
281. G. Scherer, On the numerical modelling of the transitional flow in rarefied gases. *J. Comput. Appl. Math.*, 10 (1999) p. 165.
282. R. W. Barber, D. R. Emerson and X. J. Gu, Rarefied Gas Dynamics in Micro-Devices. Centre for Microfluidics, Computational Science and Engineering Department, Daresbury Laboratory, Daresbury, Warrington, U.K.
283. G. A. Bird, *Molecular Gas Dynamics and the Direct Simulation of Gas Flows*. Oxford University Press, New York, (1994).
284. C. E. Glass and T J. Horvath, Comparison of a 3-D CFD-DSMC solution methodology with a wind tunnel experiment, *AIP Conf. Proc.*, 663 (2003) p. 441.
285. M. Ikegawa and J. Kobayashi, Deposition profile simulation using the direct simulation Monte Carlo method. *J. Electrochem. Soc.*, 136 (1989) p. 2983.
286. A. G. Coronell, K. F. Jensen, Analysis of transition regime flows in low pressure chemical deposition reactors using the direct simulation Monte Carlo method. *J. Electrochem. Soc.* 139 (1992) p. 2264.
287. D. E. Kotecki, Richard A. Conti, S. G. Barbee, T. D. Cacouris, J. D. C. Sokol, R. J. Eschbach, D. L. Wilson, J. Wong, and S. P. Zuhoski, Applications of computational fluid dynamics for improved performance in chemical-vapor-deposition reactors. *J. Vac. Sci. Tech. B*, 12 (1994) p. 2752.
288. Ana N. R. da Silva, N. I. Morimoto, Gas Flow Simulation in a PECVD Reactor. Technical Proceedings of the Fifth International Conference on Modeling and Simulation of Microsystems, San Juan, Puerto Rico (2002) p.434.

289. T. Theiler, N. Sacher and B. Froeschle, TiN barriers for high-k capacitors: simulations and experimental results. *Microelectron. Eng.*, 56 (2001) p. 181
290. H. Wolf, J. Röber, S. Riedel, R. Streiter and T. Gessner, Process and equipment simulation of copper chemical vapor deposition using Cu(hfac)vtms. *Microelectron. Eng.*, 45 (1999) p. 15.
291. F. de Jong and M. Meyyappan, Numerical simulation of silicon carbide chemical vapor deposition. *Diam. Relat. Mater.*, 5 (1996) p. 141.
292. T. G. Mihopoulos, S. G. Hummel, K. F. Jensen, Simulation of flow and growth phenomena in a close-spaced reactor. *J. Cryst. Growth.*, 195 (1998) p. 725.
293. S. Desa, S. Ghosal, R. L. Kosut, J. L. Ebert, T. E. Abrahamson, A. Kozak, D. W. Zou, X. Zhou, J. F. Groves, and H. N. G. Wadley, Reactor-scale models for rf diode sputtering of metal thin films. *J. Vac. Sci. Tech. A*, 17 (1999) p. 1926.
294. J. W. Bradley, R. D. Arnell and D. G. Armour, Measurement and modelling of the bulk plasma in magnetron sputtering sources. *Surf. Coat. Technol.*, 97 (1997) p. 538.
295. H. M. Urbassek, Molecular-dynamics simulation of sputtering. *Nucl. Instrum. Methods. Phys. Res. Sect. B*, 122 (1997) p. 427.
296. M. H. Shapiro, Using molecular dynamics simulations to investigate surface modification processes. *Surf. Coat. Technol.*, 103-104 (1998) p. 1.
297. F. Yan, Numerical Simulations of High Knudsen Number Gas Flows and Microchannel Electrokinetic Liquid Flows. PhD. Thesis, Drexel University, USA, (2003).
298. C. H. Shon and J. K. Lee, Modeling of magnetron sputtering plasmas. *Appl. Surf. Sci.*, 192 (2002) p. 258.
299. T. Kobayashi, Monte Carlo simulation of gas transport in a TiN reactive sputtering apparatus for large area deposition. *Vacuum.*, 74 (2004) p. 379.
300. T. Kobayashi, Computer simulation of gas rarefaction effects and film deposition characteristics in a magnetron sputtering apparatus. *Appl. Surf. Sci.*, 169-170 (2001) p. 405.
301. L. A. Gochberg, Comparison of Navier-Stokes and DSMC Gas Flow Models in Semiconductor Process Chambers. *AIP Conf. Proc.*, 663 (2003) p. 1073.
302. S. A. Logtenberg and A. G. Dixon, Computational fluid dynamics studies of fixed bed heat transfer. *Chem. Eng. Process.*, 37 (1998) p. 7.
303. U. Goehner, H. Mauch, FLOTRAN: Numerical method and industrial applications. *Int. J. Comput. Appl. Technol.*, 11 (1998) p. 199.
304. A Dollet, Multiscale modeling of CVD film growth—a review of recent works. *Surf. Coat. Technol.*, 177-178 (2004) p. 245.
305. ANSYS CFD FLOTRAN Analysis Guide, Release 7.0, ANSYS, Inc., Houston, PA (2003).
306. M. Buchmann, R. Gadow and J. Tabellion, Experimental and numerical residual stress analysis of layer coated composites. *Mater. Sci. Eng. A*, 288 (2000) p. 154.
307. Y. Islamoglu, E. Celik, C. Parmaksizoglu and Y. S. Hascicek, Effects on residual stresses of annealing parameters in high-temperature ZrO₂ insulation coatings on Ag/Bi-2212 superconducting tapes using finite element method. *Mater. Des.*, 23 (2002) p. 531.
308. V. Teixeira, Residual stress and cracking in thin PVD coatings. *Vacuum.*, 64 (2002) p. 393.
309. K. A. Khor and Y. W. Gu, Effects of residual stress on the performance of plasma sprayed functionally graded ZrO₂/NiCoCrAlY coatings. *Mater. Sci. Eng. A*, 277 (2000) p. 64.
310. H. Ljungcrantz, L. Hultman and J. E. Sundgren, Residual stress and fracture properties of magnetron sputtered Ti films on Si microelements. *J. Vac. Sci. Technol. A*, 11 (1993) p. 543.
311. M. Ohring, *The Material Science of Thin Films*. Academic Press, New York (1991).
312. H. Oettel and R. Wiedemann, Residual stresses in PVD hard coatings. *Surf. Coat. Technol.*, 76-77 (1995) p. 265.

313. J. A. Thornton, D. W. Hoffman, Stress-related effects in thin films. *Thin Solid Films.*, 171 (1989) p. 5.
314. S. Tamulevicius, Stress and strain in the vacuum deposited thin films. *Vacuum.*, 51 (1998) p. 127.
315. M. Levit, I. Grimberg and B. -Z. Weiss, Residual stresses in ceramic plasma-sprayed thermal barrier coatings: Measurement and calculation. *Mater. Sci. Eng. A*, 206 (1996) p. 30.
316. B. Boley and J. H. Weiner. *Theory of thermal stresses*. Kreiger Publishing, Florida (1985).
317. P. Fogarassy, F. Turquier and A. Lodini, Residual stress in plasma sprayed zirconia on cylindrical components. *Mech. Mater.*, 35 (2003) p. 633.
318. J. Gunnars and U. Wiklund, Determination of growth-induced strain and thermo-elastic properties of coatings by curvature measurements. *Mater. Sci. Eng. A*, 336 (2002) p. 7.
319. C. H. Hsueh, A. G. Evans, Residual stresses in metal/ceramic bonded strips. *J. Am. Ceram. Soc.*, 68 (1985) p. 241.
320. M. Toparli, S. Sahin, E. Ozkaya and S. Sasaki, Residual thermal stress analysis in cylindrical steel bars using finite element method and artificial neural networks. *Comput. Struct.*, 80 (2002) p. 1763.
321. M. Grujicic and H. Zhao, Optimization of 316 stainless steel/alumina functionally graded material for reduction of damage induced by thermal residual stresses. *Mater. Sci. Eng. A*, 252 (1998) p. 117.
322. S. Widjaja, A. M. Limarga and T. H. Yip, Modeling of residual stresses in a plasma-sprayed zirconia/alumina functionally graded-thermal barrier coating. *Thin Solid Films.*, 434 (2003) p. 216.
323. A. Liu and Y. Wei, Finite element analysis of anti-spallation thermal barrier coatings. *Surf. Coat. Technol.*, 165 (2003) p. 154.
324. J. -h. Jeong, S. -Y. Lee, W. -S. Lee, Y. -J. Baik and D. Kwon, Mechanical analysis for crack-free release of chemical-vapor-deposited diamond wafers. *Diamond Relat. Mater.*, 11 (2002) p. 1597.
325. V. Ucar, A. Ozel, A. Mimaroglu, I. Taymaz, I. Call and M. Gur U. Kocabcak, Use of the finite element technique to analyze the influence of coating materials, material phase state and the purity on the level of the developed thermal stresses in plasma coating systems under thermal loading conditions. *Surf. Coat. Technol.*, 142-144 (2001) p. 950.
326. A. Özel, V. Ucar, A. Mimaroglu and I. Calli, Comparison of the thermal stresses developed in diamond and advanced ceramic coating systems under thermal loading. *Mater. Des.*, 21 (2000) p. 437.
327. A. Mimaroglu, A. Ozel and S. Genc, Influence of interlayer material and geometry on stress levels in MgO.ZrO₂-GG coatings subjected to thermal shock. *Mater. Des.*, 18 (1997) p. 73.
328. A. Mimaroglu, U. Kocabicak and S. Genc, Influence of porosity characteristics in MgO.ZrO₂-GG coating subjected to thermal loading. *Mater. Des.*, 18 (1997) p. 77.
329. S. Manning and S. Fuchs, Finite element analysis of thermal stresses in high-power substrates for hybrid circuits. *Mater. Des.*, 18 (1997) p. 61.
330. M. Andritschky, P. Alpuim, D. Stöver and C. Funke, Study of the mechanics of the delamination of ceramic functional coatings. *Mater. Sci. Eng. A*, 271 (1999) p. 62.
331. O. Sarikaya and E. Celik, Effects of residual stress on thickness and interlayer of thermal barrier ceramic MgO-ZrO₂ coatings on Ni and AlSi substrates using finite element method, *Mater. Des.*, 23 (2002) p. 645.
332. S. Haque and K. L. Choy, Finite element modelling of the effect of a functionally graded protective coating for SiC monofilaments on Ti-based composite behaviour. *Mater. Sci. Eng. A*, 291 (2000) p. 97.
333. V. Teixeira, Numerical analysis of the influence of coating porosity and substrate elastic properties on the residual stresses in high temperature graded coatings. *Surf. Coat. Technol.*, 146-147 (2001) p. 79.

334. A. Polat, O. Sarikaya and E. Celik, Effects of porosity on thermal loadings of functionally graded Y_2O_3 ZrO_2 /NiCoCrAlY coatings. *Mater. Des.*, 23 (2002) p. 641.
335. Q. Xu, S. Yu and Y. Kang, Residual Stress Analysis of Functionally Gradient Materials. *Mech. Res. Commun.*, 26 (1999) p. 55.
336. A. F. Okyar and M. Gosz, Finite element modeling of a microelectronic structure under uniform thermal loading. *Finite Elem. Anal. Des.*, 37 (2001) p. 961.
337. P. M. Igit and P. A. Mawby, An advanced finite element strategy for thermal stress field investigation in aluminium interconnections during processing of very large scale integration multilevel structures. *Microelectron. J.*, 30 (1999) p. 1207.
338. J. K. Wright, R. L. Williamson, D. Rensch, B. Veal, M. Grimsditch, P. Y. Hou and R. M. Cannon, Residual stresses in convoluted oxide scales. *Mater. Sci. Eng. A*, 262 (1999) p. 246.
339. J. K. Wright, R. L. Williamson and R. M. Cannon, Finite element analysis of the effects of corners on residual stresses in protective oxide scales. *Mater. Sci. Eng. A*, 230 (1997) p. 202.
340. R. L. Williamson, J. K. Wright, E. D. Steffler and R. M. Cannon, Numerical analysis of surface cracks at regions of curvature in oxide scales. *Mater. Sci. Eng. A*, 342 (2003) p. 109.
341. D. Griffin, A. Daadbin and P. K. Datta, Deformation and fracture, during cooling, of the alumina scale developed on Fe_3Al . *Surf. Coat. Technol.*, 126 (2000) p. 142.
342. J. Gunnars and A. Alahelsten, Thermal stresses in diamond coatings and their influence on coating wear and failure. *Surf. Coat. Technol.*, 80 (1996) p. 303.
343. U. Wiklund, J. Gunnars and S. Hogmark, Influence of residual stresses on fracture and delamination of thin hard coatings. *Wear.*, 232 (1999) p. 262.
344. Y. C. Tsui and T. W. Clyne, An analytical model for predicting residual stresses in progressively deposited coatings. Part 1: Planar geometry. *Thin Solid Films.*, 306 (1997) p. 23.
345. S. J. Howard, Y. C. Tsui and T. W. Clyne, The effect of residual stresses on the debonding of coatings--I. A model for delamination at a bimaterial interface. *Acta Metallurgica et Materialia*, 42 (1994) p. 2561.
346. G. G. Stoney, The tension of metallic films deposited by electrolysis. *Proc. R. Soc. London, Ser. A*, 82 (1909) p. 172.
347. M. S. Kilijanski and Y. -L. Shen, Analysis of thermal stresses in metal interconnects with multilevel structures. *Microelectron. Reliab.*, 42 (2002) p. 259.
348. A. Rouzaud, E. Barbier, J. Ernoult and E. Quesnel, A method for elastic modulus measurements of magnetron sputtered thin films dedicated to mechanical applications. *Thin Solid Films.*, 270 (1995) p. 270.
349. R. O. E. Vijgen and J. H. Dautzenberg, Mechanical measurement of the residual stress in thin PVD films. *Thin Solid Films.*, 270 (1995) p. 264.
350. J. K. Wright, R. L. Williamson and K. J. Maggs, Finite element analysis of the effectiveness of interlayers in reducing thermal residual stresses in diamond films. *Mater. Sci. Eng. A*, 187 (1994) p. 87.
351. ANSYS-the general-purpose finite element software (version 7.0). Houston, TX: Swanson Analysis Systems, Inc. International, USA.
352. K. Dai and L. Shaw, Thermal and stress modeling of multi-material laser processing. *Acta Materialia*, 49 (2001) p. 4171.
353. J. Mencik, In: *Mechanics of Components with Treated or Coated Surfaces*. Kluwer Academic, Dordrecht (1995) p. 33.
354. M. D. Thouless, Cracking and delamination of coatings. *J. Vac. Sci. Tech. A*, 9 (1991) p. 2510.
355. J. Michler, M. Mermoux, Y. von Kaenel, A. Haouni, G. Lucazeau and E. Blank, Residual stress in diamond films: origins and modelling. *Thin Solid Films.*, 357 (1999) p. 189.

356. J Valli, J Pälöjarvi and U. Mäkelä, Pinnoitten paksuuden mittaaminen kuulakokeella (Finnish) / (coating thickness measurement using ball cratering). Technical Research Centre of Finland, Research notes, 435 (1985) p. 22.
357. M. G. Gee, A. Gant, I. Hutchings, R. Bethke, K. Schiffman, K. Van Acker, S. Poulat, Y. Gachon and J. von Stebut, Progress towards standardisation of ball cratering. *Wear.*, 255 (2003) p. 1.
358. J. D. Verhoeven, Scanning Electron Microscopy, Materials Characterization, Vol. 10, ASM Metals Handbook, 9th edition (1986) p. 490.
359. J. I. Goldstein, D. E. Newbury, P. Echlin, D. C. Joy, C. Fiori, and E. Lifshin, Scanning Electron Microscopy and X-Ray Microanalysis, Plenum Press (1981).
360. C. R. Brundle, C. A. Evans, Jr., Shaun Wilson, Encyclopedia of materials characterization: surfaces, interfaces, thin films. Elsevier (1992).
361. J. J. Friel, X-Ray and image analysis in electron microscopy. Princeton Gamma-Tech, Princeton, New Jersey, 2nd edition (1998).
362. I. Bertoti, Characterization of nitride coatings by XPS. *Surf. Coat. Technol.*, 151/152 (2002) p. 194.
363. ASM Handbook. Mechanical testing. Vol. 8, Metals Park (9th ed) Ohio (1985).
364. ASM Handbook. Surface Engineering. Vol. 5, ASM International (1999).
365. P. A. Steinmann and H. E. Hintermann, A review of the mechanical tests for assessment of thin-film adhesion. *J. Vac. Sci. Technol. A*, 7 (1989) p. 2267.
366. N. Vidakis, A. Antoniadis and N. Bilalis, The VDI 3198 indentation test evaluation of a reliable qualitative control for layered compounds. *J. Mater. Proc. Technol.*, 143-144 (2003) p. 481.
367. W. Heinke, A. Leyland, A. Matthews, G. Berg, C. Friedrich and E. Broszeit, Evaluation of PVD nitride coatings, using impact, scratch and Rockwell-C adhesion tests. *Thin Solid Films.*, 270 (1995) p. 431.
368. K. Tominaga, K. Kusaka, T. Hanabusa, S. Inoue and R. P. Howson, TiN films prepared by unbalanced planar magnetron sputtering under control of photoemission of Ti. *Thin Solid Films*, 281-282 (1996) p. 182.
369. H. Jiang, K. Tao and H. Li, Structure of TiN_x (0 < x < 1.1) films prepared by ion beam-assisted deposition. *Thin Solid Films.*, 258 (1995) p. 51.
370. M. Bromark, P. Hedenqvist and S. Hogmark, The influence of substrate material on the erosion resistance of TiN coated tool steels. *Wear.*, 186-187 (1995) p. 189.
371. Q. Yang and L. R. Zhao, Dry sliding wear of magnetron sputtered TiN/CrN superlattice coatings. *Surf. Coat. Technol.*, 173 (2003) p. 58.
372. I. L. Singer, S. D. Dvorak, K. J. Wahl, and T. W. Scharf, Role of third bodies in friction and wear of protective coatings. *J. Vac. Sci. Technol. A*, 21 (2003) p. S232.
373. M. R. Hilton, R. Bauer and P. D. Fleischauer, Tribological performance and deformation of sputter-deposited MoS₂ solid lubricant films during sliding wear and indentation contact. *Thin Solid Films.*, 188 (1990) p. 219.
374. H. Ronkainen, J. Likonen, J. Koskinen and S. Varjus, Effect of tribofilm formation on the tribological performance of hydrogenated carbon coatings. *Surf. Coat. Technol.*, 79 (1996) p. 87.

PUBLISHED PAPERS AND POSTER

JOURNALS

Julfikar Haider, Mahfujur Rahman, Brian Corcoran, M. S. J. Hashmi, Simulation of thermal stress in magnetron sputtered thin coating by finite element analysis. *Journal of Material Processing Technology*, In press (Available online 1 January 2005).

REFEREED INTERNATIONAL CONFERENCE PROCEEDINGS

Julfikar Haider, Mahfujur Rahman, Brian Corcoran and M. S. J. Hashmi, Deposition and characterization of hard-solid lubricant coating by closed-field magnetron sputtering. 9th International Conference on Plasma Surface Engineering (PSE 2004), 13-17th September 2004, Garmisch-Partenkirchen, Germany, Abstract p. 522. (Submitted to *Surface and Coatings Technology Journal*. final version has been sent to editor after correcting referee's comment.)

Mahfujur Rahman, Julfikar Haider, D. P. Dowling, P. Duggan and M. S. J. Hashmi, Deposition of magnetron sputtered TiN+MoS_x coating with Ti-TiN graded interlayer, 9th International Conference on Plasma Surface Engineering (PSE 2004), 13-17th September 2004, Garmisch-Partenkirchen, Germany, Abstract p. 184 (Submitted to *Surface and Coatings Technology Journal*. final version has been sent to editor after correcting referee's comment.)

Mahfujur Rahman, Julfikar Haider, Brian Corcoran and M. S. J. Hashmi, Finite element modeling of thermal stresses in sputter deposited graded coating system. *Proceedings of the 21st International Manufacturing Conference (IMC 21)*, 1st -3rd September 2004, University of Limerick, Limerick, Ireland, p. 175-182.

Julfikar Haider, Mahfujur Rahman, Brian Corcoran, M. S. J. Hashmi, Simulation of thermal stress in magnetron sputtered thin coating by finite element analysis. *Proceedings of the Third International Conference on Advanced Manufacturing Technology (ICAMT 2004)*, 11-13 May, 2004, Kuala Lumpur, Malaysia, p. 790-795.

POSTER PRESENTATIONS

Julfikar Haider, Brian Corcoran, M. S. J. Hashmi, Deposition of composite hard and solid lubricant thin film by magnetron sputtering. 6th Annual Sir Bernard Crossland Symposium and Postgraduate Research Workshop, 9th to 10th April, 2003, National University of Ireland Galway, Galway, Ireland, p. 103.

Julfikar Haider, M. S. J. Hashmi, Thin film coating deposition on 3-dimensional objects by DC magnetron sputtering. National Centre for Plasma Science and Technology, Dublin City University, Dublin, Ireland, 30th May 2001.

MANUSCRIPT IN PROGRESS

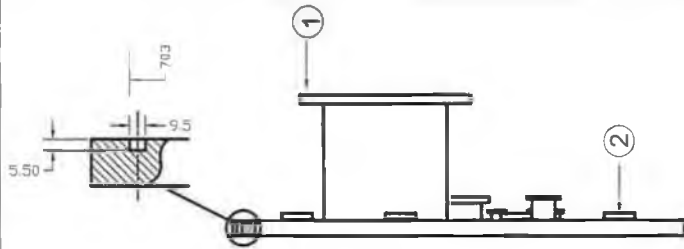
Julfikar Haider, Brian Corcoran and M. S. J. Hashmi, Cheap design of substrate rotational control for higher material utilization in closed-field magnetron sputtering.

Julfikar Haider, Brian Corcoran and M. S. J. Hashmi, Surface Engineering-Issues concerning to solid lubricant based thin coating.

APPENDIX A

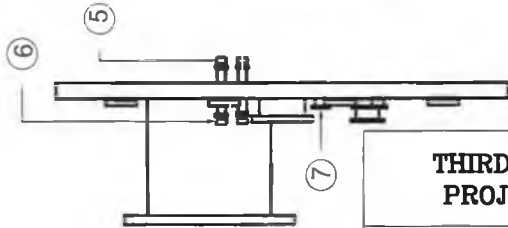
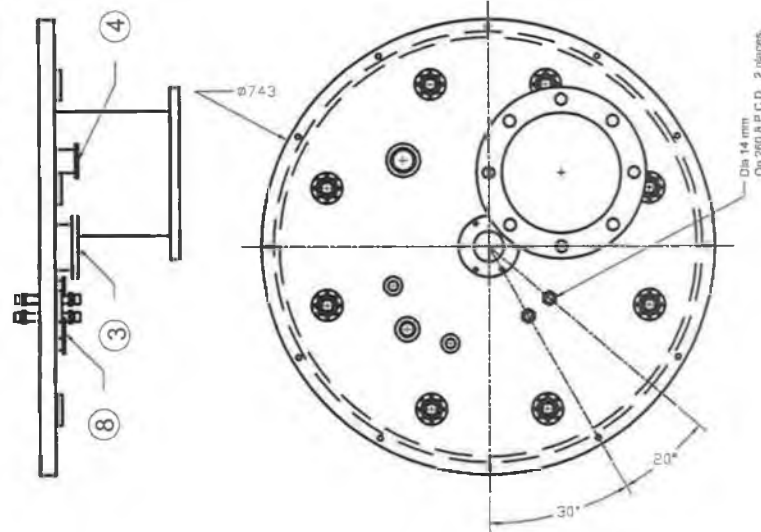
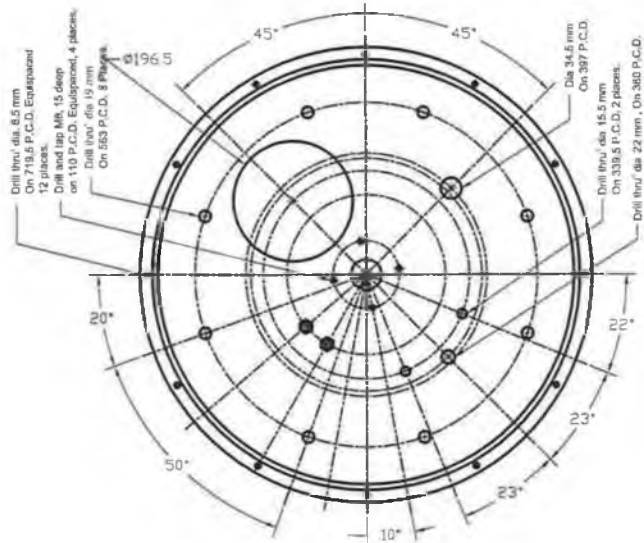
Drawings of Rotary Table

I-A-1



Item #	Qty.	Description
1	1	SW Pump Flange
2	3	Blank Plug
3	1	Control Operating Flange
4	1	Blank Valve Flange
5, 6	4	Feed Strips with orange lock
7	2	Feed through
8	1	Feed through

N.B. All items are welded to base plate



REV.	DESCRIPTION	BY	DATE
------	-------------	----	------

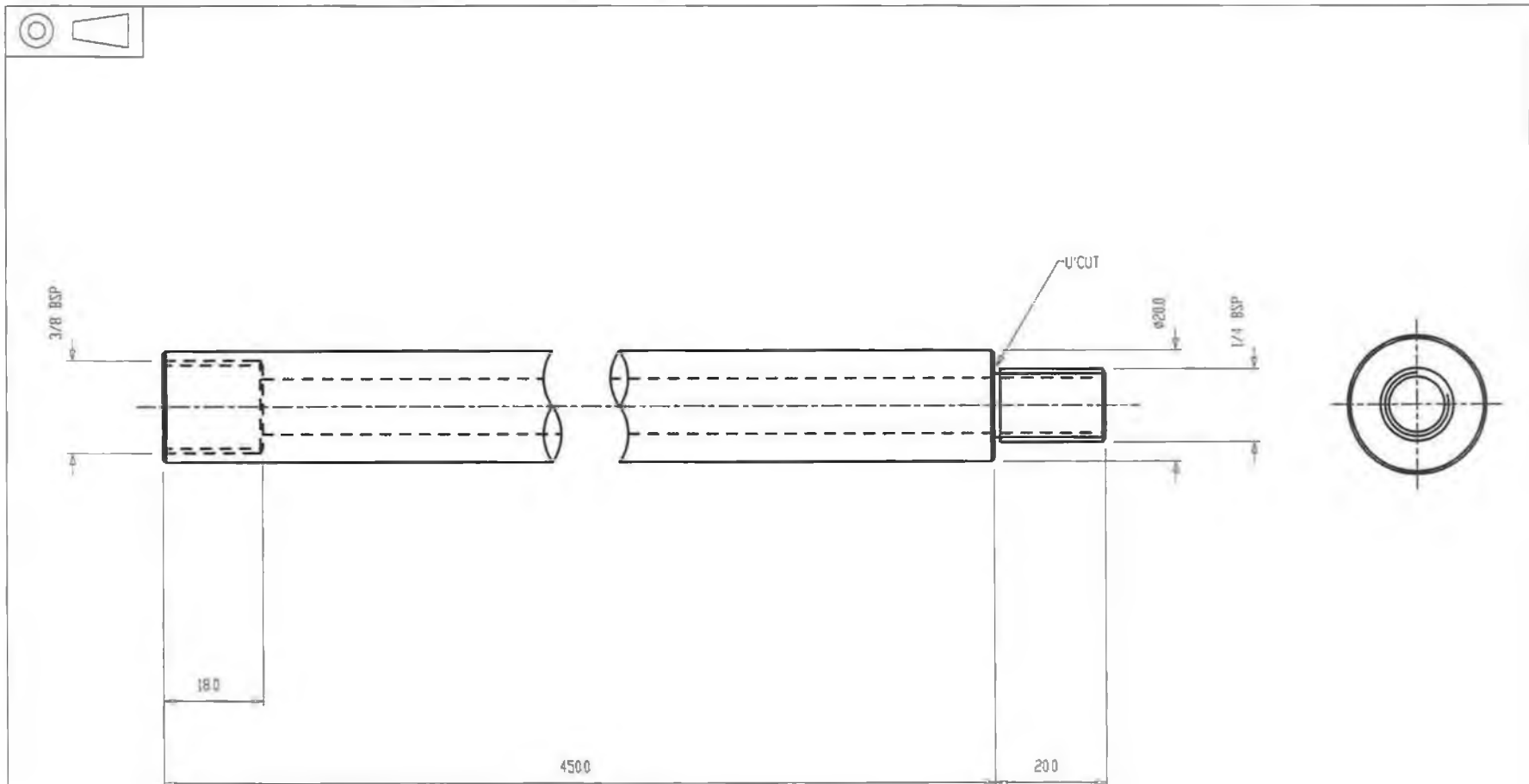
DRG. No.

THIRD ANGLE PROJECTION		TOLERANCES UNLESS SPECIFIED	
DRAWN HAIDER		FRACTIONS	
DATE 14-09-02		DECIMALS	± .25
CHECKED LIAM		ANGLES	± 1
APPROVED		SURFACE FIN.	
		MAT'L	SS
		HEAT TREAT.	NONE

DCU MECHANICAL ENG. DEPT.			
BASE PLATE			
QTY.	ASS'Y DRG.	PARTS LIST	
SCALE	PROJECT SPUTTER	SHEET 1 OF 1	

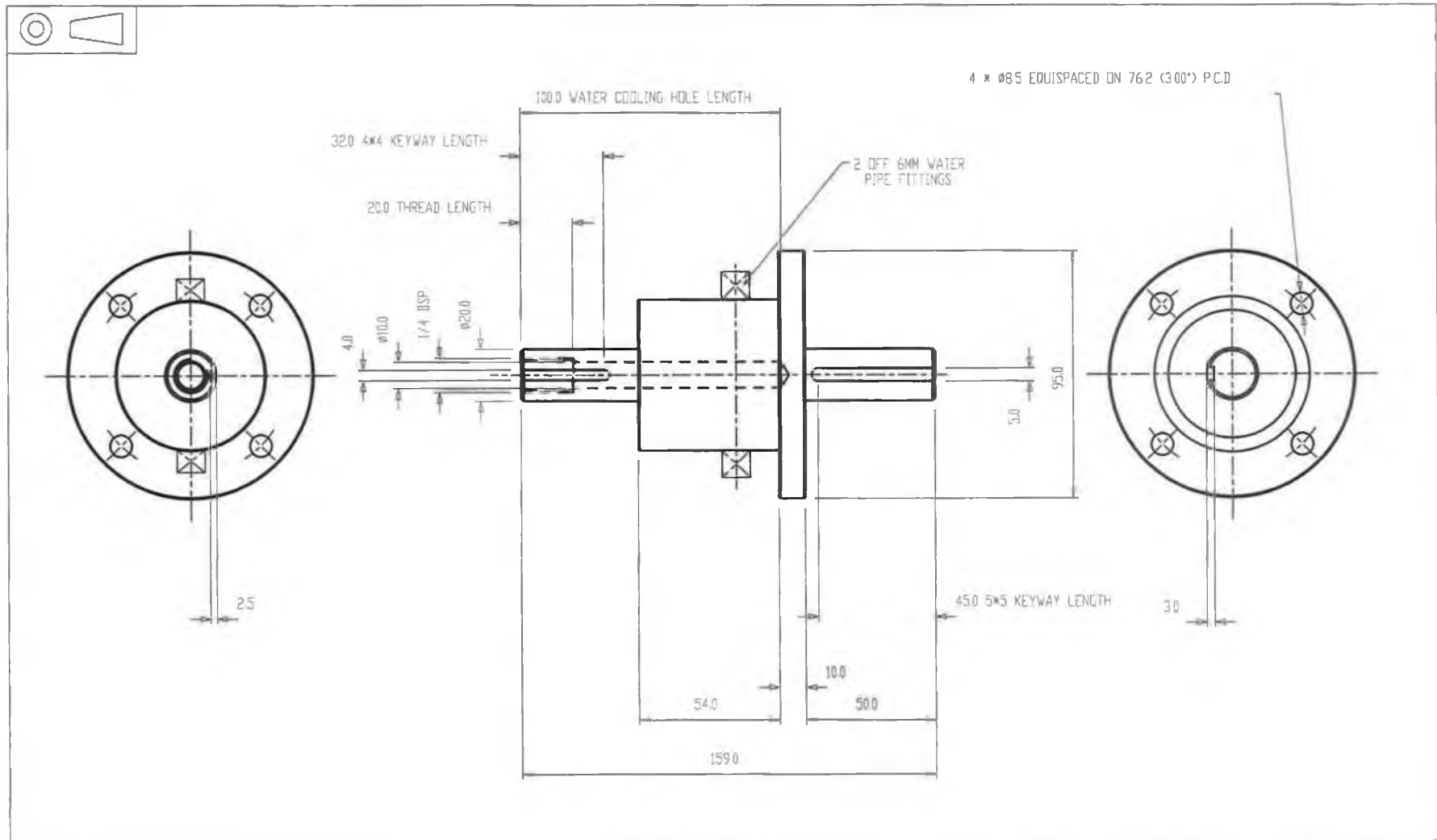
PART No.

A-2



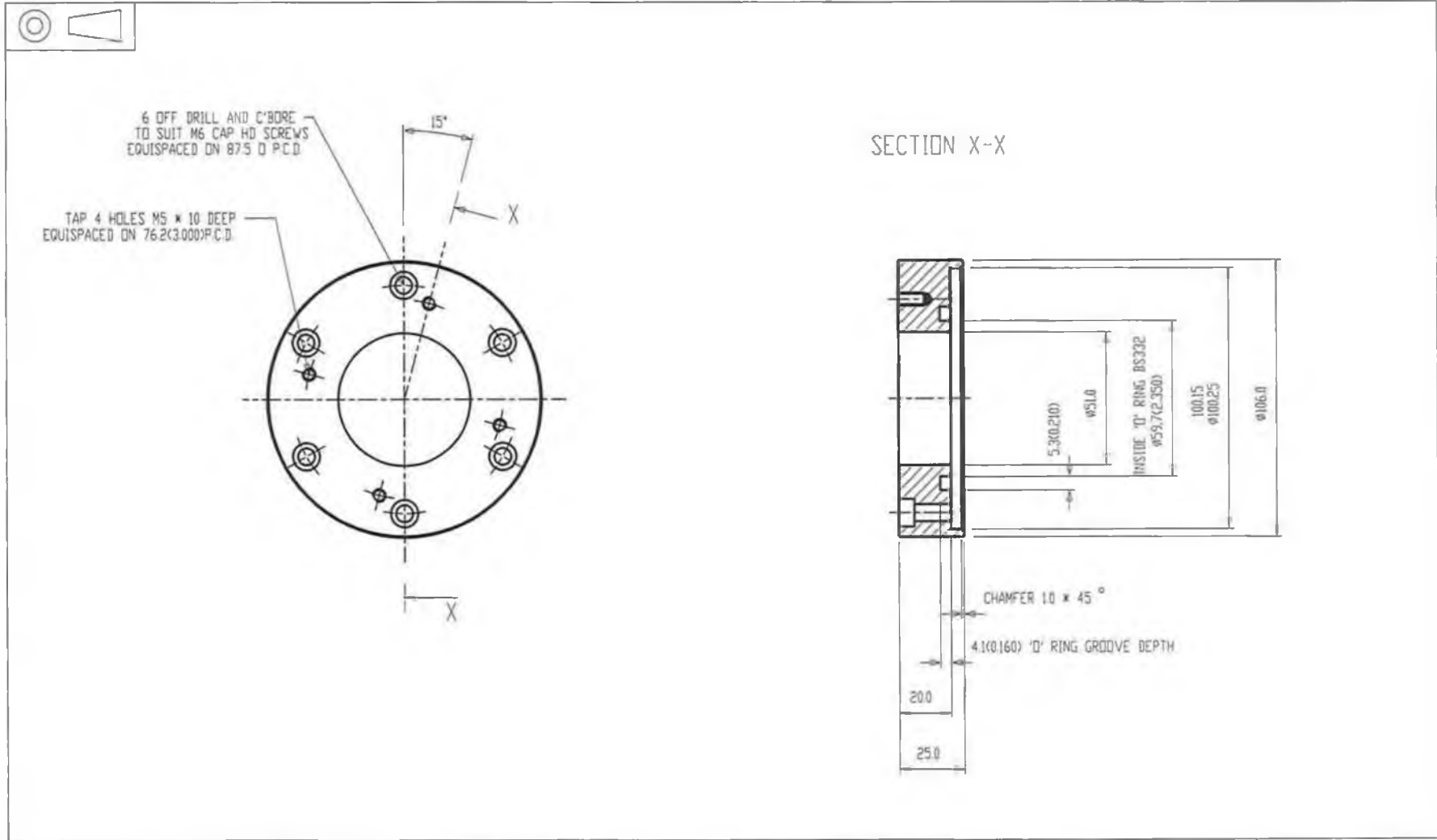
MATERIAL: AL OR BRASS				DRAWING TITLE:	CHKD BY:	DATE: 14-09-02
No OFF:	2	ISSUE	DESCRIPTION	3/8 TO 1/4 BSP EXTENSION PIPE	DRAWN BY: AJM	SCALE 1:1
ALL DIMENSIONS IN MILLIMETERS		MECHANICAL & MANUFACTURING ENGG., DCU.			DRAWING No:	2

A-3



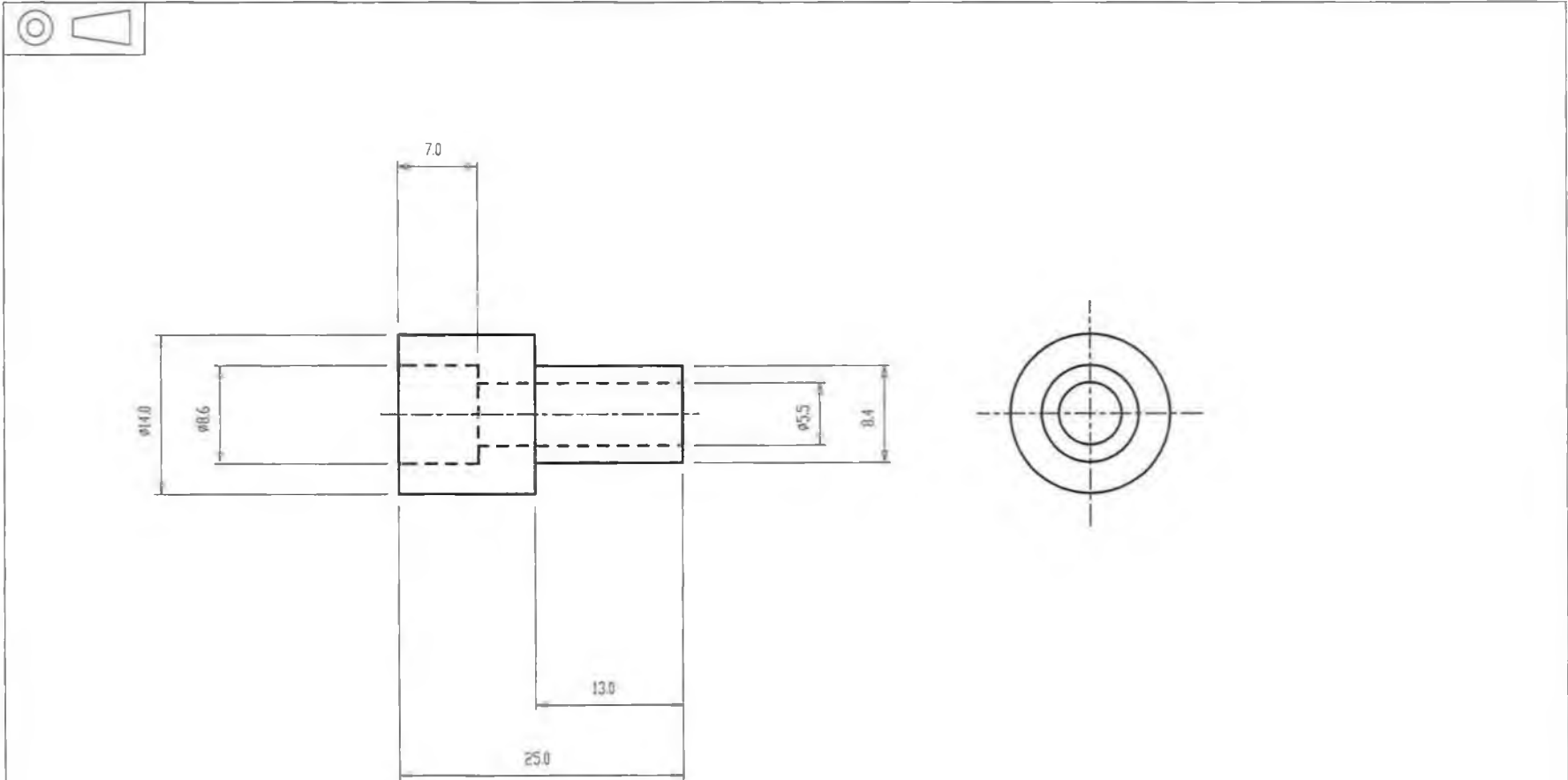
MATERIAL:				DRAWING TITLE:		CHKD BY:		DATE: 14-09-02	
No OFF: 1				FEEDTHROUGH		DRAWN BY: AJM		SCALE 1:2	
ALL DIMENSIONS IN MILLIMETERS		MECHANICAL & MANUFACTURING ENGG., DCU.				DRAWING No: 3			

A-4



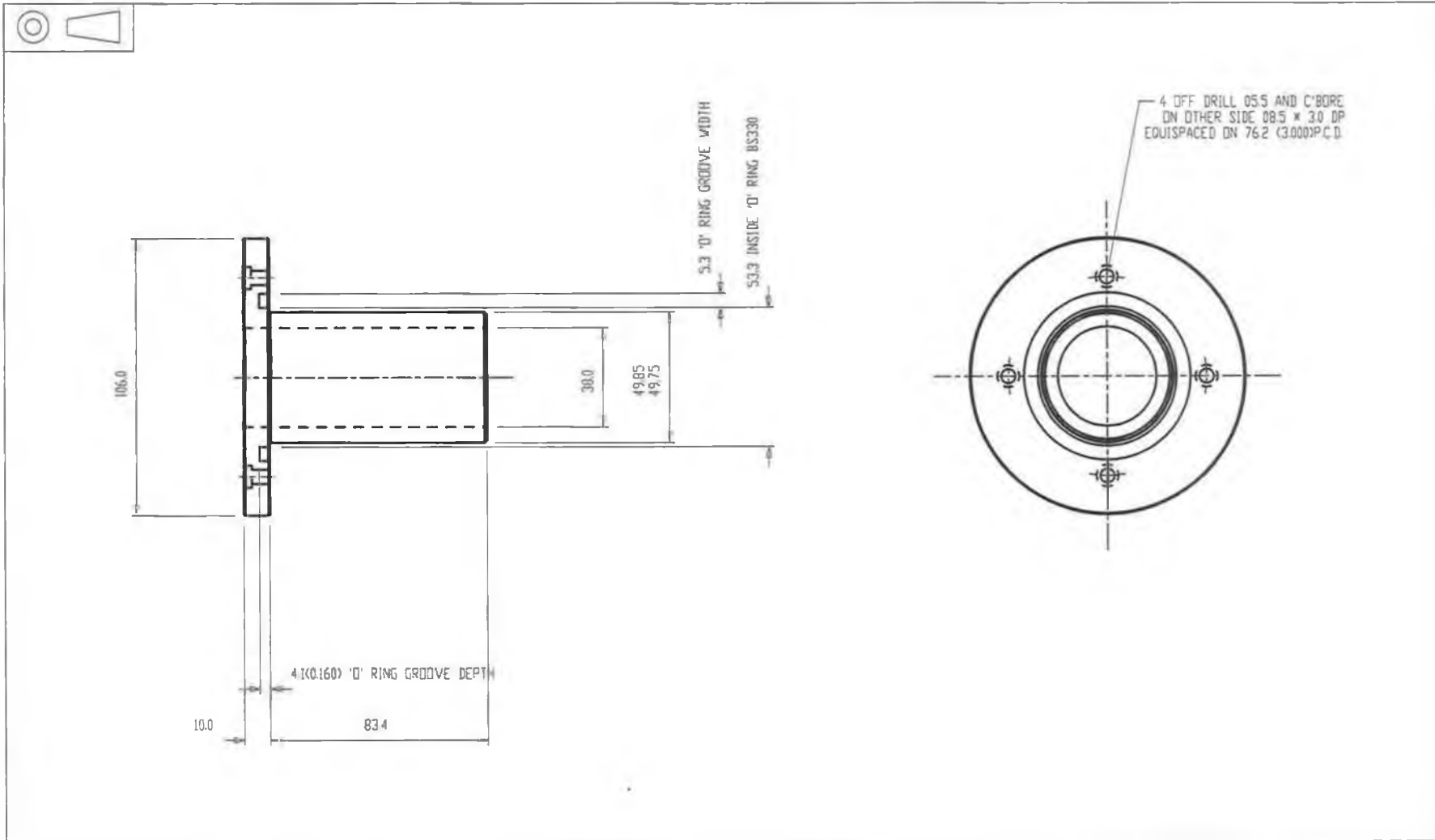
MATERIAL: 304L SS			DRAWING TITLE:	CHKD BY:	DATE: 14-09-02
No OFF: 1	2	ALTERED HOLE POSITIONS	ADAPTOR FLANGE	DRAWN BY: AJM	SCALE 1:2
ALL DIMENSIONS IN MILLIMETERS	ISSUE	DESCRIPTION		DRAWING No:	4
MECHANICAL & MANUFACTURING ENGG., DCU.					

A-5



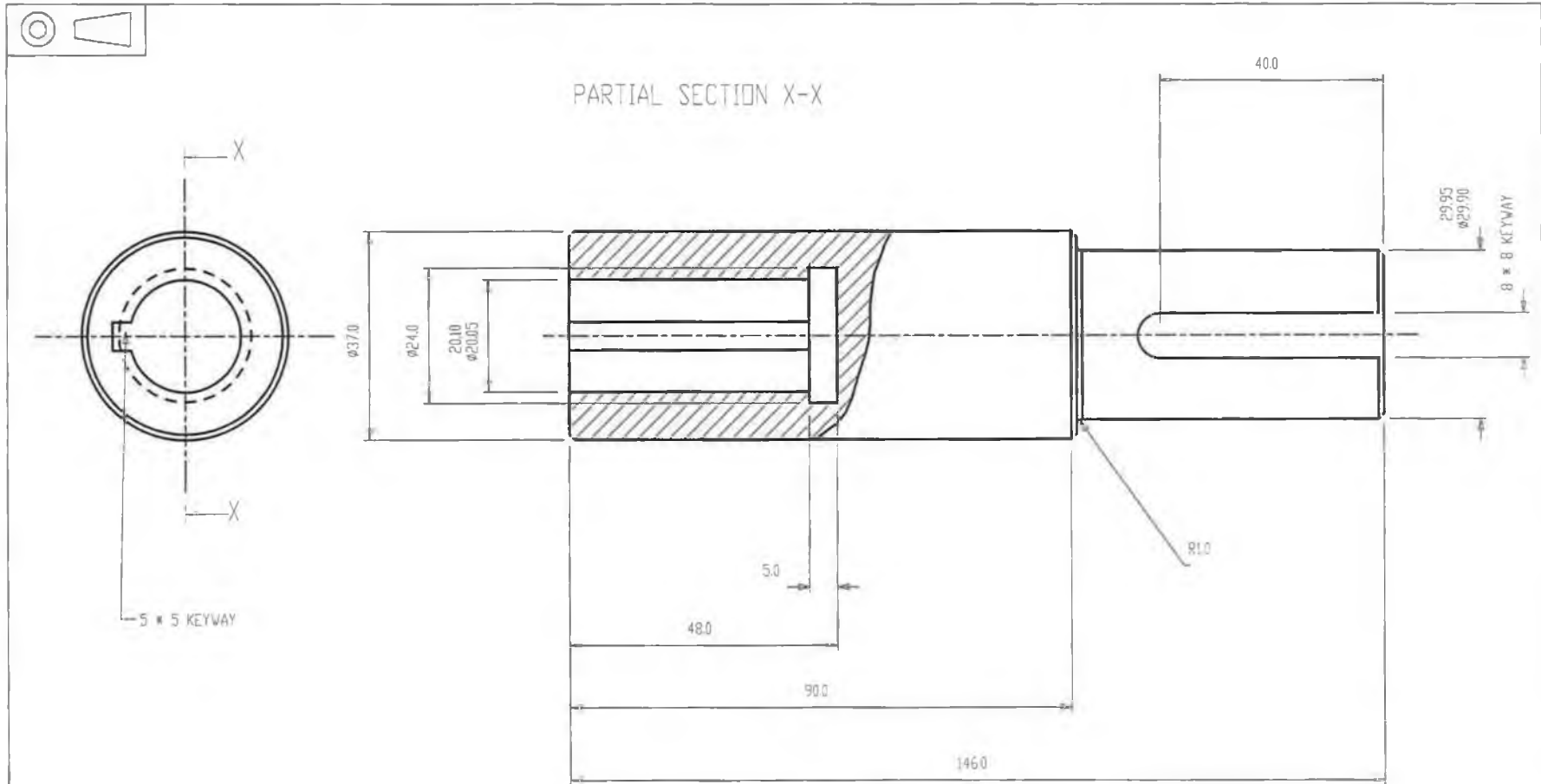
MATERIAL: PTFE				DRAWING TITLE:	CHKD BY:	DATE: 14-09-02
No OFF: 4	ISSUE	DESCRIPTION	DATE	M5 BOLT INSULATOR	DRAWN BY: AJM	SCALE 2:1
ALL DIMENSIONS IN MILLIMETERS				MECHANICAL & MANUFACTURING ENGG., DCU.	DRAWING No: 5	

A-6



MATERIAL: P.T.F.E.			DRAWING TITLE:	CHKD BY:	DATE: 14-09-02
No OFF: 1	2	ALTERED HOLE POSITIONS	FEEDTHROUGH INSULATOR	DRAWN BY: AJM	SCALE 1:2
ALL DIMENSIONS IN MILLIMETERS	ISSUE	DESCRIPTION		DRAWING No:	6
MECHANICAL & MANUFACTURING ENGG., DCU.					

A-7



MATERIAL: 304L SS

No OFF: 1

ALL DIMENSIONS IN MILLIMETERS

MECHANICAL & MANUFACTURING ENGG., DCU.

ISSUE	DESCRIPTION	DATE
	INCREASED LENGTH AND INTERNAL KEYWAY SIZE	

DRAWING TITLE:

SHAFT EXTENSION

CHKD BY:

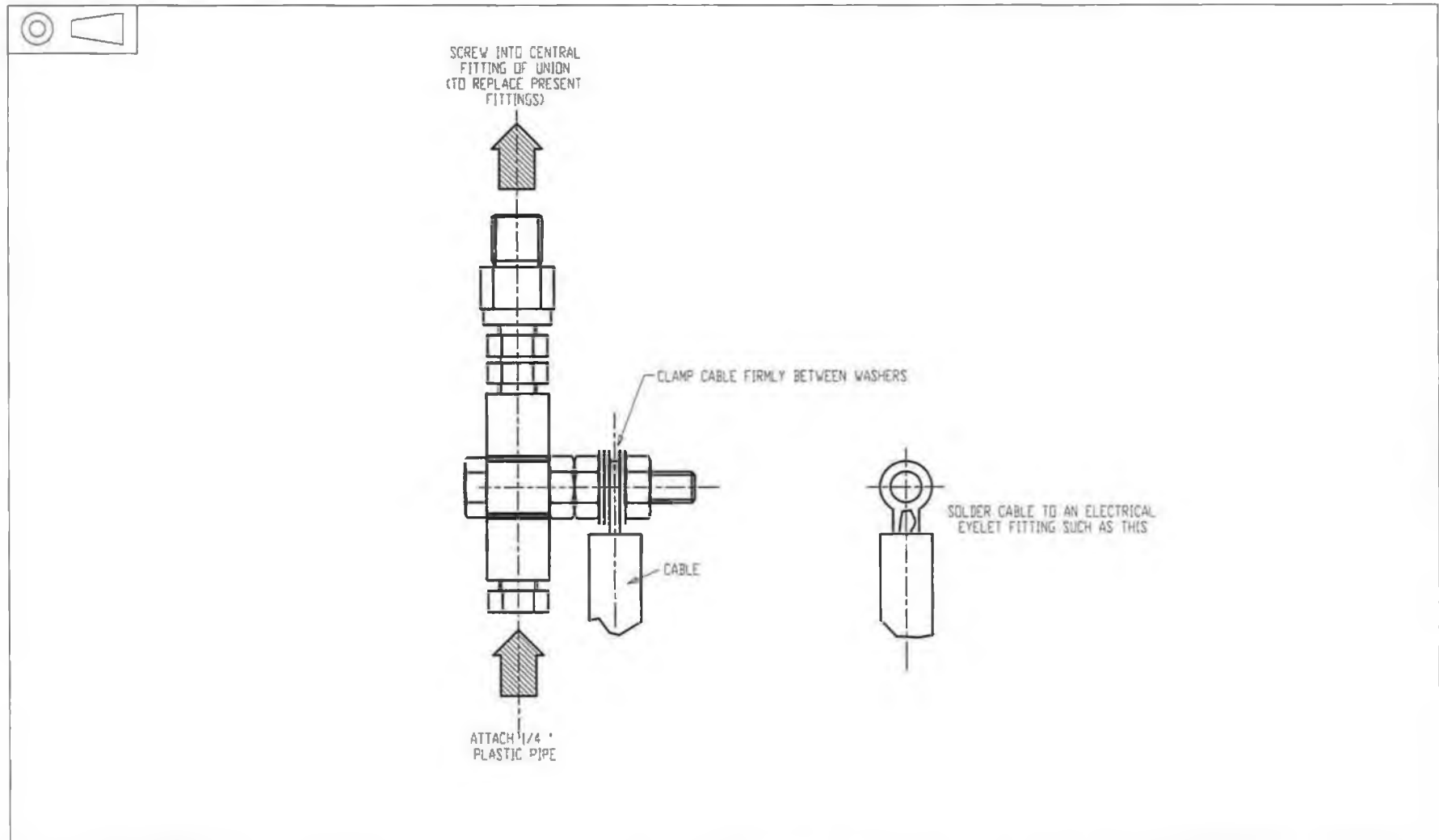
DRAWN BY: AJM

DRAWING No:

DATE: 14-09-02

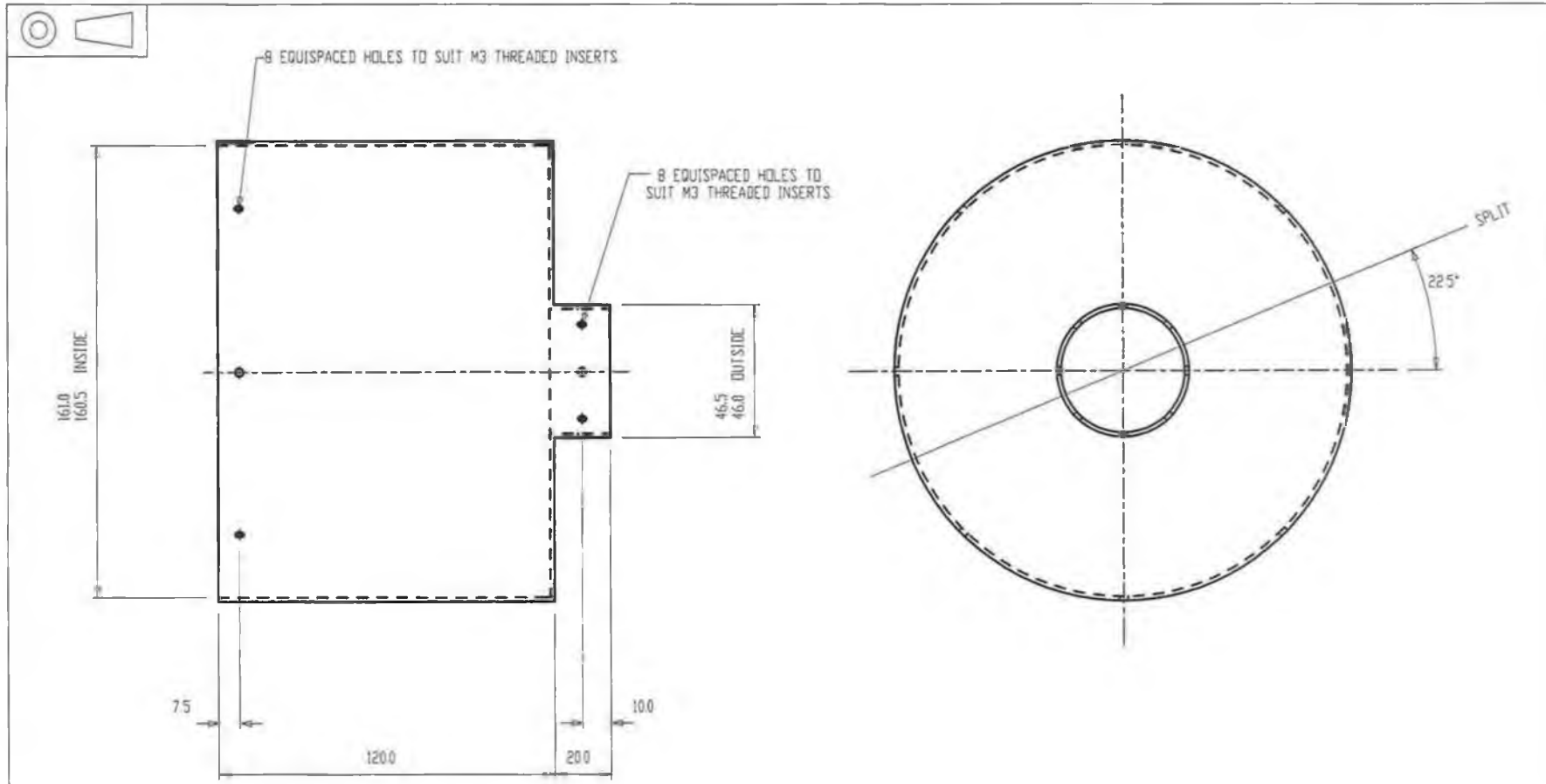
SCALE 1:1

7



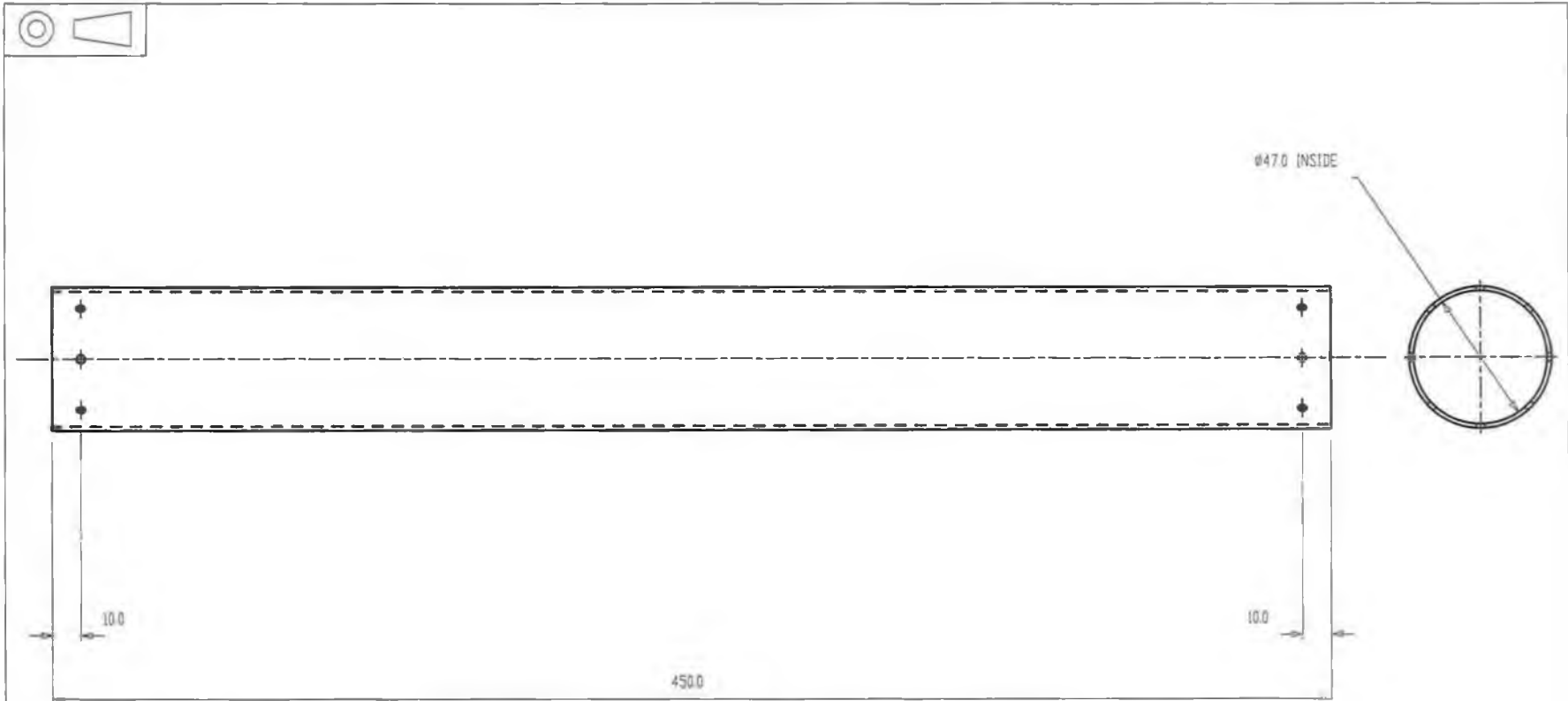
MATERIAL: STEEL				DRAWING TITLE:	CHKD BY:	DATE: 15/5/02
No OFF: 1	ISSUE	DESCRIPTION	DATE	ELECTRICAL FITTING	DRAWN BY: AJM	SCALE 1:1
ALL DIMENSIONS IN MILLIMETERS				DRAWING No: 8		
MECHANICAL & MANUFACTURING ENGG., DCU.						

6-V



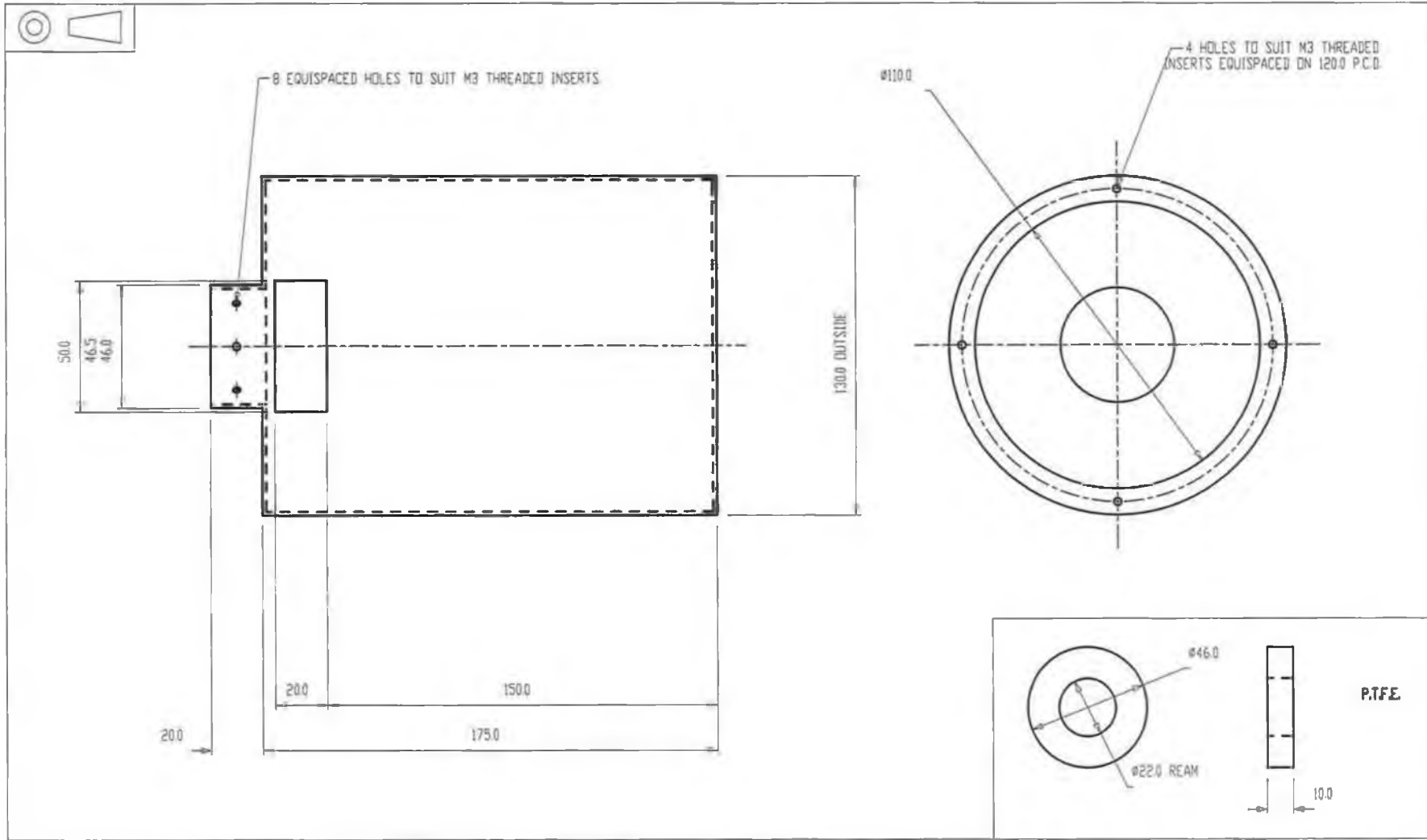
MATERIAL: 16g 304L SS			DRAWING TITLE:	CHKD BY:	DATE: 14-09-02
No OFF: 1	2	ALTERED SIZE	UPPER SHIELD	DRAWN BY: AJM	SCALE 1:2
ALL DIMENSIONS IN MILLIMETERS	ISSUE	DESCRIPTION		DRAWING No:	9
MECHANICAL & MANUFACTURING ENGG., DCU.					

A-10



MATERIAL: 16g 304L SS			DRAWING TITLE:	CHKD BY:	DATE: 14-09-02
No OFF: 1	ISSUE	DESCRIPTION	MIDDLE SHIELD	DRAWN BY: AJM	SCALE 1:2
ALL DIMENSIONS IN MILLIMETERS	MECHANICAL & MANUFACTURING ENGG., DCU.			DRAWING No:	10

A-11



MATERIAL: 16g 304L SS

No OFF: 1

ALL DIMENSIONS IN MILLIMETERS

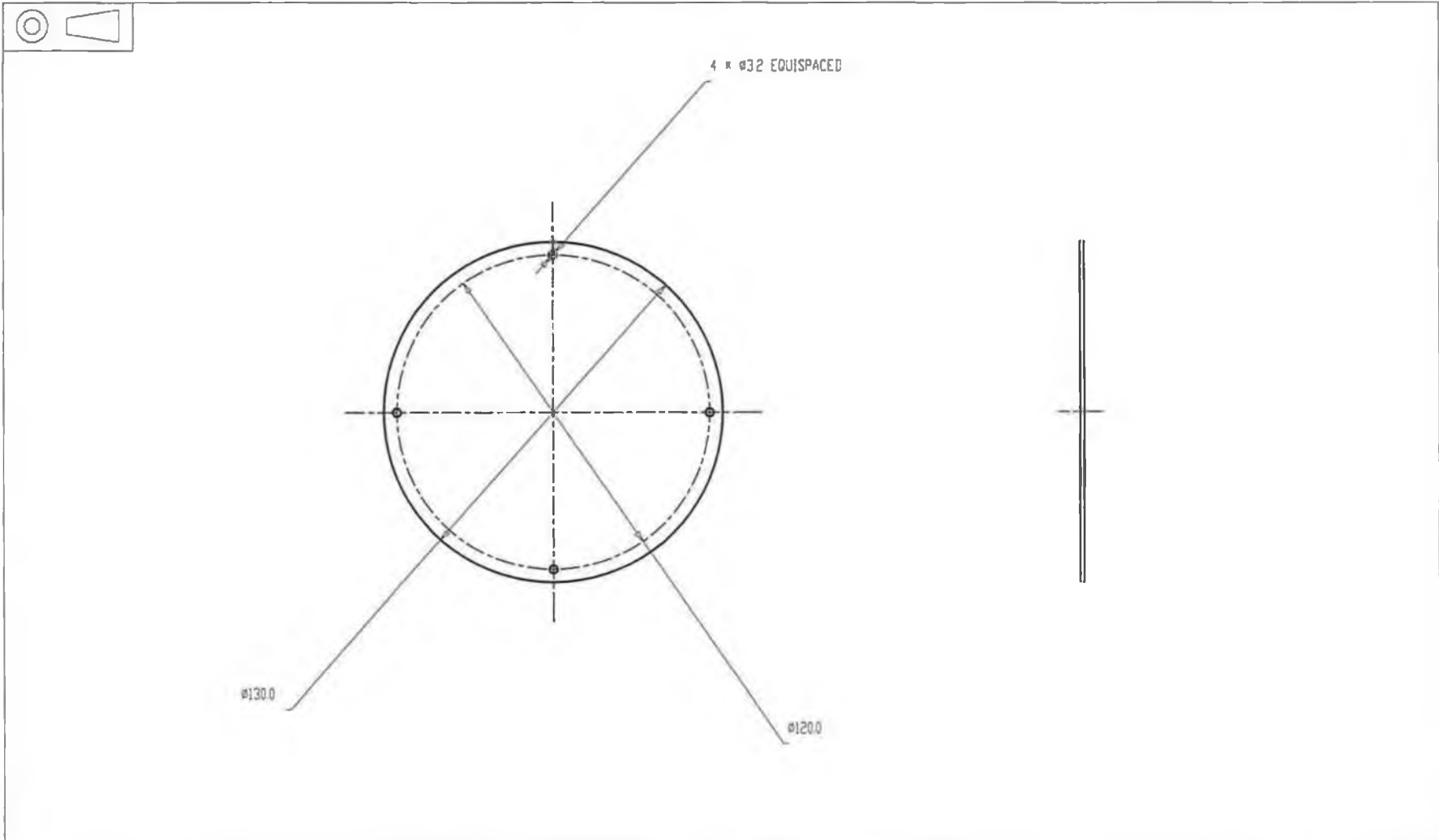
ISSUE	DESCRIPTION	DATE
3	ADDED SLOT	
2	ALTERED SIZE	

MECHANICAL & MANUFACTURING ENGG., DCU.

DRAWING TITLE:
LOWER SHIELD

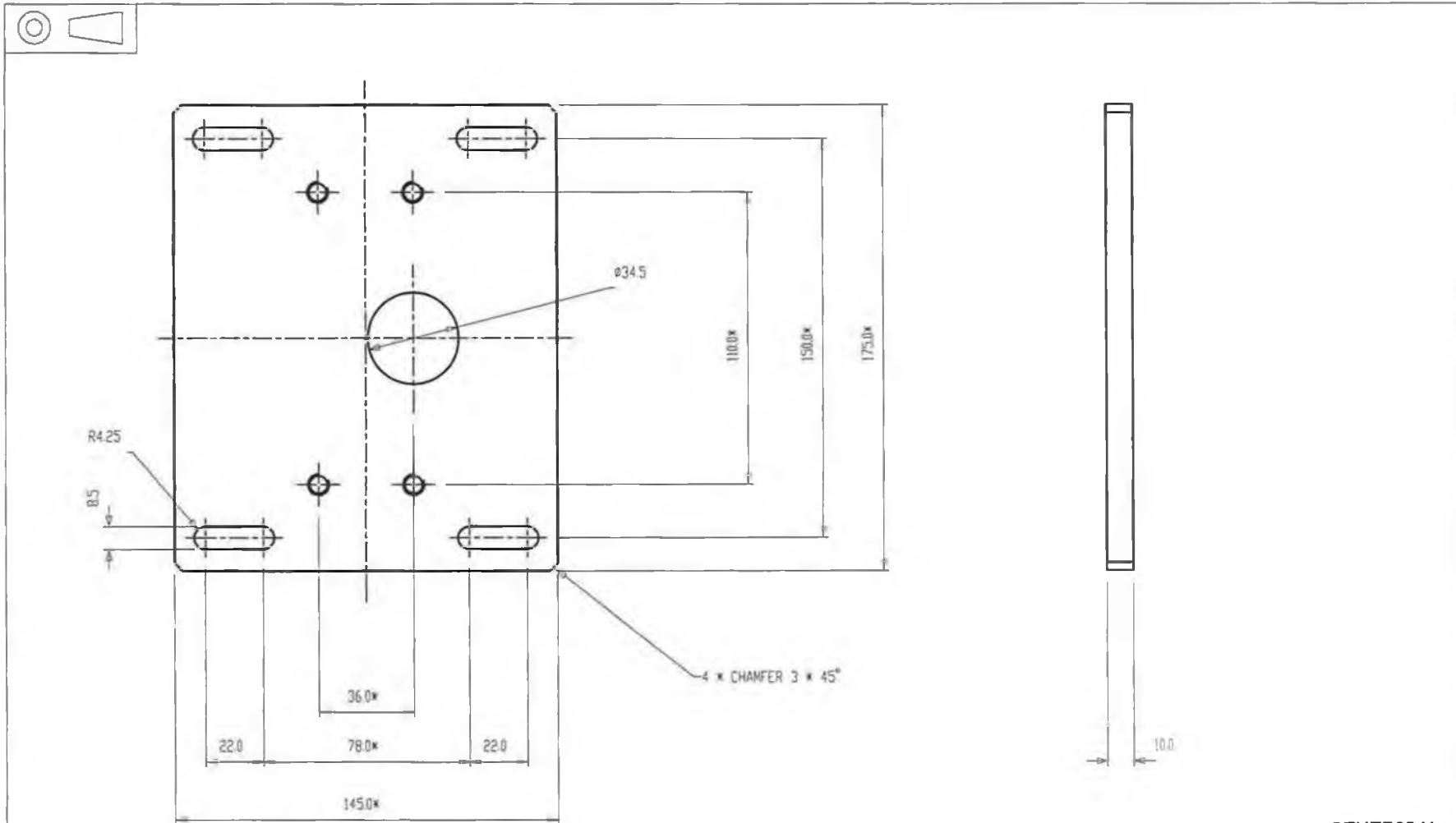
CHKD BY:	DATE: 14-09-02
DRAWN BY: AJM	SCALE: 1:2
DRAWING No:	11

A-12



MATERIAL: 16g 304L SS				DRAWING TITLE:	CHKD BY:	DATE: 14-09-02
No OFF: 1	ISSUE	DESCRIPTION	DATE	LOWER SHIELD PLATE	DRAWN BY: AJM	SCALE 1:2
ALL DIMENSIONS IN MILLIMETERS				MECHANICAL & MANUFACTURING ENGG., DCU.	DRAWING No:	12

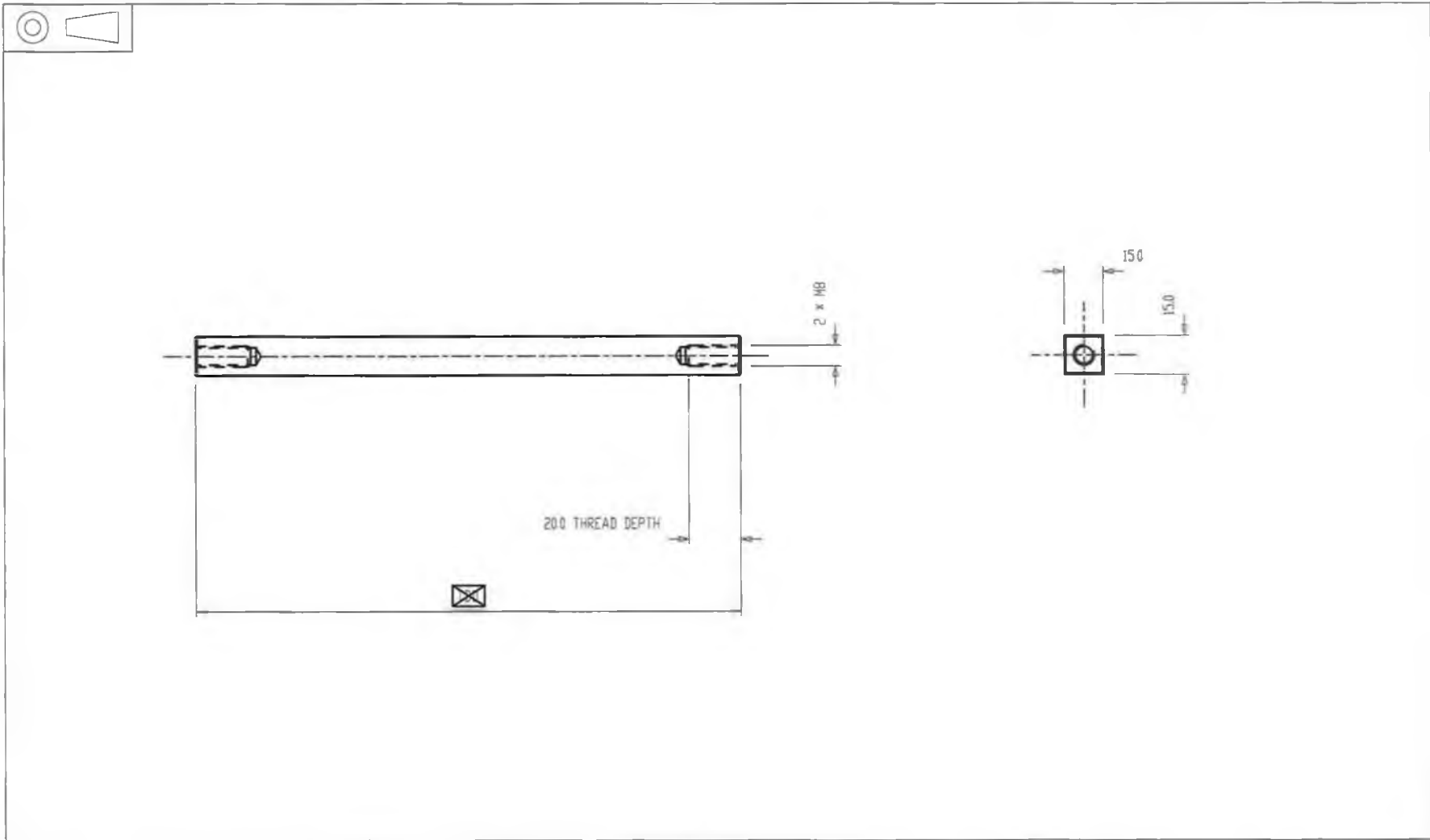
A-13



* CENTRICAL

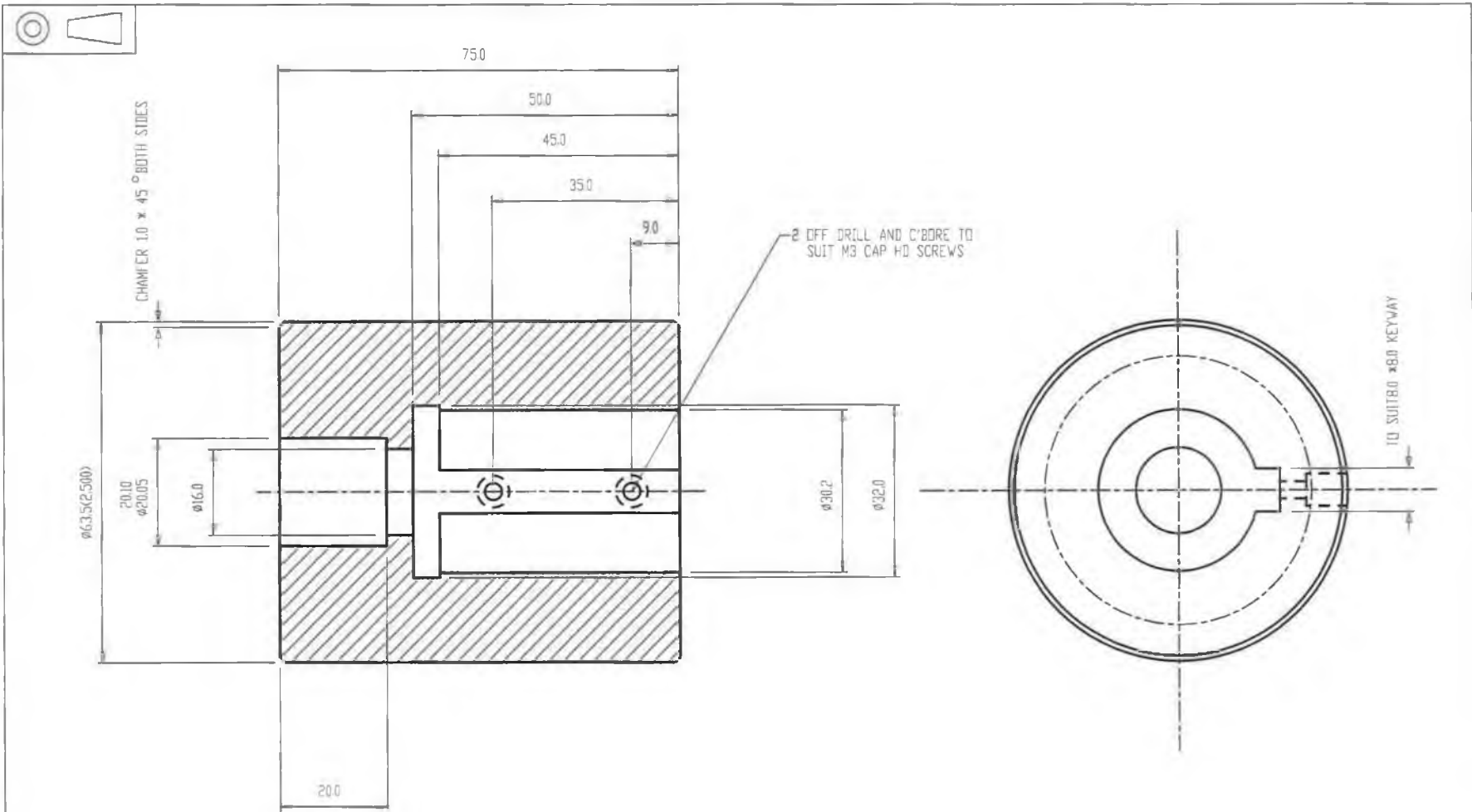
MATERIAL: MILD STEEL				DRAWING TITLE:		CHKD BY:	DATE: 14-09-02
No OFF: 1		ISSUE	DESCRIPTION	DATE	MOTOR PLATE	DRAWN BY: AJM	SCALE 1:2
ALL DIMENSIONS IN MILLIMETERS					DRAWING No: 13		
MECHANICAL & MANUFACTURING ENGG., DCU.							

A-14



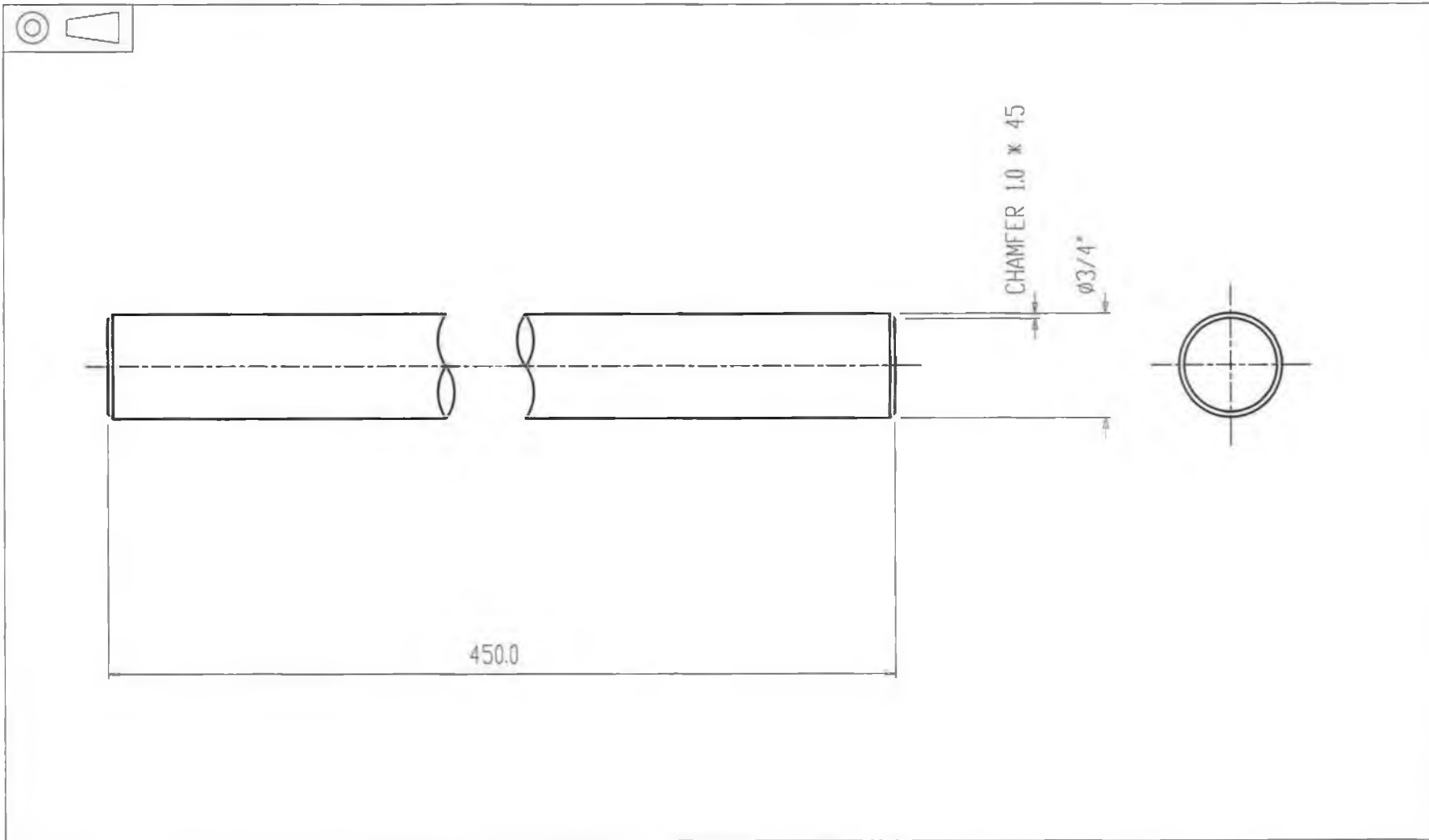
MATERIAL: STEEL				DRAWING TITLE:	CHKD BY:	DATE: 14-09-02
No OFF: 4	ISSUE	DESCRIPTION	DATE	MOTOR POSTS	DRAWN BY: AJM	SCALE 1:2
ALL DIMENSIONS IN MILLIMETERS				MECHANICAL & MANUFACTURING ENGG., DCU.	DRAWING No: 14	

A-15



MATERIAL: 304L SS	DRAWING TITLE:		CHKD BY:	DATE: 14-09-02
No OFF: 1	ADAPTOR FOR CNTR POLE		DRAWN BY: AJM	SCALE 1:1
ALL DIMENSIONS IN MILLIMETERS	ISSUE	DESCRIPTION	DATE	DRAWING No: 15
MECHANICAL & MANUFACTURING ENGG., DCU.				

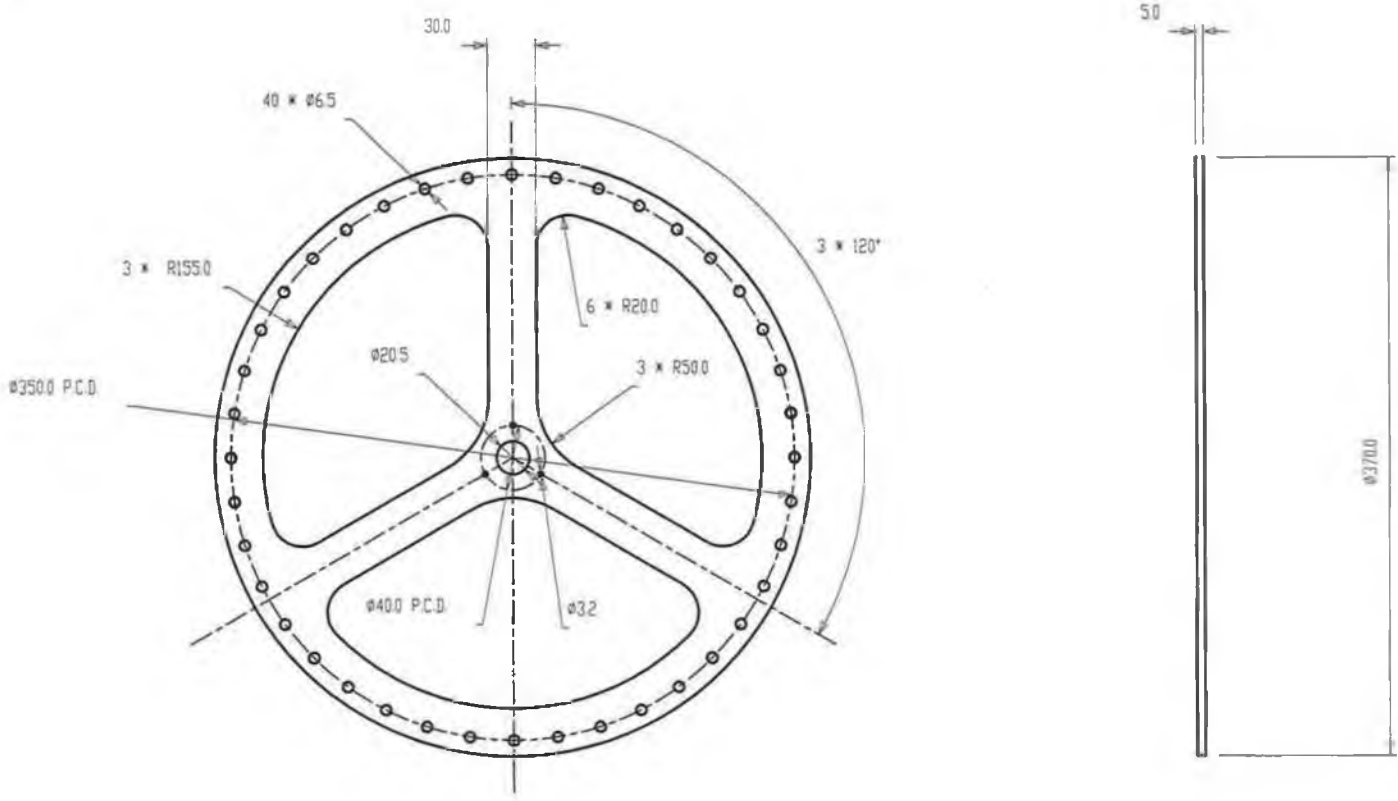
A-16



MATERIAL: 304L SS				DRAWING TITLE:	CHKD BY:	DATE: 14-09-02
No OFF: 1	ISSUE	DESCRIPTION	DATE	CENTRE POLE	DRAWN BY: AJM	SCALE 1:1
ALL DIMENSIONS IN MILLIMETERS					MECHANICAL & MANUFACTURING ENGG., DCU.	DRAWING No: 16



A-17



MATERIAL: 304L SS

No OFF: 1

ALL DIMENSIONS IN MILLIMETERS

ISSUE	DESCRIPTION	DATE

MECHANICAL AND MANUFACTURING ENGG., DCU

DRAWING TITLE:
SAMPLE PLATE 1

CHKD BY:

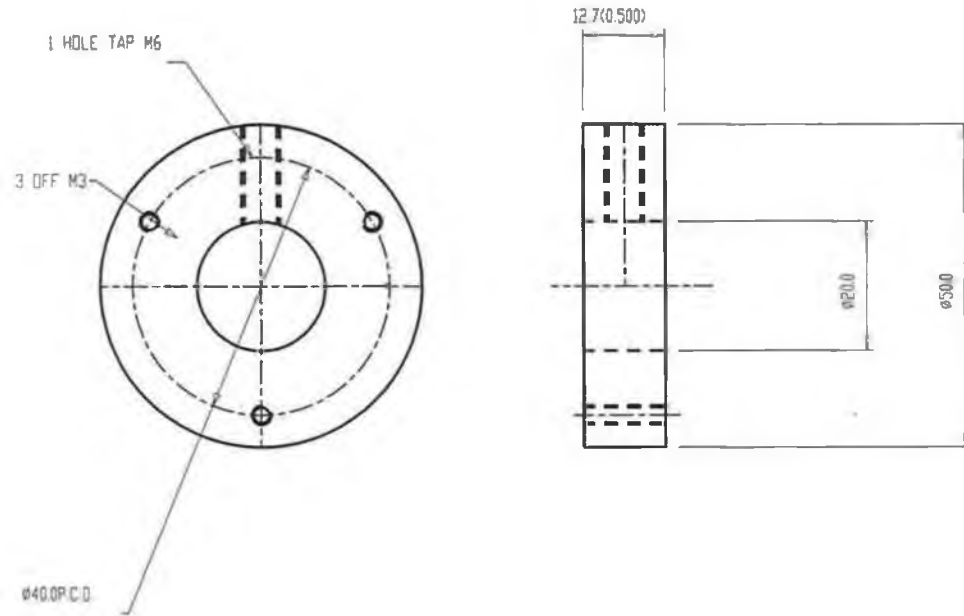
DRAWN BY: **AJM**

DRAWING No: **17**

DATE: **14-09-02**

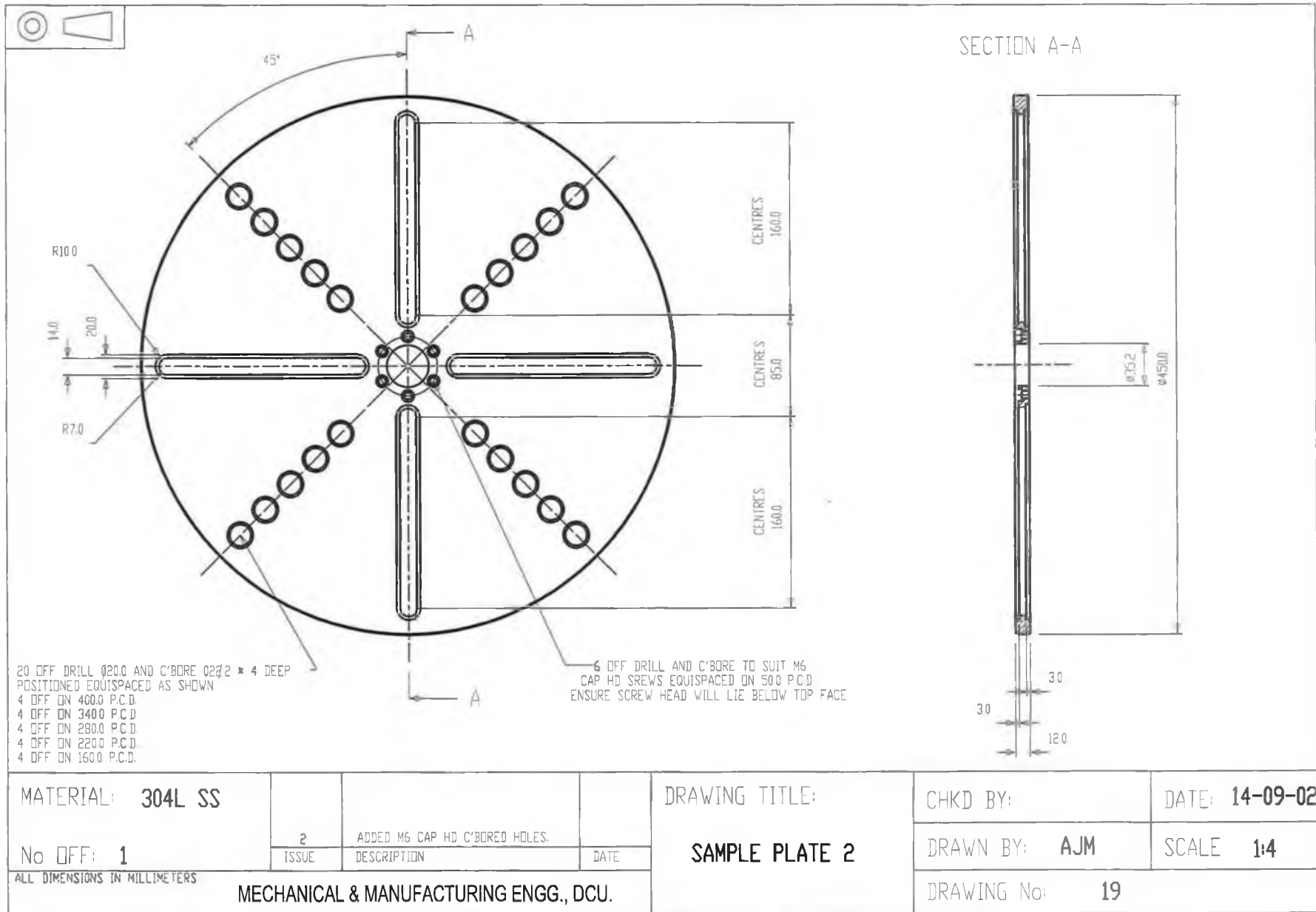
SCALE **1:4**

A-18

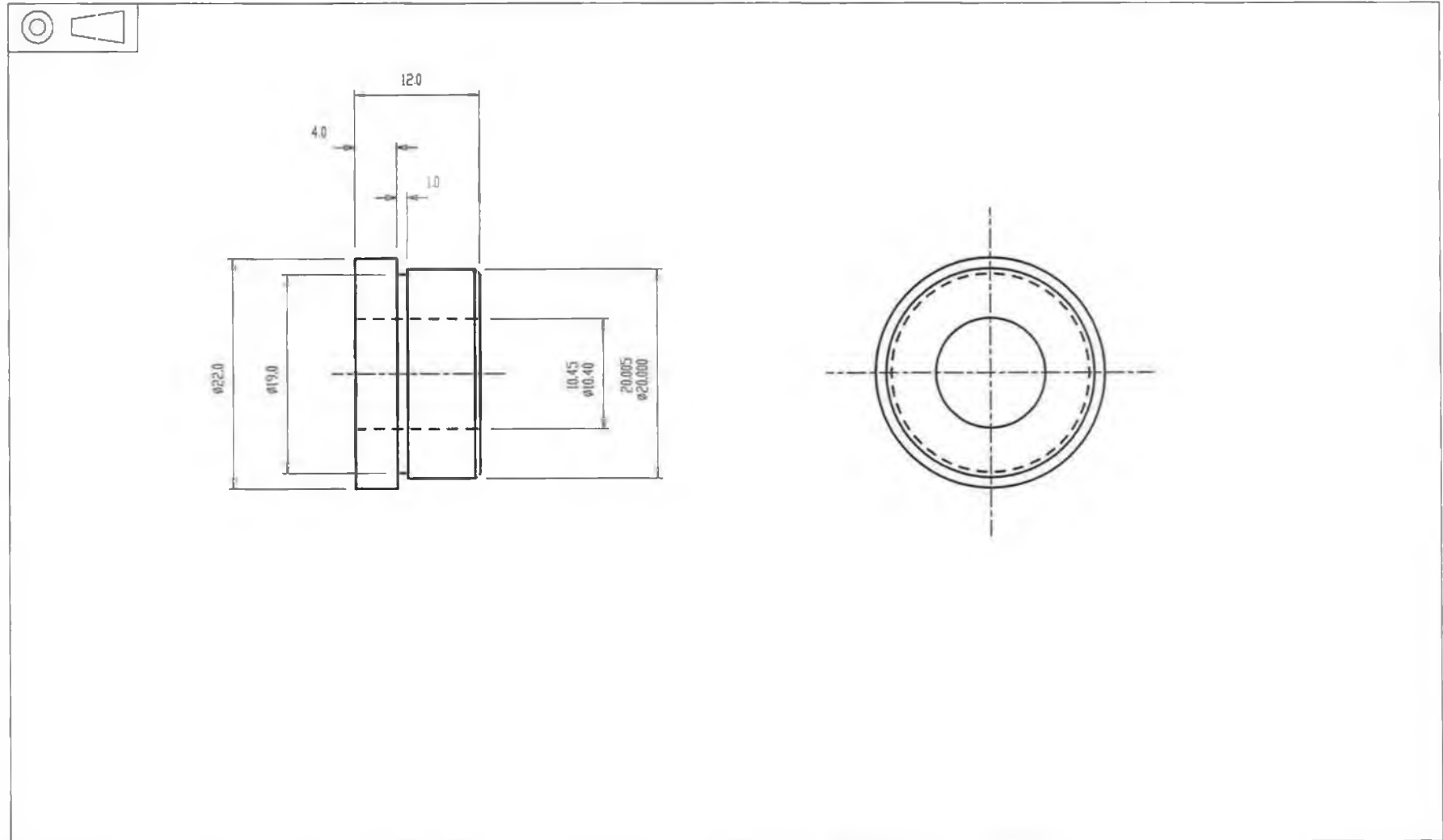


MATERIAL: 304L SS			DRAWING TITLE: STANDARD COLLAR	CHKD BY:	DATE: 14.09.02
NO OFF: 1	ISSUE	DESCRIPTION		DRAWN BY: AJM	SCALE 1:1
ALL DIMENSIONS IN MILLIMETERS	MECHANICAL & MANUFACTURING ENGG., DCU.			DRAWING No: 18	

A-19

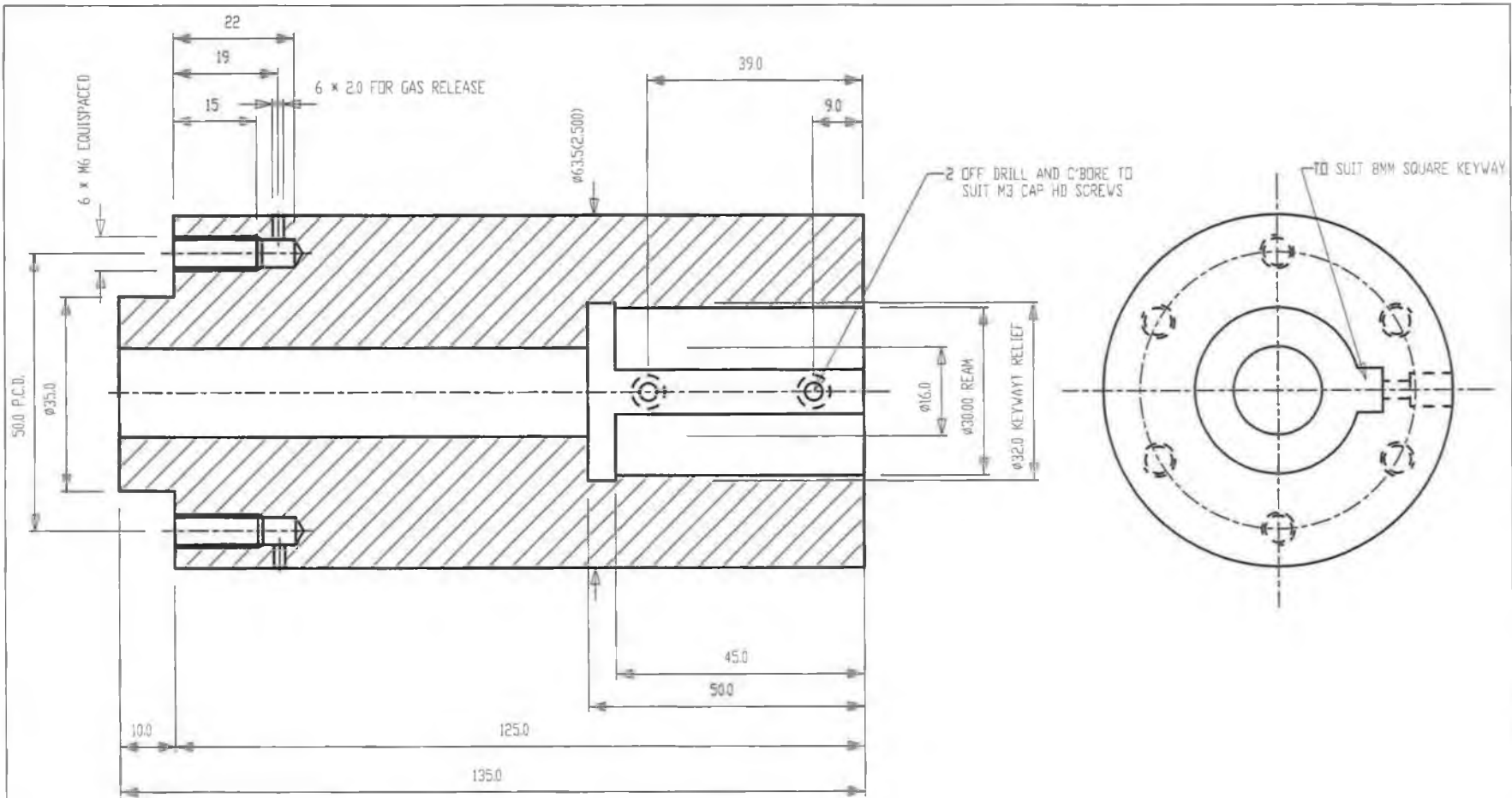


A-20



MATERIAL: PHOSPHOR BRONZE				DRAWING TITLE: BUSH	CHKD BY:	DATE: 14-09-02
No OFF: 20		ISSUE	DESCRIPTION		DATE	DRAWN BY: AJM
ALL DIMENSIONS IN MILLIMETERS				MECHANICAL & MANUFACTURING ENGG., DCU.		DRAWING No: 20

A-21



MATERIAL: 304L SS

NO OFF 1

ALL DIMENSIONS IN MILLIMETERS

ISSUE

ADDED TAPPED M6 HOLES
INCREASED BORE LENGTH

DESCRIPTION

DATE

MECHANICAL & MANUFACTURING ENGG., DCU.

DRAWING TITLE:

SAMPLE PLATE SUPPORT

CHKD BY:

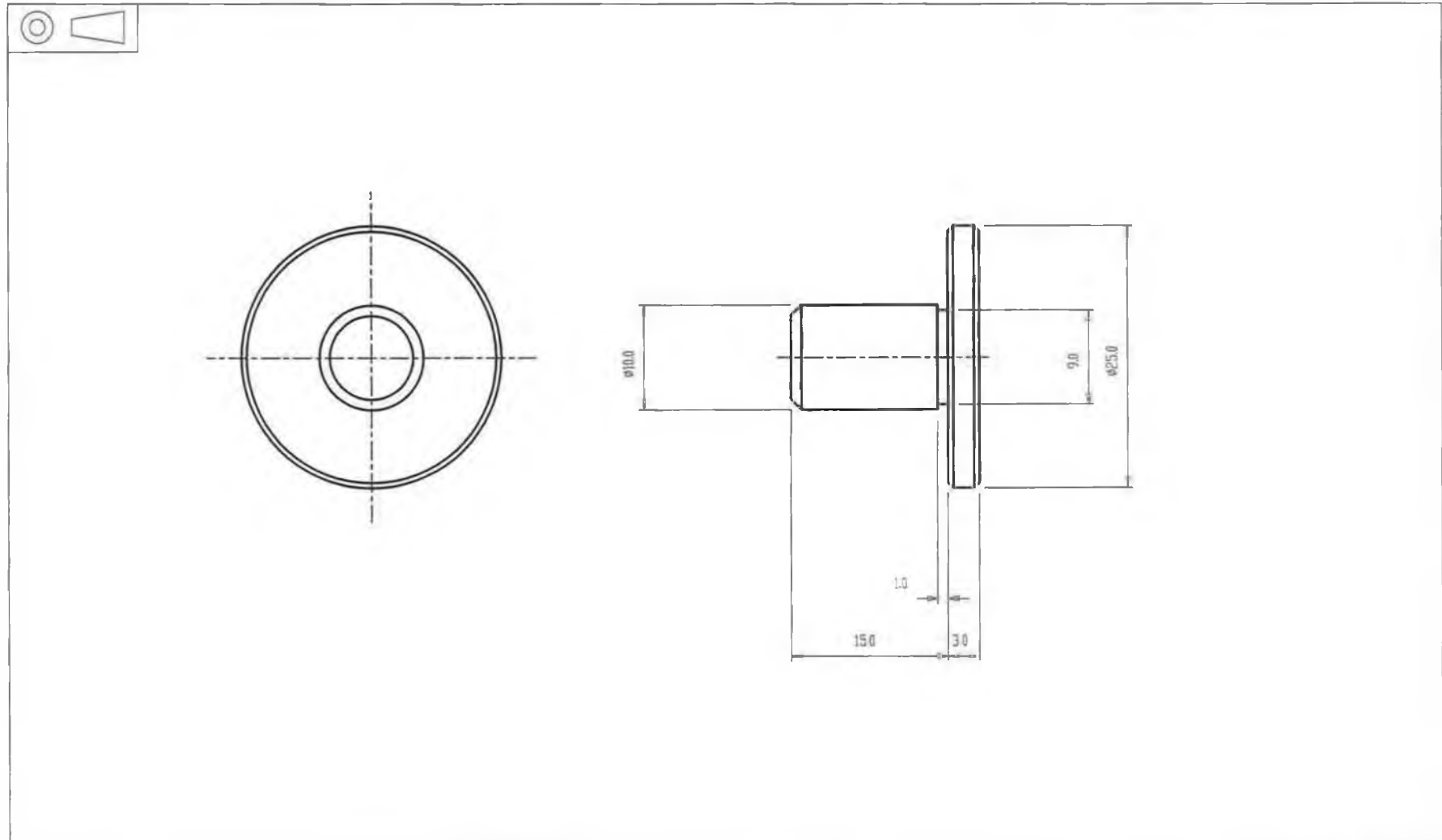
DATE: 14-09-02

DRAWN BY: AJM

SCALE 21

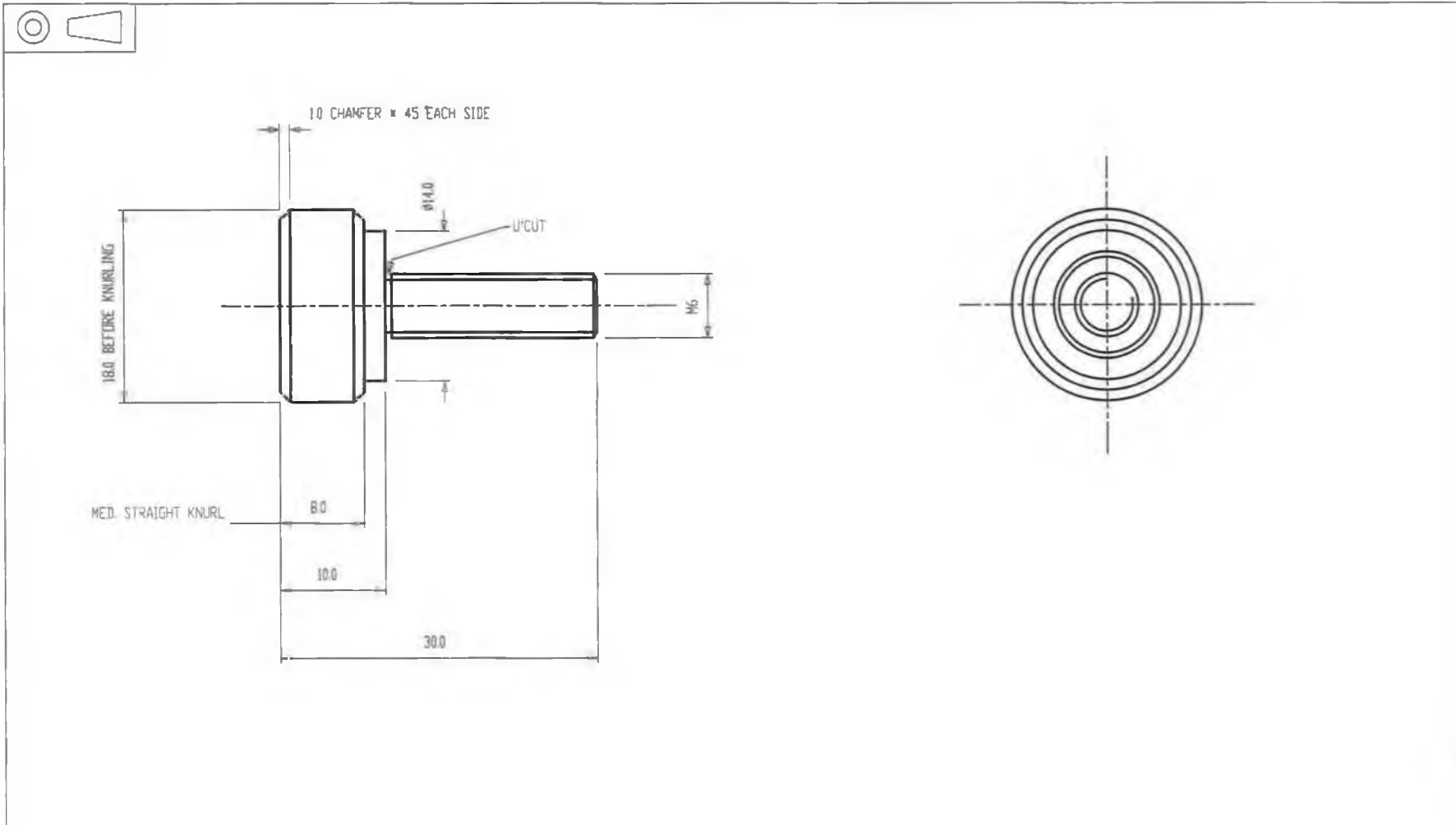
DRAWING No: 21

A-22



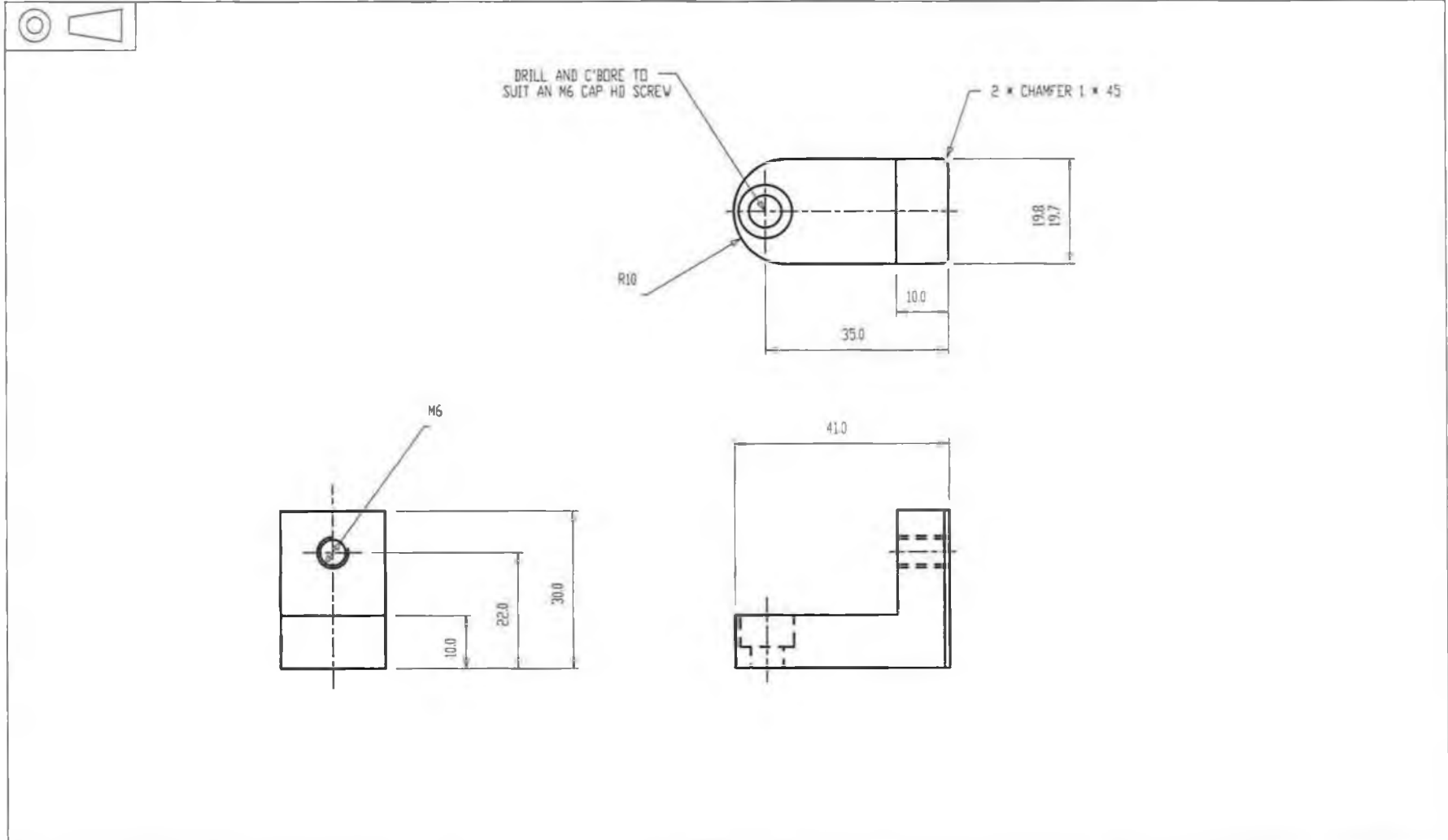
MATERIAL: 304L SS			DRAWING TITLE:	CHKD BY:	DATE: 14-09-02
No OFF: 16	ISSUE	DESCRIPTION	PLUG	DRAWN BY: AJM	SCALE 2:1
ALL DIMENSIONS IN MILLIMETERS	MECHANICAL & MANUFACTURING ENGG., DCU.			DRAWING No: 22	

A-23



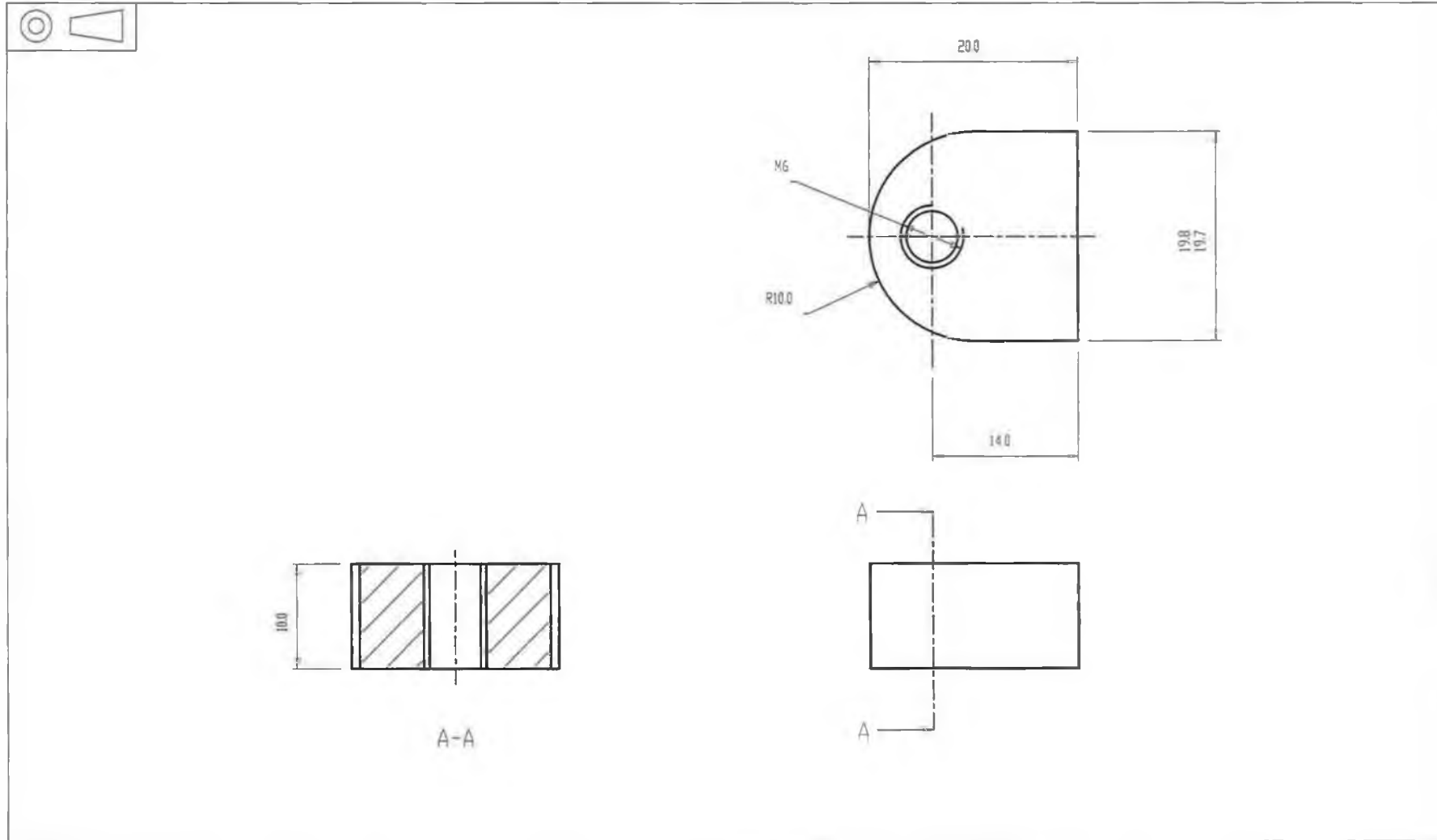
MATERIAL: 304L SS				DRAWING TITLE:	CHKD BY:	DATE: 14-09-02
No OFF: 4	ISSUE	DESCRIPTION	DATE	LOCKING THREAD	DRAWN BY: AJM	SCALE 2:1
ALL DIMENSIONS IN MILLIMETERS					DRAWING No: 23	
MECHANICAL & MANUFACTURING ENGG., DCU.						

A-24



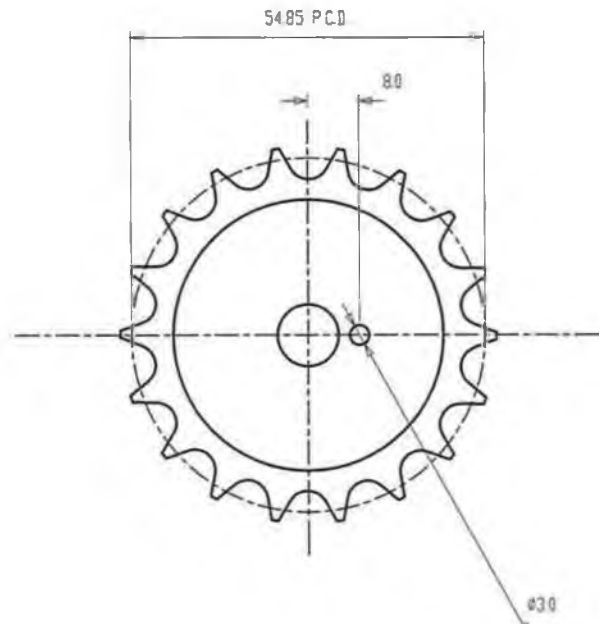
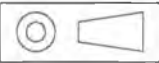
MATERIAL: 304L SS		DRAWING TITLE:		CHKD BY:	DATE: 14-09-02
No OFF: 1		SLIDING CARRIAGE		DRAWN BY: AJM	SCALE 1:1
ALL DIMENSIONS IN MILLIMETERS		MECHANICAL & MANUFACTURING ENGG., DCU.		DRAWING No: 24	
ISSUE	DESCRIPTION	DATE			

A-25



MATERIAL: ALUMINIUM			DRAWING TITLE:	CHKD BY:	DATE: 14-09-02
No OFF: 4	ISSUE	DESCRIPTION	SLIDING NUT	DRAWN BY: AJM	SCALE 2:1
ALL DIMENSIONS IN MILLIMETERS	MECHANICAL & MANUFACTURING ENGG., DCU.			DRAWING No: 25	

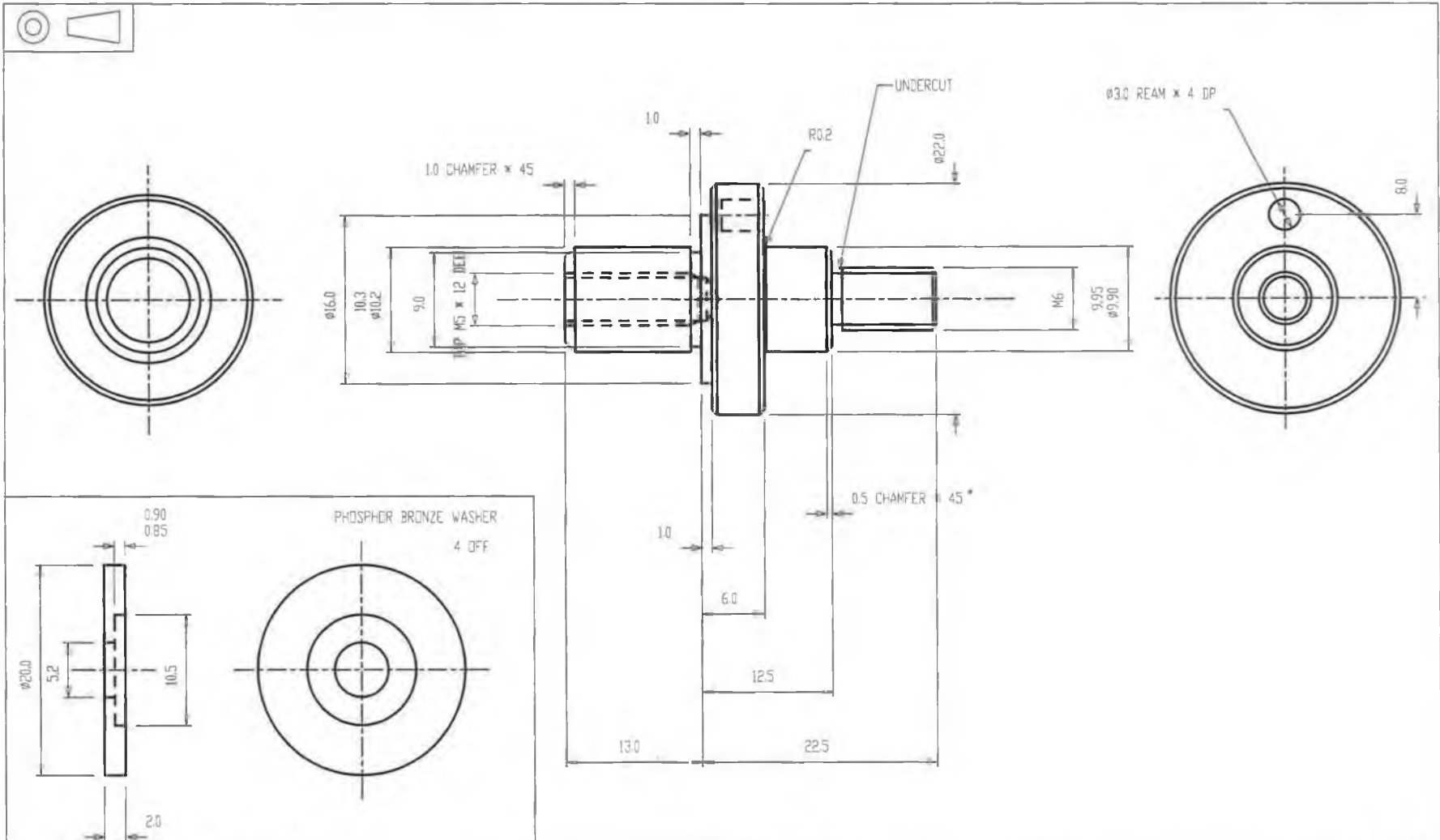
A-26



SPROCKET: AS 37-18
 3/8" PITCH, 1/4" ROLLER, 1/4" THICK

MATERIAL: ST. STEEL	2	CTR HOLE WAS 6mm	DATE	DRAWING TITLE: SPROCKET	CHKD BY:	DATE: 14-09-02
					No OFF: 4	ISSUE
ALL DIMENSIONS IN MILLIMETERS				MECHANICAL & MANUFACTURING ENGG., DCU.	DRAWING No:	26

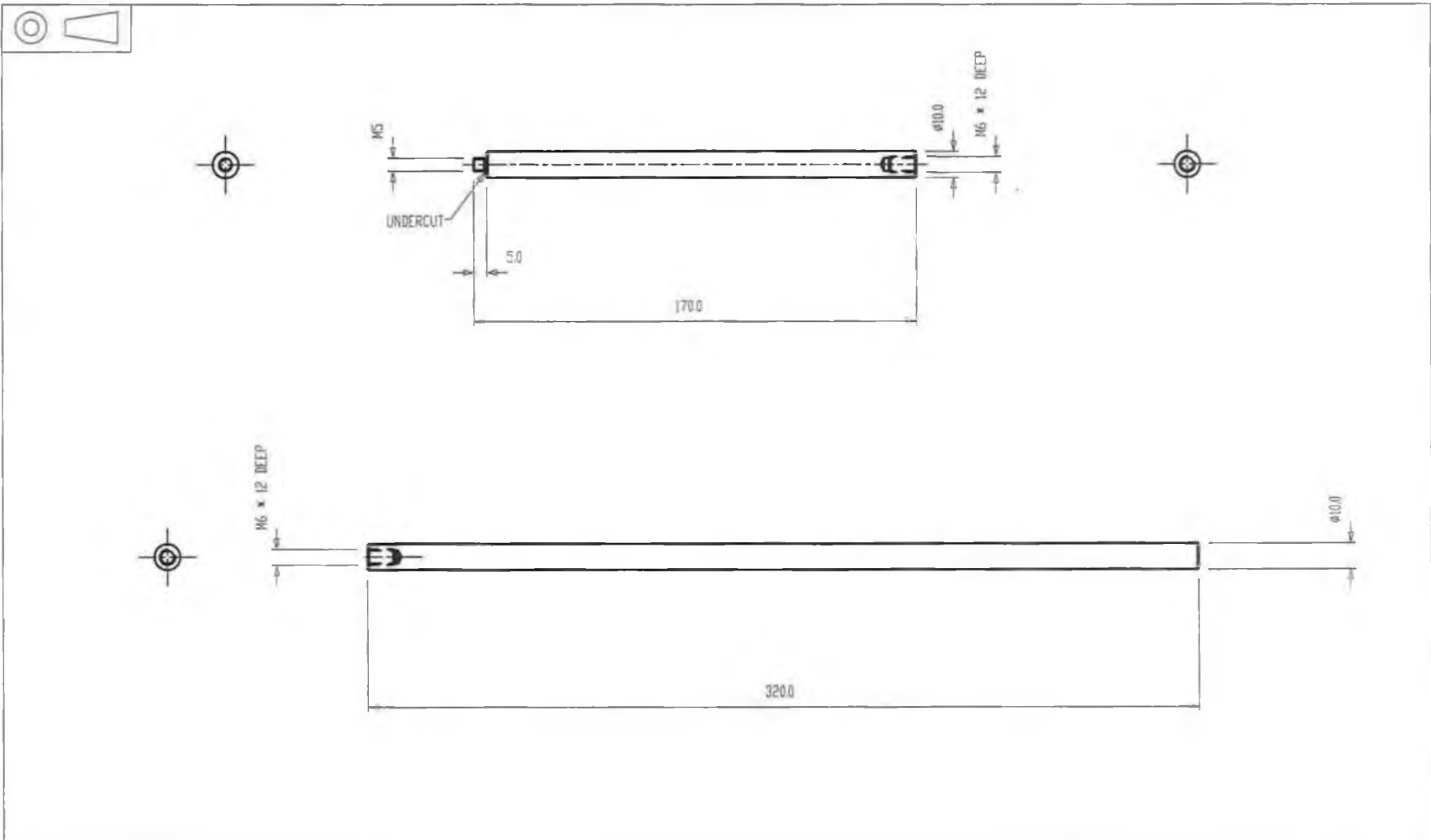
A-27



MATERIAL: 304L SS		DRAWING TITLE		CHKD BY:	DATE: 14-09-02
No OFF: 4		SHAFT		DRAWN BY: AJM	SCALE 2:1
3	ADDED WASHER	MECHANICAL & MANUFACTURING ENGG., DCU.		DRAWING No: 27	
2	ADDED TAPPED HOLE				
ISSUE	DESCRIPTION	DATE			

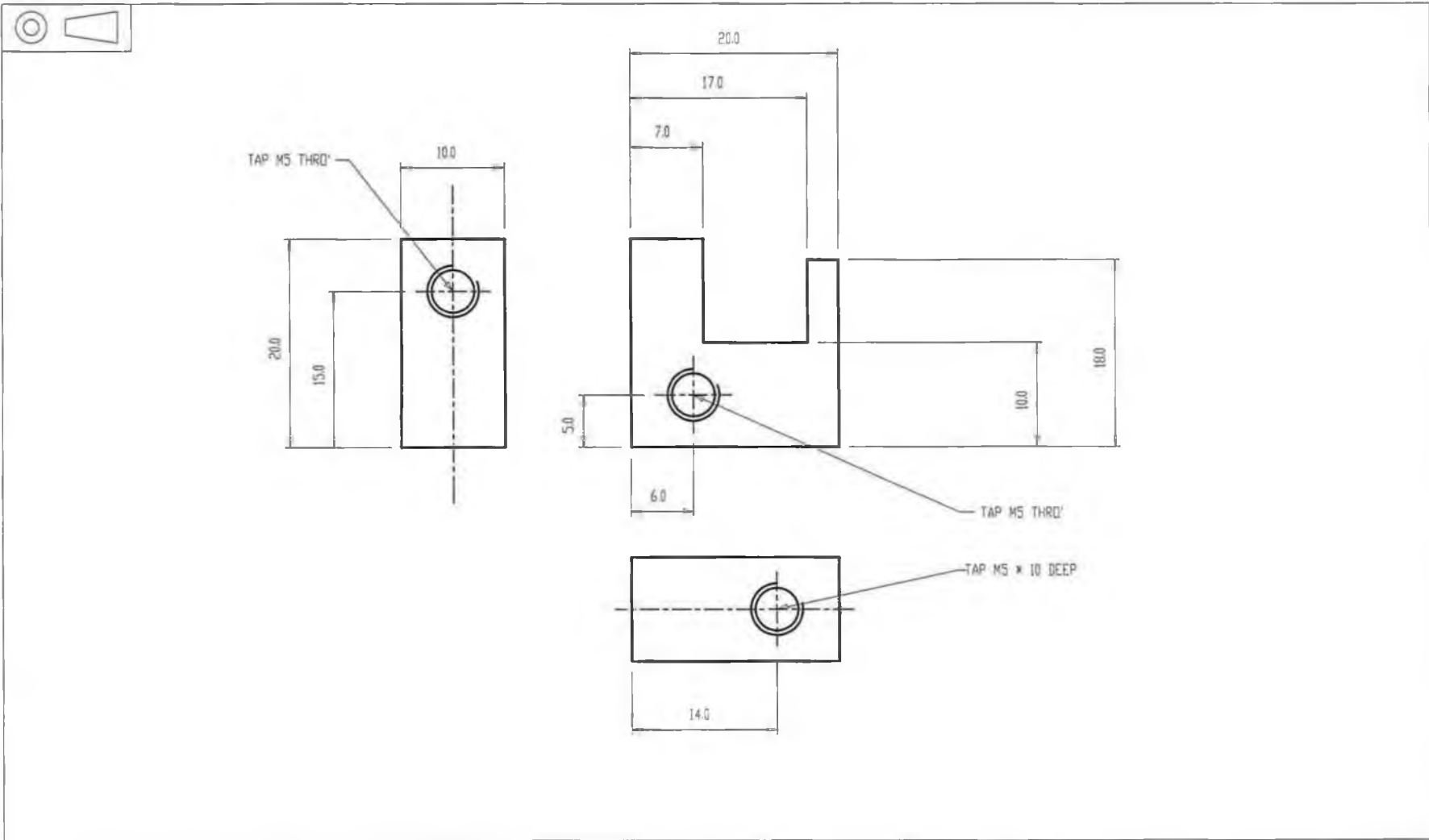
ALL DIMENSIONS IN MILLIMETERS

A-28



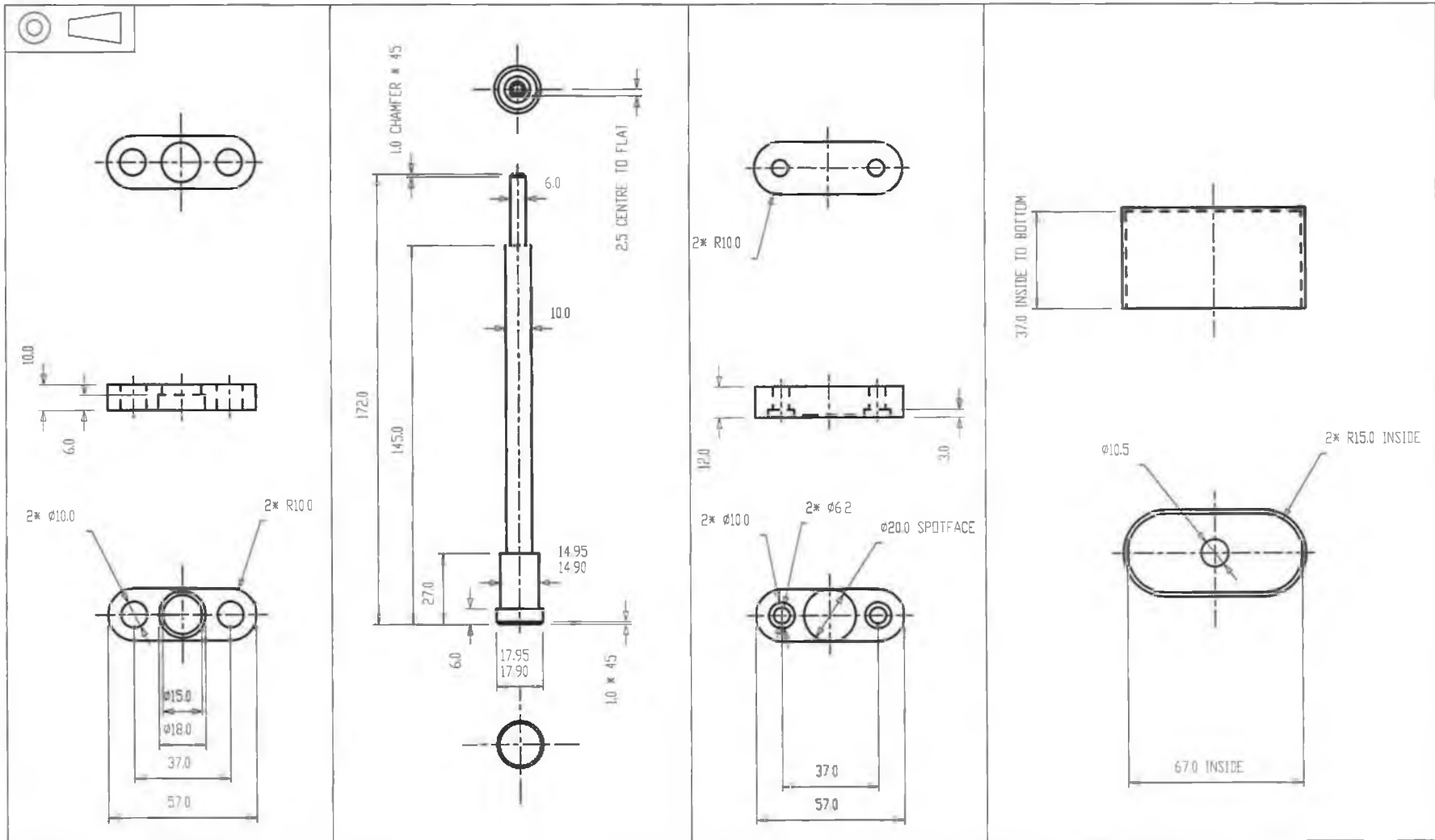
MATERIAL: 304L SS		DRAWING TITLE:		CHKD BY:	DATE: 14-09-02
No OFF: 4		SAMPLE POSTS		DRAWN BY: AJM	SCALE 1:2
ALL DIMENSIONS IN MILLIMETERS		ISSUE	DESCRIPTION	DATE	DRAWING No: 28
MECHANICAL & MANUFACTURING ENGG., DCU.					

A-29



MATERIAL: 304L SS		DRAWING TITLE:		CHKD BY:	DATE: 14-09-02
No OFF: 1		SAMPLE CLAMP		DRAWN BY: AJM	SCALE 2:1
ALL DIMENSIONS IN MILLIMETERS		MECHANICAL & MANUFACTURING ENGG., DCU.		DRAWING No:	29
ISSUE	DESCRIPTION	DATE			

A-30



MATERIAL:

No OFF: 1 OF EACH

ISSUE	DESCRIPTION	DATE

ALL DIMENSIONS IN MILLIMETERS

MECHANICAL & MANUFACTURING ENGG., DCU.

DRAWING TITLE:

KICKER PARTS

CHKD BY:

DATE: 14-09-02

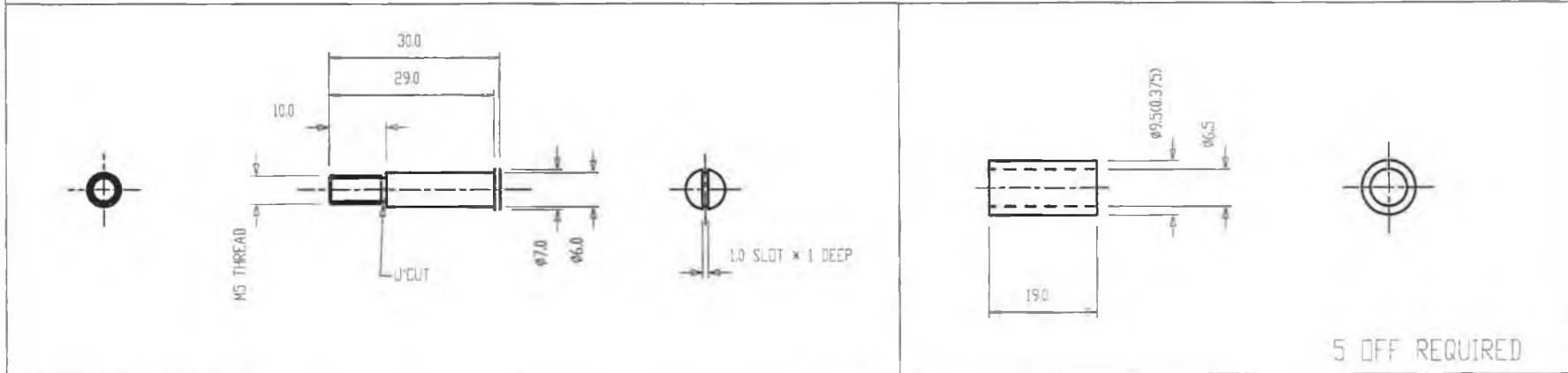
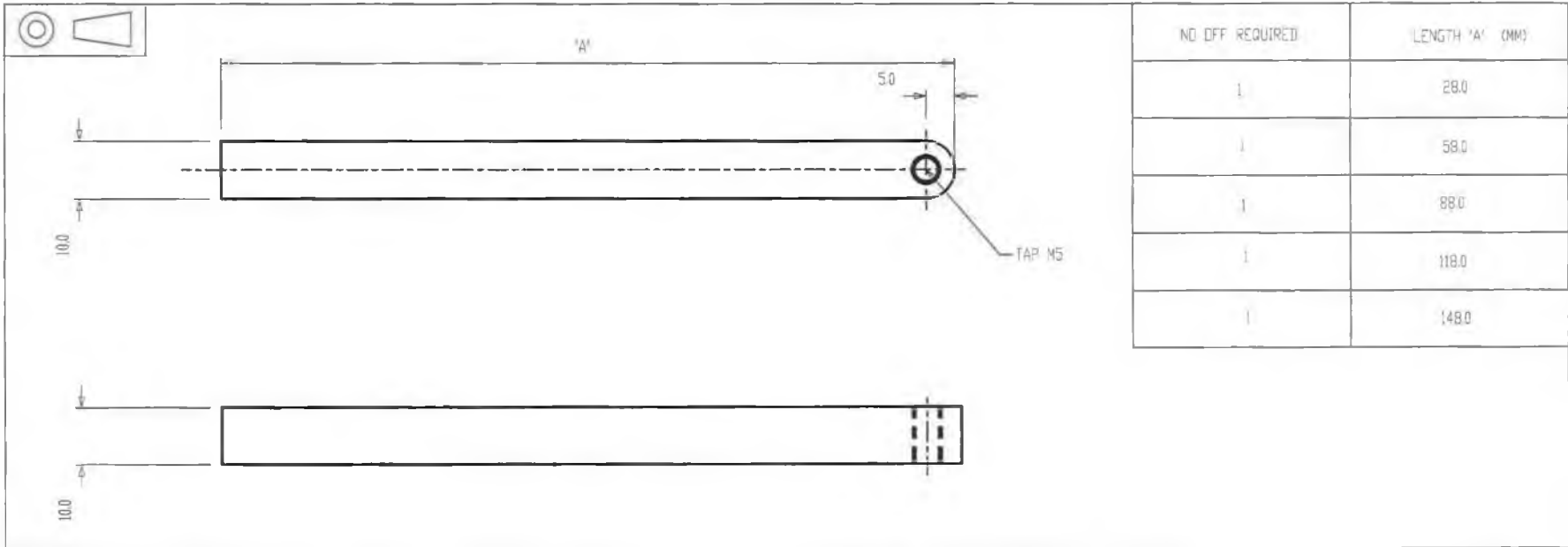
DRAWN BY: AJM

SCALE: 1:2

DRAWING No:

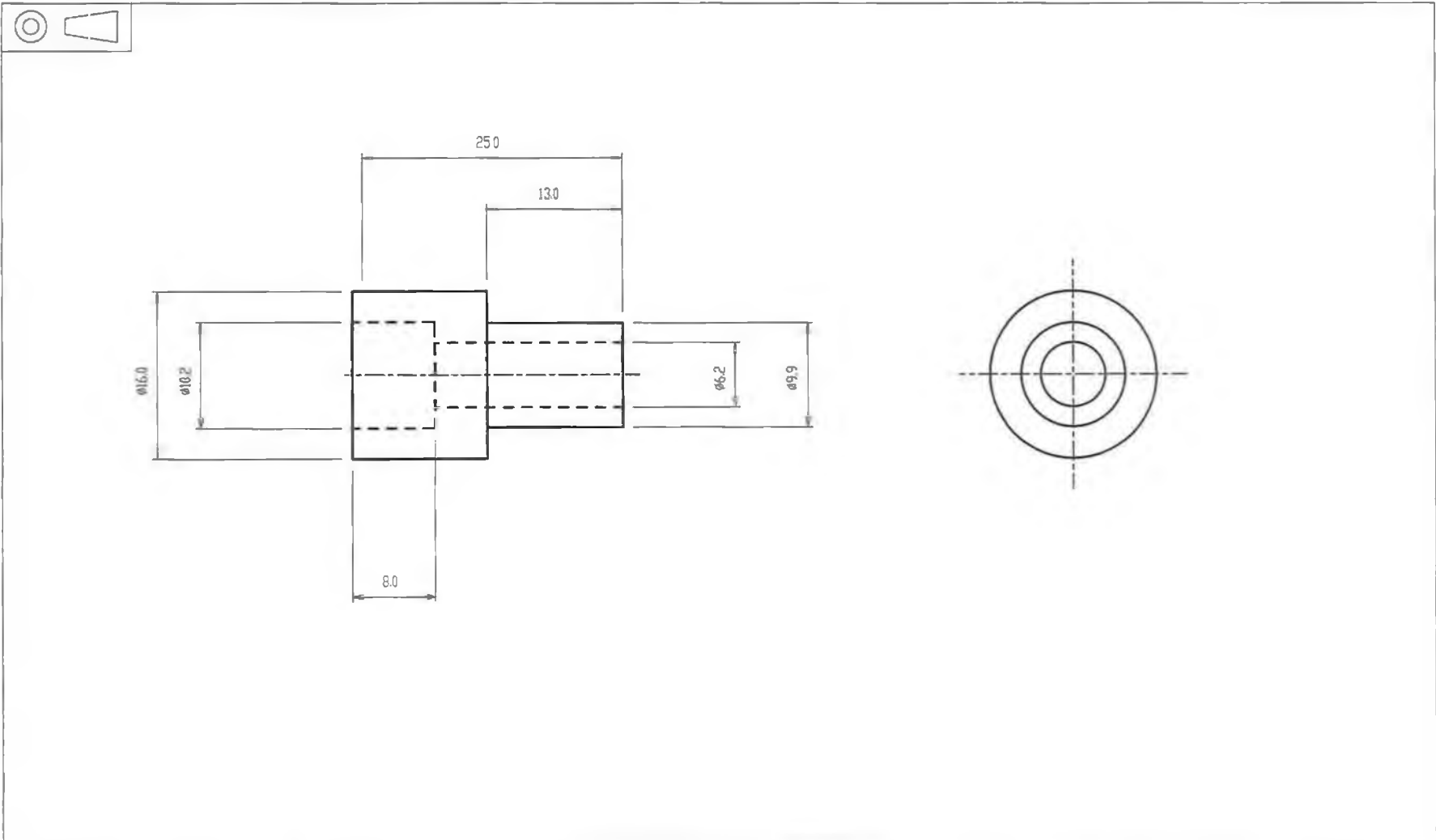
30

A-31



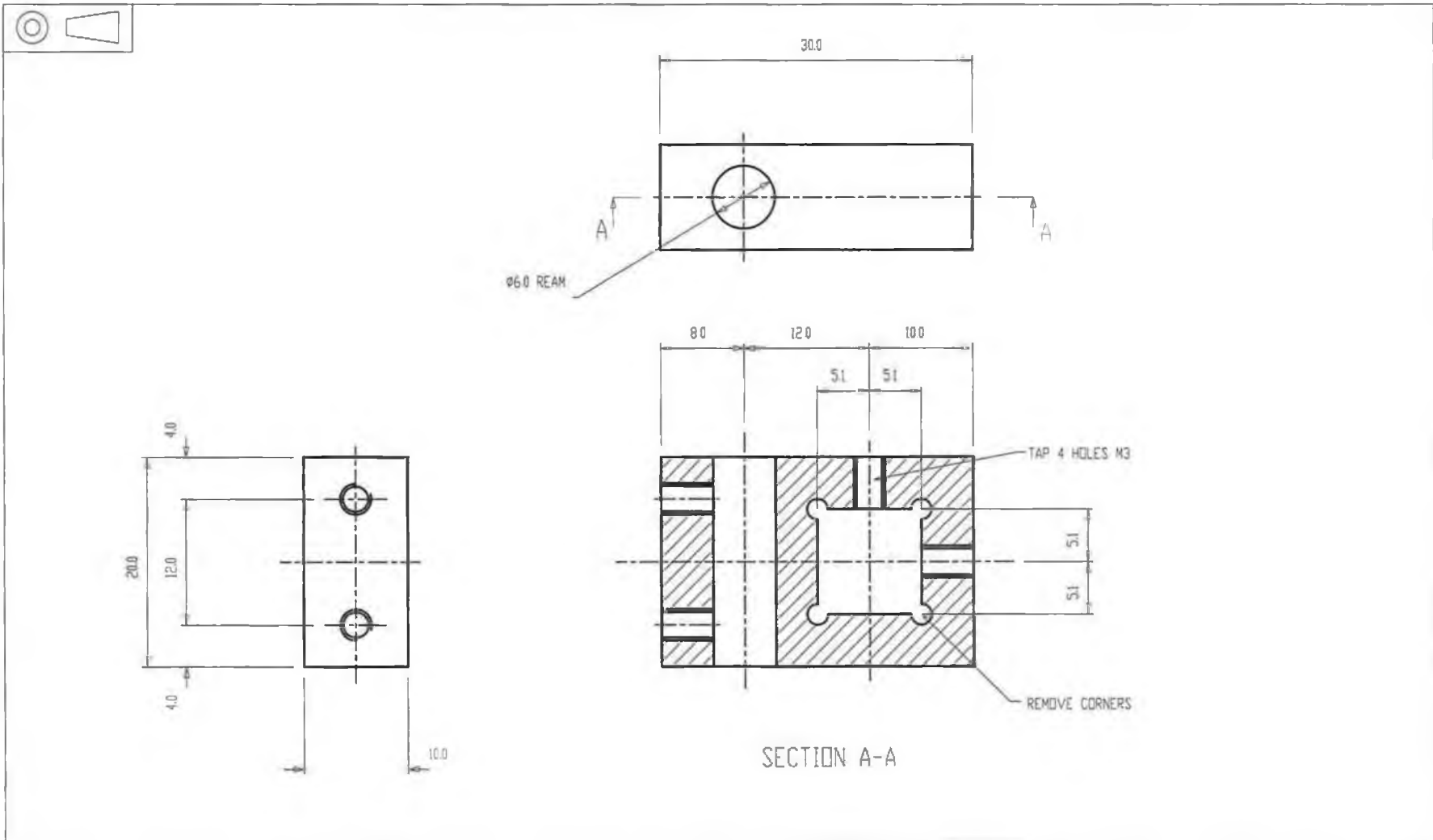
MATERIAL: 304L SS			DRAWING TITLE:	CHKD BY:	DATE: 14-09-02
No OFF: AS ABOVE	ISSUE	DESCRIPTION	KICKER PARTS	DRAWN BY: AJM	SCALE 1:1
ALL DIMENSIONS IN MILLIMETERS				DRAWING No:	31
MECHANICAL & MANUFACTURING ENGG., DCU.					

A-32



MATERIAL: PTFE				DRAWING TITLE:	CHKD BY:	DATE: 14-09-02
No OFF: 2	ISSUE	DESCRIPTION	DATE	BOLT INSULATOR	DRAWN BY: AJM	SCALE 2:1
ALL DIMENSIONS IN MILLIMETERS	MECHANICAL & MANUFACTURING ENGG., DCU.				DRAWING No:	32

A-33



MATERIAL: 304L SS				DRAWING TITLE:	CHKD BY:	DATE: 14-09-02
No OFF: 1	ISSUE	DESCRIPTION	DATE	KICKER ADAPTOR	DRAWN BY: AJM	SCALE 2:1
ALL DIMENSIONS IN MILLIMETERS					DRAWING No:	33
MECHANICAL & MANUFACTURING ENGG., DCU.						

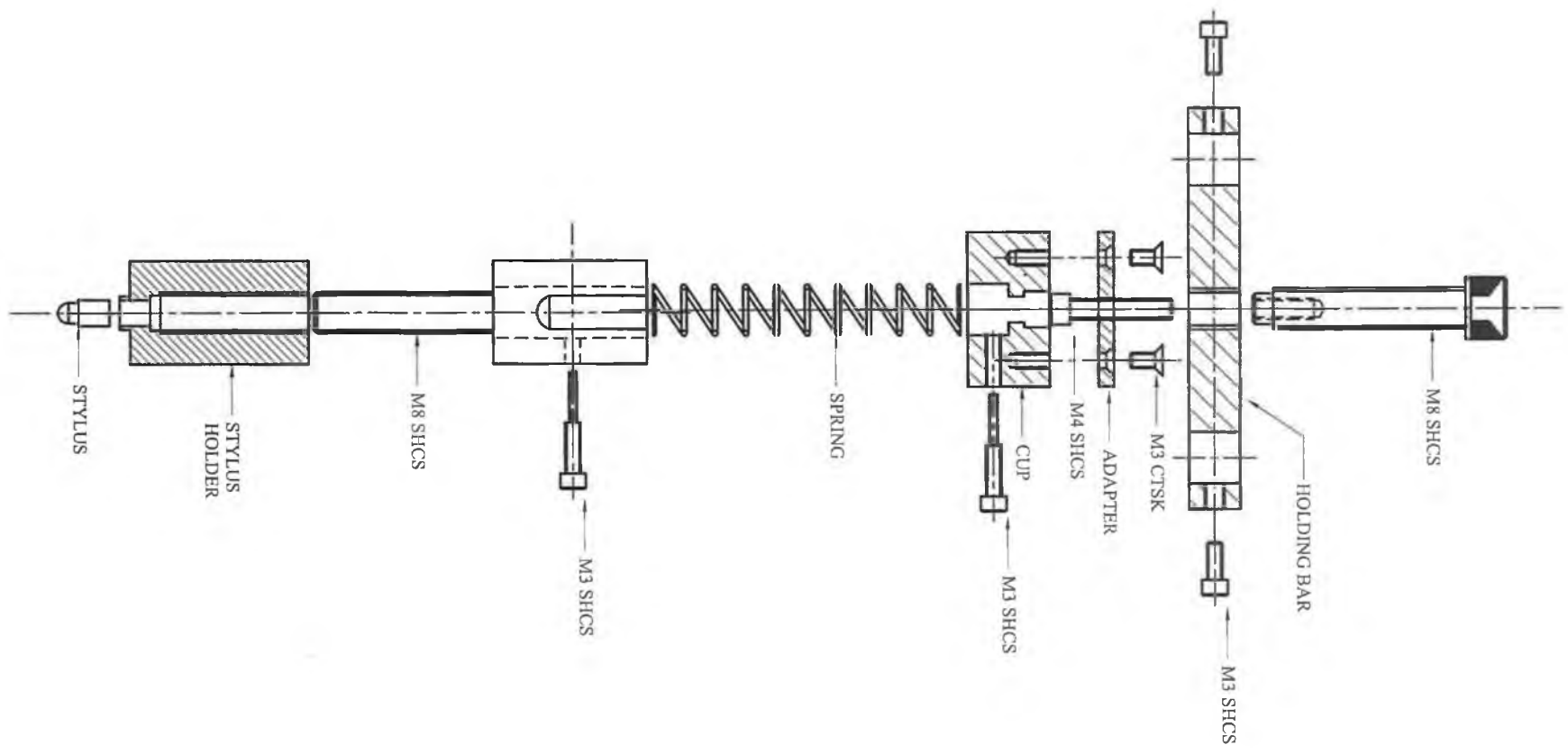
APPENDIX B

Drawings of Modified Wear Tester

DRG. No.

PART No.

REV.	DESCRIPTION	BY	DATE
------	-------------	----	------

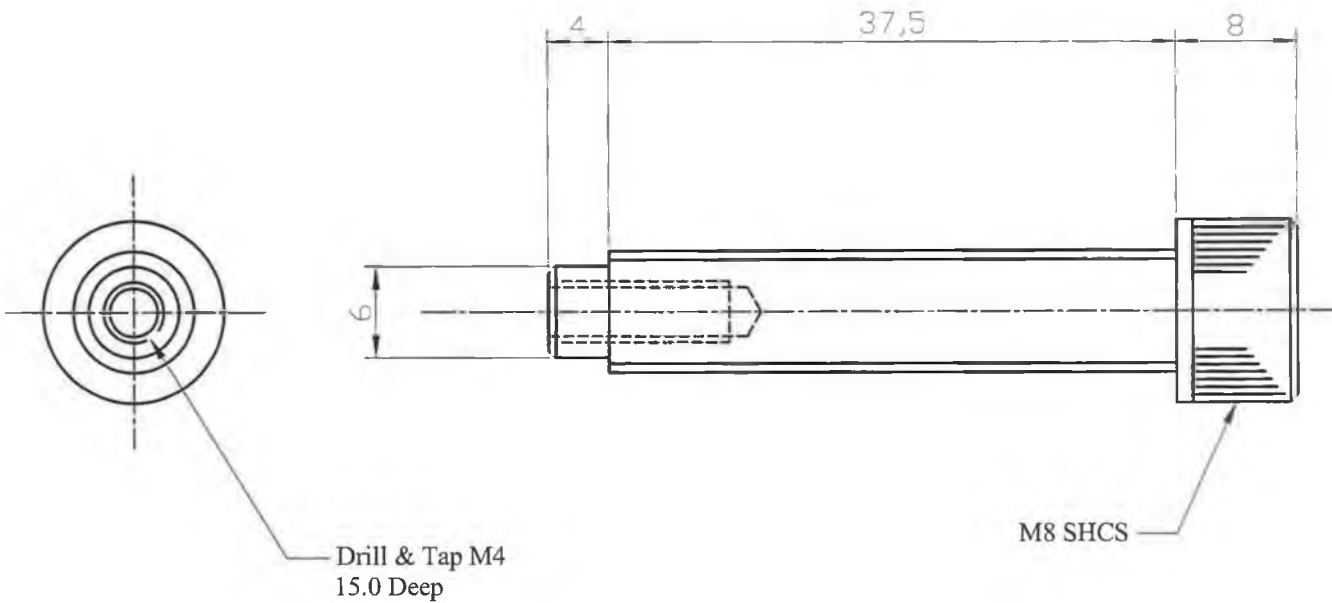


THIRD ANGLE PROJECTION		TOLERANCES UNLESS SPECIFIED		MECHANICAL & MANUFAC. ENGG. DCU		
DRAWN HAIDER		FRACTIONS		WEAR RIG ASSEMBLY		
DATE 14-09-02		DECIMALS	+ .1			
CHECKED LIAM		ANGLES	+ .5	QTY.	ASS'Y DRG.	PARTS LIST
APPROVED		SURFACE FIN.		SCALE	PROJECT SPUTTERING	SHEET 1 OF 6
		MAT'L				
		HEAT TREAT.	NONE			

B-1

REV.	DESCRIPTION	BY	DATE
------	-------------	----	------

DRG. No.

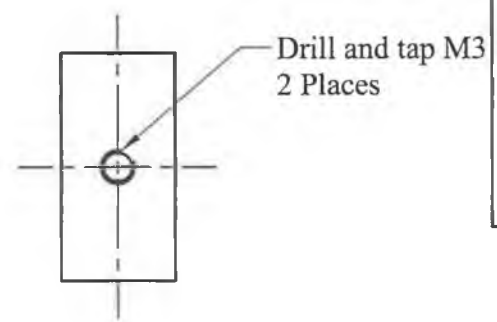
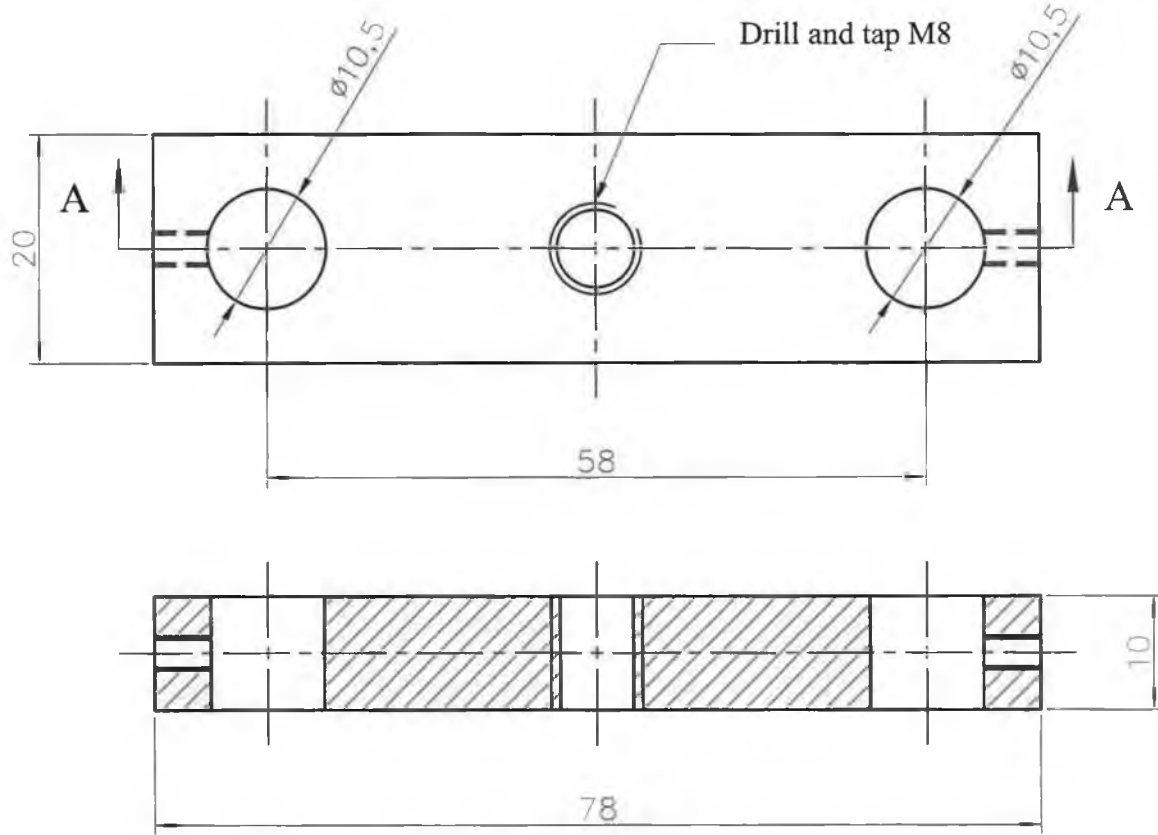


B-2

THIRD ANGLE PROJECTION		TOLERANCES UNLESS SPECIFIED		MECHANICAL & MANUFAC. ENGG. DCU		
DRAWN HAIDER	DECIMALS ± .1	FRACTIONS		M8 SCREW		
DATE 14-09-02	ANGLES ± .5	SURFACE FIN.				
CHECKED LIAM	MAT'L ALUMINUM	QTY. 1	ASS'Y DRG.	PARTS LIST		
APPROVED	HEAT TREAT. NONE	SCALE	PROJECT SPUTTERING	SHEET 2 OF 6		

PART No.

B-3



REV.	DESCRIPTION	BY	DATE
------	-------------	----	------

DRG. No.

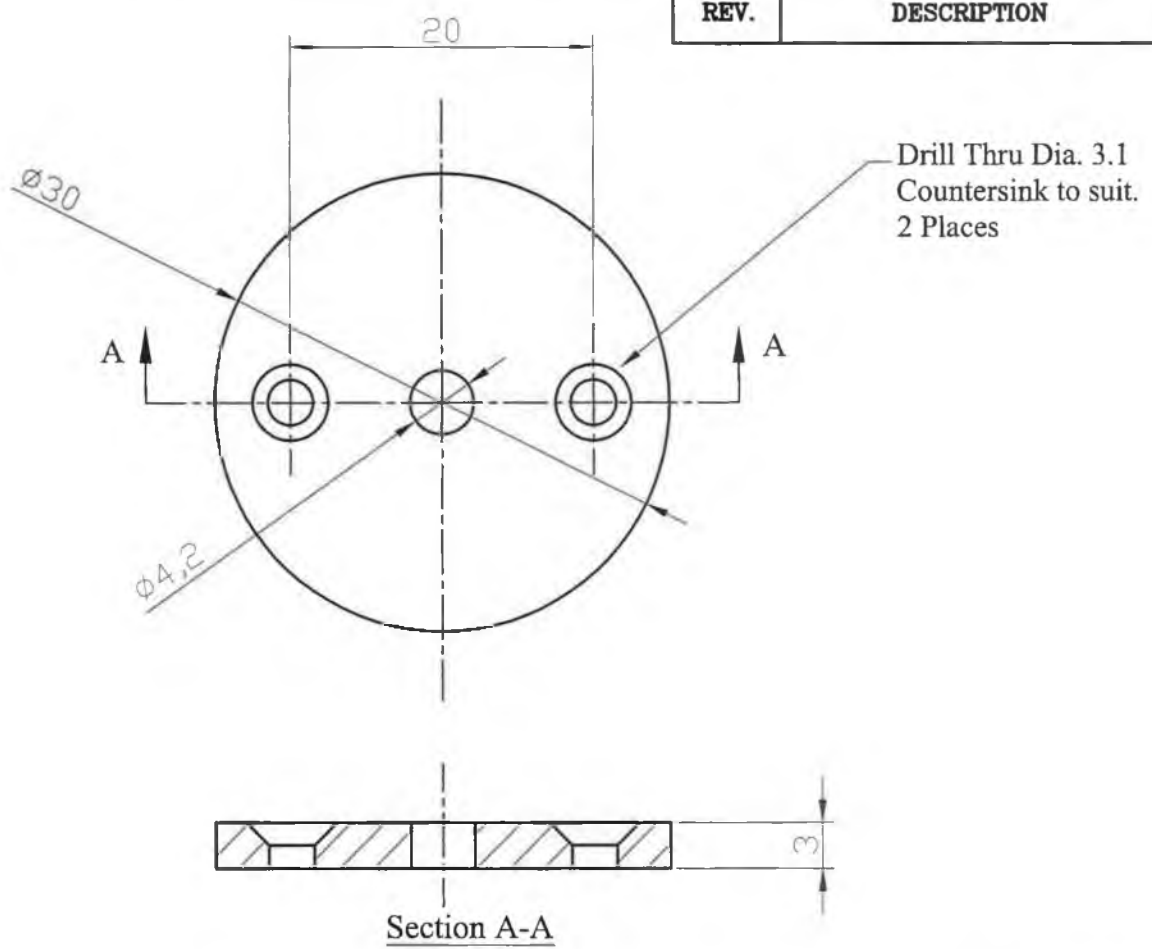
Section A-A

THIRD ANGLE PROJECTION		TOLERANCES UNLESS SPECIFIED		MECHANICAL & MANUFAC. ENGG. DCU		
DRAWN HAIDER		FRACTIONS		HOLDING BAR		
DATE 14-09-02		DECIMALS ± .1				
CHECKED LIAM		ANGLES ± .5		QTY. 1	ASS'Y DRG.	PARTS LIST
APPROVED		SURFACE FIN.		SCALE	PROJECT SPUTTERING	SHEET 3 OF 6
		MAT'L ALUMINUM/MS				
		HEAT TREAT. NONE				

PART No.

REV.	DESCRIPTION	BY	DATE
------	-------------	----	------

DRG. No.



Drill Thru Dia. 3.1
Countersink to suit.
2 Places

Section A-A

THIRD ANGLE PROJECTION		TOLERANCES UNLESS SPECIFIED		MECHANICAL & MANUFAC. ENGG. DCU		
DRAWN HAIDER	DATE 14-09-02	FRACTIONS	DECIMALS ± .1	ADAPTOR		
CHECKED LIAM		ANGLES ± .5	SURFACE FIN.			
APPROVED		MAT'L ALUMINUM/MS	HEAT TREAT. NONE	QTY. 1	ASS'Y DRG.	PARTS LIST
				SCALE	PROJECT SPUTTERING	SHEET 4 OF 6

PART No.

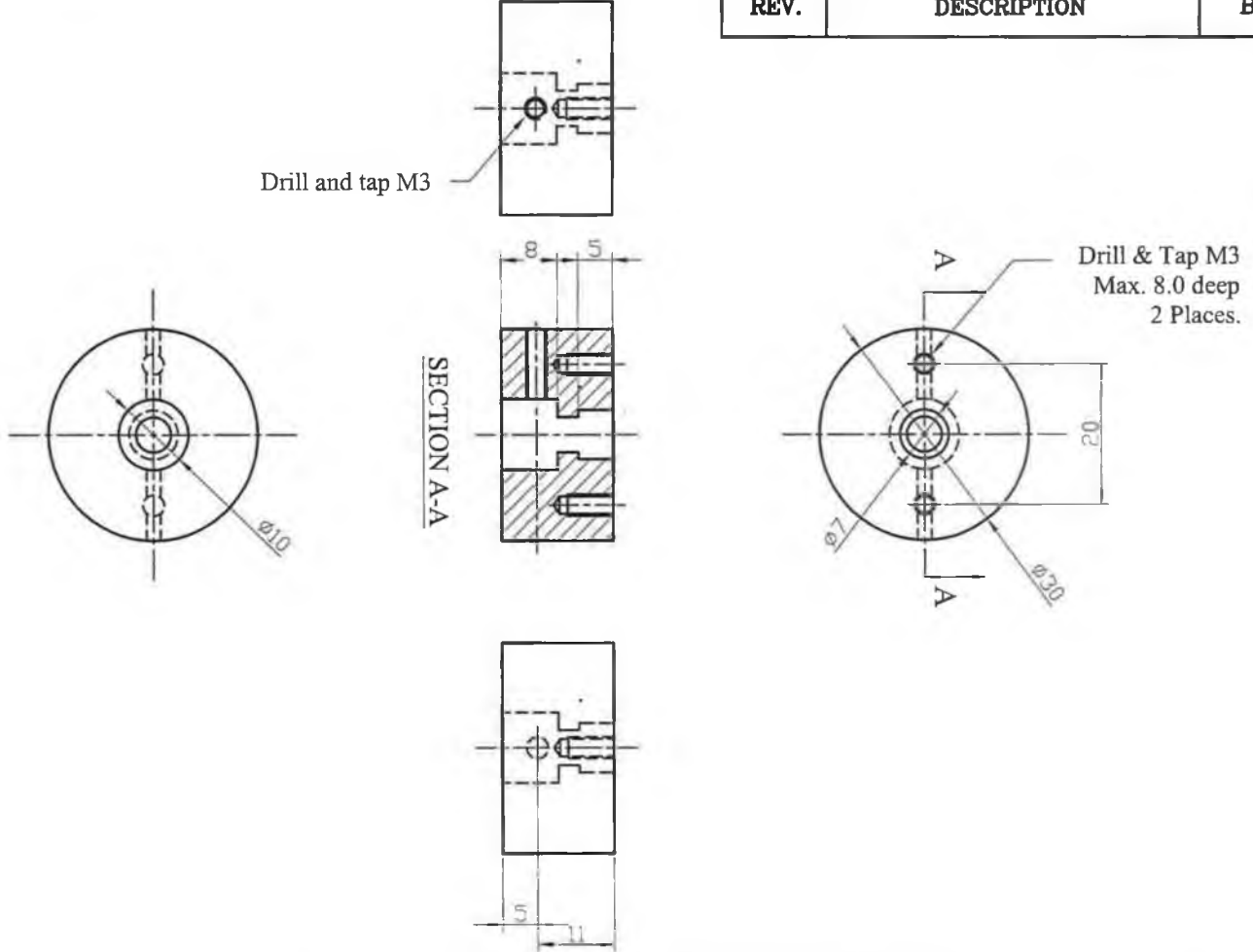
B-4

B-5

DRG. No.

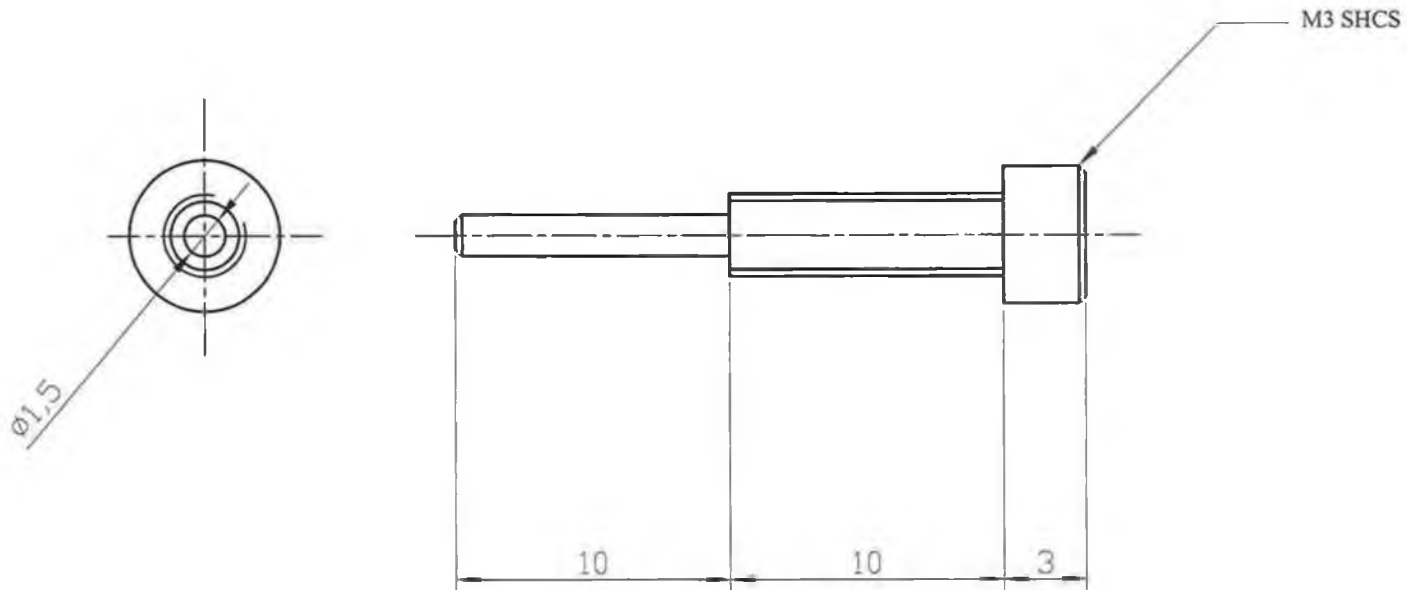
PART No.

REV.	DESCRIPTION	BY	DATE
------	-------------	----	------



THIRD ANGLE PROJECTION		TOLERANCES UNLESS SPECIFIED		MECHANICAL & MANUFAC. ENGG. DCU		
DRAWN HAIDER	DATE 14-09-02	FRACTIONS		CUP		
CHECKED LIAM	APPROVED	DECIMALS ± .1	ANGLES ± .5			
		SURFACE FIN.		QTY. 1	ASS'Y DRG.	PARTS LIST
		MAT'L ALUMINUM		SCALE	PROJECT SPUTTERING	SHEET 5 OF 6
		HEAT TREAT. NONE				

B-6



REV.	DESCRIPTION	BY	DATE
------	-------------	----	------

DRG. No.

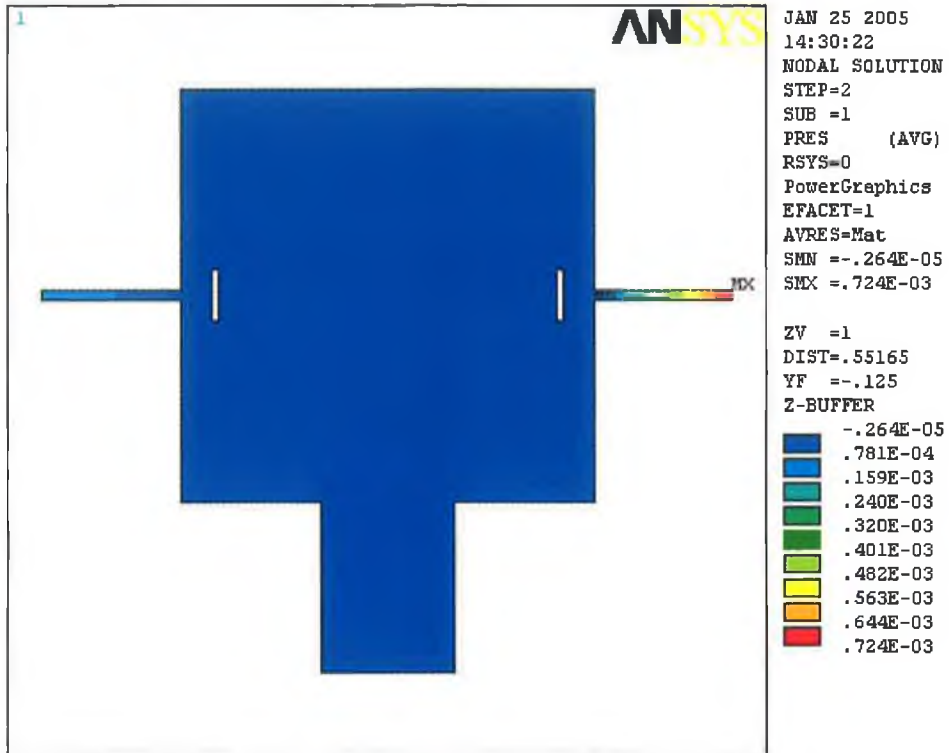
THIRD ANGLE PROJECTION		TOLERANCES UNLESS SPECIFIED		MECHANICAL & MANUFAC. ENGG. DCU		
DRAWN HAIDER	DATE 30-09-02	FRACTIONS	DECIMALS ± .1	M3 SCREW		
CHECKED LIAM	APPROVED	ANGLES ± .5	SURFACE FIN.			
		MAT'L	HEAT TREAT. NONE	QTY. 2	ASS'Y DRG.	PARTS LIST
				SCALE	PROJECT SPUTTER	SHEET 6 OF 6

PART No.

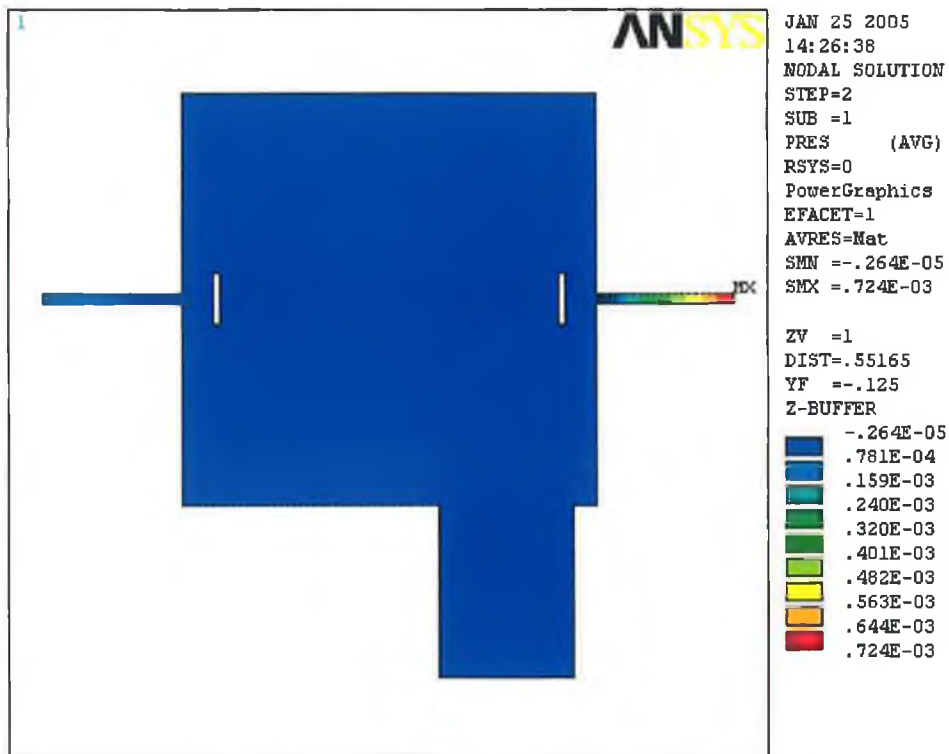
APPENDIX C

COMPARISONS OF 2-D RESULTS FOR OUTLET POSITIONS IN GAS FLOW MODELLING

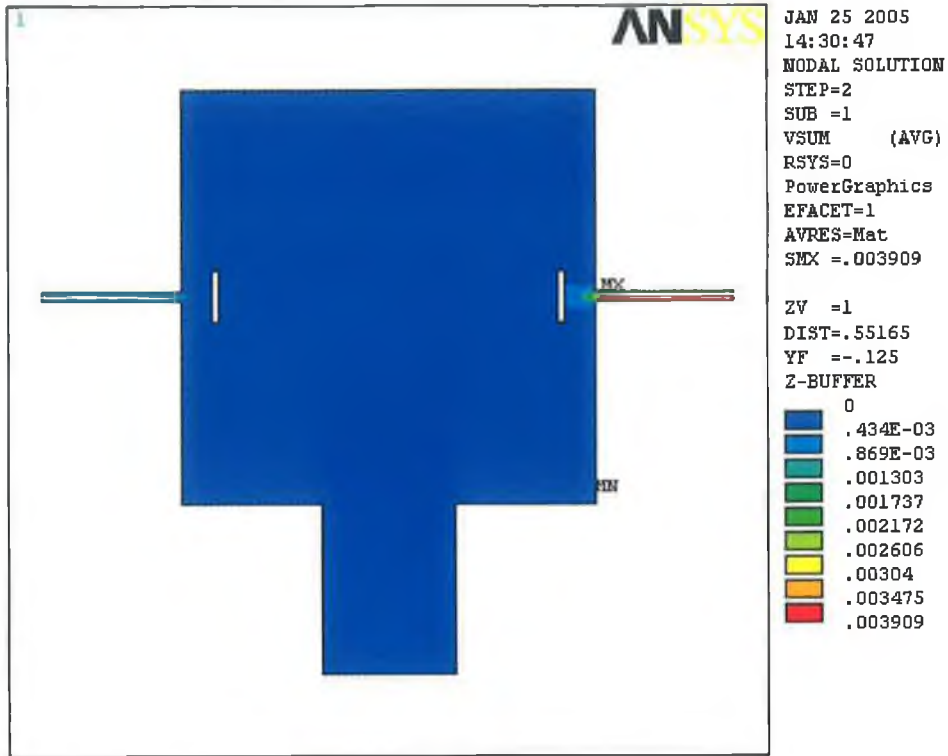
Pressure distribution plot (outlet centred)



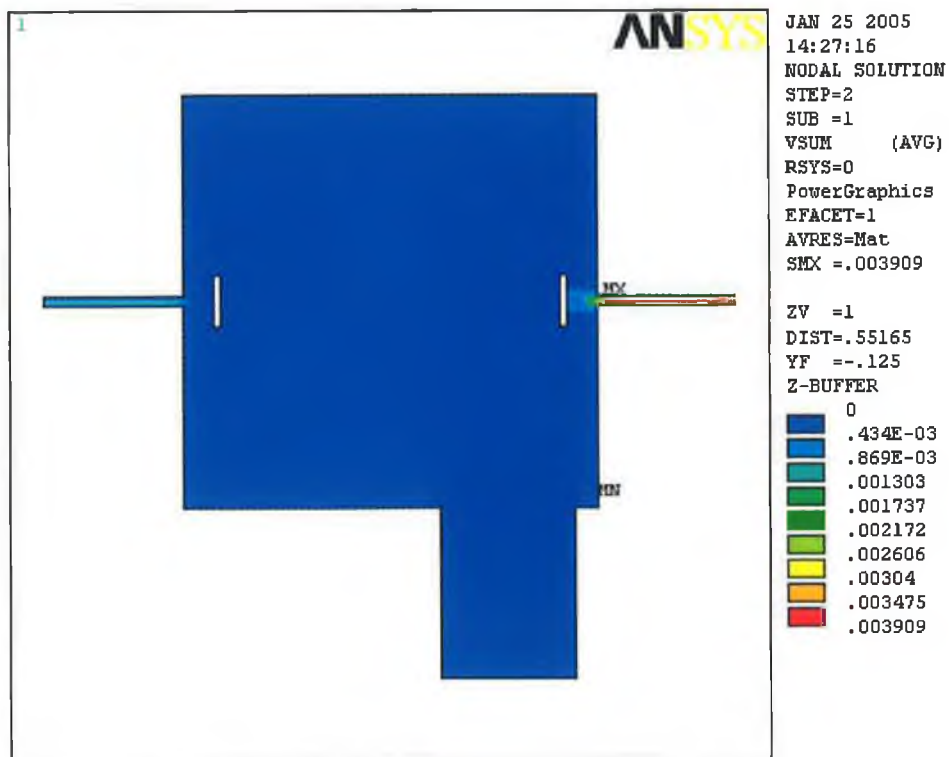
Pressure distribution plot (outlet off-centred)



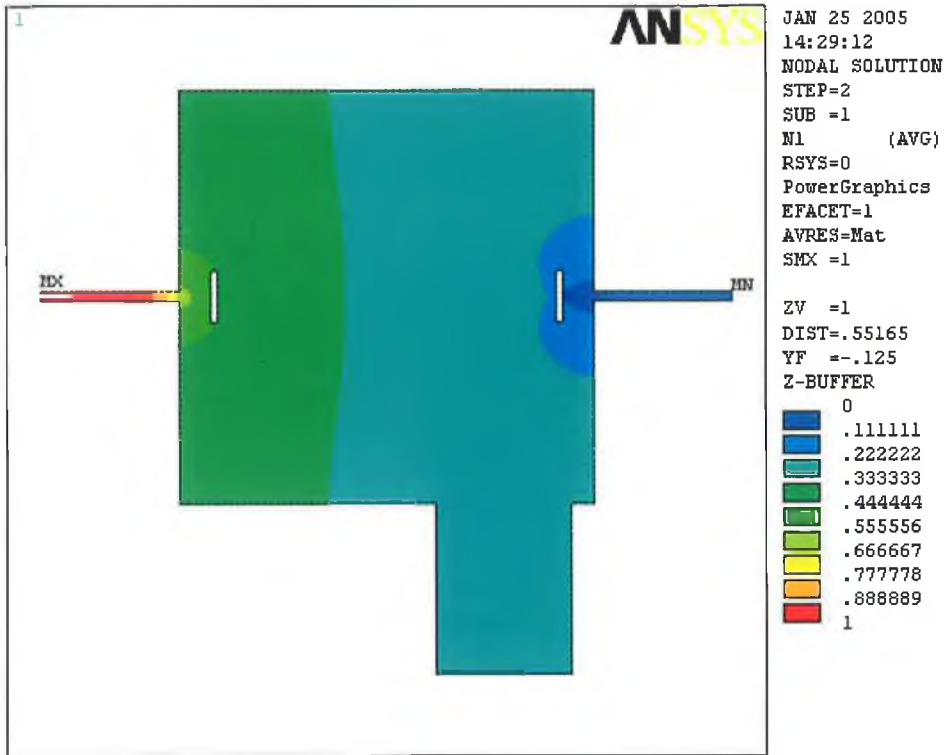
Velocity distribution plot (outlet centred)



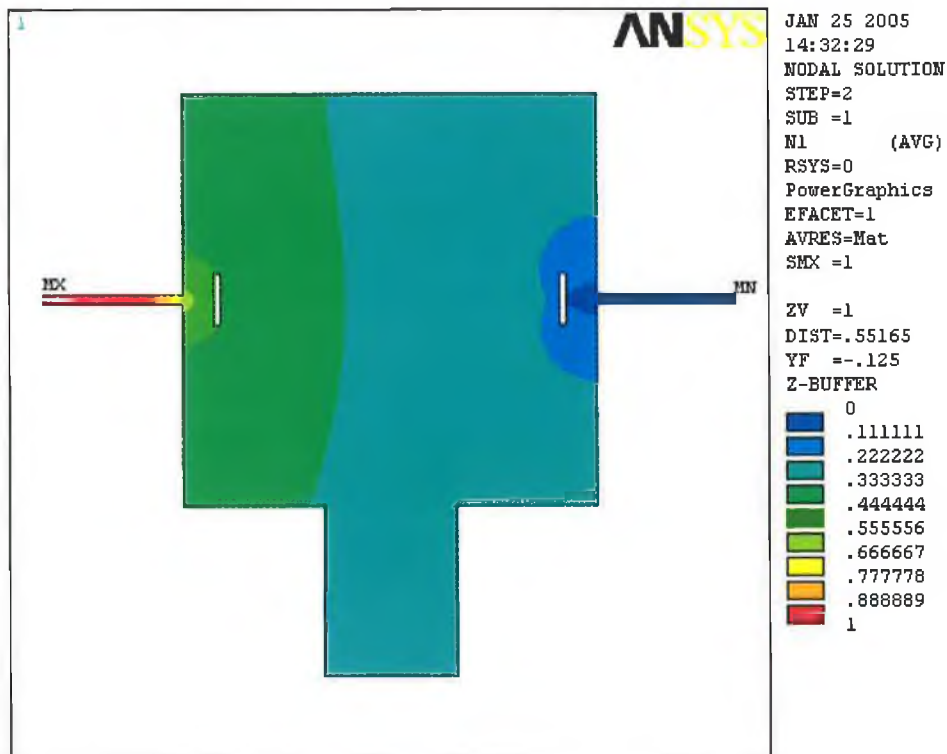
Velocity distribution plot (outlet off-centred)



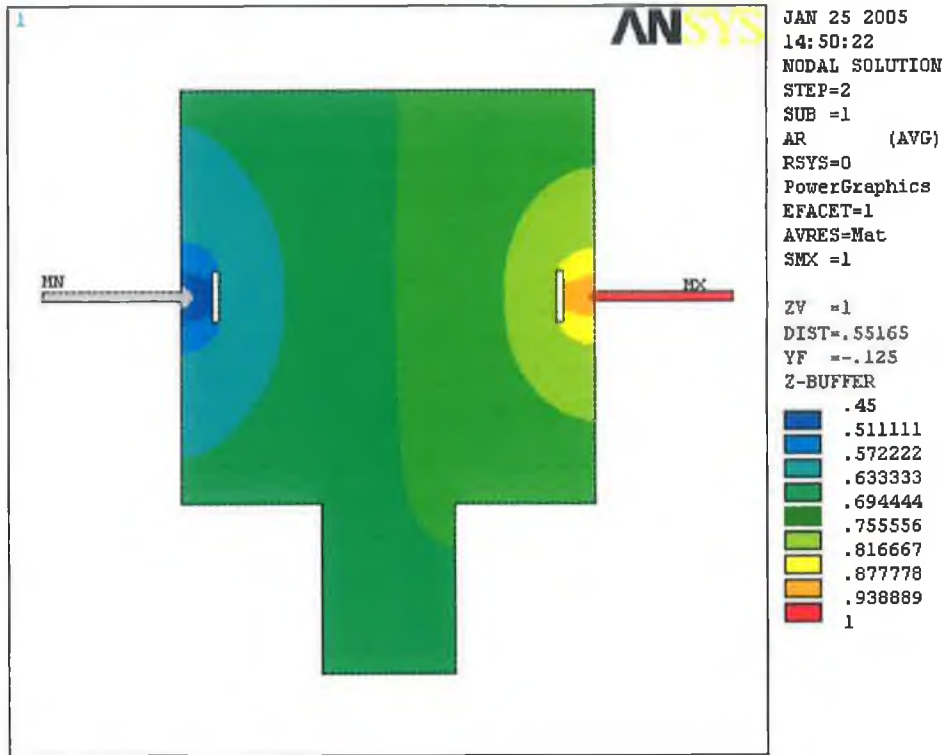
Nitrogen concentration plot (outlet centred)



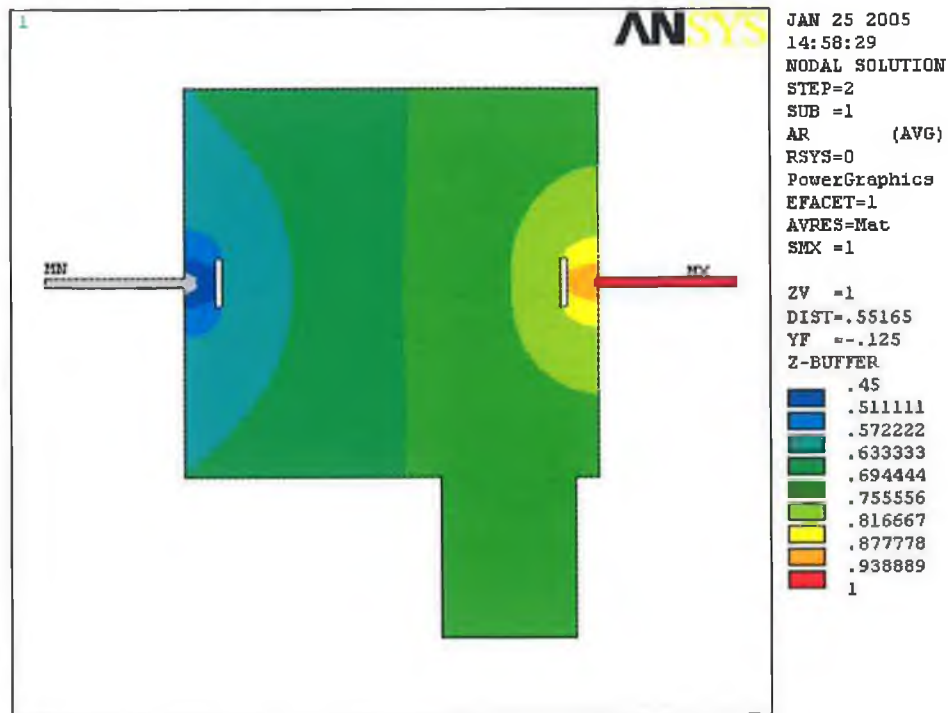
Nitrogen concentration plot (outlet centred)



Argon concentration plot (outlet centred)



Argon concentration plot (outlet off-centred)



APPENDIX D

INPUT FILE OF GAS MIXING IN SPUTTERING CHAMBER

```

/com,Author
/com,Julfikar Haider
/com,School of MME
/com,Dublin City University, Ireland
/com,Gas mixing in sputtering chamber
!
finish
/clear,start      !Clears previous database
/batch,list       !Sets the program mode to
                  !"batch."
/filename,gasmixing,1 !Changes the Jobname for the
                  !analysis.
/triad,rbot       !Triode is at right bottom
/replot          !
-----
/com ** Set-up element types, etc.
-----
/units,si        !Annotates the database with SI
                  !unit system
keyw,pr_cfd,1    !Preferences for CFD in GUI
                  !filtering
/prep7           !Enters the preprocessor
et,1,fluid142    !Defines a local element type
/title,Gas mixing in sputtering chamber
-----
/com ** Parameter of the chamber geometry
-----
chr = .3015      !Chamber radius (m)
chr1 = .29       !Radius of inlet position
chh = .610       !Chamber height (m)
inr = .007       !Inlet radius (m)
inh = .2         !Inlet height
outr = .09825   !Outlet radius (m)
outh = .2        !Outlet height
sx = .2015      !x position of substrate
-----
/com ** Quarter chamber modelling
-----
cyl4,0,0,chr,0,chr,90 !Chamber quarter circle (QC)
!area
cyl4,0,0,outr,0,outr,90 !Outlet QC area
voffst,1,chr,0,      !Extrude chamber QC area
voffst,2,-outh,0,    !Extrude outlet QC area
wpave,0,chr1,chr/2   !Moving working plane (wp)
!origin
wprot,-,90,          !Rotates working plane about x
!axis
pcirc,inr, ,90,-90,  !Top inlet half circle
voffst,1,inh,0,      !Extrude top inlet half circle
csys,0               !Cartesian co-ordinate system
wpave,0,0,0          !Moving wp to global origin
wpstyle,,,,,,,,,1
wpave,chr1,0,chr/2  !Moving working plane (wp)
!origin
wpro,,,90           !Rotates working plane about y
!axis
pcirc,inr,,90,270,   !Right inlet half circle
voffst,16,inh,0,     !Extrude right inlet half circle
vadd,all             !Add all volumes
wprot,0,90,0
wprot,90,0,0
wpave,0,0,0
wpave,sx,0,chr/2
blc4,0,0,.01,.0125  !Substrate cross-section area
voffst,1,.0375,,     !Extrude substrate cross-section
voffst,1,-.0375,,
vadd,1,2             !Add two substrate volumes
vsbv,5,3,,          !Subtract substrate from chamber
gplot
wpave,0,0,0
-----
/com, Meshing
-----
/com ** Parameters defined for meshing
-----
dpcurv = 18        !No of divisions (NOD)in plates
spcurv = 1         !Spacing ratio (SR) in plates
dwcuvr = 14        !NOD in chamber wall
swcurv = 1/2       !SR in chamber wall
dcisym = 26        !NOD in chamber inner symmetry !line
scisym = 1         !SR in chamber inner symmetry line
dupsym = 12        !NOD in upper plate symmetry line
supsym = 1         !SR in upper plate symmetry line
dbpsym = 10        !NOD in bottom plate symmetry !line
sbpsym = 1         !SR in bottom plate symmetry line
dinli = 8          !NOD in inlet area
sinli = 1          !SR in inlet area
dinwal = 4         !NOD in inlet wall
sinwal = 1         !SR in inlet wall
disym = 15         !NOD in inlet symmetry line
sisym = 1          !SR in inlet symmetry line
doutwal = 12       !NOD in outlet wall
soutwal = 1        !SR in outlet wall
dout = 10          !NOD in outlet area
sout = 1           !SR in outlet area
dosym = 15         !NOD in wall symmetry line
sosym = 1          !SR in wall symmetry line
-----
/com ** Discretization of lines
-----
lsel,s,,,60,63,1    !Chamber wall
lesize,all,,,dwcuvr,swcurv
lsel,s,,,1,7,6,     !Chamber plate
lesize,all,,,dpcurv,spcurv
lsel,s,,,12         !Chamber inner symmetry
lesize,all,,,dcisym,scisym
lsel,s,,,8,9        !Upper plate symmetric lines
lesize,all,,,dupsym,supsym
lsel,s,,,40,41      !Bottom plate symmetric lines
lesize,all,,,dbpsym,sbpsym
lsel,s,,,14,15,     !Outlet inner and outer area
lsel,a,,,42,44,2
lesize,all,,,dout,sout
lsel,s,,,4,13,9     !Outlet wall
lesize,all,,,doutwal,soutwal
lsel,s,,,16,17      !Outlet symmetric lines
lsel,a,,,43
lesize,all,,,dosym,sosym
lsel,s,,,22,31,9    !Inlet area
lsel,a,,,52,59,7
lesize,all,,,dinli,sinli
lsel,s,,,47,49,2    !Inlet wall
lsel,a,,,23,24
lsel,a,,,39,56,17
lsel,a,,,32,33
lesize,all,,,dinwal,sinwal
lsel,s,,,37,38     !Inlet symmetry wall
lsel,a,,,53,58,5
lsel,a,,,50,51
lesize,all,,,disym,sisym
allsel             !Select everything
!
mshape,1,3d        !3-d mesh with tetrahedral-shaped elements
mshkey,0           !Free meshing
vmesh,all          !Mesh all volumes
-----
/com ** Applying loads and bc's
-----
/solu              !Enter solution processor
-----
/com ** Parameters for velocities and pressure
-----

```

```

VTOP = .866e-03      !Velocity at top inlet
VRIG = 3.79e-03     !Velocity at right inlet
OUTPRES = 0         !Pressure at outlet
RPRES = .4          !Working pressure
TEMP = 300          !Gas temperature
!-----
/com ** Symmetry boundary conditions
!-----
asel,s,,28,29      !Selecting symmetric areas
asel,a,,35,
asel,a,,23
asel,a,,25,26
nsla,s,1
d,all,vx,0        !Zero velocity in x direction
asel,s,,1
asel,a,,33
asel,a,,21,24,3
asel,a,,30,31,
nsla,s,1
d,all,vy,0        !Zero velocity in y direction
!-----
/com, Wall boundary conditions
!-----
asel,s,,3         !Selecting wall areas
asel,a,,34
asel,a,,8,
asel,a,,27,32,5
asel,a,,22
nsla,s,1         !Selecting nodes of selected areas
d,all,vx,0        !Zero velocity in the x direction
d,all,vy,0        !Zero velocity in the y direction
d,all,vz,0        !Zero velocity in the z direction
!-----
/com, Inlet boundary conditions
!-----
asel,s,,12        !Selecting top inlet area
nsla,s,0
d,all,vx,0        !Zero velocity in x direction
d,all,vy,-VTOP   !Specified velocity in y direction
d,all,vz,0        !Zero velocity in z direction
asel,s,,17        !Selecting right inlet area
nsla,s,0
d,all,vx,-VRIG   !Specified velocity in x direction
d,all,vy,0        !Zero velocity in y direction
d,all,vz,0        !Zero velocity in z direction
!-----
/com, Outlet boundary conditions
!-----
asel,s,,7         !Selecting outlet area
nsla,s,1
d,all,pres,OUTPRES !Zero pressure at outlet
allsel
!-----
/com ** Reference conditions
!-----
flda,pres,refe,RPRES !Reference pressure
flda,bulk,beta,1e+015,!Bulk modulus parameters
flda,gamm,comp,1.4, !Ratio of Cp and Cv
flda,temp,nomi,300, !Nominal temperature
flda,temp,tot,300, !Stagnation (total) temperature
flda,temp,bulk,300, !Reference (Bulk) temperature
toff,0           !Offset temperature
!-----
/com ** Steady-state execution control
!-----
flda,iter,exec,40 !No of global iterations
flda,iter,over,0  !Results (.rfl) overwrite
!frequency
flda,iter,appc,0  !Results (.rfl) append frequency
flda,term,vx,0.01, !vx termination criteria
flda,term,vy,0.01, !vy termination criteria
flda,term,pres,1e-08, !Pressure termination criteria
flda,term,temp,1e-08 !Temperature termination criteria
flda,outp,sumf,10 !Output summary frequency
!-----
/com ** Solution algorithm control
!-----

```

```

fldata,algr,segr,simplef !Specify original segregated algorithm
!-----
/com ** Primary fluid (air) properties
!-----
flda,prot,dens,air-si !Specify air density in si unit
flda,vary,dens,true !Allow density variation
flda,prot,visc,air-si !Specify air viscosity in si unit
flda,vary,visc,true !Allow viscosity variation
flda,prot,cond,air-si !Specify air conductivity in si unit
flda,vary,cond,true !Allow conductivity variation
flda,prot,spht,air-si !Specify air specific heat in si unit
flda,vary,spht,true !Allow specific heat variation
!-----
/com ** Flotran general solution options
!-----
flda,solu,tran,0 !No activation of transient solution algorithm
flda,solu,flow,1 !Solves the momentum and pressure
!equations
flda,solu,temp,1 !No solution of temperature equation
flda,solu,turb,0 !No activation of turbulence model
flda,solu,comp,0 !No activation of compressible algorithm
flda,solu,vof,0 !No activation of volume of fluid method
flda,solu,sfts,0 !No activation of surface tension
flda,solu,ivsh,0 !No activation of viscous heating for
!incompressible flow
flda,solu,swrl,0 !No activation of swirl option
flda,solu,ale,0 !No activation of Arbitrary Lagrangian-
!Eulerian formulation
flda,solu,rdsf,0 !No activation of the surface-to-surface
!radiation solution
!-----
/com ** Property based output option (nodal solution)
!-----
flda,outp,dens,1 !Output laminar density
flda,outp,spht,1 !Output laminar specific heat
flda,outp,visc,1 !Output laminar viscosity
flda,outp,cond,1 !Output laminar conductivity
!-----
/com ** Derived output option (elemental solution)
!-----
flda,outp,ptot,1 !Output total pressure
flda,outp,ttot,1 !Output total temperature
flda,outp,strm,1 !Output stream function
flda,outp,pcoe,1 !Output pressure co-efficient
flda,outp,mach,1 !Output Mac number
flda,outp,yplu,1 !Output y plus
flda,outp,tauw,1 !Output wall shear stress
!-----
/com ** Convergence monitor option
!-----
flda,conv,outp,land !Output convergence monitor in
!landscape mode
flda,conv,iter,5, !No of iterations for which the
!convergence monitor information is
!stored in memory before being printed
!-----
/com ** vx and vy solver specifications
!-----
flda,meth,vx,1 !TDMA for solving vx
flda,meth,vy,1 !TDMA for solving vy
flda,meth,vz,1 !TDMA for solving vz
!-----
/com ** Pressure solver specifications
!-----
flda,meth,pres,3 !Precond con grad algorithm for solving
!pressure
flda,maxi,pres,1000 !No of conjugate direction iterations
flda,srch,pres,10 !No of conjugate direction search vectors
flda,conv,pres,1e-12 !Pressure convergence criteria
flda,delt,pres,1e-10 !Minimum delta
flda,relx,pres,0.5 !Pressure relaxation factor
!-----
/com ** Quadrature orders control
!-----
flda,quad,momd,0 !Quadrature orders (QO) for momentum
!diffusion
flda,quad,moms,0 !QO for momentum source
flda,quad,prsd,1 !QO for pressure diffusion

```

```

flda,quad,prss,1      !QO for pressure source
flda,quad,thrd,0     !QO for thermal diffusion
flda,quad,thrs,0     !QO for thermal source
!-----
/com ** Advection option
!-----
flda,advn,mome,supg   !Discretize momentum eq.
                        !using SUPG approach
flda,advn,pres,msu    !Discretize pressure eq. using
                        !MSU approach
flda,advn,temp,supg   !Discretize temperature eq.
                        !using SUPG approach
solve                 !Solve with air at 300K
save
finish                !Exits from solution
                        !processor
!-----
/com ** Multiple species solution option
!-----
/prep7                !Enter into preprocessor
flda,prot,dens,cmix   !Composite mixture for density
flda,prot,visc,cmix   !Composite mixture for
                        !viscosity
keyopt,1,1,2          !Specify that there are 2 species
flda,solu,spec,t       !Turn on solution for multiple
                        !species transport
msdata,2              !Specify species 2 (Ar) as the
                        !algebraic species
flda,outp,lmd1,1      !Output laminar mass diffusion
                        !(OLMD) for N2
flda,outp,lmd2,1      !OLMD diffusion for Ar
allsel
!-----
/com ** Species property input
!-----
!n1=nitrogen (species 1)
snum=1
msspec,snum,n1,28.018 !Specifies the name
                        !and molecular weight
                        !of N2.
msprop,snum,dens,constant,1.1381 !Define
                        !const density of N2
msnomf,snum,0.2        !Nominal mass
                        !fraction for N2
msprop,snum,visc,constant,1.663e-5 !Define
                        !const viscosity of N2
msprop,snum,mdif,constant,1.601e-5 !Define
                        !const mass diff coef
                        !of N2
msprop,snum,cond,constant,.0242 !Define
                        !const conductivity of
                        !N2
mscap,snum,1          !Activates and controls mass
                        !fraction capping for N2
!
!ar=argon (species 2)
!
snum=2
msspec,snum,ar,39.948 !Specifies the name
                        !and molecular weight
                        !of Ar.
msprop,snum,dens,constant,1.6228 !Define
                        !const density of Ar
msnomf,snum,.8         !Nominal mass
                        !fraction for Ar
msprop,snum,visc,constant,2.125e-5 !Define
                        !const viscosity of Ar
msprop,snum,mdif,constant,2.42e-5 !Define
                        !const mass diff coef.
                        !of Ar
msprop,snum,cond,constant,.0158 !Define
                        !const conductivity of
                        !Ar
mscap,snum,1          !Activates and controls mass
                        !fraction capping for Ar

```

```

!-----
/com ** Solution option for multiple species transport
!-----
msrelx,1,1,1.0        !Relaxation factor for species 1
msmeth,1,3            !PCR method for solution of species 1
                        !transport equations
mssolu,1,,2,1.0e-8    !Specifies solution options for species 1
!-----
/com ** Species boundary conditions
!-----
asel,s,,12            !Top inlet (n1)
nsla,,1
d,all,n1,1.0          !100% of species 1
d,all,ar,0.0          !0% of species 2
!
asel,s,,17            !Right inlet (ar)
nsla,,1
d,all,n1,0.0          !0% of species 1
d,all,ar,1.0          !100% of species 2
allsel
!-----
/com ** Execution and output control
!-----
flda,iter,exec,40     !Ask for 100 global iterations
flda,conv,outp,land   !Adjust convergence monitor output style
finish                !Exiting from preprocessor
!
/solu
solve
save
finish                !Exiting from solution processor
!-----
/com ** Post-processing of results
!-----
/post1                !Entering into post-processor
set,last              !Defining last data set to be read !from results
!file
/dscale,1,auto        !Automatic scaling
plnsol,pres           !Displaying pressure distribution
plnsol,v,x            !Displaying velocity in x direction
plnsol,v,y            !Displaying velocity in y direction
plnsol,v,z            !Displaying velocity in z direction
plnsol,v,sum          !Displaying sum of velocity
plnsol,n1             !Displaying nitrogen concentration
plnsol,ar             !Displaying argon concentration
finish                !Exiting from post processor

```

APPENDIX E

INPUT FILE OF THERMAL STRESS IN THIN COATING

```

/com,Author
/com,Julfikar Haider
/com,School of MME
/com,Dublin City University, Ireland
/com,Thermal stress modelling in thin coating
!
finish
/clear,start      !Clearing previous database
/batch,list       !Setting "batch" mode
/filename,thstress,1 !Setting the jobname
/triad,off        !Triode not shown
-----
/com ** Set-up element types, etc.
-----
/units,si        !Annotating the database with SI
                  !unit system
keyw,pr_struc,1 !Setting preferences for Structural
/prep7           !Entering into the pre-processor
et,1,plane42    !Defining a local element type
keyopt,1,3,1    !Setting axisymmetric option
keyopt,1,5,0
keyopt,1,6,0
!
/pnum,mat,1     !Controlling numbering/colouring
                  !on plots.
/num,1          !Specifying the number is used for
                  !displays
/title,Thermal stress modelling in thin coating
-----
/com ** Setting temperatures
-----
tdep = 500      !Deposition temperature
troom = 25      !Room temperature
-----
/com ** Specifying coating material properties
-----
scte = 13e-6    !Thermal expansion coefficient
smod = 200e9    !Young's modulus
snu = 0.3       !Poisson's ratio
-----
/com ** Specifying substrate material properties
-----
fcte = 9.4e-6   !Thermal expansion coefficient
fmod = 600e9    !Young's modulus
fnu = 0.25      !Poisson's ratio
-----
/com ** Parameters for substrate geometry
-----
subx = 0.01     !Substrate length
suby = 0.00005 !Substrate thickness
-----
/com ** Parameters for coating geometry
-----
filmx = subx    !Coating length
filmy = 0.00005 !Coating thickness
-----
/com ** Defining substrate property
-----
mp,ref1,1,tdep  !Reference temperature
mp,alpx,1,scte !Thermal expansion coefficient
mp,ex,1,smod    !Young's modulus
mp,nuxy,1,snu   !Poisson's ratio
-----
/com ** Defining coating property
-----
mp,ref2,2,tdep  !Reference temperature
mp,alpx,2,fcte !Thermal expansion coefficient
mp,ex,2,fmod    !Young's modulus
mp,nuxy,2,fnu   !Poisson's ratio
-----
-----
/com ** Model creation for coating and substrate
-----
rectng,0,subx,0,suby !Coating geometry
rectng,0,subx,suby,suby+filmy !Substrate geometry
aglue,all            !Gluing coating and substrate areas
-----
/com ** Parameters defined for meshing
-----
dcthik = 10         !No of divisions (NOD) in coating
                    !thickness
scthik = 3          !Spacing ratio (SR) in coating
                    !thickness
dclent = 450        !NOD in coating length
sclel = 20          !SR in coating length
dsthik = 50         !NOD in substrate thickness
ssthik = 10         !SR in substrate thickness
dslent = 450        !NOD in substrate length
sslent = 20         !SR in substrate length
-----
/com ** Discretization of lines and meshing
-----
mshape,0,2d        !Quadrilateral-shaped elements
mshkey,1           !Mapped meshing
!
mat,2              !Assigning coating material
lsel,s,,,9,10,     !Selecting vertical lines of coating
                    !area
lesize,all,,,dcthik,scthik,,,1 !Dividing vertical lines
                    !of coating area
lsel,s,,,3,7,4     !Selecting horizontal lines of
                    !coating area
lesize,all,,,dclent,sclel,,,1 !Dividing horizontal
                    !lines of coating area
amesh,3            !Meshing coating area
!
mat,1              !Assigning substrate material
lsel,s,,,4,        !Selecting vertical line of substrate !
                    !area
lesize,all,,,dsthik,ssthik,,,1 !Dividing vertical line of
                    !substrate area
lsel,s,,,2,        !Selecting vertical line of substrate
                    !area
lesize,all,,,dsthik,1/ssthik,,,1 !Dividing vertical line of
                    !substrate area
lsel,s,,,1,        !Selecting horizontal line !of
                    !substrate area
lesize,all,,,dslent,1/sslent,,,1 !Dividing horizontal line
                    !of substrate area
amesh,1           !Meshing substrate area
save              !Save everything
finish            !Exiting from pre-processor
-----
/com ** Applying loads and bc's
-----
/solu             !Entering into the solution processor
allsel           !Selecting everything
lsclear,all      !Clearing loads from the database
antype,0         !Setting static analysis
nlgeom,0         !Excluding large-deflection effects
-----
/com ** Structural boundary condition
-----
lsel,s,loc,x,0   !Selecting the axisymmetric lines
dl,all,,symm     !Applying symmetric bc's on lines
origin = kp(0,0,0)
dk,origin,0,,0,all !Defining DOF constraints at
                    !bottom left corner
-----

```

```

/com ** Thermal boundary condition
-----
bf,all,temp,troom      !Setting node temperatures to room
                        !temperature
allsel                 !Selecting everything
-----
/com ** Solving the problem
-----
solve                  !Starting the solution
save
finish                 !Exiting from solution processor
-----
/com ** Post-processing of results
-----
/post1                 !Entering into post-processor
set,last               !Defining last data set to be read
                        !from results file
/dscale,1,auto         !Automatic scaling
plnsol,s,eqv,0,1      !Displaying von Mises stress
/wait,10               !Waiting for 10 sec
asel,s,,3             !Selecting coating area
allsel,below,area     !Selecting everything below coating
                        !area
plnsol,s,eqv,0,1      !Displaying von Mises stress in
                        !coating only
allsel                 !Selecting everything
/wait,10               !Waiting for 10 sec
asel,s,,1             !Selecting substrate area
allsel,below,area     !Selecting everything below
                        !substrate area
plnsol,s,eqv,0,1      !Displaying von Mises stress in
                        !substrate only
allsel
ancnt,10,0.3          !Animating contoured deformed
                        !shape
-----
! Path operation
-----
path,edge,2,30,20,    !Defining a path name for path.
ppath,1,,01,0,0       !Location of 1st path point
ppath,2,,01,000055,  !Location of 2nd path point
path,status            !Displaying the status for path
                        !settings
/pbc,path,1           !Showing path geometry on displays
pdef,sx,s,x,avg       !Interpolating stress in X onto a path
/pbc,path,,0
pdef,sy,s,y,avg
/pbc,path,,0
pdef,sz,s,z,avg
/pbc,path,,0
pdef,sxy,s,xy,avg
/pbc,path,,0
pdef,seqv,s,eqv,avg
!
plpath,sx              !Displaying stress in X on a graph
plpath,sy
plpath,sz
plpath,sxy
plpath,seqv
!
prpath,sx              !Printing stress in X along path
prpath,sy
prpath,sz
prpath,sxy
prpath,seqv
!
allsel                 !Selecting everything
!
-----
/com ** Equation of thermal stress
-----
smode = smod/(1-snu)  !Effective Young's
                        !modulus of substrate
fmode = fmod/(1-fnu)  !Effective Young's
                        !modulus of coating

```

```

!
deps = (fcte-scte)*(tdep-troom) !Differential strain (delta
                                !epsilon)
!
! Theoretical film stress
!
fstrs =
(deps*smode*fmode*suby)/((smode*suby)+(4*fily*fmo
de))
-----
/com ** Calculate area-weighted average stress in coating
-----
esel,s,mat,,2         !Select coating elements
nsls,s,1              !Selecting coating nodes
etable,erase          !Erasing any previous element table
etable,vt,volu        !Define table for element volume
etable,sx,s,x         !Define table for x component stress
etable,sy,s,y         !Define table for y component stress
etable,sz,s,z         !Define table for z component stress
etable,sxy,s,xy       !Define table for xy component
                        !stress
smult,vsx,vt,sx       !Forming table by multiplying
                        !element volume and x component
                        !stress
smult,vsy,vt,sy
smult,vsz,vt,sz
smult,vsxy,vt,sxy
ssum                  !Calculating and printing sum of
                        !element table items
*get,svsx,ssum,,item,vsx !Retrieving the sum of x
                        !component stress
*get,svsy,ssum,,item,vsy !Retrieving the sum of y
                        !component stress
*get,svsz,ssum,,item,vsz !Retrieving the sum of z
                        !component stress
*get,svsxy,ssum,,item,vsxy !Retrieving the sum of
                        !xy component stress
*get,svt,ssum,,item,vt !Retrieving the sum of
                        !element volume
sxavg = svsx/svt      !Calculating the average
                        !x component stress
syavg = svsy/svt      !Calculating the average
                        !y component stress
szavg = svsz/svt      !Calculating the average
                        !z component stress
sxyavg = svsxy/svt    !Calculating the average
                        !xy component stress
-----
/com ** Comparing theoretical and FEA results
-----
allsel                 !Selecting everything
/annot,delete
/annot,on
/tspec,15,1.000,1,0,0
/tlab,0.40,-0.600,fea film stress (x) = %sxavg%
/tlab,0.40,-0.700,fea film stress (y) = %syavg%
/tlab,0.40,-0.800,fea film stress (z) = %szavg%
/tlab,0.40,-0.900,fea film stress (xy) = %sxyavg%
/tlab,0.40,-0.100,theory film stress = %fstrs%
!
save
finish                 !Exiting from Post-processor

```